universität
wien

DISSERTATION / DOCTORAL THESIS

Titel der Dissertation /Title of the Doctoral Thesis

„Heavy Quark Mass Determinations with Sum Rules and Jets“

verfasst von / submitted by

Bahman Dehnadi, MSc

angestrebter akademischer Grad / in partial fulfilment of the requirements for the degree of

Doktor der Naturwissenschaften (Dr. rer. nat)

Wien, 2016 / Vienna 2016

Studienkennzahl lt. Studienblatt / degree programme code as it appears on the student record sheet:	A 796 605 411
Dissertationsgebiet lt. Studienblatt / field of study as it appears on the student record sheet:	Doktoratsstudium Physik UG2002
Betreut von / Supervisor:	Univ.-Prof. Dr. André H. Hoang

Abstract

In this thesis I discuss the charm, bottom and top quark mass determinations. In the first part, I present new determinations of the $\overline{\mathrm{MS}}$ charm and bottom quark masses using relativistic QCD sum rules at $\mathcal{O}(\alpha_s^3)$. For the charm quark mass extraction we use the moments of the vector and the pseudoscalar current correlators where we take into account the available experimental measurements from $e^+ e^-$ collisions and lattice simulation results, respectively. For the bottom quark mass determination we use the vector current correlator for which we compute the corresponding experimental moments including a modeling uncertainty associated to the continuum region where no data is available. Our analysis of the theoretical uncertainties is based on independent variations of the renormalization scales for the mass and the strong coupling. In addition we apply a convergence test to discard the perturbative series for which the convergence behavior is significantly worse than the average convergence rate. As the final result we obtain $\overline{m}_c(\overline{m}_c) = 1.288 \pm 0.020\,\mathrm{GeV}$ and $\overline{m}_b(\overline{m}_b) = 4.176 \pm 0.023\,\mathrm{GeV}$ from the vector correlator analyses.

In the second part, I present a complete theoretical description of the entire thrust distribution for boosted heavy quark initiated jets in $e^+ e^-$ colliders. The results are given in terms of various factorization theorems in the dijet limit within a variable flavor number scheme (VFNS) for final state jets. In this limit we use Soft-Collinear Effective Theory (SCET), including mass modes, in order to factorize the cross section and to sum large logarithms at N^{2}LL order. When the invariant mass of the massive jet is close to the heavy quark mass we match onto a boosted Heavy Quark Effective Theory (bHQET) to sum up a new class of large logarithms along with the treatment of finite width effects. In this regime one cannot use the $\overline{\mathrm{MS}}$ mass for the heavy quark, as it would break the power counting of bHQET. We solve this issue by switching to a more suitable short-distance scheme for the mass, which we call the MSR scheme. Finally we also apply a VFNS to the gap subtractions, used to define a scheme for the leading power correction in which the leading renormalon of the soft function is removed. At the end, we show the perturbative convergence of the resulting thrust distributions for stable and unstable top and bottom quark production and discuss the sensitivity of the peak region of the distributions to the heavy quark masses. Our hadron-level results can be used to find a numerical relation between the top (bottom) mass parameters in parton-shower Monte Carlo generators and the well defined short-distance schemes for quark masses in QCD.

Zusammenfassung

Diese Dissertation befasst sich mit Massenbestimmungen des Charm, Bottom und Top Quarks. Im ersten Teil werden neue Untersuchungen beschrieben, welche relativistische QCD *sum rules* zur Ordnung $\mathcal{O}(\alpha_s^3)$ verwenden um die $\overline{\mathrm{MS}}$ Charm und Bottom Quark Masse zu bestimmen. Für die Bestimmung der Charm Quark Masse werden Momente des Vektor- und Pseudoskalar *current correlators* verwendet, wobei für ersteren experimentelle Messdaten von e^+e^- Kollisionen und für letzteren Ergebnisse von *lattice* Simulationen verwendet werden. Für die Bestimmung der Bottom Quark Masse verwenden wir den Vektor *current correlator* für welchen wir die experimentell messbaren Momente berechnen. Diese beinhalten eine zusätzliche Modellierungsunsicherheit um die *continuum region*, für welche keine experimentellen Daten existieren, zu berücksichtigen. Unsere nachfolgenden Untersuchungen der theoretischen Unsicherheiten basieren auf unabhängigen Variationen der Renormierungsskala für die Masse und für die Kopplungskonstante der starken Wechselwirkung. Ein zusätzlicher Konvergenztest wird abschließend dazu verwendet Störungsreihen mit einem deutlich unterdurchschnittlichen Konvegenzverhalten zu verwerfen. Von der jeweiligen Vektor *correlator* Untersuchung erhalten wir als Endergebnis $\overline{m}_c(\overline{m}_c) = 1.288 \pm 0.020$ GeV und $\overline{m}_b(\overline{m}_b) = 4.176 \pm 0.023$ GeV.

Im zweiten Teil dieser Arbeit wird eine vollständige theoretische Beschreibung der gesamten Thrust Verteilung für e^+e^- Kollisionen präsentiert. Im Besonderen werden dabei Jets untersucht, welche von geboosteten schweren Quarks stammen. Die erhaltenen Ergebnisse werden danach in einer Reihe von Faktorisierungstheoremen in einem *variable flavor number scheme* (VFNS) präsentiert, welche im 2-jet Limes gültig sind. Um in diesem Limes die erwähnte Faktorisierung zu erreichen und damit sogenannte große Logarithmen bis zur Ordnung NNLL zu resummieren, verwenden wir *Soft-Collinear Effective Theory* (SCET) mit Massen Moden. Sobald die typische invariante Masse der involvierten massiven Jets nahe an der Masse des schweren Quarks liegt, *matchen* wir auf eine geboostete Version von *Heavy Quark Effective Theory* (bHQET) um eine neue Klasse von großen Logarithmen zu resummieren und zusätzlich Effekte der endlichen Zerfallsbreite miteinzubeziehen. Da die $\overline{\mathrm{MS}}$ Masse in diesem Regime das *power counting* von bHQET verletzen würde kann sie hier nicht verwendet werden. Deshalb wird hier eine geeignetere *short distance* Masse, die sogenannte MSR Masse, verwendet. Zusätzlich wird das zuvor verwendete VFNS auch auf die *gap* Subtraktionen angewandt. Diese definieren ein Schema für die *power corrections* in welchem das führende Renormalon der *soft function* nicht vorhanden ist. Abschließend wird die perturbative Konvergenz der resultierenden Thrust Verteilung sowie die Massensensitivität der *peak region* der Verteilung untersucht. Die dadurch erhaltenen Hadron-level Resultate können weiterführend dazu benutzt werden einen numerischen Zusammenhang zwischen dem Top (Bottom) Massenparameter in *parton-shower Monte Carlo generators* und einer wohldefinierten *short distance* Masse in QCD herzustellen.

Acknowledgements

Here, I wish to express my gratitude to the people who helped and supported me during my PhD studies. Foremost, I am profoundly indebted to my supervisor André Hoang for his cooperation and great efforts throughout the projects. I am specially grateful for his patience, helpful discussions and instructive comments on different aspects of my career during the time of my PhD, that are also useful in other areas of my personal life. Furthermore, I really appreciate his understanding and concern considering the future of my scientific career, supporting me to present our work in various conferences and participating in different workshops which brought me valuable experiences as well as nice memories.

Secondly, my sincere thanks goes to Vicent Mateu without whom it would have been impossible to accomplish the works that are presented in this thesis. During our collaboration he has been always kindly taking the time to reply to my questions and discuss about physics, even while we have been communicating from long distances. Moreover, I acknowledge his deep insights in mathematics and his exceptional skills in computational science which helped throughout various stages of our research. In brief, he has been indeed a personal advisor as well as a very dear friend for me who persuaded and guided me through my PhD studies.

Moreover, I would like to thank all the members of the particle physics group at the University of Vienna and the Vienna Doktoratskollegs "Particles and Interactions" (DK-PI) for providing such a great working atmosphere to carry out my research. In particular, I am very grateful to all my colleagues and friends Piotr Pietrulewicz, Moritz Preisser, Daniel Samitz, Ilaria Jemos, Mathias Butenschoen, Elke Aeikens, Maximilian Löschner, Christopher Lepenik, Kyrylo Simonow, Daniel Lechner and Angelika Widl for all the fruitful discussions on physics, besides the social interaction along the "legendary" breaks for lunch and coffee with the joyful conversations.

I acknowledge that the writing of this thesis would not have been possible without the encouragement and help of André Hoang. I wish to thank Christopher Lepenik and Vicent Mateu for reading the preliminary draft of this manuscript and giving useful comments. The work presented in this thesis has been partially supported by the FWF DK-PI (DK W 1252-N27).

Last but not least, I dedicate my hearthful thanks to my family and my girlfriend Lena for their love, understanding and unconditional supports.

Contents

Chapter 1

Introduction

The Standard Model (SM) of particle physics represents an outstanding synthesis of several decades of experiments in high energy physics. Since it is an effective field theory of a more fundamental high energy theory, it leaves us with many free parameters to be measured. An essential ingredient to identify possible new physics at higher energies is accurate calculations and precise determinations of the SM parameters with reliable uncertainties. One important set of parameters is quark masses. It is customary to call quarks "heavy" if $m_q \gg \Lambda_{\rm QCD}$ (charm, bottom and top are heavy quarks) and light otherwise. Due to confinement, quark masses are not physical observables. Rather, they are scheme-dependent parameters of the QCD Lagrangian which have to be determined from quantities that strongly depend on them. This remark will be further elaborated in Sec. 1.1 when discussing the concept of the mass of fundamental particles.

Accurate determinations of the heavy quark masses are important from various perspectives. Precise and reliable determinations of the charm and bottom quark masses are an important input for a number of theoretical predictions, such as Higgs branching ratios to charm and bottom quarks or for the corresponding Yukawa couplings [1,2]. They also affect the theoretical predictions of radiative and inclusive B decays, as well as rare kaon decays. For example, the inclusive semileptonic decay rate of B mesons depends on the fifth power of the bottom quark mass. These weak decays provide crucial methods to determine elements of the CKM matrix, which in turn are important for testing the validity of the Standard Model, as well as for indirect searches of new physics. Likewise, the top quark plays an important role in the studies of the electroweak sector of the Standard Model. The top quark mass is an important parameter in the analysis of precision electroweak observables and resulting constraints on the extension of the Standard Model. Also it is an essential ingredient for verifying the stability of the electroweak vacuum. Hence, in this context, having a reliable estimate of uncertainties for the heavy quark masses is as important as knowing their precise values [3].

In the past decades several methods have been used to determine the charm and bottom quark masses. Amongst them, QCD sum rule is one of the most precise tools. In this method, the weighted averages of the normalized cross section $R_{e^+e^-\to\, q\bar{q}+X}$ with $q = c, b$, which are measured in experiments, are related to moments of the quark vector current correlator Π_V [4,5], that can be calculated to high accuracies with perturbative QCD. This results in perturbative equations which can be used to extract different theoretical parameters, such as the mass of heavy quarks or the strong coupling constant. Alternatively one can also consider moments of the pseudoscalar current correlator to extract the heavy quark masses. Experimental information on the pseudoscalar correlator Π_P is not available in a form useful for quark mass determinations, but for the charm quark very precise lattice calculations have become available recently [6], which can be used to obtain very precise determinations.

As a matter of fact, the most accurate determinations of charm and bottom quark masses have been provided by a number of recent sum rule analyses [6–15] based on $\mathcal{O}(\alpha_s^3)$ perturbation theory [7,16–23]. As it will be discussed, in order to obtain mass determination with accuracies better than $\mathcal{O}(\Lambda_{\rm QCD})$ one has to avoid the renormalon ambiguity of the perturbative series in the pole mass scheme by employing a short-distance mass scheme such as $\overline{\rm MS}$ [24], which renders the quark mass $\overline{m}_q(\mu_m)$

dependent on its renormalization scale μ_m, similar to the strong coupling $\alpha_s(\mu_\alpha)$, which depends on μ_α. Interestingly in some previous analyses a specific constraint was employed, namely $\mu_m = \mu_\alpha$. We will discuss that this specific choice for the renormalization scales can lead to very small perturbative uncertainties, which are however strongly depending on the specific way to arrange the α_s expansions in the heavy quark mass extractions. Our findings shows that scale variation with correlated scales μ_α and μ_m can lead to an underestimate of the perturbative uncertainty.

Based on this realization, in the first part of this thesis we propose a more reliable method to estimate the perturbative uncertainties for heavy quark mass determinations from QCD sum rules. Using this method we provide new determinations for the charm and bottom quark masses.

Measurements of the top quark mass constitute one of the challenges of recent theoretical and experimental particle physics. Several techniques have been used to measure the top mass: Direct measurements, which are based on the original "template method" [25–27] to fit the Monte Carlo (MC) output and data for the kinematic reconstruction of the top decay products, and indirect measurements, which are using more inclusive observables such as the total hadronic cross section, top-antitop plus jet final states, etc [28–30] . The most accurate determinations are provided by direct reconstruction at Tevatron and LHC independently with uncertainties below 1 GeV whereas the indirect measurements are less precise (less sensitive to top quark mass), yielding uncertainties of the order of 2 GeV . The recent determination of the top quark mass from combination of direct measurements by CDF and D0 experiments at Tevatron and ATLAS and CMS experiments at the LHC yields $m_t = 173.34 \pm 0.27 \pm 0.71\,\mathrm{GeV}$ [31] . Even further improvement with uncertainties below 0.5 GeV might be possible with the upcoming data from the new run of LHC at 14 TeV with high luminosity. As the precision on the direct determination is increasing due to smaller uncertainties, it is relevant to address an important issue which is usually ignored, namely the conceptual meaning of the top quark mass parameter which is determined in direct measurements. Strictly speaking, the measured mass in the direct approach is the mass parameter used in the Monte Carlo generators m_t^{MC}. So far no unambiguous relation for the extracted MC mass parameter to the well defined mass schemes in QCD has been provided. Nevertheless, the current value has been usually interpreted and identified as the pole mass which is conceptually illegitimate [32] [see Sec. 3.9] . In fact it is argued by Ref. [33, 34] that any feasible relation between the appropriate short distance masses and the Monte Carlo mass m_t^{MC} contains a conceptual ambiguity of the order of 1 GeV which is comparable to the current accuracies and has to be taken into account when using the direct top mass measurement values as input for theoretical predictions. Therefore it is quite essential for the current and future accuracy to systematically relate the MC mass parameters to short distance mass definitions in QCD.

As explained, the essential tools in the template method to determine the top mass are Monte Carlo event generators. Monte Carlo generators are providing a good description to many collider observables. They are in principle based on a simple factorization. The partonic contribution is implemented at the hard scale using perturbation theory, considering hard matrix elements (at most with one loop computations) supported by the leading logarithmic parton showers. The parton shower evolution is employed down to a typical cutoff scale of $\Lambda = 1\mathrm{GeV}$ where the quark and gluon degrees of freedom are not used any more and some models are used to account for nonperturbative hadronization. The models consist of parameters which are tuned to available data (e.g. LEP data) at the hadronic level. These parameters are not purely related to hadronization properties through the tuning procedure. They unavoidably encode also information about higher order missing terms in perturbative corrections, such as virtual and real radiation corrections, which are not taken into account in leading log parton showers. Hence, regardless of the question whether Monte Carlo generators are good QCD calculators or not the final tuning procedure is resulting in a good description of hadron level data by event generators. Therefore we conclude that not only understanding the specific top mass parameter in Monte Carlo generators is impoartant but from a more fundamental point of view one has to investigate whether MC generators are more like very good models or more related to first principle QCD [34] . To this end, one can test the Monte Carlo generators using a theoretically clean observable, such as differential cross sections (like double hemisphere mass distribution, thrust distribution, etc), which are highly sensitive to the heavy quark masses.

Thus, in the second part of this thesis we develop a complete description of the e^+e^- thrust cross section at the observable inclusive hadron level for high energetic jets initiated by heavy quarks, at N^{2}LL order. This theoretical framework can be used to test MC generators (for that observable) and eventually to identify the top mass parameter measured in template methods.

The outline of this thesis is as follows: In chapter 2 , we will provide new charm and bottom quark mass determinations using the QCD sum rule method. On the theoretical side, we propose a new prescription to estimate the theoretical uncertainty in QCD sum rules. Our method is capable of assigning a rather more conservative and reliable perturbative uncertainty, which is independent of the type of α_s expansion series in which the observable is written. On the experimental side, for the first time in the charmonium analysis, we account for all the available experimental data by using a clustering method to combine different experimental measurements of the total hadronic cross section. In the bottomonium analysis we will provide a rather more systematic estimation for the experimental moment uncertainties. Furthermore, based on our new approach we will provide overwhelming evidence that the small uncertainties which are claimed by previous analyses using lattice simulation data were underestimated. Indeed, it turns out that the perturbative convergence of the pseudoscalar moments is worse than for the vector moment, in contrast to claims made by lattice groups [6, 14, 15, 35], resulting in a larger theoretical uncertainty for the resulting charm mass determination.

In chapter 3 , we provide a complete description of the thrust cross section for the jets that are initiated from the primary and secondary boosted massive quark production in e^+e^- collisions. In this context, we use an effective field theory (EFT) language to describe the jet cross section in the dijet limit. The EFT framework provides convenient factorization theorems for the most singular terms in different kinematic regimes and furthermore allows us to systematically sum the large logarithms which are appearing in the this limit. The appropriate EFTs for jet processes that are employed in this work are soft collinear effective field theory (SCET) [36–38] and boosted heavy quark effective theory (bHQET) [32, 39] . In order to incorporate secondary massive corrections, we will adopt a variable flavor number scheme (VFNS) [40–43] within our EFT framework to take into account the different role of the massive quark at various kinematic regimes. We will include the subleading partonic corrections of the jet cross section via an additive nonsingular contribution. In order to take into account the decay of an unstable heavy quark, we will adopt an effective inclusive treatment at leading order using the finite total width as an imaginary mass term within the bHQET description of the peak region. We will remove the $\mathcal{O}(\Lambda_{\rm QCD})$ renormalon ambiguity in the soft function by means of the gap formalism in a short distance scheme (namely the R-gap scheme). Moreover, we switch to proper short distance mass schemes to reduce the IR-sensitivities of the perturbative expansion due to the pole mass scheme which is also related to an $\mathcal{O}(\Lambda_{\rm QCD})$ renormalon. After constructing a set of profile functions for the different renormalization scales that are appearing in our factorization theorems, we will provide a thorough numerical analysis on the convergence behavior of the entire thrust cross section for the bottom, unstable top and stable top production. We will discuss the sensitivity of the resulting thrust cross sections to the relevant parameters of the theory, i.e. the heavy quark mass, strong coupling constant and the leading moment of the nonperturbative (soft) model function. We conclude the analyses with performing a simple toy fit of the theoretical predictions at various orders and using a random scan over different sets of profile functions to the best prediction (N^{2}LL/NLO + R-gap scheme + short-distance mass schemes) for default parameters in order to provide an estimate of the theoretical uncertainty that can be obtained for a future analysis where the MC top quark mass parameter shall be connected to the short-distance mass we employ in our theoretical QCD predictions. Finally, in chapter 4 , we summarize our results and stress again the major theoretical developments in this thesis.

The results of the first part of this thesis concerning the charm and bottom quark mass determinations from QCD sum rules at $\mathcal{O}(\alpha_s^3)$ have been published in two extensive papers [44, 45] in collaboration with André Hoang, Vicent Mateu and Seyyed Mohammad Zebarjad and they have been presented at different conferences [46–49]. The content of these papers constitutes a large part of chapter 2 . The results of the second part concerning the theoretical description of the primary and secondary massive quark production in e^+e^- thrust and the consequent phenomenological application in the calibration of the top mass in MC event generators will be presented in future publications in collaboration with André Hoang, Vicent Mateu, Moritz Preisser, Iain Stewart and Mathias Butenschoen. Nevertheless, the theoretical developments of this project at different stages have been reported on in different conferences, e.g. in the annual SCET conferences at 2014 [50] and 2015 [51] , QCD15 [52] , LHC top quark working group meetings in 2014 [53] and 2015 [54] , TOP 2014 (7th international workshop on top-quark physics) [55] , the ILC top quark meeting [56] . At the time of writing my thesis, we are carrying out the very first analysis on the top mass determination from Pythia 8.2. Due to the complexity of this analysis it could not be reported on in this thesis. The preliminary results for the top mass calibration have already been reported on in the SCET conference 2016 [57] and 51st Rencontres de Moriond [58] . The final results will be published in close future.

For the numerical analyses that we carry out here we have created two completely independent codes: one using Mathematica [59] and another using Fortran [60], which is much faster and suitable for parallelized runs on computer clusters. The two codes agree for the extracted charm and bottom quark masses at the level of 1 eV and for the normalized thrust cross section determination up to 10^{-5} .

In the rest of this introduction we provide a chronological review of the concept of the mass parameter in theoretical physics, starting from the mass definitions in classical mechanics up to quantum field theory.

1.1 Mass

Mass is one of the most fundamental concepts in physics and its definition has been revised due to our more complete perception of nature within the history of science. In classical mechanics the mass of an object has an absolute meaning. In this framework the mass has been introduced based on Newton's second law of motion $F = m\,a$ and gravitational law $F = G\,\frac{mM}{r^2}$, known as Inertial mass and Gravitational mass, respectively. The Inertial mass is the measure for the resistance of the object to the changes of velocity when a force is applied. The gravitational mass can be defined in an active or passive way, as a measure of the gravitational force exerted or experienced by an object. Since the late 16th century, it has been experimentally proved that the Inertial and Gravitational mass are identical. This observation is the basis of the so called equivalence principle.

One of the most important features of the classical definition of the mass is that it is a conserved quantity. Therefore the mass of an object can be realized as the sum of individual masses of the constituents. Hence, in this context the concept of mass is irreducible though we can reduce the matter into subatomic elements. This means that talking about "the origin of mass" is not quite well defined and the mass is a primary concept.

In 1905, Einstein doubted the classical notion of mass in his paper on special theory of relativity, originally entitled as "Does the Inertia of a Body Depend on its Energy Content?". In this theory a coherent concept of space-time (unification of space and time concepts) has been demonstrated based on the two postulates of special relativity: I) postulate of relativity, II) postulate of a universal speed of light. In this framework, the invariant definition of the mass (named as "rest mass") of an on-shell particle is introduced by the energy-momentum relation, $E^2 - \vec{p}^{\,2} = m^2$, where m is the rest mass, E is the energy and $\vec{p}$ is the momentum of the particle[1]. Thus the rest mass is identical to the energy content of the particle in its rest frame as expressed by the famous equation of the 20th century $E = m$. Based on this principle, today we are accelerating particles in high energy colliders and creating enormous number of heavy particles. In the relativistic picture, not the mass of an object but the total mass-energy is conserved. Thus, the concept of mass is now tied to the dynamics of the system of constituent elementary particles rather than being an absolute static feature of individual

[1]For convenience we take "Natural Units" where $\hbar = c = 1$.

elements. This reduces the question of "the origin of the mass of particles" to the question of "the dynamics of the elementary particles".

In the last century an almost complete explanation of the dynamics of elementary particles was established named as "Standard Model of particle physics". The Standard Model is a quantum field theory which is providing a coherent quantum mechanical description of the relativistic (high energy) elementary particles. In the Standard Model, particles are represented by field value operators made from creation and annihilation operators. The dynamics of particles is given by a Lagrangian which is constructed according to basic principles such as Lorentz invariance (to respect the relativistic nature of particles), local gauge invariance, symmetries, etc. In the SM Lagrangian, the masses of particles originate from the so called Higgs mechanism and spontaneous symmetry breaking.

Since in this work we are concerned about the quark masses we will devote the rest of this discussion on the specif sector of the SM Lagrangian which is describing the strong interaction of quarks, called Quantum Chromodynamic (QCD). The QCD Lagrangian is given by

$$\mathcal{L}_{\rm QCD} = \sum_q \bar{\psi}_{q,a}(i\not{D}_{ab} - m_q\delta_{ab})\psi_{q,b} - \frac{1}{4}G^A_{\mu\nu}G^{A\,\mu\nu}\,, \tag{1.1.1}$$

where the repeated indices are summed over. The $\psi_{q,a}$ are quark-field Dirac spinors for a quark of flavor q with color a and mass m_q. The gauge covariant derivative is defined by $\not{D}_{ab} = \gamma^\mu\partial_\mu\delta_{ab} + ig_s\gamma^\mu t^C_{ab}A^C_\mu$. The A^C_μ is referring to gluon fields with $N_c^2 - 1 = 8$ types of color combinations, where C is the index for the color. The term g_s is the strong coupling constant. Finally, the gluon field strength tensors is given by

$$G^B_{\mu\nu} = \partial_\mu A^B_\nu - \partial_\nu A^B_\mu - g_s f_{BCD}A^C_\mu A^D_\nu\,,$$

with $[t^B, t^C] = if_{BCD}\,t^D$, where t^B correspond to the eight generators of the SU(3) group and f_{BCD} are the structure constants of the SU(3) group. The QCD Lagrangian has a chiral symmetry in the massless limit referring to the fact that right-handed and left-handed fermion fields transform independently. This symmetry is dynamically broken. The process is usually referred as spontaneous chiral symmetry breaking. The scale of spontaneous chiral symmetry breaking is the nonperturbative hadronization scale $\Lambda_{\rm QCD}$ of the order of 1 GeV. In addition, the massive quarks break the chiral symmetry of QCD explicitly. Conventionally, the quarks with $m > \Lambda_{\rm QCD}$ that are explicitly breaking the chiral symmetry, are called heavy quarks (c, b and t quarks are heavy). In contrast the quarks with $m < \Lambda_{\rm QCD}$ where the chiral symmetry is spontaneously broken are referred to as the light quarks (u, d and s quark are light).

The QCD Lagrangian at the lowest order (tree level) is in fact not more than a classical description of the quarks dynamics. At this classical level, the mass is in principle the rest mass of the relativistic particle in the classical field theory. Using perturbative QCD to calculate the tree level amplitude for a particle to propagate with momentum p, one obtains

$$\frac{i}{\not{p} - m + i\epsilon}\,.$$

Hence, at the amplitude level, one can identify the rest mass as the pole of the propagator.

The coherent classical description dramatically fails as soon as one considers quantum corrections. The typical loop integrations which arise in quantum corrections are producing ultraviolet (UV) divergences which cause the amplitudes to be infinite. The common prescription to cope with this problem is the process of redefinition of bare fields, coupling and masses in the classical action such that physical quantities remain finite. This procedure is called renormalization.

Let us shortly recall the process of renormalization. The very first step in renormalization is the regularization of the infinities which are arising due to integration over the virtualities of the particles in the loops, ranging from 0 to ∞. The rest of the corrections are the finite terms which are indeed a sum over many quantum fluctuations. One of the most convenient regularization methods is the so called dimensional regularization. It is based on the analytic continuation of the 4-dimensional

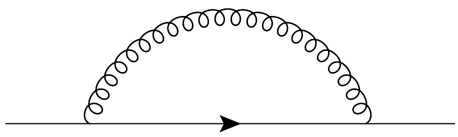

Figure 1.1: Feynman diagram of the quark self energy.

integration to arbitrary dimensions, where commonly $d = 4 - 2\,\epsilon$ has been used. Using this method, the UV infinities appear as $\frac{1}{\epsilon^n}$ terms in the limit of $d \to 4$ ($\epsilon \to 0$). In addition, to keep the renormalized coupling dimensionless, one has to formally introduce an arbitrary scale parameter μ.

The second step is to specify a renormalization condition to absorb all $\frac{1}{\epsilon^n}$ infinities and some finite contributions to redefine the couplings. Renormalization conditions are somewhat arbitrary and one can use various schemes that could have physical or practical motivations. The renormalization schemes are defined by which finite quantum fluctuations are kept in the dynamical matrix elements and which are absorbed into the couplings and parameters.

As the result of the renormalization process, the coupling constants acquire μ dependence and their evolution to different scales is performed by means of differential equations, know as the renormalization group equations (RGE).

Now let's concentrate on the mass renormalization and the consequences on the notion of quark masses. The leading quantum correction to the quark propagator in perturbative QCD (NLO accuracy) arises from the self energy diagram displayed in Fig. 1.1 . The resulting perturbative corrections can be absorbed into the denominator of the quark propagator as follows,

$$\frac{i}{\not{p} - m - \Sigma(\not{p}, m) + i\epsilon}\,, \qquad \Sigma(\not{p}, m) = m\frac{\alpha_s}{\pi}\big[-\frac{1}{\epsilon} + f(\not{p}, m)\big]\,, \tag{1.1.2}$$

where $\Sigma(\not{p}, m)$ indicates the self-energy correction, consisting of UV divergences and finite terms $f(p, m)$ due to the loop integration over all momentum values for the virtual gluon. Note that here we use dimensional regularization for regulating the UV divergences. Now one can use a suitable renormalization scheme to absorb the infinities in the mass definition. One of the very well known prescription is the on-shell renormalization scheme. This scheme is based on a physical condition where all the quantum corrections are absorbed in the coupling, fields and masses in the on-shell limit $p^2 \to M^2$. Based on this prescription, one can define the quark pole mass as the pole of the corrected propagator in the on-shell limit $\not{p} - m - \Sigma(\not{p}, m)|_{\not{p}=M} = 0$. Following this prescription one obtains a perturbative relation between the bare and pole quark masses which reads

$$m = M + \delta M\,, \qquad \delta M = \Sigma(m, m)\,. \tag{1.1.3}$$

Here, M and m denote the pole and bare masses, respectively. Note that the pole mass scheme is defined uniquely, and furthermore is μ-independent.

The notion of pole mass for leptons is well defined and perturbatively converges to the physical rest mass of free leptons. However, the concept of pole mass for quarks is a priori invalid since quarks are confined into hadrons, so that we have never observed a free quark. This can be understood as the fact that in full nonperturbative QCD, a quark propagator does not have any pole. In fact it turns out the quark pole mass suffers from low scale infrared enhancements (factorial growth) in perturbation theory which spoils the convergence of perturbative expansions asymptotically. This issue is known as the pole mass renormalon problem [61]. The pole mass renormalon arises in the on-shell renormalization condition, because all the perturbative self energy corrections, even the ill-defined contributions below $1\,\mathrm{GeV}$ are absorbed into the mass definition. This renormalon ambiguity intrinsically restricts the precision of pole mass determinations to $\Lambda_{\mathrm{QCD}} \sim 1\,\mathrm{GeV}$ accuracy, where the perturbation theory breaks down.

Instead of the pole mass scheme, one can consider the mass as a formal theory parameter that appears in the QCD Lagrangian and exploit an arbitrary renormalization prescription for which the perturbative result exhibits the best convergence for a specific observable. Such renormalization schemes where the renormalon ambiguities are removed are known as short distance mass schemes. Different short distance schemes are useful and appropriate for different applications. Hence the notion of the quark masses in QCD has completely reduced to a formal theory parameter, defined using the perturbative language, and does not have any physical relevance.

A conventional scheme which is commonly used for high energy processes (such as QCD sum rules) is the $\overline{\text{MS}}$ mass scheme. In this scheme only the infinite term is absorbed in the mass definition,

$$m = \overline{m}(\mu) - \frac{\alpha_s(\mu)}{\pi}\frac{1}{\epsilon} + \mathcal{O}(\alpha_s^2)\,, \tag{1.1.4}$$

where $\overline{m}(\mu)$ denotes the $\overline{\text{MS}}$ scheme mass. $\overline{m}(\mu)$ is renormalization scale dependent and the μ-running is given by the renormalization group equation,

$$\mu\frac{d}{d\mu}\overline{m}^{(n_f)}(\mu) = \gamma_m^{(n_f)}\big(\alpha_s^{(n_f)}(\mu)\big)\,\overline{m}^{(n_f)}(\mu)\,, \tag{1.1.5}$$

where the term n_f denotes the number of active flavors. Here, $\gamma_m^{(n_f)}$ is the mass anomalous dimension where the coefficients of its expansion series are known up to $\mathcal{O}(\alpha_s^4)$ in perturbation theory [62,63] as given in Eq. (3.9.11). In Sec. 3.9, we will also discuss the MSR (and jet) mass scheme which is more suitable for the event shape description in the peak region.

To conclude this section let us summarize our discussion on the mass concept. First we described how the definition of the mass has evolved from a primary irreducible concept in classical mechanics to the measure of energy in the rest frame in relativistic theories. Then we noted that this consistent picture fails as soon as we include quantum corrections where the UV divergences arise in loop integrals within the perturbation theory, so that one needs to renormalize the particle masses with a somewhat arbitrary prescription. Here, the notion of free particles in QED (leptons) allowed us to reconcile the rest mass definition with the pole mass scheme in perturbation theory. However, due to the confinement of quarks in hadrons, the low energy dynamics cannot be decoupled from the mass concept. Thus one has to give up any relevant physical quark mass definition which is based on the notion of free quarks. Hence we concluded that the quark mass should be considered as a formal parameter like a Yukawa coupling in the QCD Lagrangian and one has to use a convenient short distance mass scheme according to the observable of interest to obtain a good perurbative convergence behavior.

On the other hand it is necessary to remark that this discussion was based on the standard model of particle physics which suggests that the origin of particle masses is a dynamical mechanism at very high energies. Unavoidably, the fundamental theory of everything should resolve all the loopholes in our understanding of the mass concept, resulting in a more fundamental perception of the origin of mass.

Chapter 2

Part I: Charm and Bottom Quark

The most important feature of heavy quarks is that the mass lays in the region where perturbative QCD is applicable. This allows us to use various methods and observables to determine heavy quark masses to high precision. QCD sum rule is one of the primary methods which has been used to extract the heavy quark masses. Thanks to high order perturbative computations in the last decade, recent analyses have obtained the most accurate charm and bottom quark mass measurements from QCD sum rules [6–9, 14–16, 35]. In this chapter we present our recent determinations [44, 45, 48] of the $\overline{\mathrm{MS}}$ charm and bottom quark masses using relativistic QCD sum rules at $\mathcal{O}(\alpha_s^3)$.

This chapter is organized as following. In Sec. 2.1 we give a brief review on the basics of QCD and the operator product expansion (OPE). We introduce the QCD sum rule method in Sec. 2.2. In Sec. 2.3 we present the current status of charm and bottom quark mass determinations. We concentrate on the most accurate and recent measurements with QCD sum rule methods, addressing possible issues, available room for improvements and outline the main resolutions of this work. The discussion is based on our approach that having a reliable and appropriate error estimation for quark mass measurements is as important as obtaining precise values. In Sec. 2.4, we discuss the theoretical computations and we present a method to achieve a reliable determination for perturbative uncertainties. Sec. 2.5 is devoted to the extraction of the charm and bottom quark experimental moments from the available data on the hadronic cross section. We emphasize that having a conservative approach which has the least model dependence is essential. Finally, we present our final results for charm and bottom quark mass determinations in Sec. 2.6.

2.1 Quantum Chromodynamics and Operator Product Expansion

Quantum Chromodynamics (QCD) is a non-Abelian gauge theory with the SU(3) gauge group, which is believed to describe the strong interaction of colored elementary particles known as quarks and gluons. The QCD Lagrangian is given by Eq. (1.1.1). In this theory quarks are regarded as the $N_c = 3$ fundamental representation of the SU($N_c = 3$) local gauge group whereas the gluons are said to be in the adjoint representations, appearing in 8 color combinations. The quarks are replicated in 6 different flavours: u (up), d (down), s (strange), c (charm), b (bottom) and t (top).

In principle QCD results from series of experiments on hadronic physics. The pioneering study by Gell-Mann and Zweig in 1963 on the spectrum of hadronic bound sates leaded to the notion of quarks and their characteristic color quantum number. Furthermore deep-inelastic scattering experiments (DIS) verified that the constituent partons in hadrons are asymptoicaly free [64, 65]. On the other hand, later developments in quantum field theory showed that non-Abelian gauge theories are indeed explaining the asymptotic freedom of particles in bound states [66–69]. These lines of reasoning leaded into QCD as the model of strong interaction for quarks and gluons [70].[1]

QCD is successfully describing two major aspects of the observed strong interaction: 1) confine-

[1] We refer to Refs. [71, 72] for standard text books.

ment[2], and 2) asymptotic freedom. Confinement is referring to the fact that free quarks are never observed. The only finite-energy asymptotic sates of the theory are singlets color states, representing the hadrons. This feature corresponds to the sufficiently strong coupling constant at low energies of the order of the stable hadronic mass $\mathcal{O}(\Lambda_{\rm QCD}) \sim 1\,\text{GeV}$. On the other hand asymptotic freedom, as verified by DIS processes, demonstrates that the quarks and gluons at high energies are approximately free. This effect can also be understood in terms of a weak coupling of the theory for processes involving large momentum transfers (hard processes). Thus the energy dependence of the strong coupling constant $\alpha_s(\mu)$ controls the strength of effective interactions in the theory. The running of the strong coupling constant with energy is given by the following renormalization group equation

$$\mu\,\frac{d}{d\mu}\alpha_s^{(n_f)}(\mu) = \beta^{(n_f)}\big(\alpha_s^{(n_f)}(\mu)\big)\,, \tag{2.1.1}$$

where the series expansion of $\beta^{(n_f)}$-function is know to five-loop in perturbation theory [63, 79, 80] as given in Eq. (C.15). In this relation, n_f is the number of active light flavors of the effective theory at the corresponding energy. The β-function has a global minus sign which is compatible with asymptotic freedom, see Eq. (C.15). Thus at high energies where the effective quark-gluon coupling is small one can use perturbative QCD, whereas, at low energies of the order of $\mathcal{O}(1\,\text{GeV})$, the perturbative approach is not applicable. Therefore it is common to study QCD in the hard process where the short-distance effects are dominant[3].

Nevertheless even in hard interactions, the observables constitutes of the hadronic final states where nonperturbative effects are significant. A popular approach in this context is to use so called "inclusive observables" in hard scattering processes, so that the hadronization effects are suppressed by powers of $\Lambda_{\rm QCD}/Q$. Here Q is the energy at which the hard interaction is taking place. The intuitive reasons for this suppression are:

1. Factorization, which is referring to the fact that the hard scattering is taking place at high energies where the short-distance physics is dominant whereas the hadronization is happening at low energies, long time afterwards.

2. Unitarity of inclusive observables, meaning that the observable definition does not depend on the details of final states so that the overall probability of hard scattering does not change significantly due to showering and hadronization. Hence one can use perturbative QCD to obtain a leading hadronic level prediction.

Including nonperturbative corrections in a systematic way is a nontrivial exercise. In order to deal with this problem one has to understand better the nature of nonperturbative physics in QCD. For this purpose let's take the correlation functions which are related to the S-matrices of scattering in the sense of the LSZ reduction formula. An n-point Green's function in QCD reads

$$G_n(x_n, \ldots, x_1) = \langle\Omega| T\left\{\mathcal{O}_n(x_n)\ldots\mathcal{O}_1(x_1)\right\}|\Omega\rangle\,, \tag{2.1.2}$$

where $\mathcal{O}_i(x_i)$ is the ith field operator located at x_i . It is relevant to emphasize that in this expression we have used the physical QCD vacuum $|\Omega\rangle$ in the interacting theory. In contrast to the perturbative vacuum $|0\rangle$, the physical vacuum $|\Omega\rangle$ is populated by soft quark and gluon fields. Thus, it encodes the non-trivial long-distance physics (confinement, spontaneous chiral symmetry breaking, etc.). These fluctuations are arising due to the nonlinear structure of the QCD Lagrangian. Indeed various nonperturbative approaches (e.g. Lattice QCD, instanton model) indicate that the corresponding effects involve fluctuations of the order of $\mathcal{O}(\Lambda_{\rm QCD}) \sim 1\,\text{GeV}$.

[2]There is not yet a concrete theoretical proof of confinement, however we have lots of evidence [73–78].

[3]The alternative nonperturbative approach is Lattice QCD where the calculations are limited by some theoretical challenges and simulation power. Other than Lattice QCD which is directly using the QCD Lagrangian, it is popular to use models, such as instanton models or Ads/CFT correspondence, to treat nonperturbative long-distance physics.

Now let us consider a hard processes at a typical energy of Q with $Q \gg \Lambda_{\rm QCD}$ where the perturbative approach is legitimate. To the leading approximation, one can ignore the soft vacuum fluctuations at high energies, replace the $|\Omega\rangle$ with perturbative vacuum $|0\rangle$ and use perturbation theory. In order to incorporate nonperturbative effects one can introduce soft vacuum fluctuations as external fields. Hence to first approximation the high energy quarks are short distance probes that scatter in these external vacuum fluctuations so that they only perceive an average and static behavior of the soft vacuum fields. Based on this argument Wilson introduced a quantitative framework called the operator product expansion (OPE) [81,82] where the product of two (or more) operators e.g. $\mathcal{O}_1(0)$ and $\mathcal{O}_2(x)$, which are located close to each other in space-time (i.e. $x \to 0$) are described effectively with a general expansion in terms of higher dimensional local operators,

$$\lim_{x\to 0} \mathcal{O}_2(x)\,\mathcal{O}_1(0) = \sum_n C_n^{2\,1}(x)\tilde{\mathcal{O}}_n(0)\,, \tag{2.1.3}$$

where the coefficients $C_n^{2\,1}(x)$ are c-number functions. All the possible higher dimensional operators, denoted with $\tilde{\mathcal{O}}_n(0)$, should preserve the symmetries and quantum numbers of the operator product $\mathcal{O}_2(x)\,\mathcal{O}_1(0)$. In this relation we are capturing the short-distance physics and singular parts in the x-dependent Wilson coefficients while the long distance physics are encoded in the higher dimensional local operators. The generalized OPE for generic n-point Green functions reads

$$\lim_{x_n\ldots x_1\to\, 0} \langle\Omega|T\left\{\mathcal{O}_n(x_n)\ldots\mathcal{O}_1(x_1)\right\}|\Omega\rangle = \sum_k C_k^{n\ldots 1}(x_n,\ldots,x_1)\langle\Omega|\tilde{\mathcal{O}}_k(0)|\Omega\rangle\,. \tag{2.1.4}$$

We have to stress that in the renormalized theory all the operators and Wilson coefficients will have a renormalization scale dependence.

In Fourier space, the OPE can be understood in terms of a simple factorization principle with a strict cutoff scale Λ_F where $\Lambda_{\rm QCD} \ll \Lambda_{\rm F} \ll Q$. The expansion of a correlation function, Eq. (2.1.4), in Fourier space can be represented by

$$\begin{aligned}\lim_{x_n\ldots x_1\to 0} i^n \int \prod_{j=1}^{n} \mathrm{d}^4x_j\, e^{i\sum_{k=1}^n x_k\cdot p_k}\langle\Omega|T\left\{\mathcal{O}_n(x_n,\Lambda_F)\ldots\mathcal{O}_1(x_1,\Lambda_F)\right\}|\Omega\rangle = \\ \sum_k C_k^{n\ldots 1}(p_n,\ldots,p_1,\Lambda_F)\langle\Omega|\tilde{\mathcal{O}}_k(\Lambda_F)|\Omega\rangle\,.\end{aligned} \tag{2.1.5}$$

In this relation the Wilson coefficients $C_k^{n\ldots 1}$ contain the contribution from momenta $p_n > \Lambda_F$. The vacuum condensates , $\langle\Omega|\tilde{\mathcal{O}}_k(\Lambda_{\rm F})|\Omega\rangle$, are universal nonperturbative matrix elements which encode the interactions of soft fluctuations where $p_n < \Lambda_F$. In principle these long distance matrix elements are calculable in QCD using nonperturbative approaches but they could also be treated as phenomenological parameters that can be determined by fitting to experimental data. Using dimensional analysis one can show that the higher dimensional operator corrections in the OPE are power suppressed by $(\Lambda_{\rm QCD}/Q)^k$ where k is the dimension of the corresponding local operator. Thus, we have obtained a systematic procedure to include long-distance effects as power corrections to perturbation theory.

Although the strict cutoff approach in the OPE provides a clean factorization basis, it has some practical subtleties. It is usually difficult in the strict cutoff method to define the factorization scale $\Lambda_{\rm F}$ and retain gauge symmetry and Lorantz invariance. Hence, it is convenient to use the OPE in the $\overline{\rm MS}$ scheme with dimensional regularization. Eq. (2.1.5) in this scheme reads

$$\begin{aligned}\lim_{x_n\ldots x_1\to 0} i^n \int \prod_{j=1}^{n} \mathrm{d}^4x_j\, e^{i\sum_{k=1}^n x_k\cdot p_k}\langle\Omega|T\left\{\mathcal{O}_n(x_n,\mu)\ldots\mathcal{O}_1(x_1,\mu)\right\}|\Omega\rangle = \\ \sum_k C_k^{n\ldots 1}(p_n,\ldots,p_1,\mu)\langle\Omega|\tilde{\mathcal{O}}_k(\mu)|\Omega\rangle\,,\end{aligned} \tag{2.1.6}$$

where μ is the renormalization scale. The $C_k^{n\ldots 1}(p_n,\ldots,p_1,\mu)$ are normalized Wilson coefficients and the evolution of them is given by a renormalization group equation.

Let us summarize this section. Here, we discussed that a systematic study of the strong interactions with perturbation theory needs a careful use and definition of observables such that the short-distance physics is the dominant effect. Nevertheless, the accuracy of perturbative QCD is intrinsically restricted by long-distance effects. Therefore to improve the accuracy of calculations one should systematically incorporate nonperturbative effects. The operator product expansion is a robust tool which can tackle this problem using the factorization principle in high energy processes.

2.2 QCD sum rules

QCD sum rules is one of the most powerful methods in hadron phenomenology, developed in 1979 by Shifman, Vainshtien and Zakharov (ITEP group) [4, 5].[4] It is based on the primary concepts which have been discussed in the previous section. The basic observables in QCD sum rules are the n-point current correlation functions.

Let us first consider the correlation function of two quark vector currents:

$$\big(q^2\, g_{\mu\nu} - q_\mu q_\nu\big)\Pi_V(q^2) = -\,i\int \mathrm{d}x\, e^{iqx}\,\langle\,\Omega\,|T\, j_\mu(x) j_\nu(0)|\,\Omega\,\rangle\ , \qquad j^\mu(x) = \bar\psi(x)\gamma^\mu\psi(x)\,, \tag{2.2.1}$$

where $\psi(x)$ is the quark Dirac field. Here q_μ denotes the four-momentum of the virtual photon, so that q^2 is the e^+e^- center-of-mass energy. In the limit $x \to 0$ (at high virtualities $q^2 \to -\infty$) short distance physics dominates and thus perturbative QCD is applicable. Therefore one can use the OPE framework for the current production in the space-like region to separate the short and long distance quark-gluon interactions,

$$\begin{aligned}\Pi_V(q^2) &= \sum_n C_n(q^2<0)\langle 0|\mathcal{O}_n(0)|0\rangle \\ &= C^{\rm pert}(q^2)\,\cdot\,1 + C^{\bar\psi}(q^2)\,\langle 0|\bar\psi\psi|0\rangle + C^{\rm GG}(q^2)\,\langle 0|G^{A\,\mu\nu}G^A_{\mu\nu}|0\rangle \\ &\quad + C^{\psi G\psi}(q^2)\,\langle 0|\bar\psi\,\sigma_{\mu\nu}\,\frac{\lambda^A}{2}G^{A\,\mu\nu}\,\psi|0\rangle + C^{\rm GGG}(q^2)\,\langle 0|f_{ABC}\,G^A_{\mu\nu}G^{B\,\nu}_{\sigma}G^{C\,\mu\sigma}|0\rangle\ +\ \ldots\,,\end{aligned} \tag{2.2.2}$$

where the higher dimension colorless operators are respectively, quark condensates $\mathcal{O}_3 = \bar\psi\,\psi$, gluon condensates $\mathcal{O}_4 = G^{A\,\mu\nu}G^A_{\mu\nu}$, quark-gluon condensates $\mathcal{O}_5 = \bar\psi\,\sigma_{\mu\nu}\,\frac{\lambda^A}{2}G^{A\,\mu\nu}\,\psi$, three-gluon condensates $\mathcal{O}_6 = f_{ABC}\,G^A_{\mu\nu}G^{B\,\nu}_{\sigma}G^{C\,\mu\sigma}$, etc.

On the other hand, in the time-like region $q^2 > 0$, the vector current correlator is saturated by hadronic intermediate states. This region is called the resonance region and the Green's function is dominated by long-distance interactions of quarks and gluons. Therefore the OPE is not valid. This behavior manifests itself as a branch cut of the analytic correlation function on the positive axis in the complex q^2-plane. Here one can use the optical theorem to relate the vector correlator to the quark-antiquark production rate in e^+e^- annihilation

$$R_{e^+e^-\to\, q\bar q\,+X}(q^2)\ =\ 12\,\pi\,Q_q^2\,{\rm Im}\,\Pi_V(q^2)\,, \tag{2.2.3}$$

where Q_q is the charge of the quark and $R_{e^+e^-\to\, q\bar q\,+X}(q^2)$ is the normalized cross section,

$$R_{e^+e^-\to\, q\bar q\,+X}(q^2) = \frac{\sigma_{e^+e^-\to\, q\bar q\,+X}(q^2)}{\sigma_{e^+e^-\to\,\mu^+\mu^-}(q^2)}\,. \tag{2.2.4}$$

Now the major task is to match the results of QCD in the deep euclidean region (the space-like region) given by Eq. (2.2.2), to the hadronic spectrum in the physical region (the time-like region) in Eq. (2.2.3). The trick is to use dispersion relations to connect the result of the QCD calculation and the physical cross section. The derivation of the dispersion relation is a straightforward task, by employing the Cauchy formula for the analytic correlation function $\Pi_V(q^2)$ and using the contour shown in Fig. 2.1 .

[4] This method is known as SVZ sum rules too.

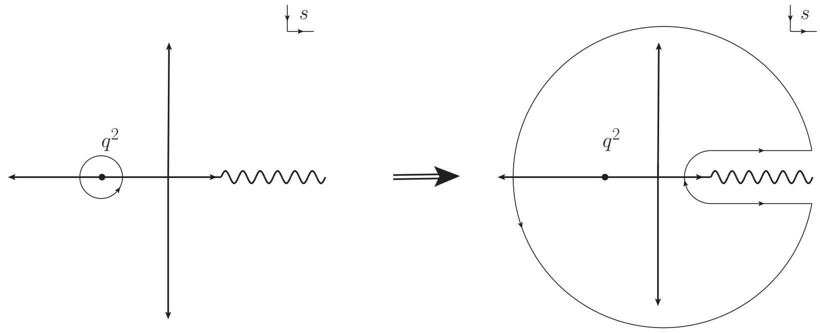

Figure 2.1: Contours of integration in the complex s-plane which are used for the derivation of the dispersion relation in QCD sum rules. The left contour is the initial contour in the Cauchy formula which is deformed into the right contour to match the pQCD calculations of the two-point function at euclidean q^2 and the hadronic cross section related to the branch cut on the positive axis.

The resulting dispersion relation reads

$$\Pi_V(q^2) \;=\; \frac{1}{2\pi i}\int_{|s|=R} \mathrm{d}s\,\frac{\Pi_V(s)}{s-q^2} + \frac{1}{2\pi i}\int_0^R \mathrm{d}s\,\frac{\Pi_V(s+i\epsilon)-\Pi_V(s-i\epsilon)}{s-q^2}\,. \tag{2.2.5}$$

where R is the radius of the contour shown in Fig. 2.1 . The contribution from the circular path at infinity vanishes if $\Pi_V(q^2)$ is tending sufficiently fast to zero at $|q^2| \sim R \to \infty$. Now by applying the Schwarz reflection principle

$$2\,i\,\mathrm{Im}\,\Pi_V(q^2) = \Pi_V(q^2+i\epsilon) - \Pi_V(q^2-i\epsilon)$$

for the time-like region, the dispersion relation becomes

$$\Pi_V(q^2) \;=\; \frac{1}{\pi}\int_{s_{\mathrm{min}}}^{\infty} \mathrm{d}s\,\frac{\mathrm{Im}\,\Pi_V(s)}{s-q^2-i\epsilon} \;=\; \frac{1}{12\,\pi^2\,Q_q^2}\int_{s_{\mathrm{min}}}^{\infty} \mathrm{d}s\,\frac{R(s)}{s-q^2-i\epsilon}\,, \tag{2.2.6}$$

where s_{min} is the physical threshold i.e. the beginning of the branch cut of the correlator on the positive axis. In the second equation we use the optical theorem given in Eq. (2.2.3) to replace the term $\mathrm{Im}\,\Pi_V(s)$ with the hadronic cross section $R(s)$. In general, correlation functions have $\Pi(q^2) \sim q^{2n}\log q^2$ terms which diverge in the limit of $q^2 \to \infty$. Therefore it is common to subtract the first few terms of the tailor expansion to make the dispersion relation convergent. The alternative method is to apply a transformation. A typical transformation for regulating the heavy quark correlation functions is the nth derivative of the dispersion relation

$$M_n^V(q^2) = \frac{12\pi^2 Q_q^2}{n!}\,\frac{\mathrm{d}^n}{\mathrm{d}s^n}\Pi_V(s)\Big|_{s=q^2} = \int_{s_{\mathrm{min}}}^{\infty} \mathrm{d}s\,\frac{R_{e^+e^-\to q\bar{q}+X}(s)}{(s-q^2)^{n+1}}\,. \tag{2.2.7}$$

The resulting observables are the moments of the current correlators, M_n^V . Each derivative in this transformation corresponds to one order of subtraction.

It is conventional to use $M_n^V(q^2=0)$ in heavy quark sum rules where the effective virtuality of the quarks is $|p| \sim m_q/n$. For small values of n where $m_q/n \gtrsim \Lambda_{\mathrm{QCD}}$, theoretical moments $M_n^V(q^2=0)$ can be computed in the OPE framework given in Eq. (2.2.2) where the $\mathcal{O}_3$ contribution vanishes and the leading OPE corrections are due to the gluon condensates $\mathcal{O}_4$. The resulting sum rules at $q^2=0$ for small values of n is the final form of relativistic sum rules which will be used in this thesis to determine the heavy quark masses.[5]

Alternatively one can also consider moments of the pseudoscalar current correlator. For the pseudoscalar correlator it turns out that the first two Taylor coefficients in the small-q^2 expansion need to

[5]The relativistic sum rule method using the vector correlator to determine the $\overline{\mathrm{MS}}$ charm mass is frequently called charmonium sum rules.

be regularized and defined in a given scheme, and that the third term (which we will denote by M_0^P) is hardly sensitive to m_q . Hence for this case we adopt the following definitions

$$\Pi_P(s) = i\int \mathrm{d}x\, e^{iqx}\,\langle\, 0\,|T\, j_P(x) j_P(0)|\, 0\,\rangle\,, \quad j_P(x) = 2\, m_q\, i\, \bar{q}(x)\gamma_5 q(x)\,, \tag{2.2.8}$$
$$M_n^{P,\,\mathrm{th}} = \frac{12\pi^2 Q_q^2}{n!}\,\frac{\mathrm{d}^n}{\mathrm{d}s^n} P(s)\Big|_{s=0}\,, \qquad P(s) = \frac{\Pi_P(s) - \Pi_P(0) - \Pi'_P(0)\, s}{s^2}\,,$$

where the explicit mass factor in the definition of the pseudoscalar current ensures that it is renormalization scheme independent. Experimental information on the pseudoscalar correlator Π_P is not available but it is possible to use lattice simulations to extract the heavy quark masses. In the following sections we will discuss the theoretical and experimental moment calculations in more detail.

2.3 Status of Charm and Bottom Quark Mass Determinations

Charm Mass

The common reference value of comparison for heavy quark masses is $\overline{m}_q(\mu = \overline{m}_q)$ in the $\overline{\mathrm{MS}}$ mass scheme. The latest average of the charm mass by the particle data group (PDG) [83] is $\overline{m}_c(\overline{m}_c) = 1.275 \pm 0.025$ GeV . One can use the perturbative relation between the $\overline{\mathrm{MS}}$ and pole mass schemes [63] to convert this value to the corresponding pole mass value M_c . Using the two-loop relations PDG obtains $M_c = 1.67 \pm 0.07$ GeV . Note that the resulting uncertainty of the quark mass in the pole scheme is increased. This is a clear manifestation of the renormalon ambiguity in the pole mass scheme discussed in Sec. 1.1 . Fig. 2.2 , taken from the PDG [83], summarizes the recent charm mass determinations. The classical methods in extracting the charm mass are relativistic (low-n moments) and non-relativistic (high-n moments) QCD sum rules, finite energy sum rules, global fits to B decays, deep inelastic experiments (THEO) and lattice QCD (LATT). We refer to Ref. [83] for a review on recent determinations, methods and the corresponding references.

Amongst the listed methods, QCD Sum rules are the most powerful ones to determine the charm quark mass. The most recent charmonium sum rule analysis carried out by Chetyrkin et al. [9] using input from perturbative QCD at $\mathcal{O}(\alpha_s^3)$ for the perturbative contribution, obtained $\overline{m}_c(\overline{m}_c) = 1279 \pm (2)_{\mathrm{pert}} \pm (9)_{\mathrm{exp}} \pm (9)_{\alpha_s} \pm (1)_{\langle \mathrm{GG}\rangle}$ MeV where the first quoted error is the perturbative uncertainty and the second is the experimental one. The third and the fourth quoted uncertainties come from α_s and the gluon condensate correction, respectively. To our knowledge this result, the outcome of similar analyses in Ref. [16] and by Boughezal, Czakon and Schutzmeier [7][6], a closely related analysis based on lattice results instead of data for pseudoscalar moments [6, 14, 15, 35] , and the finite-energy sum rules analysis by Bodenstein et al. [13] represent the analyses with the highest precision achieved so far in the literature. We remark that Ref. [15] has the smallest uncertainty claimed so far for the charm mass. If confirmed, any further investigations and attempts concerning a more precise charm quark $\overline{\mathrm{MS}}$ mass would likely be irrelevant for any foreseeable future. We therefore found it warranted to reexamine the charmonium sum rule analysis with special attention on the way how perturbative and experimental uncertainties have been treated in Refs. [8, 9].

To initiate the discussion let us first note the status of theoretical computations and experimental data on the charm cross section. For the theoretical moments $M_n^V(q^2 = 0)$ defined in Eq. (2.2.7) the perturbative coefficient $C^{\mathrm{pert}}(q^2 = 0)$ is known at $\mathcal{O}(\alpha_s^0)$ and $\mathcal{O}(\alpha_s)$ for any value of n [85]. At $\mathcal{O}(\alpha_s^2)$ the moments are known to high values of n [86–90], and to $\mathcal{O}(\alpha_s^3)$ for $n = 1$ [7, 16], $n = 2$ [18], and $n = 3$ [19]. Higher moments at $\mathcal{O}(\alpha_s^3)$ have been determined by a semianalytical procedure [20, 21] (see also [22]). The Wilson coefficient of the gluon condensate contribution $C^{\mathrm{GG}}(q^2 = 0)$ is known to $\mathcal{O}(\alpha_s)$ [91]. On the experimental side the total hadronic cross section in e^+e^- annihilation is known

[6]Since the analyses of Refs. [7, 16] were based on outdated and less precise data for the J/ψ and ψ' electronic partial widths [84], we frequently only compare our numerical results with those of Refs. [8, 9]. However the perturbative input of Refs. [7–9, 16] and ours is identical.

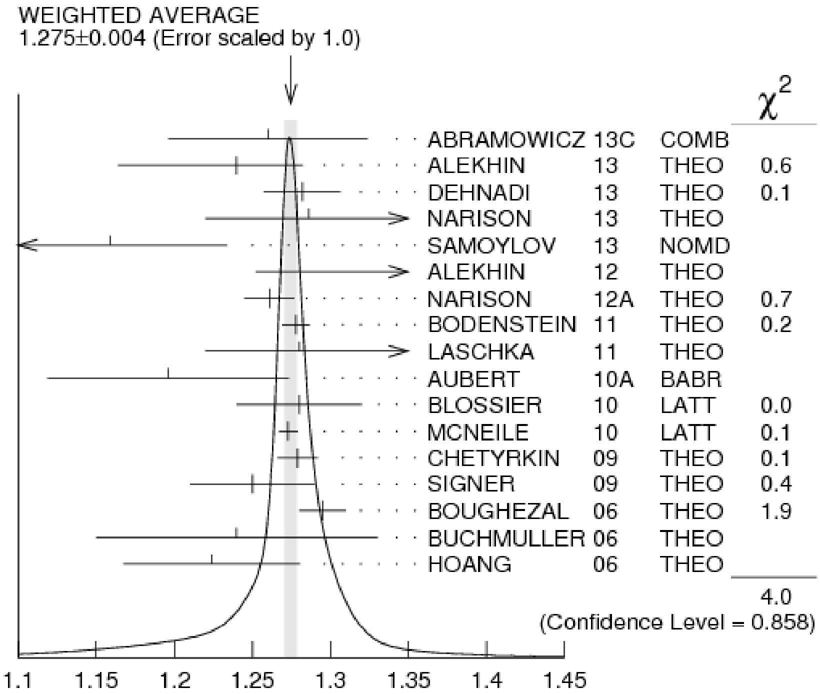

Figure 2.2: Status of charm mass $\overline{m}_c(\overline{m}_c)$ determinations taken from the PDG [83]. The first column references the collaborations. The second is referring to the year of publication and the third is related to the corresponding method. The quoted uncertainty on top refers to the statistical uncertainty that is determined form taking the weighted average of the various determinations. As the final number PDG has rescaled this error with a factor of 6.25 that leads to a 25 GeV error estimation. The reasoning of this inflation is that the statistical average value form the existed determinations is dominated by the sum rule methods. However in our analyses [44, 45] , which will be explained in the following, we have argued a possible underestimation of theoretical uncertainties in previous sum rule analyses. Therefore the PDG has inflated the theoretical uncertainties to obtain a rather more reliable and conservative determination.

from various experimental measurements for c.m. energies up to 10.538 GeV. None of the experimental analyses actually ranges over the entire energy region between the charmonium region and 10.538 GeV, but different analyses overlapping in energy exist such that energies up to 10.538 GeV are completely covered [92–109].[7]

In our analyses in Refs. [44, 45] we take a closer look into the charm quark mass determination using charmonium sum rules by Refs. [6–9, 13, 14, 16] . We demonstrated that the quoted perturbative uncertainty in the previous analyses, resulting from a specific way to arrange the α_s expansion for the charm mass extractions and, in addition, by setting the $\overline{\rm MS}$ renormalization scales in α_s and in the charm mass (which we call μ_α and μ_m, respectively) equal to each other (i.e., they use $\mu_\alpha = \mu_m$). Moreover, the lowest bound of renormalization scale variation was chosen to be 2 GeV, while our investigations showed that variations down to the charm mass value should be considered. After all the charm mass is the scale that governs the perturbative series.

On the other hand, concerning the experimental moments, only data up to $\sqrt{s} = 4.8$ GeV from the BES experiments [93, 96] were used, while for $\sqrt{s} > 4.8$ GeV perturbative QCD predictions were

[7] As a word of caution we mention that, except for the contributions of the J/ψ and ψ' resonances, no experimental separation of the charm and non-charm contributions in the hadronic cross section has been provided in available data, although charm-tagged measurements are possible, see e.g. Ref. [103] (CLEO collaboration). So the charm pair production rate from above the J/ψ and ψ' that enters the charmonium sum rules in Eq. (2.2.7) is usually obtained partly from the measured total R-ratio with theory motivated subtractions of the non-charm rate, and partly by using theory predictions for the charm production rate.

employed. Conceptually this approach was somewhat related to the method of finite energy sum rules (see e.g. Ref. [110]). While this approach might be justified to estimate the overall nominal contribution for the experimental moments from $\sqrt{s} > 4.8$ GeV, since perturbative QCD predictions describe quite well the measured total hadronic cross section outside the resonance regions, it is not obvious how this method can provide an experimental uncertainty. Since the region $\sqrt{s} > 4.8$ GeV constitutes about 30% of the first moment M_1, which is theoretically most reliable, this approach contains a significant intrinsic model dependence that cannot be quantified unambiguously.

In our analyses [44, 45] we revised the charmonium sum rules analysis for low values of n using the latest $\mathcal{O}(\alpha_s^3)$ perturbative results, and we implemented improvements which concern the two issues just mentioned:

1. In Ref. [44] we analyzed several different types of perturbative expansions and examined in detail how the result for the $\overline{\mathrm{MS}}$ charm mass depends on independent choices of μ_α and μ_m. We showed in particular that the interplay of certain choices for the perturbative expansion and the scale setting $\mu_\alpha = \mu_m$ used in previous $\mathcal{O}(\alpha_s^3)$ analyses leads to sizable cancellations of the dependence on μ_α and μ_m that in the light of our new analysis has to be considered as accidental. We demonstrated that for achieving an estimate of perturbative uncertainties based on scale variations that is independent of the perturbative expansion method one needs to vary μ_α and μ_m independently, albeit with ranges that avoid large logs. As the outcome of our analysis we quantify the current $\mathcal{O}(\alpha_s^3)$ perturbative error as around 19 MeV, which is an order of magnitude larger than that of Refs. [7–9, 16].

2. In our updated analysis in Ref. [45] we addressed the problem that the double scale variation might also leads to an overestimate of the perturbative uncertainties. Therefore, we supplemented the analysis by a convergence test that allows to quantify the overall convergence of QCD perturbation theory for each moment, and to discard series that are artificially spoiled by specific choices of the renormalization scales. This results in a reduction of the perturbative uncertainty from 19 to 14 MeV, and the corresponding result for the $\overline{\mathrm{MS}}$ charm mass supersedes the main result given in Ref. [44].

3. Using a clustering method [111–113] to combine correlated data from many different experimental measurements we demonstrated in [44] that the e^+e^- total hadronic cross section relevant for the charmonium sum rules can be determined with a complete coverage of center of mass energies above the J/ψ and ψ' resonances up to 10.538 GeV. Conservatively estimated modeling uncertainties coming from the energy range above 10.538 GeV then only leaded to an insignificant contribution to the total uncertainty of the experimental moments. We also took the opportunity to include recent updates concerning the data on the ψ' charmonium resonance.

4. We applied our improved method of estimating theory uncertainties to determine the charm mass from the pseudoscalar moment [45] . Here, in contrast with the results of the HPQCD collaboration [6, 14, 15, 35] , where small theoretical uncertainties are claimed, we obtain values with one order of magnitude larger perturbative uncertainties which leads to a charm mass determination with less accuracy in comparison with the vector moment analysis.

Bottom Mass

The recent average by the PDG [83] for the $\overline{\mathrm{MS}}$ bottom mass is $\overline{m}_b(\overline{m}_b) = 4.18 \pm 0.03$ GeV (where the corresponding pole mass using two-loop relations is quoted as $M_b = 4.78 \pm 0.06$ GeV). Various methods like non-relativistic QCD sum rules, relativistic QCD sum rules, exclusive B decays physics (THEO) and lattice QCD (LATT) are well studied approaches to extract the bottom mass. For a brief review of these methods, related references and recent measurements we refer to the latest update of the PDG. [83] [see Fig. 2.3].

Here, similar to the charm mass status, the bottom mass determinations form the bottomonium sum rules using the low-n moments are among the most accurate measurements. To the best of our

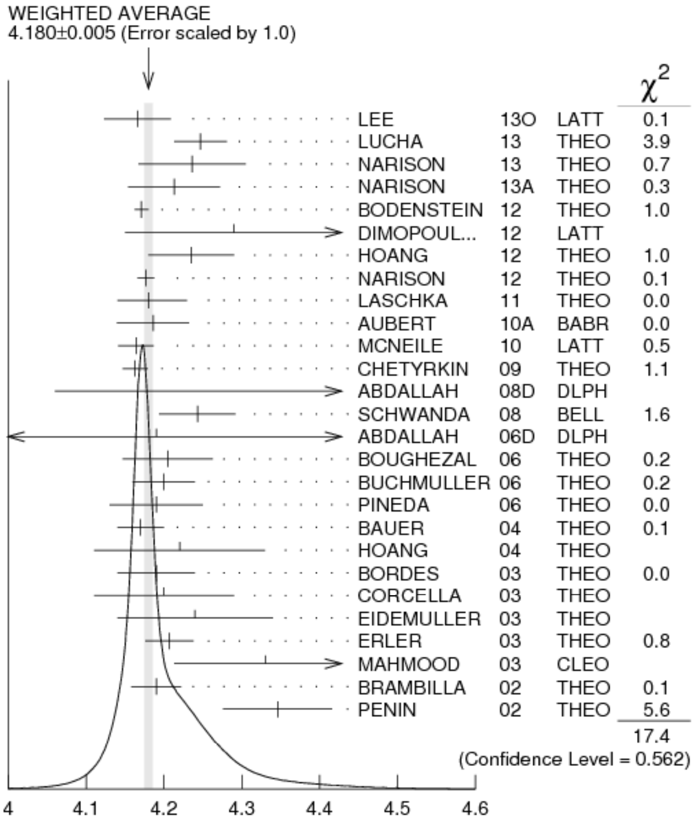

Figure 2.3: Status of bottom mass $\overline{m}_b(\overline{m}_b)$ determinations taken from PDG [83]. For the final result PDG rescales the weighted average uncertainty by a factor of 6 . For the reasoning see Fig. 2.2 .

knowledge, the most recent and precise determinations are from Refs. [9, 114], using input from pQCD at $\mathcal{O}(\alpha_s^3)$ for the perturbative contribution, respectively obtained $\overline{m}_b(\overline{m}_b) = 4163 \pm (3)_{\rm pert} \pm (10)_{\rm exp} \pm (12)_{\alpha_s}$ MeV and $\overline{m}_b(\overline{m}_b) = 4171 \pm (2)_{\rm pert} \pm (6)_{\rm exp} \pm (6)_{\alpha_s}$ MeV where the first quoted error is the perturbative uncertainty and the second is the experimental one. The third quoted uncertainty comes from α_s. The effect of the gluon condensate correction is negligible. These two analyses estimated their perturbative uncertainties in the same way as the corresponding charm mass extractions from the same collaborations [9, 13], taking the mass and coupling renormalization scales equal. Furthermore, when it comes to compute the experimental moments, they used the theoretical input at $\mathcal{O}(\alpha_s^3)$ with perturbative uncertainties to model the high-energy region (continuum region) of the spectrum. As we discussed in our analyses [45], similar caveats as for their charm analyses can be argued to also affect the bottom quark results by Refs. [9, 13] .

In Ref. [45], in analogy with the charm mass determination, we applied the improved method of estimating theory uncertainties to extract the bottom mass from the vector correlator. Moreover, we computed the bottom experimental moments by combining contributions from narrow resonances, experimental data taken in the continuum, and a theoretical model for the continuum region. We carefully studied the assignment of adequate uncertainties to this last contribution, to make sure that the model dependence is reduced to an acceptable level.

2.4 Theoretical Input

In the following sections we explain the theoretical framework which we used in Refs. [44, 45] to determine the charm and bottom quark masses from relativistic QCD sum rules. This section is organized as follows. In Sec. 2.4.1 we present different versions of the perturbative expansion series for vector and axial vector moments which could be employed to extract heavy quark masses. The nonperturbative corrections are collected in Sec. 2.4.2. In this context one can also use the ratio of moments to extract the heavy quark masses from sum rules [6]. We calculate the perturbative expansions of the moments ratio in Sec. 2.4.3. In Sec. 2.4.4 we discuss the appropriate method to assign a reliable perturbative uncertainty to the quark mass determinations from sum rules.

2.4.1 Perturbative Contribution

The moments of the vector and pseudoscalar current correlators are defined in Eqs. (2.2.7) and (2.2.8), respectively. In the framework of OPE the most dominant contribution is the perturbative moment. Thus, let us first focus on the respective contribution for the vector and pseudoscalar current correlator. As already mentioned in Sec. 2.3 these perturbative moments are computed up to $\mathcal{O}(\alpha_s^3)$ [7, 16, 18–21, 85–90] . An important feature of the results is that the perturbative series expansion has a non-linear dependence on the charm quark mass. Thus in principle no conceptual preference can be imposed on any of the possible perturbative series that arises when solving for the charm mass. As a consequence, different versions of the expansion should be considered to obtain reliable estimates of the perturbative uncertainty. As indicated in Sec. 2.3 we use in the following μ_α as the renormalization scale in α_s and μ_m as the renormalization scale in the $\overline{\rm MS}$ charm quark mass $\overline{m}_c$.

(a) Standard fixed-order expansion
We write the perturbative vacuum polarization function as

$$\widehat{\Pi}_X(s, n_f, \alpha_s^{(n_f)}(\mu_\alpha), \overline{m}_q(\mu_m), \mu_\alpha, \mu_m) \;=\; \frac{1}{12\pi^2 Q_q^2}\sum_{n=0}^{\infty} s^n \hat{M}_n^X\,, \tag{2.4.1}$$

where $X = V, P$ for vector and pseudoscalar currents, respectively. Here, we use the hat notation to indicate the perturbative contribution of the vacuum polarization function $\widehat{\Pi}_X$ and the corresponding moments $\hat{M}_n^X$. Note that for notation reasons, in Eqs. (2.4.1, 2.4.8, 2.4.10, 2.4.11) we use $\widehat{\Pi}_P(q^2) = P(q^2)$, where $P(q^2)$ is the twice-subtracted pseudoscalar correlator defined in Eq. (2.2.8). Here Q_q is the quark electric charge with $q = c, b$, and $n_f = 4, 5$ for charm and bottom, respectively. In full generality, the perturbative moments $\hat{M}_n$ can be expressed as the following sum:

$$\hat{M}_n^X \;=\; \frac{1}{[4\,\overline{m}_q^2(\mu_m)]^n}\sum_{i,a,b}\left(\frac{\alpha_s^{(n_f)}(\mu_\alpha)}{\pi}\right)^i [C_X(n_f)]_{n,i}^{a,b}\,\ln^a\!\left(\frac{\overline{m}_q^2(\mu_m)}{\mu_m^2}\right)\ln^b\!\left(\frac{\overline{m}_q^2(\mu_m)}{\mu_\alpha^2}\right). \tag{2.4.2}$$

This is the standard fixed-order expression for the perturbative moment. The numerical values for the $[C_V(n_f = 4)]_{n,i}^{a,b}$ and $[C_V(n_f = 5)]_{n,i}^{a,b}$ coefficients are given in Table B.3. Likewise, $[C_P(n_f = 4)]_{n,i}^{a,b}$ are collected in a numerical form in Table B.4. The nonlinear dependence on $\overline{m}_q$ of the standard fixed-order expansion has the disadvantage that for charm (bottom) quarks there are frequently no solutions for the mass in the sum rule mass determination, for moments higher than the first (second), for some set of values of the renormalization scales.

(b) Linearized expansion
One can linearize the the fixed-order form expansion of Eq. (2.4.2) with respect to the exponent of the quark mass pre-factor by taking the $2n$-th root. This choice is e.g. made in Ref. [14], and in general one can write:

$$\left(\hat{M}_n^X\right)^{1/2n} = \frac{1}{2\,\overline{m}_q(\mu_m)}\sum_{i,a,b}\left(\frac{\alpha_s^{(n_f)}(\mu_\alpha)}{\pi}\right)^i [\bar{C}_X(n_f)]_{n,i}^{a,b}\,\ln^a\!\left(\frac{\overline{m}_q^2(\mu_m)}{\mu_m^2}\right)\ln^b\!\left(\frac{\overline{m}_q^2(\mu_m)}{\mu_\alpha^2}\right). \tag{2.4.3}$$

The coefficients $[\bar{C}_V(n_f = 4)]_{n,i}^{a,b}$, $[\bar{C}_V(n_f = 5)]_{n,i}^{a,b}$ and $[\bar{C}_P(n_f = 4)]_{n,i}^{a,b}$ are given in Tables B.5, B.5 and B.6, respectively. Even though relation (2.4.3) still exhibits some nonlinear dependence on $\overline{m}_q$ through perturbative logarithms, we find that it always has a solution for the quark mass.

(c) Iterative linearized expansion

For the expansion methods (a) and (b) shown in Eqs. (2.4.2) and (2.4.3), one solves for the quark masses $\overline{m}_{c,b}(\mu_m)$ numerically keeping the exact mass dependence on the theory side of the equation. Alternatively, one can solve for $\overline{m}_{c,b}(\mu_m)$ iteratively order by order, which is perturbatively equivalent to the exact numerical solution, but gives different numerical results. The method consists of inserting the lower order values for $\overline{m}_{c,b}(\mu_m)$ in the higher order perturbative coefficients, and re-expanding consistently.

In the first step we determine $\overline{m}_q(\mu_m)$ employing the tree-level relation

$$\overline{m}_q^{(0)} = \frac{1}{2\big(\hat{M}_n^X\big)^{1/2n}}\,[\tilde{C}_X(n_f)]_{n,0}^{0,0}\,, \tag{2.4.4}$$

giving the tree-level quark mass $\overline{m}_q^{(0)}$. In the next step one employs the relation

$$\overline{m}_q^{(1)}(\mu_m) = \frac{1}{2\Big(\hat{M}_n^X\Big)^{1/2n}}\left\{[\tilde{C}_X(n_f)]_{n,0}^{0,0} + \frac{\alpha_s(\mu_\alpha)}{\pi}\left[[\tilde{C}_X(n_f)]_{n,1}^{0,0} + [\tilde{C}_X(n_f)]_{n,1}^{1,0}\ln\left(\frac{\overline{m}_q^{(0)\,2}}{\mu_m^2}\right)\right]\right\} \tag{2.4.5}$$

to determine the $\mathcal{O}(\alpha_s)$ quark mass $\overline{m}_q^{(1)}(\mu_m)$. In the $\mathcal{O}(\alpha_s)$ terms on the RHS of Eq. (2.4.5) the tree-level quark mass $\overline{m}_q^{(0)}$ is used, which is consistent to $\mathcal{O}(\alpha_s)$. At $\mathcal{O}(\alpha_s^2)$ for the determination of $\overline{m}_q^{(2)}(\mu_m)$ one uses $\overline{m}_q^{(0)}$ for the $\mathcal{O}(\alpha_s^2)$ coefficient and $\overline{m}_q^{(1)}(\mu_m)$ for the $\mathcal{O}(\alpha_s)$ correction, which in the strict α_s expansion yields

$$\begin{aligned}
\overline{m}_q^{(2)}(\mu_m) \;=\; & \frac{1}{2\Big(\hat{M}_n^X\Big)^{1/2n}}\left\{[\tilde{C}_X(n_f)]_{n,0}^{0,0} + \frac{\alpha_s(\mu_\alpha)}{\pi}\left[[\tilde{C}_X(n_f)]_{n,1}^{0,0} + [\tilde{C}_X(n_f)]_{n,1}^{1,0}\ln\left(\frac{\overline{m}_q^{(0)\,2}}{\mu_m^2}\right)\right] + \right.\\
& \left(\frac{\alpha_s(\mu_\alpha)}{\pi}\right)^2\left[2\,\frac{[\tilde{C}_X(n_f)]_{n,1}^{1,0}\,[\tilde{C}_X(n_f)]_{n,1}^{0,0}}{[\tilde{C}_X(n_f)]_{n,0}^{0,0}} + 2\,\frac{([\tilde{C}_X(n_f)]_{n,1}^{1,0})^2}{[\tilde{C}_X(n_f)]_{n,0}^{0,0}}\ln\left(\frac{\overline{m}_q^{(0)\,2}}{\mu_m^2}\right) + \right.\\
& \left.\left.\sum_{a,b}[\tilde{C}_X(n_f)]_{n,2}^{a,b}\ln^a\left(\frac{\overline{m}_q^{(0)\,2}}{\mu_m^2}\right)\ln^b\left(\frac{\overline{m}_q^{(0)\,2}}{\mu_\alpha^2}\right)\right]\right\}.
\end{aligned} \tag{2.4.6}$$

Here the second line contains the derivative of the $\mathcal{O}(\alpha_s)$ terms with respect to the quark mass. The determination of the $\mathcal{O}(\alpha_s^3)$ quark mass $\overline{m}_q^{(3)}(\mu_m)$ is then carried out in an analogous way involving the second (first) derivative with respect to the mass in the $\mathcal{O}(\alpha_s)$ ($\mathcal{O}(\alpha_s^2)$) correction and using again $\overline{m}_q^{(0)}$ for the $\mathcal{O}(\alpha_s^3)$ coefficient.

In general we can write the iterative expansion as follows:

$$\overline{m}_q(\mu_m) = \overline{m}_q^{(0)}\sum_{i,a,b}\left(\frac{\alpha_s^{(n_f)}(\mu_\alpha)}{\pi}\right)^i[\tilde{C}_X(n_f)]_{n,i}^{a,b}\,\ln^a\left(\frac{\overline{m}_q^{(0)\,2}}{\mu_m^2}\right)\ln^b\left(\frac{\overline{m}_q^{(0)\,2}}{\mu_\alpha^2}\right), \tag{2.4.7}$$

where the numerical value of the coefficients $[\tilde{C}_V(n_f = 4,5)]_{n,i}^{a,b}$ and $[\tilde{C}_P(n_f = 4)]_{n,i}^{a,b}$ are collected in Tables B.7 and B.8.

By construction, the iterative expansion always has a solution for the quark mass. Accordingly, potential biases on the numerical analysis related to any possible nonlinear dependence are eliminated.

(d) Contour-improved expansion

For the expansions (a), (b) and (c) the moments and the quark masses are computed for a fixed value of the renormalization scale μ_α. Using the analytic properties of the vacuum polarization function, one can rewrite the fixed-order moments as integrals in the complex plane. This opens the possibility of making μ_α dependent on the integration variable, in analogy to the contour-improved methods used for τ-decays (see e.g. Refs. [115–120]). Therefore we define the contour-improved moments [121] as (see Fig. 2.1),

$$\hat{M}_n^{X,\mathcal{C}} \;=\; \frac{6\pi Q_q^2}{i}\int_{\mathcal{C}}\frac{\mathrm{d}s}{s^{n+1}}\widehat{\Pi}_X(s,n_f,\alpha_s^{(n_f)}(\mu_\alpha^q(s,\overline{m}_q^2)),\overline{m}_q(\mu_m),\mu_\alpha^q(s,\overline{m}_q^2),\mu_m)\,, \tag{2.4.8}$$

and we employ the following path-dependent μ_α^q, first used in Ref. [121]

$$(\mu_\alpha^q)^2(s,\overline{m}_q^2) \;=\; \mu_\alpha^2\left(1-\frac{s}{4\,\overline{m}_q^2(\mu_m)}\right). \tag{2.4.9}$$

It weights in a different way the threshold versus the high energy parts of the spectrum. It is straightforward to prove that the resulting moments $\hat{M}_n^{X,\mathcal{C}}$ can be obtained analytically from the Taylor expansion around $s=0$ of the vacuum polarization function using an s-dependent $\mu_\alpha^q(s,\overline{m}_q^2)$:

$$\widehat{\Pi}_X^{\overline{\rm MS}}\Big(s,\alpha_s^{(n_f)}(\mu_\alpha^q(s,\overline{m}_q^2)),\overline{m}_q(\mu_m),\mu_\alpha^q(s,\overline{m}_q^2),\mu_m\Big) \;=\; \sum_{n=0}^{\infty} s^n\,\hat{M}_n^{X,\mathcal{C}}\,. \tag{2.4.10}$$

This trick works because $\alpha_s(\mu_\alpha^q(s,\overline{m}_q^2))$ has the same cut as the fixed-order expression for $\widehat{\Pi}_X$. Other choices of path for $\mu_\alpha^q(s)$ could spoil this property. Expanding the analytic expression for $\hat{M}_n^{X,\mathcal{C}}$ on α_s at a given finite order, one recovers the fixed-order moments $\hat{M}_n^X$. This shows that the dependence on the contour is only residual and represents an effect from higher order terms from beyond the order one employs for the calculation.

The contour-improved moments have a residual sensitivity to the value of the vacuum polarization function at zero momentum transfer.[8] For the case of the vector correlator $\widehat{\Pi}(0)=\hat{M}_0^V$ depends on the UV-subtraction scheme. For the case of the pseudoscalar correlator, $\hat{M}_0^P$ is scheme-independent, since $P(q^2)$ already includes two UV subtractions. However, one could as well define a three-times-subtracted pseudoscalar correlator of the form $\overline{P}(q^2)=P(q^2)-P(0)$. Slightly abusing notation, we denote $\overline{P}$ as the "on-shell" scheme for $P(q^2)$, and the twice subtracted (original) definition as the $\overline{\rm MS}$ scheme for $P(q^2)$. Using the OS scheme with $\widehat{\Pi}^X(0)=0$ for either vector or pseudoscalar correlator, we find that the first moment for the contour-improved expansion gives exactly the first fixed-order moment, $\hat{M}_1^{X,\mathcal{C}}=\hat{M}_1^X$. Thus, in order to implement a non-trivial modification, we employ the $\overline{\rm MS}$ scheme for $\widehat{\Pi}_V(0)$ defined for $\mu=\overline{m}_q(\overline{m}_q)$, and the twice-subtracted expression for $P(q^2)$. Generically it can be written as

$$\widehat{\Pi}_X^{\overline{\rm MS}}(0,n_f) \;=\; \sum_{i,a,b}\left(\frac{\alpha_s^{(n_f)}(\mu_\alpha)}{\pi}\right)^i[C_X(n_f)]_{0,i}^{a,b}\,\ln^a\!\left(\frac{\overline{m}_q^2(\mu_m)}{\mu_m^2}\right)\ln^b\!\left(\frac{\overline{m}_q^2(\mu_m)}{\mu_\alpha^2}\right). \tag{2.4.11}$$

The numerical values for the coefficients $[C_X]_{0,i}^{a,b}$ are collected in Table B.1 for the vector correlator with 4 and 5 flavors and the pseudoscalar correlator with 4 flavors.

2.4.2 Nonperturbative Contribution

The leading power correction of the OPE in Eq. (2.2.2) is the quark condensate. In heavy quark sum rule this term vanishes, because the charm and bottom quark are too heavy to condensate. Therefore the leading power correction of OPE for the moments [122, 123] is the dimension-4 matrix element of the gluon condensate contribution,

$$M_n^X \;=\; \hat{M}_n^X+\Delta M_n^{X,\langle G^2\rangle}+\ldots \tag{2.4.12}$$

[8] This means that the dependence vanishes in the large-order limit.

Here the ellipses represent higher-order power corrections of the OPE involving condensates with dimensions bigger than 4. The Wilson coefficients of the gluon condensate corrections are known to $\mathcal{O}(\alpha_s)$ accuracy [91]. Following Ref. [124], we express the Wilson coefficient of the gluon condensate in terms of the pole mass M_q, since in this way the correction is numerically more stable for higher moments. However, we still write the pole mass in terms of the $\overline{\mathrm{MS}}$ quark mass at one loop. The resulting expression reads

$$\begin{aligned}
\Delta M_n^{X,\langle G^2\rangle} &= \frac{1}{(4M_q^2)^{n+2}}\Big\langle\frac{\alpha_s}{\pi}G^2\Big\rangle_{\mathrm{RGI}}\left[[a_X(n_f)]_n^0+\frac{\alpha_s^{(n_f)}(\mu_\alpha)}{\pi}\,[a_X(n_f)]_n^1\right], \qquad (2.4.13)\\
M_q &= \overline{m}_q(\mu_m)\left\{1+\frac{\alpha_s^{(n_f)}(\mu_\alpha)}{\pi}\left[\frac{4}{3}-\ln\left(\frac{\overline{m}_q^2(\mu_m)}{\mu_m^2}\right)\right]\right\}.
\end{aligned}$$

We use the renormalization group invariant (RGI) scheme for the gluon condensate $\langle G^2\alpha_s/\pi\rangle_{\mathrm{RGI}}$ [125]. The numerical value of the $[a_V(n_f=4)]_n^a$, $[a_V(n_f=5)]_n^a$ and $[a_P(n_f=4)]_n^a$ coefficients are collected in Table B.2. For methods (b) and (c) one can obtain the gluon condensate contribution by performing simple algebra operations and re-expansions in $\alpha_s^{(n_f)}$ and $\langle G^2\rangle$. For method (d) we employ Eqs. (2.4.12) and (2.4.13) as shown. For the RGI gluon condensate we adopt [126]

$$\Big\langle\frac{\alpha_s}{\pi}G^2\Big\rangle_{\mathrm{RGI}} = 0.006\pm 0.012\ \mathrm{GeV}^4\,. \qquad (2.4.14)$$

The overall contribution of the gluon condensate correction in Eq. (2.4.13) in the charm quark mass analysis is quite small. Its contribution to the moments amounts to around 0.4%, 2%, 5%, and 9% for the first four moments, respectively. For $n=1$ it leads to a correction in the $\overline{\mathrm{MS}}$ charm quark mass at the level of 2 MeV and is an order of magnitude smaller than our perturbative uncertainty. The gluon condenstae contribution in the bottom quark mass analysis is absolutely negelegible. Nevertless, including that in final result leads corrections less than 0.1 MeV. We therefore ignore the condensate correction for the discussion of the perturbative uncertainties in Sec. 2.4.4. Its contribution is, however, included for completeness in the final charm mass results presented in Secs. 2.6.

2.4.3 Ratios of Moments

An alternative set of observables which are also highly sensitive to the quark masses are the ratios of consecutive moments. To that end we define $R_n^X(n_f)\equiv M_{n+1}^X(n_f)/M_n^X(n_f)$. Such ratios are proportional to the inverse square of the quark mass for any value of n. Their perturbative series can be expressed as an expansion in powers of $\alpha_s^{(n_f)}$ analogous to Eq. (2.4.2), with the replacements $[4\,\overline{m}_q^2(\mu_m)]^n\to 4\,\overline{m}_q^2(\mu_m)$ and $[C_X(n_f)]_{a,b}^{i,j}\to[R_X(n_f)]_{a,b}^{i,j}$. Their computation is trivial, as one only needs to take the ratio of the two consecutive theoretical moments and re-expand as a series in $\alpha_s^{(n_f)}$. We call this the standard fixed-order expansion, analogous to the expansion (a) of Sec. 2.4.1. The numerical expressions for the $[R_X(n_f)]_{a,b}^{i,j}$ coefficients for the vector correlator with $n_f=4,5$ are given in Table B.9, and for the pseudoscalar correlator with $n_f=4$ in Table B.10. As for the regular moments, we find that the nonlinear dependence of R_n^X on the quark mass sometimes causes that there is no numerical solution for $\overline{m}_q$.

By taking the square root of the ratio of two consecutive moments one gets a linear dependence on the inverse of the quark mass. The corresponding theoretical expression is obtained by re-expanding the perturbative expansion of $\sqrt{R_n^X(n_f)}$ as a series in powers of $\alpha_s^{(n_f)}$. Thus we obtain an expression of the form of Eq. (2.4.3) with the replacement $[\bar{C}_X(n_f)]_{a,b}^{i,j}\to[\bar{R}_X(n_f)]_{a,b}^{i,j}$. This is referred to as the linearized expansion, in analogy to the expansion (b) of Sec. 2.4.1. The numerical values for the $[\bar{R}_X(n_f)]_{a,b}^{i,j}$ coefficients are collected for the vector correlator with $n_f=4,5$ in Table B.11, and for the pseudoscalar correlator with $n_f=4$ in Table B.12.

Finally, one can use $\sqrt{R_n^X(n_f)}$ to solve for $\overline{m}_q(\mu_m)$ in an iterative way, exactly as explained in Sec. 2.4.1 for expansion (c). The theoretical expression is analogous to Eq. (2.4.7) with the replacement $[\tilde{C}_X(n_f)]_{a,b}^{i,j}\to[\tilde{R}_X(n_f)]_{a,b}^{i,j}$. We collect the numerical values for the $[\tilde{R}_X(n_f)]_{a,b}^{i,j}$ coefficients, in

Tabs. B.13 and B.14 for the vector ($n_f = 4, 5$) and pseudoscalar ($n_f = 4$) correlators, respectively. We call this the iterative linearized expansion.

One cannot implement a contour-improved expression for the ratios of moments, as they cannot be computed as the contour integral of a correlator. For the ratios of moments, in any of the three expansions, one can include nonperturbative corrections in the form of a gluon condensate OPE term, just using Eq. (2.4.13) and performing simple algebra operations and re-expansions in $\alpha_s^{(n_f)}$ and $\langle G^2 \rangle$.

2.4.4 Perturbative Uncertainties

Scale Variations

In this section we discuss in detail the perturbative series for the determination of the $\overline{\mathrm{MS}}$ heavy quark mass $\overline{m}_q$ and how to set up an adequate scale variation to estimate the perturbative uncertainty. In the previous section we have discussed four different ways to carry out the perturbative expansion and we presented the corresponding order-by-order analytic expressions. As described there, we can determine at each order of the perturbative expansion for the moments M_n^{th} a value for $\overline{m}_q(\mu_m)$ which also has a residual dependence on μ_α, the renormalization scale used for α_s. To compare the different mass determinations we then evolve $\overline{m}_q(\mu_m)$ to obtain $\overline{m}_q(\overline{m}_q)$ using the 4-loop renormalization group equations for the mass and the strong coupling [80, 127–130]. The obtained value of $\overline{m}_q(\overline{m}_q)$ thus has a residual dependence on the scales μ_m and μ_α, on the order of perturbation theory and on the expansion method. Of course the extracted mass depends on the moment considered as well. Since in our analysis we focus on the first moment for charm and second moment for bottom, for simplicity we drop that label. For the results we can therefore use the notation

$$\overline{m}_q(\overline{m}_q)[\mu_m, \mu_\alpha]^{i,n}\,, \tag{2.4.15}$$

where $n = 0, 1, 2, 3$ indicates perturbation theory at $\mathcal{O}(\alpha_s^n)$ and

$$i \;=\; \begin{cases} a & \text{(fixed-order expansion)},\\ b & \text{(linearized expansion)},\\ c & \text{(iterative linearized expansion)},\\ d & \text{(contour improved expansion)}.\end{cases} \tag{2.4.16}$$

As already mentioned, in a number of recent low-n sum rule analyses [6–9, 13–15, 114], which determined the charm and bottom quark masses with very small uncertainties using $\mathcal{O}(\alpha_s^3)$ theoretical computations for the moments [20–23], the theory uncertainties from the truncation of the perturbative series have been estimated with the scale setting $\mu_m = \mu_\alpha$ based on just one type of expansion, which was either the fixed-order [expansion (a)] for the vector correlator, or the linearized [expansion (b)] for the pseudoscalar correlator. Nevertless, we repeated the analysis of the perturbative series at $\mathcal{O}(\alpha_s^3)$ using four different expansion methods (a) – (d) and we focused on the question whether the renormalization scale variation restricted to $\mu_m = \mu_\alpha$ is suitable for error estimate.

In the following, we will use the first moment of the vector and pseudoscalar current correlator to discuss the charm mass analysis and the second vector moment to discuss the bottom mass. Though the discussion here is limited to these set of moments, the results are generic and tested for the ratio of moments and higher moments. To compute the charm and bottom masses in this section we use $M_1^{P,\,\mathrm{latt}} = 0.1402\,\mathrm{GeV}^{-2}$ for the charm pseudoscalar correlator, from Ref. [6], and our own computation $M_1^{V,\,\mathrm{exp}} = 0.2121\,\mathrm{GeV}^{-2}$ for the charm vector correlator and $M_2^{V,\,\mathrm{exp}} = 2.834 \times 10^{-5}\,\mathrm{GeV}^{-4}$ for the bottom vector correlator, see Sec. 2.5. We also use $\alpha_s(m_Z) = 0.1184$..

Let us start with the charm mass. Quite conspicuous, we deduce that the extractions for the $\overline{\mathrm{MS}}$ charm mass using various expansion methods with correlated scale variations $\mu_m = \mu_\alpha$ lead to very small scale variations, which can be very different depending on the method. The results are shown in Fig. 2.4(a), for the expansion methods (a) – (d) we obtain for the correlated scale variation 1.2893 ± 0.0007, 1.2904 ± 0.0004, 1.2963 ± 0.0045 and $1.3009 \pm 0.0020\,\mathrm{GeV}$, respectively, for $\overline{m}_c(\overline{m}_c)$.

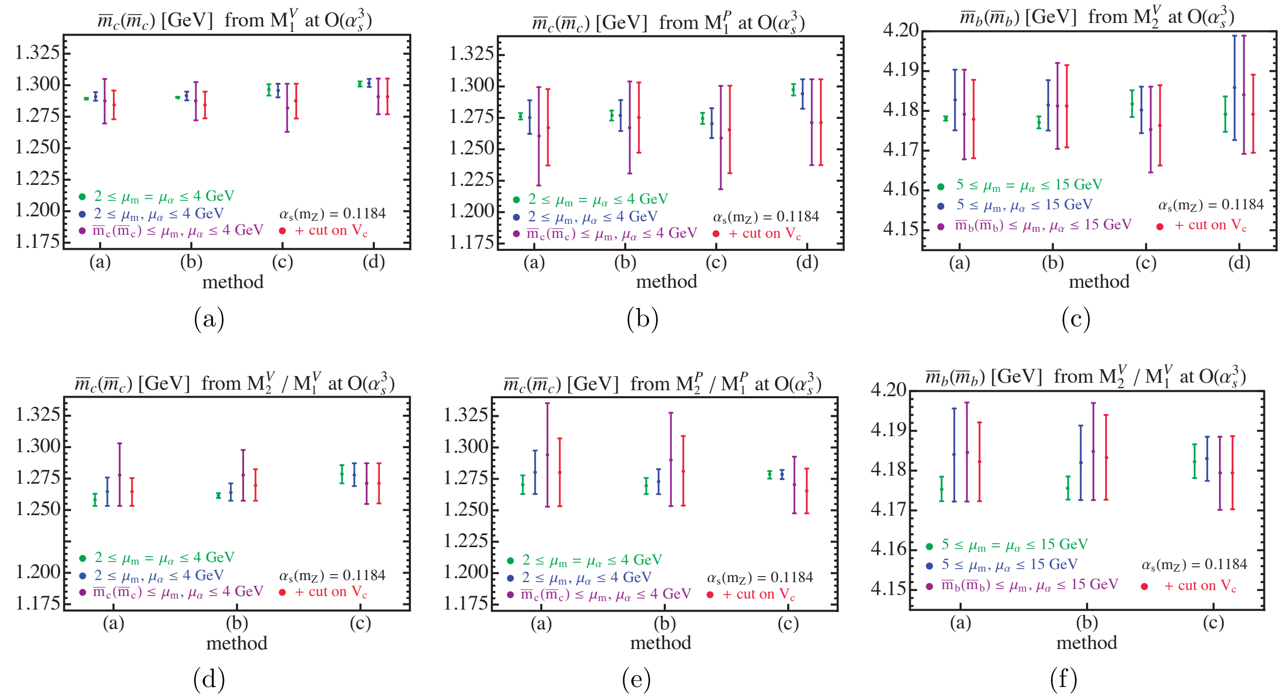

Figure 2.4: Charm and bottom mass values from the first [second] moment of the vector (a) for charm [(c) for bottom] and pseudoscalar [(b), charm] currents at $\mathcal{O}(\alpha_s^3)$; and for the ratio of the second over the first moment for the vector [(d) for charm, (g) for bottom] and pseudoscalar [(e), charm] correlators. We show the outcome of various scale variations for the perturbative expansions (a) – (d) [(a) – (c) for ratios], where green (rightmost) corresponds to $2\,\text{GeV} \le \mu_m = \mu_\alpha \le 4\,\text{GeV}$ [$5\,\text{GeV} \le \mu_m = \mu_\alpha \le 15\,\text{GeV}$ for bottom], blue (second from the left) $2\,\text{GeV} \le \mu_m, \mu_\alpha \le 4\,\text{GeV}$ [$5\,\text{GeV} \le \mu_m, \mu_\alpha \le 15\,\text{GeV}$ for bottom], purple (second from the right) $\overline{m}_c(\overline{m}_c) \le \mu_m, \mu_\alpha \le 4\text{GeV}$ [$\overline{m}_b(\overline{m}_b) \le \mu_m, \mu_\alpha \le 15\,\text{GeV}$ for bottom] and in red (rightmost) we supplement the latter variation with a cut on the series with larger values of V_c.

The outcome of different methods are inconsistent. Moreover, for some expansions also the results from the different orders can be incompatible to each other. [9]

An illustrative way to demonstrate how a small scale variation can arise is given in Fig. 2.5(a) - 2.5(d). For all four expansion methods contour curves of constant $\overline{m}_c(\overline{m}_c)$ are displayed as a function of (the residual dependence on) μ_m and μ_α. For the fixed-order (a) and the linearized expansions (b) we see that there are contour lines closely along the diagonal $\mu_m = \mu_\alpha$. For the fixed-order expansion (a) this feature is almost exact and thus explains the extremely small scale-dependence seen in Fig. 2.4(a). For the linearized expansion (b) this feature is somewhat less exact and reflected in the slightly larger scale variation seen in Fig. 2.4(a). On the other hand, the contour lines of the iterative (c) and contour improved (d) expansions have a large angle with respect to the diagonal $\mu_m = \mu_\alpha$ leading to the much larger scale variations at $\mathcal{O}(\alpha_s^3)$ visible in Fig. 2.4(a). Hence we conclude:

- The small scale variations observed for the fixed-order and linearized expansions for $\mu_m = \mu_\alpha$ result from strong cancellations of the individual μ_m and μ_α dependences that arise for this correlation.

- Other correlations between μ_m and μ_α that do not generate large logarithms do not lead to such cancellations. One therefore has to consider the small scale variations observed for $\mu_m = \mu_\alpha$ in the fixed-order and linearized expansions as accidental.

In order to avoid the accidental cancellation of correlated scale variations a natural and conservative choice is to apply an independent variation of μ_m and μ_α. However, the ranges of independent

[9] Fig. 1 of Ref. [48] shows the order-by-order dependence of the results.

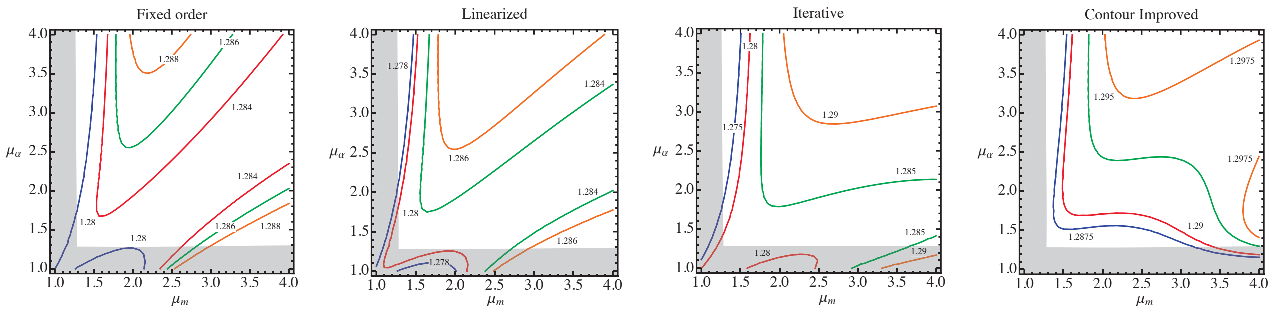

(a) (b) (c) (d)

Figure 2.5: Contour plots for $\overline{m}_c(\overline{m}_c)$ as a function of μ_α and μ_m at $\mathcal{O}(\alpha_s^3)$, for methods (a)–(d). The shaded areas represent regions with $\mu_m, \mu_\alpha < \overline{m}_c(\overline{m}_c)$, and are excluded of our analysis.

scale variation are somewhat arbitrary. For instance using independent variations between 2 GeV and 4 GeV, $2\,\text{GeV} \leq \mu_\alpha, \mu_m \leq 4\,\text{GeV}$, motivated by correlated variations, we obtain 1.291 ± 0.003, 1.291 ± 0.003, 1.296 ± 0.005 and 1.302 ± 0.003 GeV, respectively, for expansions (a) – (d). These results are not consistent either. We find out that an adequate variation range should include the charm mass itself (after all, that is the scale that governs the series), motivated by the range $2\,m_c \pm m_c$ around the pair production threshold. We also stress that there are no perturbative instabilities concerning the use of the RGE down to the scale $\overline{m}_c(\overline{m}_c)$. Thus, adopting independent scale variation in the range $\overline{m}_c(\overline{m}_c) \leq \mu_m, \mu_\alpha \leq 4\,\text{GeV}$ one obtains 1.287 ± 0.018, 1.287 ± 0.015, 1.282 ± 0.019 and 1.291 ± 0.014 GeV respectively. The results show consistency and demonstrate the strong dependence on the lower bound of the renormalization scale variation. The outcome is illustrated graphically in Fig. 2.4(a). Overall, we draw the following conclusion:

- Uncorrelated (i.e. independent) variation of μ_m and μ_α leads to charm mass extractions with perturbative uncertainty estimates that are in general larger, but fully compatible among the expansions (a) – (d) and for the different orders. We therefore conclude that μ_m and μ_α should be varied independently in the range

$$\overline{m}_c(\overline{m}_c) \;\leq\; \mu_m, \mu_\alpha \;\leq\; 4\ \text{GeV}\,, \tag{2.4.17}$$

  to obtain a reliable and conservative estimate of the perturbative uncertainty.

We have repeated this analysis for the first moment of the pseudoscalar correlator M_1^P. Ref. [6] used the method (b) with the same scale variation as Ref. [9], quoting 4 MeV for the truncation error. For methods (a) – (d) and using $2\,\text{GeV} \leq \mu_m = \mu_\alpha \leq 4\,\text{GeV}$ we obtain 1.276 ± 0.003, 1.277 ± 0.004, 1.275 ± 0.005 and 1.297 ± 0.004 GeV, respectively. For independent double scale variation between 2 and 4 GeV we obtain, 1.276 ± 0.013, 1.277 ± 0.012, 1.271 ± 0.012 and 1.294 ± 0.012 GeV, and if we use $\overline{m}_c(\overline{m}_c)$ as the lower bound to we obtain 1.260 ± 0.039, 1.267 ± 0.037 GeV, 1.259 ± 0.041 and 1.272 ± 0.034. These results are displayed graphically in Fig. 2.4(b). The contour lines for the mass extraction from the first moment of the pseudoscalar correlator for all methods are shown in Fig. 2.6. We see that the results show a qualitative agreement with the situation for the vector current, but at a level of perturbative scale variations that are in general roughly larger by a factor of two.

A similar study can be performed for the extraction of the bottom mass $\overline{m}_b(\overline{m}_b)$ from the second moment of the vector correlator M_2^V. In this context Ref. [9] used the fixed-order expansion [method (a)] and correlated scale variation between $5\,\text{GeV} \leq \mu_m = \mu_\alpha \leq 15\,\text{GeV}$, quoting a perturbative error of 3 MeV. For the same variation we obtain 4.1781 ± 0.0005, 4.1771 ± 0.0015, 4.1818 ± 0.0034 and 4.1792 ± 0.0044 GeV for methods (a) and (d), respectively. As in the charm case the results are not consistent, but the variations of the results have a much smaller size, as is expected from the fact that for the bottom the renormalization scales are much larger. For independent variation between the same values we get 4.183 ± 0.008, 4.181 ± 0.006, 4.180 ± 0.006 and 4.186 ± 0.013 GeV. Finally, if the

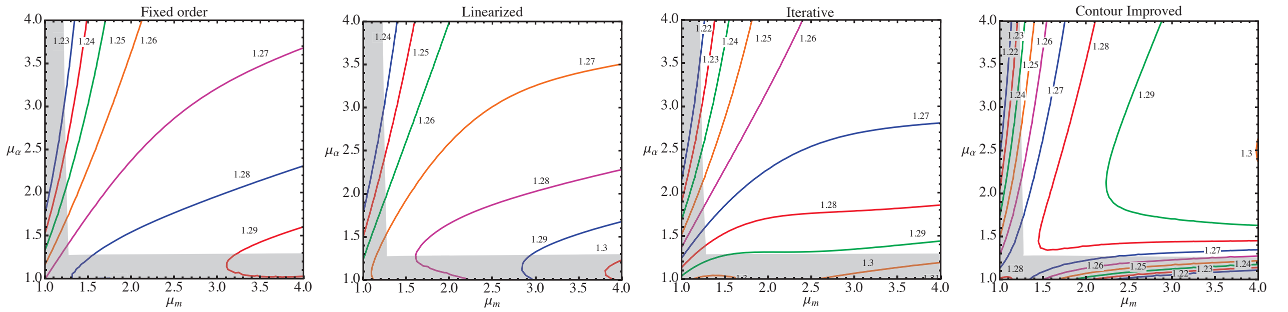

(a) (b) (c) (d)

Figure 2.6: Contour plots for $\overline{m}_c(\overline{m}_c)$ as obtained from the first moment of the pseudoscalar correlator M_1^P, as a function of μ_α and μ_m at $\mathcal{O}(\alpha_s^3)$, for methods (a) – (d). The shaded areas represent regions with $\mu_m, \mu_\alpha < \overline{m}_c(\overline{m}_c)$, and are excluded of our analysis. For this plot we employ $\alpha_s(m_Z) = 0.118$.

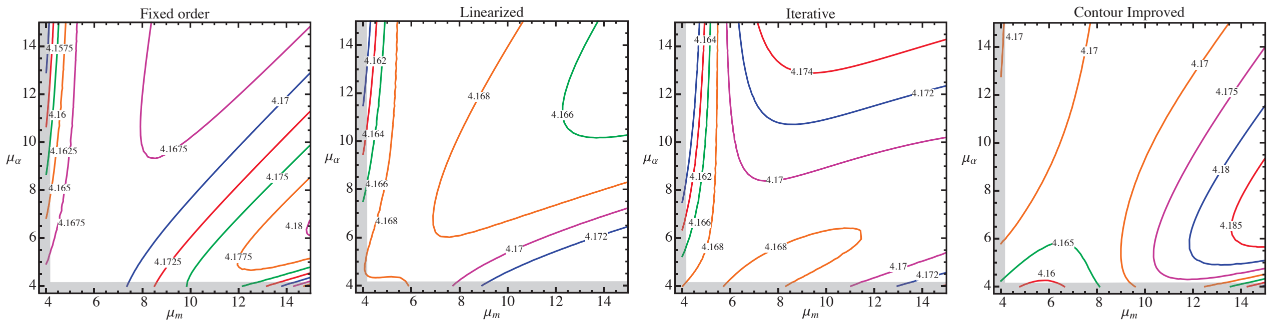

(a) (b) (c) (d)

Figure 2.7: Contour plots for $\overline{m}_b(\overline{m}_b)$ as obtained from the second moment of the vector correlator M_2^V with $n_f = 5$, as a function of μ_α and μ_m at $\mathcal{O}(\alpha_s^3)$, for methods (a) – (d). The shaded areas represent regions with $\mu_m, \mu_\alpha < \overline{m}_b(\overline{m}_b)$, and are excluded of our analysis. For this plot we employ $\alpha_s(m_Z) = 0.118$.

lower limit of the double variation starts at $\overline{m}_b(\overline{m}_b)$ we find 4.179 ± 0.011, 4.181 ± 0.011, 4.175 ± 0.011 and 4.184 ± 0.0015 GeV. These results are collected in Fig. 2.4(c). The corresponding $\overline{m}_b(\overline{m}_b)$ contours in the $\mu_m - \mu_\alpha$ plane are shown in Fig. 2.7. As for the charm case, we find fully consistent results for the independent scale variation and using $\overline{m}_b(\overline{m}_b)$ as the lower bound.

We have also studied the ratio of the first over the second moments for the three cases, and observe a very similar pattern. We do not provide a detailed discussion in the text, but display the outcome graphically in Figs. 2.4(d) to 2.4(f).

Convergence Test

At this point it is useful to consider the perturbative series for all choices of μ_α and μ_m as different perturbative expansions, which can have different convergence properties. To estimate the perturbative uncertainties one analyzes the outcome of this set of (truncated) series. While the uncorrelated scale variation certainly is a conservative method, one possible concern is that it might lead to an overestimate of the size of the perturbative error. For instance, this might arise for a non-vanishing value of $\ln(\mu_m/\mu_\alpha)$ in connection with sizeable values of $\alpha_s(\mu_\alpha)$ for μ_α close to the charm mass scale, which might artificially spoil the convergence of the expansion. One possible resolution might be to simply reduce the range of scale variation (such as increasing the lower bound). However, this does not resolve the issue, since the resulting smaller variation merely represents a matter of choice. Furthermore, there is in general no guarantee that the series which are left have a better convergence despite the fact that the overall scale variation might become reduced. Preferably, the issue should be fixed from inherent properties of the perturbative series themselves. It is possible to address this issue by supplementing the uncorrelated scale variation method with a convergence test constraint, which we explain in the following.

We implement a finite-order version of the root convergence test. Let us recall that in mathematics, the root test (also known as Cauchy's radical test) states that for a series of terms a_n, $S[a] = \sum_n a_n$, if the quantity V_∞ defined as

$$V_\infty \equiv \limsup_{n\to\infty} (a_n)^{1/n}\,, \tag{2.4.18}$$

is smaller (bigger) than 1, the sum is absolutely convergent (divergent). If V_∞ approaches 1 from above then the series is still divergent, otherwise the test is not conclusive. In Eq. (2.4.18) lim sup stands for the superior limit, which essentially means that in case of oscillating series, one takes the maximum value of the oscillation. In the context of our analysis with truncated series the relevant property is that a smaller V_∞ implies a better convergent series. For the different expansion methods we use, it is simplest to apply the method directly to the sequence of quark masses that are extracted order by order, rewriting the results as a series expansion. Since we only know a finite number of coefficients of the perturbative series, we need to adapt the test. We now introduce the quantity V_c and proceed as follows: [10]

(a) For each pair of renormalization scales (μ_m, μ_α) we define the convergence parameter V_c from the charm mass series $\overline{m}_c(\overline{m}_c) = m^{(0)} + \delta m^{(1)} + \delta m^{(2)} + \delta m^{(3)}$ resulting from the extractions at $\mathcal{O}(\alpha_s^{0,1,2,3})$:

$$V_c = \max\left[\frac{\delta m^{(1)}}{m^{(0)}}\,, \left(\frac{\delta m^{(2)}}{m^{(0)}}\right)^{1/2}, \left(\frac{\delta m^{(3)}}{m^{(0)}}\right)^{1/3}\right]. \tag{2.4.19}$$

(b) The resulting distribution for V_c values can be conveniently cast as a histogram, and the resulting distribution is a measure for the overall convergence of the perturbative expansion being employed. We apply the convergence analysis to the region $\overline{m}_c(\overline{m}_c) \le \mu_\alpha, \mu_m \le 4\,\mathrm{GeV}$ for charm, and $\overline{m}_b(\overline{m}_b) \le \mu_\alpha, \mu_m \le 15\,\mathrm{GeV}$ for bottom. If the distribution is peaked around the average $\langle V_c\rangle$ it has a well-defined convergence. Hence discarding series with $V_c \gg \langle V_c\rangle$ (particularly if they significantly enlarge the estimate of the perturbative error) is justified.

Fig. 2.8(a) shows the V_c distributions for expansions (a) – (d) for the extraction of the charm mass from the vector moment M_1^V. We find $\langle V_c\rangle_{\rm double} = (0.15,\, 0.15,\, 0.17,\, 0.19)$[11] and that the distributions are peaked around $\langle V_c\rangle$, indicating a very good overall convergence. The scale variation error (defined as half the overall variation) as a function of the fraction of the series (with the largest V_c values) that are being discarded is shown in Fig. 2.9(a). We see that only around 2% of the series with the highest V_c values by themselves cause the increase of the scale variation from well below 15 MeV to up to 20 MeV. These series are located at the upper-left and lower-right corners of Figs. 2.5 and 2.7, and Fig. 6 of Ref. [44], corresponding to values of μ_m and μ_α far from each other. Given that these series have very large V_c values and do not reflect the overall good convergence behavior of the bulk of the series, it is justified to remove them from the analysis.

The V_c distributions for the pseudoscalar first moment M_1^P are shown in Fig. 2.8(b), again showing a clear peak. However, with $\langle V_c\rangle_{\rm double} = (0.24,\, 0.24,\, 0.25,\, 0.21)$ [for correlated variation $\langle V_c\rangle_{\rm corr} = (0.22,\, 0.23,\, 0.22,\, 0.15)$ with 2 GeV as the lower bound], the average V_c values are significantly larger than for the vector correlator, indicating that the overall perturbative convergence for the pseudoscalar moment is still excellent but worse than for the vector moment. This means that the vector correlator method is superior, and we expect that the perturbative uncertainty in the charm mass from the pseudoscalar is larger. This expectation is indeed confirmed as we discussed in Sec. 2.4.4, see also Sec. 2.6. Fig. 2.9(b) shows that the effect of discarding the series with the worst convergence is very similar to that of the vector correlator.

[10] One could think of implementing the ratio test as well. However, since we only known a small number of terms, it is likely that one of them becomes close to zero, making one of the ratios blow up. This makes this test very unstable.

[11] Interestingly, the same analysis for the correlated variation with $2\,\mathrm{GeV} \le \mu_\alpha = \mu_m \le 4\,\mathrm{GeV}$ yields $\langle V_c\rangle_{\rm corr} = (0.14,\, 0.16,\, 0.19,\, 0.19)$, which is similar to the outcome for the double variation. This same observation can be made for the rest of the correlators.

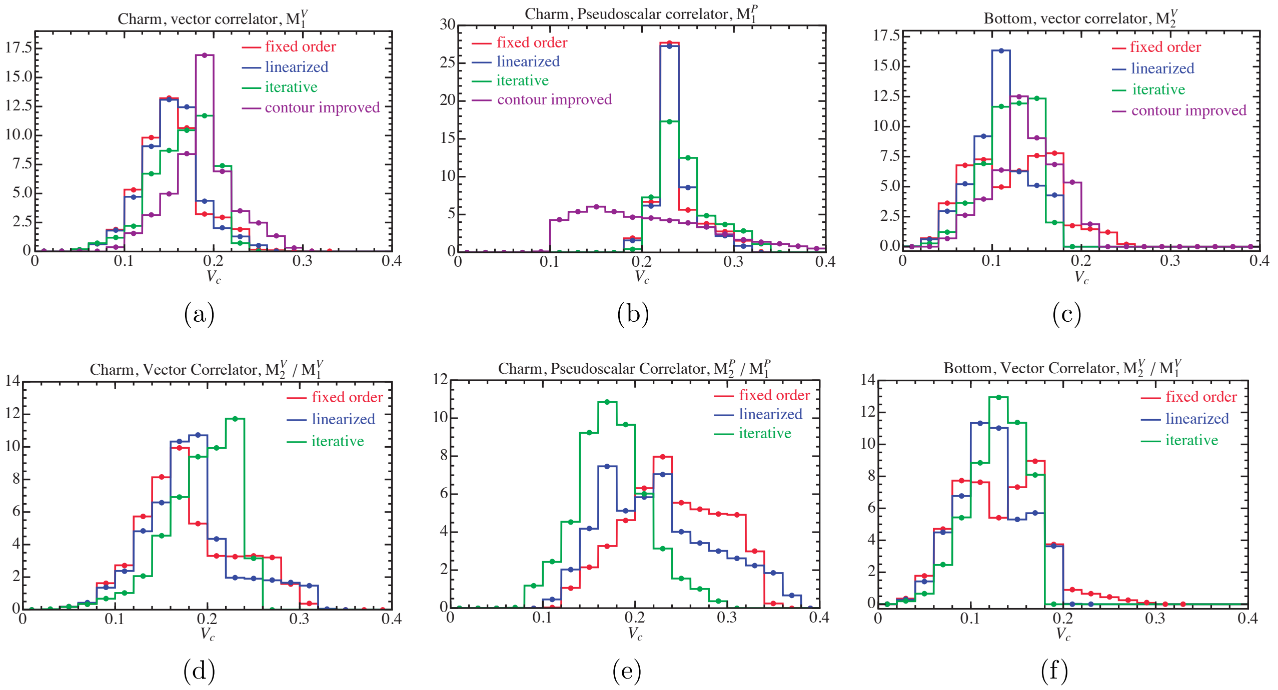

Figure 2.8: V_c distribution for $\overline{m}_c(\overline{m}_c)$ from the first moment of the vector (a) and pseudoscalar (b) correlator, and for $\overline{m}_b(\overline{m}_b)$ for the second moment of the vector correlator (c), for expansions (a) – (d). The three lower panels show the same for the ratio of the second over the first moment for expansions (a) – (c).

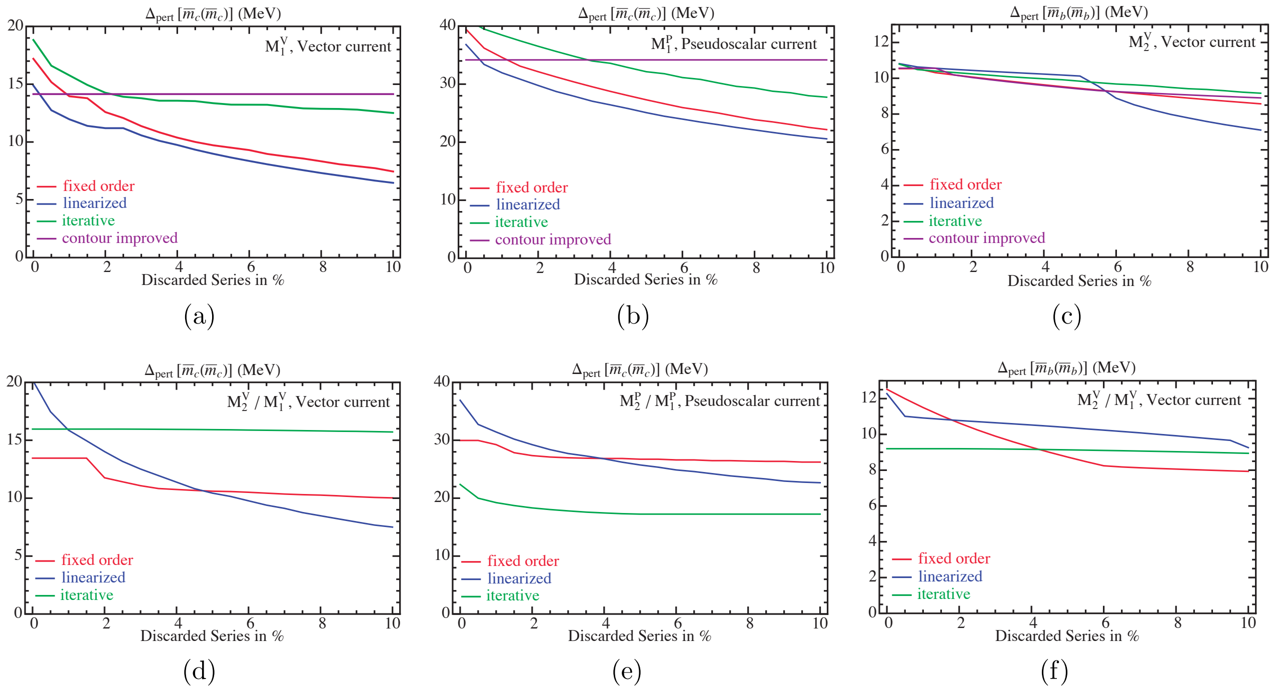

Figure 2.9: Half of the scale variation of $\overline{m}_q(\overline{m}_q)$ at $\mathcal{O}(\alpha_s^3)$ as a function of the fraction of the discarded series with highest V_c values for the first moment of the vector (a) and pseudoscalar (b) correlators for charm, the second moment of the vector correlator for bottom (c); the ratio of the second over the first moment for the vector [charm (d) and bottom (f)] and pseudoscalar [charm (e)] correlators.

For our determination of the bottom mass we use the second moment M_2^V (see Sec. 2.5 for a discussion on why we discard the first moment), and employ uncorrelated scale variations in the range

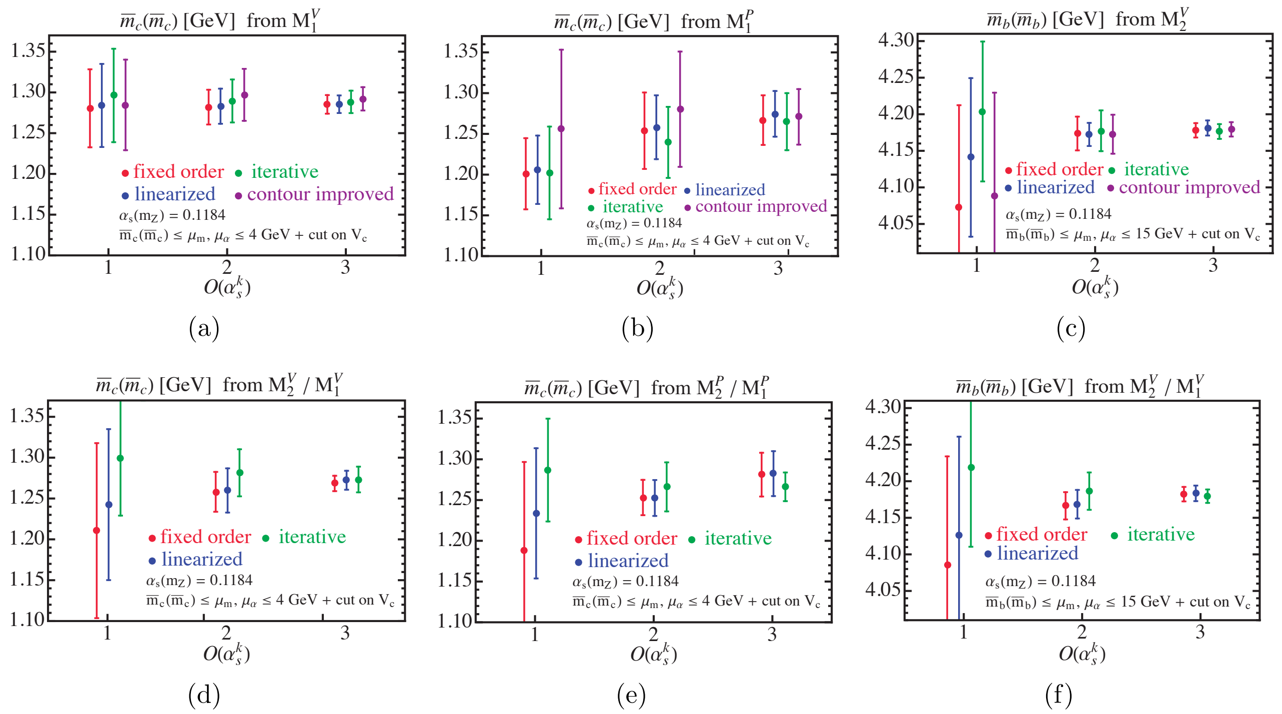

Figure 2.10: Charm and bottom mass values from the first [second] moment of the vector (a) for charm [(c) for bottom] and pseudoscalar [(b), charm] currents at $\mathcal{O}(\alpha_s^{1,2,3})$; and for the ratio of the second over the first moment for the vector [(d) for charm, (g) for bottom] and pseudoscalar [(e), charm] correlators for expansions (a) – (d) [(a) – (c) for ratios], in red, blue, green and purple, respectively.

$\overline{m}_b(\overline{m}_b) \le \mu_m, \mu_\alpha \le 15\,\text{GeV}$. Fig. 2.8(c) shows the corresponding histograms, and we find that the convergence test yields $\langle V_c \rangle_{\text{double}} = (0.13,\, 0.11,\, 0.12,\, 0.15)$ for expansions (a) – (d) [for the correlated variation with scales set equal and $5\,\text{GeV} \le \mu_\alpha = \mu_m \le 15\,\text{GeV}$ we find $\langle V_c \rangle_{\text{corr}} = (0.13,\, 0.09,\, 0.13,\, 0.15)$]. As expected, the averages for the bottom are much smaller than for the charm. We further find that discarding series with the highest V_c values only has minor effects on the perturbative error estimate for fractions up to 5%, see Fig 2.9(c). This is a confirmation that the series for bottom moments overall are more stable, which is again expected from the fact that perturbation theory should work better for the bottom than for the lighter charm.

The behavior of the ratios of moments is very similar as that for regular moments, as can be seen in Figs. 2.9 and 2.8, panels (d) – (f). We find the following average values for V_c for methods (a) – (d): ratios of charm vector moments $\langle V_c \rangle_{\text{double}} = (0.19,\, 0.18,\, 0.19)$ [$\langle V_c \rangle_{\text{corr}} = (0.16,\, 0.16,\, 0.23)$]; ratios of charm pseudoscalar moments $\langle V_c \rangle_{\text{double}} = (0.25,\, 0.23,\, 0.18)$ [$\langle V_c \rangle_{\text{corr}} = (0.25,\, 0.20,\, 0.16)$]; ratios of bottom vector moments $\langle V_c \rangle_{\text{double}} = (0.13,\, 0.12,\, 0.13)$ [$\langle V_c \rangle_{\text{corr}} = (0.13,\, 0.11,\, 0.14)$]. Therefore we conclude that the perturbative convergence of the ratios of moments is in general terms a bit worse than that of regular moments, except for the linearized iterative method of the pseudoscalar ratios.

In our final numerical analyses we discard 3% of the series with the worst V_c values. As can be seen from Fig. 2.8, this only affects series with V_c values much larger than the average values for the whole set of series. It is our intention to keep the fraction of discarded series as small as possible, since it is our aim to remove only series with convergence properties that are obviously much worse than those of the bulk of the series. We call this procedure *trimming* in the following. As we see in Figs. 2.10, the results including the trimming show a very good order-by-order convergence for the heavy quark mass determinations, and at each order every expansion method gives consistent results for the central values as well as for the estimate of the perturbative uncertainties. Figs. 2.10(a) and 2.10(b) show the results for $\overline{m}_c(\overline{m}_c)$ from the vector and pseudoscalar correlators, respectively, for expansions (a) – (d) at $\mathcal{O}(\alpha_s^{1,2,3})$ and with $\overline{m}_c(\overline{m}_c) \le \mu_m, \mu_\alpha \le 4\,\text{GeV}$, using the first moment. Figs. 2.10(d) and 2.10(e) show results for methods (a) – (c), using the ratio of the second over the first moment. Analogously, Figs. 2.10(c) and 2.10(f) show the results for $\overline{m}_b(\overline{m}_b)$ for the second moment, and the ratio of the second over the first moment, respectively, with the uncorrelated variation $\overline{m}_b(\overline{m}_b) \le \mu_m, \mu_\alpha \le 15\,\text{GeV}$.

2.5 Experimental Input

In this section we are calculating the experimental moments. In Sec. 2.5.1, we provide a complete collection of the available experimental data on hadronic cross section in the region between 2 GeV and 10.538 GeV. Then we use the clustering method to combine data and compute the experimental moments for the charm vector current correlators. This is the first analysis of charmonium sum rules which accounts for all available e^+e^- hadronic cross section data. In Sec. 2.5.2 we present our computation of the experimental moments for the bottom correlator. Sec. 2.5.3 is devoted to a short discussion on the lattice simulation data. The computation of the ratio of experimental moments is presented in Sec. 2.5.4.

2.5.1 Computation of the Experimental Moments for the Charm Correlator

In the following we compute the moments for the charm vector current correlator from experimental data. The moments consist of three distinct contributions: the charmonium narrow resonances, the region of broader resonances which is covered by various experiments, and the continuum region, where no data has been taken and some modeling is required.

Data Collections

Region (I): Narrow resonances

Below the open charm threshold there are the J/ψ and ψ' narrow charmonium resonances. Their masses, and electronic widths are taken from the PDG [83] and are collected in Tab. 2.1 together with the value of the pole-subtracted effective electromagnetic coupling at their masses. The total widths are not relevant since we use the narrow width approximation for their contributions to the moments. The uncertainty for the contribution to the moments coming from the masses and the effective electromagnetic coupling can be neglected.

	J/ψ	ψ'
M (GeV)	3.096916(11)	3.686109(13)
Γ_{ee} (keV)	5.55(14)	2.37(4)
$(\alpha/\alpha(M))^2$	0.9580(3)	0.9557(6)

Table 2.1: Masses and electronic widths [83] of the narrow charmonium resonances with total uncertainties and effective electromagnetic coupling, where $\alpha = 1/137.035999084(51)$ is the fine structure constant, and $\alpha(M)$ stands for the pole-subtracted effective electromagnetic coupling at the scale M [131]. We have also given the uncertainties in $\alpha(M)$ due to its hadronic contributions. Compared to the uncertainties of the widths, the uncertainties on $\alpha(M)$ and the masses are negligible.

Region (II): Threshold and data continuum region

The open charm threshold is located at $\sqrt{s} = 3.73$ GeV. We call the energies from just below the threshold and up to 5 GeV the threshold region, and the region between 5 GeV and 10.538 GeV, where the production rate is dominated by multiparticle final states the data continuum region. In these regions quite a variety of measurements of the total hadronic cross section exist from BES [92–97], CrystalBall [98,99], CLEO [100–103], MD1 [104], PLUTO [105], and MARKI and II [106–109]. Taken together, the entire energy region up to 10.538 GeV is densely covered with total cross section mea-

Numbering	Reference	Experiment	Year	Systematical	Data points
1	[92]	BES	2000	no splitting given	6
2	[93]	BES	2002	splitting given	85
3	[94]	BES	2004	only one point	1
4	[95]	BES	2006	splitting given	3
5	[96]	BES	2006	splitting given	68
6	[97]	BES	2009	no splitting given	3
7	[98]	CrystalBall	1986	splitting given	98
8	[99]	CrystalBall (Run 1)	1990	splitting given	4
9	[99]	CrystalBall	1990	splitting given	11
10	[100]	CLEO	1979	only one point	1
11	[101]	CLEO	1998	only one point	1
12	[102]	CLEO	2007	splitting given	7
13	[103]	CLEO	2008	no splitting given	13
14	[104]	MD1	1996	splitting given	31
15	[105]	PLUTO	1982	no splitting given	45
16	[106]	MARKI	1976	no splitting given	59
17	[107]	MARKI	1977	no splitting given	21
18	[108]	MARKII	1979	splitting given	24
19	[109]	MARKI	1981	splitting given	78

Table 2.2: Complete data set of measurements of the total hadronic R-ratio used in this work. Each data set is assigned a number to simplify referencing in discussions and figures of this work. Also given is information on the name of the experimental collaboration, the year of the publication, on whether the splitting of the systematical error in correlated and uncorrelated contributions is provided, and on the number of data points.

surements from these 19 data sets.[12] The measurements from BES and CLEO have the smallest uncertainties. They do, however, not cover the region between 5 and 7 GeV. Here CrystalBall and MARKI and II have contributed measurements albeit with somewhat larger uncertainties. The statistical and total systematical uncertainties of the measurements can be extracted from the respective publications. For some data sets the amount of uncorrelated and correlated systematical uncertainties is given separately (BES [93, 95, 96], CrystalBall [98, 99], CLEO [102], MARKI and II [108, 109], MD1 [104]) while for all the other data sets only combined systematical uncertainties are quoted. All these data sets are shown in Figs. 2.11, where the displayed error bars represent the (quadratically) combined statistical and systematical uncertainties.

Interestingly, none of the previous charm mass analyses, to the best of our knowledge, ever used the complete set of available data. As examples, Bodenstein et al. [10] used data sets [92, 93, 96, 103] from BES and CLEO. Jamin and Hoang [121] used the data sets of Refs. [93], [104] and [100] from BES, MD1 and CLEO, covering the regions 2 GeV $\leq E \leq$ 4.8 GeV and 6.964 GeV $\leq E \leq$ 10.538 GeV. Boughezal et al. [7], Kuhn et al. [24], and Narison [11] use only one data set from BES [93]. Kuhn et al. [8, 9] used the data sets of Refs. [93, 96] from BES covering the energy region 2.6 GeV $\leq E \leq$ 4.8 GeV.

We consider three different selections of data sets to study the dependence of the experimental moments on this choice:

1. The *minimal selection* contains all data sets necessary to cover the whole energy region between 2 and 10.538 GeV without any gaps and keeping only the most accurate ones. These 8 data sets are from BES [92, 93, 95, 97], CrystalBall [99], CLEO [102, 103] and MD1 [104] corresponding to the data sets 1, 2, 5, 6, 9, 12, 13, and 14 (see Tab. 2.2 for references).

[12] There are 18 references quoted since Ref. [99] provides results from two independent runs that we treat as two different data sets.

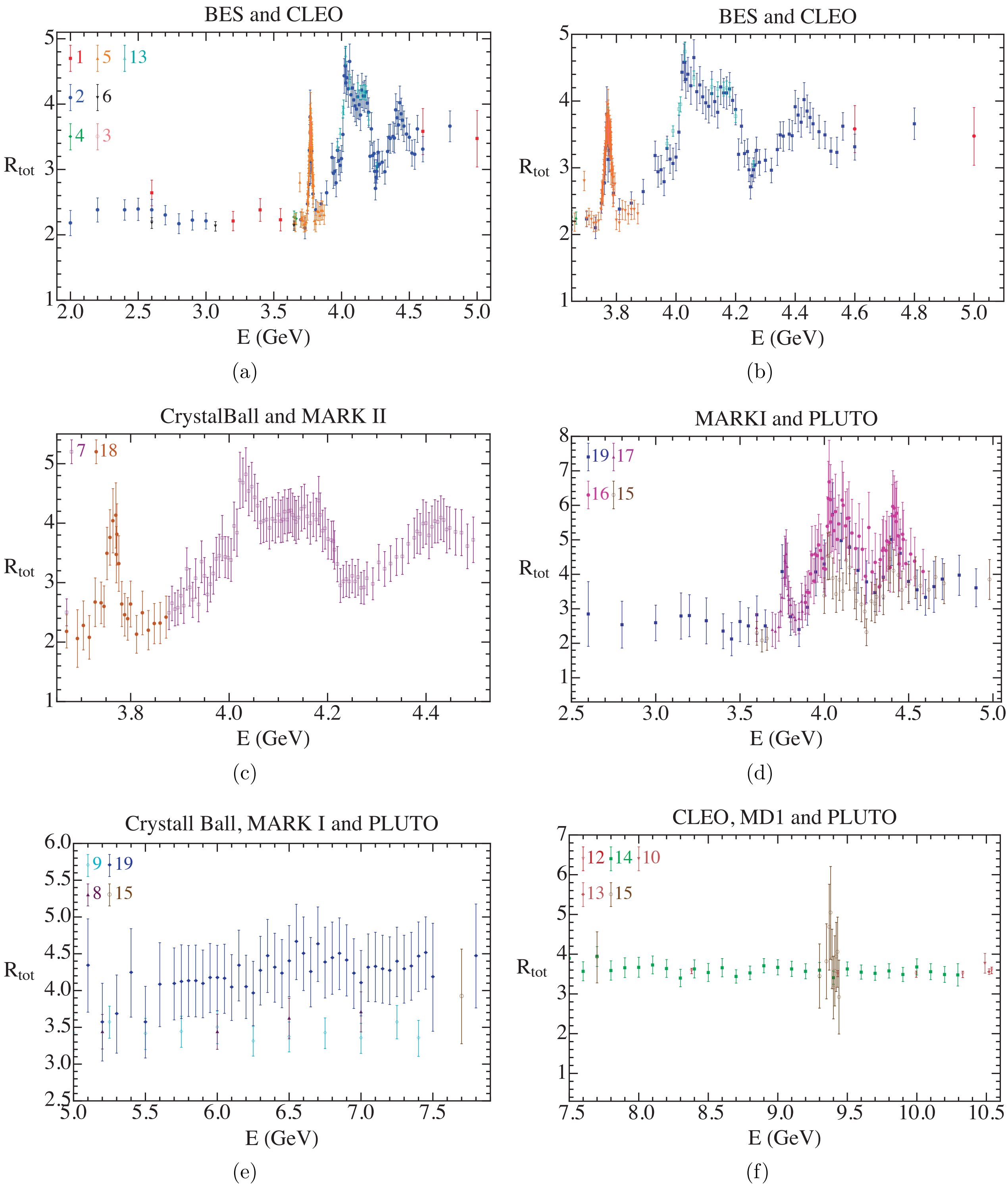

Figure 2.11: Experimental data. In the two top figures we show BES and CLEO data in the non-charm, low charm and threshold regions (a) and low charm region and threshold region (b). The two pictures in the middle show less precise data in the threshold region: CrystalBall and MARKII (c) and MARKI and PLUTO (d). The two pictures on the bottom show data in the continuum region: below 8 GeV data from CrystalBall, MARKI and PLUTO (e) and above 8 GeV data from CLEO, MD1 and PLUTO (f).

2. The *default selection* contains all data sets except for the three ones with the largest uncertainties. It contains 16 data sets and fully includes the minimal selection. It contains all data sets except for Mark I and II data sets 16, 17 and 19 from Refs. [106, 107, 109].

3. The *maximal selection* contains all 19 data sets.

We use the default selection as our standard choice for the charm mass analysis, but we will also quote results for the other data selections.

Region (III): Perturbative QCD region

Above 10.538 GeV there are no experimental measurements of the total hadronic R-ratio that might be useful for the experimental moments. In this energy region we will therefore use perturbative QCD to provide estimates for the charm production R-ratio. As a penalty for not using experimental data we assign a 10% total relative uncertainty to the contribution of the experimental moments coming from this region, which we then treat like an uncorrelated experimental uncertainty for the combination with the moment contribution from lower energies. We stress that this error is not related to the theoretical uncertainty of perturbative QCD in this region (which amounts to less than 0.5%), but represents a conservative error assignment that allows to trace the impact of this region in the analyses. We have fixed the value of 10% as twice the overall offset between the combined data and the perturbative QCD prediction for the charm cross section in the energy region between 4.55 and 10.538 GeV, see the discussion at the end of Sec. 2.5.1. As we see in Sec. 2.5.1 the energy region above 10.538 GeV contributes only $(6, 0.4, 0.03, 0.002)\%$ to $M^{\rm exp}_{1,2,3,4}$. In the first moment $M^{\rm exp}_1$ the total contribution is about three times larger than the combined statistical and systematical (true) experimental uncertainties from the other energy regions. So the 10% penalty we assign to this approach represents a subleading component of the final quoted uncertainty.[13] In the second and higher moments $M^{\rm exp}_{n\geq 2}$ the contributions from above 10.538 GeV and the corresponding uncertainty are negligible compared to the uncertainties from the lower energy regions. This means that our experimental moments are completely free from any theory-driven input or potential bias.

As the theoretical formula to determine the moment contribution from the perturbative QCD region we use the $\mathcal{O}(\alpha_s)$ [85], $\mathcal{O}(\alpha_s^2)$ [132–134], and $\mathcal{O}(\alpha_s^3)$ [135, 136] nonsinglet massless quark cross section including charm mass corrections up to $\mathcal{O}(\overline{m}_c^4/s^2)$ [137–141]:

$$R^{\rm th}_{cc}(s) \;=\; N_c\, Q_c^2\, R^{\rm ns}(s, \overline{m}_c^2(\sqrt{s}), n_f = 4, \alpha_s^{n_f=4}(\sqrt{s}), \sqrt{s})\,, \tag{2.5.1}$$

where

$$\begin{aligned}
& R^{\rm ns}(s, \overline{m}_c^2(\mu), n_f = 4, \alpha_s^{n_f=4}(\mu), \mu) \\
&= 1 + \frac{\alpha_s}{\pi} + \Big(\frac{\alpha_s}{\pi}\Big)^2 [1.52453 - 2.08333 L_s] + \Big(\frac{\alpha_s}{\pi}\Big)^3 \big[-11.52034 + 34028 L_s^2 - 9.56052 L_s\big] \\
&+ \frac{\overline{m}_c^2(\mu)}{s}\Big\{12\,\frac{\alpha_s}{\pi} + \Big(\frac{\alpha_s}{\pi}\Big)^2 [109.167 - 49 L_s] + \Big(\frac{\alpha_s}{\pi}\Big)^3 \big[634.957 - 799.361 L_s + 151.083 L_s^2\big]\Big\} \\
&+ \frac{\overline{m}_c^4(\mu)}{s^2}\Big\{-6 + \frac{\alpha_s}{\pi}[-22 + 24 L_s] + \Big(\frac{\alpha_s}{\pi}\Big)^2 \big[140.855 + 221.5 L_s - 5.16667 L_m - 73 L_s^2\big] \\
&\qquad + \Big(\frac{\alpha_s}{\pi}\Big)^3 \big[3776.94 - 509.226 L_s - 174.831 L_m - 1118.29 L_s^2 \\
&\qquad\qquad + 10.3333 L_m^2 + 42.1944 L_m L_s + 198.722 L_s^3\big]\Big\}\,,
\end{aligned} \tag{2.5.2}$$

with

$$L_s \,\equiv\, \ln\Big(\frac{s}{\mu^2}\Big)\,, \qquad L_m \,\equiv\, \ln\Big(\frac{\overline{m}_c^2(\mu)}{s}\Big)\,. \tag{2.5.3}$$

For the computation of the contribution to the experimental moments we determine $\overline{m}_c(\sqrt{s})$ and $\alpha_s(\sqrt{s})$ appearing in Eq. (2.5.1) using $\overline{m}_c(\overline{m}_c) = 1.3$ GeV and $\alpha_s(m_Z) = 0.118$ as initial conditions.

[13] The situation is quite different if experimental data from the region above 4.8 GeV is discarded and perturbative QCD is used already from 4.8 GeV. Here the contribution to the moments $M^{\rm exp}_{1,2,3,4}$ from energies above 4.8 GeV amounts to $(30, 10, 3, 1)\%$. For the first moment the 10% penalty would then represent the largest source of uncertainty and correspond to an uncertainty in the charm mass of around 18 MeV.

n	Mass corrections	Secondary Radiation	Singlet	Z-boson
1	0.02	0.038	3×10^{-4}	0.006
2	0.001	9×10^{-4}	2×10^{-5}	0.004
3	1×10^{-4}	4×10^{-5}	2×10^{-6}	0.003
4	8×10^{-6}	3×10^{-6}	1×10^{-7}	0.003

Table 2.3: Relative size (in percent) of some subleading contributions for the first four moments originating from energies $\sqrt{s} > 10.538$ GeV. The second column shows the charm mass corrections contained in $R_{cc}^{\rm th}$ as a reference. The third column shows the contributions from $\mathcal{O}(\alpha_s^2)$ secondary $c\bar{c}$ radiation through gluon splitting. The effects from secondary charm radiation accounting all energies from threshold to infinity are $(0.042, 0.002, 3\times10^{-4}, 7\times10^{-5})$% for the first four moments. The fourth column depicts the contribution from the $\mathcal{O}(\alpha_s^3)$ singlet gluon corrections accounting for the mass corrections up to order $\overline{m}_c^4$. Integrating the known singlet corrections from threshold to infinity the contributions amount to $(0.005, 0.003, 0.002, 0.001)$% for the first four moments. The last column shows the relative corrections from the Z-boson exchange integrated from threshold to 10.538 GeV.

It is instructive to examine for the moment contributions from $\sqrt{s} > 10.538$ GeV terms related to charm production that we do not account for in Eq. (2.5.2). In Tab. 2.3 the relative size with respect to the full first four moments (in percent) of the most important neglected contributions are given. In the second column the size of the mass corrections up to order $\overline{m}_c^4$, which we have included in $R_{cc}^{\rm th}$, are shown as a reference. The third column shows the contributions coming from secondary $c\bar{c}$ radiation through gluon splitting, see Fig. 3.1. The fourth column depicts the contributions from the $\mathcal{O}(\alpha_s^3)$ singlet corrections (including the mass corrections up to order $\overline{m}_c^4$), which one can take as an rough estimate for the actual contributions from the charm cut, see Fig. 3.7. Finally in the last column we show the size of the Z-boson exchange terms integrated from threshold to 10.538 GeV. This contribution represents the Z-exchange contribution that is contained in the data, but - by definition - not accounted for in the theory moments. We see that at least for the first two moments, the contributions neglected are much smaller than the charm mass corrections we have accounted for in the nonsinglet production rate,[14], which are already constituting a very small effect. Overall the numerical effect on the charm mass of all these contributions is tiny considering the scaling $\overline{m}_c \sim M_n^{1/2n}$. Since we assign a 10% error on the moments' contribution from the energy region $\sqrt{s} > 10.538$ GeV where we use theory input, our approach to neglect subleading effects is justified.

Non-charm background

Experimentally only the total hadronic cross section is available. Although charm-tagged rate measurements are in principle possible [103] they have not been provided in publications. On the other hand, they would also exhibit sizable additional uncertainties related to the dependence on simulations of the decay of charmed mesons into light quark final states. So to obtain the charm production cross section from the data we have to subtract the non-charm background using a model based on perturbative QCD related to the production of u, d and s quarks. A subtle point is related to the secondary radiation of $c\bar{c}$ pairs off the u, d and s quarks from gluon splitting and to which extent one has to account theoretically for the interplay between real and virtual secondary $c\bar{c}$ radiation which involves infrared sensitive terms [142]. Since in this work we define the moments from primary $c\bar{c}$ production (see Eq. (2.2.7)), secondary $c\bar{c}$ production is formally counted as non-charm background. Thus for the model for the non-charm background for $\sqrt{s} > 2\,\overline{m}_c$ we employ the expression

$$\begin{aligned} R_{uds}(s) \;=\; & N_c(Q_u^2 + 2Q_d^2)\Bigg[R^{\rm ns}(s,0,n_f=3,\alpha_s^{n_f=4}(\sqrt{s}),\sqrt{s}) \\ & + \left(\frac{\alpha_s^{n_f=4}(\sqrt{s})}{\pi}\right)^2 \frac{2}{3}\left(\rho^V + \rho^R + \frac{1}{4}\log\frac{\overline{m}_c^2(\overline{m}_c)}{s}\right)\Bigg]. \end{aligned} \tag{2.5.4}$$

[14]See Sec. 3.6 for the nonsinglet contribution explanation.

The second term on the RHS describes the contributions from real and virtual secondary $c\bar{c}$ radiation. The analytic expressions for ρ^R and ρ^V can be found in Eqs. (2) and (6) of Ref. [143]. We have checked that the numerical impact of real (ρ^R) and virtual (ρ^V) secondary radiation individually as well as the complete second term on the RHS of Eq. (2.5.4) on the moments is negligible, see Tab. 2.3. We use Eq. (2.5.4) and fit the non-charm background including also data in the region 2 GeV $\leq E \leq$ 3.73 GeV via the ansatz $R_{\mathrm{non}-c\bar{c}}(s) = n_{\mathrm{ns}}\, R_{uds}(s)$, where the constant n_{ns} represents an additional fit parameter. We determine n_{ns} from a global combined fit including many data sets, as explained below. This is similar in spirit to Refs. [8], where an analogous constant n_- was determined. Their approach, however, differs from ours as they fitted n_- separately for the two considered BES data sets [93] and [96] accounting only energies below 3.73 GeV.

Data Combination

Combining different experimental measurements of the hadronic cross section one has to face several issues: (a) the measurements are given at individual separated energy points, (b) the set of measurements from different publications are not equally spaced, cover different, partly overlapping energy regions and have different statistical and systematical uncertainties, (c) the correlations of systematical errors are only known (or provided) for the data sets within each publication, (d) there are a number of very precise measurements at widely separated energies.

In this section we discuss the combination of the experimental data from the threshold and the data continuum regions between 2 and 10.538 GeV using a method based on a fitting procedure used before for determining the hadronic vacuum polarization effects for $g-2$ [113]. In this work we extend this approach and also account for the subtraction of the non-charm background.

Combination method

The method uses the combination of data in energy bins (clusters) assuming that the R-value within each cluster changes only very little and can thus be well approximated by a constant. Thus clusters for energies where R varies rapidly need to be small (in this case the experimental measurements are also denser). The R-value in each cluster is then obtained by a χ^2 fitting procedure. Since each experimental data set from any publication covers an energy range overlapping with at least one other data set, the clusters are chosen such that clusters in overlapping regions contain measurements from different data sets. Through the fitting procedure correlations are then being communicated among different data sets and very accurate individual measurements can inherit their precision into neighboring clusters. Both issues are desirable since the hadronic R-ratio is a smooth function with respect to the sequence of clusters.

To describe the method we have to set up some notation:

- All measurements $R(E)$ are distinguished according to the energy E at which they have been carried out.
- Each such energy point having a measurement is written as $E_i^{k,m}$, where $k = 1, \ldots, N_{\mathrm{exp}}$ refers to the N_{exp} data sets, $m = 1, \ldots, N_{\mathrm{cluster}}$ runs over the N_{cluster} clusters and $i = 1, \ldots, N^{k,m}$ assigns the i-th of the $N^{k,m}$ measurements.
- Each individual measurement of the R-ratio is then written as

$$R(E_i^{k,m}) \;=\; R_i^{k,m} \pm \sigma_i^{k,m} \pm \Delta_i^{k,m}\,, \tag{2.5.5}$$

  where $R_i^{k,m}$ is the central value, $\sigma_i^{k,m}$ the combined statistical and uncorrelated systematical uncertainty and $\Delta_i^{k,m}$ the correlated systematical experimental uncertainty.
- For convenience we define $\Delta f_i^{k,m} = \Delta_i^{k,m}/R_i^{k,m}$ to be the relative systematical correlated uncertainty.

As our standard choice concerning the clusters we use 5 different regions each having equidistant cluster sizes ΔE. The regions are as follows:

(0) **non-charm region**: has 1 cluster for 2 GeV $\leq E \leq$ 3.73 GeV ($\Delta E = 1.73$ GeV).

(1) **low charm region**: has 2 clusters for 3.73 GeV $< E \leq$ 3.75 GeV ($\Delta E = 10$ MeV).

(2) $\psi(3S)$ **region/threshold region 1**: has 20 cluster for 3.75 GeV $< E \leq$ 3.79 GeV ($\Delta E =$ 2 MeV).

(3) **resonance region 2**: has 20 cluster for 3.79 GeV $< E \leq$ 4.55 GeV ($\Delta E = 38$ MeV).

(4) **continuum region**: has 10 cluster for 4.55 GeV $< E \leq$ 10.538 GeV ($\Delta E = 598.8$ MeV).

We assign to this choice of $52 + 1$ clusters the notation (2,20,20,10) and later also examine alternative cluster choices demonstrating that the outcome for the moments does within errors not depend on them. The cluster in the non-charm region is used to fit for the normalization constant $n_{\rm ns}$ of the non-charm background contribution, see Eq. (2.5.4).

Our standard procedure to determine the central energy E_m associated to each cluster is just the weighted average of the energies of all measurements falling into cluster m,

$$E_m \;=\; \frac{\sum_{k,i} \dfrac{E_i^{k,m}}{(\sigma_i^{k,m})^2 + (\Delta_i^{k,m})^2}}{\sum_{k,i} \dfrac{1}{(\sigma_i^{k,m})^2 + (\Delta_i^{k,m})^2}}\,. \tag{2.5.6}$$

The corresponding R-value for the charm cross section that we determine through the fit procedure described below is called

$$R_m \;\equiv\; R_{c\bar{c}}(E_m)\,. \tag{2.5.7}$$

We note that using instead the unweighted average or simply the center of the cluster has a negligible effect on the outcome for the moments since the clusters we are employing are sufficiently narrow.

Fit procedure and χ^2-function

We determine the charm cross section $R_{c\bar{c}}$ from a χ^2-function that accounts for the positive correlation among the systematical uncertainties $\Delta_i^{k,m}$ within each experiment k and, at the same time, also for the non-charm background. To implement the correlation we introduce the auxiliary parameters d_k ($k = 1, \ldots, N_{\rm exp}$) that parametrize the correlated deviation from the experimental central values $R_i^{k,m}$ in units of the correlated systematical uncertainty $\Delta_i^{k,m}$, see Eq. (2.5.5). In this way we carry out fits to $R_i^{k,m} + d_k\,\Delta_i^{k,m}$ and treat the d_k as additional auxiliary fit parameters that are constraint to be of order one (one standard deviation) by adding the term

$$\chi^2_{\rm corr}(\{d_k\}) \;=\; \sum_{k=1}^{N_{\rm exp}} d_k^2\,, \tag{2.5.8}$$

to the χ^2-function. To implement the non-charm background we assume that the relative energy dependence of the non-charm cross section related to primary production of u, d and s quarks is described properly by R_{uds} given in Eq. (2.5.4). We then parametrize the non-charm background cross section by the relation

$$R_{{\rm non}-c\bar{c}}(E) \;=\; n_{\rm ns}\,R_{uds}(E) \tag{2.5.9}$$

as already described in Sec. 2.5.1, where the fit parameter $n_{\rm ns}$ is determined mainly from the experimental data in the first clusters below 3.73 GeV by adding the term

$$\chi^2_{\rm nc}(n_{\rm ns},\{d_k\}) \;=\; \sum_{k=1}^{N_{\rm exp}}\sum_{i=1}^{N^{k,1}}\left(\frac{R_i^{k,1}-(1+\Delta f_i^{k,1}\,d_k)\,n_{ns}\,R_{uds}(E_i^{k,1})}{\sigma_i^{k,1}}\right)^2 , \tag{2.5.10}$$

to the χ^2-function. The complete χ^2-function then has the form

$$\chi^2(\{R_m\},n_{\rm ns},\{d_k\}) \;=\; \chi^2_{\rm corr}(\{d_k\}) + \chi^2_{\rm nc}(n_{\rm ns},\{d_k\}) + \chi^2_{\rm c}(\{R_m\},n_{\rm ns},\{d_k\}) , \tag{2.5.11}$$

where

$$\chi^2_{\rm c}(\{R_m\},n_{\rm ns},\{d_k\}) = \tag{2.5.12}$$
$$\sum_{k=1}^{N_{\rm exp}}\sum_{m=2}^{N_{\rm clusters}}\sum_{i=1}^{N^{k,m}}\left(\frac{R_i^{k,m}-(1+\Delta f_i^{k,m}\,d_k)\,(R_m+n_{\rm ns}\,R_{uds}(E_i^{k,m}))}{\sigma_i^{k,m}}\right)^2 .$$

Note that in our approach the non-charm normalization constant $n_{\rm ns}$ is obtained from a combined fit together with the cluster values R_m. We have checked that the effect of using $R_{uds}(E_m)$ instead of $R_{uds}(E_i^{k,m})$ is totally negligible.

This form of the χ^2-function is an extended and adapted version of the ones used in Refs. [111,112]. A special characteristic of the χ^2-functions in Eqs. (2.5.10) and (2.5.12) is that the relative correlated experimental uncertainties $\Delta f_i^{k,m}$ enter the χ^2-function by multiplying the fit value R_m rather than the experimental values $R_i^{k,m}$. This leads to a non-bilinear dependence of the χ^2-function on the d_m and the R_m fit parameters and avoids spurious solutions where the best fit values for the R_m are located systematically below the measurements. Such spurious solutions can arise for data points with substantial positive correlation when χ^2-functions with strictly bilinear dependences are employed [111, 112].

We also note that the implementation of the non-charm background subtraction as given in Eq. (2.5.12) leads to a partial cancellation of systematical uncertainties for the R_m best fit values for the charm cross section. Moreover, it is interesting to mention that in the limit where each cluster contains exactly one measurement (except below threshold, in which we always keep one cluster) the χ^2-function decouples, after performing the change of variables $R'_m = R_m + n_{\rm ns}\,R_{uds}(E^{k,m})$, into the sum of two independent χ^2-functions, one containing data below threshold and depending only on $n_{\rm ns}$ and d_k, and another one containing data above threshold $R^{k,m}$ (we drop the label i because having only one data per cluster it can take only the value 1) and depending only on R'_m. After minimizing the first χ^2-function one can obtain the best fit values for $n_{\rm ns}$ and d_k, denoted by $n_s^{(0)}$ and $d_k^{(0)}$, respectively. The second χ^2 has a minimal value of 0 and the best fit parameters read $R_m^{(0)} = R^{k,m}/(1+d_k^{(0)}\Delta^{k,m}) - n_{\rm ns}^{(0)}R_{uds}(E^{k,m})$.

Close to the minimum the χ^2-function of Eq. (2.5.11) can be written in the Gaussian approximation

$$\chi^2(\{p_i\}) = \chi^2_{\rm min} + \sum_{i,j}(p_i-p_i^{(0)})V_{ij}^{-1}(p_j-p_j^{(0)}) + \mathcal{O}\Big((p-p^{(0)})^3\Big) , \tag{2.5.13}$$

where $p_i = (\{R_m\},n_{\rm ns},\{d_k\})$ and the superscript (0) indicates the respective best fit value. After determination of the correlation matrix V_{ij} by numerically inverting V_{ij}^{-1} we can drop the dependence on the auxiliary variables $n_{\rm nc}$ and d_k and obtain the correlation matrix of the R_m from the R_m-submatrix of V_{ij} which we call $V^R_{mm'}$. In order to separate uncorrelated statistical and systematical uncertainties from correlated systematical ones we compute the complete $V^R_{mm'}$ accounting for all uncertainties and a simpler version of the correlation matrix, $V^{R,u}_{mm'}$ accounting only for uncorrelated uncertainties. The latter is obtained from dropping all correlated errors $\Delta_i^{k,m}$ from the χ^2-function (2.5.11).[15]

[15] In a very good approximation, it can be also obtained by dropping in $V_{i,j}^{-1}$ the rows and columns corresponding to d_k and inverting the resulting matrix. After that one also drops the row and column corresponding to $n_{\rm nc}$. We adopt this simplified procedure for our numerical fits.

The outcome of the fit for the sum of the charm and the non-charm cross section in the threshold and the data continuum region using the standard data set explained above is shown in Figs. 2.12(a)-(f) together with the input data sets. The red line segments connect the best fit values and the brown band represents the combined total uncertainty. The clusters are indicated by dashed vertical lines. For completeness we have also given all numerical results for the R_m values in Appendix A. There we also give results for the minimal and maximal data set selections.

The fit results in the continuum region for the energies between 4.55 GeV and 10.538 GeV allow for an interesting comparison of the R-values obtained from perturbative QCD and from experimental data based on our combined fit procedure. In the left panel of Fig. 2.13 the fit results for the charm cross section are shown together with the perturbative QCD prediction from Eq. (2.5.2) (black solid line). Within the total experimental errors, which are around 5%, there is good agreement between data and the perturbative QCD result (which itself has a perturbative error due to scale variations of less than 1%). Interestingly, there appears to be some oscillatory behavior of the data around the perturbative QCD result, although the statistical power of the data is insufficient to draw definite conclusions concerning the physics of these oscillations. Concerning the contributions to the moments we find $M_{1,\rm ex}^{(4.55-10.538)\rm GeV} = 4.81 \pm 0.18$ from the data compared to $M_1^{(4.55-10.538)\rm GeV} = 5.010 \pm 0.011$ from perturbative QCD based on Eq. (2.5.2). The central value from perturbative QCD is 4% above the experimental moment. This shows that adopting perturbative QCD predictions instead of data gives a contribution to the central value of the moments compatible within the experimental uncertainties. However, using theoretical uncertainties as an estimate for the experimental ones leads to an underestimate. In the right panel of Fig. 2.13 the experimental data and the perturbative QCD predictions are compared for the total hadronic cross section. Here the perturbative QCD result is shifted downward with respect to the data due to the non-charm normalization constant $n_{\rm ns}$ obtained from our combined fit being slightly larger than unity, see Eq. (A.2). Overall, the agreement between the combined data and perturbative QCD appears to be even better than for the charm cross section in particular for the energy region above 9 GeV.

Final Results for the Charm Experimental Moments

Region (I): Narrow resonances

For the J/ψ and ψ' charmonium contributions to the experimental moments we use the narrow width approximation,

$$M_n^{\rm res} \;=\; \frac{9\,\pi\,\Gamma_{ee}}{\alpha(M)^2 M^{2n+1}}\,, \tag{2.5.14}$$

with the input numbers given in Tab. 2.1. We neglect the tiny uncertainties in the charmonium masses as their effects are negligible.

Region (II): Threshold and data continuum region

For the determination of the moment contributions from the threshold and the continuum region between 3.73 and 10.538 GeV we use the results for the clustered $c\bar{c}$ cross section values R_m determined in Sec. 2.5.1 and the trapezoidal rule. We employ a linear interpolation for the cross section but keep the analytic form of the integration kernel $1/s^{n+1}$ exact by including it into the integration measure. Using the relation $\mathrm{d}s/s^{n+1} = \mathrm{d}(E^{-2n}/n)$ we thus obtain

$$\begin{aligned} M_n^{\rm thr+cont} &= \frac{1}{2n}\Bigg[\sum_{i=1}^{N_{\rm clusters}} R_i\left(\frac{1}{E_{i-1}^{2n}}-\frac{1}{E_{i+1}^{2n}}\right)+R_0\left(\frac{1}{E_0^{2n}}-\frac{1}{E_1^{2n}}\right)\\ &+ \quad R_{N_{\rm clusters}+1}\left(\frac{1}{E_{N_{\rm clusters}}^{2n}}-\frac{1}{E_{N_{\rm clusters}+1}^{2n}}\right)\Bigg]\,, \end{aligned} \tag{2.5.15}$$

where R_0 and E_0 are the R and energy values at the lower boundary of the smallest energy cluster, and $R_{N_{cl}+1}$ and $E_{N_{cl}+1}$ are the corresponding values of the upper boundary of the highest energy

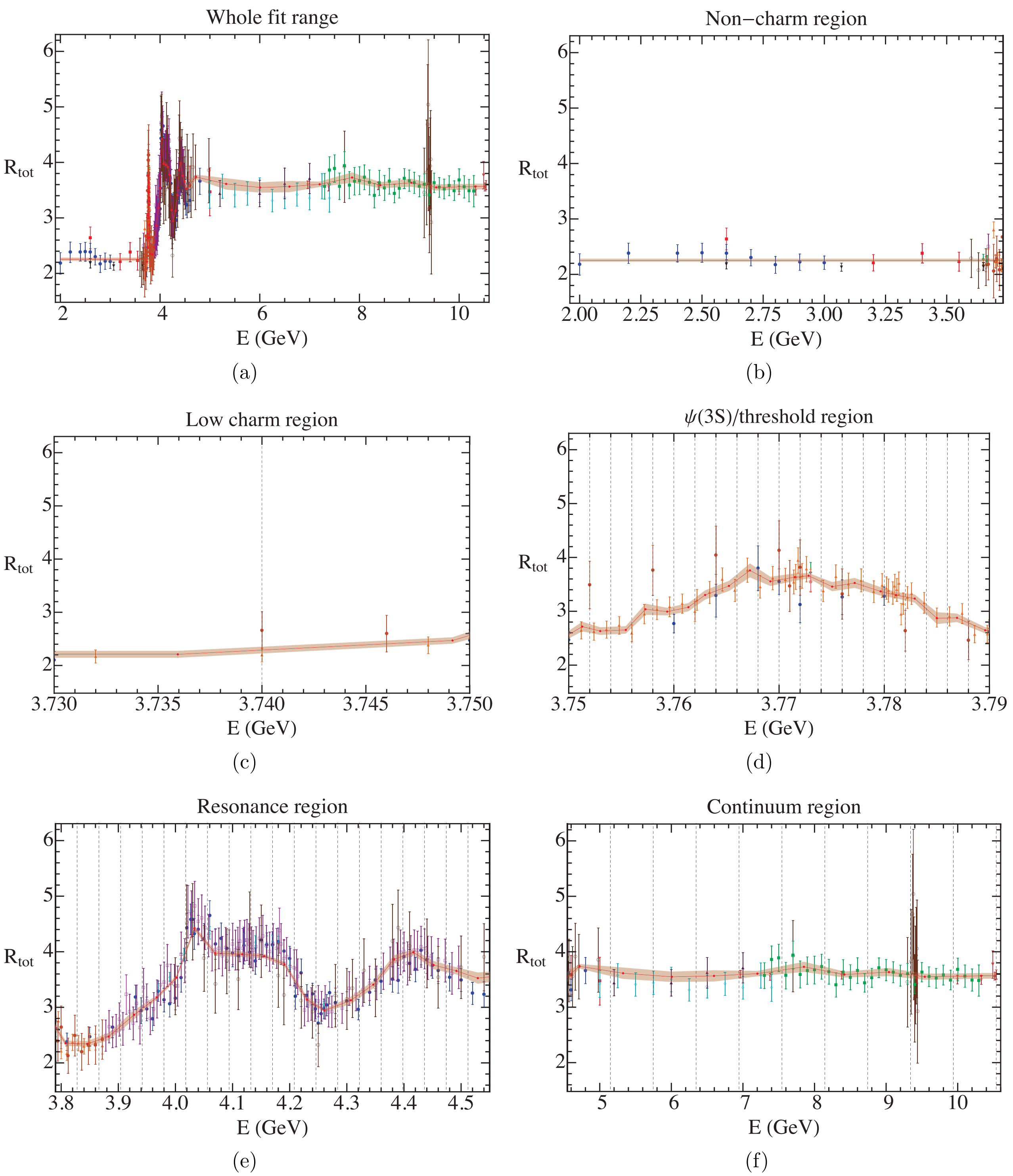

Figure 2.12: Result of the fit for the default selection of data sets. On the top, (a) and (b) show the entire fit region and the non-charm region, respectively. In the middle row, (c) illustrates the low charm region and (d) the threshold region 1. In the bottom line (e) and (f) depict threshold region 2 and the data continuum region, respectively.

cluster. The values for R_0 and $R_{N_{cl}+1}$ are obtained from linear extrapolation using the R_m values of

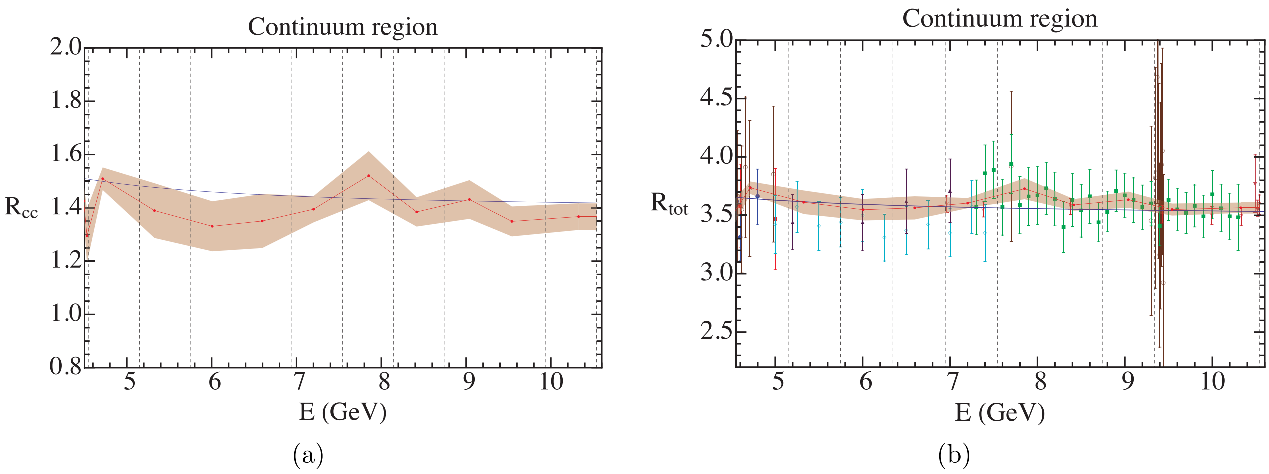

Figure 2.13: Comparison of experimental data (red dots) with uncertainties (brown error band) and the predictions from perturbative QCD (black solid line) for the charm cross section $R_{c\bar{c}}$ (left panel) and the total cross section $R_{\rm tot}$ (right panel).

the two closest lying clusters[16] m' and $m'+1$ with the formula

$$R(E) \;=\; \frac{R_{m'+1} - R_{m'}}{E_{m'+1} - E_{m'}}\,(E - E_{m'}) + R_{m'}\,. \tag{2.5.16}$$

For the computation of the moment contributions from subintervals within the range between 3.73 and 10.538 GeV we also use Eq. (2.5.15) using corresponding adaptations for the boundary values at $m = 0$ and $m = N_{cl} + 1$.

Region (III): Perturbative QCD region

For the region above 10.538 GeV where we use the perturbative QCD input described in Eqs. (2.5.1) and (2.5.2) for the charm R-ratio the contribution to the experimental moment is obtained from the defining equation (2.2.7) with a lower integration limit of 10.538 GeV:

$$M_n^{\rm QCD} \;=\; \gamma \times \int_{(10.538\,{\rm GeV})^2}^{\infty} {\rm d}s\, \frac{R_{cc}^{\rm th}(s)}{s^{n+1}}\,. \tag{2.5.17}$$

The variable γ is an auxiliary variable used to parametrize the 10% uncertainty we assign to the perturbative QCD contribution,

$$\gamma \;=\; 1.0 \pm 0.1\,. \tag{2.5.18}$$

Final Results for the Charm Experimental Moments

The experimental moments are obtained from the sum of the resonance, threshold plus continuum and perturbative QCD contributions described just above,

$$M_n^{\rm exp} \;=\; M_n^{\rm res} + M_n^{\rm thr+cont} + M_n^{\rm QCD}\,. \tag{2.5.19}$$

To determine the uncertainties we account for the errors in the e^+e^- widths of J/ψ and ψ' and in the cluster values R_m, and for the 10% assigned uncertainty in $M_n^{\rm QCD}$. For the evaluation we use the usual error propagation based on a $\bar{m} \times \bar{m}$ correlation matrix with $\bar{m} = N_{cl} + 3$. The correlation matrix of the experimental moments thus has the form

$$C_{nn'}^{\rm exp} \;=\; \sum_{i,j=1}^{N_{cl}+3} \left(\frac{\partial M_n^{\rm exp}}{\partial \bar{R}_i}\right)\left(\frac{\partial M_{n'}^{\rm exp}}{\partial \bar{R}_j}\right) V_{ij}^{\bar{R}}\,, \tag{2.5.20}$$

[16]For R_0 we have $m' = 1$ and for $R_{N_{cl}+1}$ we have $m' = N_{cl} - 1$.

n	Resonances	3.73 − 4.8	4.8 − 7.25	7.25 − 10.538	10.538 − ∞	Total
1	11.91(17|20)	3.23(4|6)	3.39(8|13)	1.42(2|5)	1.27(0|13)	21.21(20|30)
2	11.68(18|20)	1.78(2|3)	1.06(3|4)	0.200(3|7)	0.057(0|6)	14.78(18|21)
3	11.63(18|20)	1.00(1|2)	0.350(9|13)	0.0294(6|10)	0.0034(0|3)	13.02(19|20)
4	11.73(19|20)	0.571(7|11)	0.121(3|4)	0.00448(9|15)	$2.3(0\|2) \times 10^{-4}$	12.43(19|20)

Table 2.4: Result for the experimental moments for the standard selection of data sets. The second column collects the contribution from the narrow resonances J/ψ and ψ' treated in the narrow width approximation. Third to fifth columns are shown only as an illustration, but use the outcome of the fit to the entire fit region, 3.73 − 10.538 GeV. The sixth column is obtained using perturbation theory, and the last column shows the number for the complete moment. For the moment $M_n^{\rm exp}$ all numbers are given in units of $10^{-(n+1)}\,{\rm GeV}^{-2n}$.

n	Resonances	3.73 − 4.8	4.8 − 7.25	7.25 − 10.538	10.538 − ∞	Total
1	11.91(17|20)	3.14(6|8)	3.24(9|16)	1.38(2|6)	1.27(0|13)	20.95(21|33)
2	11.68(18|20)	1.75(3|4)	1.01(3|5)	0.195(4|9)	0.057(0|6)	14.69(18|21)
3	11.63(18|20)	0.99(2|3)	0.33(1|2)	0.0287(6|12)	0.0034(0|3)	12.99(19|20)
4	11.73(19|20)	0.57(1|1)	0.114(4|5)	0.0044(1|2)	$2.3(0\|2) \times 10^{-4}$	12.42(19|20)

Table 2.5: Results for the experimental moments for the minimal selection of data sets. Conventions are as in Tab. 2.4. All moments are given in units of $10^{-(n+1)}\,{\rm GeV}^{-2n}$.

n	Resonances	3.73 − 4.8	4.8 − 7.25	7.25 − 10.538	10.538 − ∞	Total
1	11.91(17|20)	3.19(3|5)	3.60(6|6)	1.54(2|4)	1.27(0|13)	21.50(19|27)
2	11.68(18|20)	1.77(2|3)	1.11(2|2)	0.217(4|5)	0.057(0|6)	14.83(18|20)
3	11.63(18|20)	1.00(1|2)	0.361(7|7)	0.0319(6|8)	0.0034(0|3)	13.03(19|20)
4	11.73(19|20)	0.57(1|1)	0.123(3|2)	0.0049(1|1)	$2.3(0\|2) \times 10^{-4}$	12.43(19|20)

Table 2.6: Results for the experimental moments for the maximal selection of data sets. Conventions are as in Tab. 2.4. All moments are given in units of $10^{-(n+1)}\,{\rm GeV}^{-2n}$.

where we have $\bar{R}_i = (\{R_m\}, \Gamma_{e^+e^-}(J/\psi), \Gamma_{e^+e^-}(\psi'), \gamma)$. The entries of $V^{\bar{R}}$ in the R_m subspace are just the entries of the correlation matrix V^R obtained from the cluster fit. The diagonal entries in the $\Gamma_{e^+e^-}$ subspace are the combined statistical and systematical uncertainties of the e^+e^- widths and the $\delta\gamma = 0.1$ for $M_n^{\rm QCD}$, respectively. We treat the latter uncertainty as uncorrelated with all other uncertainties. So all non-diagonal entries of $V_{ij}^{\bar{R}}$ for i or $j = N_{cl}+3$ are zero. For the uncertainty of the e^+e^- widths we adopt a model where the (quadratic) half of the error is uncorrelated and the other (quadratic) half is positively correlated among the two narrow resonances, while we assume no correlation between the narrow resonances and the R_n cluster values.[17] Thus for the corresponding non-diagonal entries of $V_{i,j}^{\bar{R}}$ with $i \in \{1, N_{cl}\}$ and $j = \{N_{cl}+1, N_{cl}+2\}$ we have the entries $V_{ij}^{\bar{R}} = 0$, and for $i = N_{cl}+1$ and $j = N_{cl}+2$ we have $V_{ij}^{\bar{R}} = \delta\Gamma^1_{e^+e^-}\delta\Gamma^2_{e^+e^-}/2$, where $\delta\Gamma^{1,2}_{e^+e^-}$ are the respective e^+e^- width total uncertainties for J/ψ and ψ', respectively. The results for the moments showing separately the contributions from the resonances, various energy subintervals and their total sum using the defaults data set collection (see Sec. 2.5.1) are given in Tab. 2.4. Using Eq. (2.5.20) it is straightforward to compute the correlation matrix of the moments, and we obtain

$$C^{\rm exp} \;=\; \begin{pmatrix} 0.128 & 0.084 & 0.077 & 0.075 \\ 0.084 & 0.076 & 0.074 & 0.075 \\ 0.077 & 0.074 & 0.075 & 0.077 \\ 0.075 & 0.075 & 0.077 & 0.079 \end{pmatrix}, \tag{2.5.21}$$

for the total correlation matrix accounting for all correlated and uncorrelated uncertainties. We remind

[17] We thank J. J. Hernández Rey for pointing out that, although a coherent study of these correlations does not exist, treating resonances as uncorrelated to the continuum represents the most appropriate correlation model.

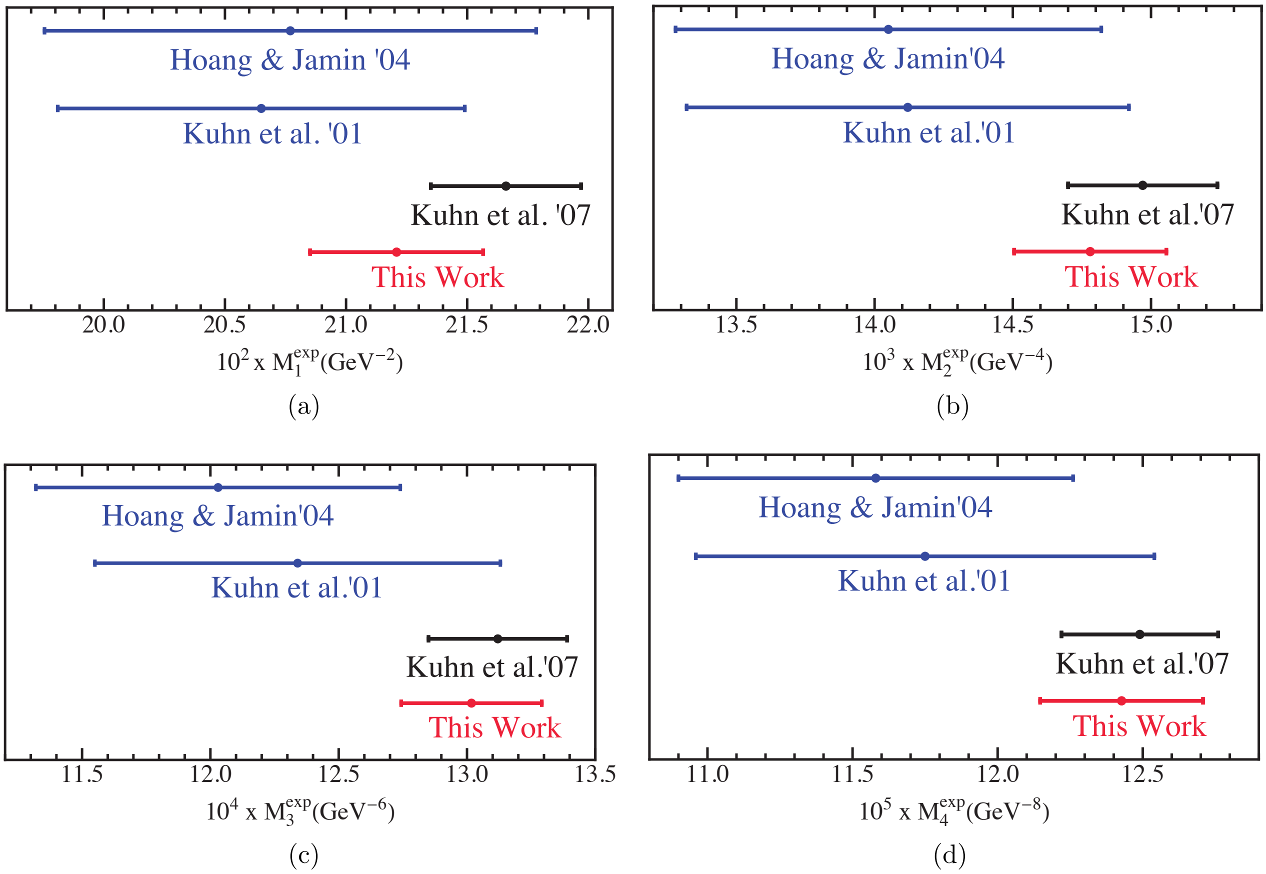

Figure 2.14: Comparison of determinations of the experimental moments. Blue lines refer to analyses in which outdated values for the parameters of the narrow resonances [84] have been used.

n	This work	Kuhn et al.'07 [8]	Kuhn et al.'01 [24]	Hoang & Jamin'04 [121]
1	21.21(20|30)	21.66(31)	20.65(84)	20.77(47|90)
2	14.78(18|21)	14.97(27)	14.12(80)	14.05(40|65)
3	13.02(18|20)	13.12(27)	12.34(79)	12.20(41|57)
4	12.43(19|20)	12.49(27)	11.75(79)	11.58(43|53)

Table 2.7: Comparison of our results for experimental moments to those from previous publications with a dedicated data analysis. The second column contains our results using the default setting. The third and fourth columns were determined from the same collaboration and use data from Refs. [93, 95] (our datasets 2, 4) and [93] (our dataset 2), respectively. The results in the fourth column were also used in the charm mass analysis of Ref. [7]. The numbers in the fifth column used data from Refs. [93, 100, 104] (our datasets 2, 10, 14). The moments in the third column use (slightly less precise) experimental data on the narrow resonances from [144]. The moments in the last two columns were obtained using (less precise) experimental data on the narrow resonances [84]. These data have been updated later [145]. All moments are given in units of $10^{-(n+1)}\,\mathrm{GeV}^{-2n}$.

the reader that all numbers related to the moment $M_n^{\rm exp}$ are given in units of $10^{-(n+1)}\,\mathrm{GeV}^{-2n}$. To quote correlated and uncorrelated uncertainties separately it is also useful to show the correlation matrix that is obtained when only uncorrelated uncertainties are accounted for

$$C_{\rm uc}^{\rm exp} = \begin{pmatrix} 0.04 & 0.034 & 0.033 & 0.034 \\ 0.034 & 0.033 & 0.034 & 0.034 \\ 0.033 & 0.034 & 0.034 & 0.036 \\ 0.034 & 0.034 & 0.036 & 0.037 \end{pmatrix} . \tag{2.5.22}$$

These results can be used to carry out combined simultaneous fits to several of the moments. This is, however, not attempted in this work.

2.5.2 Computation of the Experimental Moments for the Bottom Correlator

In this section we present our computation of the moments for the bottom vector current correlator from experimental data. Similar to charm calculations, the bottom experimental moments are made of three distinct contributions: the narrow resonances below threshold, the region of broader resonances, explored by BABAR [146], and the continuum region, where no data has been taken and requires modeling.

Narrow Resonances

The contribution of resonances below the open bottom threshold $\sqrt{s} = 10.62\,\mathrm{GeV}$ includes $\Upsilon(1S)$ up to $\Upsilon(4S)$. We use the narrow width approximation in Eq. (2.5.14) to compute their contribution to the experimental moments. The masses and electronic widths of these four resonances are taken from the PDG [83], and the values of the effective electromagnetic coupling constant evaluated at the Υ masses are taken from Ref. [8]. This information is collected in Table 2.8. We have also checked

	$\Upsilon(1S)$	$\Upsilon(2S)$	$\Upsilon(3S)$	$\Upsilon(4S)$
$M_\Upsilon(\mathrm{GeV})$	9.46030(26)	10.02326(31)	10.3552(5)	10.5794(12)
$\Gamma_{\mathrm{ee}}(\mathrm{KeV})$	1.340(18)	0.612(11)	0.443(8)	0.272(29)
$\left(\frac{\alpha_{\mathrm{QED}}}{\alpha(M_\Upsilon)}\right)^2$	0.932069	0.93099	0.930811	0.930093

Table 2.8: Masses and electronic widths of narrow Υ resonances [83] and effective electromagnetic coupling constant [8]. $\alpha_{\mathrm{QED}} = 1/137.035999084(51)$ represents the fine structure constant.

that if one uses a Breit-Wigner instead of the narrow width approximation the results change by an amount well within the error due to the uncertainty in the electronic width. In analogy to what we found in our study of the charm moments, the effect of the mass uncertainty in the moments is negligible. Therefore one only needs to consider the experimental uncertainty in the electronic widths. There is no information on the correlation between the measurements of these widths. The PDG averages of the electronic partial widths for the first three resonances is dominated by the CLEO measurement [147].[18] Therefore we take the approach that half of the width's uncertainty (in quadrature) is uncorrelated (therefore mainly of statistical origin), whereas the other half is correlated among the various resonances (therefore coming from common systematics in the measurements).

Threshold Region

The region between the open bottom threshold and the experimental measurement of the R_b-ratio at the highest energy, $10.62\,\mathrm{GeV} \leq \sqrt{\mathrm{s}} \leq 11.2062\,\mathrm{GeV}$, is referred to as the threshold region. The region above the last experimental measurement will be collectively denoted as the continuum region. The first experimental data close to the B meson threshold were taken by the CLEO [100, 101, 148] and CUSB [149] collaborations. The measurements at each c.m. energy have a 6% systematic uncertainty. More recently the BABAR collaboration [146] has measured the R_b-ratio in the energy region between 10.54 GeV and 11.20 GeV, with significantly higher statistics and better control of systematic uncertainties (of the order of 3%). These measurements are taken in small energy bins, densely populating the threshold region. The BABAR data supersedes the older data of CLEO and CUSB, and it has already been used in Refs. [9, 114, 124], in which the bottom mass was also determined.

[18] Refs. [8, 9] assume that the error of the electronic width for the first three narrow resonances is 100% correlated, and uncorrelated to that of the $\Upsilon(4S)$.

This BABAR data for the R_b-ratio has not been corrected for initial-state radiation and vacuum polarization effects. Moreover, the effect of the $\Upsilon(4S)$ resonance has not been subtracted,[19] so we have performed the subtraction ourselves, using the Breit-Wigner approximation and using for the total width the PDG value $\Gamma_{4S} = 20.5\,\mathrm{MeV}$:

$$R^{\mathrm{BW}}(s) = \frac{9\,M_{4S}^2\,\Gamma_{\mathrm{ee}}^{4S}}{\alpha(M_{4S})^2}\frac{\Gamma_{4S}}{(s-M_{4S}^2)^2+\Gamma_{4S}^2 M_{4S}^2}\,. \tag{2.5.23}$$

For the subtraction of the $\Upsilon(4S)$ resonance and the correction for the initial state radiation we take an approach similar to Ref. [9].

Subtraction of the $\Upsilon(4S)$ Radiative Tail

Before subtracting the radiative tail of the $\Upsilon(4S)$ resonance one has to account for vacuum polarization effects. BaBar experimental data has been normalized to the theoretical Born level dimuon cross section (using the fine structure constant rather than the running effective electromagnetic coupling), instead of normalizing to the number of events with muons in the final state. Therefore one has to multiply the BaBar data with $[\alpha(s)/\alpha_{\mathrm{em}}]^2$, which we take as constant with value 0.93.

The contribution to be subtracted from the BABAR data (already corrected for vacuum polarization effects) is the ISR-distorted tail of the $\Upsilon(4S)$, which reaches to energies above its mass. The cross section R and the ISR-distorted cross-section $\hat{R}$ are related by a convolution relation

$$\hat{R}(s) = \int_{z_0}^{1}\frac{\mathrm{d}z}{z}\,G(z,s)\;R(s\,z)\,, \tag{2.5.24}$$

which can be used to determine the ISR effects on the $\Upsilon(4S)$ resonance given in Eq. (2.5.23). Here the lower integration bound is $z_0 = (10\,\mathrm{GeV})^2/\mathrm{s}$. This value is not fully fixed by theoretical arguments, and it is chosen such that it excludes the narrow resonances, but keeps the major part of the $\Upsilon(4S)$ line shape. The radiator function G is given as [150, 151]

$$\begin{aligned} G(z,s) &= (1-z)^{\beta(s)\,-\,1}\,\tilde{G}(z,s)\,, \\ \widetilde{G}(z,s) &= \beta(s)\,e^{\delta_{\mathrm{yfs(s)}}}\,F(s)\big[\,\delta_C^{V+S}(s)+\delta_C^{H}(s,z)\,\big]\,, \end{aligned} \tag{2.5.25}$$

where the specific form of β, F and the two δ's can be found in Eq. (7) of [9]. Note that the function $G(z,s)$ is divergent as $z\to 1$, but since $0<\beta-1<-1$, it is integrable. The divergent behavior is absent in $\widetilde{G}$, which in the limit $z\to 1$ reduces to

$$\widetilde{G}(1,s) \;=\; \beta(s)\,e^{\delta_{\mathrm{yfs}}(s)}\,F(s)\,\delta_C^{V+S}(s)\,. \tag{2.5.26}$$

After subtracting the radiative tail of the $\Upsilon(4S)$ we find that to a good approximation the cross section vanishes for energies below 10.62 GeV. Therefore we add an additional point to our BABAR dataset: $R_b(10.62\,\mathrm{GeV}) = 0$ and take $R_b = 0$ for energies below 10.62 GeV. Since the subtracted cross section does not exactly vanish between 10.5408 GeV and 10.62 GeV, we take the (small) contribution of the subtracted cross section in that region to the moments as an additional source of systematic correlated uncertainty.

Deconvolution of Initial-State Radiation

After subtraction of the radiative tails and correcting for vacuum polarization effects, the BABAR threshold data are corrected for ISR. The inversion of the convolution in Eq. (2.5.24), can be carried

[19] The radiative tails of the first three resonances are provided by BABAR, so they can be subtracted at the data level, before correcting for vacuum polarization effects.

out in an iterative way [9]. Defining $\delta G(z,s) = G(z,s) - \delta(1-z)$ one can use a successive series of approximations

$$R^j(s) = R^0(s) - \int_{z_0}^{1} \frac{\mathrm{d}z}{z}\, \delta G(z,s)\, R^{j-1}(s\,z), \tag{2.5.27}$$

where we denoted the j-th approximation of $R(s)$ as $R^j(s)$ and use as starting point $R^0(s) = \hat{R}(s)$, the BABAR data after correcting for vacuum polarization effects and subtracting the radiative tails. In Eq. (2.5.27) we take $z_0 = (10.62\,\mathrm{GeV})^2/s$, using as a starting point the energy value for which the cross section vanishes after the subtraction of the radiative tails. To isolate the singularity at the higher endpoint one can perform a subtraction at $z = 1$, resulting in:

$$\begin{aligned} R^j(s) \;&=\; R^0(s) + R^{j-1}(s) - \int_{z_0}^{1} \frac{\mathrm{d}z}{z}\, \big(1-z\big)^{\beta(s)\,-\,1} \Big[\widetilde{G}(z,s)\, R^{j-1}(s\,z) - z\, \widetilde{G}(1,s)\, R^{j-1}(s)\Big] \\ &-\; \frac{1}{\beta(s)}\, \widetilde{G}(1,s)\, R^{j-1}(s) \big(1-z_0\big)^{\beta(s)} . \end{aligned} \tag{2.5.28}$$

We use the trapezoidal rule to evaluate the integration on the discrete set of experimental data measurements labeled by the index i. Changing the integration variable from z to energy we find

$$\begin{aligned} R^j_i &= R^0_i + R^{j-1}_i + \widetilde{G}(1,E_i^2) R^{j-1}_i \left(1 - \frac{E_1^2}{E_i^2}\right)^{\beta(E_i^2)} \left(\frac{E_1(E_2 - E_1)}{E_i^2 - E_1^2} - \frac{1}{\beta(E_i^2)}\right) \\ &- \sum_{k=2}^{i-1} \left(1 - \frac{E_k^2}{E_i^2}\right)^{\beta(E_i^2)\,-\,1} E_k \left[\widetilde{G}\left(\frac{E_k^2}{E_i^2}, E_i^2\right) \frac{R^{j-1}_k}{E_k^2} - \widetilde{G}(1,E_i^2) \frac{R^{j-1}_i}{E_i^2}\right] (E_{k+1} - E_{k-1})\,, \end{aligned} \tag{2.5.29}$$

where we have used $R^j_1 = R(10.62\,\mathrm{GeV}) \equiv 0$ for all iterations. After applying the procedure as many times as necessary to obtain a stable solution, one obtains the ISR-corrected cross section. Among the experimental measurements one finds two data points taken at very similar values of the energy: 10.86 GeV and 10.8605 GeV. It turns out that the fact that they lie very close makes the iterative procedure unstable. Therefore we drop the latter point from our analysis.

In Fig. 2.15 we show the BABAR data after the subtraction of all radiative tails, before (red) and after (blue) ISR and vacuum polarization corrections.

Determination of the Unfolding Error Matrix

The BABAR collaboration splits the experimental uncertainties into statistical, systematic uncorrelated, and systematic correlated. We add the two former in quadrature to obtain the total uncorrelated uncertainty $\epsilon^{\mathrm{uncor}}$ and rename the latter as the total correlated uncertainty ϵ^{cor}. The removal of the radiative tails of the Υ mesons has no effect on these uncertainties. Therefore, the correlation matrix for the BABAR data after the subtraction of the radiative tails, before it is corrected for ISR effects, can be written as

$$M^{0\,0}_{ij} = (\epsilon^{\mathrm{uncor}}_i)^2\, \delta_{ij} + \epsilon^{\mathrm{cor}}_i \epsilon^{\mathrm{cor}}_j\,. \tag{2.5.30}$$

One needs to compute a new correlation matrix after each iteration. In this way we determine the unfolding error matrix.

The master formula in Eq. (2.5.29) can be cast in a matrix form as follows:

$$R^j_i = R^0_i + \sum_{k=2}^{i} G_{ik} R^{j-1}_k\,, \tag{2.5.31}$$

where R^j_i is to be thought as the i-th component of the column vector R^j, and G_{ik} represents the (i,k)-component of a matrix G. Here R^j_i depends only on the initial value R^0_i and the result of the

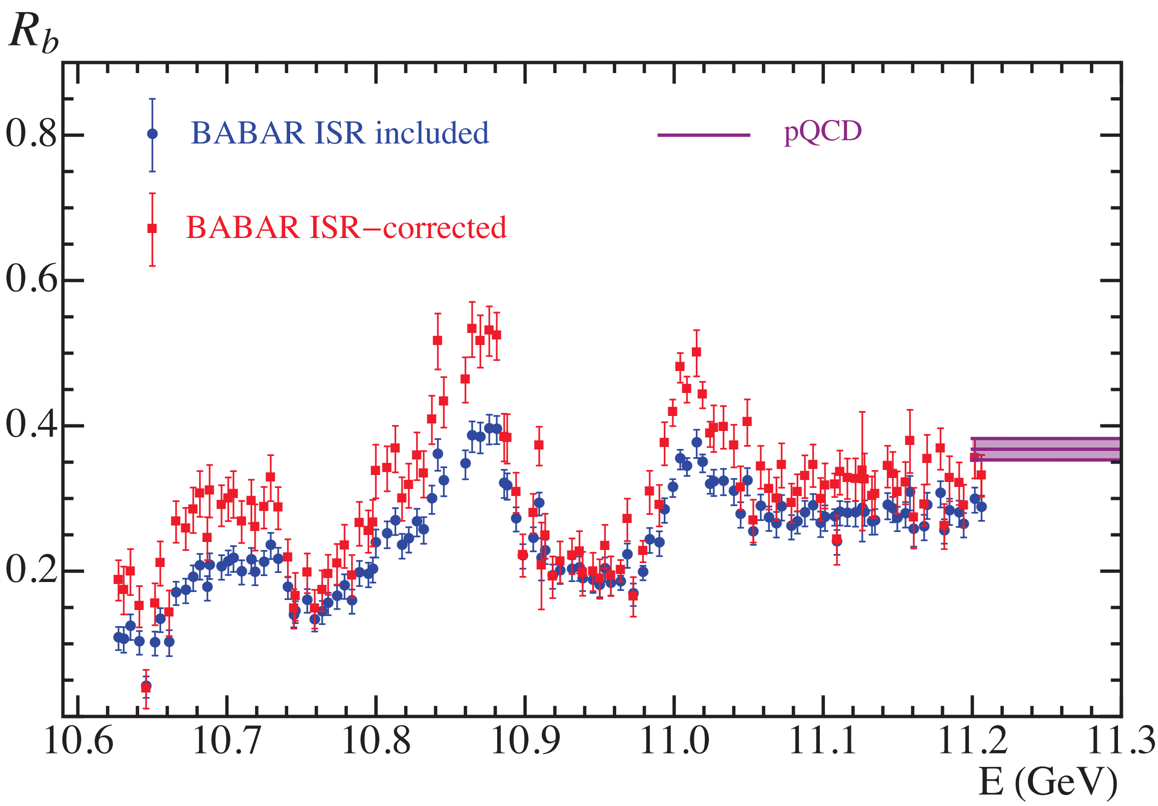

Figure 2.15: BABAR experimental data before (blue) and after (red) the ISR correction is applied. The purple bar on the right refers to the pQCD prediction for the continuum region. We have removed one data point at $E = 10.8605\,\text{GeV}$.

previous iteration R_i^{j-1}. The G_{ik} do not depend on R_k^j or the iteration step j. Therefore, for the error propagation one uses

$$\frac{\partial R_i^j}{\partial R_k^0} = \delta_{ik}\,, \qquad \frac{\partial R_i^j}{\partial R_k^{j-1}} = G_{ik}\,, \tag{2.5.32}$$

both of them j-independent. We will denote with $M^{j\,j}$ the correlation matrix among the entries of the vector R^j for a given iteration j. We also find it convenient to introduce the correlation matrix among R^j and R^0, referred to as $M^{j\,0}$. Finally we use the notation $M^{0\,j} \equiv (M^{j\,0})^T$. We find for the correlation matrix after j iterations:

$$\begin{aligned} M^{j\,j} &= M^{0\,0} + M^{0\,j-1}\,G^T + G\,M^{(j-1)\,0} + G\,M^{(j-1)\,(j-1)}\,G^T, \\ M^{j\,0} &= M^{0\,0} + G\,M^{(j-1)\,0}, \end{aligned} \tag{2.5.33}$$

were the elements of the matrix $M^{0\,0}$ are given in Eq. (2.5.30). We find that after five iterations the result has converged already to a level well below the experimental uncertainties. Our unfolded BaBar data agrees well with that worked out in Ref. [124].

Contribution of the Threshold Region

After having corrected BABAR data for ISR and vacuum polarization effects, we use the trapezoidal rule (similar to Eq. (2.5.15)) for integrating the threshold region between 10.62 GeV and 11.20 GeV:

$$M_n^{\rm thr} = \frac{1}{2n}\left[\sum_{i=2}^{N-1} R_i\left(\frac{1}{E_{i-1}^{2n}} - \frac{1}{E_{i+1}^{2n}}\right) + R_N\left(\frac{1}{E_{N-1}} - \frac{1}{E_N}\right)\right], \tag{2.5.34}$$

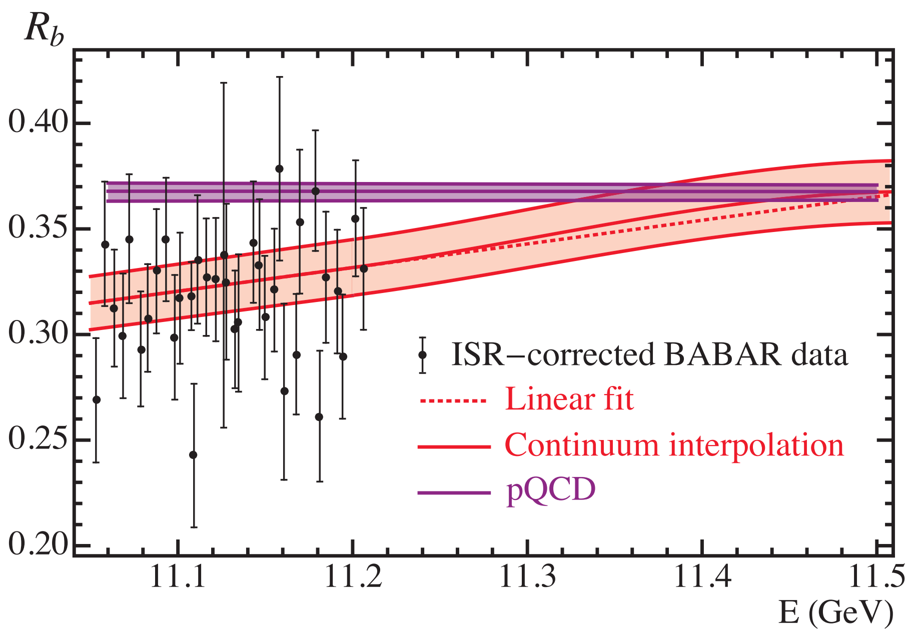

Figure 2.16: Comparison of ISR-corrected BABAR data in the continuum region (black dots with error bars) with pQCD (purple band). The red band shows our reconstruction of the continuum, which includes a linear fit to the BaBar data, patched to the pQCD prediction in a smooth way using a cubic polynomial in the energy.

where R_i has been already ISR corrected and N is the number of data points. We have added the boundary condition point $R_1 = R(10.62) = 0$. From Eq. (2.5.34) one can compute the correlation matrix among M_n^{thr} for various n values, using the unfolding matrix among the R_i computed in Sec. 2.5.2.

Continuum Region

For the determination of the experimental moments from the region above 11.2 GeV we use pQCD (which has essentially negligible errors) supplemented by a modeling uncertainty. Comparing pQCD (purple line in Fig. 2.16) to a linear fit to the BaBar data in the region between 11.06 GeV and 11.2 GeV (red dotted line in Fig. 2.16) we find a 10% discrepancy concerning the central values. The fit function has a roughly constant 4% relative uncertainty. The fit linear function shows a growing pattern such that it would meet the pQCD prediction at around 11.5 GeV. This result is very robust, since a quadratic fit yields the same meeting point. To model the continuum in the region between 11.2 GeV and 11.52 GeV we patch together the linear fit function to the BaBar data and the result of pQCD above 11.52 GeV using a cubic function, demanding continuity and smoothness at 11.2 GeV and 11.52 GeV. The result is shown as the central red line in Fig. 2.16. Given that the relative discrepancy between experiment and pQCD for R_b at the Z-pole is about 0.3% [152], we adopt a relative modeling error that decreases linearly from 4% at 11.2 GeV to 0.3% at m_Z, and stays constant for energies larger than m_Z. This is shown as the red band in Fig. 2.16. This uncertainty makes up for 96.9% of the total error for the first moment M_1^V (which has an total 2.45% relative error), and 86.15% of the second moment M_2^V (which has a total 1.85% relative error). Note that if we would adopt a constant 4% error for all energies above 11.2 GeV, this continuum uncertainty would make up for 97.24% of the total error for the first moment M_1^V (from a total 2.60% relative error), and 86.46% of the second moment M_2^V (from a total 1.87% relative error). The difference is small because contributions from higher energies are suppressed. Following the procedure i.e. described in the charm experimental moments, we consider this uncertainty as fully correlated for the various moments, but without any correlation to the narrow resonances or the threshold region.

We use the same theoretical expression which is given in Eq. (2.5.1) for perturbative QCD while the number of active flavors is set to $n_f = 5$. This includes the non-singlet massless quark cross section supplemented with bottom mass corrections up to $O(\overline{m}_b^4/s^2)$.[20] It takes into account only contributions from the electromagnetic current coupled to the bottom quark. It reads: [137–141][21]

$$R_{b\bar{b}}^{\rm th}(s) = N_c\, Q_b^2\, R^{\rm ns}(s, \overline{m}_b^2(\sqrt{s}), n_f = 5, \alpha_s^{(n_f=5)}(\sqrt{s}))\,, \tag{2.5.35}$$

where

$$\begin{aligned}
&R^{\rm ns}(s, \overline{m}_b^2(\mu), n_f = 5, \alpha_s^{(n_f=5)}(\mu), \mu)\\
&= 1 + \frac{\alpha_s}{\pi} + \Big(\frac{\alpha_s}{\pi}\Big)^2 (1.40923 - 1.91667\, L_s) + \Big(\frac{\alpha_s}{\pi}\Big)^3 (-\,12.7671 - 7.81872\, L_s + 3.67361\, L_s^2\,)\\
&+ \frac{\overline{m}_b^2(\mu)}{s}\Big[12\frac{\alpha_s}{\pi} + \Big(\frac{\alpha_s}{\pi}\Big)^2 (104.833 - 47\, L_s) + \Big(\frac{\alpha_s}{\pi}\Big)^3 (541.753 - 724.861\, L_s + 137.083\, L_s^2\,)\Big]\\
&+ \frac{\overline{m}_b^4(\mu)}{s^2}\Big[-\,6 + \Big(\frac{\alpha_s}{\pi}\Big)(-\,22 + 24\, L_s) + \Big(\frac{\alpha_s}{\pi}\Big)^2 (139.014 - 4.83333\, L_m + 214.5\, L_s - 71\, L_s^2\,)\\
&+ \Big(\frac{\alpha_s}{\pi}\Big)^3\,(3545.81 - 158.311\, L_m + 9.66667\, L_m^2 - 538.813\, L_s + 37.8611\, L_m\, L_s\\
&-\,1037.79\, L_s^2 + 185.389\, L_s^3\,)\Big]\,,
\end{aligned} \tag{2.5.36}$$

with

$$L_s \equiv \ln\Big(\frac{s}{\mu^2}\Big), \quad L_m \equiv \ln\Big(\frac{\overline{m}_b^2(\mu)}{s}\Big), \quad \alpha_s = \alpha_s^{(n_f=5)}(\mu)\,. \tag{2.5.37}$$

We use the initial conditions $\overline{m}_b(\overline{m}_b) = 4.2\,$GeV and $\alpha_s(m_Z) = 0.118$. Therefore, for the continuum region we use the following expression,

$$\begin{aligned}
M_n^{\rm pQCD} = &\int_{s_0}^{s_1} {\rm d}s\, \frac{R_{bb}^{\rm cubic}(s)}{s^{n+1}}\Big[1 + \gamma'\frac{0.04(m_Z^2 - s) + 0.003(s - s_0)}{m_Z^2 - s_0}\Big]\\
&+ \int_{s_1}^{m_Z^2} {\rm d}s\, \frac{R_{bb}^{\rm th}(s)}{s^{n+1}}\Big[1 + \gamma'\frac{0.04(m_Z^2 - s) + 0.003(s - s_0)}{m_Z^2 - s_0}\Big]\\
&+ (1 + 0.003\,\gamma')\int_{m_Z^2}^{\infty} {\rm d}s\, \frac{R_{bb}^{\rm th}(s)}{s^{n+1}}\,, \qquad \gamma' = 0 \pm 1\,,
\end{aligned} \tag{2.5.38}$$

with $s_0 = (11.2062\,{\rm GeV})^2$, $s_1 = (11.52\,{\rm GeV})^2$ and $R_{bb}^{\rm cubic}$ is a cubic function that smoothly interpolates between the linear fit to BaBar data and pQCD. Here γ' is the auxiliary variable used to parametrize our uncertainty, which we consider as 100% correlated among the various moments. The related entries of the correlation matrix are trivially computed as

$$C_{nn'}^{\rm pQCD} = \frac{\partial M_n^{\rm pQCD}}{\partial\gamma'}\,\frac{\partial M_{n'}^{\rm pQCD}}{\partial\gamma'}\,. \tag{2.5.39}$$

Final Results for the Bottom Experimental Moments

The full result for the experimental moments is obtained by summing up all the portions described before,

$$M_n^{\rm exp} = M_n^{\rm res} + M_n^{\rm thr} + M_n^{\rm pQCD}\,. \tag{2.5.40}$$

We determine two correlation matrices among the first four moments. One of them comes from the various uncorrelated uncertainties, whereas the other encodes the systematic uncertainties. We denote

[20] We note that the double massive fermion bubble contribution to R_{bb} in Eq. (2.5.36) includes both virtual and real radiation terms in the large energy expansion. However, when this formula is used to compare pQCD to the existing BABAR data, below the four-bottom-quarks threshold, the real radiation should be excluded. We have checked that this inconsistency has an effect below 0.1%.

[21] The authors of Ref. [124] use the pole mass instead of the $\overline{\rm MS}$, and include α_s^4 and QED corrections. This explains some numerical differences in the analyses.

n	Resonances	10.62 − 11.2062	11.2062 − ∞	Total
1	1.394(12|22)	0.270(2|9)	2.862(0|108)	4.526(12|111)
2	1.459(12|22)	0.226(1|8)	1.148(0|45)	2.834(12|51)
3	1.538(12|22)	0.190(1|7)	0.611(0|24)	2.338(12|34)
4	1.630(13|22)	0.159(1|6)	0.365(0|15)	2.154(13|27)

Table 2.9: Results for our computations of the experimental moments. The second column collects the contribution from the first four Υ resonances (using the narrow width approximation). The third to fifth columns show the contributions from the threshold (using ISR-corrected BABAR data) and continuum (using an interpolation between a linear fit to the BaBar data with highest energy and pQCD as a model for the lack of data) regions, and the total moment determinations, respectively. The two numbers quoted in parentheses correspond to the uncorrelated and correlated experimental uncertainties, respectively. All numbers are given in units of $10^{-(2n+1)}\,\mathrm{GeV}^{-2\mathrm{n}}$.

them as the correlated and uncorrelated correlation matrices, respectively. These are computed by summing up the respective individual matrices from each region, and in the same way as we did for our charm analysis, we assume there is no region-to-region correlation. We find:

$$C_{\rm uc}^{\rm exp} = \begin{pmatrix} 0.0002 & 0.0002 & 0.0002 & 0.0002 \\ 0.0002 & 0.0002 & 0.0002 & 0.0002 \\ 0.0002 & 0.0002 & 0.0002 & 0.0002 \\ 0.0002 & 0.0002 & 0.0002 & 0.0002 \end{pmatrix}, \; C_{\rm cor}^{\rm exp} = \begin{pmatrix} 0.0122 & 0.0055 & 0.0032 & 0.0021 \\ 0.0055 & 0.0026 & 0.0017 & 0.0012 \\ 0.0032 & 0.0017 & 0.0011 & 0.0009 \\ 0.0021 & 0.0012 & 0.0009 & 0.0007 \end{pmatrix}, \tag{2.5.41}$$

where the (n,m) entry of each matrix is given in units of $10^{-2(n+m+1)}\,\mathrm{GeV}^{-2(\mathrm{n+m})}$, and the total correlation matrix is the sum of $C_{\rm uc}^{\rm exp}$ and $C_{\rm cor}^{\rm exp}$. The contribution of each region to the final experimental moments and the corresponding uncertainties are presented in Table 2.9.

Comparison to other Determinations of the Bottom Experimental Moments

In this section we compare our result for the experimental moments for the bottom vector current correlator with previous determinations. These are collected in Table 2.10.[22] The most relevant comparison is between the second and third columns, where the most recent data on the narrow resonances and the BABAR continuum data are used. For the contributions from the narrow resonances we have a perfect agreement with [9], although slightly larger errors. For the threshold region our results are slightly smaller, and our uncertainties are almost identical; however, this is not a one-to-one comparison, since our integration region is slightly smaller. Indeed if we consider their energy range we agree with their numbers almost perfectly. The main difference between these two determinations is the estimate of the uncertainties coming from the continuum region, where the pQCD prediction for the R_b-ratio is employed. Whereas we adopt the more conservative approach described in Sec. 2.5.2, Ref. [9] employs only the perturbative uncertainties related to the purple band in Fig. 2.16. In Ref. [124] the same collaboration presents a more critical analysis of their errors. In particular they observe that the last experimental measurement of BABAR, after being corrected for ISR, disagrees with the pQCD prediction at the 20% level (way outside the corresponding uncertainties).[23] To resolve this discrepancy they assume two possible scenarios: a) pQCD starts being reliable at energies above 13 GeV (therefore the authors interpolate between the last experimental point and pQCD at 13 GeV); b) BABAR systematic errors have been underestimated (therefore the central values of the

[22] In the case of Ref. [153], we reconstruct the experimental moments from their Table 3, where the moments are split in several different contributions. For the reconstructed uncertainty, we take one half of the error of the narrow resonances correlated to each other, and the other half as uncorrelated. The errors from patches where theory input is used are taken as fully correlated to one another. The total narrow-resonance error, and the total "theory-patch" error are added in quadrature to get the final uncertainty.

[23] From our own computation of the ISR-corrected R_b-ratio, we only observe a 10% deviation between the last data point and the pQCD prediction, see Fig. 2.16.

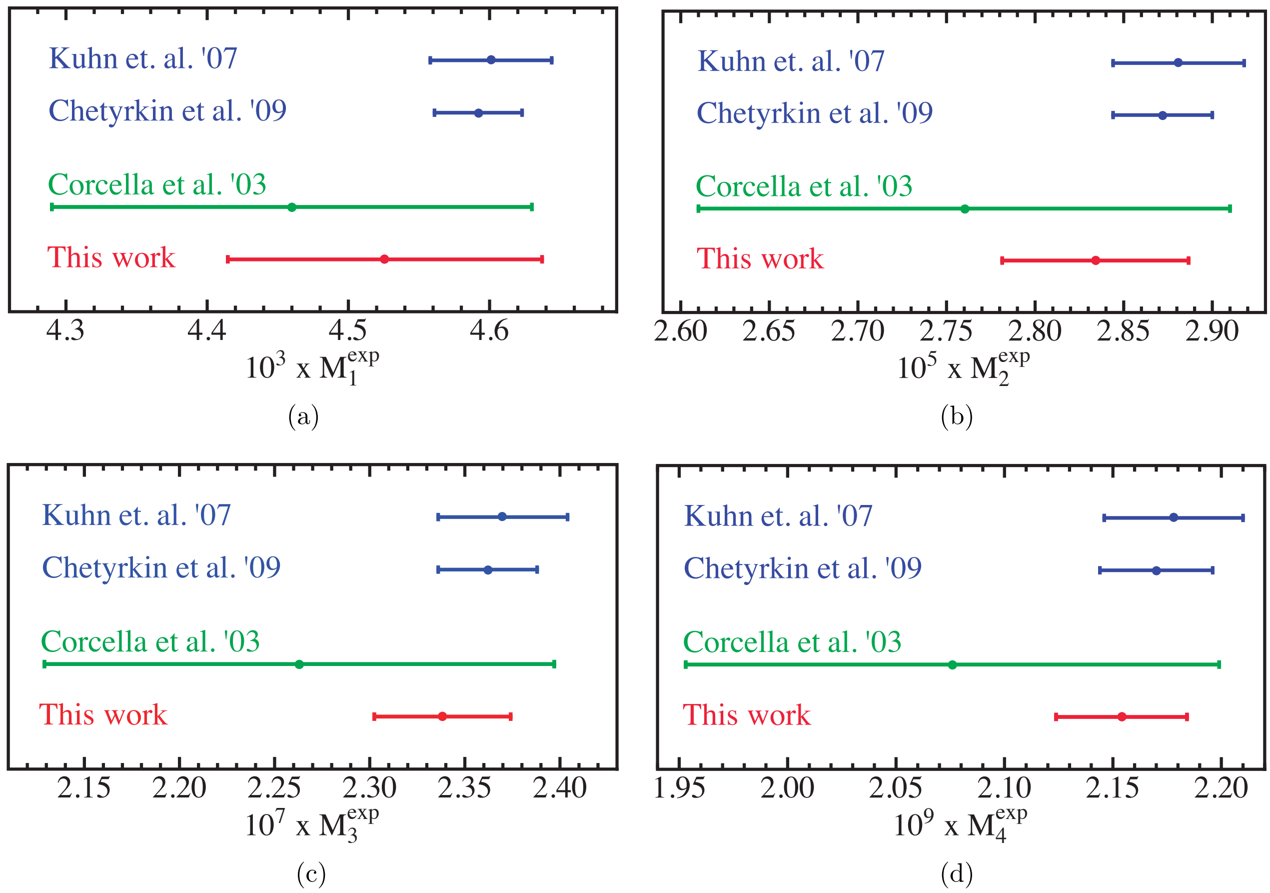

Figure 2.17: Comparison of various determinations of the experimental moments for the bottom vector correlator. Results in blue correspond to analyses of the same collaboration. The green result and the determination at the top do not use the new BABAR results.

experimental measurements are rescaled by a factor of 1.21). Ref. [124] quotes the values of the experimental moments and the resulting values for the bottom mass for these two scenarios. Since the effect of these differences of the two bottom masses obtained from M_2^V is only slightly larger than the size of the other uncertainties (that is, the uncertainties of the theoretical moments plus the other experimental errors) added quadratically, it is argued that this issue can be ignored. We disagree with this argument, since the issue constitutes an independent source of uncertainty not covered by the other errors and, in particular, being unrelated to uncertainties in the theoretical moments. Therefore this shift must be taken as an additional source of error on the experimental moments (and indeed would then dominate the corresponding total error). The additional error (to be added in quadrature to the one in round brackets) is quoted in square brackets in the third column of Table 2.10. It amounts to an additional error of 30, 18, 11 and 7 MeV for $\overline{m}_b(\overline{m}_b)$ extracted from moments M_1^V to M_4^V, respectively.

Refs. [7, 8, 153] have used the older CLEO and CUSB experimental measurements, resulting in relatively large uncertainties. In Ref. [8] the CLEO measurements are divided by a factor of 1.28, and an error of 10% is assigned. It is argued that this procedure is necessary to reconcile old and new CLEO measurements, as well as to improve the agreement with pQCD predictions. Ref. [153] uses values for the Υ-states electronic partial widths given by the PDG 2002, which have larger uncertainties. This makes their determination of the experimental moments rather imprecise.

Concerning the continuum region where no measurements exist, while some previous analyses have taken a less conservative approach than ours, in Ref. [154] a much more conservative approach is adopted. In this region they consider the R_b-ratio as constant with a 66% uncertainty. In Ref. [153]

n	This work	Chetyrkin et al. '09 [9]	Kuhn et al. '07 [8]	Corcella et al. '03 [153]
1	4.526(12|111)	4.592(31)[67]	4.601(43)	4.46(17)
2	2.834(12|51)	2.872(28)[51]	2.881(37)	2.76(15)
3	2.338(12|34)	2.362(26)[40]	2.370(34)	2.26(13)
4	2.154(13|27)	2.170(26)[35]	2.178(32)	2.08(12)

Table 2.10: Comparison of our results for the experimental moments of the bottom vector correlator (2nd column) to previous determinations (3rd to 5th columns). The 2nd and 3rd columns use BABAR data from Ref. [146], while 4th and 5th use older data from Refs. [100,101]. The 3rd and 4th columns use perturbative uncertainties in the continuum region, while 2nd and 5th use a more conservative estimate based on the agreement of data and pQCD. In the 3rd column, we quote in square brackets our own estimate of an additional systematic error from the considerations made in Ref. [124]. All numbers are given in units of $10^{-(2n+1)}\,\mathrm{GeV}^{-2n}$.

also a more conservative approach is adopted. Between 11.1 and 12 GeV $\mathcal{O}(\alpha_s^2)$ pQCD errors are used, which are larger than 10%; for energies above 12 GeV a global 10% correlated error is assigned.

2.5.3 Lattice Simulation Data

The pseudoscalar current is not realized in nature in a way which is useful to compute the moments of the corresponding correlator from experimental data. Results for the moments of the pseudoscalar current correlator can, however, be obtained from simulations on the lattice. The strategy of these numerical simulations is to tune the lattice parameters (such as bare coupling constant and masses) to a selected number of observables (e.g. the energy splitting of Υ resonances). Once this tuning is performed, the lattice action is fully specified and no further changes are implemented. The tuned lattice action can then be used to perform all sorts of predictions, moments of correlators among them. Lattice simulations have to face a number of challenges, which usually translate into sizeable uncertainties. Among those are the extrapolations to the infinite volume and the zero lattice spacing (the latter being much harder), as well as the extrapolation to physical quark masses. On top of these systematic uncertainties, there are also statistical ones, which are related to the finite sampling used to perform the path integrations. On the other hand there are also concerns on the type of lattice action which is being used for the fermions. According to Ref. [6], the moments of the pseudoscalar correlator are least affected by systematic uncertainties, and so HPQCD has focused on those for their subsequent high-precision analyses.

To the best of our knowledge, HPQCD is the only lattice collaboration which has published results on QCD correlators. They have used the staggered-quarks lattice action, and MILC configurations for gluons. These results have been used to determine the charm mass and the strong coupling constant [6, 14, 15] with high accuracy, as well as the bottom mass [14, 35], with smaller precision. We will use the simulation results as given in Ref. [6], even if the results quoted in of [14, 15] are a bit more precise. The reason for this choice is that while [6] makes a straightforward extrapolation to the continuum, which is independent of the charm mass and α_s extractions, in [14,15] the fit for the quark masses, the strong coupling constant and the extrapolation to the continuum is performed all at once, in a single fit. Furthermore that fits contains a lot of priors for the parameters one is interested in fitting. In any case, as we have seen, the charm mass extraction from the pseudoscalar correlator is dominated by perturbative uncertainties, as a result of the bad convergence of the series expansion for its moments.

Ref. [6] provides simulation results for the so-called reduced moments R_k, which are collected in their Table II. The index k takes only even values, and starts with the value $k = 4$, which is fairly insensitive to the charm mass. Hence the lowest moment we consider is R_6. Reduced moments are defined as (up to a global power) the full moment divided by the tree-level result. By taking this ratio, the authors of Ref. [6] claim that large cancellations between systematic errors take place. The reduced moments are scaleless, and the mass-dimension that one obviously needs to determinate the charm quark mass is regained by dividing with the mass of the η_c pseudoscalar particle. Thus one

M_1^P	M_2^P	M_3^P	M_4^P
1.402(20)	1.361(40)	1.426(59)	1.558(89)

Table 2.11: Lattice simulation results for the moments of the twice-subtracted pseudoscalar correlator $P(q^2)$ for $n_f = 4$. Moments given in units of $10^{-n} \times \mathrm{GeV}^{-2n}$.

can easily translate the reduced moments into the more familiar correlator moments M_n^P with the following relation:

$$M_n^P = [C_P(n_f = 4)]_{n,0}^{0,0} \left(\frac{R_{2n+4}}{m_{\eta_c}} \right)^{2n}, \tag{2.5.42}$$

where the C_P coefficients correspond to the tree-level terms of the standard fixed-order expansion of Eq. (2.4.2). Although the experimental value for η_c is 2.9836(7) GeV, we use the value $m_{\eta_c} = 2.980\,\mathrm{GeV}$ given in Ref. [6], in order to ease comparison with that analysis. In Ref. [15] the value $m_{\eta_c} = 2.9863(27)\,\mathrm{GeV}$ is used. It is claimed that (as for the lattice action) it has no QED effects, and the error accounts for $c\bar{c}$ annihilation. Using the quote in Ref. [15] changes M_1^P by 0.4% and the effect on the charm mass is of the order of 2 MeV. The uncertainty in the η_c mass has no effect on the M_n^P errors. In Table 2.11 we quote the lattice simulation results written as regular moments M_n^P.

2.5.4 Computation of the Experimental Values for the Ratios of Moments

Once the experimental values for the moments of the vector and pseudoscalar correlators have been computed, it is in principle a straightforward exercise to calculate ratios of them. The central value is obtained by simply taking the ratio of the corresponding central values. The correlation matrix $\Delta R_n^{\mathrm{exp}}$ among the different ratios of moments can be calculated from

$$\Delta R_n^{\mathrm{exp}} = \sum_{i,j} \left(\frac{\partial R_n^X}{\partial M_i^X} \right) \left(\frac{\partial R_n^X}{\partial M_j^X} \right) C_{ij}^{\mathrm{exp}} \tag{2.5.43}$$

Therefore one needs to have access to the complete correlation matrix among the moments C^{exp}. Our computation for the charm and bottom experimental moments which is quoted in Eqs. (2.5.22), (2.5.21) and (2.5.41), yield the desired correlation matrices, for statistical and systematical correlations. For the pseudoscalar moments the information on correlations is not provided in Ref. [6]. Therefore we make the simplest possible assumption, which is that the moments are fully uncorrelated. This will most certainly overestimate the uncertainties for the ratios of moments, but given that we are anyway dominated by perturbative uncertainties, our approach appears justified. We collect our results for the computation of the ratios of experimental moments in Table. 2.12.

n	Vector $n_f = 4$	Vector $n_f = 5$	Pseudoscalar $n_f = 4$
1	6.969(32|59)	6.262(10|53)	0.971(32)
2	8.807(23|26)	8.251(09|48)	1.048(53)
3	9.547(14|13)	9.212(08|35)	1.092(77)

Table 2.12: Ratios of experimental moments for the vector correlator with 4 and 5 flavors (second and third column, respectively), and for the pseudoscalar correlator with 4 flavors (fourth column). For the vector current, the first error in parenthesis corresponds to the statistical uncertainty, whereas the second corresponds to the systematic one. For the pseudoscalar correlator we only quote the lattice error. Moments given in units of $10^{-2}\,\mathrm{GeV}^{-2}$, $10^{-3}\,\mathrm{GeV}^{-2}$ and, $10^{-1}\,\mathrm{GeV}^{-2}$ for the second, third, and fourth column, respectively.

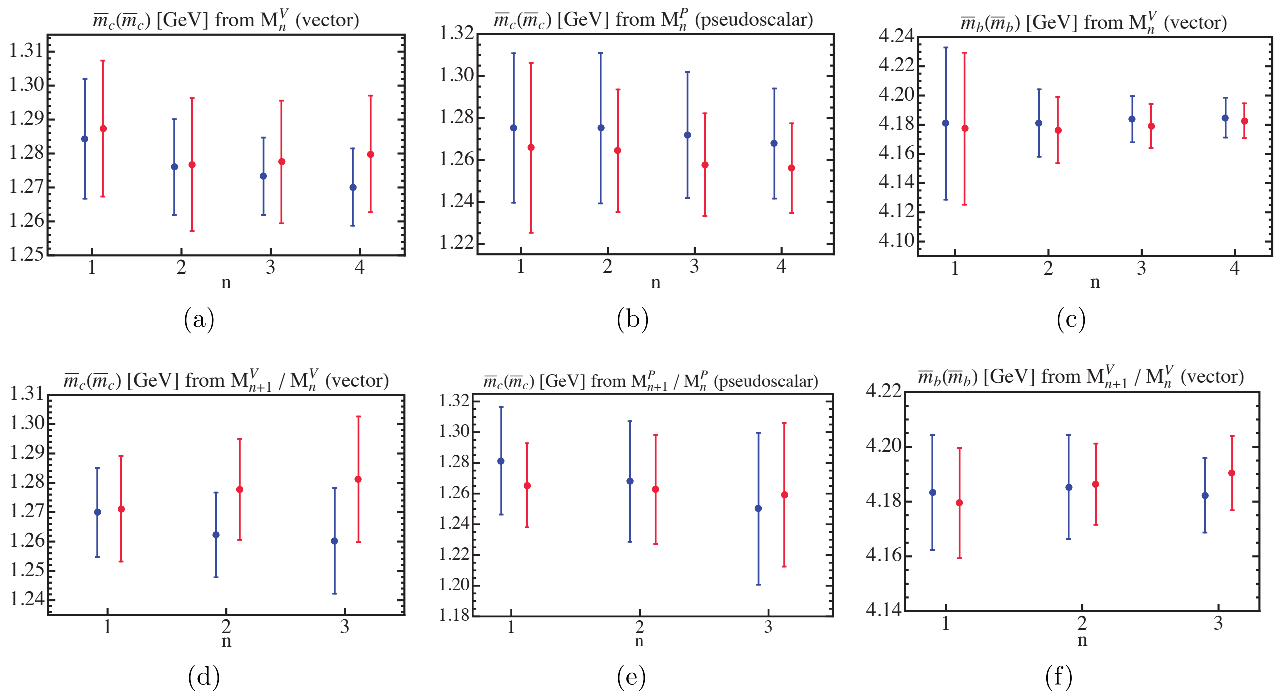

Figure 2.18: Charm and bottom quark mass determinations for different moments (upper row) or ratios of moments (lower row), for the linearized (in blue) and iterative (in red) methods. Panels (a), (b) [(e), (f)] show the results for the charm mass from moments [ratios of moments] of the vector and pseudoscalar correlator, respectively. Panels (c) and (g) show the results for the bottom mass from the vector correlator, for moments and ratios of moments, respectively.

2.6 Results

In this section we present the final results for our analyses at $\mathcal{O}(\alpha_s^3)$. We take method (c) (linearized iterative expansion) as our default expansion. For the estimate of the perturbative uncertainty, we perform double scale variation in the ranges $\overline{m}_c(\overline{m}_c) \le \mu_\alpha, \mu_m \le 4\,\mathrm{GeV}$ for charm (either correlator), and $\overline{m}_b(\overline{m}_b) \le \mu_\alpha, \mu_m \le 15\,\mathrm{GeV}$ for bottom, and we discard 3% of the series with the worst convergence (that is, with highest values of the V_c convergence parameter). For the charm mass determinations (either vector or pseudoscalar correlator) we use the first moment as our default, given that it is theoretically more reliable than the higher moments. For the analysis of the bottom mass from regular moments, we use M_2^V as our default, since it is less afflicted by systematic experimental errors than the first moment, and is nevertheless theoretically sound. For the charm and the bottom mass analyses we also examine the ratio of the second over the first moment as a cross check and validation of the results from regular moments. The results for the experimental moments are collected in: the last column of Table 2.4 (charm vector correlator regular moments); the last column of Table 2.9 (bottom vector correlator regular moments); Table 2.11 (lattice regular moments); and Table 2.12 (all ratios of moments).

We also analyzed higher (and also lower for the case of bottom) moments and ratios of moments for all correlator and quark species. Since, as already discussed, fixed-order and contour-improved higher moments are particularly afflicted by their nonlinear dependence on the quark mass, we only consider the linearized and iterative methods for this analysis. In any case, since higher moments have a larger sensitivity to infrared effects and are therefore theoretically less sound, the analysis involving higher moments mainly aims at providing cross checks. The results are collected in a graphical form in Fig. 2.18.

Our final determinations include nonperturbative effects through the gluon condensate including its Wilson coefficients at order $\mathcal{O}(\alpha_s)$. Furthermore, we assign as a conservative estimate of the

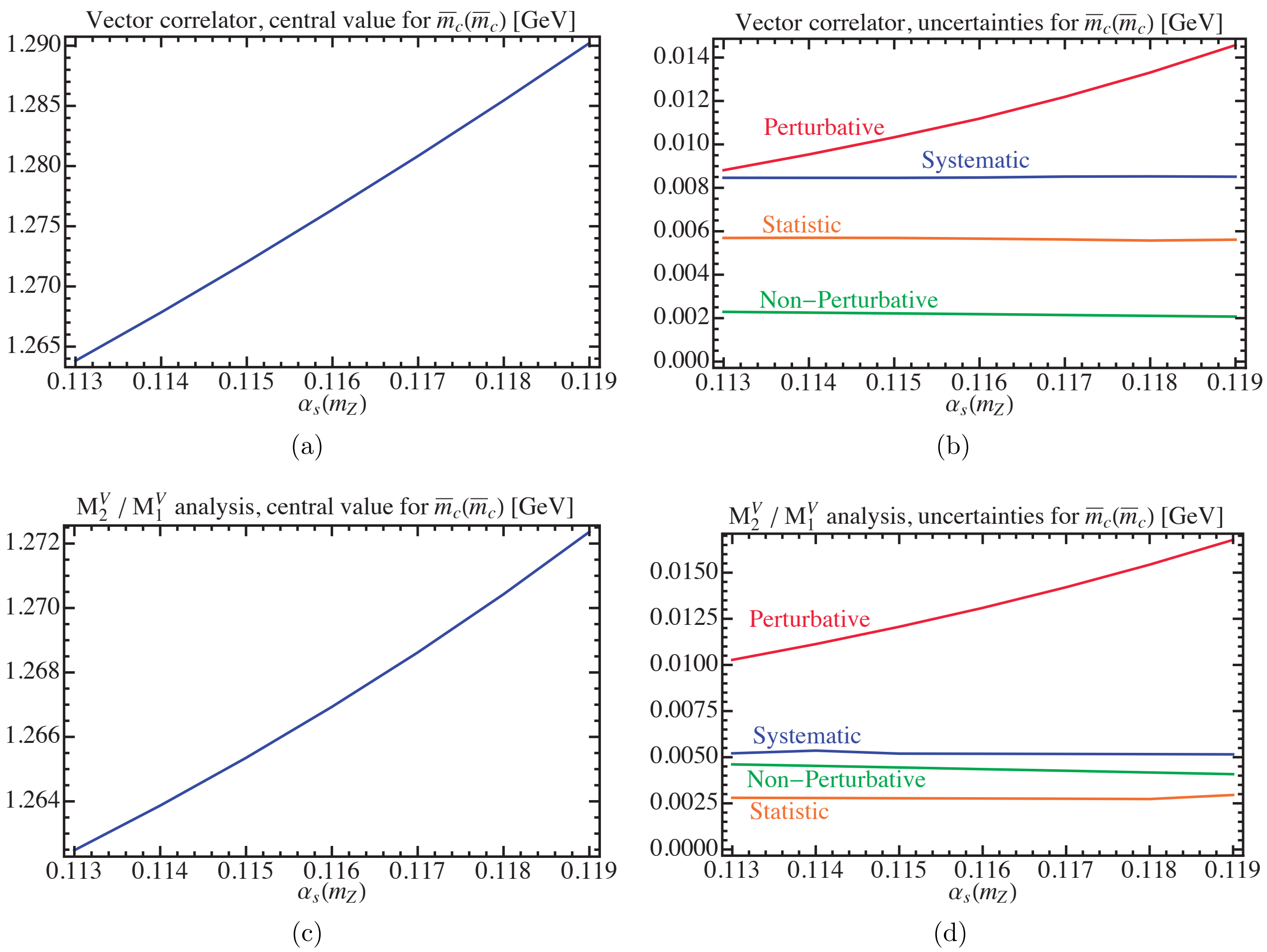

Figure 2.19: Dependence on $\alpha_s(m_Z)$ of the central values of $\overline{m}_c(\overline{m}_c)$ and the corresponding perturbative (red), statistical (orange), systematical (blue) and nonperturbative uncertainties (green), for the analysis of the first moment [panels (a) and (b)] and the ratio of the second over the first moment, [panels (c) and (d)], corresponding to the vector correlator.

nonperturbative uncertainty twice the shift caused by including the gluon condensate. In any case, this error is very small, particularly for the bottom mass determination. One source of uncertainty which we have not discussed so far is that coming from the strong coupling constant. Although the world average $\alpha_s(m_Z) = 0.1185 \pm 0.006$ has a very small error, see Ref. [83], one cannot ignore the fact that it is fairly dominated by lattice determinations, e.g. [15]. Furthermore, there are other precise determinations with lower central values and in disagreement with the world average from event-shapes [155–158] and DIS [159]. A review on recent α_s determinations can be found in Refs. [160–162]. Therefore, in analogy with Ref. [44], we perform our analyses for several values of $\alpha_s(m_Z)$ between 0.113 and 0.119, and provide the central values and perturbative errors as (approximate) linear functions of $\alpha_s(m_Z)$. The other uncertainties are essentially α_s-independent, so we just provide the average. We also quote quark mass results for α_s taken from the world average:

$$\alpha_s(m_Z) = 0.1185 \pm 0.0021\,, \tag{2.6.1}$$

where we adopt an uncertainty 3.5 times larger than the current world average [83]. We note that in Ref. [44] we have taken $\alpha_s(m_Z) = 0.1184 \pm 0.0021$ as an input which causes only tiny sub-MeV differences in the quark masses.

2.6.1 Results for the Charm Mass from the Vector Correlator

For the analysis using the first moment of the charm vector correlator we use the experimental value quoted in table 2.4 : $M_1^{V,\,\rm exp} = (0.2121 \pm 0.0020_{\rm stat} \pm 0.0030_{\rm syst})\,{\rm GeV}^{-2}$. The outcome of this analysis is:

$$\begin{aligned}\overline{m}_c(\overline{m}_c) = &\,1.288 \,\pm\, (0.006)_{\rm stat} \,\pm\, (0.009)_{\rm syst} \,\pm\, (0.014)_{\rm pert}\\ &\pm\, (0.010)_{\alpha_s} \,\pm\, (0.002)_{\langle GG\rangle}\,{\rm GeV}\,,\end{aligned} \tag{2.6.2}$$

where the quoted errors are (from left to right) experimental uncorrelated, experimental correlated, peturbative, due to the uncertainty in α_s as given in Eq. (2.6.1), and nonperturbative. If we adopt the correlated scale variation $2\,{\rm GeV} \le \mu_\alpha = \mu_m \le 4\,{\rm GeV}$, we obtain for method (c) $1.297 \pm (0.005)_{\rm pert}$, with the other errors essentially unchanged. For method (a) we would get $1.290 \pm (0.0007)_{\rm pert}$, with a scale variation even smaller than the nonperturbative uncertainty, and 20 times smaller than our perturbative error estimate with double scale variation [3 times for method (c)]. The dependence on $\alpha_s(m_Z)$ is shown graphically in Figs. 2.19(a) and 2.19(b), and analytically the result reads:

$$\begin{aligned}\overline{m}_c(\overline{m}_c) \;\;=\;\; & (1.288 + 4.40 \times [\alpha_s(m_Z) - 0.1185]) \,\pm\, (0.006)_{\rm stat} \,\pm\, (0.009)_{\rm syst}\\ & \pm (0.014 + 0.95 \times [\alpha_s(m_Z) - 0.1185])_{\rm pert} \,\pm\, (0.002)_{\langle GG\rangle}\,.\end{aligned} \tag{2.6.3}$$

For the ratio of the second over the first moment of the vector correlator we use as the experimental input $R_1^{V,\,\rm exp} = (6.969 \pm 0.032_{\rm stat} \pm 0.059_{\rm syst}) \times 10^{-2}\,{\rm GeV}^{-2}$, which yields the following result for the charm mass:

$$\begin{aligned}\overline{m}_c(\overline{m}_c) = &\,1.271 \,\pm\, (0.003)_{\rm stat} \,\pm\, (0.005)_{\rm syst} \,\pm\, (0.016)_{\rm pert}\\ &\pm\, (0.004)_{\alpha_s} \,\pm\, (0.004)_{\langle GG\rangle}\,{\rm GeV}\,.\end{aligned} \tag{2.6.4}$$

With correlated variation $2\,{\rm GeV} \le \mu_\alpha = \mu_m \le 4\,{\rm GeV}$ we get $1.258 \pm (0.005)_{\rm pert}$ and $1.279 \pm (0.007)_{\rm pert}$ for methods (a) and (c), respectively. In this case the scale variations are a factor of 2 to 3 smaller than our perturbative error estimate.[24] The α_s dependence, which can be seen in Figs. 2.19(c) and 2.19(d), has the form:

$$\begin{aligned}\overline{m}_c(\overline{m}_c) = &\,(1.271 + 1.64 \times [\alpha_s(m_Z) - 0.1185]) \,\pm\, (0.003)_{\rm stat} \,\pm\, (0.005)_{\rm syst}\\ &\pm\, (0.016 + 1.081 \times [\alpha_s(m_Z) - 0.1185])_{\rm pert} \,\pm\, (0.004)_{\langle GG\rangle}\,.\end{aligned} \tag{2.6.5}$$

We observe that the central value for the ratios of moments is 17 MeV smaller than for the first moment analysis, but fully compatible within theoretical uncertainties. Furthermore, the dependence on α_s of the central value obtained from the regular moment analysis is larger, which translates into a corresponding larger error due to the uncertainty in α_s. Both determinations have very similar perturbative uncertainties for any value of α_s. We also see that the charm mass from the ratio of moments has smaller experimental uncertainties, as a result of cancellations between correlated errors. Moreover, the charm mass result from R_1^V has a nonperturbative error twice as large as that from M_1^V. The two charm mass results from the first moment and the moment ratio are compared graphically in Fig. 2.22(a).

2.6.2 Results for the Charm Mass from the Pseudoscalar Correlator

For the analysis of the first moment of the charm pseudoscalar correlator we employ $M_1^{P,\,\rm latt} = (0.1402 \pm 0.0020_{\rm latt})\,{\rm GeV}^{-2}$ [6], which yields the following charm mass determination:

$$\overline{m}_c(\overline{m}_c) = \;1.267 \,\pm\, (0.008)_{\rm lat} \,\pm\, (0.035)_{\rm pert} \,\pm\, (0.019)_{\alpha_s} \,\pm\, (0.002)_{\langle GG\rangle}\,{\rm GeV}\,. \tag{2.6.6}$$

[24] Had we taken the fixed-order expansion (a) and correlated scale variation $2\,{\rm GeV} \le \mu_\alpha = \mu_m \le 4\,{\rm GeV}$ as the estimate for the perturbative uncertainty, the result from R_1^V with all errors added quadratically would be $1.258 \pm 0.013\,{\rm GeV}$, whereas the result from M_1^V would read $1.290 \pm 0.015\,{\rm GeV}$. Both results would not be consistent to each other.

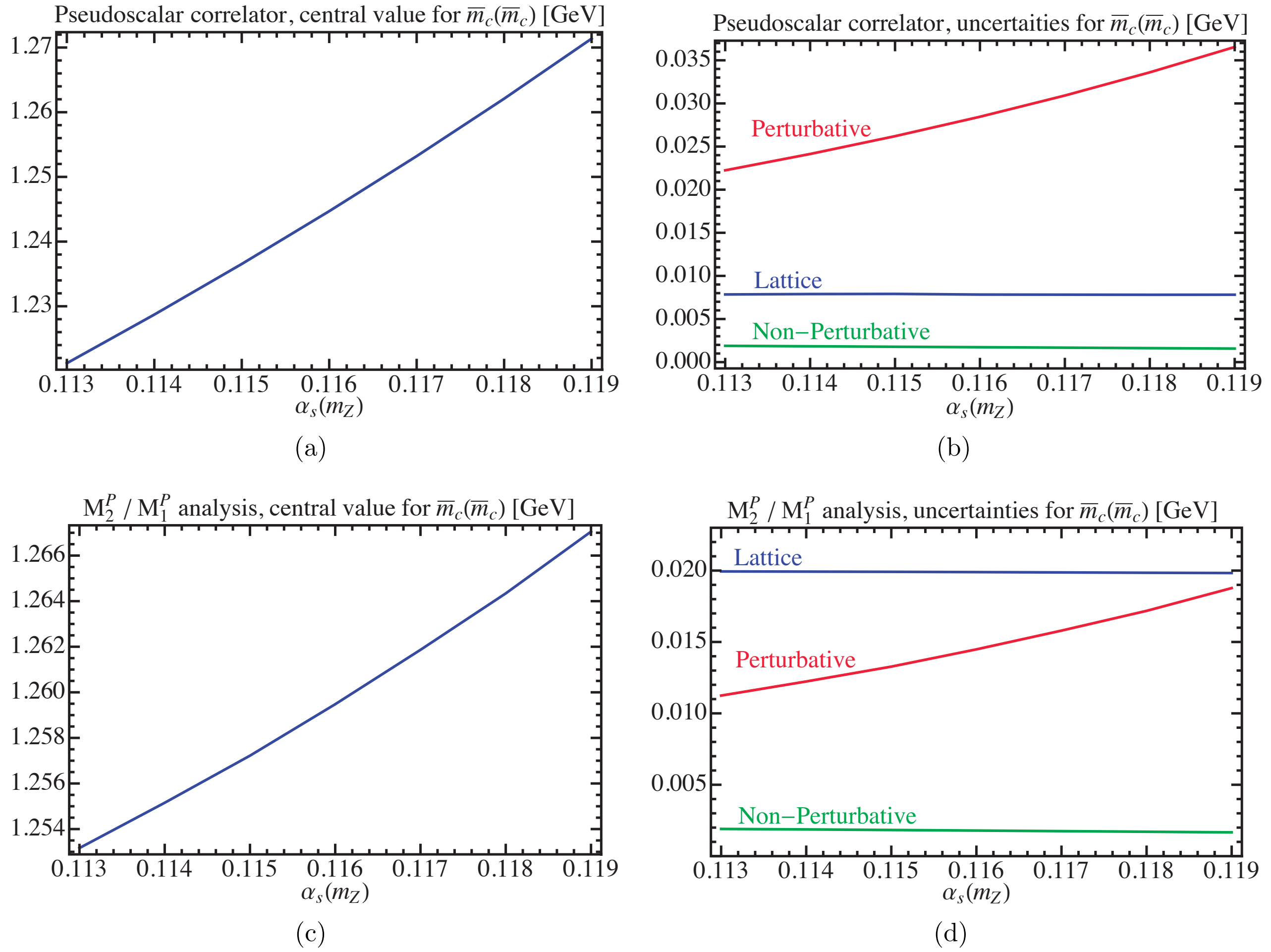

Figure 2.20: Dependence on $\alpha_s(m_Z)$ of the central values of $\overline{m}_c(\overline{m}_c)$ and the corresponding perturbative (red), lattice (blue) and nonperturbative uncertainties (green), for the analysis of the first moment [panels (a) and (b)] and the ratio of the second over the first moment, [panels (c) and (d)], corresponding to the pseudoscalar correlator.

With correlated scale variation $2\,\text{GeV} \leq \mu_\alpha = \mu_m \leq 4\,\text{GeV}$ we obtain the central values 1.278 and 1.276 GeV, for methods (b) and (c), respectively. In both cases the scale variation is 4 MeV, 8 times smaller than our perturbative error estimate with double scale variation. For the α_s dependence, we find

$$\begin{aligned}\overline{m}_c(\overline{m}_c) = (1.267 + 8.36 \times [\alpha_s(m_Z) - 0.1185]) \,\pm\, (0.008)_{\text{lat}} \\ \pm\, (0.035 + 2.38 \times [\alpha_s(m_Z) - 0.1185])_{\text{pert}} \,\pm\, (0.002)_{\langle GG\rangle}\,,\end{aligned} \tag{2.6.7}$$

which is also displayed in Figs. 2.20(a) and 2.20(b). As expected, the perturbative error is much larger than for the vector correlator, and has a stronger dependence on α_s. We see that the central value has a much stronger dependence on α_s as well, which again translates into a large error due to the uncertainty in the strong coupling. The central value is 21 MeV lower than Eq. (2.6.2), but fully compatible within errors [see Fig 2.22(a)]. The nonperturbative uncertainties are identical to the vector current case.

For the ratio of second over the first moment of the pseudoscalar correlator we use $R_1^{P,\,\text{latt}} = (0.0971 \pm 0.0032_{\text{latt}})\,\text{GeV}^{-2}$. We find for the charm mass

$$\overline{m}_c(\overline{m}_c) = 1.266 \pm (0.020)_{\text{latt}} \pm (0.018)_{\text{pert}} \pm (0.006)_{\alpha_s} \pm (0.002)_{\langle GG\rangle}\,\text{GeV}\,. \tag{2.6.8}$$

Using correlated variation $2\,\text{GeV} \leq \mu_\alpha = \mu_m \leq 4\,\text{GeV}$ one obtains $1.270 \pm (0.007)_{\text{pert}}$ and $1.278 \pm (0.003)_{\text{pert}}$ for methods (a) and (c), respectively. These scale variations are a factor 3 and 6 smaller

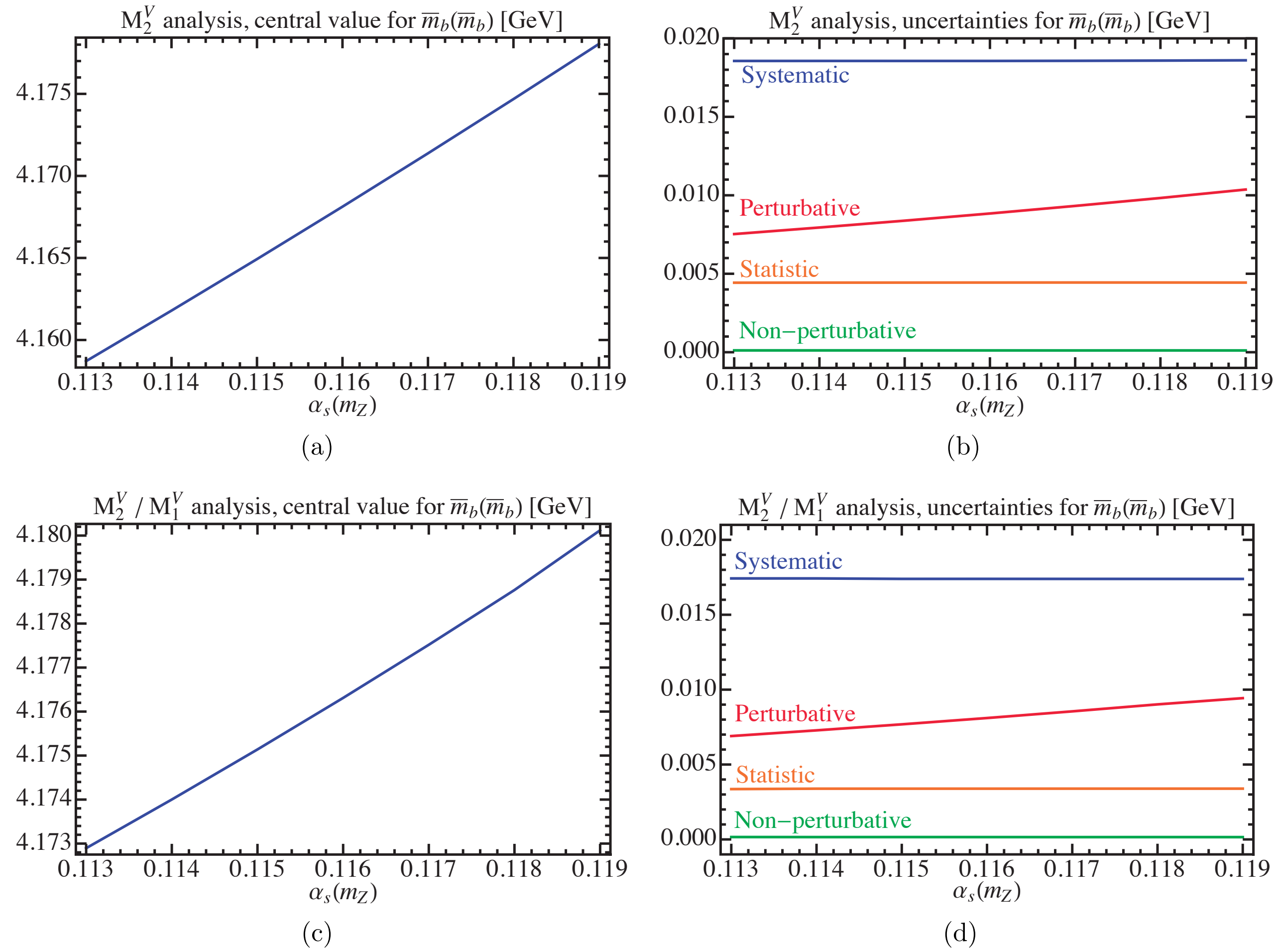

Figure 2.21: Dependence on $\alpha_s(m_Z)$ of the central values of $\overline{m}_b(\overline{m}_b)$ and the corresponding perturbative (red), statistical (orange), systematical (blue) and nonperturbative uncertainties (green), for for the analysis of the second moment [panels (a) and (b)] and the ratio of the second over the the first moment [panels (c) and (d)] of the vector correlator.

than our perturbative error estimate, respectively. The α_s dependence is

$$\begin{aligned}\overline{m}_c(\overline{m}_c) = {} & (1.266 + 2.31 \times [\alpha_s(m_Z) - 0.1185]) \pm (0.020)_{\rm latt} \\ & \pm (0.018 + 1.25 \times [\alpha_s(m_Z) - 0.1185])_{\rm pert} \pm (0.002)_{\langle GG \rangle} \,.\end{aligned} \tag{2.6.9}$$

The central values for both M_1^P and R_1^P are almost identical, but their α_s dependence is not: the latter is much smaller (even smaller than for M_1^V, but larger than for R_1^V). Note that the lattice error is larger for the ratio since we made the very conservative assumption that they are fully uncorrelated. This is because the correlation matrix for various lattice moments is unknown. The perturbative error reduces by a factor of two for any value of α_s when using the ratio, but we have checked that this only happens for the iterative expansion. On the other hand, the α_s dependence of the perturbative uncertainty is smaller for the regular moment determination. The nonperturbative errors are identical.

All charm determinations are illustrated graphically in Fig. 2.22(a), where in red we show our preferred determination from the first moment of the vector correlator.

2.6.3 Results for the Bottom Mass from the Vector Correlator

For our determination of the bottom quark mass from the second moment of the vector correlator we use for the experimental moment $M_2^{V,\,\rm exp} = (2.834 \pm 0.012_{\rm stat} \pm 0.051_{\rm syst}) \times 10^{-5}\,{\rm GeV}^{-4}$, and we obtain

$$\overline{m}_b(\overline{m}_b) = 4.176 \,\pm\, (0.004)_{\rm stat} \,\pm\, (0.019)_{\rm syst} \,\pm\, (0.010)_{\rm pert} \\ \pm\, (0.007)_{\alpha_s} \,\pm\, (0.0001)_{\langle GG\rangle}\,\mathrm{GeV}\,. \tag{2.6.10}$$

The perturbative error is 30% smaller than for the charm vector correlator analysis, as a result of the smaller value of α_s at the scales close to the bottom mass. This is consistent with our discussion on the convergence properties of perturbation series for the bottom quark carried out in Sec. 2.4.4. The total error is dominated by the experimental systematic uncertainty, which in turn mainly comes from the continuum region where one relies on modeling in the absence of any experimental measurements. The nonperturbative error is completely negligible. This is expected since it is suppressed by two powers of the bottom mass. Using the correlated scale variation $5\,\mathrm{GeV} \le \mu_\alpha = \mu_m \le 15\,\mathrm{GeV}$ for methods (a) and (c) we get 4.178 and 4.182 for the central values and scale variations which are 20 and 3 times smaller, respectively. The α_s dependence reads

$$\overline{m}_b(\overline{m}_b) = (4.176 + 3.22 \times [\alpha_s(m_Z) - 0.1185]) \,\pm\, (0.004)_{\rm stat} \,\pm\, (0.019)_{\rm syst} \\ \pm\, (0.010 + 0.472 \times [\alpha_s(m_Z) - 0.1185])_{\rm pert} \,\pm\, (0.0001)_{\langle GG\rangle}\,. \tag{2.6.11}$$

For the analysis based on the ratio of the second moment over the first, we use $R_2^{V,\,\rm exp} = (6.262 \pm 0.010_{\rm stat} \pm 0.053_{\rm syst}) \times 10^{-3}\,\mathrm{GeV}^{-2}$, and with this value we obtain the bottom mass

$$\overline{m}_b(\overline{m}_b) = 4.179 \,\pm\, (0.003)_{\rm stat} \,\pm\, (0.017)_{\rm syst} \,\pm\, (0.009)_{\rm pert} \\ \pm\, (0.003)_{\alpha_s} \,\pm\, (0.0002)_{\langle GG\rangle}\,\mathrm{GeV}\,. \tag{2.6.12}$$

With correlated scale variation $5\,\mathrm{GeV} \le \mu_\alpha = \mu_m \le 15\,\mathrm{GeV}$ we obtain $4.175 \pm (0.003)_{\rm pert}$ and $4.182 \pm (0.004)_{\rm pert}$ for methods (a) and (c), respectively. In this case the scale variation is smaller by a factor 3 and 2, respectively. The α_s dependence reads as follows:

$$\overline{m}_b(\overline{m}_b) = (4.179 + 1.199 \times [\alpha_s(m_Z) - 0.1185]) \,\pm\, (0.003)_{\rm stat} \,\pm\, (0.017)_{\rm syst} \\ \pm\, (0.009 + 0.426 \times [\alpha_s(m_Z) - 0.1185])_{\rm pert} \,\pm\, (0.0002)_{\langle GG\rangle}\,. \tag{2.6.13}$$

Although the central value for the ratio analysis is 3 MeV higher, this has no significance given the size of the uncertainties. The dependence of the central value on α_s is three times smaller for the ratio analysis. The perturbative error and its α_s dependence are roughly the same for the ratio and the single moment analysis. Moreover, the two experimental errors are very similar. This is because, even though there is some cancellation of correlated errors in the ratio, a significant part of the huge systematic error of the first moment remains uncanceled.

A graphical illustration of the two bottom mass determinations is shown in Fig. 2.22(b). Both combined uncertainties and central values are rather similar, and we adopt the result from the second moment (in red) as our default result.

2.6.4 Comparison to other Determinations

In this section we make a comparison of our charm mass determination from the vector correlator, from the pseudoscalar current correlator and of our bottom mass determination, to previous analyses. We restrict our discussion to determinations which use QCD sum rules with infinite as well as finite energy range for the vector or pseudoscalar current correlators, and including relativistic and nonrelativistic versions of the sum rules. We do not cover charm mass determinations from DIS or bottom mass determinations from jets (which are in any case rather imprecise), as well as determinations which are based on the mass of bound states (B mesons or quarkonia) or B decays.

In Figs. 2.23(a) and 2.23(b) we present in a graphical form a compilation of recent sum rule determinations of the charm and bottom masses, respectively. We have labeled them from top to bottom with numbers from 1 to 14. We note that comparing these results, one has to keep in mind that different analyses in general employed different values and uncertainties for the strong coupling. Only the analyses in Refs. [9, 10, 44, 121, 163] and ours have provided the dependence of their results on the value of $\alpha_s(m_Z)$.

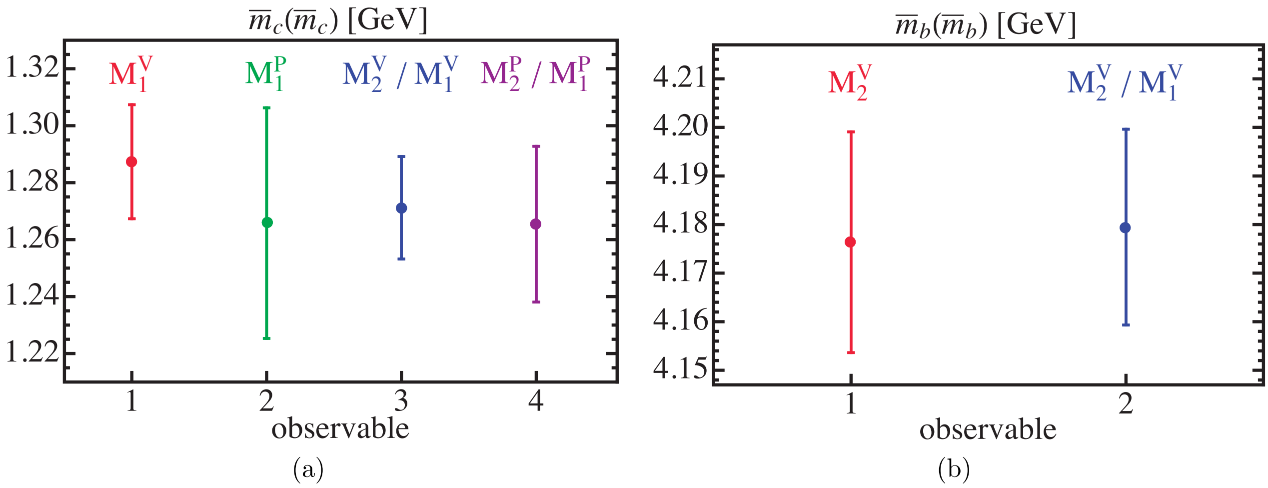

Figure 2.22: Charm (a) [bottom (b)] mass determinations from the first [second] moment of the vector correlator (in red), the first moment of the pseudoscalar correlator (green, charm only), and the ratio of the second over the first moment of the vector (blue) and pseudoscalar correlator (purple, charm only).

Charm Mass

Let us first focus our attention on the charm mass, Fig. 2.23(a). Within each color, determinations are ordered according to publication date. In red (determinations 12 to 14) we show the results of our collaboration: 12 and 13 for the vector correlator, the former (dashed) corresponding to Ref. [44] without trimming procedure, and the latter (solid) corresponding to Ref. [45], which includes the trimming procedure, presented in this thesis. Determinations 12 to 14 are the only analyses using uncorrelated scale variation. Determination 6 (gray) [121] sets $\mu_m = \overline{m}_c(\overline{m}_c)$, and all the other analyses have set $\mu_m = \mu_\alpha$. Determinations in blue (1 [15], 2 [14] and 3 [6]) were performed by the HPQCD collaboration, which employ method (b) for the pseudoscalar correlator moments used for the mass determination in their lattice analyses. Only 1 to 3 and 14 use pseudoscalar moments, while all the other analyses use the vector correlator. Among those 7 [13], 8 [9], 9 [8] and 10 [7] use data in the threshold region only up to 4.8 GeV; analysis 6 uses two patches of data in the threshold region, one from threshold to 4.7 GeV, and another between 7.2 and 11 GeV; analyses 12 and 13 use all available data (see Sec. 2.5.1 for the complete bibliographic information on charm data). The result in 6 uses only $\mathcal{O}(\alpha_s^2)$ perturbative input [all the other analyses utilize $\mathcal{O}(\alpha_s^3)$ computations] and older information on the narrow resonances, from the PDG 2006. They also study the fixed-order expansion and two methods of contour improvement. In black (8 to 10) we display results using fixed order analyses at $\mathcal{O}(\alpha_s^3)$ from the Karlsruhe (8 and 9) and Würzburg (10) collaborations.

Analysis 7 (orange) corresponds to weighted finite-energy sum rules. They employ a kernel which enhances the sensitivity to the charm mass, and at the same time reduces the sensitivity to the continuum region. Green color analyses, collected in 4 [11, 12] and 5 [10], apply other kinds of sum rules. Analysis 5 uses a finite energy sum rule similar to 7, but the kernel makes the sensitivity to the charm mass quite small. On the other hand, the two determinations of 4 use shifted moments, ratios of shifted moments, and exponential sum rules, and consider only the contributions from the first 6 vector resonances in the narrow width approximation, and the pQCD prediction for the continuum. The lower analysis of 4 [11] includes contributions from condensates up to dimension 6; the higher [12] includes condensates up to dimension 8. In purple (11 [164]) we show the only analysis which uses large-n moments for the charm mass fits, employing NRQCD methods to sum up large logs and threshold enhanced perturbative corrections, supplemented with fixed order predictions for the formally power suppressed terms. This analysis uses contributions from narrow resonances, plus a crude model for the threshold and continuum patches, for which a conservative uncertainty is assigned. We note, however, that this analysis might be questioned since perturbative NRQCD is in general not applicable for the

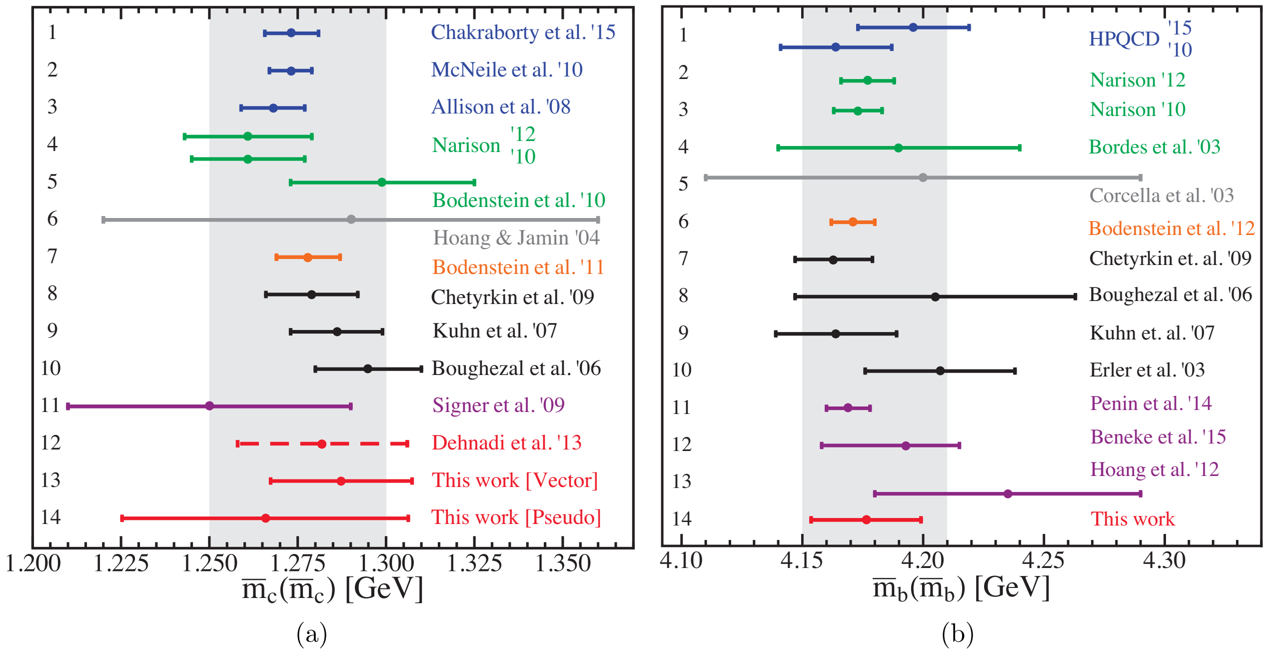

Figure 2.23: Comparison of recent determinations of charm (a) and bottom (b) quark masses from sum rule analyses. Red results correspond to our determination. Black and gray correspond to $\mathcal{O}(\alpha_s^2)$ and $\mathcal{O}(\alpha_s^3)$ analyses, respectively. Purple results use nonrelativistic sum rules. Orange use weighted finite energy sum rules. Blue results are based on QCD sum rules using lattice simulation results as experimental data. Green labels other kinds of sum rule analyses (FESR, Q^2-dependent moments, ratios of moments).

charmonium states.

Our vector correlator result agrees well with the world average, having a similar uncertainty. Our result is fully compatible with the other determinations shown in Fig. 2.23(a). As mentioned already before, we disagree with the small perturbative uncertainties related to the scale variations of the vector and/or pseudoscalar moments adopted in analyses 1 to 3 and 7 to 10.

Bottom Mass

Let us now turn our attention to the bottom mass results, see Fig. 2.23(b). The coloring and chronological conventions are analogous to Fig. 2.23(a), and we try to keep a similar ordering. We show three nonrelativistic determinations (11 [163], 12 [154] and 13 [165]) in purple; $\mathcal{O}(\alpha_s^2)$ fixed-order analyses are shown in gray (5 [153]), black (10 [166]) and green (4 [167]); finite energy sum rules also based on fixed-order appear in orange (6 [114]) and green (4); there are two lattice analyses in blue, collected in 1 [14, 35]. Analyses 3, 6, 7 and 11 to 13 use the new BABAR data, whereas the others use the older CLEO and CUSB data. Analyses 4 and 11 include only the contributions of the first six vector resonances. Analyses 4 and 5 use older measurements of the electronic width for the narrow resonances. Analyses 3, 4, 6 to 9 use pQCD in the high-energy spectrum for the experimental moments. The theoretical treatment of the bottom mass analyses in red, gray, black, blue and green are in complete analogy to their charm mass analyses: 3 and 4 for bottom correspond to 4 and 5 for charm, respectively; 1 in bottom corresponds to 1 and 2 for charm.

The upper analysis of 1 [35] uses a nonrelativistic lattice action to compute ratios of large-n moments, which are later compared to relativistic continuum perturbation theory. Because the continuum computation do not sum up Sommerfeld enhanced terms, this procedure is questionable. The analysis 10 uses a combination of M_6^V with the infinite momentum transfer moment, both in fixed-order, in order to constrain the continuum region. They only use experimental information on narrow resonances, and model the rest of the spectrum with theory predictions. Finally, they make the following scale choice: $\mu_\alpha = \mu_m = \overline{m}_b(\overline{m}_b)$ and estimate the truncation error from an ansatz for the $\mathcal{O}(\alpha_s^3)$ term.[25] Analyses 11 and 13 use large-n moments and NRQCD methods for their theoretical moments. Analysis 12 uses NRQCD fixed-order perturbation theory at N^{3}LO (which accounts for the summation of the Coulomb singularities) and 13 uses renormalization group improved perturbation theory in the framework of vNRQCD at N^{2}LL order. Both analyses employ low-scale short-distance masses to avoid ambiguities related to the pole mass renormalon. Analysis 12 also uses N^{3}LO NRQCD fixed-order input, but is incomplete concerning the contributions from the continuum region in the theoretical moments. Moreover, they extract the pole mass which is then converted to the $\overline{\text{MS}}$ scheme.

Our result 14 is in full agreement with the world average, having a slightly smaller uncertainty. It also agrees with the other analyses shown, with slightly smaller or comparable uncertainties. We disagree with the small perturbative uncertainties related to scale variations quoted in 6 to 10.

[25] Ref. [166] also makes a determination of the charm mass. We exclude it from our comparison since it is not used in the PDG average.

Chapter 3

Part II: Massive Quark Production in The Thrust Distribution

In this chapter we present a complete description of the full thrust distribution for boosted heavy quark initiated jets in $e^+ e^-$ colliders. The results are given in terms of various factorization theorems in the dijet limit within a variable flavor number scheme (VFNS) for final state jets. In this limit we use Soft-Collinear Effective Theory (SCET) [36], including mass modes, in order to factorize the cross section and to sum large logarithms at $\mathrm{N^2LL}$ order. When the invariant mass of the massive jet is close to the heavy quark mass we need to integrate out the small component of the heavy quark field and match onto a boosted Heavy Quark Effective Theory (bHQET) [32] to sum up a new class of large logarithms along with the treatment of finite width effects.

This chapter is organized as follows: After a short introduction in Sec. 3.1 , we initiate the discussion with the description of the event shape variables in Sec. 3.2. Here, in particular we have a closer look into the thrust variable which exhibits a high sensitivity to the mass of the heavy quark. In Sec. 3.3 we provide a basic review on SCET and bHQET, which are essential ingredients of our theoretical description. In Sec. 3.4 we give a short presentation of the factorization theorem using SCET for the fully massless thrust distribution in the dijet limit. Then, we explain the key ideas of Refs. [42, 43] to incorporate secondary heavy quark effects using a VFNS for final state jets. This discussion provides a useful guideline to construct a VFNS for our more complicated problem with both primary and secondary massive quark production in the thrust distribution. We establish our VNFS for the fully massive thrust distribution in Sec. 3.5 .

In order to obtain a complete theoretical description it is necessary to incorporate the nonsingular contribution which consists of subleading contributions that are not contained in the factorized cross section. These subleading terms are significant in the far-tail region of the distribution, however they can also be numerically large and cause instabilities close to the threshold of the cross section, in particular at low energies. In Sec. 3.6 we suggest a prescription to incorporate certain formally non-singular contributions into the factorization theorem such that the effect of subdominant singularities is suppressed.

The resulting framework provides full control over the mass dependence of various matrix elements and the corresponding kinematic scenarios where we can switch to suitable short-distance schemes for the heavy quark masses such that the power counting of relevant fluctuations is respected in each sector independently. In Sec. 3.7 we describe the shape function that accounts for hadronization effects. Specifically we apply also a VFNS to the gap subtractions, used to define a scheme for the leading power correction in which the leading renormalon of the soft function is removed. In order to take into account the decay of unstable heavy quarks inclusively, we provide an effective treatment at leading order in Sec. 3.8, which leads to a factorization theorem for the finite width effects where we carry out an additional smearing of the stable cross section with a Breit-Wigner function. In Sec. 3.9 we briefly review the proper short-distance mass schemes which can be used in this context.

The mass dependent profile functions for the various renormalization scales of the factorization theorems are described in Sec. 3.10. They are designed such that all large logarithms are resummed and a smooth transition between various regions of the distribution is obtained. The resulting profile functions are compatible with those for the massless thrust distribution in Refs. [155, 158]. The variation of parameters in the profile function equip us with a common method to estimate the theoretical uncertainties from residual dependence of perturbative expansions on the profile function parameters.

The resulting hadron-level predictions can be used to compare the top (bottom) mass parameters in parton-shower Monte Carlo (MC) generators to well defined short-distance schemes for massive thrust distributions. However, the corresponding analysis is not provided in this thesis. In Sec. 3.11 we present numerical studies on the theoretical uncertainties of the predictions for the bottom, unstable and stable top thrust distributions where we discuss the perturbative convergence of the results. Then we display the sensitivity of the thrust distribution to the quark mass, the coupling constant and the first moment of the model function at different energies. Finally we estimate the theoretical uncertainty for the mass fit which might be obtained from a future calibration analysis of the MC bottom and top mass parameters.

3.1 Introduction

Production of hadronic jets in electron-positron colliders has been playing a key role in our understanding of the strong interactions. In this context event shapes [168–173] are an important class of jet observables which have been used to test QCD (for example determinations of the strong coupling constant) and tune Monte Carlo generators. For instance thrust and C-parameter distributions with massless quarks have been employed to determine the strong coupling constant with high precision using accurate experimental data at $e^- e^+$ colliders (e.g. LEP) [155,156,158,174]. Event shape distributions are differential cross sections where the corresponding kinematics of the final states is varying along the spectrum. Therefore one cannot use fixed order perturbative QCD to describe all different regions of distribution. For instance, in the tail region of event shapes, where the c.m. energy is the only relevant scale, the perturbative expansion in α_s provides a good description. However, in the peak region of the distribution, where the governing scales are highly separated, one encounters large logarithms of the ratios of kinematic scales in FO perturbative QCD. These large logarithms spoil the perturbative series and need to be summed. A very popular approach which provides a systematic summation of large logarithmic terms is to construct an effective filed theory regarding the hierarchies of the relative scales. In this context SCET has been frequently used to properly describe the energetic hadronic final states and various jet observables in the regions where resummation is necessary.

One of the first attempts to study event shapes for boosted heavy quark jets based on an effective field theory has been provided by Refs. [32,39]. Here the double differential hemisphere invariant mass distribution (and thrust distribution) has been studied in the peak region, considering the production of a pair of boosted top-antitop close to the mass-shell at e^+e^- colliders. It was shown that due to the large separation of governing scales in the dijet configuration, $Q \gg m \gg \Gamma \geq \Lambda_{\rm QCD}$, one can use a sequence of effective field theories (SCET with massive quarks and bHQET) to integrate out all the fluctuations of the order of the mass and higher scales. Consequently, Ref. [32] derived a factorization theorem which describes the heavy quark jet dynamics in the peak region. Moreover, the resummation of all sets of large logarithms has been achieved by means of individual Renormalization Group Evolution (RGE) for various matrix elements in the factorization theorem. It was also demonstrated that the location of the peak of the thrust distribution is highly sensitive to the heavy quark mass, and can be used to determine the top mass. It has been shown that based on this method a certain class of short distance mass schemes can be measured with accuracies that are in principle better than $\Lambda_{\rm QCD}$.

The calculation of the thrust distribution at Next-to-Leading logarithm resummation with one-loop matrix elements (NLL$'$) for bHQET is carried out in Ref. [39] . The accuracy of the theoretical description is improved since then by separating the computation of different sectors of the factorization

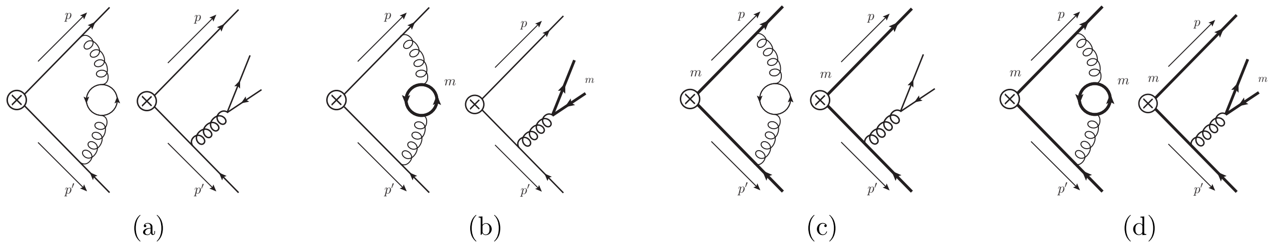

Figure 3.1: Feynman diagrams at order $\mathcal{O}(\alpha_s^2)$ for virtual and real secondary radiation of massive (b,d) and massless (a,c) pairs of quarks.

theorems. The two-loop corrections for the massless soft function and the bHQET jet function are computed in Refs. [175–177] and Ref. [178] , respectively. In addition, the known massless form factors with higher order perturbative corrections were used to determine the two-loop corrections to the hard matching coefficient [179, 180]. The only missing component to have a full Next-to-Next-to-Leading logarithm resummation with two-loop matrix elements ($\mathrm{N^2LL'}$) prediction for the differential cross section in the bHQET region was the mass mode matching of HQET to SCET at $\mathcal{O}(\alpha_s^2)$. Here a complication arises since one needs to account for secondary massive quark effects[1]. The proper treatment of these effects has been addressed just recently in Refs. [42, 43], by incorporating the additional soft and collinear mass mode degrees of freedom into the SCET framework. Based on that, Ref. [181] has recently computed the missing mass mode matching contribution for a $\mathrm{N^2LL'}$ analysis in the bHQET regime. However, the suggested theoretical framework in Refs. [32, 39, 181] is a particular setup that is designed for boosted top production and is confined to the peak region of the distribution with particular kinematics. Nevertheless, Refs. [32, 39] also provided a factorization theorem based on SCET for massive quarks which can be used to predict the far-tail region of the distribution. This computation was carried out up to $\mathcal{O}(\alpha_s)$ considering only the primary production of massive quarks where the issue of producing massive secondary quarks was not properly addressed. Only recently Ref. [43] has shown that accounting for the secondary production of arbitrary massive quarks in jet cross sections is a challenging subject and has non-trivial effects (large corrections at $\mathcal{O}(\alpha_s^2)$ known as rapidity logarithms) which has to be taken into account even at Next-to-Next-to-Leading logarithm resummation with one-loop matrix element ($\mathrm{N^2LL}$).[2] Thus, we have yet to provided a consistent framework to describe the production of the primary and secondary boosted heavy quarks in jet cross sections.

In this work we aim to provide such description of the entire thrust distribution for boosted heavy quark jets in $e^-\,e^+$ collision at $\mathrm{N^2LL}$. We build a coherent setup where the quark mass can be arbitrary. This is a challenging subject in perturbative QCD since now one encounters different physical situations where the hierarchy of the mass with respect to the other kinematic scales (such as Q and Λ_{QCD}) could vary significantly. The full theoretical description of the entire event shape distribution, must take into account various scenarios where the role of the heavy quark mass is continuously changing from the threshold region (where heavy quarks are relevant degrees of freedom as typical massive particles) to the asymptotic limits (i.e. the decoupling limit for $m \gg Q$ where the massive quark can be integrated out or the massless limit $m \ll Q$ where heavy quark is regarded as a light dynamical flavor). This issue has been thoroughly discussed in Ref. [43] considering the production of secondary massive quarks in light hadronic jets where a variable flavor number scheme (VFNS) has been accommodated to incorporate these effects in a consistent framework with factorization theorems.

Therefore, based on previous works in Ref. [32] for massive primary production and inspired by the

[1]The production of heavy quarks in various high energy processes can be understood through two different mechanisms. Primary production where the massive quarks are directly produced in the hard interaction; and Secondary processes where a pair of massive quark-antiquark is produced through the splitting of gluon radiation [see Figs. 3.1].

[2]The study in Refs. [42,43] concerns the final state jets where massive quarks are produced only through the secondary mechanism.

ideas in Ref. [43] for accounting massive secondary quark effects, here we construct a VFNS for fully massive thrust distribution in order to deal with primary and secondary productions of heavy quarks in a unique framework. We emphasize that although the study of the top quark mass is essentially the ultimate aim of our work, we have constructed a generic framework for any arbitrary massive particles in order to examine MC generators. In particular we provide a bottom quark mass analysis in Sec. 3.11. The reason is that the bottom quark mass has been determined to high precision using various methods [see Sec. 2]. Therefore the study of the bottom quark mass parameter in MC parton showers using the theoretical framework which is suggested here, can be considered as a good test. It can be also employed to calibrate some relevant parameters in MC, such as hadronization parameters or the strong coupling constant. Hence, the bottom quark mass analysis would be a complementary study which estimates the reliability of the theoretical framework and in particular justifies the possible outcomes of the top quark mass analysis.

3.2 Event Shape Distributions

Event shape variables are characterizing the geometrical properties of the energy-momentum flow of hadrons in the final state. In other words, event shapes are classifying the shape of an event as seen in detectors in terms of continuous variables. For example the small values of event shape variables are typically referring to dijet events where a smooth transition to three-jet and multijet region events can be represented by larger event shape values. The typical event shape distribution consists of a peak which is populated by the, most likely, dijet events and a tail region where the events with more spherical configurations with gluon radiation are taking place and hence suppressed by powers of α_s.

Event shapes are not fully inclusive observables, nevertheless, by construction, they are infrared and collinear safe observables[3]. This means the perturbative QCD calculation at the partonic level can be used to describe the dominant behavior of the event shape in the OPE region [182–185]. The intuitive reasoning for this property is that infrared and collinear safe observables, by definition, are mostly sensitive to the main directions of energy momentum flow of hadronic final states while the showering and hadronization do not significantly change the distribution.

One of the common features of event shape variables is the behavior of the perturbative series in the dijet limit, where the emission of soft and collinear gluons is logarithmically enhanced. This behavior arises because of the tight restriction which is imposed by the small event shape values on the real emissions while there is no counterpart restriction on the virtual contributions. This results in an incomplete cancellation of logarithmic divergences between virtual and real contributions. These large logarithms spoil the perturbative convergence of fixed order computations of QCD in the dijet limit. Therefore one has to sum the logarithmic terms to all orders in perturbation theory in order to properly describe the event shape distributions. There are various techniques to carry out the resummation of large logarithmic terms [186–192]. One of the most systematic methods is to use Soft Collinear Effective Theory (SCET), where the most singular contributions are factorized [32, 38, 193] and the resummation is achieved by means of renormalization group equations [36, 38, 174, 194–197].

To be more precise, one has to note that the large logarithms are not the only source of possible poor convergences in fixed order calculations. The factorial growth of the coefficients of the perturbative series of the partonic contribution is an important issue which needs to be taken into account in order to obtain high precision in perturbation theory. A similar problem is already noted in the context of sum rules, Sec. 2 , where the use of the pole mass in perturbative expansion of the cross section leads to a renormalon ambiguity. We will discuss some of the modern approaches to cope with this problem in the following sections, Sec. 3.7 and Sec. 3.9.

The deeper reasoning of the renormalon ambiguities are in fact the nonperturbative effects which can be significant in jet observables such as event shapes. These hadronization effects are verified to contribute in terms of power series correction in $\Lambda_{\mathrm{QCD}}/Q\,e$. Thus, these effects are not uniform

[3] The infrared and collinear safe observables are defined such that they are insensitive to emission of soft and/or collinear particles [71] .

over the entire distribution (i.e. e-dependence) and the numerical size of them can be comparable to the next-to-leading order perturbative corrections for small values of the event shape. Therefore it is essential to employ a systematic and consistent approach to include these corrections. A common strategy to incorporate these nonperturbative power corrections is based on QCD factorization where the perturbative and nonperturbative contributions are separated [198]. In this approach a model function (shape function) is convoluted with the partonic computation. The model function can account for the whole range of the nonuniform power corrections over the spectrum. For instance, in the tail region of the distribution where $e \sim \mathcal{O}(1)$, and $\Lambda_{\rm QCD} \ll Qe$, the model function can be expanded, and one recovers the OPE approximation. However, in the peak region, where the dominant contribution of the perturbative computation for the soft emission is enhanced at the scales of the order of hadronization scale $\Lambda_{\rm QCD} \sim Qe$, one has to use the full model function [see Sec. 3.7].

3.2.1 Thrust

To start, it is crucial to select a rather convenient and theoretically clean observable which is highly sensitive to the mass of heavy quarks to be used for phenomenological applications. One of the most commonly used event shape variables is thrust [169],

$$\tau = 1 - T = 1 - \max_{\hat{t}} \frac{\sum_i |\hat{t}\cdot\vec{p}_i|}{\sum_i |\vec{p}_i|}\,, \tag{3.2.1}$$

where the sum is overall the hadronic final states with momenta p_i (whose momentum vectors and energies are respectively $\vec{p}_i$ and E_i) and $\hat{t}$ is the thrust axis. Experimentally, the thrust determination is based on the measurements of the hadronic final states that reach the detector. These final states are in principle stable light hadrons with mass scales of the order of $\Lambda_{\rm QCD}$. Theoretically, these effects (namely hadron mass effects) are related to nonperturbative physics and will be encoded in terms of nonperturbative parameters of the model function which captures the low energy dynamics and will be fitted to experimental data. Therefore in the limit where the quarks are treated as massless particles, it is absolutely consistent at the partonic level to use conservation of energy to set $\sum_i |\vec{p}_i| = \sum_i E_i = Q$ in the denominator of the thrust definition,[4]

$$\tau = 1 - \frac{1}{Q}\max_{\hat{t}} \sum_i |\hat{t}\cdot\vec{p}_i|\,, \tag{3.2.2}$$

where Q is the center of mass energy.

In this work we adopt the event shape variable in Eq. (3.2.2) as the formal definition for the thrust variables[5] in order to study the jets that are initiated from the heavy quarks. The reason is that the event shape variable in Eq. (3.2.2) in comparison with the original thrust variable in Eq. (3.2.1) has the following advantages: the analytic calculations are significantly simpler; it exhibits a higher sensitivity to the quark mass [32,39], so that it is more appropriate for phenomenological applications; it is rather a more inclusive observable with respect to the heavy quark decaying [155], while in the original definition we have to explicitly calculate the momentum of massive quark decay products to measure the thrust.

To demonstrate that the thrust variable as defined in Eq. (3.2.2), exhibits a high sensitivity to the heavy quark mass, it is convenient to express the thrust in the dijet limit in terms of jet invariant mass variable. We remind that the jet invariant mass of quark and antiquark initiated jets in the n and $\bar{n}$ directions are defined by the total invariant mass of all the final state particles in each of the two hemispheres a and b, respectively, which are split up by the plane orthogonal to the thrust axis,

$$s_q = \Big(\sum_{i\in a} p_{q,i}\Big)^2 = \frac{Q^2}{4} - \Big(\sum_{i\in a}\vec{p}_{q,i}\Big)^2 + \mathcal{O}(\lambda^4)\,, \tag{3.2.3}$$

[4]For an extensive discussion on hadron mass effects, we refer to Ref. [199–201] where various event shape schemes are classified based on the common nonperturbative corrections.

[5]This definition agrees with 2-jettiness [201,202].

and the corresponding one for $s_{\bar{q}}$. The subscript $q(\bar{q})$ indicates the $n(\bar{n})$ hemisphere where the boosted quark (antiquark) is produced and decays. In the second equation we make use of the fact that in the dijet limit, the sum of the subsequent particles energies in each hemisphere is equal to half of the center of mass energy $Q/2$ up to power-suppressed terms $\mathcal{O}(\lambda^4)$ where $\lambda \sim m/Q$ [32] .[6] The term $\sum_i \vec{p}_{q,i}$ is the total three momentum in the quark hemisphere. Starting with Eq. (3.2.2) one can split the thrust variable into two pieces from each hemisphere,

$$\tau = 1 - \frac{1}{Q}\max_{\hat{t}}\Big(\sum_{i\in a}\vec{p}_{q,i} - \sum_{j\in b}\vec{p}_{\bar{q},j}\Big)\cdot\hat{t}\,, \tag{3.2.4}$$

where the minus sign ensure the positive contributions form each hemisphere. Now it is trivial to see that the thrust axis with $\hat{t} = \Big(\sum_i \vec{p}_{q,i} - \sum_j \vec{p}_{\bar{q},j}\Big)/\Big|\sum_i \vec{p}_{q,i} - \sum_j \vec{p}_{\bar{q},j}\Big|$ maximizes the second term on the RHS of Eq. (3.2.4). After substituting the thrust axis $\hat{t}$, Eq. (3.2.4) becomes

$$\begin{aligned}\tau &= 1 - \frac{1}{Q}\Big|\sum_{i\in a}\vec{p}_{q,i} - \sum_{j\in b}\vec{p}_{\bar{q},j}\Big| \\ &= 1 - \frac{2}{Q}\Big|\sum_{i\in a}\vec{p}_{q,i}\Big|\,,\end{aligned} \tag{3.2.5}$$

where for the second line we used the total three momentum conservation $\sum_{i\in a}\vec{p}_{q,i} = -\sum_{j\in b}\vec{p}_{\bar{q},j}$. Now we make use of Eq. (3.2.3) to replace the three momentum of each hemisphere in Eq. (3.2.5) with the invariant mass variables. At the end, the results can be expanded in the dijet limit where $s_{q,\bar{q}} \ll Q^2$. The outcome up to leading order in $s_{q,\bar{q}}/Q^2$ reads

$$\tau = \frac{s_q + s_{\bar{q}}}{Q^2} + \mathcal{O}\bigg(\Big(\frac{s_{q,\bar{q}}}{Q^2}\Big)^2\bigg)\,. \tag{3.2.6}$$

This relation clearly displays the high sensitivity of the thrust variable to the mass of the heavy quark that is produced in the dijet configuration.

Now let us discuss the partonic endpoints of the thrust distribution for the production of stable or unstable heavy quarks separately. Let us first consider the situation where a pair of stable heavy quarks is produced. It is straightforward to show from the formal definition in Eq. (3.2.2) that the limit of small thrust for stable massive quarks corresponds to two narrow, boosted, back-to-back jets where each of them carries half of the c.m. energy. This results in the minimum thrust value as

$$\tau_{\min} = 1 - \sqrt{1 - 4m_q^2/Q^2}\,. \tag{3.2.7}$$

In the massless quark limit of the partonic computation this minimum is obviously zero. The second interesting endpoint is related to the three jet configuration which corresponds to the real gluon emission at order $\mathcal{O}(\alpha_s)$ in fixed order QCD. The calculation of this contribution is shown in Sec. 3.6.1 and has an endpoint at $\tau_{max}^{3-\text{jet}} = 5/3 - 4/3\sqrt{1 - 3m_q^2/Q^2}$. Higher thrust values are obtained from configurations with lower energy jets which are interpolating continuously to the multijet endpoint. This endpoint is related to the spherical and isotropic multijet configurations. In this situation the maximum thrust value takes place in the configuration where the two heavy quarks are produced along the thrust axis, traveling in opposite directions, with small 3-momentum components $\vec{p}_{t,\bar{t}} \simeq 0$, and the rest of the energy has been uniformly distributed between an infinite number of massless particles which are scattered isotropically. Hence, one can linearly divide the c.m. energy between all the particles, $Q = 2\,m_q + N\,|\vec{p}\,|$, where N is the number of massless particles which have identical energy $E_i = |\vec{p}_i| = |\vec{p}\,|$ and m_q is the mass of each of the stable heavy quarks. In the limit of an infinite number

[6] This small correction in the dijet limit is related to the small fraction of events with large angels w.r.t. to the thrust axis which can propagate from hemisphere a to b or vice versa [32].

of jets, using spherical coordinates one can make the following substitution $\sum_i \to \rho \int \mathrm{d}\phi\, \mathrm{d}\theta\, \sin\theta$, where ρ is the uniform distribution density given by $\rho = N/(4\pi)$. Substituting the above relations into Eq. (3.2.2) to compute thrust, we obtain

$$\tau_{\max} = 1 - \frac{|\vec{p}|}{Q} \sum_i |\cos\theta_i| = \frac{1}{2} + \frac{m}{Q}. \tag{3.2.8}$$

Note that the maximal possible value for the multijet endpoint of massive quark is kinematically restricted to one. In the massless limit, the result in Eq. (3.2.8) recovers the multijet endpoint, $\lim_{m\to 0} \tau_{\max} = 1/2$. We remark that the corresponding endpoints for the original definition of thrust, given by Eq. (3.2.1), are at $\tau_{\min} = 0$ and $\tau_{\max} = 1/2$, regardless of the fact that quarks are massless or massive. Here, in comparison with the original thrust variable, the maximum and minimum values for massive quarks have moved further to the right by the amount of $2m^2/Q^2 + \mathcal{O}(m^4/Q^4)$ and m/Q, respectively.

Now, we consider the situation where heavy quarks are treated as unstable particles. Here, the small-τ endpoint does vanish due to the power suppressed events [32] where the massless decay products are crossing the hemispheres that are defined by the orthogonal plane to the thrust axis. However the position of the peak is related to dijet events where two almost on-shell tops are produced and decayed in each hemisphere. One can use conservation of momenta in each hemisphere, $\sum_i |\hat{t}\cdot\vec{p}_i| = |\sum_i \hat{t}\cdot\vec{p}_i| = (Q/2)^2 - m_q^2$, to show that the peak position does not vary due to decays at partonic level and it still locates at $\tau_{\text{peak}} = 1 - \sqrt{1 - 4m_q^2/Q^2}$. The multi particle endpoint relates to the isotropic configuration of massless decay products. Thus, this shifts the endpoint region back to $\tau_{\max} = 1/2$. We have verified that indeed the partonic decay of unstable heavy quarks is a subleading power correction which mainly affects the left side of the peak of the thrust distribution. As discussed before, the observed suppression for decay effects (in this thrust scheme) is due to the inclusive nature of the definition in Eq. (3.2.2) which is guaranteed by respecting the momentum conservation in the dijet limit.

3.3 Soft-Collinear and (Boosted) Heavy Quark Effective Field Theory

Quantum field theory (QFT) represents a robust tool to describe intricate phenomena in elementary particle physics. However the computational power of QFTs in elementary particle physics is restricted since in practice one cannot obtain exact solutions. Therefore one applies approximation procedures to determine the dominant effects. In this regard, perturbation theory is one of the most important technologies which is extensively used to perform complicated computations in QFT. The results are expressed in terms of asymptotic series in powers of the coupling constants, where in principle the higher order correction can be determined with more computational effort. Nevertheless in many cases perturbation theory is limited by the nature of the problem, e.g. in QCD the theoretical predictions are limited by the nonperturbative physics or the existence of multiple scales with large hierarchies. The former problem was discussed in Sec. 2.1 where we stressed that the inclusive nature of observables and the OPE allows us to make predictions. Here, both subtleties play an important role.

In fact the problem of highly separated multiple scales in QCD arises because of a more generic property of QFTs, namely the quantum nature of the theory which inevitably accounts for all possible virtual states (degrees of freedom), carrying different characteristic scales such as masses of quarks, the hadronic scale, binding energies, etc. A systematic approach to perform meaningful quantitative predictions in this situation is to construct an effective field theory (EFT) description from the corresponding QFT that is suitable for the kinematics of the physical system. In an EFT one separates the dynamics of degrees of freedom at different scales and then extracts the dominant contributions by a systematic expansion of the main QFT in powers of a kinematic expansion parameter determined by the ratio of scales (representing a power counting parameter of the EFT). The EFT approach improves the calculation by dividing the problem into more convenient single-scale problems at different sectors where all degrees of freedom are playing their role according to their relevance. In general an EFT has the following advantages with respect to the full theory:

- The generic philosophy is along the factorization principles i.e. the dynamics at low energies is not affected by the details of the dynamics at high energies.
- It may demonstrate enriched residual symmetries that provide a better understanding of the governing physics.
- It allows the resummation of large logarithms that are generated from the ratio of scales in full QFT.
- The perturbative computations are more convenient for the set of single scale problems.
- The precision is systematically improvable by accounting the subleading contributions in the power counting expansion of the theory.

EFTs are widely applied to different areas of high energy physics and in particular they are essential tools in QCD phenomenology. The prominent EFTs of QCD are Non-Relativistic QCD (NRQCD) [203–205], Chiral Perturbation Theory (ChPT) [206–213], Heavy Quark Effective Theory (HQET) [214–218] and Soft Collinear Effective Theory (SCET) [36–38, 219]. Here we shortly present the latter two theories (SCET and HQET) in the context where we aim to describe the jet processes.

3.3.1 Soft Collinear Effective Theory

SCET is an effective field theory of QCD which is constructed to describe the production of energetic particles such as high energetic light states in the decay of heavy hadrons [36] or the production of boosted massive quark initiated jets in collider environments [32]. To present the generic idea let us focus on a specific application i.e. when back to back boosted heavy quark-antiquark initiated jets are produced in the e^+e^- collision. In this physical situation the boosted heavy quarks (antiquarks) can emit soft and collinear gluons[7] without significantly changing their virtuality of order p^2. Note that regarding the heavy quark as a boosted particle means that $p_\perp \ll Q$ where Q is the center of mass energy and $p_\perp$ denotes the perpendicular components of the quark momentum p.

SCET is conveniently formulated in light cone coordinates which allow a clear separation of the momentum component scales. This provides a rather more convenient distinction between the soft and collinear modes according to the rapidity of boosted particles and provides an appropriate power counting for momentum components. To start let us introduce the notation by identifying the light cone four-vectors

$$n^\mu = (1, \vec{n})\,, \quad \bar{n}^\mu = (1, -\vec{n})\,, \tag{3.3.1}$$

where $\vec{n}$(-$\vec{n}$) is the direction of the top (antitop) jet with the property, $\vec{n}^2 = 1$, $n^2 = \bar{n}^2 = 0$ and $n \cdot \bar{n} = 2$. Using this basis the momentum of massive particles can be decomposed as

$$p^\mu = n \cdot p \frac{\bar{n}^\mu}{2} + \bar{n} \cdot p \frac{n^\mu}{2} + p_\perp^\mu\,. \tag{3.3.2}$$

Here we also make use of the notation $(p^+, p^-, p_\perp) = (n \cdot p, \bar{n} \cdot p, p_\perp)$ to denote the momentum components in light cone coordinates. The invariant mass of the particle with momentum p^μ hence reads $p^2 = p^+p^- + p_\perp^2$. Now considering the invariant mass of the boosted heavy quark in the $\vec{n}$ direction $p_n^2 = p_n^+ p_n^- + p_{n,\perp}^2$, we obtain the following scaling for its individual momentum components

$$p_n^\mu \sim Q(\lambda^2, 1, \lambda) \tag{3.3.3}$$

[7]Collinear in the sense that the particles are produced in the same direction as the boosted quark (antiquark).

mode	fields	$p^\mu \equiv (+,-,\perp)$	p^2
n-collinear	$(\xi_n\,, A_n^\mu)$	$p_n^\mu \sim Q(\lambda^2, 1, \lambda)$	$Q^2\lambda^2$
$\bar{n}$-collinear	$(\xi_{\bar{n}}\,, A_{\bar{n}}^\mu)$	$p_n^\mu \sim Q(1, \lambda^2, \lambda)$	$Q^2\lambda^2$
soft mode	$(q_s\,, A_s^\mu)$	$p_s^\mu \sim Q(\lambda^2, \lambda^2, \lambda^2)$	$Q^2\lambda^4$

Table 3.1: Summery of the relevant modes in SCET. The power counting parameter is $\lambda \equiv (s_n^{1/2}/Q) \ll 1$.

where the ratio $\lambda \equiv p_{n,\perp}/Q$ is a small parameter which serves as the SCET power counting parameter. According to this scaling, one can identify the soft and collinear degrees of freedom such that they do not alter the virtualty of boosted heavy quarks dramatically[8]. It is useful in this context to use the more generic variable known as the jet invariant mass in the $\vec{n}$ direction i.e. defined as $s_n \equiv [\sum_{i,j\in jet}(p_{n,i} + p_{s,j})]^2 \sim p_{n,\perp}^2$ where p_n and p_s are the collinear and soft particle momenta, respectively. Here the n and $\bar{n}$ subscripts will be used to label the collinear particles in the $\vec{n}$ (quark jet) and $-\vec{n}$ (antiquark jet) directions, respectively. The subscript s denotes the soft modes. The virtuality of the collinear and soft modes satisfy

$$p_n^2 \sim p_{\bar{n}}^2 \sim s_n\,, \quad p_s^2 \sim \frac{s_n^2}{Q^2}\,, \tag{3.3.4}$$

and the corresponding individual momentum components are respectively displayed in Tab. 3.1. The dynamics of the n- and $\bar{n}$- collinear sectors are decoupled and only the soft radiation provides the cross talk between these jets. Note that when $s_n/Q \gg \Lambda_{\rm QCD}$, the soft mode is dominated by the perturbative dynamics, so that we are in the OPE region where the nonperturbative corrections are power suppressed.

After specifying the appropriate power counting of the effective theory, one can assign the relative field modes by separating the far off-shell degrees of freedom from the relevant fluctuations which keeps the heavy quark close to its mass shell. This can be performed in momentum-position space using the so called label formalism [36, 37]. Here we only consider the dynamics of particles in the n direction. One obtains similar independent relations for the $\bar{n}$ jet as well. We first move the large momentum component into the label of the mode field and redefine the quark, $q(x)$, and gluon fields, $A(x)$, with

$$\begin{aligned} q(x) &= \sum_{\tilde{p}\neq 0} e^{-i\tilde{p}x} q_{n,\tilde{p}}(x) + q_s(x)\,, \\ A(x) &= \sum_{\tilde{p}\neq 0} e^{-i\tilde{p}x} A_{n,\tilde{p}}(x) + A_s(x)\,, \end{aligned} \tag{3.3.5}$$

where the label $\tilde{p}$ contains the large components of the quark momentum, $\tilde{p} = Q(0, 1, \lambda)$. Now the x-dependence of the fields $q_{n,\tilde{p}}(x)$ and $A_{n,\tilde{p}}(x)$ only captures the dynamics of the residual momentum scale, $k^\mu = Q(\lambda^2, \lambda^2, \lambda^2)$. The $q_{n,\tilde{p}}(x)$ constitutes from a large and a small spinor component, respectively denoted with $\xi_{n,\tilde{p}}$ and $\Xi_{\bar{n},\tilde{p}}$,

$$q_{n,\tilde{p}}(x) = \xi_{n,\tilde{p}}(x) + \Xi_{\bar{n},\tilde{p}}(x)\,. \tag{3.3.6}$$

These fields can be extracted form the $q_{n,\tilde{p}}(x)$ using projection operators

$$\xi_{n,\tilde{p}} = \frac{\not{n}\not{\bar{n}}}{4} q_{n,\tilde{p}}(x)\,, \quad \Xi_{\bar{n},\tilde{p}} = \frac{\not{\bar{n}}\not{n}}{4} q_{n,\tilde{p}}(x)\,, \tag{3.3.7}$$

[8]Strictly speaking one would also have to take the mass mode with $p_m \sim Q(\lambda, \lambda, \lambda)$ as relevant degrees of freedom. However their effect is only appearing at secondary virtual corrections. Taking these modes into account will not change the SCET derivation [38].

where $(\bar{n\!\!\!/} n\!\!\!/ + n\!\!\!/ \bar{n\!\!\!/})/4 = 1$. In fact the fields $\Xi_{\bar{n},\tilde{p}}$ are far off-shell degrees of freedom which will be integrated out in the following (which can be done by using the equations of motion). Now we have all the ingredients in hand to derive the SCET Lagrangian. Starting with the massive QCD Lagrangian

$$\mathcal{L}_{\rm QCD} = \bar{q}(x)(iD\!\!\!\!/ - m)q(x) - \frac{1}{4}F_{\mu\nu}F^{\mu\nu}\,, \tag{3.3.8}$$

where the covariant derivative, D_μ and gluon field strength tensor $F_{\mu\nu}$ are defined as

$$D_\mu = \partial_\mu + igT^a A^a_\mu\,, \quad F_{\mu\nu} = -\frac{i}{g}[D_\mu, D_\nu]\,, \tag{3.3.9}$$

respectively. We make use of the field redefinition in Eqs. (3.3.5), and the decomposition of the spinor components, in Eq. (3.3.6), to rewrite the QCD Lagrangian as

$$\begin{aligned}\mathcal{L}_{q,n} = \sum_{\tilde{p},\tilde{p}'} e^{-i(\tilde{p}-\tilde{p}')x}\Big[&\bar{\xi}_{n,\tilde{p}'} in\cdot D\frac{\bar{n\!\!\!/}}{2}\xi_{n,\tilde{p}} + \Xi_{\bar{n},\tilde{p}'}(\tilde{p\!\!\!/}_\perp + iD\!\!\!\!/_\perp - m)\xi_{n,\tilde{p}} \\ &+ \bar{\xi}_{n,\tilde{p}'}(\tilde{p\!\!\!/}_\perp + iD\!\!\!\!/_\perp - m)\Xi_{\bar{n},\tilde{p}} + \Xi_{\bar{n},\tilde{p}'}(\tilde{p} + i\bar{n}\cdot D)\frac{n\!\!\!/}{2}\Xi_{\bar{n},\tilde{p}}\Big]\,. \end{aligned}\tag{3.3.10}$$

Here one can see that the kinetic term of the small field component is power suppressed since $(i\bar{n}\cdot D) \sim Q\lambda^2$. Hence we can make use of the equation of motion to integrate out these fluctuations to all orders in perturbation theory. The equation of motion for the $\Xi_{\bar{n},\tilde{p}}$ (and similarly for $\Xi_{\bar{n},\tilde{p}'}$) reads

$$(\tilde{p} + i\bar{n}\cdot D)\frac{n\!\!\!/}{2}\Xi_{\bar{n},\tilde{p}} = -(\tilde{p\!\!\!/}_\perp + iD\!\!\!\!/_\perp - m)\xi_{n,\tilde{p}}\,. \tag{3.3.11}$$

Finally using the scaling of the relative fluctuations in momenta and fields, we can systematically expand the Lagrangian up to the leading order of the power counting parameter λ^0. The resulting expression describes the leading soft-collinear interactions, and reads

$$\mathcal{L}_{q,n} = \bar{\xi}_n[i\,n\cdot D_s + g\,n\cdot A_n + (iD\!\!\!\!/_c^\perp - m)W_n\frac{1}{\bar{n}\cdot\mathcal{P}}W_n^\dagger(iD\!\!\!\!/_c^\perp + m)]\frac{\bar{n\!\!\!/}}{2}\xi_n\,, \tag{3.3.12}$$

where the soft and collinear covariant derivatives are

$$iD_s^\mu = i\partial^\mu + gA_s^\mu\,, \quad iD_c^\mu = \mathcal{P}^\mu + gA_n^\mu\,, \tag{3.3.13}$$

respectively, with $D_c^\perp \sim m \gg D_s^\perp$. In this Lagrangian the partial derivatives are probing the residual dynamics in the field i.e. $\partial^\mu \sim \lambda^2$. The large momentum components are extracted by the label operator $\mathcal{P}^\mu$ which is defined by the action on any collinear field $\phi_{n,\tilde{p}}$,

$$\mathcal{P}^\mu\,\phi_{n,\tilde{p}} = \tilde{p}^\mu\,\phi_{n,\tilde{p}}\,, \quad \mathcal{P}^\mu\,\phi^\dagger_{n,\tilde{p}} = -\tilde{p}^\mu\,\phi^\dagger_{n,\tilde{p}}\,. \tag{3.3.14}$$

The term $W_n(x)$ in Eq. (3.3.12) is the collinear Wilson line, constructed from A_n^μ. In position space the Wilson lines read

$$W_n(x) = P\exp\big[-ig\int_{-\infty}^0 {\rm d}s\,\bar{n}\cdot A_n(\bar{n}s + x)\big]\,, \tag{3.3.15}$$

where P is the path ordering operator along the lightlike line in the $\bar{n}$ direction. After the Fourier transformation of the expression in Eq. (3.3.15) to momentum space we obtain

$$W_n(x) = \sum_{\rm perms}\exp\Big(-\frac{g}{\mathcal{P}}\bar{n}\cdot A_n(x)\Big)\,. \tag{3.3.16}$$

The strict expansion of the Wilson line in Eq. (3.3.12) recovers the fact that in the soft-collinear Lagrangian the interaction of collinear quarks with an arbitrary number of collinear gluons is allowed.

The deeper reasoning of the existence of the collinear Wilson lines in the SCET Lagrangian is the gauge structure of the theory [38].

Since the fluctuation modes in SCET have a particular momentum scaling, the theory respects residual gauge symmetries, namely the collinear gauge symmetries $U_n(x)$ with

$$\partial^\mu U_n(x) \sim Q(\lambda^2, 1, \lambda)\,, \quad \partial^\mu U_{\bar{n}}(x) \sim Q(1, \lambda^2, \lambda)\,, \tag{3.3.17}$$

and the soft gauge symmetry, $U_s(x)$, with

$$\partial^\mu U_s(x) \sim Q(\lambda^2, \lambda^2, \lambda^2)\,. \tag{3.3.18}$$

The consequent gauge transformations for various fields in SCET are presented in Ref. [38]. Amongst them, the collinear and Wilson lines transformation rules read

$$\begin{aligned}
&\xi_{n,\tilde{p}}(x) \xrightarrow{U_n} U_{n,\tilde{p}-\tilde{p}'}(x)\,\xi_{n,\tilde{p}'}(x)\,, \quad \xi_{n,\tilde{p}}(x) \xrightarrow{U_{\bar{n}}} \xi_{n,\tilde{p}}(x)\,, \quad \xi_{n,\tilde{p}}(x) \xrightarrow{U_s} U_s(x)\,\xi_{n,\tilde{p}}(x)\,,\\
&W_n(x) \xrightarrow{U_n} U_n(x)\,W_n(x)\,, \quad W_n(x) \xrightarrow{U_{\bar{n}}} W_n(x)\,, \quad W_n(x) \xrightarrow{U_s} U_s(x)\,W_n(x)\,U_s^\dagger(x)\,.
\end{aligned} \tag{3.3.19}$$

Note that the collinear transformation can change the label of a collinear quark field. The Wilson lines are important ingredients of SCET which can be employed in constructing various collinear gauge invariant operators. Given the transformation rules in Eq. (3.3.17), an important gauge invariant combination of a Wilson line with a collinear field is namely the quark jet field [36, 37]

$$\chi_n(x) \equiv W_n^\dagger(x)\,\xi_n(x)\,, \quad \chi_{\bar{n}}(x) \equiv W_{\bar{n}}^\dagger(x)\,\xi_{\bar{n}}(x)\,, \tag{3.3.20}$$

which correspond to quark and antiquark initiated jets, respectively. Jet fields provide a better sense of a jet in terms of collinear quark and an arbitrary number of gluons moving in the $n(\bar{n})$ direction. Another example of useful operators is the jet production current operator which connects the n- and $\bar{n}$- collinear sectors

$$J_{\rm SCET}(x) = \bar{\chi}_n(x)\,\Gamma\,\chi_{\bar{n}}(x)\,, \tag{3.3.21}$$

where $\Gamma \in \{\gamma^\mu, \gamma^\mu\gamma_5\}$ is the spin matrix for vector or axial-vector channel, respectively. This is the counterpart operator for the QCD current operator in SCET and is appearing in the jet cross section determinations.

To obtain the complete SCET Lagrangian one needs to include the soft interactions together with collinear sectors,

$$\mathcal{L}_{\rm SCET} = \mathcal{L}_s(A_s^\mu, q_s) + \mathcal{L}_{q,n}(A_n^\mu, A_s^\mu, \xi_n) + \mathcal{L}_{q,\bar{n}}(A_{\bar{n}}^\mu, A_s^\mu, \xi_{\bar{n}})\,. \tag{3.3.22}$$

The soft Lagrangian, $\mathcal{L}_s(A_s^\mu, q_s^\mu)$, is similar to the full QCD Lagrangian, however constructed from soft quark and gluon fields. Based on $\mathcal{L}_{\rm SCET}$, the derivation of the corresponding Feynman rules in SCET is straightforward [36] . Note that the collinear sectors contain soft gluon fields. This corresponds to the soft and collinear coupling through the term $(\xi_n\, g\, n\cdot A_s \bar{\not{n}}\xi_n)/2$ in $\mathcal{L}_{q,n}$. However, it is possible to decouple the soft and collinear modes by performing the following field redefinitions on the collinear fields [38]

$$\xi_n \to Y_n \xi_n\,, \quad A_n^\mu \to Y_n A_n^\mu Y_n^\dagger\,, \tag{3.3.23}$$

where the term Y_n ($Y_n^\dagger$) is a soft Wilson line with $Y_n Y_n^\dagger = 1$. In position space Y_n and $Y_n^\dagger$ read

$$\begin{aligned}
Y_n(x) &= \bar{P}\exp\Big(-i\,g\int_0^\infty {\rm d}s\, n\cdot A_s(ns+x)\Big)\\
Y_n^\dagger(x) &= P\exp\Big(+i\,g\int_0^\infty {\rm d}s\, n\cdot A_s(ns+x)\Big)\,,
\end{aligned} \tag{3.3.24}$$

where $P(\bar{P})$ is the path(antipath)-ordering operator. The equation of motion for the soft Wilson line is $(in\cdot\partial+gn\cdot A_s)Y_n=0$. After applying the field redefinitions in Eq. (3.3.24) to the SCET Lagrangian in Eq. (3.3.22), the A_s dependence in the n- and $\bar{n}$- collinear Lagrangians vanishes yielding

$$\mathcal{L}_{\rm SCET}=\mathcal{L}_s(A_s^\mu,q_s)+\mathcal{L}_{q,n}(A_n^\mu,\xi_n)+\mathcal{L}_{q,\bar{n}}(A_{\bar{n}}^\mu,\xi_{\bar{n}})\,, \tag{3.3.25}$$

where the collinear and soft interactions are absolutely decoupled at the Lagrangian level. This feature is the basis of the jet cross section factorization in SCET. Now the corresponding soft and collinear interactions are appearing in terms of soft Wilson lines in the effective operators. For instance the current operator after field redefinition reads

$$J_{\rm SCET}(x)=\bar{\chi}_n(x)\,Y_n^\dagger\,\Gamma\,Y_{\bar{n}}\,\chi_{\bar{n}}(x)\,. \tag{3.3.26}$$

One of the most important aspects of SCET is that it allows a convenient proof of the factorization for jet cross sections [32, 38, 220] which can be schematically displayed as

$$\mathrm{d}\sigma\sim H\otimes\mathcal{J}\otimes S+\mathcal{O}(\lambda)\,. \tag{3.3.27}$$

Here, the term H, named as the hard function, captures the short distance dynamics. It results from taking the square of Wilson coefficients obtained by matching the QCD current operator onto the SCET current operator. The jet function, $\mathcal{J}$, is the matrix element of the gauge invariant combination of collinear fields and collinear Wilson lines. The term S represents the vacuum matrix element of the soft Wilson lines which are entering the current operator in Eq. (3.3.21). The term $\mathcal{O}(\lambda)$ reminds that the SCET Lagrangian and consequent factorization are provided at leading order in λ, i.e. the most singular contributions in the jet cross section. Note that the factorization of collinear and soft dynamics is the direct consequence of decoupling property which has been achieved by the field redefinition in Eq. (3.3.24).

The advantage of factorization is that the separated sectors have simpler structures and can be computed and normalized independently in perturbation theory. Therefore one obtains individual RGEs for each function. This leads to a systematic resummation of large logarithms in powers of $\ln(\lambda)$ and in particular of the Sudakov logarithms[9] present in the dominant singular contributions. In general these logarithms are arising from the ratio of scales in the physical problem and in fact the factorization theorem provides us with a systematic understanding of the origin of these logarithms in order to sum them up via RG equations.

The generic RGE for a matrix element F in SCET such as the jet and soft function can be formulated as a nonlocal convolution with plus distributions,

$$\mu\frac{\mathrm{d}}{\mathrm{d}\mu}F(\mu,\omega)=\int\mathrm{d}\omega'\bigg(\frac{\Gamma^F[\alpha_s]}{\mu}\bigg[\frac{\mu\,\theta(\omega-\omega')}{\omega-\omega'}\bigg]_+ +\gamma^F[\alpha_s]\,\delta(\omega-\omega')\bigg)F(\mu,\omega')\,, \tag{3.3.28}$$

where $\Gamma^F[\alpha_s]$ and $\gamma^F[\alpha_s]$ are the perturbative series for cusp and noncusp anomalous dimensions. The plus distribution in the anomalous dimension has an implicit $\ln(\mu)$ dependence, hence this term in fact sums the double logarithms. The RGE for the hard function however is local and obeys

$$\mu\frac{\mathrm{d}}{\mathrm{d}\mu}H(Q,\mu)=\Big(\Gamma^H[\alpha_s]\ln\frac{\mu^2}{Q^2}+\gamma^H[\alpha_s]\Big)H(Q,\mu)\,. \tag{3.3.29}$$

The general solution of the RG equations in Eqs. (3.3.28, 3.3.29) has been performed in [39]. The consequent solutions are known as evolution factors which are summing the large logarithms between the characteristic scales, denoted with $\{\mu_H,\mu_F\}$, and the global renormalization scale μ of the factorized cross section,

$$\begin{aligned}F(\mu,\omega)&=\int\mathrm{d}\omega'\,U_F(\omega-\omega',\mu,\mu_F)F(\omega',\mu_F)\,,\\ H(Q,\mu)&=U_H(Q,\mu_H,\mu)H(Q,\mu_H)\,.\end{aligned} \tag{3.3.30}$$

[9]The Sudakov logarithms are produced from the incomplete cancellation of the overlapping IR collinear and soft divergences.

Order	Log.Term.	Cusp	Noncusp	Matching	β	nonsingular	γ_Δ	δ
LL	$\alpha_s^n L^{n+1}$	1-loop	-	Tree	1-loop	None	None	None
NLL	$\alpha_s^n L^n$	2-loop	1-loop	Tree	2-loop	None	1-loop	None
N^{2}LL	$\alpha_s^n L^{n-1}$	3-loop	2-loop	1-loop	3-loop	1-loop	2-loop	1-loop
N^{3}LL	$\alpha_s^n L^{n-2}$	4-loop	3-loop	2-loop	4-loop	2-loop	3-loop	2-loop

Table 3.2: List of perturbative corrections that are required for the resummation in SCET at different orders. The second column shows the logarithmic structures that are summed by SCET at each order of accuracy. For completeness, we have presented the necessary corrections for nonsingular contributions, gap anomalous dimension γ_Δ and gap subtraction δ in the table. These terms are discussed in Sec. 3.6 and Sec. 3.7.

The RG equations, respective anomalous dimensions and resulting evolution factors for various matrix elements are given in App. C explicitly.

To understand which perturbative information is needed to sum the large logarithms via SCET, let us first illustrate the order counting in the jet cross section. The logarithmic structure of the differential cross section can be easily demonstrated using the cumulant of the thrust distribution that is defined as

$$\Sigma(\tau) = \int_0^\tau \mathrm{d}\tau' \frac{1}{\sigma}\frac{\mathrm{d}\sigma}{\mathrm{d}\tau}(\tau') \,. \tag{3.3.31}$$

In fixed order perturbation theory the cumulant can be displayed schematically as

$$\ln\Sigma(\tau) \sim \sum_{n=1}^{\infty} \alpha_s^n \sum_{k=0}^{n+1} L^k = \Big[\alpha_s \sum_{k=0}^{2} L^k\Big]_{\mathrm{LO}} + \Big[\alpha_s^2 \sum_{k=0}^{3} L^k + \Big]_{\mathrm{NLO}} + \Big[\alpha_s^3 \sum_{k=0}^{4} L^k + \Big]_{\mathrm{NNLO}} + \cdots \tag{3.3.32}$$

where $L \sim \ln(\tau)$. The subscript LO, NLO and N^{2}LO indicates the fixed order counting for the perturbative series in α_s. However these logarithms can be large while the kinematic scales are highly separated such that $\alpha_s L \sim \mathcal{O}(1)$. This can deteriorate the convergence of the perturbative series in Eq. (3.3.32). Hence one needs to rearrange the perturbative expansion in Eq. (3.3.32) with the counting criteria $\alpha_s L \sim \mathcal{O}(1)$ in order to capture more information and obtain the best convergence. This requires the summation of the logarithms which can be displayed in a schematic expansion as

$$\ln\Sigma(\tau) \sim \Big[L \sum_{k=1}^{\infty} (\alpha_s L)^k\Big]_{\mathrm{LL}} + \Big[\sum_{k=1}^{\infty} (\alpha_s L)^k\Big]_{\mathrm{NLL}} + \Big[\alpha_s \sum_{k=1}^{\infty} (\alpha_s L)^k\Big]_{\mathrm{N^2LL}} + \Big[\alpha_s^2 \sum_{k=1}^{\infty} (\alpha_s L)^k\Big]_{\mathrm{N^3LL}} + \cdots \tag{3.3.33}$$

Here the brackets are grouping the logarithmic structures which are summed at the so called LL, NLL, N^{2}LL, N^{3}LL accuracies. Based on this counting one can identify the necessary ingredients to determine the resummed cross section in SCET up to N^{3}LL accuracy. We have summarized the list of requirements in Tab. 3.2, taken from Ref. [155].

3.3.2 (Boosted) Heavy Quark Effective Theory

Hadronic systems where the heavy quark interacts with soft degrees of freedom, such as B mesons or heavy baryons, are conveniently described with heavy quark effective field theory. The natural hierarchy of scales in such systems is $m \gg \Lambda_{\mathrm{QCD}}$ where m is the mass of the heavy quark and Λ_{QCD} is the typical scale of soft interactions that fluctuates the heavy quarks close to the mass shell. Hence the momentum of a heavy quark in such physical systems can be written as

$$p^\mu = m v^\mu + k^\mu \,, \tag{3.3.34}$$

where v is the 4-velocity of the hardon which carries the heavy quark, conventionally taken as $v = (1, \vec{0})$ in the rest frame of heavy hadron. The term k^μ is the momentum fluctuation resulting from the soft

mode	fields	$p^\mu \equiv (+,-,\perp)$
n-ucollinear	$(h_{v_+}\,, A^\mu_+)$	$k^\mu \sim \hat{s}(\lambda, \lambda^{-1}, 1)$
n-ucollinear	$(h_{v_-}\,, A^\mu_-)$	$k^\mu \sim \hat{s}(\lambda^{-1}, \lambda, 1)$
soft mode	$(q_s\,, A^\mu_s)$	$k^\mu \sim \hat{s}(\lambda, \lambda, \lambda)$

Table 3.3: Summery of the fluctuation modes in bHQET. The power counting parameter $\lambda_{\rm bHQET} = \hat{s}_t \ll 1$.

interactions with light partons. For a nearly on shell quark with $|k^\mu| \ll m$ one can separate the large momentum and soft fluctuations and then decompose the resulting quark field into large and small components, i.e.

$$q(x) = e^{-imv\cdot x}\big[h_v(x) + H_v(x)\big]\,, \tag{3.3.35}$$

where the h_v and H_v are the upper (i.e. large) and lower (i.e. small) components of spinor field, respectively. Note that now these dynamical fields correspond to the soft interacting modes which have the residual momentum $k^2 \sim \Lambda^2_{\rm QCD}$. This decomposition can be performed by applying the projection operators, $\mathcal{P}^+_v = (1+\not{v})/2$ and $\mathcal{P}^-_v = (1-\not{v})/2$ on the quark field

$$h_v(x) = e^{imv\cdot x}\mathcal{P}^+_v\, q(x)\,, \quad H_v(x) = e^{imv\cdot x}\mathcal{P}^-_v\, q(x)\,. \tag{3.3.36}$$

It is easy to show that the resulting field satisfies the following projection relations

$$\not{v} h_v = h_v\,, \quad \not{v} H_v = -H_v\,. \tag{3.3.37}$$

By inserting these field redefinitions into the Dirac Lagrangian, i.e. the quark sector of the QCD Lagrangian in Eq. (3.3.8), we obtain

$$\mathcal{L}_q = \bar{h}_v iv\cdot D h_v + \bar{H}_v(-iv\cdot D - 2m)H_v + \bar{h}_v i\vec{\not{D}} H_v + \bar{H}_v i\vec{\not{D}} h_v\,, \tag{3.3.38}$$

where $i\vec{\not{D}} = iD^\mu - v^\mu iv\cdot D$ only contains the 3-spatial component of the covariant derivative. Here the h_v is a massless degree of freedom which describes the soft fluctuations of the heavy quark close to its mass shell, while the H_v describes the massive mode interactions. The coupling of the two modes is performed by the last two terms in the effective Lagrangian. Now to integrate out the off-shell massive mode H_v, we make use of the equation of motion i.e.

$$H_v = \frac{1}{2\,m + iv\cdot D} i\vec{\not{D}} h_v\,. \tag{3.3.39}$$

This relation manifests the suppression of the H_v mode in the power counting parameter of HQET $H_v = \lambda_{\rm HQET} h_v$, where $\lambda_{\rm HQET} = \Lambda_{\rm QCD}/m$. After substituting the H_v in Eq. 3.3.38 using Eq. (3.3.39) and performing the expansion of Eq. (3.3.38) up to the leading order in λ_{HQET}, we obtain the leading HQET Lagrangian,

$$\mathcal{L}_{HQET} = \bar{h}_v iv\cdot D_s h_v - \frac{1}{4}F_{\mu\nu}F^{\mu\nu} + \mathcal{O}\Big(\frac{\Lambda_{\rm QCD}}{m}\Big)\,, \tag{3.3.40}$$

where $iD^\mu_s = i\partial^\mu + gA^\mu_s$. The additional term $\frac{1}{4}F_{\mu\nu}F^{\mu\nu}$ accounts for soft gluon interactions. The field strength tensor $F_{\mu\nu}$ carries only the soft gluon fields, denoted with A^μ_s, and thus the resulting soft dynamic is similar to the full QCD.

An interesting application of HQET is in collider physics, e.g. to describe the highly energetic jets in the dijet configuration that are initiated from unstable top-antitop production at e^+e^- colliders, while the jet invariant mass is $(s_t - m_t^2) \ll m_t^2$ [32]. The term s_t denotes the invariant mass of the top (antitop) jet. Note that in the previous section we introduced SCET to describe the same process. In SCET the quark fluctuations can have virtualities of the order of the mass that can kick the top quark far off-shell. However, here we aim to use HQET to describe the top quark dynamics near its mass shell which corresponds to a kinematical constraint over the scale of fluctuation $\Gamma_t \lesssim k^\mu \ll m$, where k^μ indicates the momentum of soft interactions in the rest frame of the top quark. The term Γ_t denotes the total decay width of the top quark which provides an IR cutoff over the residual soft scale. Hence the top (antitop) quark momentum, in its rest frame, follows the relation in Eq. (3.3.34). The convenient frame to study the jet cross section is the center of mass frame, so that we adopted two copies of HQET to separately describe the boosted top and antitop quark jets in the n- and $\bar{n}$-direction in the c.m. frame. The resulting effective theory is known as boosted HQET (bHQET). The bHQET Lagrangian reads [32]

$$\mathcal{L}_\pm = \bar{h}_{v_\pm}\Big(iv_\pm \cdot D_\pm - \delta m + \frac{i}{2}\Gamma_t\Big)h_{v_\pm}\,, \tag{3.3.41}$$

where

$$D_+ = i\partial_+^\mu + gA_+^\mu + \frac{\bar{n}^\mu}{2} g\, n\cdot A_s\,, \quad D_- = i\partial_-^\mu + gA_-^\mu + \frac{n^\mu}{2} g\, \bar{n}\cdot A_s\,, \tag{3.3.42}$$

and the $\pm$ subscript refers to jet in the $\pm\vec{n}$ directions. The corresponding velocity vectors in light cone coordinates are

$$v_+^\mu = \Big(\frac{m}{Q}, \frac{Q}{m}, 0_\perp\Big)\,, \quad v_-^\mu = \Big(\frac{Q}{m}, \frac{m}{Q}, 0_\perp\Big)\,, \tag{3.3.43}$$

which are easily obtained by boosting $v = (1, \vec{0})$. Here the soft interactions of the massive quarks (antiquarks) in the boosted frame are accounted by the ultra-collinear modes $A_\pm^\mu$, that are collinear modes obtained from boosting the typical soft modes in the rest frame of the top quark, which preserve the invariant mass of the jet. The momentum components of $A_\pm^\mu$ are

$$k_+^\mu \sim \hat{s}_t\Big(\frac{m}{Q}, \frac{Q}{m}, 1\Big)\,, \quad k_-^\mu \sim \hat{s}_t\Big(\frac{Q}{m}, \frac{m}{Q}, 1\Big)\,. \tag{3.3.44}$$

The term $\hat{s}_t = (s_t - m_t^2)/m_t$ is the scale of the soft fluctuations that leaves the top quark close to the mass shell, so that $\hat{s}_t \ll m_t$. The cross talk of the top-antitop jets is mediated with additional (ultra)soft modes A_s. These modes are in fact playing the same role as the soft modes in the SCET [32], having uniform momentum scaling in the light cone coordinate, given in Tab. 3.3. The term δm denotes the residual mass term which specifies the scheme of the mass parameter in bHQET. The term $\frac{i}{2}\Gamma_t$ provides an effective description of the inclusive decay of the unstable top quark close to the mass shell [32]. This approach is suitable for applications when the coherent sum of the momenta of top decay products enters the observable as it happens for thrust. The latter two terms will be discussed further in Sec. 3.9 and Sec. 3.7, respectively.

The effective current operator in bHQET is given by

$$J_{\rm bHQET} = (\bar{h}_{v_+} W_n)\, \Gamma\, (W_{\bar{n}}^\dagger h_{v_-})\,, \tag{3.3.45}$$

where the term W_n are the same collinear Wilson lines as defined in SCET in Eq. (3.3.15), except here we replace the collinear field $A_n(A_{\bar{n}})$ with ultracollinear fields $A_+(A_-)$. The ultracollinear Wilson lines are essential ingredients which are restoring the ultracollinear gauge invariance in the bHQET current.

Furthermore, similar to SCET, one can use the soft Wilson lines Y_n and $Y_{\bar{n}}$, given in Eq. (3.3.24), to redefine the heavy quark and ultracollinear gluon fields,

$$h_{v_+} \to Y_n h_{v_+}\,, \quad h_{v_-} \to Y_{\bar{n}} h_{v_-}\,, \quad A_+^\mu \to Y_n A_+^\mu Y_n^\dagger\,, \quad A_-^\mu \to Y_{\bar{n}} A_-^\mu Y_{\bar{n}}^\dagger\,, \tag{3.3.46}$$

and decouple the (ultra)soft interactions from the collinear sector. This decoupling allows us to write a factorization theorem for the jet cross section in bHQET that will be discussed further in Sec. 3.5.

Note that the matching of bHQET to the high energy theory is taking place at the mass scale, whereas the jet production itself is taking place at the hard scale Q. Thus one needs to use an intermediate effective theory to decrease the effective fluctuations of the theory from the scale Q down to the mass scale. This has been performed by Ref. [32] where they employ SCET to integrate out the hard fluctuation at the scale of Q and then match the SCET theory to bHQET at the mass scale, in order to describe the top-antitop jets close to the mass shell.

3.4 VFNS for Primary Massless and Secondary Heavy Quark Production in Thrust

A systematic description of heavy quark effects with arbitrary mass for fully inclusive cross sections at hadron colliders has been provided by Aivazis, Collins, Olness and Tung (ACOT) in Refs. [40, 41]. This approach is the basis of the so called variable flavor number scheme (VFNS) which is based on employing different renormalization conditions depending on whether the quarks are heavy, light or fluctuate close to the mass-shell.[10] The basic idea in Ref. [40, 41] has been adopted by Refs. [42, 43] for final state jets to integrate in (out) the heavy quark effects in event shape descriptions within the effective field theory framework. In particular they have adopted a VFNS for final state jets in SCET to take into account the production of heavy quarks in e^+e^- collisions via secondary radiation through the splitting of virtual gluons at order $\mathcal{O}(\alpha_s^2)$.

In this section we shortly present the key ideas of Refs. [42, 43] considering the secondary heavy quark effects for massless event shapes. We start with a brief review of the massless factorization theorem for the singular contributions in the dijet limit where we set up the notation and basic framework. Then we will discuss the essential ingredients and underlying ideas for incorporating the secondary heavy quark effects into the massless factorization theorem. The results will be formulated in terms of various scenarios which are valid to all orders in perturbation theory. However matrix elements will be presented only at $\mathcal{O}(\alpha_s)$. We also address the nontrivial contributions at $\mathcal{O}(\alpha_s^2)$ which contain large rapidity logarithms, resulting from massive secondary radiation corrections. This is an important ingredient which has to be taken into account for the analyses at Next-to-Next-to leading logarithmic accuracy.

3.4.1 The Massless Factorization Theorem

To discuss the relevant dynamical fluctuations in the dijet limit, we use the representation of thrust in Eq. (3.2.6) valid in the dijet limit. The invariant mass of each jet is proportional to the square of the momentum transverse to the thrust axis of the collinear particles in each hemisphere $s_q \sim p_T^2$. Hence, in the dijet limit configuration, where the boosted jets are pencil like (i.e. narrow jet cones with small opening angle $\theta \sim p_T/Q \ll 1$), the allowed final states are restricted to $p_T \ll Q$. Writing this restriction in terms of the thrust variable lead to $\tau \ll 1$ which implies the peak (i.e. $\tau \sim 2\Lambda_{\rm QCD}/Q$) and the tail ($2\Lambda_{\rm QCD}/Q \leq \tau \lesssim 1/3$) regions of the distribution. The dynamics of the system in this region is essentially dictated by three highly separated scales and the corresponding modes. The hard scale $\mu_H \sim Q$ which is the c.m. energy in the hard interaction (e^+e^- collision), the jet scale $\mu_J \sim Q\lambda$ which is related to the invariant mass of jets via $\mu_J^2 \sim s_q$, and the soft scale $\mu_S \sim Q\lambda^2$ that is the energy of soft radiations at large angles, where λ is the power counting parameter which scales as $\lambda \sim \max(\tau^{1/2}, (\Lambda_{\rm QCD}/Q)^{1/2})$. The corresponding hard, n- , $\bar{n}$- collinear and soft modes are displayed in Fig. 3.2.

Based on these degrees of freedom in the dijet limit, one can employ SCET [see Sec. 3.3.1] to calculate the most singular contributions within perturbation theory. It has been shown in Refs. [32, 38, 193] that the jet cross section in the dijet limit within the SCET formalism can be factorized

[10] We note that a similar renormalization procedure is customarily used for accounting the massive quark effects in the strong coupling constant Ref. [221]. The formulation of VFNS for DIS in the OPE region is also based on analogous concepts.

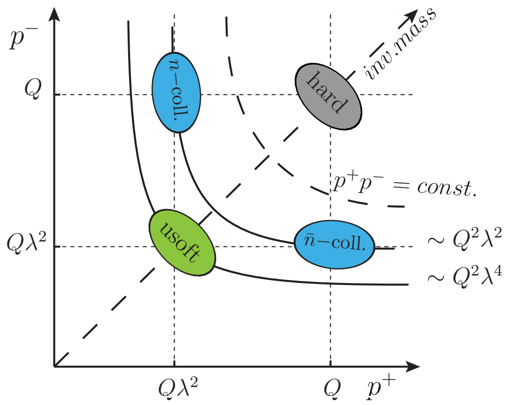

(a)

Figure 3.2: Visualization of collinear and soft mode fluctuations in SCET, illustrated in the p^+-p^- plane. The modes are induced by the effective degrees of freedom in the dijet limit of jet cross section. The hard modes are off-shell effects which are integrated out at the scale μ_H, as schematically denoted with the dashed hyperbola. The n and $\bar{n}$ collinear modes with different rapidity are placed on the same invariant mass scale $s_q \sim s_{\bar{q}} \sim Q^2\lambda^2$, shown with the blue circles on the middle hyperbola.

into various sectors which are describing the relevant hard interactions, collinear dynamics and soft radiation in terms of separated gauge invariant structures. The resulting factorization theorem for the thrust distribution with (n_l) quarks in the massless limit reads

$$\begin{aligned}\frac{1}{\sigma_0}\frac{\mathrm{d}\sigma(\tau)}{\mathrm{d}\tau} =& \, Q\, H_Q^{(n_l)}(Q,\mu_H) U_{H_Q}^{(n_l)}(Q,\mu_H,\mu) \int \mathrm{d}s \int \mathrm{d}s'\, U_S^{(n_l)}\big(s-s',\mu,\mu_J\big) J^{(n_l)}(s',\mu_J) \\ & \times \int \mathrm{d}k\, U_S^{(n_l)}\big(k,\mu,\mu_S\big) S^{(n_l)}\big(Q\tau - \frac{s}{Q} - k,\mu_S\big)\,, \end{aligned} \tag{3.4.1}$$

where the term σ_0 is the total tree-level cross section and H_Q, J and S are the hard, jet and soft functions respectively. The terms $U_H^{(n_l)}$, $U_J^{(n_l)}$ and $U_S^{(n_l)}$ are the counterpart evolution kernels of the hard, jet and soft sectors which are summing the large logarithmic terms between the characteristic scales of each sector and the global μ [see appendix C]. We note that the global μ dependence cancels out. Therefore it is convenient to fix the global μ scale such that it eliminates one of the evolution kernels. For convenience we will take $\mu = \mu_J$. Hence we write the basic factorization theorem as

$$\begin{aligned}\frac{1}{\sigma_0}\frac{\mathrm{d}\sigma(\tau)}{\mathrm{d}\tau} =& \, Q\, H_Q^{(n_l)}(Q,\mu_H) U_{H_Q}^{(n_l)}(Q,\mu_H,\mu_J) \int \mathrm{d}s \int \mathrm{d}k\, J^{(n_l)}(s,\mu_J) \\ & \times U_S^{(n_l)}\big(k,\mu_J,\mu_S\big) S^{(n_l)}\big(Q\tau - \frac{s}{Q} - k,\mu_S\big)\,. \end{aligned} \tag{3.4.2}$$

We emphasize that all the distinct sectors of the factorized cross section are color and spin singlet matrix elements which can be independently computed in perturbation theory.

Now let us have a closer look into various sectors. The factor H_Q, known as the hard function, is the square of the Wilson coefficient correction resulting from the matching of the SCET current to the full QCD counterpart,

$$J_\mu^{\mathrm{QCD}}(x) \to \int \mathrm{d}\omega \int \mathrm{d}\omega' C(\omega,\omega')\, \bar{\chi}_{n,\omega'}\, Y_n^\dagger\, \gamma_\mu\, Y_{\bar{n}}\, \chi_{\bar{n},\omega}\,, \tag{3.4.3}$$

where the $\chi_{\bar{n},\omega}$ $(\chi_{\bar{n},\omega})$ is the quark (antiquark) jet field defined in Eq. (3.3.20) and $C(\omega,\omega')$ is the Wilson coefficient. $Y_n(x)$ and $\overline{Y}_{\bar{n}}(x)$ are the soft Wilson lines given in Eq. (3.3.24). The hard function has been calculated at $\mathcal{O}(\alpha_s)$ in Ref. [39]. The higher (non-singlet) corrections up to $\mathcal{O}(\alpha_s^3)$ can be extracted from the on-shell current form factors [179, 180, 222–225]. The resulting hard function at one loop reads,

$$H_Q^{(n_l)}(Q,\mu) = 1 + \frac{C_F\,\alpha_s^{(n_l)}(\mu)}{4\pi}\bigg\{ -2\ln^2\Big(\frac{Q^2}{\mu^2}\Big) + 6\ln\Big(\frac{Q^2}{\mu^2}\Big) - 16 + \frac{7\pi^2}{3}\bigg\}. \tag{3.4.4}$$

The thrust jet function J_τ accounts for the dynamics of collinear radiation in the two sets of final state jets which are initiated by the quark and antiquark, respectively in the n- and $\bar{n}$- direction along the thrust axis. It can be calculated via the convolution of the n- and $\bar{n}$- hemisphere jet functions $J = J_n \otimes J_{\bar{n}}$, where the hemisphere jet function J_n is defined as

$$J_{\bar{n}}(Qr^+,\mu) \equiv \frac{1}{2\pi N_c Q}\,\mathrm{Im}\Big[\,i\int \mathrm{d}^4x\, e^{ir_n\cdot x}\,\langle 0|\,\mathrm{T}\{\bar{\chi}_n(0)\,\bar{n}\!\!\!/\,\chi_n(x)\}\,|0\rangle\,\Big]. \tag{3.4.5}$$

T indicates that the product of operators is time ordered. The hemisphere jet function in the massless quark limit has been computed at order $\mathcal{O}(\alpha_s)$ [226, 227] and $\mathcal{O}(\alpha_s^2)$ [228]. Moreover the logarithmic terms at $\mathcal{O}(\alpha_s^3)$ can be extracted from the known anomalous dimensions at three loops [155, 229]. The resulting expression for the thrust jet function at order $\mathcal{O}(\alpha_s)$ reads

$$J^{(n_l)}(s,\mu) \equiv \delta(s) + \frac{C_F\,\alpha_s^{(n_l)}(\mu)}{4\pi}\bigg\{\delta(s)\,(14-2\,\pi^2) - \frac{6}{\mu^2}\Big[\frac{\theta(s/\mu^2)}{s/\mu^2}\Big]_+ + \frac{8}{\mu^2}\Big[\frac{\theta(s/\mu^2)\ln\big(s/\mu^2\big)}{s/\mu^2}\Big]_+\bigg\}. \tag{3.4.6}$$

The dynamics of the soft cross-talk radiation of the quark and antiquark jets in the factorization theorem is taken into account via a convolution of the jet function with the soft function S. The thrust soft function is defined by

$$S(\ell,\mu) \equiv \frac{1}{N_c}\sum_{X_s}\delta(\ell - \bar{n}\cdot k_s^R - n\cdot k_s^L)\,\langle 0|\,\bar{Y}_{\bar{n}}Y_n(0)\,|X_s\rangle\,\langle X_s|\,Y_n^\dagger\bar{Y}_{\bar{n}}^\dagger(0)\,|0\rangle\;, \tag{3.4.7}$$

where the summation is overall soft final states $|X_s\rangle$ in the left (right) hemisphere with momentum $k_s^R\,(k_s^L)$. The soft function should account for the long distance physics such as large angle soft radiations between the jets. In order to incorporate these nonperturbative effects one can further factorize [198] the soft function into a partonic component $S_{\rm part}$ and a nonperturbative hadronization model function (known as shape function) $S_{\rm mod}$, yielding

$$S^{(n_l)}(\ell,\mu) = \int \mathrm{d}\ell\, S_{\rm part}^{(n_l)}(\ell-\ell',\mu)\,S_{\rm mod}(\ell'). \tag{3.4.8}$$

A popular approach to construct the model function has been adopted by Ref. [230] using a linear combination of an infinite set of basis functions. We present the suitable parametrization of the shape function in Sec. 3.7.2. The partonic thrust soft function at one loop reads

$$S_{\rm part}^{(n_l)}(\ell,\mu) = \delta(\ell) + \frac{C_F\,\alpha_s^{(n_l)}(\mu)}{4\pi}\bigg\{\frac{\pi^2}{3}\,\delta(\ell) - \frac{16}{\mu}\Big[\frac{\theta(\ell)\ln\big(\ell/\mu\big)}{\ell/\mu}\Big]_+\bigg\}. \tag{3.4.9}$$

The main advantage of using the factorization formalism for the soft radiation is that it provides a smooth transition for the nonperturbative corrections in different regions of the distribution. To verify this feature we note that the typical support of the soft model is at $\mathcal{O}(\Lambda_{\rm QCD})$ whereas the scale of perturbative soft radiation can vary substantially along the thrust distribution. Hence, in the peak region where $\ell \sim \ell' \sim \Lambda_{\rm QCD}$, one has to account for the full model function whereas in the tail region where $\ell' \ll \ell$, the expression in Eq. (3.4.8) can be expanded up to suitable orders. Therefore the exact form of the soft model function is not relevant any more and Eq. (3.4.8) can be expanded in the form

$$S(\ell,\mu) = S_{\rm part}(\ell) - \frac{\mathrm{d}\,S_{\rm part}(\ell)}{\mathrm{d}\,\ell}\,2\,\overline{\Omega}_1 + \cdots \tag{3.4.10}$$

where the second term on the RHS is the leading power correction and the dots are referring to higher order power corrections. The $\overline{\Omega}_1$ is related to the first moment of the shape function,

$$2\,\overline{\Omega}_1 = \int \mathrm{d}\,\ell'\,\ell' S_{\mathrm{mod}}(\ell')\,. \tag{3.4.11}$$

Note that the resulting expression in Eq. (3.4.10) is precisely the OPE for the soft function where the term $\overline{\Omega}_1$ indicates the leading nonperturbative matrix element and $\mathrm{d}S_{\mathrm{part}}/\mathrm{d}\ell$ is the Wilson coefficient which can be calculated from the matching to all orders in perturbation theory.

The factorization in Eq. (3.4.8) is conveniently performed in the $\overline{\mathrm{MS}}$ scheme with dimensional regularization. This approach simplifies the higher order computations and provides the proper renormalization scale dependence. However, the integrations in dimensional regularization are carried out overall momentum scales which leads to an IR-sensitivity of the partonic soft function. It was shown in Ref. [198] that in fact the perturbative soft function suffers from an $\mathcal{O}(\Lambda_{\mathrm{QCD}})$ renormalon ambiguity which leads to a corresponding ambiguity in the leading OPE term $\overline{\Omega}_1$. This poor convergence is associated with the unphysical partonic threshold at $\ell = 0$ in $S_{\mathrm{part}}(\ell)$. The better approximation is to introduce the gap parameter $\Delta \sim \Lambda_{\mathrm{QCD}}$ as the minimum hadronic energy deposit due to soft radiation. The gap enters the soft model function in terms of a simple shift, $S_{\mathrm{mod}}(\ell - 2\,\Delta)$, so that the soft model function only has support for $\ell \geq \Delta$. Consequently the relation in Eq. (3.4.11) is modified as following

$$2\,\overline{\Omega}_1 = 2\,\Delta + \int \mathrm{d}\ell'\,\ell'\,S_{\mathrm{mod}}(\ell')\,. \tag{3.4.12}$$

From this equation one can deduce that the gap accounts for the renormalon ambiguity that arises in the leading power corrections of the OPE expansion in Eq. (3.4.10). Note that Δ is a bare parameter which is flavor scheme independent and renormalization scale invariant. The essential feature of the gap formalism is that one can split the bare gap into a renormalon-free $\bar{\Delta}^{(n_l)}(R,\mu_S)$ component and a perturbative subtraction $\delta^{(n_l)}(R,\mu_S)$ [198],

$$\Delta = \bar{\Delta}^{(n_l)}(R,\mu) + \delta^{(n_l)}(R,\mu)\,, \tag{3.4.13}$$

where R is the renormalon subtraction scale (cutoff scale) occurring in namely R-scheme [231].[11] The subtraction term $\delta^{(n_l)}(R,\mu_S)$ can be extracted conveniently from the partonic soft function to all orders in perturbation theory such that it captures the appropriate power dependence to eliminate the linear IR sensitivities [232]. For convenience we postpone the explicit presentation of the gap subtraction and corresponding RG evolutions in the scale R to Sec. 3.7. The superscript (n_l) indicates the number of active flavors in the perturbative subtraction and the gap parameter. Now, one can shift the perturbative subtraction from the gap term in the shape function to the partonic soft function, so that the factorization in Eq. (3.4.8) becomes

$$S^{(n_l)}(\ell,\mu) = \int \mathrm{d}\ell'\,S^{(n_l)}_{\mathrm{part}}(\ell - \ell' - 2\,\delta^{(n_l)}(R,\mu),\,\mu)\,S_{\mathrm{mod}}(\ell' - 2\bar{\Delta}^{(n_l)}(R,\mu))\,, \tag{3.4.14}$$

where the term δ is constructed such that it cancels the renormalon problem of the partonic soft function order-by-order in perturbation theory.

On the other hand the perturbative subtraction in Eq. (3.4.12) can be pulled to the LHS to obtain a renormalon free scheme (known as the R-gap scheme) for $\overline{\Omega}_1$ which is defined

$$\overline{\Omega}_1^{(n_l)}(R,\mu) = \overline{\Omega}_1 - \delta^{(n_l)}(R,\mu)\,. \tag{3.4.15}$$

Note that within this formalism the gap is an extra nonperturbative parameter in the soft function that needs to be simultaneously fit with the rest of shape function parameters. In the tail region,

[11] The R-scheme introduces the appropriate power corrections of (R/Q) into the Wilsonian coefficient of the OPE in the $\overline{\mathrm{MS}}$ scheme with dimensional regularization such that it cancels the factorial growth of the perturbative coefficients.

the gap dependence is fully encoded in the nonperturbative parameter of the leading power correction which makes it convenient for phenomenological applications.

To conclude we stress that the systematic subtraction of the renormalon ambiguity is an important ingredient of this analysis as it enhances the stability of the perturbative series and improves the accuracy of the nonperturbative parameters determination. In particular accounting for the renormalon subtraction ensures the possibility to determine the quark mass with precision better than $\Lambda_{\rm QCD}$.

3.4.2 Mass Mode Setup

Now let us discuss how the secondary heavy quark correction can be incorporated into the massless factorization theorem. Here we consider a generic setup which consists of one heavy quark with mass $m \gg \Lambda_{\rm QCD}$ and (n_l) light quark flavors. In order to account for the fluctuation of the order of the mass shell of the heavy quark one has to introduce new degrees of freedom known as mass modes in addition to the usual massless collinear and soft degrees of freedom in SCET [42]. When massive quarks are highly boosted, i.e. $\lambda_m \equiv m/Q \ll 1$, the mass modes separate into three different types of mass-shell fluctuations, n-, $\bar{n}$-collinear and soft mass modes which have the scaling $p_n^\mu \sim Q(\lambda_m^2, 1, \lambda_m)$, $p_{\bar{n}}^\mu \sim Q(1, \lambda_m^2, \lambda_m)$ and $p_s^\mu \sim Q(\lambda_m, \lambda_m, \lambda_m)$, respectively. Note that the consequent modes have the same virtualities and are only discriminated by different boosts and rapidity (the rapidity variable is defined as $y = p^-/p^+$). We remark that the collinear mass mode fields are defined with soft mass mode bin subtractions to avoid double counting with the soft sector. This ensures that the results are gauge-invariant. The Feynman rules for collinear massive quark interactions can be extracted from Eq. (3.3.25). The coupling of soft mass mode quarks with collinear quarks is through the soft Wilson lines where the interaction obeys the usual QCD Feynman rules.

Since the hierarchy of the mass scale (m) with respect to the hard (Q), collinear $(Q\lambda)$ and soft $(Q\lambda^2)$ scales can vary substantially one has to take into account various kinematical scenarios where the associated mass modes are treated properly in the matrix elements and evolution kernels [see Fig. 3.3]. To this end, Ref. [43] imposes $\overline{\rm MS}$ or on-shell renormalization conditions with respect to the massive quark corrections depending on the hierarchy between the mass mode matching scale $\mu_m \sim m$ and the global evolution scale μ. They always employ the $\overline{\rm MS}$ renormalization for the massless degrees of freedom which corresponds to (n_l) running flavor.

To explain the underlying idea let us recall the important features of using these two renormalization schemes in a simplified example where the correction of secondary massive quarks for a matrix element is schematically given by

$$\delta M^{\rm bare}(m,\mu) = \frac{\alpha_s^2\, C_F\, T_F}{(4\pi)^2}\Big(\text{UV terms proportional to}\,\frac{1}{\epsilon^n} + \text{finite term}\, f(m,\mu) + \mathcal{O}(\epsilon)\Big)\,. \tag{3.4.16}$$

Note that α_s is not renormalized yet.

In the $\overline{\rm MS}$ renormalization scheme only the divergent terms are absorbed into the counterterm. Hence the massive quark contributes to the anomalous dimensions in the same way as the massless quarks and participates as an active flavor in the RG evolution. The remaining finite terms in Eq. (3.4.16) will be considered as the massive quark corrections to the matrix element. The resulting matrix element has the correct massless limit (i.e. $m \to 0$) when the massive quark becomes massless. Therefore using the $\overline{\rm MS}$ scheme one obtains the correct asymptotic behavior in the massless limit where the effective description has $(n_l + 1)$ massless quark flavors.

In the on-shell renormalization condition, the counterterm accounts for all the UV and low energy finite terms such that the anomalous dimension vanishes. Hence the massive quark does not contribute in the RG evolution.[12] Furthermore the remaining correction in the normalized matrix element does vanish for low energy scales much smaller than the mass. Therefore the on-shell renormalization scheme is appropriate to recover the correct decoupling limit (i.e. $m \to \infty$) where the effective description has (n_l) massless quark flavors.

[12]In this case one has to analogously use the OS scheme for the coupling constant which results to the anomalous dimension with (n_l) running flavors, i.e. $\beta = \beta^{(n_l)}$.

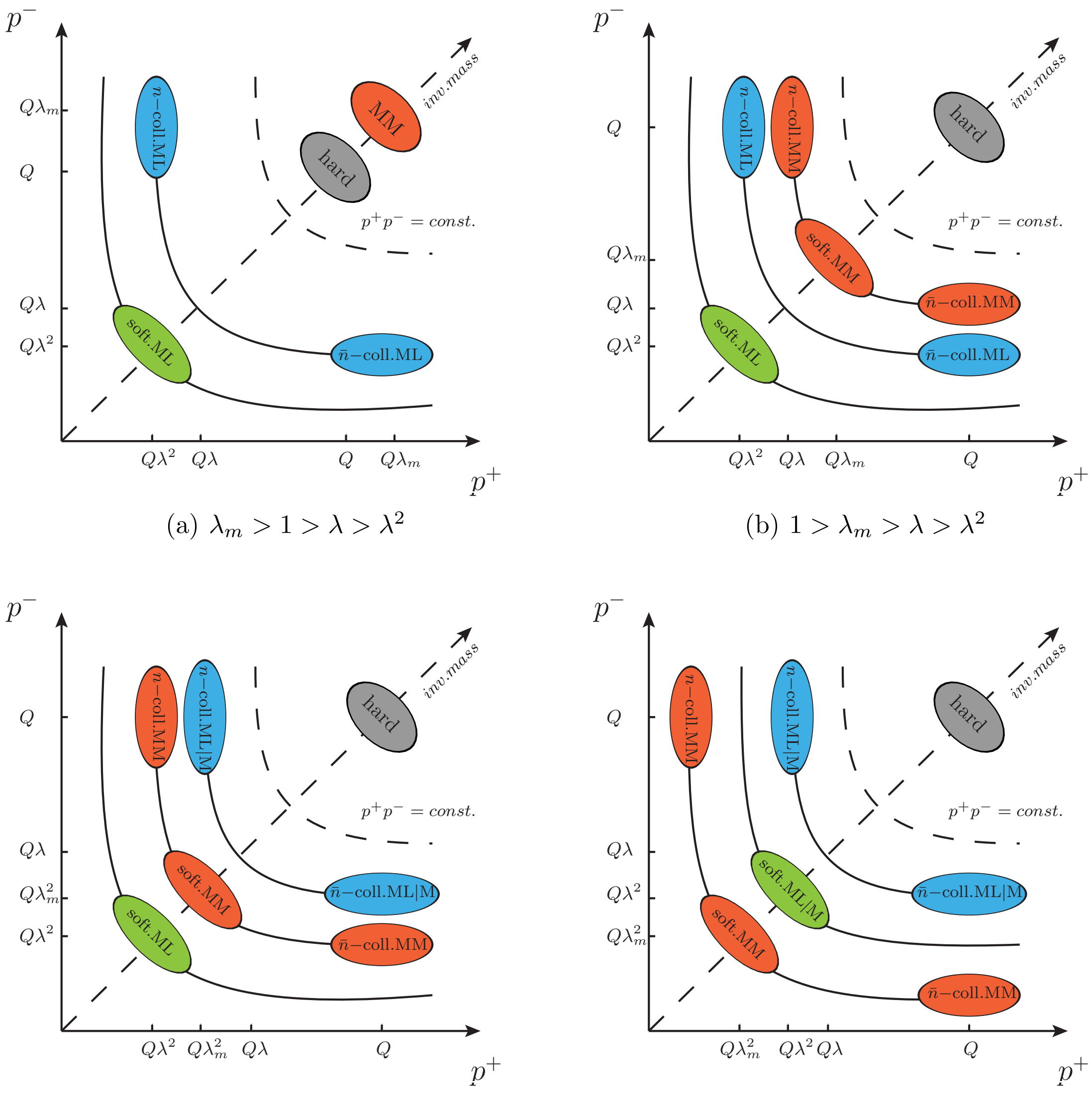

(a) $\lambda_m > 1 > \lambda > \lambda^2$ (b) $1 > \lambda_m > \lambda > \lambda^2$

(c) $1 > \lambda > \lambda_m > \lambda^2$ (d) $1 > \lambda > \lambda^2 > \lambda_m$

Figure 3.3: The location of relevant degrees of freedom in the $p^- - p^+$ plane according to different kinematical scenarios. ML(M) indicate the regular soft and collinear modes for massless(massive) particles. We denote the mass-shell fluctuations(mass mode) with MM. We note that the regular massive mode (M) in SCET represents the off-shell massive quark fluctuations which scale as their massless counterparts.

The matching condition for the renormalized matrix elements with respect to both renormalization schemes specifies the threshold corrections. These corrections need to be taken into account whenever the mass threshold is crossed by evolution kernels and the massive quark fluctuations are integrated out(in).

The constructed VFNS for thrust in Ref [43] is in principle a systematic implementation of these two renormalization schemes for the various sectors of the factorized cross section according to the relevant kinematic scenarios as illustrated in Figs. 3.3 and 3.4. The resulting framework provides a coherent and continuous theoretical description of the jet cross section where the role of the heavy quark is smoothly changing in the RG evolutions with variable number of active flavors and accounts for the corresponding threshold corrections.

In the following we summarize the mass mode setup of Ref [43] which is based on four different factorization formulas associated to the kinematic scenarios in Fig. 3.4. We only display the partonic thrust distribution, denoted with $\mathrm{d}\hat{\sigma}(\tau)/\mathrm{d}\tau$, and postpone the discussion on the nonperturbative

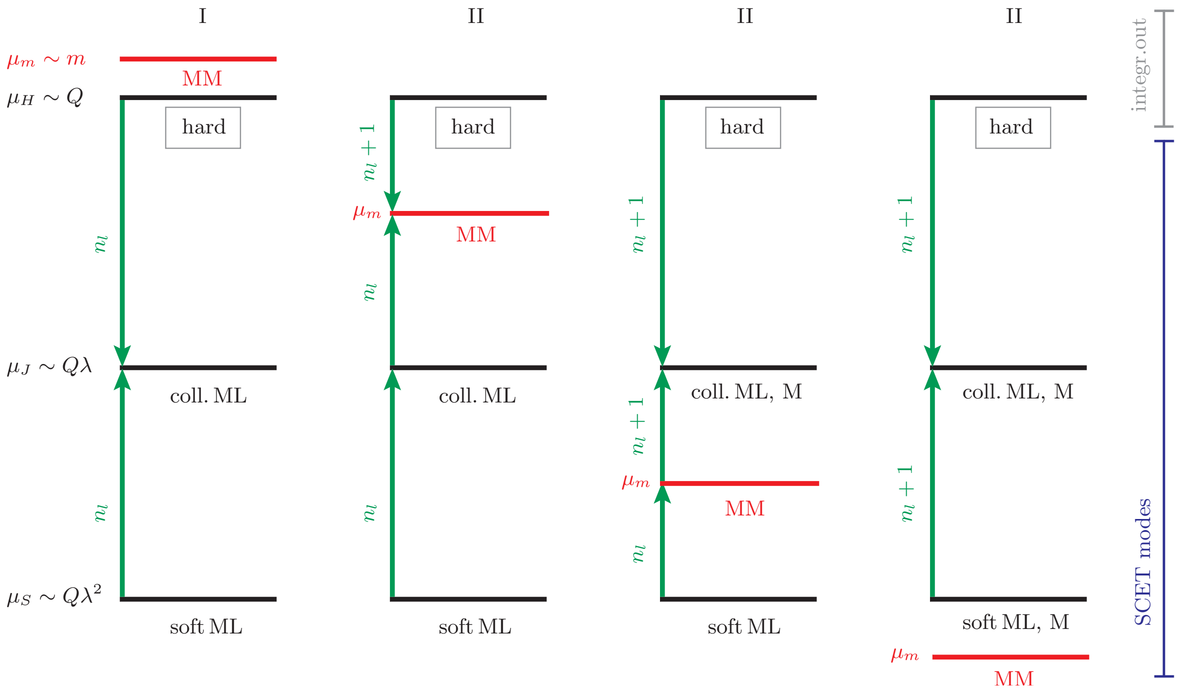

Figure 3.4: The different kinematical scenarios according to the mass scale in comparison with the hard, jet and soft scales. MM denotes the scaling of mass-shell fluctuations, and ML represents the massless scaling. M indicates the modes that have mass m but scale as massless fluctuations. The arrows displays the conventional RG evolution in the factorization theorem where the global scale is fixed at $\mu = \mu_J$. The number of active flavor which are participating in the RG evolutions are shown explicitly next to the arrows. While the evolution is crossing the massive quark threshold, the mass modes fluctuations are integrated out. The corresponding matching conditions at μ_m introduces the threshold corrections.

correction and gap formalism to Sec. 3.7. It is also more convenient to proceed with the pole mass scheme for all mass dependent terms in the factorization theorem and implement the appropriate short distance distance scheme later in Sec. 3.9. This allows us to outline and deal with the theoretical issues in a more systematic manner.

Scenario I: $m > Q > Q\lambda > Q\lambda^2$

The first scenario relates to the kinematic situation where the mass scale m is larger than the hard interaction scale Q. Here, the heavy quark (and corresponding mass mode fluctuation) is integrated out already while matching SCET to QCD and does not affect the SCET setup. Therefore the massive quark is not an active flavor in the matrix elements and their RG evolutions, which are located below the hard scale. The factorization theorem is similar to Eq. (3.4.2) with (n_l) active flavors, except the hard matching coefficient which accounts for the virtual massive quark bubble contribution to the QCD form factor at order $\mathcal{O}(\alpha_s^2)$ [see the diagrams in Fig. 3.1]

$$\begin{aligned}\frac{1}{\sigma_0}\frac{\mathrm{d}\hat{\sigma}(\tau)}{\mathrm{d}\tau} =& \, Q\, H_Q^{(n_l)}(Q,m,\mu_H) U_{H_Q}^{(n_l)}(Q,\mu_H,\mu_J) \int \mathrm{d}s \int \mathrm{d}k\, J^{(n_l)}(s,\mu_J) \\ &\times U_S^{(n_l)}(k,\mu_J,\mu_S) S_{\text{part}}^{(n_l)}\big(Q\tau - \frac{s}{Q} - k, \mu_S\big)\,. \end{aligned} \tag{3.4.17}$$

Here the strong coupling constant in all factors run with (n_l) active flavors, related to the massless quarks. The hard function $H_Q^{(n_l)}(Q,m,\mu)$ at $\mathcal{O}(\alpha_s)$ is given by Eq. (3.4.4). Note that in this scenario the massive quark threshold is always above the global scale which is set to the jet scale $\mu = \mu_J$. Hence, the on-shell renormalization scheme is employed for the massive secondary quark contribution in the QCD form factor (i.e. with zero momentum subtraction) [13]. This yields the manifest decoupling in the infinite mass limit for the hard function,

$$\lim_{m\to\infty} H_Q^{(n_l)}(Q,m,\mu) = H_Q^{(n_l)}(Q,\mu)\,, \tag{3.4.18}$$

and the corresponding factorization scenario in Eq. (3.4.17) which reduces to the massless factorization formula given in Eq. (3.4.2) with (n_l) active flavors. We emphasize that Eq. (3.4.17) does not have the proper massless limit since the hard function $H_Q^{(n_l)}(Q,m,\mu)$ contains mass shell contributions, exhibiting large mass logarithms which need to be summed.

Scenario II: $Q > m > Q\lambda > Q\lambda^2$

The mass scale is below the hard scale but larger than jet and soft scales. Here the collinear and soft mass modes participate in the SCET setup and account for mass shell fluctuations. Hence in the matching procedure of SCET to QCD, these mass shell contributions are subtracted from the hard matching coefficient. This leads to an IR-safe hard coefficient such that all the mass singularities for $m \ll Q$ in $H_Q^{(n_l)}(Q,m,\mu)$ are eliminated and the hard function approaches the proper massless limit $m \to 0$. The jet invariant mass and soft radiation scales are smaller than the mass scale $\mu_m > \mu_J > \mu_S$, so the mass mode effects are only via virtual diagrams. The factorization theorem in this scenario reads

$$\begin{aligned}\frac{1}{\sigma_0}\frac{\mathrm{d}\hat\sigma(\tau)}{\mathrm{d}\tau} =& \,Q\, H_Q^{(n_l+1)}(Q,m,\mu_H)\, U_{H_Q}^{(n_l+1)}(Q,\mu_H,\mu_m)\mathcal{M}_H^{(n_l+1)}(Q,m,\mu_H,\mu_m)U_{H_Q}^{(n_l)}(Q,\mu_m,\mu_J)\\ &\times\int \mathrm{d}s\int \mathrm{d}k\, J^{(n_l)}(s,\mu_J)U_S^{(n_l)}(k,\mu_J,\mu_S)S_{\rm part}^{(n_l)}\big(Q\tau-\frac{s}{Q}-k,\mu_S\big)\,. \end{aligned}\tag{3.4.19}$$

Similar to the previous scenario in Eq. (3.4.17), the jet function, soft function and relative RG evolutions are carried out with (n_l) active flavors. This is an automatic consequence of imposing the on-shell renormalization scheme with respect to the massive quark contribution for these sectors. However the hard evolution factor has a more complicated structure because it crosses the heavy quark threshold during the evolution. For the hard matching we apply the $\overline{\rm MS}$ renormalization prescription when the RG evolution is running above μ_m. This implies that the heavy quark is an active flavor for the hard coefficient and its evolution from μ_H to μ_m . We emphasize that the non-vanishing virtual mass mode contributions in SCET together with $\overline{\rm MS}$ renormalization prescription for α_s leads to the correct massless limit, i.e.

$$\lim_{m\to 0} H_Q^{(n_l+1)}(Q,m,\mu) = H_Q^{(n_l+1)}(Q,\mu). \tag{3.4.20}$$

Note that the perturbative expression for $H_Q^{(n_l+1)}(Q,m,\mu)$ at one loop is identical to the massless hard matching coefficient in Eq. (3.4.4) with (n_l+1) numbers of active flavors.

At μ_m all the collinear and soft mass shell fluctuations are integrated out and we switch to the on-shell renormalization scheme for the hard matching below the mass scale. Thus only (n_l) massless degrees of freedom take part in the RG evolution of the hard function from μ_m to μ_J. The difference of these two renormalization prescriptions leads to the current threshold correction. This correction has been computed in Ref. [43] at $\mathcal{O}(\alpha_s^2)$, where it has been demonstrated that the resulting expression contains a log-enhanced contribution proportional to $\alpha_s^2\ln(\mu_H^2/\mu_m^2)$ which cannot be summed by the usual RG evolution. Such terms are known as rapidity logarithms which arise due to incomplete cancellation of the rapidity singularities in the overlap region of collinear and soft mass modes which have the same invariant masses. There are different approaches in order to sum these logarithmic terms which eventually results in a simple exponentiation, see Refs. [43,174,194–197,233]. We refer to Ref. [43] for the explicit computation of the anomalous dimension. Nevertheless one can safely expand

[13] We always use the $\overline{\rm MS}$ renormalization prescription for massless bubble contributions.

the exponential expression using the logarithmic counting in SCET, $\alpha_s \ln(m^2/Q^2) \sim \mathcal{O}(1)$. At $\mathcal{O}(\alpha_s)$ the threshold correction reads

$$\mathcal{M}_H^{(n_l+1)}(Q,m,\mu_H,\mu_m) = 1 + \bigg[C_F\, T_F \Big(\frac{\alpha_s^{(n_l+1)}(\mu_m)}{4\pi}\Big)^2 \ln\Big(\frac{\mu_H^2}{\mu_m^2}\Big)\Big\{ -\frac{4}{3}L_m^2 - \frac{40}{9}L_m - \frac{112}{27}\Big\}\bigg]_{\mathcal{O}(\alpha_s)} + \mathcal{O}(\alpha_s^2)\,, \tag{3.4.21}$$

where $L_m \equiv \ln(m^2/\mu_m^2)$. Here the term $\alpha_s^2\ln(\mu_H^2/\mu_m^2)$ is counted as $\mathcal{O}(\alpha_s)$ and needs to be kept at N^{2}LL order, whereas the higher order terms in the fixed order expansion e.g. $\alpha_s^4\ln^2(\mu_H^2/\mu_m^2) \sim \mathcal{O}(\alpha_s^2)$, constitute the subleading corrections. The term $\mathcal{O}(\alpha_s^2)$ in Eq. (3.4.21) refers to such subleading large logs and the remaining two-loop contributions containing the small logarithms of L_m , which can be neglected at N^{2}LL order.

Scenario III: $Q > Q\lambda > m > Q\lambda^2$

The mass scale is below the hard and jet invariant scales, however it is still above the soft scale. In this setup the hard and soft functions are similar to scenario II with (n_l+1) and (n_l) active flavors in Eqs. (3.4.4) and (3.4.9), respectively. Here, the collinear and soft mass mode dynamics enter in terms of both real and virtual contributions in the jet sector. Thus the heavy quark is an active flavor in the jet function and we employ the $\overline{\text{MS}}$ renormalization prescription to recover the massless description in the limit $m \to 0$. Since in our factorization formulation we set the global RG evolution equal to the jet scale $\mu = \mu_J$, all large logarithms in the jet function are automatically summed. On the other hand, the current evolution from μ_H all the way down to μ_J is running above μ_m, so that it is carried out with (n_l+1) flavors. In this scenario, the soft function evolves with (n_l) massless flavors from μ_S up to the heavy quark threshold at μ_m, where we integrate in the heavy quark fluctuations, and perform the rest of the evolution from μ_m to μ_J with (n_l+1) active flavors. The threshold correction $\mathcal{M}_S^{(n_l+1)}$ results from the matching of the renormalized soft function in the $\overline{\text{MS}}$ and on-shell schemes at μ_m. The factorization formula in this scenario reads

$$\begin{aligned}\frac{1}{\sigma_0}\frac{\mathrm{d}\hat\sigma(\tau)}{\mathrm{d}\tau} &= Q\, H_Q^{(n_l+1)}(Q,m,\mu_H) U_{H_Q}^{(n_l+1)}(Q,\mu_H,\mu_J) \int \mathrm{d}s \int \mathrm{d}k \int \mathrm{d}k' \int \mathrm{d}k''\, J^{(n_l+1)}(s,m,\mu_J)\\ &\times U_S^{(n_l+1)}(k'',\mu_J,\mu_m)\, \mathcal{M}_S^{(n_l+1)}(k'-k'',m,\mu_m,\mu_S)\, U_S^{(n_l)}(k-k',\mu_m,\mu_S)\\ &\times S_{\text{part}}^{(n_l)}\big(Q\tau - \frac{s}{Q} - k,\mu_S\big)\,,\end{aligned} \tag{3.4.22}$$

where the jet function exhibits the proper massless limit

$$\lim_{m\to 0} J^{(n_l+1)}(s,m,\mu) = J^{(n_l+1)}(s,\mu)\,. \tag{3.4.23}$$

Note that the mass dependent corrections enter at two loops so that the one loop jet function is identical to the massless expression in Eq. (3.4.6) with (n_l+1) active flavors. The soft mass mode matching $\mathcal{M}_S$ has been determined up to N^{3}LL in Ref. [43]. In analogy with the current mass mode matching, $\mathcal{M}_S$ contains a large rapidity logarithm at order $\mathcal{O}(\alpha_s^2)$ i.e. $\alpha_s^2\ln(\mu_S^2/\mu_m^2)$ which can not be summed via the RGE for the UV singularities at large invariant mass scales. This rapidity logarithm is also summed by simple exponentiation as shown by Ref. [43]. However, using the logarithmic counting in SCET, $\alpha_s\ln(m^2/l^2) \sim \mathcal{O}(1)$, one can expand the exponential expression. The resulting threshold correction at leading order reads

$$\mathcal{M}_S^{(n_l+1)}(l,m,\mu_m,\mu_S) = \delta(\tilde l) + \bigg[C_F\, T_F \Big(\frac{\alpha_s^{(n_l+1)}(\mu_m)}{4\pi}\Big)^2 \delta(\tilde l)\, \ln\Big(\frac{\mu_S^2}{\mu_m^2}\Big)\Big\{\frac{8}{3}L_m^2 + \frac{80}{9}L_m + \frac{224}{27}\Big\}\bigg]_{\mathcal{O}(\alpha_s)} + \mathcal{O}(\alpha_s^2) \tag{3.4.24}$$

where $\tilde{l} = l/\mu_S$ and $L_m = \ln(m^2/\mu_m^2)$. The term $\mathcal{O}(\alpha_s^2)$ refers to subleading effects that are not relevant at N^{2}LL order analyses. As for the current mass mode matching, the leading rapidity correction in the soft matching threshold given in Eq. (3.4.24) counts as $\mathcal{O}(\alpha_s)$ and are necessary ingredients at N^{2}LL accuracy.

Scenario IV: $\boldsymbol{Q > Q\lambda > Q\lambda^2 > m}$

The heavy quark threshold is below the soft scale. The collinear and soft mass modes are entering as dynamical degrees of freedom in all sectors in analogy with their massless counterparts. According to our convention for the evolution scale, all the RG evolution is taking place above the mass scale and we never cross the mass threshold. Hence we employ the $\overline{\text{MS}}$ prescription to renormalize the hard, jet and soft functions so that the massive quark contributes in the evolution factors as an active flavor in addition to the massless quarks. This leads to the hard and jet functions with secondary massive corrections at two loops, that are already addressed in Scenarios II and III, respectively. Only the soft function is modified such that it accounts for the real and virtual massive quark correction at $\mathcal{O}(\alpha_s^2)$. The thrust factorization for this scenario reads,

$$\begin{aligned}\frac{1}{\sigma_0}\frac{\mathrm{d}\hat{\sigma}(\tau)}{\mathrm{d}\tau} =& \,Q\, H_Q^{(n_l+1)}(Q,m,\mu_H) U_{H_Q}^{(n_l+1)}(Q,\mu_H,\mu_J) \int \mathrm{d}s \int \mathrm{d}s' \int \mathrm{d}k\, J^{(n_l+1)}(s,m,\mu_J) \\ &\times U_S^{(n_l+1)}(k,\mu_J,\mu_S) S_{\text{part}}^{(n_l+1)}\Big(Q\tau - \frac{s}{Q} - k, m, \mu_S\Big)\,. \end{aligned} \tag{3.4.25}$$

The renormalized soft function in $\overline{\text{MS}}$ scheme exhibits the manifested massless limit

$$\lim_{m\to 0} S_{\text{part}}^{(n_l+1)}(l,m,\mu) = S_{\text{part}}^{(n_l+1)}(l,\mu)\,. \tag{3.4.26}$$

The one loop soft function has the form of Eq. (3.4.9) with (n_l+1) flavors. Note that in this setup, all the matrix elements have the appropriate small quark mass limit such that in the limit $m \to 0$ Eq. (3.4.25) recovers the massless factorization in Eq. (3.4.2) with (n_l+1) active flavors.

3.5 VFNS for Primary and Secondary Heavy Quark Production in Thrust

In this section we aim to construct a variable flavor number scheme for the production of primary massive quarks with secondary massive corrections of the same flavor in the e^+e^- thrust distribution. This is in close analogy with the VFNS for the secondary production of heavy quarks in light quark initiated processes which was described in the previous section. However, in comparison with the previous setup, we have to account for the real production of primary massive quarks in the final state jet. This confines the viable kinematics to the scenarios where the invariant mass of the jet is larger than the heavy quark mass square, i.e. $s_q > m^2$. Therefore only scenarios III (with $Q > Q\lambda > Q\lambda_m > Q\lambda^2$) and IV (with $Q > Q\lambda > Q\lambda > Q\lambda_m$) are kinematically allowed. Furthermore, since the transverse momentum of collinear particles is larger than the mass scale, the collinear Lagrangian must include the mass term [234] in Eq. (3.3.10). Therefore the real production of the heavy quark modifies the jet function already at leading order in α_s [see Eq. (3.5.3)]. The hard function does not change since the current matching condition at leading order expansion in m/Q agrees with the massless relation. The soft function is a universal matrix element which does not depend on the mass of the primary collinear particles [32] . This is the direct consequence of the leading SCET factorization at the level of the Lagrangian where the soft modes are absolutely decoupled from massive collinear modes. In order to account for secondary mass effects, similar to the previous setup, we consider additional mass-shell fluctuations. As shown these correction contains large rapidity logarithms which have to be considered at N^{2}LL accuracy.

On the other hand, in this context we encounter an additional kinematic regime where the invariant mass of the boosted jets is close to the mass-shell of the heavy quark

$$\hat{s}_q \equiv (s_q - m^2)/m \ll m\,. \tag{3.5.1}$$

This constraint is related to the peak region of the distribution where the heavy quarks are produced close to on-shell and boosted. In particular, this scenario describes the relevant kinematics for the production of boosted top quarks and the subsequent decay in the peak region where $\Gamma_t \lesssim \hat{s}_q \ll m_t$[14]. In this limit a new type of large logarithms appears in perturbation theory which is not summed by SCET. The reason is that the typical virtuality of fluctuations in SCET is $\hat{s}_q \sim m$. Thus one has to integrate out these fluctuations to describe the quark dynamics near the mass shell where the virtuality of the fluctuations scale as $\hat{s}_q \ll m$. To this end Ref. [32] adopted two copies of a boosted version of Heavy Quark Effective Theory (bHQET) in the n and $\bar{n}$ directions described in Sec. 3.3.2 . In this framework the decay of unstable quarks can be treated as an inclusive process in terms of the total decay width Γ that acts as an imaginary residual mass term. We have a closer look into this scenario in Sec. 3.5 where we present the corresponding factorization theorem.

To have a more convenient presentation in the following, we first establish a complete VFNS framework regarding the production of stable heavy quarks in jet cross sections. We demonstrate later, in Sec. 3.8, the procedure to incorporate the leading effects of decay processes into the factorization theorem for stable quark production such that the resulting theory describes the unstable massive quark production. In analogy with the previous section we adopt factorization scenarios where the global renormalization scale μ is fixed at the jet scale. In this discussion we concentrate on the generic aspects of the factorization scenarios, thus we only present the partonic singular contributions and consider all the mass parameters in the pole scheme. This simplifies the formulation of scenarios. In Sec. 3.9, we will employ different short distance schemes for the quark mass parameter of each sector to preserve the power counting. We provide the hadronic level formulation in Sec. 3.7 where a VFNS gap formalism will be properly adopted according to each kinematic scenario. In the following discussion, first we present scenarios IV and III and afterwards describe the bHQET scenario.

Scenario IV: $Q > Q\lambda > Q\lambda^2 > m$

The mass of the heavy quark is below all the other kinematic scales. Since in our formulation of factorization theorem we use the convenient choice where the global scale is $\mu = \mu_J$, the RG evolutions do not cross the mass threshold in this scenario. Therefore the massive quarks are participating as active flavors in all the matrix elements and evolution kernels. The corresponding factorization theorem is similar to Eq. (3.4.25),

$$\begin{aligned}\frac{1}{\sigma_0}\frac{\mathrm{d}\hat{\sigma}(\tau)}{\mathrm{d}\tau} =\, & Q\, H_Q^{(n_l+1)}(Q,\mu_H) U_{H_Q}^{(n_l+1)}\big(Q,\mu_H,\mu_J\big) \int \mathrm{d}s \int \mathrm{d}k\, J^{(n_l+1)}(s,m,\mu_J) \\ & \times U_S^{(n_l+1)}\big(k,\mu_J,\mu_S\big) S_{\mathrm{part}}^{(n_l+1)}\Big(Q(\tau-\tau_{\min}) - \frac{s}{Q} - k, m, \mu_S\Big)\,,\end{aligned} \tag{3.5.2}$$

where $\tau_{\min} = 1 - \sqrt{1-4\,m^2/Q^2}$ is the minimum thrust value. The shift by $\tau_{\min}$ is the direct consequence of the kinematical constraint $s_q > m_q$ which implies the real production of primary massive quarks in final states. Here m is the heavy quark mass in the pole scheme. The soft matrix element is the same as scenario IV in the primary massless quark setup where we use the $\overline{\mathrm{MS}}$ renormalization prescription with respect to the secondary massive quark corrections. The resulting expression for the soft function manifests the massless limit and can be read from Eq. (3.4.9) at order α_s with (n_l+1) active flavors. The hard function is obtained by performing the current matching condition at leading order expansion in m/Q. The outcome is in precise agreement with the massless hard function $H_Q^{(n_l+1)}(Q,\mu_H)$, given in Eq. (3.4.20), to all orders in perturbation theory. The corresponding

[14] Γ_t denotes the total top quark decay width.

expression at $\mathcal{O}(\alpha_s)$ can be read from Eq. (3.4.4). Note that $H_Q^{(n_l+1)}$ and $S_{\rm part}^{(n_l+1)}$ get m-dependence at $\mathcal{O}(\alpha_s^2)$. The thrust jet function with primary massive quarks is obtained from Eq. (3.4.5) using the Feynman rules for massive collinear jet fields [234]. The resulting expression at one-loop reads [39]

$$\begin{aligned}
J^{(n_l+1)}(s,m,\mu) = \delta(s) + \frac{C_F\,\alpha_s^{(n_l+1)}(\mu)}{4\pi}\bigg\{&\delta(s)\Big[4\ln^2\Big(\frac{m^2}{\mu^2}\Big)+2\ln\Big(\frac{m^2}{\mu^2}\Big)+16-\frac{2\pi^2}{3}\Big]\\
&+\frac{16}{\mu^2}\Big[\frac{\theta(s/\mu^2)\ln\big(s/\mu^2\big)}{s/\mu^2}\Big]_+ - \frac{8}{\mu^2}\Big(1+\ln\Big(\frac{m^2}{\mu^2}\Big)\Big)\Big[\frac{\theta(s/\mu^2)}{s/\mu^2}\Big]_+\\
&+\theta(s)\Big[\frac{2s}{(s+m^2)^2}-\frac{8}{s}\ln\Big(1+\frac{s}{m^2}\Big)\Big]\bigg\}\,.
\end{aligned}\tag{3.5.3}$$

It is straightforward to show that the massive jet function in Eq. (3.5.3) has the proper small mass limit, exactly reducing to the expression in Eq. (3.4.6) for $m\to 0$.

Scenario III: $Q > Q\lambda > m > Q\lambda^2$

In this scenario the mass scale is between the jet and the soft scales. The factorization formula looks similar to scenario III for the massless primary setup. The RG evolution of the hard and the jet functions is taking place above the heavy quark threshold, so that the number of active flavors in the corresponding sectors are set to (n_l+1). The soft function is running from μ_S up to μ_J scale and is crossing μ_m. Hence one should take into account secondary mass effects in the RG evolution of soft matrix elements by considering different renormalization prescriptions and including the mismatch in terms of the soft threshold correction $\mathcal{M}_S$, given in Eq. (3.4.24). The factorization theorem reads

$$\begin{aligned}
\frac{1}{\sigma_0}\frac{{\rm d}\hat\sigma(\tau)}{{\rm d}\tau} = {}& Q\,H_Q^{(n_l+1)}(Q,\mu_H)U_{H_Q}^{(n_l+1)}(Q,\mu_H,\mu_J)\int{\rm d}s\int{\rm d}k\int{\rm d}k'\int{\rm d}k''\,J^{(n_l+1)}(s,m,\mu_J)\\
&\times U_S^{(n_l+1)}\big(k'',\mu_J,\mu_m\big)\mathcal{M}_S^{(n_l+1)}(k'-k'',m,\mu_m,\mu_S)U_S^{(n_l)}\big(k-k',\mu_m,\mu_S\big)\\
&\times S_{\rm part}^{(n_l)}\big(Q(\tau-\tau_{\rm min})-\frac{s}{Q}-k,\mu_S\big)\,.
\end{aligned}\tag{3.5.4}$$

Here, the hard and jet functions are exactly identical to the corresponding expressions in scenario IV. We adopt the $\overline{\rm MS}$ (on-shell) renormalization for the soft function above (below) μ_m. This accounts for whether the heavy quark is an active or passive flavor in the RG evolution, indicated with $U_S^{(n_l+1)}$ and $U_S^{(n_l)}$, respectively. Note that the on-shell renormalization for the soft function at $\mu_S<\mu_m$ ensures that the universal soft Wilson lines are only coupling to (n_l) massless flavors. Hence in Eq. (3.5.4) we have adopted $S_{\rm part}^{(n_l)}$ which is identical to the massless soft function given in Eq. (3.4.9).

bHQET Scenario: $Q > Q\lambda \sim m > \hat s_q > \hat s_q\, m/Q$

The jet scale is close to the heavy quark mass. This kinematic regime occurs in the peak region of the thrust distribution where the virtuality of typical fluctuations involving the boosted heavy quarks is much smaller than the mass scale, $\hat s_q \ll m$. Note that this scenario is not always taking place since the jet invariant mass is bounded from below to $s_q \gtrsim Q\Lambda_{\rm QCD}$. Thus when $m^2 \ll Q\Lambda_{\rm QCD}$ this scenario is irrelevant. For instance, due to the small mass of the bottom quark, we do not encounter the bHQET region for energies above 40 GeV, see Sec. 3.11.1.

The resulting hierarchy in this regime leads to a set of large logarithms in perturbation theory which are not summed by means of RGEs in SCET. It is easy to verify these large logarithms as powers of $\ln(\hat s/m)$ in scenario III and IV by setting $\mu^2\sim m^2$ in the massive jet function in Eq. (3.5.3). This kinematic regime is in analogy with a heavy meson (such as the B meson) situation where the momentum fluctuations of the heavy quark in the interactions are $p^\mu = mv^\mu + k^\mu$ with $|k^\mu|\ll m$. Based on that we match bHQET to SCET in order to describe the quark and antiquark jets close to their

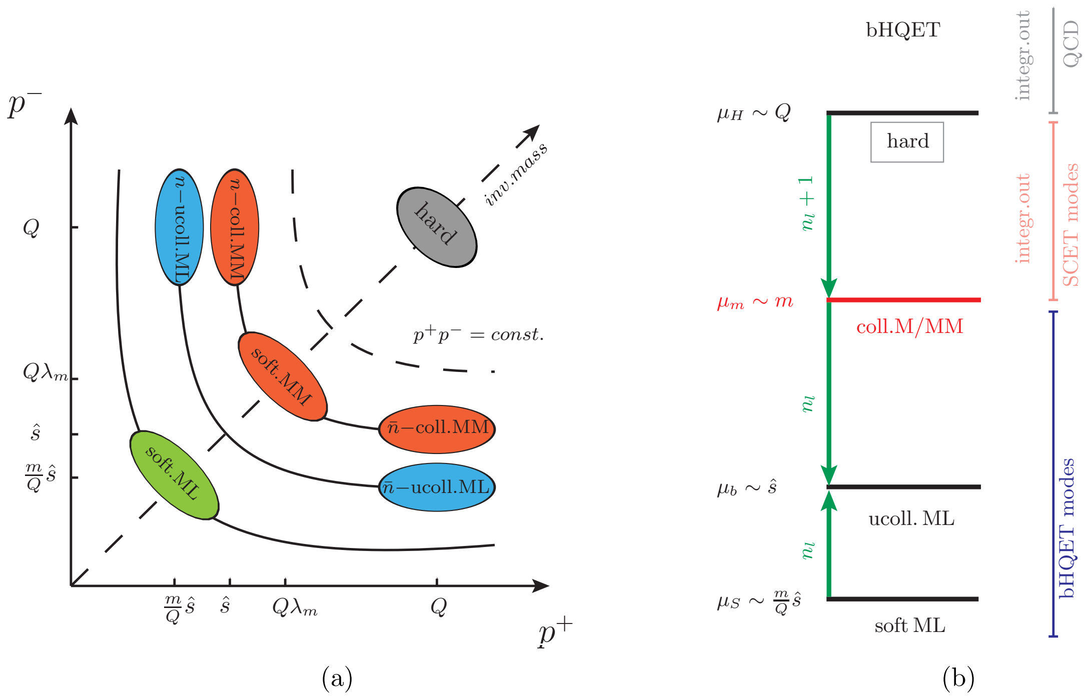

Figure 3.5: a) displays the position of relevant degrees of freedom in bHQET and SCET in the $p^- - p^+$ phase space. MM represents the mass modes which are now unified with the regular collinear modes in SCET. The ultracollinear modes in bHQET are denoted with n- and $\bar{n}$- ucoll.ML which consists of massless degrees of freedom. b) shows the kinematics of bHQET scenario. The arrows illustrate the RG evolution in the factorization theorem where the global scale is fixed at $\mu = \mu_b$. We present the sequence of EFTs with the vertical lines on the right side. We switch from QCD to SCET at the hard scale. At the mass scale we integrate out the fluctuations with virtualities of the order of $\hat{s} \sim m$ in SCET by matching to bHQET. The number of active flavors below (above) the mass scale, in the bHQET (SCET), is indicated with (n_l) (with (n_l+1)).

mass-shell [32]. We remind the reader that the relevant degrees of freedom in bHQET are ultracollinear and soft modes which have the $\hat{s}_q^2$ and $\hat{s}_q^2 m^2/Q^2$ invariant masses, respectively, see Sec. 3.3.2. This sequence of EFTs allows us to sum all the large logarithms including the ones between the mass scale and $\hat{s}_q$ which was left over in the SCET factorization theorems. The EFT setup and corresponding modes which are used to describe this kinematic regime are illustrated in Fig. 3.5 .

The standard procedure to carry out the matching between SCET and bHQET is to construct the effective currents in both theories and then write down the matching condition at the factorization scale μ_m [32]. The alternative approach is based on the factorization properties in SCET which states that the n-collinear , $\bar{n}$-collinear and soft sector are absolutely decoupled at leading order at the level of the Lagrangian, therefore the matching and running of each sector of the factorization theorem to the low-energy theory can be performed independently. In the following discussion we take the second approach since the factorization theorem is granted from SCET since the beginning.

Let us take the generic factorization formula as given by scenario IV in Eq. (3.5.2). We note that while switching from SCET to bHQET, we integrate out the hard-collinear and mass modes fluctuations with $\hat{s}_q \sim m$. It is straightforward to trace the resulting modifications in the factorization theorem. First, in bHQET all the real and virtual effects due to massive quarks are absent. This yields (n_l) active flavors for all sectors below the mass scale in the bHQET description. Second, in principle bHQET represents an expansion in $\hat{s}/m$ of the collinear Lagrangian while the soft interactions with momentum scales of the order of $m\hat{s}_q/Q$ are unexpanded. Therefore only the jet sector of the factorization needs to be matched from SCET to bHQET.

In order to determine the jet matrix element in bHQET, one can boost the SCET hemisphere jet functions, given in Eq. (3.4.5), to the heavy quark (antiquark) rest frame in n ($\bar{n}$) direction, then match the field operators onto the HQET ones, and afterwards boost back the result to the c.m. frame [32]. The resulting hemisphere jet function in bHQET reads [32]

$$B_n(\hat{s}_q,\mu) \equiv \frac{-1}{4\pi N_c m}\,\mathrm{Im}\Big[\, i\int \mathrm{d}^4x\, e^{ir.x}\,\langle 0|\,\mathrm{T}\{\bar{h}_{v_+}(0)\,W_n(0)\,W_n^\dagger(x)\,h_{v_+}(x)\}\,|0\rangle\,\Big]\,, \tag{3.5.5}$$

with $\hat{s} = 2v_+\cdot r$ where v_+ is the rest frame of the quark which is boosted in the n direction [see Sec. 3.3.2]. The heavy quark fields are denoted by $h_{v_{+,-}}$ where the $+$ and $-$ subscript refer to the quark and antiquark directions. The collinear Wilson lines W_n are the same as in SCET, except here we have ultracollinear gluon fields $A_{+,-}$. The thrust jet function is obtained by the convolution of the n and $\bar{n}$ hemisphere jet functions, $B = B_n \otimes B_{\bar{n}}$. The perturbative result of the bHQET jet function at $\mathcal{O}(\alpha_s)$ reads

$$mB^{(n_l)}\Big(\hat{s},\mu,m\Big) = \delta(\hat{s}) + \frac{C_F\,\alpha_s^{(n_l)}(\mu)}{4\pi}\bigg\{\delta(\hat{s})\big(8-\pi^2\big) + \frac{16}{\mu}\bigg[\frac{\theta(\hat{s}/\mu)\ln(\hat{s}/\mu)}{\hat{s}/\mu}\bigg]_+ - \frac{8}{\mu}\bigg[\frac{\theta(\hat{s}/\mu)}{\hat{s}/\mu}\bigg]_+\bigg\}\,, \tag{3.5.6}$$

which describes the dynamics of heavy quarks close to the mass shell inside the jet and thus the characteristic jet scale μ is of the order of $\sim \hat{s}$. The matching condition between the SCET and bHQET jet functions at leading order expansion in $\hat{s}/m$ reads

$$J^{(n_l)}(s,m,\mu_m) = H_m^{(n_l)}(m,\mu_m)B^{(n_l)}(\hat{s},\mu_m)\,. \tag{3.5.7}$$

The matching coefficient H_m has been computed recently with two-loop corrections in Ref. [181] using two different methods, direct calculation by matching the bHQET and SCET current operators and indirect extraction using the known Wilson coefficient in the matching of QCD and SCET currents and the matrix elements of current operators in QCD and bHQET in pure dimensional regularization. The resulting expression for H_m contains large rapidity logarithms which are of the same origin as the similar threshold matching in previous scenarios (see $\mathcal{M}_{S/H}^{(n_l+1)}$) due to the overlap of collinear and soft mass modes. As mentioned these large logarithms can be summed by simple exponentiation [181]. We stress once more that although this large logarithms arise at order α_s^2, one has to account them for an N^{2}LL analysis with the counting $\mathcal{O}(\alpha_s)$ together with one loop matrix element corrections. The relevant expression for H_m at N^{2}LL is

$$\begin{aligned}H_m^{(n_l+1)}(m,\mu_m) = 1 &+ C_F\bigg(\frac{\alpha_s^{(n_l+1)}(\mu_m)}{4\pi}\bigg)\bigg\{2L_m^2 - 2L_m + 8 + \frac{\pi^2}{3}\bigg\}\\ &+ C_F\,T_F\,\bigg(\frac{\alpha_s^{(n_l+1)}(\mu_m)}{4\pi}\bigg)^2\ln\bigg(\frac{m^2}{Q^2}\bigg)\bigg\{\frac{8}{3}L_m^2 + \frac{80}{9}L_m + \frac{224}{27}\bigg\}\,,\end{aligned} \tag{3.5.8}$$

where $L_m = \ln(m^2/\mu_m^2)$.

Thus the factorization formula in this scenario becomes

$$\begin{aligned}\frac{1}{\sigma_0}\frac{\mathrm{d}\hat{\sigma}(\tau)}{\mathrm{d}\tau} &= Q\,H_Q^{(n_l+1)}(Q,\mu_Q)\,U_{H_Q}^{(n_l+1)}(Q,\mu_H,\mu_m)\,H_m^{(n_l+1)}(m,\mu_m)\,U_{H_m}^{(n_l)}(\frac{Q}{m},\mu_m,\mu_b)\\ &\times\int \mathrm{d}\hat{s}\int \mathrm{d}k\, m\,B^{(n_l)}\Big(\hat{s},\mu_b,m\Big)\,U_S^{(n_l)}(k,\mu_b,\mu_S)\,S_{\mathrm{part}}^{(n_l)}\Big(Q(\tau-\tau_{\min}) - \frac{m\hat{s}}{Q} - k,\mu_S\Big)\,.\end{aligned} \tag{3.5.9}$$

Here we adopt the same convention as in previous scenarios, setting the global evolution scale to the bHQET jet scale $\mu = \mu_b \sim \hat{s}$, so that all large logarithms in the jet function $B^{(n_l)}(\hat{s},\mu_b,m)$ are automatically summed up and we do not need to account for its evolution factor. The hard function, H_Q, is identical to the expression in scenario III (IV) with (n_l+1) active flavors that are taking part in the running of U_{H_Q} form the hard scale down to the mass scale. At μ_m we integrate out all the fluctuations with $\hat{s} \sim m$, resulting into a matching coefficient H_m defined in Eq. (3.5.8) arising from the jet matching condition. We stress that by matching SCET to bHQET we explicitly integrate out all the virtual massive loop corrections which were induced in previous scenarios by means of mass modes. Hence there are only (n_l) flavors in the $\overline{\mathrm{MS}}$ running coupling in bHQET. Here the evolution factor U_{H_m} sums all the large logarithms between $\hat{s}$ and m. This evolution factor contains (n_l) massless active flavor while evolving below μ_m. The jet function B encodes the dynamics of the massive quarks and antiquarks close to their mass-shell inside the jets. We explain in Sec. 3.8 how one can incorporate the decay of the unstable quarks inside the jet by using a simple convolution of the jet function with a Breit-Wigner function [39]. The term $S_{\rm part}$ indicates the partonic soft function which accounts for the soft cross talk between the jets. Note that by switching to bHQET the soft function, defined in Eq. (3.4.7), does not change since the soft interactions are completely decoupled from the collinear sector. Furthermore due to the absence of the mass modes in the bHQET regime, only (n_l) massless flavors are active in the soft matrix element and the RGE factor U_S. The perturbative expression for the soft function at $\mathcal{O}(\alpha_s)$ is given in Eq. (3.4.9).

As already noted in Sec. 3.3, one of the most important aspects of using an effective field theory description is that it provides a systematic power expansion of the main QFT Lagrangian up to a certain order in the power counting. The resulting leading EFT describes the most singular contributions and the subleading contributions can be incorporated in terms of additional nonsingular expression which is simply the difference of the full theory and the leading EFT.

As already explained, in this work we use a sequence of two EFTs, therefore one has to account for two types of nonsingular contributions. The first type of the nonsingular contributions arises while matching QCD onto SCET. Note that SCET factorization theorems only account for the leading contributions in the SCET power counting parameter $\lambda_{\rm SCET} \sim \max\{\tau^{1/2}, (\Lambda_{\rm QCD}/Q)^{1/2}\}$ with $\lambda_{\rm SCET} \ll 1$. The second type of nonsingular contributions arises in the peak region when matching SCET onto bHQET. We remind the reader that bHQET factorization theorem only accounts for the leading contributions in the bHQET power counting parameter $\lambda_{\rm bHQET} \sim (Q^2\tau - 2m^2)/m^2$ with $\lambda_{\rm bHQET} \ll 1$.

Let us first address the second type of nonsingular contributions.[15] In the peak region we are continuously switching from the kinematics of scenario III to bHQET. Hence the second type of nonsingular contributions is simply the remnant of matching of scenario III to bHQET at μ_m,

$$\left|\frac{1}{\sigma_0}\frac{\mathrm{d}\hat{\sigma}(\tau)}{\mathrm{d}\tau}\right|_{\rm nsb} = \left|\frac{1}{\sigma_0}\frac{\mathrm{d}\hat{\sigma}(\tau)}{\mathrm{d}\tau}\right|_{\rm scenario-III} - \left|\frac{1}{\sigma_0}\frac{\mathrm{d}\hat{\sigma}(\tau)}{\mathrm{d}\tau}\right|_{\rm bHQET}, \tag{3.5.10}$$

where the subscript nsb indicates the nonsingular contributions in bQHET with respect to SCET. Using the matching condition in Eq. (3.5.7) we obtain

$$\begin{aligned}\left|\frac{1}{\sigma_0}\frac{\mathrm{d}\hat{\sigma}(\tau)}{\mathrm{d}\tau}\right|_{\rm nsb} &= Q\, H_Q^{(n_l+1)}(Q,\mu_H)\, U_{H_Q}^{(n_l+1)}\big(Q,\mu_H,\mu_{\rm nsb}\big) \int \mathrm{d}s \int \mathrm{d}k \int \mathrm{d}k' \int \mathrm{d}k''\, J_{\rm ND}^{(n_l+1)}(s,m,\mu_{\rm nsb}) \\ &\quad\times U_S^{(n_l+1)}\big(k,\mu_{\rm nsb},\mu_m\big)\, \mathcal{M}_S^{(n_l+1)}\big(k'-k,m,\mu_m,\mu_s\big)\, U_S^{(n_l)}\big(k'-k'',\mu_m,\mu_S\big) \\ &\quad\times S_{\rm part}^{(n_l)}\Big(Q(\tau-\tau_{\rm min}) - \frac{s}{Q} - k'',\mu_S\Big),\end{aligned} \tag{3.5.11}$$

where we indicate the nonsingular jet scale with $\mu_{\rm nsb}$. Note that this scale is in principle arbitrary in the bHQET regime however it should merge smoothly with μ_m while switching from the bHQET scenario to scenario III to ensure the continuity of the transition between scenarios. The term $J_{\rm ND}^{(n_l+1)}$ contains the non-distribution contribution of the massive jet function in Eq. (3.5.3),

$$J_{\rm ND}^{(n_l+1)}(s,m,\mu) = \frac{C_F\,\alpha_s^{(n_l+1)}(\mu)}{4\pi}\left[\frac{2s}{(s+m^2)^2} - \frac{8}{s}\ln(1+\frac{s}{m^2})\right]\theta(s). \tag{3.5.12}$$

[15] The first type of nonsingular contribution has to be considered as an overall correction in addition to the SCET and bHQET factorization theorems. We will discuss the extraction and appropriate treatment of these contributions in Sec. 3.6.

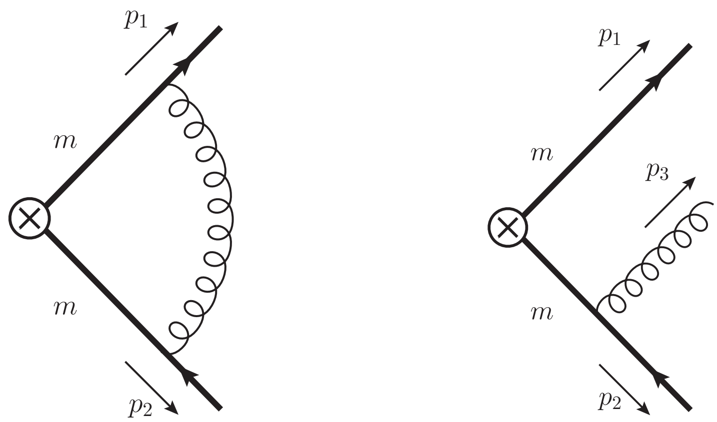

Figure 3.6: Virtual (a) and real (b) Feynman diagrams for the production of massive primary quark with mass m.

3.6 Nonsingular Distribution

In the following we present the calculation of the thrust distribution in fixed order QCD. Then we will discuss the possible prescriptions to incorporate the nonsingular effects in the content of our singular factorization framework.

3.6.1 Fixed Order Full Theory Results

In this section we present the $\mathcal{O}(\alpha_s)$ computation of the thrust distribution in full QCD. The relevant real and virtual Feynman diagrams for the production of primary massive quarks are shown in Fig. 3.6. In the corresponding calculation one has to take into account that the annihilation of $e^+ e^-$ into hadrons is taking place via two channels related to photon and Z-boson exchange processes, $e^+ e^- \to \gamma^*, Z^* \to \bar{q}q + X$. In the following sections we present the results for the vector and axial-vector contributions of the above channels in parallel.

Before starting we briefly remind how the full cross section involving the photon and Z-boson exchange can be split into vector and axial-vector contributions. We consider the total cross section as an example which can be easily generalized to differential cross sections. In the presence of both channels, the total cross section at leading order in the electroweak coupling reads [235]

$$\hat{\sigma} = N_C \frac{4\pi\alpha^2}{3\,s}\left[\frac{\nu_e^2 + a_e^2}{(1-\hat{m}_Z^2)^2 + \left(\frac{\Gamma_Z}{m_Z}\right)^2}(R^V_{Z^*} + R^A_{Z^*}) - 2\nu_e \frac{1-\hat{m}_Z^2}{(1-\hat{m}_Z^2)^2 + \left(\frac{\Gamma_Z}{m_Z}\right)^2} R^V_{\mathrm{Int}} + R^V_{\gamma^*}\right], \tag{3.6.1}$$

with

$$\nu_f = \frac{T_3^f - 2Q_f sin^2\theta_{\mathrm{W}}}{\sin(2\,\theta_{\mathrm{W}})}\,, \quad a_f = \frac{T_3^f}{\sin(2\theta_{\mathrm{W}})}\,, \quad \hat{m}_Z = \frac{m_Z}{\sqrt{s}}\,, \tag{3.6.2}$$

where m_Z is the mass of the Z-boson and s is the center of mass energy squared. To have a consistent notation, we use $\hat{\sigma}$ to indicate the partonic contributions. The hadron level cross sections will be referred later as σ, see Eq. (3.7.1). Note that $e = \sqrt{4\pi\alpha}$ is the elementary charge while $Q_{e/f}$ is the electric charge quantum number of the electron or the quark with flavor f. Various terms in this relation are induced by pure electromagnetic interactions ($R^V_{\gamma^*}$), vector ($R^V_{Z^*}$) and axial-vector ($R^A_{Z^*}$) couplings of the Z-boson and an interference contribution (R^V_{Int}) which has to be taken into account for the vector current. Each of these contributions decomposes into two classes of diagrams, namely singlet and nonsinglet diagrams. The nonsinglet diagrams are related to the topologies where one fermion loop couples to both the external currents. All these amplitudes have a simple charge structure related to the flavor of the fermion loop. The second class of diagrams, singlet contributions,

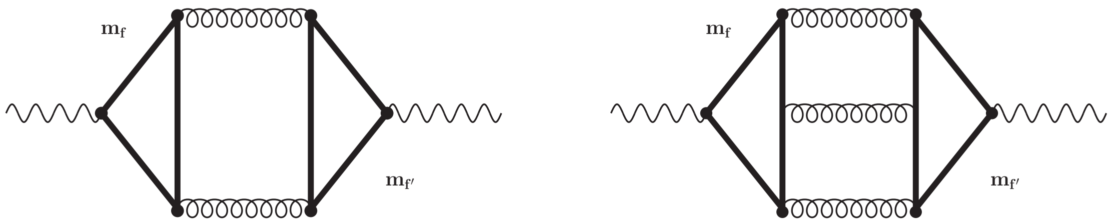

Figure 3.7: Singlet contribution of order $\mathcal{O}(\alpha_s^2)$ and $\mathcal{O}(\alpha_s^3)$.

arise when two fermion loops are coupled to two currents. These diagrams can be cut into two parts by cutting gluon lines [see Fig. 3.7]. Hence, the contributions cannot be assigned to an individual quark. With this consideration one can rewrite the R-functions by factorising the charge,

$$R^V_{Z^*} = \sum_f \nu_f^2\, r^V_{NS}(f) + \sum_{f,f'} \nu_f\, \nu'_f\, r^V_S(f,f')\,, \qquad R^A_{Z^*} = \sum_f a_f^2\, r^A_{NS}(f) + \sum_{f,f'} a_f\, a'_f\, r^A_S(f,f')$$
$$R^V_{\mathrm{Int}} = \sum_f \nu_f Q_f\, r^V_{NS} + \sum_{f,f'} \nu_f\, Q_{f'}\, r^V_S(f,f')\,, \quad R^V_{\gamma^*} = \sum_f Q_f^2\, r^V_{NS} + \sum_f \sum_{f'} Q_f\, Q_{f'}\, r^V_S(f,f')\,. \quad (3.6.3)$$

The r^X_S and r^X_{NS} with $X \in \{V, A\}$ are the singlet and nonsinglet contributions, respectively. Note that the singlet contributions are off-diagonal terms which depend on the flavor of the quarks in both loops whereas the nonsinglet terms are just depending on the single quark flavor running in the fermion loop. The leading singlet diagram is appearing at $\mathcal{O}(\alpha_s^2)$. Therefore, one can ignore the singlet contributions give in Eq. (3.6.3) at NLO.[16] Thus we can rewrite the total cross section as a sum overall individual flavor production rates,

$$\hat\sigma = \sum_f \hat\sigma^V_f\, r^V_{NS} + \hat\sigma^A_f\, r^A_{NS}\,, \tag{3.6.4}$$

with

$$\begin{aligned}\hat\sigma^V_f &= N_C\,\frac{4\pi\alpha^2}{3\,s}\left(\frac{\nu_f^2(\nu_e^2+a_e^2)}{(1-\hat m_Z^2)^2+\left(\frac{\Gamma_Z}{m_Z}\right)^2} - 2\nu_e\nu_f Q_f\,\frac{1-\hat m_Z^2}{(1-\hat m_Z^2)^2+\left(\frac{\Gamma_Z}{m_Z}\right)^2} + Q_f^2\right),\\ \hat\sigma^A_f &= N_C\,\frac{4\pi\alpha^2}{3\,s}\left(\frac{a_f^2(\nu_e^2+a_e^2)}{(1-\hat m_Z^2)^2+\left(\frac{\Gamma_Z}{m_Z}\right)^2}\right).\end{aligned} \tag{3.6.5}$$

The $\hat\sigma^X_f$ with $X \in \{V, A\}$ are the vector and axial-vector born cross sections in the massless quark limit.

The $e^+e^- \to q\bar q + X$ Thrust Distribution up to $\mathcal{O}(\alpha_s)$

The thrust distribution of primary massive quark productions at order $\mathcal{O}(\alpha_s)$ consists of different parts: Born cross section at tree level, virtual correction to the dijet event $e^+e^- \to q\bar q$ and the three body events corresponding to real radiation of a gluon $e^+e^- \to q\bar q g$. Adding the vector and axial-vector contributions we obtain the following result,

$$\frac{\mathrm{d}\hat\sigma^{\mathrm{FO}}(\tau)}{\mathrm{d}\tau} = \sum_{X=V,A} \frac{\mathrm{d}\hat\sigma(\tau)}{\mathrm{d}\tau}\bigg|^X_{\mathrm{full.}}\,, \tag{3.6.6}$$

[16] The discussion on the singlet diagrams he is unnecessary. Nevertheless we include it for completeness to stress that one has to account for these contributions at higher orders.

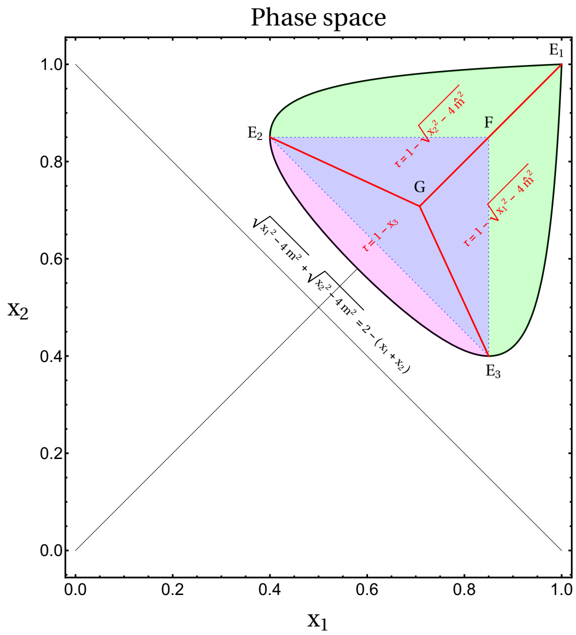

Figure 3.8: Phase space for the real radiation of a gluon off a massive quark-antiquark in terms of x_1 and x_2 with mass ratio $\hat{m} = 0.2$ where x_i is the energy fraction $2E_i/Q$. x_3 is fixed by the conservation of energy relation, $x_3 = 2 - x_1 + x_2$. The area bounded by the black curve is the allowed phase space for production of three partons. The available phase space is divided into 3 regions by red lines. The thrust relation in each region is represented by the red formula. G is the location of the maximal thrust. The colored areas are representing various contributions of the thrust distribution, $B(\tau, \hat{m})$ (Green), $C(\tau, \hat{m})$ (Blue) and $D(\tau, \hat{m})$ (Red) which are distinguished by different threshold structures [see Eq. (3.6.7)]. The vector and axial-vector contributions are shown in figure 3.9.

where

$$\begin{aligned}\frac{\mathrm{d}\hat{\sigma}(\tau)}{\mathrm{d}\tau}\bigg|^{X}_{\text{full.}} &= \hat{\sigma}_f^X \bigg\{ \bar{\sigma}^X_{\text{Born}}(\hat{m})\, \delta(\tau - \tau_{\min}) + \frac{C_F\, \alpha_s}{4\pi} \bigg[A^X(\hat{m}) \delta(\tau - \tau_{\min}) \\ &\quad + \Big(B^X(\tau, \hat{m}) \left[\frac{\theta(\tau - \tau_{\min})}{\tau - \tau_{\min}} \right]_+ + D^X(\tau, \hat{m})\, \theta\left(\tau - 4\hat{m}^2\right) \Big)\, \theta\left(\bar{\tau} - \tau\right) \\ &\quad + C^X(\tau, \hat{m})\, \theta\left(\tau - \bar{\tau}\right)\, \theta(\tau^{3-\text{jet}}_{\max} - \tau) \bigg] \bigg\}, \end{aligned} \tag{3.6.7}$$

with $\hat{m} = m/Q$ and $\alpha_s = \alpha_s^{n_f}(\mu)$. m is the pole mass of the heavy quark and Q is the center-of-mass energy. Here, $\tau_{\min} = 1 - \sqrt{1 - 4\hat{m}^2}$ is the minimum value of τ, related to the pair production at threshold, and $\tau^{3-\text{jet}}_{\max} = (5 - 4\sqrt{1 - 3\hat{m}^2})/3$ is the maximal possible value of τ for three events. The term $\bar{\tau} = \frac{\hat{m}}{1-\hat{m}}$ is related to the line $x_2 = 1 - x_1 - \frac{\hat{m}}{1-\hat{m}}$ in the phase space which is separating the $C^X(\tau)$ and $D^X(\tau)$ contribution regions (i.e. the border between the blue and magenta areas in Fig. 3.8). The normalized Born cross sections for the vector and axial-vector channels read

$$\bar{\sigma}^V_{\text{Born}}(\hat{m}) = \sqrt{1 - 4\hat{m}^2}(1 + 2\hat{m}^2)\,, \quad \bar{\sigma}^A_{\text{Born}}(\hat{m}) = (1 - 4\hat{m}^2)^{3/2}\,. \tag{3.6.8}$$

The distribution in Eq. (3.6.7) has a generic threshold structure for vector and axial-vector contributions. The $A^X(\hat{m})$ coefficient consists of both virtual and real corrections whereas the rest of the distribution at order $\mathcal{O}(\alpha_s)$ are due to the gluon real radiation. We will present the computation of all coefficient functions in the following. As a cross-check we verify that with a numeric integration of Eq. (3.6.7) from $\tau_{\min}$ to $\tau_{\max}$ we recover the known total cross section result at order $\mathcal{O}(\alpha_s)$ given in Ref. [235] .

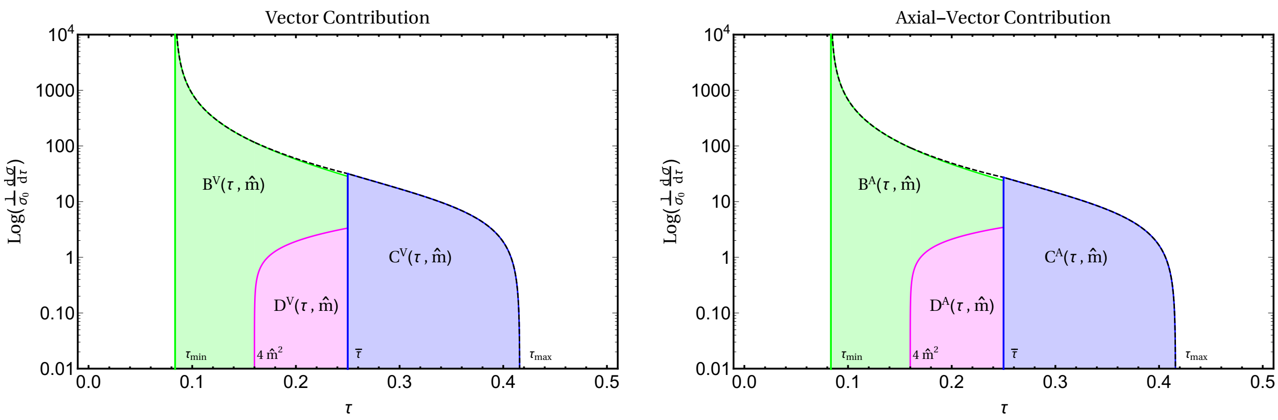

Figure 3.9: Logarithmic plot of the three contributions $B(\tau,\hat{m})$ (Green), $C(\tau,\hat{m})$ (Blue) and $D(\tau,\hat{m})$ (Red) of fixed order thrust distribution at $\mathcal{O}(\alpha_s)$ for the real radiation of gluons in the pair production of massive quarks with $\hat{m}=0.2$. These contributions are obtained by projecting the double differential distribution along the thrust axis in each region of phase space and collecting the similar threshold structures [see Fig. 3.8]. The sum of all terms is depicted by the dashed black line. The left and right panels are representing the vector and axial-vector contributions, respectively.

Computation of $B^X(\tau,\hat{m})$, $C^X(\tau,\hat{m})$ and $D^X(\tau,\hat{m})$ Coefficients

In this section we will compute the $B^X(\tau,\hat{m})$, $C^X(\tau,\hat{m})$ and $D^X(\tau,\hat{m})$ coefficients. As already mentioned these coefficient functions are arising completely from three jet events. First, we compute the matrix element for real radiation diagrams with a massive quark and perform the integration of the three-body phase space. It is convenient to use the energy fraction variables, $x_i = 2\,p_i^0/Q$ with i running from 1 to 3, representing the quark, antiquark and gluon, respectively. Here, energy conservation implies $x_1+x_2+x_3=2$. We obtain the double differential cross section for vector and axial-vector channels as (agrees with Refs. [236, 237])

$$\begin{aligned}\frac{\mathrm{d}^2\hat{\sigma}^{V,\,\mathrm{real}}(\tau)}{\mathrm{d}x_1\mathrm{d}x_2} =&\frac{C_F\alpha_s}{2\pi}\Bigg[\frac{x_1^2+x_2^2-2\hat{m}^2\left(6-\frac{7}{2}(x_1+x_2)+x_1x_2+4\hat{m}^2\right)}{(1-x_1)(1-x_2)}\\&+\frac{\hat{m}^2}{(1-x_1)^2}\left(x_1^2-4\hat{m}^2-3x_1\right)+\frac{\hat{m}^2}{(1-x_2)^2}\left(x_2^2-4\hat{m}^2-3x_2\right)\Bigg]\,,\\\frac{\mathrm{d}^2\hat{\sigma}^{A,\,\mathrm{real}}(\tau)}{\mathrm{d}x_1\mathrm{d}x_2} =&\frac{C_F\alpha_s}{2\pi}\Bigg[\frac{8\hat{m}^4-2\hat{m}^2}{(1-x_1)^2}+\frac{8\hat{m}^4-2\hat{m}^2}{(1-x_2)^2}+\frac{8\hat{m}^2-2}{1-x_1}+\frac{8\hat{m}^2-2}{1-x_2}+4\hat{m}^2\\&+\frac{(1+2\hat{m}^2)\left((1-x_1)^2+(1-x_2)^2\right)+2-12\hat{m}^2+16\hat{m}^4}{(1-x_1)(1-x_2)}\Bigg]\,,\end{aligned}\tag{3.6.9}$$

The second step is to define the observable in terms of kinematic variables. It is straightforward to show, using the algorithm in [238], that the thrust variable τ is simply related to the maximum momentum of the three particles in tree jet events;

$$\tau = 1-\max_{\hat{\mathbf{t}}}\frac{\sum_{i=1}^{3}\hat{\mathbf{t}}\cdot\mathbf{p}_i}{Q} = 1-\max\left(\sqrt{x_1^2-4\hat{m}^2},\sqrt{x_2^2-4\hat{m}^2},x_3\right),\tag{3.6.10}$$

where $\hat{\mathbf{t}}$ is the normalized thrust axis and $\mathbf{p}_{1/2/3}$ are the three-momentum of the quark, the antiquark or the gluon in the center-of-mass frame. The last step is to evaluate the thrust distribution by projecting the double differential cross section onto the thrust

$$\frac{\mathrm{d}\hat{\sigma}^{X,\,\mathrm{real}}(\tau)}{\mathrm{d}\tau} = \int\mathrm{d}x_1\mathrm{d}x_2\frac{\mathrm{d}^2\hat{\sigma}^{X,\,\mathrm{real}}}{\mathrm{d}x_1\mathrm{d}x_2}\delta\left(\tau-1+\max\left(\sqrt{x_1^2-4\hat{m}^2},\sqrt{x_2^2-4\hat{m}^2},2-x_1-x_2\right)\right),\tag{3.6.11}$$

where we integrate over the whole allowed phase space of final states, illustrated in Fig. 3.8 . In order to simplify the integration we have used the following substitutions and defined the x and t parameters

$$x_1 = \frac{1}{2}\left(x + t + 1\right), \qquad x_2 = \frac{1}{2}\left(x - t + 1\right). \tag{3.6.12}$$

After performing the integrals in Eq. (3.6.11), we obtain the $B^{V,A}(\tau,\hat{m})$, $C^{V,A}(\tau,\hat{m})$, $D^{V,A}(\tau,\hat{m})$ coefficient functions in Eq. (3.6.7) for vector and axial-vector

$$\begin{aligned}
B^V(\tau,\hat{m}) &= \frac{(\tau-1)(\tau-\tau_{\min})}{2(t_1-1)t_1}\Bigg[4(1-t_1)\left(3+8\hat{m}^2+t_1\right) + \frac{(t_1-1)^2\left(1-2\hat{m}^2+t_1-\tau\right)^2}{(1+\hat{m}^2-t_1)^2} \\
&-\frac{32\hat{m}^2\left(1+2\hat{m}^2\right)\left(1+\hat{m}^2-t_1\right)}{2\hat{m}^2-1-t_1+\tau} + 8\left(1+2\hat{m}^2\right)\left(2\hat{m}^2-1-t_1+\tau\right) \\
&+8\left(1-8\hat{m}^4+4\hat{m}^2(t_1-1)+t_1^2\right)\ln\left(\frac{1-2\hat{m}^2+t_1-\tau}{2+2\hat{m}^2-2t_1}\right)\Bigg],
\end{aligned}$$

$$\begin{aligned}
B^A(\tau,\hat{m}) &= \frac{(\tau-1)(\tau-\tau_{\min})}{2(t_1-1)t_1}\Bigg[4(1-t_1)\left(3+t_1+2\hat{m}^2(5t_1-13)\right) \\
&+\frac{\left(1+2\hat{m}^2\right)(t_1-1)^2\left(1-2\hat{m}^2+t_1-\tau\right)^2}{\left(1+\hat{m}^2-t_1\right)^2} + \frac{32\hat{m}^2\left(4\hat{m}^2-1\right)\left(1+\hat{m}^2-t_1\right)}{2\hat{m}^2-1-t_1+\tau} \\
&-\frac{8\left(4\hat{m}^4-1+t_1+\hat{m}^2(5+2(t_1-4)t_1)\right)\left(2\hat{m}^2-1-t_1+t\right)}{1+\hat{m}^2-t_1} \\
&+8\left(1+16\hat{m}^4+t_1^2+2\hat{m}^2(t_1(t_1-6)-1)\right)\ln\left(\frac{1-2\hat{m}^2+t_1-\tau}{2+2\hat{m}^2-2t_1}\right)\Bigg],
\end{aligned}$$

$$\begin{aligned}
C^V(\tau,\hat{m}) &= \frac{4\left(2\hat{m}^2+4\hat{m}^4-(t_1-1)(t_1-\tau)\right)(2t_1-1-\tau)}{(t_1-1)(t_1-\tau)} \\
&+\frac{4\left(1-8\hat{m}^4+4\hat{m}^2(\tau-1)+\tau^2\right)}{\tau-1}\ln\left(\frac{1-t_1}{t_1-\tau}\right) + \frac{2(1-\tau)(2t_1-1-\tau)}{(t_1-1)^2t_1(t_1-\tau)} \\
&\times\Big[8\hat{m}^4(\tau-1)+(t_1-1)(t_1-\tau)(3+\tau)+4\hat{m}^2(3\tau+2t_1(t_1-1-\tau)-1)\Big] \\
&+\frac{4(1-\tau)\left(1-8\hat{m}^4+4\hat{m}^2(t_1-1)+t_1^2\right)}{(t_1-1)t_1}\ln\left(\frac{1-t_1}{t_1-\tau}\right),
\end{aligned}$$

$$\begin{aligned}
C^A(\tau,\hat{m}) &= \frac{4\left(8\hat{m}^4-2\hat{m}^2+(t_1-1)(t_1-\tau)\right)(2t_1-1-\tau)}{(1-t_1)(t_1-\tau)} \\
&+\frac{4\left(1+16\hat{m}^4+\tau^2+2\hat{m}^2(\tau^2-6\tau-1)\right)}{\tau-1}\ln\left(\frac{1-t_1}{t_1-\tau}\right) \\
&+\frac{2(1-\tau)(2t_1-1-\tau)}{(t_1-1)^2t_1(t_1-\tau)}\Big[16\hat{m}^4(1-\tau)+(t_1-1)(t_1-\tau)(3+\tau) \\
&+2\hat{m}^2\left(4t_1^3-2+(\tau-11)\tau-t_1^2(17+3\tau)+t_1(13-(\tau-16)\tau)\right)\Big] \\
&+\frac{4(1-\tau)\left(1+16\hat{m}^4+t_1^2+2\hat{m}^2(t_1(t_1-6)-1)\right)}{(t_1-1)t_1}\ln\left(\frac{1-t_1}{t_1-\tau}\right),
\end{aligned} \tag{3.6.13}$$

$$D^V(\tau,\hat{m}) = \frac{4}{\tau-1}\left[t_2\left(1+4\hat{m}^2\tau+\tau^2\right)+\left(1-8\hat{m}^4+4\hat{m}^2(\tau-1)+\tau^2\right)\ln\left(\frac{1-t_2}{1+t_2}\right)\right],$$

$$D^A(\tau,\hat{m}) \;=\; \frac{4}{\tau-1}\left[t_2\left(1-8\hat{m}^2\tau+\tau^2\right)+\left(1+16\hat{m}^4+\tau^2+2\hat{m}^2(\tau^2-6\tau-1)\right)\ln\left(\frac{1-t_2}{1+t_2}\right)\right],$$

where we abbreviated $t_1=\sqrt{4\hat{m}^2+(1-\tau)^2}$ and $t_2=\sqrt{1-4\hat{m}^2/\tau}$.

A straightforward examination of the real radiation result is to check the massless limit $\hat{m}\to 0$. In this limit the only distribution which survives is the $C^X(\tau,\hat{m})$ function. This contribution corresponds to the triangular shaped region (Blue area in Fig. 3.8) in the core of available phase space for real gluon radiation. In the massless limit this region inflates and merges to the massless phase space, the upper half triangle. Taking the massless limit of our result in Eq. (3.6.7) we obtain

$$\frac{\mathrm{d}\hat{\sigma}^{X,\,\mathrm{real}}(\tau)}{\mathrm{d}\tau} = \frac{1}{\tau(1-\tau)}\bigg(-3+9\tau+3\tau^2-9\tau^3-(4-6\tau+6\tau^2)\ln\left(\frac{1-2\tau}{\tau}\right)\bigg)\,\theta(\tau)\,\theta(1/3-\tau)\,, \tag{3.6.14}$$

in agreement with Refs. [155, 172] . Note that the threshold is now located at $\tau=0$ and the endpoint of the distribution at $\tau=1/3$.

Computation of the $A^X(\hat{m})$ Coefficient

In this section the $A^V(\hat{m})$ and $A^A(\hat{m})$ coefficients for the thrust distribution given in Eq. (3.6.7) are determined. One way to determine these is to integrate the B, C and D terms in Eq. (3.6.7) and subtract the results from the corresponding contributions in the total cross section. Though the numerical extraction of these coefficients using the total cross section is then straightforward, here we provide a method to calculate the expressions analytically. The method is generic and can be used for various event shape distributions.[17]

Before starting we note that the $A^V(\hat{m})$ and $A^A(\hat{m})$ are the coefficients of the $\delta(\tau-\tau_{\min})$ term that is located at the threshold $\tau_{\min}$. Therefore in the following procedure we simplify the calculations by exploiting different expressions in the threshold limit, i.e. when $\tau-\tau_{\min}\ll 1$. Based on the above discussion the strategy of our method is to compute separately the real (related to $e^+e^-\to q\bar{q}g$ process) and the virtual (related to $e^+e^-\to q\bar{q}$ process) contributions from the threshold region in the total cross section at NLO. Then by comparing the results with the total cross section that can be obtained from the integration of the thrust differential cross section given in Eq. (3.6.7) expanded in the limit $\tau-\tau_{\min}\ll 1$, we extract the analytic expressions for the $A^V(\hat{m})$ and $A^A(\hat{m})$ coefficients.

To start, we first compute the virtual corrections in dimensional regularization with $D=4-2\epsilon$ space-time dimensions, so that the infrared divergences are explicit. These infrared divergent terms will be canceled by the (infrared) divergences arising in the real gluon radiation. The total $e^+e^-\to q\bar{q}$ Born cross sections for vector and axial-vector up to order $\mathcal{O}(\epsilon)$ are given by

$$\hat{\sigma}^V_{\mathrm{Born}}=\hat{\sigma}^V_f\left(1+2\hat{m}^2-\frac{3}{2}\epsilon\right)\beta\,,\qquad \hat{\sigma}^A_{\mathrm{Born}}=\hat{\sigma}^A_f\beta^3\left(1-\frac{3}{2}\epsilon\right), \tag{3.6.15}$$

where $\hat{m}=m/Q$ and $\beta=\sqrt{1-4\hat{m}^2}$. The terms $\hat{\sigma}^A_f$ and $\hat{\sigma}^V_f$ are given by Eq. (3.6.5). The virtual corrections to the total $e^+e^-\to q\bar{q}$ cross section up to order $\mathcal{O}(\epsilon^0)$ are given by

$$\begin{aligned}
\hat{\sigma}^{V,\mathrm{virtual}}_{q\bar{q}} &= \hat{\sigma}^V_{\mathrm{Born}}\frac{\alpha_s C_F}{2\pi}C_\epsilon\left[\frac{2}{\epsilon}\left(-1+\frac{1+\beta^2}{2\beta}\ln\left(\frac{1+\beta}{1-\beta}\right)\right)+A^V_V\right],\\
\hat{\sigma}^{A,\mathrm{virtual}}_{q\bar{q}} &= \hat{\sigma}^A_{\mathrm{Born}}\frac{\alpha_s C_F}{2\pi}C_\epsilon\left[\frac{2}{\epsilon}\left(-1+\frac{1+\beta^2}{2\beta}\ln\left(\frac{1+\beta}{1-\beta}\right)\right)+A^A_V\right],
\end{aligned} \tag{3.6.16}$$

[17] Another method is to extract $A^X(\hat{m})$ form the cumulant of the thrust distribution (3.3.31) in the threshold limit $\tau-\tau_{\min}\ll 1$. There one has to compute the real and virtual corrections in dimensional regularization with D space-time dimensions.

where we abbreviated $C_\epsilon = (4\pi\mu^2 m^{-2} e^{-\gamma_E})^\epsilon$, and

$$
\begin{aligned}
A_V^V &= \frac{3+4\hat{m}^2}{1+2\hat{m}^2}\beta \ln\Big(\frac{1+\beta}{1-\beta}\Big) - 4 + \frac{1+\beta^2}{\beta}\bigg(-\frac{1}{2}\ln^2\Big(\frac{1-\beta}{1+\beta}\Big) + 2\ln\Big(\frac{1-\beta}{1+\beta}\Big)\ln\Big(\frac{2\beta}{1+\beta}\Big) \\
&\quad + 2\mathrm{Li}_2\Big(\frac{1-\beta}{1+\beta}\Big) + \frac{2}{3}\pi^2\bigg),
\end{aligned}
$$

$$
\begin{aligned}
A_V^A &= \frac{3-4\hat{m}^2}{\beta} \ln\Big(\frac{1+\beta}{1-\beta}\Big) - 4 + \frac{1+\beta^2}{\beta}\bigg(-\frac{1}{2}\ln^2\Big(\frac{1-\beta}{1+\beta}\Big) + 2\ln\Big(\frac{1-\beta}{1+\beta}\Big)\ln\Big(\frac{2\beta}{1+\beta}\Big) \\
&\quad + 2\mathrm{Li}_2\Big(\frac{1-\beta}{1+\beta}\Big) + \frac{2}{3}\pi^2\bigg). \qquad (3.6.17)
\end{aligned}
$$

The infrared singularity in (3.6.16) is manifest in the term $1/\epsilon$. Note that the virtual corrections are contributing to the $A^X(\hat{m})$ coefficients in the thrust distribution.

For the calculation of the real radiation contributions in the threshold regime, we follow the so called two cutoff phase space slicing method [239]. Based on this method, we first decompose the three-body phase space for $e^+e^- \to q\bar{q}g$ process into two regions, the threshold region where $\tau - \tau_{\rm min} \le \delta$ with $\delta \ll 1$, and the rest of phase space i.e. $\tau - \tau_{\rm min} > \delta$. As already mentioned here we only focus on the threshold region which corresponds to a small region close to the point of minimal gluon energy (where $(1-x_1) \sim (1-x_2) \ll 1$ so that $x_3 \ll 1$) that is indicted with E_1 in the three-body phase space in Fig. 3.8. The thrust value in this region is given by

$$
\tau(x_1,x_2) = \begin{cases} 1 - \sqrt{x_1^2 - 4\hat{m}^2} & \text{region } E_1GE_3 \\ 1 - \sqrt{x_2^2 - 4\hat{m}^2} & \text{region } E_1GE_2 \end{cases}, \qquad (3.6.18)
$$

where the regions E_1GE_3 and E_1GE_2 are visualized in Fig. 3.8 [see also Fig. 3.10]. The equations for the boundary of the threshold region read

$$
\tau(x_1,x_2) = \tau_{\rm min}(\hat{m}) + \delta\,, \qquad \text{with} \qquad \delta \ll 1\,. \qquad (3.6.19)
$$

By solving this equation and expanding the results up to leading order in δ we obtain,

$$
x_1 = x_1^{thr} = 1 - \beta\,\delta\,, \qquad \text{and} \qquad x_2 = x_2^{thr} = 1 - \beta\,\delta\,, \qquad (3.6.20)
$$

that are equations of two straight lines in the x_1–x_2 plane, shown in Fig. 3.10. A rather more general relation to find the threshold region of phase space for different event shapes is presented in Appendix. D.

In the next step we split the threshold region into three sub-regions denoted with S and E. The region S refers to the soft gluon region where $0 < x_3 < x_3^{\max}$ and $x_3^{\max}$ refers to the maximum gluon energy which can be obtained while keeping the $x_1 = x_2$. The value of $x_3^{\max}$ depends on the specific event shape and the generic relation is given in Appendix. D. For the thrust event shape variable the result reads $x_3^{\max} = 2\beta\delta$. The boundary of the soft gluon region S in the $x_1 - x_2$ plane is given by $x_3 = 2 - (x_2 + x_1) = x_3^{\max}$. The remaining pieces of the threshold region that are not included in the soft region constitute the E regions. The S and E regions are displayed, respectively with blue and yellow color in Fig. 3.10.

The partitioning of the phase space into S and E regions allows us to calculate the corresponding contributions to the total cross section separately. For the S region where the emitted gluon is soft, one can use the eikonal (double pole) approximation of the matrix element [188, 240–243] and the phase space integral will be carried out conveniently in dimensional regularization with $D = 4-2\epsilon$ space-time dimensions. The resulting contributions contains a single logarithm, $\ln(x_3^{\max})$, which depends on the specific event shape, non-logarithmic terms that are universal for all event shapes and the complete infrared divergences that arises from the real radiation. The region E consists of two identical finite contributions that can be simply computed by using the same eikonal approximation for the matrix element, however performing the phase space integrations in 4 space-time dimension. The outcome in this region depends on the boundary lines of the threshold region which are related to the particular event shape. Below, we demonstrate the particular calculations for the thrust variable however as noted the method is generic and can be conveniently applied to the other event shape variables.

The differential cross section of the real radiation process $e^+(k_1)e^-(k_2) \to q(p_1)\overline{q}(p_2)g(p_3)$ in the limit of a soft gluon energy $p_3^0 \to 0$ is given by

$$\mathrm{d}\hat{\sigma}_{\mathrm{S}}^{X,\mathrm{real}} = \mathrm{d}\hat{\sigma}_{\mathrm{Born}}^{X}\,\mathrm{d}\Gamma_{p_3}\,4\pi\alpha_s C_F\left(-\frac{m^2}{(p_1\cdot p_3)^2}-\frac{m^2}{(p_2\cdot p_3)^2}+\frac{2\,p_1\cdot p_2}{(p_1\cdot p_3)(p_2\cdot p_3)}\right), \tag{3.6.21}$$

where $X=\{V,A\}$ and we use the eikonal approximation for the matrix elements given in Ref. [239] . In this notation we have factorized the three-body phase space as $\mathrm{d}\Gamma_3 = \mathrm{d}\Gamma_2\mathrm{d}\Gamma_{p_3}$ where $\mathrm{d}\Gamma_2$ refer to the two body phase space that is implicitly included in the differential Born cross section in Eq. (3.6.21), and the term $\mathrm{d}\Gamma_{p_3}$ is the differential phase space factor belonging to the outgoing gluon given by

$$\mathrm{d}\Gamma_{p_3} = \frac{\mu^{2\epsilon}\mathrm{d}^{D-1}p_3^0}{2(2\pi)^{D-1}p_3^0} = \frac{(\pi\mu^2)^\epsilon}{(2\pi)^3}\,\frac{\Gamma(1-\epsilon)}{\Gamma(1-2\epsilon)}(p_3^0)^{1-2\epsilon}\mathrm{d}p_3^0\sin^{1-2\epsilon}\theta_1\mathrm{d}\theta_1\sin^{-2\epsilon}\theta_2\mathrm{d}\theta_2\,. \tag{3.6.22}$$

Since we are considering the soft gluon limit we can parametrize the momenta of the outgoing particles as $p_1 = \frac{Q}{2}(1,0,0,\beta)$, $p_2 = \frac{Q}{2}(1,0,0,-\beta)$, and $p_3 = p_3^0(1,\sin\theta_1\sin\theta_2,\sin\theta_1\cos\theta_2,\cos\theta_1)$. Then integrating Eq. (3.6.21) in D dimensions and restricting the p_3^0 integration to $p_3^0 = x_3Q/2 < x_3^{\max}Q/2$, we arrive at

$$\hat{\sigma}_{\mathrm{S}}^{X,\mathrm{real}} = \hat{\sigma}_{\mathrm{Born}}^{X}\frac{\alpha_s C_F}{2\pi}C_\epsilon\left[\frac{2}{\epsilon}\left(1-\frac{1+\beta^2}{2\beta}\ln\left(\frac{1+\beta}{1-\beta}\right)\right)+A_S+4\left(-1+\frac{1+\beta^2}{2\beta}\ln\left(\frac{1+\beta}{1-\beta}\right)\right)\ln\left(x_3^{\max}\right)\right], \tag{3.6.23}$$

with

$$\begin{aligned} A_S = {} & 2\left(1-\frac{1+\beta^2}{2\beta}\ln\left(\frac{1+\beta}{1-\beta}\right)\right)\ln(\hat{m}^2) \\ & +4\left(\frac{1}{2\beta}\ln\left(\frac{1+\beta}{1-\beta}\right)-\frac{1+\beta^2}{2\beta}\left(\mathrm{Li}_2\left(\frac{2\beta}{1+\beta}\right)+\frac{1}{4}\ln^2\left(\frac{1+\beta}{1-\beta}\right)\right)\right). \end{aligned} \tag{3.6.24}$$

Note that the infrared divergences appearing as $1/\epsilon$ terms are precisely canceling the corresponding terms in the virtual contributions in Eq. (3.6.16) .

The cross section contributions arising from the region E consist of two pieces that are identical. In the following we compute only the upper one. Here the cross section can be evaluated in four space-time dimensions using the eikonal matrix elements in the soft gluon limit, given in Eq. (3.6.21). In this computation, it is more convenient to use the energy fraction variables and the double differential cross section given by

$$\frac{\mathrm{d}^2\hat{\sigma}_E^{X,\mathrm{real}}}{\mathrm{d}x_1\mathrm{d}x_2} = \hat{\sigma}_{\mathrm{Born}}^{X}\frac{C_F\alpha_s}{2\pi}\left(-\frac{2\hat{m}^2}{\beta(1-x_1)^2}-\frac{2\hat{m}^2}{\beta(1-x_2)^2}+\frac{2-4\hat{m}^4}{\beta(1-x_1)(1-x_2)}\right). \tag{3.6.25}$$

One can also extract this expression by expanding the double differential cross section in Eq. (3.6.9) in the limit $(1-x_1)\sim(1-x_2)\ll 1$. To obtain the corresponding cross section we perform the following integration over the phase space region E (the upper piece),

$$\hat{\sigma}_E^X = \int_{1-\beta\delta}^{1-\xi\beta\delta}\mathrm{d}x_2\int_{1-\psi+\psi x_2}^{2-2\beta\delta-x_2}\mathrm{d}x_1\,\frac{\mathrm{d}^2\hat{\sigma}_E^{X,\mathrm{real}}}{\mathrm{d}x_1\mathrm{d}x_2}\,, \tag{3.6.26}$$

where $\xi = 2-4\hat{m}^2/\tau_{\min}$, $\psi = 2\hat{m}^2/(\tau_{\min}-2\hat{m}^2)$. The lower boundary of the integration over x_1 that is given by $x_1 = 1+\psi(x_2-1)$, is obtained by solving the three-body phase space boundary equation

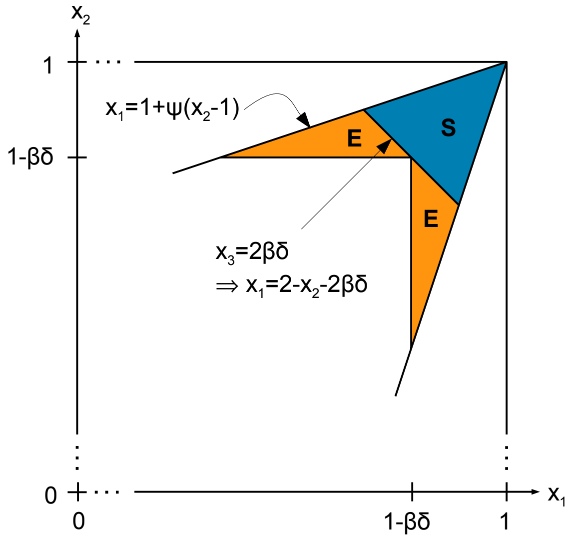

Figure 3.10: The x_1–x_2 phase space of the process $e^+e^- \to q\bar{q}g$ limited to $\tau < \tau_{\min} + \delta$ with $\delta \ll 1$. The phase space is split into two parts, a region S, which is the region, in which the gluon energy $E_5 = x_3 Q/2 < Q\beta\delta$, and two regions E, which comprise the difference to the whole region in which $\tau < \tau_{\min} + \delta$. We abbreviated $\psi = 2\hat{m}^2/(\tau_{\min} - 2\hat{m}^2)$.

$\sqrt{x_2 - 4\hat{m}^2} + \sqrt{x_1 - 4\hat{m}^2} = 2 - (x_1, x_2)$ for x_1 and expanding the outcome in the limit of $(1 - x_2) \ll 1$ up to $\mathcal{O}((x_1 - 1)^2)$. After carrying out the integration in Eq. (3.6.25) for the upper E region, the cross section reads

$$\hat{\sigma}_E^X = \hat{\sigma}_{\text{Born}}^X \frac{C_F \alpha_s}{2\pi} A_E \,, \tag{3.6.27}$$

with

$$\begin{aligned} A_E = &-\frac{2}{\beta\psi}\biggl[2\hat{m}^2\psi - \frac{\pi^2}{12}\psi + \frac{1}{6}\hat{m}^2\pi^2\psi - \frac{2\hat{m}^2\psi}{\xi} + \frac{1}{2}\psi\ln^2(2) - \hat{m}^2\psi\ln^2(2) + \hat{m}^2\psi\ln(2-\xi) \\ &+ \hat{m}^2\ln(\xi) - \hat{m}^2\psi\ln(\xi) - \hat{m}^2\psi^2\ln(\xi) - \psi\ln(2)\ln(\xi) + \hat{m}^2\psi\ln(4)\ln(\xi) + \psi\ln(\psi)\ln(\xi) \\ &- 2\hat{m}^2\psi\ln(\psi)\ln(\xi) + \frac{1}{2}\psi\ln^2\xi - \hat{m}^2\psi\ln^2(\xi) + (\psi - 2\hat{m}^2\psi)\text{Li}_2\left(\frac{\xi}{2}\right)\biggr] \,. \end{aligned} \tag{3.6.28}$$

Note that the expression is independent of the term δ.

Now we have all the ingredients at hand to obtain the $\mathcal{O}(\alpha_s)$ fixed order $e^+e^- \to q\bar{q} + X$ cross section from the threshold region. The result is

$$\begin{aligned} \hat{\sigma}^{\text{FO}}_{\tau<\tau_{\min}+\delta} &= \sum_{X=A,V} \hat{\sigma}^X_{\text{Born}} + \hat{\sigma}^{X,\text{virtual}} + \hat{\sigma}_S^{X,\text{real}} + 2\,\hat{\sigma}_E^{X,\text{real}} \\ &= \frac{\alpha_s C_F}{2\pi}\left(\hat{\sigma}_0^V(1+2\hat{m}^2)\beta A_V^V + \hat{\sigma}_0^A \beta^3 A_V^A\right) + \hat{\sigma}^{q\bar{q}}_{\text{Born}}\biggl[1 + \frac{\alpha_s C_F}{2\pi} \\ &\quad\times\left(2A_E + A_S + 4\left(-1 + \frac{1+\beta^2}{2\beta}\ln\left(\frac{1+\beta}{1-\beta}\right)\right)\ln(2\beta\delta)\right)\biggr] . \end{aligned} \tag{3.6.29}$$

where $\hat{\sigma}^{q\bar{q}}_{\text{Born}} = \sum_{X=A,V} \hat{\sigma}^X_{\text{Born}}$. In the first line we multiply the $\hat{\sigma}_E$ with the factor 2 to account for the second piece of region E.

On the other hand, expanding Eq. (3.6.7) for $\tau - \tau_{\min} \ll 1$ yields

$$\begin{aligned} \frac{\mathrm{d}\hat{\sigma}^{\text{FO}}(\tau)}{\mathrm{d}\tau} &= \delta(\tau-\tau_{\min})\frac{\alpha_s C_F}{2\pi}\left(\hat{\sigma}_0^V \frac{A^V(\hat{m})}{2} + \hat{\sigma}_0^A \frac{A^A(\hat{m})}{2}\right) + \hat{\sigma}^{q\bar{q}}_{\text{Born}}\biggl\{\delta(\tau-\tau_{\min}) + \frac{\alpha_s C_F}{2\pi} \\ &\quad\times\left[\frac{\theta(\tau-\tau_{\min})}{\tau-\tau_{\min}}\right]_+ 4\left(-1 + \frac{1+\beta^2}{2\beta}\ln\left(\frac{1+\beta}{1-\beta}\right)\right)\biggr\} + \mathcal{O}\left((\tau-\tau_{\min})^0\right) . \end{aligned} \tag{3.6.30}$$

Integrating Eq. (3.6.30) from $\tau_{\min}$ to $\tau_{\min}+\delta$ we arrive at

$$\begin{aligned}\hat{\sigma}^{\rm FO}_{\tau<\tau_{\min}+\delta} &= \frac{\alpha_s C_F}{2\pi}\left(\hat{\sigma}^V_0\frac{A^V(\hat{m})}{2}+\hat{\sigma}^A_0\frac{A^A(\hat{m})}{2}\right)+\hat{\sigma}^{q\bar{q}}_{\rm Born}\bigg[1+\frac{\alpha_s C_F}{2\pi}\\ &\quad\times 4\left(-1+\frac{1+\beta^2}{2\beta}\ln\Big(\frac{1+\beta}{1-\beta}\Big)\right)\ln(\delta)\bigg]\end{aligned}\tag{3.6.31}$$

Finally, since the total cross section in Eqs. (3.6.29) and (3.6.31) must be equal, we can identify $A^V(\hat{m})$ and $A^A(\hat{m})$ to be

$$\begin{aligned}A^V(\hat{m}) &= (1+2\hat{m}^2)\beta\left[4A_E+2A_S+2A^V_V+8\left(-1+\frac{1+\beta^2}{2\beta}\ln\Big(\frac{1+\beta}{1-\beta}\Big)\right)\ln(2\beta)\right]\\ A^A(\hat{m}) &= \beta^3\left[4A_E+2A_S+2A^A_V+8\left(-1+\frac{1+\beta^2}{2\beta}\ln\Big(\frac{1+\beta}{1-\beta}\Big)\right)\ln(2\beta)\right].\end{aligned}\tag{3.6.32}$$

After plugging in (3.6.17), (3.6.24), and (3.6.28) and doing some simplification of the resulting expressions we obtain

$$\begin{aligned}A^V(\hat{m}) &= -4(5-8\hat{m}^2-24\hat{m}^4)\ln\left(\frac{1-\beta}{2\hat{m}}\right)+2(1-4\hat{m}^4)\bigg[\frac{2(1-\beta-4\hat{m}^2)}{1-2\hat{m}^2}+\pi^2\\ &\quad+6\ln^2(1-\beta)+8\ln\Big(\frac{(1-\beta)\beta}{2\hat{m}^2}\Big)\ln\Big(\frac{1-\beta}{2\hat{m}}\Big)+\frac{4\beta}{1-2\hat{m}^2}\ln\Big(\frac{(1-\beta)\hat{m}}{2\beta}\Big)\\ &\quad-4\ln(1-\beta)\ln(8\hat{m}^2)+2\ln(2)\ln(8\hat{m}^4)-4\,{\rm Li}_2\left(\frac{1-\beta}{2}\right)+8\,{\rm Li}_2\left(\frac{1-\beta}{1+\beta}\right)\bigg],\end{aligned}$$

$$\begin{aligned}A^A(\hat{m}) &= 4\beta^3\left(\beta-1-2\ln\Big(\frac{\beta(1+\beta)}{2\hat{m}^3}\Big)\right)-4\beta^2(5-8\hat{m}^2)\ln\Big(\frac{1-\beta}{2\hat{m}}\Big)\\ &\quad+8\beta^2(1-2\hat{m}^2)\bigg[\frac{\pi^2}{4}+\frac{7}{2}\ln^2\Big(\frac{1-\beta}{2}\Big)+2\ln(\beta)\ln\Big(\frac{1-\beta}{2\hat{m}}\Big)-4\ln\Big(\frac{(1-\beta)^2}{4\hat{m}}\Big)\ln(\hat{m})\\ &\quad-{\rm Li}_2\left(\frac{1-\beta}{2}\right)+2\,{\rm Li}_2\left(\frac{1-\beta}{1+\beta}\right)\bigg].\end{aligned}\tag{3.6.33}$$

3.6.2 Nonsingular Contributions

The partonic thrust distribution obtained from the perturbative fixed order computation consists of singular and nonsingular contributions. We defined our first type partonic nonsingular contributions in Sec. 3.5 , denoted here with $\frac{1}{\hat{\sigma}^X_f}\frac{{\rm d}\hat{\sigma}(\tau)}{{\rm d}\tau}\big|^{\rm X}_{\rm n.sing.}$, to be equal to the remainder of the differential cross section in full QCD after subtracting the singular contributions which are accounted by SCET factorization (expanded up to $\mathcal{O}(\alpha_s)$),

$$\frac{1}{\hat{\sigma}^X_f}\frac{{\rm d}\hat{\sigma}(\tau)}{{\rm d}\tau}\bigg|^{\rm X}_{\rm n.sing.}\equiv\frac{1}{\hat{\sigma}^X_f}\frac{{\rm d}\hat{\sigma}(\tau)}{{\rm d}\tau}\bigg|^{\rm X}_{\rm full.}-\frac{1}{\hat{\sigma}^X_f}\frac{{\rm d}\hat{\sigma}(\tau)}{{\rm d}\tau}\bigg|_{\rm sing.},\tag{3.6.34}$$

where the terms $\hat{\sigma}^X_f$ are given in Eq. (3.6.5) and the superscript $X\in\{V,A\}$. The term $\frac{1}{\hat{\sigma}^X_f}\frac{d\hat{\sigma}(\tau)}{d\tau}\big|^X_{\rm full.}$ refers to the vector and axial-vector contributions that constitute the fixed-order thrust distribution given in Eq. (3.6.7).

The term $\frac{1}{\hat{\sigma}^X_f}\frac{{\rm d}\hat{\sigma}(\tau)}{{\rm d}\tau}\big|_{\rm sing.}$ refers to the singular terms which are accounted in the SCET factorization theorem expanded at $\mathcal{O}(\alpha_s)$. One can extract this contribution from the FO results in Eq. (3.6.7) . To this end we take the correct threshold information which is clearly related to the terms proportional to $\theta(\tau-\tau_{\rm min})$ and $\delta(\tau-\tau_{\rm min})$. Expanding the corresponding coefficients for small $\lambda\sim\hat m^2\sim\tau\ll 1$ yields [18]

$$\frac{1}{\hat\sigma_f^X}\frac{\mathrm{d}\hat\sigma(\tau)}{\mathrm{d}\tau}\bigg|_{\rm sing.}=\delta(\tau-\tau_{\rm min})+\frac{C_F\alpha_s}{4\pi}\bigg\{\delta(\tau-\tau_{\rm min})\Big(2\pi^2+4\ln^2(\hat m^2)+2\ln(\hat m^2)\Big)$$
$$-8\big(1+\ln(\hat m^2)\big)\left[\frac{\theta(\tau-\tau_{\rm min})}{\tau-\tau_{\rm min}}\right]_++\left(\frac{2(\tau-\tau_{\rm min})}{(\tau-\tau_{\rm min}+\hat m^2)^2}-\frac{8\ln(1+\frac{\tau-\tau_{\rm min}}{\hat m^2})}{\tau-\tau_{\rm min}}\right)\theta(\tau-\tau_{\rm min})\bigg\}\,, \quad (3.6.35)$$

where $\alpha_s=\alpha_s^{(n_l+1)}(\mu)$ is a natural choice [19] with (n_l+1) number of active flavors, since $\mu\sim\mathcal{O}(Q)$ and the primary massive quark is an active flavor in the hard interaction. One can also determine the singular contributions from the factorization formula in scenario IV, using Eq. (3.5.2) while all the scales in different sectors are set to be equal, $\mu_H=\mu_J=\mu_S$, so that the evolution factors are dropped. Note that the resulting SCET limit does not depend on the type of current and is identical for vector and axial-vector.

Following the definition in Eq. (3.6.34), the resulting nonsingular contribution can be expressed as

$$\frac{1}{\hat\sigma_f^X}\frac{\mathrm{d}\hat\sigma(\tau)}{\mathrm{d}\tau}\bigg|^X_{\rm n.sing.}=\mathcal{A}_0^{X,\rm n.sing.}(\hat m)\,\delta(\tau-\tau_{\rm min})+\frac{C_F\,\alpha_s}{4\pi}\bigg\{\mathcal{A}_1^{X,\rm n.sing.}(\hat m)\,\delta(\tau-\tau_{\rm min})$$
$$+\mathcal{B}_1^{X,\rm n.sing.}(\hat m)\left[\frac{\theta(\tau-\tau_{\rm min})}{(\tau-\tau_{\rm min})}\right]_++\mathcal{C}_1^{X,\rm n.sing.}(\tau,\hat m)\bigg\}\,, \quad (3.6.36)$$

where $\alpha_s=\alpha_s^{(n_l+1)}(\mu_{\rm ns})$. The $\mu_{\rm ns}$ denotes the renormalization scale in the strong coupling constant of the nonsingular contribution that will be discussed in Sec. 3.10. The subscript $\{0,1\}$ indicates the order of perturbative contributions. The corresponding coefficients read

$$\begin{aligned}
\mathcal{A}_0^{X,\rm n.sing.}(\hat m)&=\bar\sigma^X_{\rm Born}(\hat m)-1\,,\\
\mathcal{A}_1^{X,\rm n.sing.}(\hat m)&=A^X(\hat m)-\Big(2\pi^2+4\ln^2(\hat m^2)+2\ln(\hat m^2)\Big)\,,\\
\mathcal{B}_1^{X,\rm n.sing.}(\hat m)&=B^X(\tau_{\rm min},\hat m)+8\Big(1+\ln(\hat m^2)\Big)\,,\\
\mathcal{C}_1^{X,\rm n.sing.}(\tau,\hat m)&=C^X(\tau,\hat m)\,\theta\,(\tau-\bar\tau)\;\theta(\tau^{\rm 3-jet}_{\rm max}-\tau)\\
&\quad+\bigg[D^X(\tau,\hat m)\,\theta\left(\tau-4\hat m^2\right)+\Big(\frac{B^X(\tau,\hat m)-B^X(\tau_{\rm min},\hat m)}{\tau-\tau_{\rm min}}\Big)\,\theta(\tau-\tau_{\rm min})\bigg]\,\theta\,(\bar\tau-\tau)\\
&\quad-\bigg(\frac{2(\tau-\tau_{\rm min})}{(\tau-\tau_{\rm min}+\hat m^2)^2}-\frac{8\ln(1+\frac{\tau-\tau_{\rm min}}{\hat m^2})}{\tau-\tau_{\rm min}}\bigg)\,\theta(\tau-\tau_{\rm min})\,.
\end{aligned} \quad (3.6.37)$$

where the terms $\bar\sigma^X_{\rm Born}$, $A^X(\hat m)$, $B^X(\tau,\hat m)$, $C^X(\tau,\hat m)$ and $D^X(\tau,\hat m)$ are various contribution for the thrust distribution given in Eq. (3.6.6), and the analytic expressions are presented, respectively, in Eqs. (3.6.8), (3.6.33) and (3.6.13). Furthermore the term $B^X(\tau_{\rm min},\hat m)$ can be extracted from the threshold expansion of the thrust distribution given in Eq. (3.6.30)

$$B^X(\tau_{\rm min},\hat m)=8\,\bar\sigma^X_{\rm Born}(\hat m)\left(\frac{1+\beta^2}{2\beta}\ln\Big(\frac{1+\beta}{1-\beta}\Big)-1\right)\,. \quad (3.6.38)$$

[18] In order to provide the expansion for the SCET limit i.e. $\hat m^2\sim\tau\ll 1$ one has to substitute $\tau\to x\hat m^2$ and expand the expressions for the small $\hat m^2$ variable up to leading order, and finally substitute back the term x with $\tau/\hat m^2$. The resulting expression contains singularities of the form $1/(\tau-2\hat m^2)$ where the full threshold, i.e. $\tau_{\rm min}$, has been expanded and in practice has been replaced with term $2\hat m^2$. Nevertheless, since a priori we know the exact form of the threshold and singularities, we make use of the following replacement, $\tau\to\tau-\tau_{\rm min}+2\hat m^2$, to obtain Eq. (3.6.35). We note here that the same prescription has been employed for the different factorization scenarios for massive thrust. We stress that the difference between the exact threshold $\tau_{\rm min}$ and the expanded form $2\hat m^2$ is only in a subleading correction in powers of $\hat m^2$ that will be accounted by the nonsingular contribution.

[19] Note that one can use the one loop relation between the strong coupling constants with (n_l) and (n_l+1) active flavors, $\alpha_s^{(n_l+1)}=\alpha_s^{(n_l)}+\mathcal{O}\big((\alpha_s^{(n_l)})^2\big)$, to expand the expression in Eq. (3.6.35) in powers of $\alpha_s^{(n_l)}$. Hence, the difference between the two choices of flavor scheme appears at higher perturbative orders.

We note that $B^X(\tau,\hat{m}) - B^X(\tau_{\rm min},\hat{m}) \propto (\tau-\tau_{\rm min})$ so that the second term in the fifth line of Eq. (3.6.37) is finite when $\tau \to \tau_{\rm min}$.

The nonsingular contribution introduced in Eq. (3.6.34) contains subleading terms including the subdominant singularities that are not accounted by the SCET factorization theorems at the leading order in the power counting parameter $\lambda_{\rm SCET}$ (an example of subleading terms is $\hat{m}^2/(\tau-\tau_{\rm min})$). We notice that the effects of these subdominant singularities can be numerically large in the peak region of the thrust distribution. This issue is more critical for the top quark production at low energies and can cause some singular behavior close to the threshold of the thrust distribution [see Sec. 3.11].

To cope with this problem one would have to employ the subleading SCET theory [244] to provide resummation of the large logarithms in the subleading contributions. However, this computation cannot been performed yet. Nevertheless, here we provide a prescription to absorb certain subleading contribution into the leading SCET factorization theorems such that the effects of subdominant singularities are strongly suppressed.

To this end we have absorbed the subdominant singularities that are appearing in $\frac{1}{\hat\sigma_f^X}\frac{{\rm d}\hat\sigma(\tau)}{{\rm d}\tau}\big|^{\rm X}_{\rm n.sing.}$ in the hard and the jet sectors of the SCET factorization theorem,

$$\begin{aligned}
\tilde{H}_Q^{X,(n_l+1)}(Q,m,\mu_H) &= H_Q^{(n_l+1)}(Q,\mu_H) + \left(\frac{C_F\,\alpha_s^{(n_l+1)}(\mu_H)}{4\pi}\right)(1-\xi_j)\,\frac{h^X(\hat{m})}{\mathcal{A}_0^{X,\,\rm n.sing.}(\hat{m})}\,,\\
\tilde{J}^{X,(n_l+1)}(s,m,\mu_J) &= \mathcal{A}_0^{X,\,\rm n.sing.}(\hat{m})\,J^{(n_l+1)}(s,m,\mu_J) + \left(\frac{C_F\,\alpha_s^{(n_l+1)}(\mu_J)}{4\pi}\right)\Big\{\xi_j\,h^X(\hat{m})\delta(s)\\
&\quad + \Big(\mathcal{B}_1^{X,\,\rm n.sing.}(\hat{m}) - \mathcal{A}_0^{X,\,\rm n.sing.}(\hat{m})\mathcal{B}_1^{X,\,\rm sing.}(\hat{m})\Big)\frac{1}{m^2}\left[\frac{\theta(s)}{s/m^2}\right]_+\Big\}\,, \qquad (3.6.39)
\end{aligned}$$

where the term $h(\hat{m})$ is given by

$$h^X(\hat{m}) = \mathcal{A}_1^{X,\,\rm n.sing.}(\hat{m}) - \mathcal{A}_0^{X,\,\rm n.sing.}(\hat{m})\,\mathcal{A}_1^{X,\,\rm sing.}(\hat{m}) + 2\,\ln(\hat{m})\,\mathcal{B}_1^{X,\,\rm n.sing.}(\hat{m})\,. \qquad (3.6.40)$$

The terms $\tilde{H}^{X,(n_l+1)}$ and $\tilde{J}^{X,(n_l+1)}$ are the modified hard and jet functions, receptively, that will be used instead of $H_Q(Q,\mu_H)$ and $J(s,m,\mu_J)$ in the SCET factorization scenario III and scenario IV. We do not modify the soft function at $\mathcal{O}(\alpha_s)$. Massive corrections in the soft function can only raise via virtual heavy quark bubbles at higher orders in perturbation theory. Therefore it is inconceivable that the subleading singularities appear in the soft function in a systematic subleading treatment of SCET. Note that the modified hard and jet function carry the X superscript due to the different subleading terms for vector and axial-vector.

This absorption procedure is not uniquely determined, therefore the term ξ_j is used to tune the amount of corrections (related to the coefficients of the Dirac delta function) that are accounted separately by the modified jet and hard function. The parameter ξ_j can vary from 0 to 1. The limit $\xi_j \to 0$ ($\xi_j \to 1$) refers to the situation where we include all the corrections proportional to δ-function in the jet (hard) function. In the final analysis in SEC. 3.11, we assign a theoretical uncertainty to the partonic predictions that arises from this freedom in the absorption process. We have found that the overall effect of different choices for ξ_j on the resulting thrust distribution is very small.

After plugging Eq. (3.6.39) into the factorization formula in scenario III [Eqs. (3.5.4)] and IV [Eqs. (3.5.2)], we obtain the thrust distribution which truly accounts for all the singular contributions, i.e. the sum of the leading and subleading singular terms. Now, the nonsingular contributions reads

$$\frac{1}{\hat\sigma_f^X}\frac{{\rm d}\hat\sigma(\tau)}{{\rm d}\tau}\bigg|^{X}_{\rm n.sing} = \mathcal{C}_1^{X,n.sing.}(\tau,\hat{m})\,, \qquad (3.6.41)$$

which now only accounts for the truly nonsingular (non-distributional) contribution of the partonic thrust distribution.

In the bHQET regime one can make use of the matching condition in Eq. (3.5.7) to split further $\tilde{J}^{X,(n_l+1)}(s,m,\mu_J)$ between the bHQET jet function $B(\hat{s},m,\mu)$ and the bHQET current matching coefficient $H_m(m,\mu_m)$,

$$\begin{aligned}\tilde{H}_m^{X,(n_l+1)}(m,\mu_m) &= H_m^{(n_l+1)}(m,\mu_m) + \left(\frac{C_F\,\alpha_s^{(n_l+1)}(\mu_m)}{4\pi}\right)(1-\xi_b)\,\xi_j\,\frac{h^X(\hat{m})}{\mathcal{A}_0^{X,\,\text{n.sing.}}(\hat{m})}\,,\\ \tilde{B}^{X,(n_l)}(\hat{s},m,\mu_b) &= \mathcal{A}_0^{X,\,\text{n.sing.}}(\hat{m})\,B^{(n_l)}(\hat{s},m,\mu_b) + \left(\frac{C_F\,\alpha_s^{(n_l)}(\mu_b)}{4\pi}\right)\bigg\{\xi_j\,\xi_b\,h^X(\hat{m})\delta(\hat{s})\\ &\quad + \left(\mathcal{B}_1^{X,\,\text{n.sing.}}(\hat{m}) - \mathcal{A}_0^{X,\,\text{n.sing.}}(\hat{m})\mathcal{B}_1^{X,\,\text{sing.}}(\hat{m})\right)\frac{1}{m}\left[\frac{\theta(\hat{s})}{\hat{s}/m}\right]_+\bigg\}\,, \end{aligned} \tag{3.6.42}$$

where the parameter ξ_b varies from 0 to 1 . The parameter ξ_b plays a similar role as ξ_j and allows us to assign a theoretical uncertainty in the splitting procedure of the subleading corrections between the bHQET jet function and the current matching coefficient. The terms $\tilde{H}_m^{X,(n_l+1)}(m,\mu_m)$ and $\tilde{B}^{X,(n_l)}(\hat{s},m,\mu_J)$ are the modified bHQET current matching coefficient and jet functions, respectively, and will replace the $H_m^{(n_l+1)}(m,\mu_m)$ and $B^{(n_l)}(\hat{s},m,\mu_b)$ in the bHQET factorization given in Eq. (3.5.9). The result accounts for all the dominant and subdominant singularities for the massive thrust distribution. The corresponding nonsingular contribution in the bHQET scenario is also given by Eq. (3.6.41). In Sec. 3.11 we discuss further how this set of modifications suppresses the numerical effects of subleading singularities close to the threshold $\tau_{\min}$.

3.7 Nonperturbative Corrections

For convenience, in Sec. 3.4 (Sec. 3.6) we only presented the singular (nonsingular) partonic thrust distribution. In the following sections we discuss how to achieve the hadron level predictions by convoluting the partonic contributions with a model function that is determining the nonperturbative effects of hadronization at low energies. We employ the gap formalism, as introduced in Sec. 3.4.1, which equips us with means to systematically remove the leading renormalon ambiguity in the soft function. This procedure is based on introducing a gap subtraction which is extracted order by order from the perturbative partonic soft function such that it captures the leading infrared-sensitivity. In the massless factorization theorem the gap subtraction is uniquely determined by the soft function with (n_l) massless active flavors. However, while constructing the VFNS for the secondary mass corrections, we encounter different kinematic scenarios where the heavy quark is treated as an active (passive) flavor in the soft function, i.e. scenario IV (scenario I, II, III, bHQET). Hence in the consequent gap subtraction one has to account for active and passive effects of massive secondary quarks in terms of different schemes and provide a smooth interpolation by accounting for matching relations [43]. Here we initiate the discussion on the gap formalism considering a setup where the heavy quark mass is above the soft scale and thus the soft function has (n_l) light quark active flavors. After that we discuss the mass correction due to additional secondary heavy quark effects in the soft function. Finally we summarize the implementation of the formalism for different scenarios. In Sec. 3.7.2 we present a convenient parametrization of the soft model function.

3.7.1 Gap Formalism

As already discussed in Sec. 3.4.1, a systematic approach to incorporate nonperturbative effects in the jet cross section is to factorize the generic soft function into a partonic part S_{part} and a model function S_{mod} where the complete soft function is given by $S = S_{\text{part}} \otimes S_{\text{mod}}$. This method provides a continuous description of nonperturbative effects along the jet cross section such that a simple power expansion in the tail region results in the OPE formulation for this regime, see Eq. (3.4.10). Based on the soft factorization theorem, the hadronic level thrust distribution can be obtained using a simple convolution of the partonic contributions with the soft model function

$$\frac{\mathrm{d}\sigma(\tau)}{\mathrm{d}\tau} = \int \mathrm{d}\ell\,\frac{\mathrm{d}\hat{\sigma}}{\mathrm{d}\tau}\Big(\tau - \frac{\ell}{Q}\Big)\,S_{\text{mod}}\big(\ell - 2\Delta\big)\,, \tag{3.7.1}$$

where the term Δ is the bare gap parameter as introduced in Sec 3.4.1. We remind the reader again that in our notation, the term σ refers to hadron level predictions and $\hat{\sigma}$ indicates the partonic cross sections. The gap parameter allows us to subtract the renormalon ambiguity of the partonic soft function to all orders in perturbation theory. This can be achieved by splitting the bare gap parameter into a renormalon free component $\Delta^{(n_l)}(R,\mu)$ and a gap subtraction $\delta^{(n_l)}(R,\mu)$, introduced in Eq. (3.4.13). Let us first consider setups with (n_l) massless active flavors in the partonic soft function. We stress that the bare gap parameter is absolutely scheme and RG invariant, while the terms $\Delta^{(n_l)}(R,\mu)$ and $\delta^{(n_l)}(R,\mu)$ are scheme and scale dependent As already noted, the gap subtraction can be properly extracted from the perturbative soft function such that it accounts for the $\mathcal{O}(\Lambda_{\rm QCD})$ renormalon ambiguities. A convenient definition of $\delta^{(n_l)}(R,\mu)$ is given in Ref. [232] in the R-scheme which reads

$$\delta^{(n_l)}(R,\mu) = \frac{R}{2} e^{\gamma_E} \frac{\mathrm{d}}{\mathrm{d}\ln(ix)} \ln S^{(n_l)}_{\rm part}(x,\mu)|_{x=(iRe^{\gamma_E})^{-1}}\,, \tag{3.7.2}$$

where $S^{(n_l)}_{\rm part}(x,\mu)$ is the partonic soft function in position space, $S^{(n_l)}_{\rm part}(x,\mu) = \int \mathrm{d}\ell S^{(n_l)}_{\rm part}(\ell,\mu)e^{-i\ell x}$. The parameter R has the dimension of a mass and play the role of an infrared cutoff scale which is typically $R \geq \Lambda_{\rm QCD}$. Now using the convolution properties, one can shift the subtraction term into the partonic part. Thus the factorization in Eq. (3.7.1) becomes

$$\frac{\mathrm{d}\sigma(\tau)}{\mathrm{d}\tau} = \int \mathrm{d}\ell\, \frac{\mathrm{d}\hat{\sigma}}{\mathrm{d}\tau}\Big(\tau - \frac{\ell}{Q} - \frac{2\delta^{(n_l)}(R,\mu)}{Q}\Big)\, S_{\rm mod}\big(\ell - 2\bar{\Delta}^{(n_l)}(R,\mu)\big)\,. \tag{3.7.3}$$

In order to obtain an exact cancellation of the $\mathcal{O}(\Lambda_{\rm QCD})$ renormalon in the partonic soft function one has to set the renormalization scale of the gap subtraction identical to the soft scale μ_S, and expand it together with $S_{\rm part}(k,\mu_S)$ order-by-order in $\alpha_s(\mu_S)$. The perturbative expansion series of gap subtraction in $\alpha_s(\mu_S)$ reads

$$\delta^{(n_l)}(R,\mu_S) = e^{\gamma_E} R \sum_{i=1}^{\infty} \alpha_s^i(\mu_S)\, \delta_i^{(n_l)}(R,\mu_S)\,, \tag{3.7.4}$$

where $\alpha_s(\mu_S) = \alpha_s^{(n_l)}(\mu_S)$ and the coefficients $\delta_i^{(n_l)}$ are known up to 3-loops [232],

$$\begin{aligned}
\delta_1^{(n_l)}(R,\mu_S) &= -8\, C_F L_R\,,\\
\delta_2^{(n_l)}(R,\mu_S) &= C_A\, C_F\Big[-\frac{808}{27} - \frac{22}{9}\pi^2 + 28\,\zeta_3 + \Big(\frac{8}{3}\pi^2 - \frac{536}{9}\Big)L_R - \frac{88}{3}L_R^2\Big]\\
&\quad + C_F\, T_F\, n_l\Big[\frac{224}{27} + \frac{8}{9}\pi^2 + \frac{160}{9}L_R + \frac{32}{3}L_R^2\Big]\,,\\
\delta_3^{(n_l)}(R,\mu_S) &= C_A^2\, C_F\Big[-\frac{278021}{729} - \frac{25172}{243}\pi^2 + \frac{44}{9}\pi^4 + \frac{18136}{27}\,\zeta_3 - \frac{88}{9}\pi^2\,\zeta_3 - 192\,\zeta_5\\
&\quad + \Big(352\zeta_3 - \frac{62012}{81} + \frac{104}{27}\pi^2 - \frac{88}{45}\pi^4\Big)L_R + \Big(\frac{176}{9}\pi^2 - \frac{14240}{27}\Big)L_R^2 - \frac{3872}{27}L_R^3\Big]\\
&\quad + C_A\, C_F\, T_F\, n_l\Big[\frac{80324}{729} + \frac{19408}{243}\pi^2 - \frac{64}{45}\pi^4 + \frac{6032}{27}\,\zeta_3 + \Big(\frac{32816}{81} + \frac{128}{9}\pi^2\Big)L_R\\
&\quad + \Big(\frac{9248}{27} - \frac{64}{9}\pi^2\Big)L_R^2 + \frac{2816}{27}L_R^3\Big]\\
&\quad + C_F^2\, T_F\, n_l\Big[\frac{3422}{27} + \frac{8}{3}\pi^2 - \frac{16}{45}\pi^4 - \frac{6032}{27}\,\zeta_3 + \Big(\frac{440}{3} - 128\,\zeta_3\Big)L_R + \frac{2816}{27}L_R^3\Big]\\
&\quad + C_F T_F^2\, n_l^2\Big[\frac{6400}{729} - \frac{128}{9}\pi^2 + \frac{128}{9}\zeta_3 - \Big(\frac{3200}{81} + \frac{128}{27}\pi^2\Big)L_R - \frac{1280}{27}L_R^2 - \frac{512}{27}L_R^3\Big]\,,
\end{aligned} \tag{3.7.5}$$

with $L_R = \ln(\mu_S/R)$. The R scale should be set such that it satisfies two criteria [155, 230], namely the power counting and large log criterion. The power counting criterion states that according to Eq. (3.7.2) it is natural to set $R \sim 1\,\text{GeV}$ such that power correction parameter scales like $\overline{\Omega}_1 \sim \Lambda_{\text{QCD}}$ in both R-gap and bare schemes and we remain in the perturbative regime with $\alpha_s(R)$. The large log criterion is related to the logarithms of L_R which could be large in the tail region where $\mu_S \sim Q(\tau - \tau_{\min}) \gg 1\,\text{GeV}$. Hence one has to set $R \sim \mu_S$ to avoid such enhancements. This is in conflict with the power counting criterion. To resolve this issue Ref. [231] introduced an RGE in the R variable, in analogy with the RGE for μ, to sum the large logarithms while keeping the $R \sim \mu$ along the thrust spectrum. The R-RGE and μ-RGE for the gap $\bar{\Delta}^{(n_l)}(R,\mu)$ obey the following relations

$$R\,\frac{\mathrm{d}}{\mathrm{d}R}\bar{\Delta}^{(n_l)}(R,R) = -R\frac{\mathrm{d}}{\mathrm{d}R}\delta^{(n_l)}(R,R) = -R\sum_{n=0}^{\infty}\gamma_n^R\left(\frac{\alpha_s^{(n_l)}(R)}{4\pi}\right)^{n+1}, \tag{3.7.6}$$

$$\mu\,\frac{\mathrm{d}}{\mathrm{d}\mu}\bar{\Delta}^{(n_l)}(R,\mu) = 2\,R\,e^{\gamma_E}\sum_{n=0}^{\infty}\Gamma_n^{\text{cusp}}\left(\frac{\alpha_s^{(n_l)}(\mu)}{4\pi}\right)^{n+1}. \tag{3.7.7}$$

Note that the first equation is obtained simply by taking the derivatives of Eq. (3.7.4) with respect to R, keeping in mind that the bare gap does not depend on the variable R. The anomalous dimension coefficients up to three loops read

$$\begin{aligned}
\gamma_0^R &= 0\,,\\
\gamma_1^R &= e^{\gamma_E}\bigg[C_A\,C_F\bigg(-\frac{808}{27}-\frac{22}{9}\pi^2+28\zeta_3\bigg)+C_F\,T_F\,n_l\bigg(\frac{224}{27}+\frac{8}{9}\pi^2\bigg)\bigg],\\
\gamma_2^R &= e^{\gamma_E}\bigg[C_A^2\,C_F\bigg(\frac{41947}{729}-\frac{16460}{243}\pi^2+\frac{44}{9}\pi^4+\frac{7048}{27}\zeta_3-\frac{88}{9}\pi^2\zeta_3-192\zeta_5\bigg)\\
&\quad+C_A\,C_F\,T_F\,n_l\bigg(\frac{124732}{729}+\frac{13072}{243}\pi^2-\frac{64}{45}\pi^4-\frac{2000}{27}\zeta_3\bigg)\\
&\quad+C_F^2\,T_F\,n_l\bigg(\frac{3422}{27}+\frac{8}{3}\pi^2-\frac{16}{45}\pi^4-\frac{608}{9}\zeta_3\bigg)+C_F\,T_F^2\,n_l^2\bigg(\frac{38656}{729}-\frac{256}{27}\pi^2+\frac{128}{9}\zeta_3\bigg)\bigg].
\end{aligned} \tag{3.7.8}$$

Furthermore in Eq. (3.4.15) we introduced a renormalon free scheme for the first moment, denoted with $\overline{\Omega}_1^{(n_l)}(R,\mu)$. One can use Eqs. (3.4.12) and (3.4.13) to write a relation between the gap and the first moment in the R-scheme,

$$2\bar{\Delta}^{(n_l)}(R,\mu)+\int\mathrm{d}k\,k\,S_{\text{mod}}(k) = 2\overline{\Omega}_1^{(n_l)}(R,\mu)\,. \tag{3.7.9}$$

To obtain the R-RGE and μ-RGE for $\overline{\Omega}_1^{(n_l)}(R,\mu)$ one can use the fact that the second term on the LHS of Eq. (3.7.9) is scale invariant, so that the RG equations for the first moment follows the exact relations given in Eq. (3.7.6) and Eq. (3.7.8).

Now let us consider the kinematic regime where the soft scale is above the mass scale with $m > \Lambda_{\text{QCD}}$, so that the heavy quark is an active flavor in the soft function and one has to take into account the real and virtual secondary mass effects in the soft interaction [43]. Note that in this regime the finite mass of the heavy quark acts in fact as an IR-cutoff of the virtuality of the corresponding soft gluon exchanges so that the factorial enhancement of the related perturative corrections are suppressed and it might be unnecessary to include the corresponding contributions in the gap subtractions. Nevertheless Ref. [43] introduces the appropriate gap scheme such that it incorporates the secondary massive quark effects to obtain a continuous description of the gap with variable number of flavor which simultaneously respects the asymptotic limits i.e. the decoupling and the massless limits. Starting with the splitting of the bare gap parameter into a renormalon free term $\bar{\Delta}^{(n_l+1)}(R,m,\mu)$ and the gap subtraction $\delta^{(n_l+1)}(R,m,\mu)$,

$$\Delta = \bar{\Delta}^{(n_l+1)}(R,m,\mu)+\delta^{(n_l+1)}(R,m,\mu)\,, \tag{3.7.10}$$

Eq. (3.7.1) becomes

$$\frac{\mathrm{d}\sigma(\tau)}{\mathrm{d}\tau} = \int \mathrm{d}\ell \, \frac{\mathrm{d}\hat{\sigma}}{\mathrm{d}\tau}\Big(\tau - \frac{\ell}{Q} - \frac{2\delta^{(n_l+1)}(R,m,\mu)}{Q}\Big)\, S_{\mathrm{mod}}\big(\ell - 2\bar{\Delta}^{(n_l+1)}(R,m,\mu)\big)\,. \tag{3.7.11}$$

Here the resulting gap subtraction $\delta^{(n_l+1)}(R,m,\mu)$ is mass dependent. The complete presentation of this scheme is performed in Ref. [43] and we briefly review it here. One can identify the massive correction to the gap subtraction by applying Eq. (3.7.2) for the massive contribution of the soft function which arises at $\mathcal{O}(\alpha_s^2 C_F T_F)$. The resulting gap subtraction with massive correction reads

$$\delta^{(n_l+1)}(R,m,\mu) = \delta^{(n_l+1)}(R,\mu) + \delta^{(n_l+1)}_{\Delta_m}(R,m,\mu)\,, \tag{3.7.12}$$

where the term $\delta^{(n_l+1)}(R,\mu)$ is obtained from the expression in Eq. (3.7.4) when we set the number of active flavors in α_s and the expansion coefficients δ to (n_l+1). The term $\delta^{(n_l+1)}_{\Delta_m}(R,m,\mu)$ denotes the quark mass corrections. The latter contribution contains numerical integrations. A suitable parametrization of this contributions using the variable $y = m/R$ is [43]

$$\delta^{(n_l+1)}_{\Delta_m}(R,R\,y,\mu)\bigg|_{\text{param.}} = C_F\,T_F\left(\frac{\alpha_s^{(n_l+1)}(\mu)}{4\pi}\right)^2 R\,e^{\gamma_E}\left\{\tilde{h}(y) - \frac{\tilde{h}(y)+ay}{1+by+cy^2}\,e^{-\alpha y^\beta}\right\}, \tag{3.7.13}$$

where

$$\tilde{h}(y) = -\frac{8}{3}\ln^2 y^2 - \frac{80}{9}\ln y^2 - \frac{448}{27} - \frac{8}{9}\pi^2\,, \tag{3.7.14}$$

and the parameters are

$$\alpha = 0.634\,, \qquad \beta = 1.035\,, \qquad a = 23.6\,, \qquad b = -0.481\,, \qquad c = 1.19\,. \tag{3.7.15}$$

The suggested parametrization approximates the exact numerical results with a relative deviation of less than 1%. Furthermore the expression in Eq. (3.7.13) exhibits the correct massless limit, i.e. $\lim_{y\to 0}\delta^{(n_l+1)}_{\Delta_m}(R,R\,y,\mu) \to 0$. The μ-RGE for $\bar{\Delta}^{(n_l+1)}(R,m,\mu)$ is mass independent and thus obeys the same relation in Eq. (3.7.6) with n_l+1 active flavors. The R-RGE can be derived from Eq. (3.7.7), resulting into a massive correction to the R-anomalous dimension

$$\gamma_R^{(n_l+1)}\Big(\frac{m}{R}\Big) = \gamma_R^{(n_l)} + \gamma_{R,\Delta_m}^{(n_l+1)}\Big(\frac{m}{R}\Big)\,, \tag{3.7.16}$$

where

$$\gamma_{R,\Delta_m}^{(n_l+1)}\Big(\frac{m}{R}\Big)\bigg|_{\text{parm.}} = \frac{\mathrm{d}}{\mathrm{d}R}\delta^{(n_l+1)}_{\Delta_m}(R,m,R)\bigg|_{\text{param.}}\,. \tag{3.7.17}$$

Again the parametrization provides a good approximation to the numerical result with better than a 2% relative deviation. It also exhibits the correct massless limit i.e. $\lim_{m\to 0}\gamma^{(n_l+1)}_{R,\Delta_m}(m/R) \to 0$. The matching condition for $\bar{\Delta}^{(n_l)}(R,\mu)$ and $\bar{\Delta}^{(n_l+1)}(R,m,\mu)$ is obtained using the fact that the bare gap parameter is scheme-independent. This yields

$$\Delta = \bar{\Delta}^{(n_l)}(R,\mu) + \delta^{(n_l)}(R,\mu) = \bar{\Delta}^{(n_l+1)}(R,m,\mu) + \delta^{(n_l+1)}(R,m,\mu)\,. \tag{3.7.18}$$

Given the perturbative expression up to $\mathcal{O}(\alpha_s^2)$ the matching relation becomes

$$\bar{\Delta}^{(n_l)}(R,\mu) = \bar{\Delta}^{(n_l+1)}(R,m,\mu) + \delta^{(n_l+1)}(R,m,\mu) - \delta^{(n_l+1)}_{2,T_F}(R,\mu) - \frac{\alpha_s^{(n_l+1)}T_F}{3\pi}\ln\Big(\frac{m^2}{\mu^2}\Big)\delta_1^{(n_l+1)}(R,\mu)\,, \tag{3.7.19}$$

where the term δ_{2,T_F} can be read in Eq. (3.7.5) i.e. the term for $\mathcal{O}(\alpha_s^2 C_F T_F)$

$$\delta_{2,T_F}^{(n_l+1)}(R,\mu) = C_F\,T_F\,\left(\frac{\alpha_s^{(n_l+1)}(\mu)}{4\pi}\right)^2 R\,e^{\gamma_E}\left[\frac{224}{27}+\frac{8}{9}\pi^2+\frac{160}{9}L_R+\frac{32}{3}L_R^2\right], \tag{3.7.20}$$

and the last term is due to the matching of the strong coupling constant with (n_l) and (n_l+1) schemes. In order to avoid the large logarithms one has to perform the gap matching in Eq. (3.7.19) at $R\sim\mu\sim\mu_m\sim m$.

To conclude this section let us summerize the prescription for using the (n_l) and (n_l+1) gap-schemes while employing the convolution of the partonic distributions with the model function:

$$\frac{\mathrm{d}\sigma(\tau)}{\mathrm{d}\tau} = \begin{cases} \int \mathrm{d}\ell\,\frac{\mathrm{d}\hat\sigma}{\mathrm{d}\tau}\Big(\tau-\frac{\ell}{Q}-\frac{2\delta^{(n_l)}(R,\mu)}{Q}\Big)\,S_{\mathrm{mod}}\big(\ell-2\bar\Delta^{(n_l)}(R,\mu)\big) & \mu_m>\mu_S \\ \int \mathrm{d}\ell\,\frac{\mathrm{d}\hat\sigma}{\mathrm{d}\tau}\Big(\tau-\frac{\ell}{Q}-\frac{2\delta^{(n_l+1)}(R,m,\mu)}{Q}\Big)\,S_{\mathrm{mod}}\big(\ell-2\bar\Delta^{(n_l+1)}(R,m,\mu)\big) & \mu_m<\mu_S \end{cases}. \tag{3.7.21}$$

The first condition $\mu_m>\mu_S$ corresponds to the kinematic scenarios I, II, III, bHQET and massless factorization. The second condition $\mu_m<\mu_S$ refers to scenario IV. We also use this prescription for folding the partonic nonsingular corrections with the model function. The numerical code automatically switches the gap scheme indicating the use of Eq. (3.7.21) while crossing the mass scale μ_m.

3.7.2 Nonperturbative Model Function

The soft nonperturbative model (shape) function parametrizes the hadronization effects and nonperturbative soft interactions in thrust. A systematic approach for constructing the shape function has been developed by Ref. [230]. Based on this method we make use of the linear combination of an infinite set of orthonormal basis functions to parametrize the soft model function which is normalized, positive definite with $S_{\mathrm{mod}}(0)=0$ and moreover its n-th moment scales as Λ^n_{QCD}. The resulting parametrization allows us to systematically estimate the uncertainties on the shape of the soft model function by determining the uncertainty of the coefficients of this expansion. The suggested model function reads

$$S_{\mathrm{mod}}(k,\lambda,\{c_i\}) = \frac{1}{\lambda}\left[\sum_{n=0}^{N} c_n\,f_n\Big(\frac{k}{\lambda}\Big)\right]^2, \tag{3.7.22}$$

where the orthonormal basis functions are defined as

$$\begin{aligned} f_n(z) &= 8\sqrt{\frac{2}{3}z^3(2n+1)}\,e^{-2z}P_n\big(g(z)\big)\,, \\ g(z) &= \frac{2}{3}(3-e^{-4z}(3+12z+24z^2+32z^3))-1\,. \end{aligned} \tag{3.7.23}$$

Here P_n are the Legendre polynomials. The normalization condition of the soft model function now reduces to a constraint that is $\sum_i c_i^2=1$. In this model function λ specifies the width of the soft function that is usually considered to be $\lambda\sim\Lambda_{\mathrm{QCD}}$.

In the numerical analysis in Sec. 3.11 we make use of the simplest model function, i.e. only $c_0=1$ and the rest of the coefficients are set to be zero. This model has been used in Ref. [155] for the extraction of the strong coupling constant from fits of massless thrust QCD predictions in the tail region of the distribution where the dominant nonperturbative effects are encoded by the first moment of the soft model $\overline{\Omega}_1$. In this case we obtain

$$\overline{\Omega}_1(R_0,\mu_0) = \bar\Delta(R_0,\mu_0)+\frac{\lambda}{2}\,, \tag{3.7.24}$$

where R_0 and μ_0 are the reference scales for which the initial value of the gap (and thus the moments) is assigned. The further running of the gap and the first moment between (R_0, μ_0) and (R, μ_S) is determined by the RGEs in Eqs. (3.7.6) and (3.7.7). In the simple model function with $c_0 = 1$ the higher moments $\overline{\Omega}_{2,3,\ldots}$ are functions of $\bar{\Delta}$ and $\overline{\Omega}_1$, e.g. the expression for the second moment reads

$$\overline{\Omega}_2 = \frac{1}{4}(\bar{\Delta}^2 - 2\,\bar{\Delta}\,\overline{\Omega}_1 + 5\,\overline{\Omega}_1^2)\,. \tag{3.7.25}$$

3.8 Unstable Quarks with Finite Width

An effective field theory approach to incorporate the decay of an unstable boosted heavy quark (e.g. top) close to its mass shell within jets is developed by Ref. [32] . Here based on the inclusive nature of thrust[20], we treat the quark and antiquark decays as an absolute inclusive process, so that we do not aim to determine all the detailed information on the momenta of the decay products. To describe the decay of collinear particles in SCET one can use the full electroweak Lagrangian as far as the mass of the W boson is smaller than the mass of the heavy quark. For instance the decay of the top quark is described by

$$\mathcal{L}_{\rm ew} = \frac{g_2}{\sqrt{2}}\,\bar{b}\,W_\mu^- \gamma^\mu\, P_L\, t + \frac{g_2}{\sqrt{2}}\,\bar{t}\,W_\mu^+ \gamma^\mu P_L\, b\,, \tag{3.8.1}$$

where $G_F = \sqrt{2}g_2^2/(8m_W^2)$ is the Fermi constant. Nevertheless, since the fluctuations of the jet invariant mass in SCET is $s_q \geq m^2$, the top decay effects can be neglected to the leading approximation.

In fact the finite width effects are mainly relevant in the bHQET scenario. Here an effective treatment can be employed [32] where the total decay width of the unstable massive quark enters the bHQET Lagrangian as an imaginary mass term which is deduced from the matching of the imaginary part of quark-antiquark self energy corrections from SCET onto bHQET. Thus including the leading finite width effects for unstable particles, the bHQET Lagrangian(s) reads

$$\mathcal{L}_\pm = \bar{h}_{v_\pm}\bigg(iv_\pm \cdot D_\pm - \delta m + \frac{i}{2}\Gamma\bigg) h_{v_\pm}\,. \tag{3.8.2}$$

Note that the term $(i\Gamma/2)\,\bar{h}_{v_\pm}\,h_{v_\pm}$ is the only allowed operator at leading order in the Γ/m expansion. Furthermore it is proportional to a conserved current, so it does not need to be renormalized. The term δm is the residual mass term that specifies the scheme of the quark mass. This term will be discussed in Sec. 3.9. Similar to previous sections, here, we consider the pole mass scheme where $\delta m = 0$.

From Eq. (3.8.2) we see that the decay width will only affect the ultracollinear sector i.e. the bHQET jet function. The definition of the stable quark jet function was given in Eq. (3.5.5) where the $B_\pm$ are obtained from taking the imaginary part of the vacuum matrix element of two collinear jet fields. According to the form of $\mathcal{L}_\pm$ it is straightforward to conclude that the jet function for the unstable quark can be simply obtained by shifting $\hat{s} \to \hat{s} + i\,\Gamma$ in the vacuum matrix element before taking the imaginary part.

It has been shown in Ref. [39] that one can write a dispersion relation to factorize the decay width effects in the cross section. Here we only note that the proof is based on the analyticity of the vacuum matrix element in the complex $\hat{s}$-plane before taking the imaginary part with a branch cut for intermediate states which have invariant masses larger than the top quark mass. Hence one can employ the residue theorem for a contour that envelopes the cut to deduce the dispersion relation. Finally using the shifted variable $\hat{s}_0 = \hat{s} + i\,\Gamma$ and taking the imaginary part we obtain the following factorization relation for accounting the leading finite width effects,

$$B_{n,\bar{n}}(\hat{s}, \Gamma, \mu) = \int_{-\infty}^{\hat{s}} \mathrm{d}\hat{s}'\, B_{n,\bar{n}}(\hat{s} - \hat{s}', \mu)\, \frac{\Gamma}{\pi(\hat{s}'^2 + \Gamma^2)}\,, \tag{3.8.3}$$

[20]Ref. [32] has in particular studied the hemisphere invariant mass distribution which can be simply related to thrust.

where the jet function for the unstable heavy quark $B_{n,\bar{n}}(\hat{s},\Gamma,\mu)$ is obtained by the convolution of the stable jet function $B_{n,\bar{n}}(\hat{s}-\hat{s}',\mu)$, given in Eq. (3.5.6), with a Breit-Wigner function of the width Γ. Note that the relation manifests identical RG evolutions (and renormalization factors) for the jet function of stable and unstable heavy quarks.

The factorization property of width effects in the jet function allows us to shift this smearing to the other elements of the factorization theorem such as the soft function

$$S(\ell,\mu)=\int_{-\infty}^{+\infty}\mathrm{d}\ell' S(\ell-\ell',\mu)\,\frac{\left(\frac{2\,m\,\Gamma}{Q}\right)}{\pi\Big(\ell'^2+\left(\frac{2\,m\,\Gamma}{Q}\right)^2\Big)}\,. \tag{3.8.4}$$

Here the width provides a cutoff for soft scales i.e. $(2\,m\,\Gamma/Q)$. Hence it is straightforward to conclude that for $\Gamma\gg Q\,\Lambda_{\rm QCD}/m$ the nonperturbative effects are suppressed and one can use the OPE even in the peak region of distributions. On the other hand when the $\Gamma\lesssim Q\,\Lambda_{\rm QCD}/m$ the complete soft model function has to be employed in the peak region where the higher moments $\{\overline{\Omega}_2,\overline{\Omega}_3,\cdots\}$ play more significant roles. This intuitive understanding of the physical situation is an important guideline in constructing and adjusting the default scale of the profile function in Sec. 3.10.

For the sake of numerical implementation of the additional smearing due to the finite width of the unstable heavy quarks we perform the convolution of the Breit-Wigner function with all singular partonic terms in the bHQET scenario,

$$\frac{\mathrm{d}\hat{\sigma}(\tau)}{\mathrm{d}\tau}\bigg|_{\text{sing./sub.sing.}}=\int_{-\infty}^{+\infty}\mathrm{d}\tau'\,\frac{\left(\frac{2\,m\,\Gamma}{Q^2}\right)}{\pi\Big(\tau'^2+\left(\frac{2\,m\,\Gamma}{Q^2}\right)^2\Big)}\,\frac{\mathrm{d}\hat{\sigma}}{\mathrm{d}\tau}(\tau-\tau')\bigg|_{\text{sing.dist.}}\,. \tag{3.8.5}$$

Here the abbreviation "sing.dist." refers to all types of singular distributions, i.e. the dominant singularities accounted by the factorization theorems and the subdominant singularities that exist in the nonsingular contribution (which can be absorbed into the factorization theorems as discussed in Sec. 3.6). For our numerical studies in Sec. 3.11 we have carried out the convolution in Eq. (3.8.5) analytically. The details of this computation are presented in Appendix E.

Although the treatment of the finite width via Eq. (3.8.5) is strictly correct only in the context of the bHQET Lagrangian (peak region), we employ the prescription of Eq. (3.8.5) universally for all kinematic regions. We extrapolate the factorization in Eq. (3.8.5) to the singular distribution in the SCET scenarios that match onto the bHQET distributions and we switch off the width effects later in a smooth manner in the tail region where the effects are in principle negligible since $\mu_S\gg(2\,m\,\Gamma/Q)$. This procedure provides a continuous and smooth transition from the correct description in the peak to the far tail region of thrust.

3.9 Short Distance Mass Schemes

In previous sections we explored various ingredients for a complete theoretical description of the thrust distribution for massive quark production. The resulting theoretical framework allows us to have a full control over the mass dependence of all different contributions (i.e. the factorization theorems, nonsingular contributions, the gap formalism and the finite width effects). For the sake of convenience, yet we have formulated the framework in the pole mass scheme. However as we already explained in Sec. 1.1 it is a well know fact that the pole mass scheme suffers from an $\mathcal{O}(\Lambda_{\rm QCD})$-renormalon ambiguity [61]. This infrared sensitivity leads to spurious large perturbative corrections which can affect the stability of predictions for the mass dependent observables. Using the pole scheme to determine the quark mass has an intrinsic uncertainty which does not allow precise measurements with accuracies better than $\mathcal{O}(\Lambda_{\rm QCD})$.

Quark mass schemes that do not have such a problem are called short distance schemes. Short distance mass schemes are defined in perturbation theory by accounting for a finite residual term in the difference to the pole mass[21],

$$m_{\rm pole} = m_Y^{(n_f)}(\mu) + \delta m_Y^{(n_f)}(\mu)\,, \tag{3.9.1}$$

where (n_f) indicates the number of active flavors. The term $\delta m_Y(\mu)$ is the residual perturbative correction starting at order $\mathcal{O}(\alpha_s)$. The subscript Y refers to the renormalization scheme used for the mass on the RHS of Eq. (3.9.1). Note that the pole mass is renormalization scale invariant whereas short distance masses are in general scale and scheme dependent. The term μ in Eq. (3.9.1) refers to any generic scale that is induced by the definition of the short-distance mass scheme. Furthermore, we stress that one can define short distance mass schemes which depend on more scales, e.g. see the jet mass scheme in Sec. G .

There are two equivalent approaches to implement a short distance mass scheme: i) in the first approach we consider the observables in the short distance mass schemes from the beginning and add the mass counterterm in the Lagrangian with $\delta m \neq 0$ and thus include the corresponding vertex in the Feynman diagrams, ii) in the second approach we use the pole mass scheme (where $\delta m = 0$) initially for the formulation of the theory and later switch to the short distance scheme by using Eq. (3.9.1) and strictly expanding the perturbative corrections in powers of α_s . In this section we follow the second approach which is more convenient and the implementation is more straightforward. Nevertheless we use the first approach to address conceptual issues and discuss the characteristics of appropriate short distance mass schemes for our theoretical framework.

To initiate the discussion we start with the conceptual remark that the proper short distance mass scheme should be defined such that the residual mass term δm respects the power counting of the governing EFT, otherwise the theoretical prediction for the mass dependent observable exhibits instabilities. Note that in this work we make use of two different EFTs, SCET and bHQET. Hence let us have a closer look at the corresponding Lagrangians separately and see how the residual mass term enters.

The mass term in the SCET Lagrangian only affects the collinear sector [234] which reads from Eq. (3.3.12) as

$$\mathcal{L}_n = \bar{\xi}_n \Big[in\cdot\partial + gn\cdot A_n + (i\not{D}_c^{\perp} - m - \delta m) W_n \frac{1}{\overline{\mathcal{P}}} W_n^{\dagger} (i\not{D}_c^{\perp} + m + \delta m) \Big] \frac{\bar{\not{n}}}{2} \xi_n\,. \tag{3.9.2}$$

This is the leading SCET Lagrangian in the power counting parameter $\lambda_{\rm SCET} \sim s^{1/2}/Q$. In order to produce primary heavy quarks the jet invariant mass should be larger than the quark mass, i.e. $\hat{s}_q \gtrsim m$, where $\hat{s}_q = (s_q - m^2)/m$ was defined in Eq. (3.5.1). Hence the perpendicular components of the collinear quark momenta should at least scale as $\not{D}_c^{\perp} \sim Q\lambda_{\rm SCET} \sim m$. Based on this relation one can easily conclude that the suitable short distance mass scheme should have a residual correction which is consistent with the SCET power counting i.e.

$$\delta m \sim Q\lambda_{\rm SCET}\,\alpha_s \sim m\,\alpha_s\,, \tag{3.9.3}$$

where the term α_s indicates that this correction is arising at NLO. Thus in SCET, where the fluctuations of the order of mass scale are still accessible to the heavy quark, one can employ the $\overline{\rm MS}$ mass scheme. The perturbative relation between the pole and the $\overline{\rm MS}$ schemes reads

$$m_{\rm pole} = \overline{m}^{(n_f)}(\mu) + \delta\overline{m}^{(n_f)}(\mu)\,, \tag{3.9.4}$$

where the term n_f indicates the number of active flavors. Here, for convenience, we use the conventional notation for the $\overline{\rm MS}$ mass scheme i.e. $\overline{m}(\mu) \equiv m_{\rm MSB}(\mu)$. We briefly review the $\overline{\rm MS}$ scheme in Sec. 3.9.2 to fix the necessary notation for further discussions.

[21] In previous sections we used "m" for the pole mass, but in this section the term "$m_{\rm pole}$" indicates the pole mass and we employ the "m" for a generic mass scheme. We remark that the difference of short distance schemes to the pole mass scheme is only due to the finite contributions which are absorbed in the mass definition. The UV divergences absorbed into the mass definition are equivalent for all schemes.

In the peak region of the thrust distribution, however, we encounter the bHQET kinematic regime where fluctuations with virtualities of the other of mass are integrated out. As a result the remaining ultracollinear fluctuations have smaller momentum scales, $p_{uc}^2 \sim \hat{s}_q^2$. Therefore it is necessary to switch from the $\overline{\text{MS}}$ scheme to a more convenient mass scheme that preserves the power counting of bHQET. From the bHQET Lagrangian given in Eq. (3.8.2),

$$\mathcal{L}_\pm = \bar{h}_{\nu_\pm}\Big(i\nu_\pm \cdot D_\pm - \delta m + \frac{i}{2}\Gamma\Big)h_{\nu_\pm}\,, \tag{3.9.5}$$

it is easy to conclude that since $\nu_\pm \cdot D_\pm \sim \hat{s}_q$, the appropriate mass scheme should have a residual correction which scales as

$$\delta m \sim \alpha_s\,\hat{s}_q \ll m\,, \tag{3.9.6}$$

where again the term α_s indicates the residual term is arising at NLO. For an unstable massive quark the finite width serves as an additional infrared cutoff such that $\hat{s}_q \simeq \Gamma$. Thus in the bHQET region, one can use the jet [178] and the MSR mass [245] schemes when their infrared cutoff scale is set to $R \sim \hat{s}_q \sim \Gamma$ so that they respect the power counting in Eq. (3.9.6). The MSR and jet mass schemes are discussed further in Sec. 3.9.2 and App. G , respectively. For the rest of this discussion and numerical results given in Sec. 3.11 , we will take the MSR mass scheme for convenience. The implication of the jet mass scheme is in analogous. The relation between the MSR and the pole masses reads

$$m_{\text{pole}} = m_{\text{MSR}}^{(n_l)}(R_m) + \delta m_{\text{MSR}}^{(n_l)}(R_m)\,, \tag{3.9.7}$$

where the term (n_l) indicates the number of massless active flavors. We recall that in the bHQET scenario all the massive loop corrections are integrated out, so that the bHQET theory only contains (n_l) massless active flavors. Note that the MSR mass scheme only depends on a single IR-cutoff scale indicated with R_m.[22]

Following the above discussion one has to use different types of short distance mass schemes for SCET and bHQET scenarios. On the other hand, it is clear from Eqs. (3.9.2 , 3.9.5) that the residual mass term only enters the collinear (ultracollinear) Lagrangian which is decoupled from the hard and soft sector at the level of the Lagrangian. Thus while switching the theoretical description from SCET to bHQET, we still have the freedom to treat the mass scheme differently in the various sectors of the factorization theorem such that they do not violate the typical scaling of their characteristic scales. For instance, here it is crucial to use the MSR (jet) mass scheme (with $R_m \sim \hat{s}_q \sim \Gamma_t$) in the bHQET jet function where $\mu_b < m$ and the mass has a kinematic effect, whereas in the bHQET hard matching coefficient H_m one can take the $\overline{\text{MS}}$ as it is employed in the SCET scenarios since the scale of H_m is similar to m .

In general the following prescription can be adopted consistently to reconcile the presented theoretical framework with short distance mass schemes

$$m_{\text{pole}} = \begin{cases} \overline{m}^{(n_f)}(\mu) + \delta\overline{m}^{(n_f)}(\mu) & \mu \geq \mu_m \quad \text{with} \quad n_f = n_l + 1 \\[2ex] m_{\text{MSR}}^{(n_f)}(\mu) + \delta m_{\text{MSR}}^{(n_f)}(\mu) & \mu < \mu_m \quad \text{with} \quad n_f = n_l \end{cases}\,, \tag{3.9.8}$$

where in the second line the scale μ plays the role of the cutoff scale R_m in Eq. (3.9.7). In the region $\mu < \mu_m$ one can also use the jet mass scheme instead of the MSR mass scheme, see Sec. G . According to this prescription, when the mass renormalization scale μ is above the mass matching scale μ_m we use the $\overline{\text{MS}}$ scheme which provides the proper description with $(n_l + 1)$ active flavors . At the scale μ_m we integrate out the heavy quark effects and switch to the MSR mass scheme with (n_l) massless active flavors. To obtain the correct perturbative result, after plugging in the above mass schemes into mass dependent functions, we strictly expand the expressions in $\delta m \sim \mathcal{O}(\alpha_s)$.

[22] Here, we use R_m to denote the IR-cutoff scale in the jet and MSR mass schemes in order to discriminate them from the cutoff scale R which is used in the R-gap scheme for soft function.

Based on this prescription we employ the $\overline{\rm MS}$ scheme for the singular and nonsingular contributions in scenarios III and IV. This implies the $\overline{\rm MS}$ scheme in the massive corrections to the gap formalism in scenario IV too.

In the bHQET scenario given in Eq. (3.5.9), we make use of different mass schemes for various sectors of the factorization theorem according to their characteristic scales. We employ the MSR mass scheme for the mass terms involving kinematic threshold information, namely $B^{(n_l)}(\hat{s},\mu_b,m)$, $\tau_{\rm min}$ and $m\hat{s}/Q$. The replacement rule for these terms reads $m_{\rm pole}\to m_{\rm MSR}^{(n_l)}(\mu_b)+\delta m_{\rm MSR}^{(n_l)}(\mu_b)$. Afterwards we expand the result in powers of $\alpha_s^{(n_l)}(\mu_b)$. For the terms $H_m(m,\mu_m)$ and $U_{H_m}(Q/m,\mu_m,\mu_b)$ where the characteristic scale is $\sim m$, we exploit the $\overline{\rm MS}$ mass scheme and substitute the pole mass with $m_{\rm pole}\to\overline{m}^{(n_f)}(\mu_m)+\delta\overline{m}^{(n_f)}(\mu_m)$, however, here for convenience we do not expand the residual term in powers of α_s .[23] Indeed, it has been shown in Ref. [181] that the numerical difference between using the pole mass and $\overline{\rm MS}$ mass scheme for the bHQET hard matching coefficient is small. Therefore, we conclude that by expanding the results after replacing the pole mass with $\overline{\rm MS}$ mass in the bHQET hard matching coefficient and its evolution factor, no large cancellation in the perturbative coefficients takes place. Thus, the choice of expansion for these high scale quantities does not have a significant impact on the perturbative results. For the first and the second type of nonsingular contributions in the bHQET scenario we follow the prescription for the corresponding singular contributions and employ the MSR mass scheme.

Furthermore for the cross section of the unstable quark production we have included an additional smearing due to the width effects, given in Eq. (3.8.5). Since the corresponding effects are accounted for by the collinear Lagrangian, the scheme of the mass parameter in the Breit-Wigner function should match the mass scheme in the jet function. Therefore for the Breit-Wigner function we use the $\overline{\rm MS}$ scheme in scenarios III and IV, and MSR (jet) scheme in the bHQET scenario.

3.9.1 $\overline{\rm MS}$ Mass Scheme

In this short section we briefly review the basic ingredients of the $\overline{\rm MS}$ mass scheme to introduce the notation. We consider a setup where we have (n_l) massless flavors and (n_h) massive quark. The $\overline{\rm MS}$ mass scheme is defined in the $n_f=n_h+n_l$ flavor scheme in Eq. (3.9.4). The perturbative series expansion of the residual mass term reads

$$\delta\overline{m}^{(n_l+1)}(\mu)=\overline{m}^{(n_l+1)}(\mu)\sum_{n=1}^{\infty}\sum_{k=0}^{n}a_{nk}(n_h,n_l)\left(\frac{\alpha_s^{(n_l+1)}(\mu)}{4\pi}\right)^n\ln^k\left(\frac{\mu}{\overline{m}^{(n_l+1)}(\mu)}\right),\tag{3.9.9}$$

where the perturbative coefficients $a_{nk}(n_h,n_l)$ are given up to 4-loops in Eq. (F.1). Note that here the flag (n_h) controls the massive quark corrections which are due to the virtual effects in the self energy diagrams at two loops or higher orders. Hence by taking $n_h=1(0)$ we can switch on (off) the virtual heavy quark effects. The RGE for $\overline{m}(\mu)$ reads,

$$\frac{d}{d\ln\mu^2}\overline{m}^{(n_f)}(\mu)=-\overline{m}^{(n_f)}(\mu)\sum_{i=0}^{\infty}\gamma_{m,i}^{(n_f)}\left(\frac{\alpha_s^{(n_f)}(\mu)}{4\pi}\right)^{i+1}.\tag{3.9.10}$$

where $\gamma_{m,i}^{(n_f)}$ are the mass anomalous dimension coefficients that are known up to 4-loops [62,63],

$$\begin{aligned}
&\gamma_{m,0}^{n_f}=4\,,\qquad \gamma_{m,1}^{n_f}=\frac{202}{3}-\frac{20}{9}n_f\,,\qquad \gamma_{m,2}^{n_f}=1249+\left(-\frac{2216}{27}-\frac{160}{3}\zeta_3\right)n_f^2-\frac{140}{81}n_f^2\,,\\
&\gamma_{m,3}^{n_f}=\frac{4603055}{162}+\frac{135680}{27}\zeta_3-8800\zeta_5+\left(-\frac{91723}{27}-\frac{34192}{9}\zeta_3+880\zeta_4+\frac{18400}{9}\zeta_5\right)n_f\\
&\qquad+\left(-\frac{5242}{243}+\frac{800}{9}\zeta_3-\frac{160}{3}\zeta_4\right)n_f^2+\left(-\frac{332}{243}+\frac{64}{27}\zeta_3\right)n_f^3\,.
\end{aligned}\tag{3.9.11}$$

[23] Note that the bHQET current anomalous dimension given in Eq. (C.10) contains mass dependent logarithms $\ln Q^2/m^2$. Hence after substituting the pole mass with the $\overline{\rm MS}$ scheme and expanding the result one obtains an additional term in the anomalous dimensions of H_m .

It is easy to see from Eq. (3.9.9) that in the $\overline{\text{MS}}$ scheme the residual mass term scales as $\delta m \sim \alpha_s m$. Thus one can make use of this renormalon free scheme for the theoretical descriptions where the typical fluctuation are of the order of the mass scale or higher. This leads to the conclusion that the lowest meaningful scale for the mass renormalization scale is of the order of the mass itself i.e. $\overline{m}(\overline{m})$. Below this scale one has to adopt a different prescription such that it is compatible with the scale of dynamical fluctuations and also does not suffer from IR sensitivities. To this end we use the MSR mass scheme that will be discussed in the next section.

3.9.2 MSR Mass Scheme

The MSR mass scheme is a short-distance mass scheme which depends on a dynamical IR-cutoff scale R_m so that it can be used for a wide range of phenomenological applications. The relation between the MSR and pole masses is given by Eq. (3.9.7), where we use the superscript MSR to denote the MSR mass scheme. The residual mass term in the MSR mass scheme is obtained from the matching to the $\overline{\text{MS}}$ mass scheme at $R_m = \overline{m}(\overline{m})$ [245],

$$\delta_{m^{\text{MSR}}}\big(R_m = \overline{m}(\overline{m})\big) = \delta_{\overline{m}}(\mu = \overline{m}) \,, \tag{3.9.12}$$

with $\overline{m}(\overline{m}) = \overline{m}^{(n_l+1)}(\overline{m}^{(n_l+1)})$. In other words, we obtain the residual mass term in the MSR scheme $\delta m^{\text{MSR}}(R_m)$ by taking the residual mass term of the $\overline{\text{MS}}$ mass scheme at $\overline{m}(\overline{m})$, i.e. the expansion series of $\delta\overline{m}(\overline{m})$ in powers of $\alpha_s(\overline{m}(\overline{m}))$, and setting $\overline{m}(\overline{m}) \to R_m$ everywhere. Thus the MSR mass scheme provides a continuous and smooth extension of the $\overline{\text{MS}}$ mass to the lower scales where $R_m < \overline{m}(\overline{m})$.

However this naive definition has an ambiguity concerning the treatment of virtual secondary loops which was not been discussed in [245]. Obviously the IR renormalon problem in the pole mass is related to the (n_l) massless flavors. The massive quark loops do not lead to $\mathcal{O}(\Lambda_{\text{QCD}})$ renormalon ambiguity since the mass provides a cutoff scale. In this sense one has a freedom how to define the MSR mass scheme. In the first approach which we refer as the "natural prescription", we defined the residual mass term in the MSR scheme as

$$\delta m^{\text{MSR}}(R_m) = R_m \sum_{n=1}^{\infty} a_{n0}(n_h = 0, n_l) \left(\frac{\alpha_s^{(n_l)}(R_m)}{4\pi}\right)^n , \tag{3.9.13}$$

where we have dropped all the secondary massive quark corrections to all orders in perturbation theory (by setting $n_h = 0$). Note that in this prescription Eq. (3.9.12) plays the role of a matching condition to $\overline{\text{MS}}$ mass scheme. In the second approach, which we name "practical prescription", we define the residual term to exactly match the residual term in the $\overline{\text{MS}}$ scheme with $n_l + 1$ active flavor, i.e.

$$\delta m^{\text{MSR}}(R_m) = R_m \sum_{n=1}^{\infty} a_{n0}(n_h = 1, n_l) \left(\frac{\alpha_s^{(n_l+1)}(R_m)}{4\pi}\right)^n . \tag{3.9.14}$$

To reconcile this description with (n_l) active flavor, we reexpand the perturbative series in Eq. (3.9.14) in terms of $\alpha_s^{(n_l)}(R_m)$ using the perturbative relation between $\alpha_s^{(n_l)}(R_m)$ and $\alpha_s^{(n_l+1)}(R_m)$. We obtain

$$\delta m^{\text{MSR}}(R_m) = R_m \sum_{n=1}^{\infty} b_n \left(\frac{\alpha_s^{(n_l)}(R_m)}{4\pi}\right)^n . \tag{3.9.15}$$

where the b_n coefficients are determined from the β-function and $a_{n0}(n_h = 1, n_l)$ coefficients,

$$\begin{aligned}
b_1 &= \frac{16}{3}\,, \qquad b_2 = \frac{307}{2} + \frac{16}{3}\pi^2 + \frac{16}{9}\pi^2\ln 2 - \frac{8}{3}\zeta_3 + n_l\Big(-\frac{71}{9} - \frac{8}{9}\pi^2\Big)\,,\\
b_3 &= \frac{8462917}{1458} + \frac{1305682}{1215}\pi^2 - \frac{1390}{243}\pi^4 - \frac{18400}{81}\pi^2\ln 2 - \frac{1408}{81}\pi^2\ln^2 2 - \frac{1760}{81}\ln^4 2 - \frac{14080}{27}\text{Li}_4\Big(\frac{1}{2}\Big)\\
&\quad + \frac{3712}{27}\zeta_3 - \frac{5756}{27}\pi^2\zeta_3 + \frac{15800}{27}\zeta_5 + n_l\Big(-\frac{463694}{729} - \frac{7928}{81}\pi^2 + \frac{488}{243}\pi^4 - \frac{704}{81}\pi^2\ln 2 + \frac{128}{81}\pi^2\ln^2 2\\
&\quad + \frac{64}{81}\ln^4 2 + \frac{512}{27}\text{Li}_4\Big(\frac{1}{2}\Big) - \frac{1928}{9}\zeta_3\Big) + n_l^2\Big(\frac{4706}{729} + \frac{208}{81}\pi^2 + \frac{224}{27}\zeta_3\Big)\,.
\end{aligned} \tag{3.9.16}$$

The R_m RG equation for the MSR mass reads

$$R_m \frac{\mathrm{d}}{\mathrm{d}R_m} m^{\mathrm{MSR}}(R_m) = -R_m \frac{\mathrm{d}}{\mathrm{d}R_m} \delta m^{\mathrm{MSR}}(R_m) = -R_m \sum_{n=0}^{\infty} \gamma_n^{R_m} \left(\frac{\alpha_s(R_m)}{4\pi}\right)^{n+1}, \tag{3.9.17}$$

and the R_m-anomalous dimension up to N^{2}LO can be computed from the following relations

$$\gamma_0^{R_m} = b_1\,, \qquad \gamma_1^{R_m} = b_2 - 2\,\beta_0\, b_1\,, \qquad \gamma_2^{R_m} = b_3 - 4\,\beta_0\, b_2 - 2\,\beta_1\, b_1\,. \tag{3.9.18}$$

where the β_i are series expansion coefficients of the QCD β-function given in Eq. (C.15). The coefficients of the anomalous dimensions are all positive, so that $m^{\mathrm{MSR}}(R_m)$ decreases with R_m. The general solution of the R_m-RGE equation is shown in Ref. [245]. In the following analyses we will employ the practical prescription for the MSR mass scheme.

3.10 Profile Functions

So far we have presented a complete and continuous description of the entire massive thrust distribution in terms of various factorization theorems in the dijet limit. These factorization theorems are given within the SCET and bHQET frameworks to sum up all the large logarithms of the leading partonic singular contributions. The resummation is manifest by different renormalization scales in the hard, jet and soft functions, threshold corrections and corresponding evolution factors. In order to sum up these large logarithms, the renormalization scale of each sector must be set to the characteristic scale of the respective fluctuation. These characteristic scales are determined by the kinematics and the dynamics of different sectors at different regions of thrust distribution (which are related to the dijet (peak), three jet (tail) or multijet (far tail) event configurations). Hence, one has to make a careful study of the relevant scales in each region of the distribution to assign proper values to the renormalization scales. Moreover, the short distance R-scheme which are used for the mass and soft renormalon subtractions induce extra scales which control the IR subtractions and have to be respectively set to the order of the soft and mass scales to avoid large logarithms.

The common approach to obtain a continuous and smooth transition between various regions of distributions is to construct τ dependent renormalization scales, called profile functions. Here, we parametrize the profile functions of the renormalization scales such that, depending on the thrust value, they satisfy the following constraints[24],

1. **Nonperturbative:** the region where the nonperturbative effects are dominant. This region extends from the threshold up to a trust value close to the maximum of the peak:

$$\tau \le \tau_{\min}(\hat{m}) + 2\,\frac{\Lambda_{\mathrm{QCD}}}{Q}\,,$$

where

$$\tau_{\min}(\hat{m}) = 1 - \sqrt{1-4\hat{m}^2}\,, \quad \hat{m} = m/Q\,. \tag{3.10.1}$$

The appropriate scenario to describe this regime is bHQET or scenario III, depending whether the quark fluctuation in the peak region is close to the mass shell or not. We always have to sum the large logarithms in the partonic contribution, whether nonperturbative effects are significant or not. Here the renormalization scales exhibit large hierarchies $\mu_H \gg \mu_J \gg \mu_S \sim \Lambda_{\mathrm{QCD}}$ that are related to the kinematic scales as following:

$$\mu_H \sim Q\,, \quad \mu_J \sim \sqrt{\Lambda_{\mathrm{QCD}} Q}\,, \quad \mu_b \sim \frac{\Lambda_{\mathrm{QCD}} Q}{m}\,, \quad \mu_m \sim R_m \sim m\,, \quad \mu_S \sim R_s \sim \Lambda_{\mathrm{QCD}}\,. \tag{3.10.2}$$

[24] Different regions are named after the dominant theory

2. **Resummation:** the perturbative regime where singular pieces are dominant and large logarithms have to be summed up in various scenarios. In this region nonperturbative corrections are power suppressed and the OPE is a good approximation to describe the leading hadronization effects. This regime covers the tail (and partially the peak and far tail) of the thrust distribution:

$$\tau_{\rm min}(\hat{m}) + 2\,\frac{\Lambda_{\rm QCD}}{Q} \leq \tau < \tau_{\rm max}^{\rm 3-jet}(\hat{m})\,,$$

where $\tau_{\rm max}^{\rm 3-jet}(\hat{m}) = (5-4\sqrt{1-3\hat{m}^2})/3$ is the maximum value of thrust for 3-jet events (quark-antiquark production associated with real radiation of a gluon). Here, either of the factorization scenarios might be relevant to describe the cross section. There is still a large hierarchy between the hard, jet and soft scales however the soft scale is now a perturbative scale, $\mu_S \gg \Lambda_{\rm QCD}$. The renormalization scales are approximately determined by:

$$\begin{aligned}
&\mu_H \sim Q\,, \quad \mu_J \sim \sqrt{Q^2(\tau-\tau_{\rm min}(\hat{m}))}\,, \quad \mu_b \sim \frac{Q^2(\tau-\tau_{\rm min}(\hat{m}))}{m}\,,\\
&\mu_m \sim R_m \sim m\,, \quad \mu_S \sim R_s \sim Q(\tau-\tau_{\rm min}(\hat{m})) \gg \Lambda_{\rm QCD}\,.
\end{aligned} \tag{3.10.3}$$

3. **Fixed order:** the multi-jet region at far tail

$$\tau_{\rm max}^{\rm 3-jet}(\hat{m}) < \tau < \tau_{\rm max}(\hat{m})\,,$$

where $\tau_{\rm max}(\hat{m}) = \frac{1}{2} + \hat{m}$. This regime is described by scenario IV while smoothly merging to fixed order perturbation theory. In this region the nonsingular pieces are as important as singular terms. Thus, the resummation of large logarithms in the factorization theorem should be turned off to provide a proper cancellation of singular and nonsingular contributions as it happens in the fixed order determinations for the cross section. This can be achieved in scenario IV by setting all the scales equal and approximately of the order of the hard scale:

$$\mu_H = \mu_J = \mu_S = R_S \sim Q \gg \Lambda_{\rm QCD}\,, \tag{3.10.4}$$

In addition we consider the nonsingular scale to be of the order of the hard scale $\mu_{\rm ns} \sim \mu_H$, and in particular $\mu_{\rm ns} = \mu_H$ in the far tail region to ensure the previously mentioned cancellations. Note that in the nonperturbative and resummation regions we use the canonical relations between soft, hard and mass scales,

$$\mu_J = \sqrt{\mu_H\,\mu_S}\,, \quad \mu_b = \frac{\mu_H\,\mu_S}{\mu_m}\,, \tag{3.10.5}$$

to construct the jet and bHQET scales, so that all the large logarithms between these scales are summed.

It is convenient to construct the profile functions using piecewise functions [155] which are designed to satisfy the above constraints and are smoothly connected. Then we adopt various tuning parameters to provide sufficient variation for the renormalization scales. Note that the factorization theorems in the various scenarios are unchanged with respect to variations of the renormalization scales of $\mathcal{O}(1)$ which does not modify the hierarchy of scales. This residual dependence of the resummed perturbative cross section on the variation of the profile functions provides a conventional method to assign a perturbative uncertainty to the cross section prediction. We note that the available profile functions in the literature have been designed and tested for massless event shape distributions [155, 156, 158] at intermediate energies $35\,{\rm GeV} < Q < 250\,{\rm GeV}$. Here we aim to construct a rather more systematic approach in devising a profile function for event shapes with massive quarks, named massive profile functions.

The crucial consideration in constructing the massive profile functions is to obtain an efficient parameterization such that it properly manifests the quark mass and center of mass energy dependence.

The resulting massive profile functions have to exhibit consistent features in the small mass limit in order to merge into the well-studied massless profile functions. Here we use the generic idea for the massless profile functions, given in Ref. [158] as guidelines to construct the massive profile functions. In addition we implement a number of important modifications that account for mass effects and are inspired by a concrete and systematic analysis of the thrust distribution for the massive (massless) quark production at different c.m. energies.

The general strategy to construct the profile functions [158] is to first assign flat scales for hard and mass matching scales. Then we design a continuous and smooth piecewise function for the soft scale according to the constraints given in Eqs. (3.10.2), (3.10.3), (3.10.4). In the next step we make use of the canonical relations between soft, hard and mass scales, given in Eq. (3.10.5), to construct the jet and bHQET scales. In this way it is ensured that the jet, bHQET, soft and hard scales satisfy the corresponding constraints in the various regions. Finally the variation of the profile functions is implemented by an adequate number of additional auxiliary parameters which keep the canonical relationships intact.

For the renormalization scales in the hard function and mass matching scale, we use respectively

$$\mu_H(\tau) = e_H Q\,, \quad \mu_m(\tau) = e_m m\,, \tag{3.10.6}$$

where e_H and e_m are rescaling parameters. We vary e_H between 0.5 and 2, whereas e_m is varied in a correlated way, $e_m = \sqrt{e_H}$, such that the hierarchies of the mass matching scale with respect to the soft and hard scales are clearly retained.

The soft scale profile function is more complicated. We use the following piecewise function:

$$\mu_S(\tau) = \begin{cases} \mu_0 & \tau_{\min} \le \tau < t_0 \\ \zeta(\mu_0,\, \mu_H\,(\tau - \tau_{\min}(\hat{m})),\, t_0,\, t_{01},\, t_1,\, \tau) & t_0 \le \tau < t_1 \\ r_s\,\mu_H\,(\tau - \tau_{\min}(\hat{m})) & t_1 \le \tau < t_2 \\ \zeta(\mu_H\,(\tau - \tau_{\min}(\hat{m})),\, \mu_H,\, t_2,\, t_{2s},\, t_s,\, \tau) & t_2 \le \tau < t_s \\ \mu_H & t_s \le \tau < \tau_{\max} \end{cases}\,, \tag{3.10.7}$$

where the first, third and fifth lines in Eq. (3.10.7) satisfy the constraint in the various regimes independently. These regions are then smoothly connected in a small transition region with double quadratic function, ζ, that will be explained later.

The soft scale in the nonperturbative regime is controlled by μ_0 which is extended from 0 to t_0. The term t_0 represents the ending point of the nonperturbative region and the beginning of the transition to the OPE region and t_1 controls the end of this transition region. The canonical relation in the region t_1 to t_2 is obtained by demanding the resummation of large logarithms in the soft function, i.e. $\ln\left[(\mu_H(\tau-\tau_{\min})+2\Lambda_{\rm QCD})/\mu_S\right]$. The term t_2 sets the border of the resummation region and starts of transition to the fixed order region. The parameter t_s specifies the value of thrust where the second transition ends and all the scales are set equal to μ_H so that we recover the fixed order result valid for the multijet region.

The subtle point is to adopt a coherent parametrization of the boundaries of the piecewise function, the t_i's, such that the mass and energy scale dependence is explicit, i.e. finding a function $t_n(m, Q)$ with $n = \{0, 1, 2, s\}$. Here we suggest a method to specify the $t_n(m, Q)$ and assign proper variation for the parameters. To introduce the procedure let us start with the massless limit where the following relations are adopted in Ref. [158] for the transition points,

$$\begin{aligned} t_0(0,Q) &= \frac{n_0}{(Q/1\,\text{GeV})}\,, \qquad n_0 \in [1.5, 2.5] \\ t_1(0,Q) &= \frac{n_1}{(Q/1\,\text{GeV})}\,, \qquad n_1 \in [8.5, 11.5] \\ t_2(0,Q) &\in [0.225, 0.275]\,, \qquad t_s(0,Q) \in [0.375, 0.425]\,, \end{aligned} \tag{3.10.8}$$

where the notation $[x_1, x_2]$ stands for variation between x_1 and x_2. Note that only the transition borders from the nonperturbative to the perturbative region are energy dependent. We also assume that

$t_2(0,Q)$ and $t_s(0,Q)$ are energy independent. We aim to verify whether the suggested parametrization for $t_0(0,Q)$ and $t_1(0,Q)$ with the given range of variations in Eq. (3.10.8) are appropriate choices.

Let us start with the term $t_0(0,Q)$. According to its definition, $t_0(0,Q)$ represents the approximate border between the perturbative and nonperturbative regimes. In the nonperturbative regime we have to employ the full shape function to include the hadronization effects, while in the perturbative regime, the OPE provides a good description. Based on this behavior, we define $\tau < t_0(0,Q)$ to correspond the τ ranges where the OPE approximation starts to deviate at least 2% from the full shape convolution for the massless thrust distribution. We name the resulting candidate point $t_0(0,Q)$ as the deviation point. To parametrize $t_0(0,Q)$ we consider the following ansatz, inspired by known massless profiles,

$$t_0(0,Q) = \frac{n_0}{(Q/1\,\mathrm{GeV})^{a_0}} + b_0\,. \tag{3.10.9}$$

We generate two different ensembles of massless thrust distributions with different sets of input parameters for the profile functions and at different energies, $\{Q, n_0, a_0, b_0, \dots\}$. Here the dots stand for the rest of other profile function parameters that are analyzed simultaneously and will be discussed later. For the first ensemble we use the convolution of the partonic distribution with the full shape function. For the second ensemble we employ an OPE approximation for nonperturbative corrections. Then, for each set of parameters and energies, we find the τ value where the thrust distribution with full model implementation starts to deviate from the corresponding OPE approximation. By repeating this exercise for all possible variations of input parameters we collect an ensemble of deviation points. Finally we fit the generic form in Eq. (3.10.9) to the ensemble of deviation points. As the result, we obtain $a_0 \sim 1$ and $b_0 \sim 0$ which indeed acknowledges the suggested parametrization by Eq. (3.10.8) for t_0. Moreover by repeating the analysis for various choices of $\{\alpha_s, \overline{\Omega}_1\}$ in the ranges $[0.113, 0.120]$ and $[0.25, 0.55]$, respectively[25], we obtain similar ranges of variation for n_0 i.e. $n_0 \in [1.5, 2.5]$. However we notice that this result is only applicable at intermediate energies, approximately $35\,\mathrm{GeV} < Q < 250\,\mathrm{GeV}$. At very high (low) energies the constant variation of n_0 is not appropriate. We present later how to adopt a more suitable variation of t_0 that has a different energy dependence [see Eq. (3.10.12)]. We observe that the resulting t_0 is very close to the maximum peak position, shortly on the left side of the peak for high energies and on the right side of the peak for low energies. The suggested method here, in principle, represents an iterative fit to the parameters of Eq. (3.10.9), starting with arbitrary initial values of the parameters and looking for the best fit of t_0 to the ensemble of deviation points. Later we will use this general method to investigate the correct mass dependence of the massive profile function.

In contrast to t_0 the term t_1 is a somewhat more arbitrary, being located close to the lower border of the resummation region with $t_0 < t_1$ for all energies. We choose t_1 such that we have an adequate sized window for the transition from the nonperturbative to the resummation region, avoiding high-sloped curves for the double quadratic transition function. We found that the thrust value at half of the peak height is an appropriate candidate for t_1. Similar to the previous case, we provided an ensemble for the thrust values where the height of thrust distributions is half of the peak height. For this ensemble we employ the full model implementation and we run over different input parameters for profile functions and energies. After fitting the ensemble to a similar parameterization in Eq. (3.10.9), for the t_1, we obtain

$$t_1(0,Q) = \frac{n_1}{(Q/1\,\mathrm{GeV})^{0.75}}\,, \qquad n_1 \in [2, 2.5]\,. \tag{3.10.10}$$

The resulting expression exhibits a different energy dependence in comparison to the previous massless profile functions in Eq. (3.10.8). However we verified that the new parametrization is compatible with the former one at intermediate energies in the range $35\,\mathrm{GeV} < Q < 250\,\mathrm{GeV}$, where they were used in Ref. [158].

Now we aim to adopt the transition points for the massive profile functions. To account for the mass effects in the transition points we suggest a natural modification with respect to the massless profile

[25] The $\overline{\Omega}_1$ variations are taken form the massless thrust analysis in Ref. [155].

transition regions. This mass correction is motivated by the theoretical calculation (i.e. consistent with experimental observations) that the threshold and maximum endpoints of the massive thrust distribution are moved further to higher values in comparison with the massless thrust. The resulting shift due to the mass in the various regions of the distribution is different, therefore one has to treat the transition points according to the approximate position within the distribution. For instance the physical shift of the threshold for massive thrust is $\Delta^{\tau}_{\rm thr.}(\hat{m}) = \tau_{\rm min}(\hat{m}) = 1-\sqrt{1-4\hat{m}^2}$ while the effective shift in the tail region is $\Delta^{\tau}_{\rm max.}(\hat{m}) = \tau_{\rm max}(\hat{m}) - 1/2 = \hat{m}$. Hence, considering the fact that t_0 and t_1 are located in the peak region whereas t_2 and t_s are placed in the tail, here we add $\tau_{\rm min}(\hat{m})$ to the first two transition points and $\hat{m}$ to the latter two. These additive shifts should most likely capture the leading correction due to the mass in the transition parameters. We note that the mass parameter in the profile function is an unphysical parameter that in principle can be fixed freely. We found that this method works best if the profile mass parameter is set to the approximate physical mass of the distribution at the threshold which is the MSR-mass scheme at a low energy. In particular for the top and bottom profile function we take $m_t^{\rm p.f.} = m_t^{\rm MSR}(5{\rm GeV})$ and $m_b^{\rm p.f.} = m_b^{\rm MSR}(\overline{m}_b) = \overline{m}_b(\overline{m}_b)$ where the term $m^{\rm p.f}$ denotes the mass parameter in the massive profile function.

In order to check that this simple modification indeed represents the major mass effects in the massive profile transition parameters, we performed an analysis similar to the one for massless thrust, for $t_0(m,Q)$ and $t_1(m,Q)$. We provide an ensemble of deviation points, as candidates for t_0 , and the half peak height thrust values , for possible t_1 borders. Then we fit the following parametrization of the $t_0(m,Q)$ and $t_1(m,Q)$ to the ensembles,

$$t_{0,1}(m,Q) = \frac{n_{0,1}}{(Q/1\,{\rm GeV})^{a_{0,1}}} + b_{0,1} + \tau_{\rm min}(\hat{m})\,, \tag{3.10.11}$$

where we only add the threshold shift to the $t_{0,1}(0,Q)$ in Eq. (3.10.10). We note that here we also varied the mass parameter of the profile function in the ensemble. The resulting $\{n_{0,1}, a_{0,1}, b_{0,1}\}$ are in perfect agreement with the massless parameters. This sanity check certifies that the additive massive correction as discussed above properly expresses the mass dependence of the transition parameters for the massive profile functions.

As already pointed out, we observed that using the fixed ranges of variation for n_0 and n_1 lead to inconsistent variations for the massless (massive) transition parameters at very low or high energies. The reason is although the peak position is roughly proportional to $1/Q$, the energy dependence of the peak width is approximately $\Gamma \sim 1/(Q/1{\rm GeV})^{0.5}$, and the variation of the transition parameters should be rather proportional to the peak width. Since in this analysis we aim to study the top-antitop production at very high energies, instead of the usual variations of n_0 and n_1 , we adopted an additional additive energy dependent variation as $d_{0,1}/(Q/1{\rm GeV})^{0.5}$ for the first two transition parameters t_0 and t_1 that are related to the peak properties.

The transition parameters and corresponding variations for the massive profile functions can be summarized as follows,

$$\begin{array}{ll} t_0(m,Q) = \frac{2}{(Q/1{\rm GeV})} + \frac{d_0}{(Q/1{\rm GeV})^{0.5}} + \tau_{\rm min}(\hat{m}) & d_0 \in [-0.05, 0.05] \\ t_1(m,Q) = \frac{2.25}{(Q/1{\rm GeV})^{0.75}} + \frac{d_1}{(Q/1{\rm GeV})^{0.5}} + \tau_{\rm min}(\hat{m}) & d_1 \in [-0.05, 0.05] \\ t_2(m,Q) = n_2 + \hat{m} & n_2 \in [0.225, 0.275] \\ t_s(m,Q) = n_s + \hat{m} & n_s \in [0.375, 0.425] \end{array}\,, \tag{3.10.12}$$

where the default value for $d_{0,1}$ and $n_{2,s}$ is the middle-point value of the quoted range of variation. The transition values have the important feature that the order of scales $t_0 < t_1 < t_2 < t_s$ is preserved in almost all high and intermediate energies. However, at very low energies $t_1(m,Q)$ might exceed $t_2(m,Q)$, so that the soft scale does not get a chance to reach the resummation region and it transits to the hard scale directly. This property is manifest in the original massless profiles from Ref. [158] as well. As a result, the nonperturbative regime is extended over the peak and tail region such that we encounter only a tiny resummation regime in the tail region. This behavior is acceptable because for low Q the heavy quark becomes less boosted such that the theoretical description leaves the realm of the SCET approximation.

The slope parameter r_s in the canonical relation, third line of Eq. (3.10.7), controls the slope of the soft profile function in the resummation region and introduces residual logarithms in the soft function. It has been demonstrated in Ref. [158] that although $r_s = 1$ seems to be a natural default value for the slope parameter, nevertheless, setting $r_s = 2$ one achieves a better convergence of the cross section between different orders of resummation. We note that the analysis is based on the study of the massless thrust distribution at $\mathrm{N^3LL'}$ in the tail region. In Sec. 3.11 we perform a similar study to show the impact of these choices on the convergence of the results, where we confirm that $r_s = 2$ exhibits a better convergence at different orders. However, by applying the suggested range of variation in Ref. [158] for the slope parameter of the massless profile functions, i.e. $r_s \in [1.77, 2.26]$, we obtained a much larger variation from the massive profile functions. We realized that the origin of this enhancement is the nonuniform massive modification to the distribution range which rescales the peak and tail regions (difference of threshold and endpoint) for the massive thrust distribution with respect to the massless one. We fix this issue by multiplying the slope with a rescaling factor,

$$r_s \to r_s \frac{t_s(0,Q)}{t_s(m,Q) - \tau_{\min}(m,Q)}\,, \qquad r_s \in [1.77, 2.26]\,, \tag{3.10.13}$$

so that the resulting variation for the massive profiles is compatible with the massless case and has the proper massless limit.

In order to obtain both the soft scale profile function $\mu_S(\tau)$ and its first derivative continuous, we use double quadratic functions in the transition regions [158]. These functions are built out of two quadratic polynomials that are smoothly patched together at some middle point, t_m. We use this function to interpolate between two functions, $f(t)$ at t_i (initial point) and $g(t)$ at t_f (final point), in a smooth way[26]. The double quadratic function has the form

$$\zeta(f(t), g(t), t_i, t_m, t_f, t) = \begin{cases} f(t_i) + f'(t_i)(t - t_i) + d_i(t - t_i)^2 & t_i \le t \le t_m \\ g(t_2) + g'(t_f)(t - t_f) + d_f(t - t_f)^2 & t_m \le t \le t_f \end{cases}, \tag{3.10.14}$$

$$d_i = \frac{f'(t_i) - g'(t_f)}{(t_f - t_i)(t_m - t_i)}\left(t_J - \frac{t_m + t_i}{2}\right), \qquad d_f = \frac{g'(t_f) - f'(t_i)}{(t_i - t_f)(t_m - t_f)}\left(t_J - \frac{t_m + t_f}{2}\right),$$

where the t_J is the at the junctions

$$t_J = \frac{g(t_f) - f(t_i) + f'(t_i)t_i - g'(t_f)t_f}{f(t_i) - g(t_f)}\,. \tag{3.10.15}$$

In this double quadratic transition, we are free to set the matching point t_m at any value $t_i \le t_m \le t_f$. For simplicity we set $t_m = (t_i + t_f)/2$ in our profile functions.

By establishing $\mu_S(\tau)$ we obtain the most important ingredient of the profile functions. We stress again that the resulting soft profile function with mass effects is in principle a systematic extension of the massless profiles in Ref. [158] such that in the small mass limit it recovers the massless profile functions [155, 156, 158].

We use the canonical relation induced by the logarithmic terms of the jet function $\ln\left(\mu_J^2/\mu_H\mu_S\right)$, to construct the jet profile function. In order to probe the perturbative uncertainty which arises from jet scale variation, it is conventional to use the so called "trumpet" function, $f_{\mathrm{j}}(e_J, \tau)$ [158]. Thus, our jet profile function reads

$$\mu_J(\tau) = \begin{cases} f(e_J, \tau)\sqrt{\mu_H(\tau)\,\mu_S(\tau)} & \tau \le t_s \\ \mu_H(\tau) & t_s < \tau \end{cases}, \tag{3.10.16}$$

where the trumpet function reads

$$f(e_J, \tau) = \begin{cases} 1 + e_J(t_s - t_0)^2 & \tau < t_0 \\ \zeta(1 + e_J(t_s - t_0)^2, 1 + e_J(t_s - \tau)^2, t_0, t_m, t_1, \tau) & t_0 \le \tau < t_1 \\ 1 + e_J(t_s - \tau)^2 & t_1 \le \tau < t_s \end{cases}. \tag{3.10.17}$$

[26]In this context, we say two functions are smoothly connected when the resulting function and its first derivative at the joins are continuous.

The parameter e_J in the trumpet function provides the variation of the jet scale within the trumpet band [see Figs. 3.11 and 3.12]. We notice that the first derivative of the common trumpet prescription given in Refs [155, 158], with a constant multiplicative factor as $1 + e_J(t_s - \tau)^2$, is discontinuous at the transition point t_0. Therefore in Eq. (3.10.17) we make use of a piecewise function and employs the regular trumpet for $\tau < t_0$ and $\tau > t_1$ and then smoothly patch them together in $t_0 < \tau < t_1$ with an intermediate double quadratic function. Similar to our consideration for the slope parameter, we observed that the massless range of variation $e_J \in [-1.5, 1.5]$ results in a too fat trumpet band for the jet scale which are incompatible with the massless trumpets. Again, we traced back the origin of this enhancement to the stretching of the resummation region in the massive profile functions. Thus, we suggest a quadratic rescaling factor for the term e_J of the form

$$e_J \to e_J\left(\frac{t_s(0,Q) - t_0(0,Q)}{t_s(m,Q) - t_0(m,Q)}\right)^2, \qquad e_J \in [-1.5, 1.5]\,. \tag{3.10.18}$$

It seems natural to set the default value of the trumpet to $e_J = 0$ to retain the canonical relation between different scales and eliminate all the powers of $\ln\left(\mu_J^2/\mu_H\mu_S\right)$ in the cross section. In fact this has been confirmed from our studies for stable heavy quark cross sections. However we also realized that the cross section for unstable top production demonstrates better convergence at different resummation orders when $e_J = -1.5$ is taken as the default value and therefore we take a negative range of variation $e_J \in [-3, 0]$. We come back to the reasoning of this behavior in Sec. 3.11 .

The instruction for building a profile function for the bHQET scale is more involved and complicated. As already discussed, the bHQET scenario is relevant when the jet scale is getting close to the mass shell of the massive quark. Consequently a new set of large logarithms appeared which had to be summed up. Therefore we integrated out the fluctuations of the order of the mass scale and match SCET onto bHQET. The matching was performed at the mass scale μ_m . The resulting bHQET jet function contains logarithms of the form $\ln(\mu_m\mu_b/\mu_H\mu_S)$ which could be summed by tuning the bHQET scale μ_b to satisfy the canonical relation, $\mu_b \sim \mu_H\mu_S/\mu_m$. In addition, the remnant of the matching, referred as the second type of nonsingular contribution [see Sec. 3.5] has to be taken into account in the bHQET scenario to ensure the complete description of the theory. The renormalization scale of this nonsingular term is somewhat arbitrary and denoted with $\mu_{\rm nsb}$. The crucial constraint which ties μ_m , μ_J , μ_b and $\mu_{\rm nsb}$ is to obtain a continuous transition from scenario III to bHQET at their border. In the following we indicate the border between scenario III and bHQET with t_b. We recall that the bHQET scenario is only valid in the kinematic region where $t \lesssim \tau_{\min}(\hat{m}) + \hat{m}^2$. Hence one has to construct μ_b and $\mu_{\rm nsb}$ such that the crossing point of each two of these four scales remains in close vicinity to $t_b \sim \tau_{\min}(\hat{m}) + \hat{m}^2$.

Based on this criterion we tried sophisticated prescriptions, however we found that a rather simple prescription which respects the above constraint is more practical and totally sufficient. We start with specifying the t_b . It is clear from the kinematics of bHQET scenario that one should switch from the scenario III to bHQET in the region where the mass scale is approaching the jet scale. Hence we simply set t_b to the intersection point of the mass scale and the default jet scale, obtained by solving the equation:

$$\mu_m = \mu_J(t_b)\big|_{e_J=0}\,. \tag{3.10.19}$$

This equation has implicit dependence on $\{e_H, e_m, r_s\}$ which leads to values of the t_b in the vicinity of $\sim \tau_{\min}(\hat{m}) + \hat{m}^2$. When the mass scale crosses the jet scale in the resummation region, t_b can be obtained analytically from solving Eq. (3.10.19)

$$t_b = \tau_{\min}(\hat{m}) + \frac{e_m^2\hat{m}^2}{r_s e_H^2}\,. \tag{3.10.20}$$

By setting $e_m = \sqrt{e_H}$ and considering $e_H \in [0.5, 2]$ and $r_s \in [r_s^{\min}, r_s^{\max}]$ the border of scenario III and bHQET takes the value in the range $\tau_{\min}(\hat{m}) + \hat{m}^2/(2r_s^{\max}) \le t_b \le \tau_{\min}(\hat{m}) + 2\hat{m}^2/r_s^{\min}$. One can determine $r_s^{\min}$ and $r_s^{\max}$ using the rescaling factor and the range of variation for the slope parameter given in Eq. (3.10.13). We obtain $r_s^{\min} \simeq 1.4$ and $r_s^{\max} \simeq 1.8$. As a result t_b can vary approximately between $\tau_{\min}(\hat{m}) + 0.3\,\hat{m}^2$ and $\tau_{\min}(\hat{m}) + 1.5\,\hat{m}^2$ that is a reasonable region for switching from scenario III to bHQET.

For the μ_b profile function we use the canonical relation given in Eq. (3.10.5). This will automatically introduce the appropriate bHQET scale which joins to the mass and jet scales at t_b (for the default set of profile parameters). We express the bHQET scale as

$$\mu_b(\tau) = f(e_b, \tau)\,\frac{\mu_J^2(\tau)}{\mu_m(\tau)}\,, \qquad \tau \le t_b, \tag{3.10.21}$$

where the trumpet function is defined by Eq. (3.10.17). Note that in this prescription we do not impose the continuity of the first derivative of the jet and bHQET scales at t_b which otherwise leads to an unnecessary complication of the profile function. Nevertheless, we have examined other prescriptions where the first derivative of the bHQET scale profile function is continuous. We found that the effect of ignoring this constraint is negligible and the consequent kink in the thrust distribution at $\tau = t_b$ is almost invisible, e.g. see Fig. 3.15. Similar to the jet scale here the trumpet parameter, indicated with e_b, controls the variation of the bHQET scale. To preserve the continuity of the bHQET and jet scales we set $e_b = e_J$, including the same rescaling factor as in Eq. (3.10.18). We set the profile function for the renormalization scale in the second type nonsingular contributions as

$$\mu_{\rm nsb}(\tau) = \mu_J(\tau)\,. \tag{3.10.22}$$

We remark that the μ_m, μ_J, μ_b and $\mu_{\rm nsb}$ profile functions are constructed such that for the default set of parameters, they satisfy the continuity criterion at $\tau = t_b$ i.e. $\mu_{\rm nsb}(t_b) = \mu_J(t_b) = \mu_b(t_b) = \mu_m$.

Based on the discussion in Sec. 3.7.1 , to avoid large logarithms in the R-gap scheme, we choose the renormalon subtraction scale equal to the soft scale in the resummation region. Nevertheless, we have observed that in the nonperturbative region, nonvanishing α_s corrections in the gap subtraction terms are favorable, as it has been verified in the massless analyses [155,156,158] . Therefore in analogy, we use the following R profile function

$$R(\tau) = \begin{cases} R_0 & \tau < t_0 \\ \zeta(R_0,\, \mu_S(\tau), t_0,\, t_m,\, t_1,\, \tau) & t_0 \le \tau \le t_1 \\ \mu_S(\tau) & t_1 \le \tau \end{cases}, \tag{3.10.23}$$

where the R_0 controls the subtraction scale in the nonperturbative region. We have checked that the ranges of $R_0 \in [0.85\mu_0, 0.7\mu_0]$ result into an appropriate cancellation of the renormalons in the peak region and consequently a good stability of the peak position.

We also set the R_m in the MSR mass scheme in the bHQET regime as

$$R_m(\tau) = \mu_b(\tau)\,, \qquad \tau \le t_b\,, \tag{3.10.24}$$

to achieve the complete pole mass renormalon subtraction without generating large logarithms.

Finally, for the renormalization scale in the nonsingular partonic cross section, we employ the profile function already used for massless quarks [158]

$$\mu_{ns}(\tau) = \begin{cases} \frac{1}{2}\Big(\mu_H(\tau) + \mu_J(\tau)\Big) & n_{ns} = 1 \\ \mu_H(\tau) & n_{ns} = 0 \\ \frac{1}{2}\Big(3\mu_H(\tau) - \mu_J(\tau)\Big) & n_{ns} = -1 \end{cases}, \tag{3.10.25}$$

where n_{ns} identifies the different settings. Varying μ_{ns} allows us to account for the theoretical uncertainty due to the ignorance of the logarithmic resummation in the nonsingular contribution. Note that the three prescriptions have the crucial feature that μ_{ns} together with μ_J, μ_S and R merge with

μ_H at the $t > t_s$, so that we precisely recover the fixed order prediction in the far tail region. We note that using lower scales for μ_{ns} such as the soft scale results in an unnatural enhancement in the nonsingular contributions in the cross section [155].

The only open parameters which have not been discussed yet, are μ_0 and R_0. In this work, similar to the massless analyses in Ref. [158] we fix μ_0 and R_0 at particular scales and do not vary them. The reason is that these scales are tied to the definition of the parameters of the shape function and therefore are set to particular values to ensure that the shape function has a unique meaning. Moreover we have verified that varying μ_0 and R_0 while keeping the difference fixed, e.g. $\mu_0 - R_0 = 0.4$, has a small impact compared to the variation of the shape function parameters and other profile scale variations. Therefore it has been concluded in Ref. [158] that the values $\mu_0 = 1.1$ and $R_0 = 0.7$ are convenient and good choices for the massless profile functions. Based on these studies, for the stable top/bottom quark production we set the values for μ_0 and R_0 in the massive profile functions equal to the values for massless case. However we realized that for the unstable heavy quark production, due to the additional smearing with the Breit-Wigner function, one should set them to somewhat higher values to ensure that the resulting cross section remains positive for τ values below the peak position. The reason is that the total width serves as an additional IR-cutoff for the soft scale, and thus one has to set it to higher values. In order to obtain a meaningful result for the unstable top cross section, we found that $\mu_0 = 3$ and $R_0 = 2.25$ are suitable values.

In Sec. 3.7, we discussed a naive procedure which allows us to absorb the subdominant singularities in the factorization theorems and suppressing artificial instabilities that could arise close to the threshold of the thrust distribution. In our analysis we use a flag, denoted with "*sing*" to switch the absorption process off ($sing = 0$) and on ($sing = 1$). We found that for the stable heavy quark jet cross section it is necessary to absorb these subleading contributions, see Fig. 3.35 while for the unstable quark jet cross section, due to the additional smearing with the Breit-Wigner function for finite width, the subleading effects are suppressed, see Fig. 3.24. The impact of the choice of *sing* will be discussed further in Sec. 3.11. The absorption process is not unique and has a 2-dimensional arbitrariness which we parametrized by the continuous parameters ξ_j and ξ_b, that can be tuned between 0 and 1. Hence, in addition to the variation of the profile functions parameters we also use the variation of ξ_j and ξ_b to extract the theoretical uncertainty. The set of default values and range of variations for different parameters of the profile function and theory parameters are listed in Tabs. 3.5 and 3.4 for stable (unstable) top and stable bottom production, respectively. In each case we have at most 10 different parameters to vary during the theory scan.

In Figs. 3.11 and 3.12 we display the massive profile functions for bottom quark production at $Q = \{15, 22, 45\}$(GeV) and top production at $Q = \{700, 1000, 1400\}$(GeV). These plots are obtained by taking 100 random variations of the profile set parameters for the transition points, slope function and trumpets in the ranges indicated in Tabs. 3.4 and 3.5, while the rest of the parameters are set to their default values. We indicate the possible further profile variations (which are global variations like the hard scale and the mass scale variations) with up and down arrows. The gray dashed lines display the canonical relations for soft and jet (bHQET) scales in the resummation region. Note that by choosing $r_s = 1$, the soft, jet and bHQET scale profile functions exactly match the corresponding canonical curves with $r_s = 1$ in the resummation region, $t_1(m, Q) < \tau < t_2(m, Q)$, see Figs. 3.11 and 3.17.

The intersection of the gray lines indicates the profile threshold, $\tau_{\min}(m^{\rm p.f.}/Q)$ where $m^{\rm p.f.}$ is the non-dynamical mass in the profile functions and set to the values in Tabs. 3.4 and 3.5. The exact position of the partonic threshold of the thrust distribution depends on the mass scheme and renormalization scales that enter the factorization theorems close to the threshold region. In the bQHET region the jet scale adopts the role of the second type of nonsingular renormalization scale, $\mu_{\rm nsb}(\tau) = \mu_J(\tau)$. We note that we set $n_s = 0$ in the default setting of theoretical parameters, so that the renormalization scale in the first type of nonsingular contributions is given by $\mu_{\rm ns}(\tau) = \mu_H(\tau)$. The R_m-scale in the MSR mass scheme coincides with $\mu_b(\tau)$ in the bHQET region to ensure the precise renormalon subtraction.

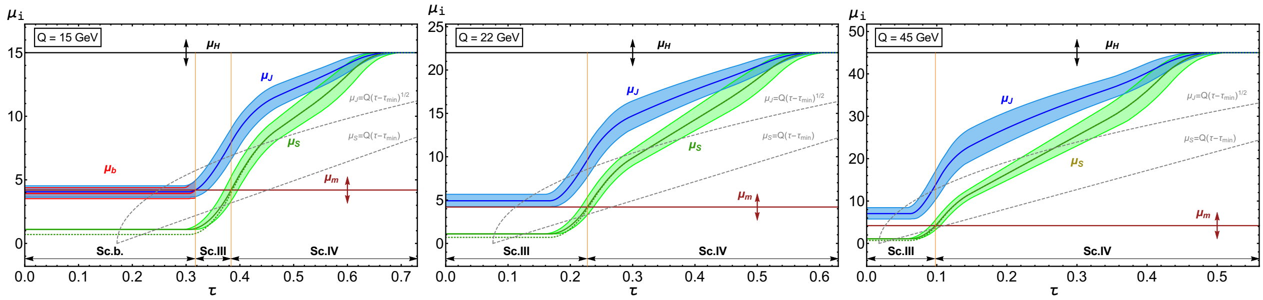

(a) Bottom Production

Figure 3.11: Massive profile functions for the renormalization scales $\mu_H(\tau)$ (solid black line), $\mu_m(\tau)$ (solid brown line), $\mu_J(\tau)$ (solid blue line), $\mu_b(\tau)$ (solid red line), $\mu_S(\tau)$ (solid green line) and $R(\tau)$ (dotted green line) for three c.m energies Q. The bands indicate the results of varying the profile function parameters, obtained by taking 100 random points for $\{d_0, d_1, n_2, n_s, e_J, e_B, e_S\}$ in the range of values given in Tab. 3.4. The more global variations of the terms $\{e_H, e_m\}$ are indicated with the up-down arrows. The flat region of the soft and R-scale μ_0 and R_0 are kept constant. All the renormalization scales except for the mass scale, merge to the hard scale at $t_s(m, Q)$. The left, center and right panels correspond to $Q = 15\,\mathrm{GeV}$, $22\,\mathrm{GeV}$ and $45\,\mathrm{GeV}$, respectively. We set $m^{\mathrm{p.f.}} = \overline{m}_b(\overline{m}_b) = 4.2\,\mathrm{GeV}$. The thin orange lines represent the borders of different scenarios for the default values of profile function parameters. The approximate regions of various kinematical scenarios for the massive thrust distribution are specified with the black double-headed arrows. The "Sc.b.", "Sc.III" and "Sc.IV" denote scenario bHQET, scenario III and scenario IV, respectively. The gray dashed lines display the canonical relations for soft and jet scales in the resummation region.

parameter	default value	range of values
μ_0	1.1	-
R_0	0.7	-
r_s	2	-
$m^{\mathrm{p.f.}}$	$\overline{m}(\overline{m})$	-
sing	1	-
e_m	1	correlated variation: $\sqrt{e_H}$
d_0	0	-0.05 to $+0.05$
d_1	0	-0.05 to $+0.05$
n_2	0.25	0.225 to 0.275
n_s	0.4	0.375 to 0.425
e_H	1	0.5 to 2
e_S	0	$1.13^{-1} - 1$ to $1.13^{+1} - 1$
$e_{J/B}$	0	-1.5 to 1.5
n_{ns}	0	-1, 0, 1
χ_j	0	0 to 1
χ_b	0	0 to 1

Table 3.4: The thrust theory parameters relevant for determining the theory uncertainty of the stable bottom cross section. The first column lists the parameters introduced in the profile function and theoretical description. The second column displays the default values. The third column presents the range of variations used for the theory scan to assign the theoretical uncertainty.

The resulting profile functions clearly manifest different kinematic scenarios. The hierarchy between the quark mass scale and other scales is changing along the thrust spectrum dynamically. This clearly illustrates the reasoning for constructing different theoretical descriptions for various kinematic regimes, as presented in Sec. 3.4.2. To obtain the entire thrust distribution one needs to patch the relevant kinematic scenarios at specific borders. We found that it is convenient to make use of the massive profile functions in Figs. 3.11 and 3.12 to identify the approximate border between kinematic

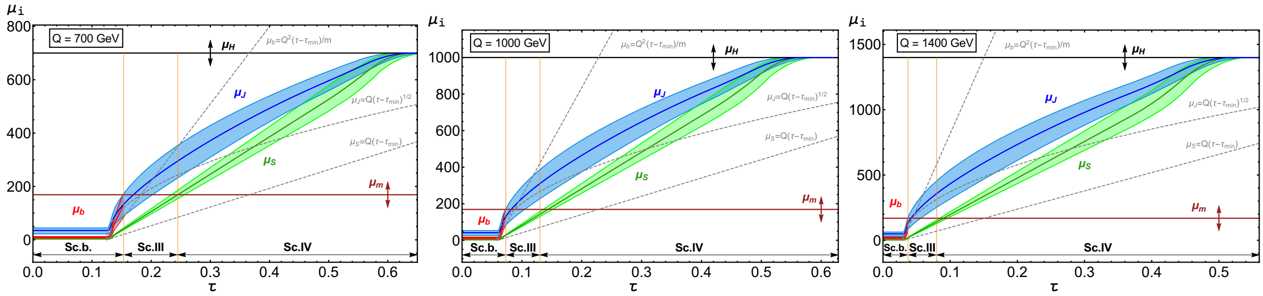

(a) Top Production

Figure 3.12: Massive profile functions for the renormalization scales $\mu_H(\tau)$ (solid black line), $\mu_m(\tau)$ (solid brown line), $\mu_J(\tau)$ (solid blue line), $\mu_b(\tau)$ (solid red line), $\mu_S(\tau)$ (solid green line) and $R(\tau)$ (dotted green line) for three c.m energies Q. The band indicates the results of the varying profile function parameters, obtained by taking 100 random points for $\{d_0, d_1, n_2, n_s, e_J, e_B, e_S\}$ in the range of values given in Tab. 3.5. The rather more global variations of the terms $\{e_H, e_m\}$ are specified with the up-down arrows. The flat region of the soft and R-scale μ_0 and R_0 are kept constant. At the resolution of this plot the $\mu_S(\tau)$ and $R(\tau)$ are not distinguishable and the variation of μ_b in the flat region is as thick as the red solid line. All the renormalization scales except for the mass scale, merge to the hard scale at $t_s(m, Q)$. The left, center and right panels correspond to $Q = 700$ GeV, 1000 GeV and 1400 GeV, respectively. We set $m^{\rm p.f.} = 168.8$ GeV. The thin orange lines represent the borders of different scenarios for the default values of profile function parameters. The approximate regions of various kinematic scenarios for the massive thrust distribution are specified with the double-headed arrows. The “Sc.b.”, “Sc.III” and “Sc.IV” denote scenario bHQET, scenario III and scenario IV, respectively. The gray dashed lines display the canonical relations for soft and jet and bHQET scales in the resummation region.

parameter	default value stable (unstable)	range of values
μ_0	1.1 (3)	-
R_0	0.7 (2.25)	-
r_s	2	-
$m^{\rm p.f.}$	$m^{\rm MSR}(5\,{\rm GeV})$	-
sing	1 (0)	-
e_m	1	correlated variation: $\sqrt{e_H}$
d_0	0	-0.05 to $+0.05$
d_1	0	-0.05 to $+0.05$
n_2	0.25	0.225 to 0.275
n_s	0.4	0.375 to 0.425
e_H	1	0.5 to 2
e_S	0	$1.13^{-1}-1$ to $1.13^{+1}-1$
$e_{J/B}$	-1.5	-3 to 0
n_{ns}	0	-1, 0, 1
χ_j	0	0 to 1
χ_b	0	0 to 1

Table 3.5: The thrust theory parameters relevant for determining the theory uncertainty of the unstable (stable) top cross section. The first column lists the parameters introduced in the profile function and theoretical description. The second column displays the default values. The third column presents the range of variations used for the theory scan to assign the theoretical uncertainty.

scenarios. We already provided a prescription to assign a border between scenario bHQET and scenario III. We indicated this border with t_b. In analogy with t_b we assign the second border between scenario III and scenario IV to correspond the thrust value where the mass scale crosses the soft scale. We denote this border with t_c, and note that we always have $t_c > t_b$. We display the t_b and t_c with the thin orange lines in the first panels of Figs. 3.11 and 3.12 for the $Q = 15$ GeV case. The orange line in the $Q = 22\,\mathrm{GeV}$ and $45\,\mathrm{GeV}$ cases represents t_c. We stress that the resulting scenario borders are flexible and can be slightly changed in the vicinity of the transition between scenarios, e.g. by varying the mass scale so that it consequently crosses the jet and soft scale at different thrust values. We indicate the different kinematic regimes with the black double-headed arrows in Figs. 3.11 and 3.12.

An interesting feature that is apparent from the bottom quark profile functions in Fig. 3.11 and the corresponding thrust distributions in Fig. 3.13 is that the bHQET scenario is not always a relevant description in the peak region. We do not encounter the bHQET regime at all for the default set of theoretical parameters at $Q = 22\,\mathrm{GeV}$ and $45\,\mathrm{GeV}$, and at $Q = 15\,\mathrm{GeV}$ it is only a marginal regime which means that the default jet and mass scale are very close to each other. While performing the random scan over the theoretical parameters we might encounter cases where the mass scale is below the jet scale so that the bHQET regime disappears completely. Note that at higher energies where $m \ll \mu_J \sim Q\Lambda_{\mathrm{QCD}}$ we do not encounter the bHQET scenario at all which is in agreement with the fact that the bHQET scenario is irrelevant in the limit of massless quarks. On the other hand, the top quark profile functions in Fig. 3.12 and the thrust distributions for stable and unstable top production in Figs. 3.34 and 3.23, respectively, illustrate that for Q values up to about 10TeV the bHQET scenario is always the relevant description in the peak region of cross sections.

3.11 Results

In this section we present the resulting thrust distributions for the bottom, unstable top and stable top production. In the following analyses we only concentrate on the theoretical aspects of the results. Finally we try to estimate the theoretical accuracy that can be achieved from the future fits to the mass parameters in MCs. We stress that the stable top analysis has no physical relevance however it can be used to check whether the top mass determination in the small width limit are compatible with the correct physical situation where the top width is finite $\Gamma_t \sim 1.5\,\mathrm{GeV}$.

In each of the upcoming analyses in Secs. 3.11.1, 3.11.2 and 3.11.3, we first show various components of the thrust distribution at N^{2}LL and NLO precision using the R-gap scheme for the non-perturbative effects and the MSR mass scheme. Moreover, we discuss how the artificial instabilities close to the partonic threshold of the distribution due to subleading contributions can be suppressed by absorbing the subdominant singularities in the factorization theorems. Next, we discuss the reasoning of choosing some specific value for some parameters of the profile functions given in Tab. 3.4 for bottom and Tab. 3.5 for top. We display the impact of various choices of theoretical parameters on the perturbative convergence of the thrust distribution at N^{2}LL and NLL. Afterward, we study the sensitivity of the thrust distributions to the theoretical parameters such as the mass, the strong coupling constant and the first moment of the shape function. Finally, we employ a simple fitting procedure as a guideline for estimating the theoretical uncertainties that can be obtained for the MC mass parameter calibration.

The presentation in each section will be performed at different energies to point out energy dependent features. In particular this allows to verify whether the parametrization of the different pieces of the profile functions suggested in Sec. 3.10 has the appropriate energy dependence. Thus for the bottom quark analysis we always display cross sections at three different energies where the left, center and right column of panels correspond to $Q = 15\,\mathrm{GeV}$, $22\,\mathrm{GeV}$ and $45\,\mathrm{GeV}$, respectively. Similarly, in the plots for the top analyses we display cross sections at $Q = 700\,\mathrm{GeV}$, $1000\,\mathrm{GeV}$ and $1400\,\mathrm{GeV}$, which are respectively located at the left, center and right panels.

In the subsequent sections, we employ to $\overline{m}_b(\overline{m}_b) = m_b^{\mathrm{MSR}}(m_b^{\mathrm{MSR}}) = 4.2\,\mathrm{GeV}$, $\overline{m}_t(\overline{m}_t) = 160\,\mathrm{GeV}$ ($m_t^{\mathrm{MSR}}(5\,\mathrm{GeV}) = 168.8\,\mathrm{GeV}$), $\alpha_s(m_Z) = 0.114$ and $\overline{\Omega}_1(R_\Delta, \mu_\Delta) = 0.5\,\mathrm{GeV}$ with reference scales $R_\Delta = \mu_\Delta = 2\,\mathrm{GeV}$ [155], as the default set of theoretical parameters. In the following analyses, we use the default set of theoretical parameters and indicate explicitly whenever we vary a specific parameter by denoting its value. We note that here we only use the simplest model function where $c_0 = 1$ and $c_{i>0} = 0$ [see Sec. 3.7.2].

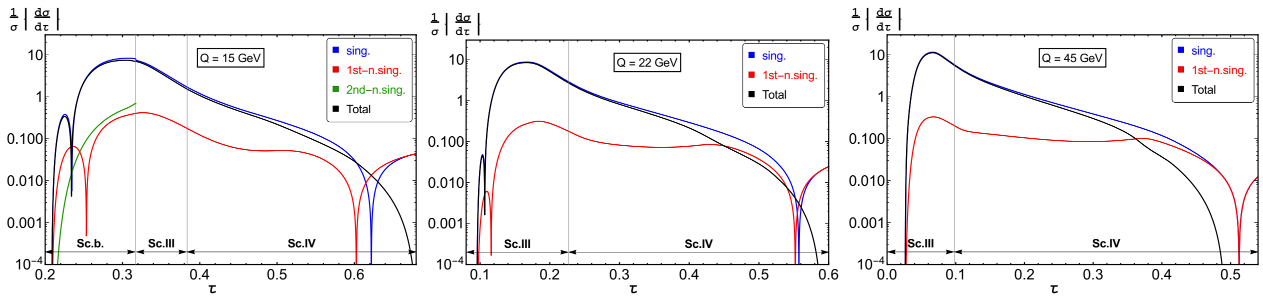

Figure 3.13: Singular and nonsingular contributions of the bottom thrust distribution at various energies at N^{2}LL including nonperturbative effects in the R-gap scheme. We use the default set of theoretical parameters for the bottom cross section given in Tab. 3.4 with $\alpha_s(m_Z) = 0.114$, $\overline{\Omega}_1(R_\Delta, \mu_\Delta) = 0.5\,\mathrm{GeV}$ and $\overline{m}_b(\overline{m}_b) = 4.2\,\mathrm{GeV}$. "1st-n.sing." and "2nd-n.sing." indicate the first and second type of nonsingular components, respectively [see Sec. 3.5]. Here the subdominant singularities are absorbed into the factorization theorems ($sing = 1$) [see Sec. 3.6.2].

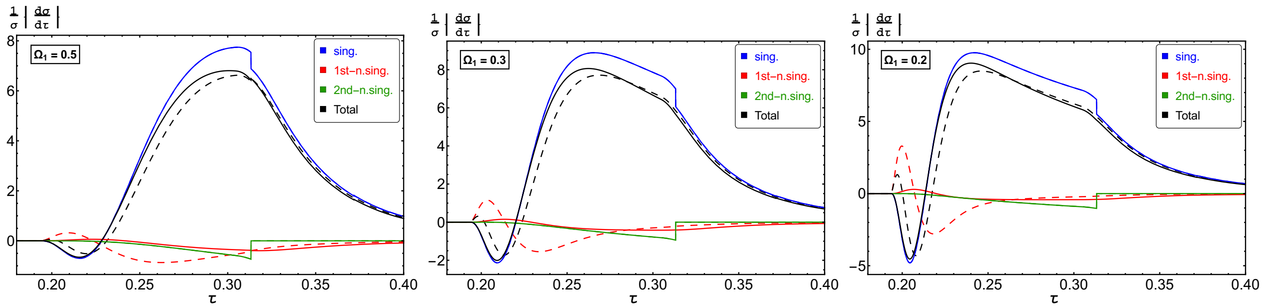

Figure 3.14: Singular and nonsingular contributions of the bottom thrust distribution at N^{2}LL including nonperturbative effects in the R-gap scheme, when the subdominant singularities are absorbed ($sing = 1$), displayed by solid lines, or not absorbed ($sing = 0$), displayed by dashed lines. Here we set $e_h = 2$. For the rest of the theoretical parameters we use the default values given in Tab. 3.4 with $\alpha_s(m_Z) = 0.114$ and $\overline{m}_b(\overline{m}_b) = 4.2\,\mathrm{GeV}$. The left, center and right panels are obtained by setting $\overline{\Omega}_1(R_\Delta, \mu_\Delta) = 0.5\,\mathrm{GeV}$, $\overline{\Omega}_1(R_\Delta, \mu_\Delta) = 0.3\,\mathrm{GeV}$ and $\overline{\Omega}_1(R_\Delta, \mu_\Delta) = 0.2\,\mathrm{GeV}$, respectively. "1st-n.sing." and "2nd-n.sing." indicate the first and second type nonsingular components, respectively [see Sec. 3.5].

3.11.1 Bottom Analysis

Thrust Distribution: Singular v.s. Nonsingular Components

Here we discuss various components of the full thrust distribution with resummation at N^{2}LL. These components are: I) the most singular contributions accounted by the factorization scenarios, II) the first type of nonsingular contribution consisting of subleading corrections that are not taken into account by the SCET factorization scenarios, III) the second type of nonsingular contributions (appearing only in the bHQET scenario), constituted of the non-distributional terms in the SCET factorization scenarios that are not accounted by the bHQET factorization theorem.

In Fig. 3.13 we display various components of the bottom thrust distribution at N^{2}LL using the default theoretical inputs and parameters. We use the R-gap scheme for the soft function and the MSR scheme for the mass parameter, to ensure that all the leading renormalon ambiguities of $\mathcal{O}(\Lambda_{\rm QCD})$ are removed. The red and green curves illustrate the first and second type of nonsingular components, respectively. The sum of the singular (blue line) and nonsingular components gives the total distribution (black line). The gray lines indicate the borders of the kinematical scenarios.

Fig. 3.13 shows the relative size of singular and nonsingular contributions in different regions of the distribution. In the peak the singular contribution is clearly dominant. In the tail, however, the singular curve falls down and its size gets closer to the first type of nonsingular contributions. Note that here the sign of the singular and nonsingular contributions is opposite. Finally in the far-tail the singular and nonsingular contributions, appearing with the same size and opposite signs, cancel each other to a large extent. This results in a rapid decrease of the total thrust distribution in the far tail which is obvious in the region where individual pieces (blue and red curves) are larger than the total thrust distribution (black curve).

In the default setting of theoretical parameters for the bottom cross section given in Tab. 3.4 we absorb the subdominant singularities in the factorization theorems which corresponds to the choice where $sing = 1$. To illustrate the impact of this choice here we study the effects of the subleading contributions for $sing = 0(1)$ on the bottom quark cross section. In Fig. 3.14 we display different components of the thrust distribution at $Q = 15\,\mathrm{GeV}$ for $sing = 0$ (solid lines) and $sing = 1$ (dashed lines) using different values for the first moment of the soft model function. The figure displays only the peak of the thrust distribution. The left, center and right panels display the resulting cross sections when the first moment of the soft model function at the reference scales $R_\Delta = \mu_\Delta = 2\,\mathrm{GeV}$ is set to $\overline{\Omega}_1(R_\Delta, \mu_\Delta) = 0.5\,\mathrm{GeV}$, $\overline{\Omega}_1(R_\Delta, \mu_\Delta) = 0.3\,\mathrm{GeV}$ and $\overline{\Omega}_1(R_\Delta, \mu_\Delta) = 0.2\,\mathrm{GeV}$, respectively. Here we set $e_h = 2$ since the impact of $sing = 0$ is more enhanced and leads to a clear oscillating pattern in the threshold region. The rest of the theoretical parameters are set to the default values. We recall that the singular and the second type of nonsingular contributions do not depend on $sing$. Therefore only one solid blue and one solid green curve are displayed in each panel.

It is obvious from Fig. 3.14 that the first type of nonsingular contributions with $sing = 0$ exhibits a more pronounced oscillating pattern close to the threshold that is enhanced for small $\overline{\Omega}_1$ values. It is apparent from the panel with $\overline{\Omega}_1(R_\Delta, \mu_\Delta) = 0.2\,\mathrm{GeV}$ that below the peak the size of these contributions is comparable to the singular contributions. However note that the choice of $sing = 0$ has no significant effect on the sum of all contributions for the bottom thrust distribution. In fact the singular contributions (blue curves) exhibit analogous oscillations in the threshold region with a similar size relative to the nonsingular instabilities (red dashed curve). On the other hand, it is manifest by the solid red curves in Fig. 3.14 that the choice of $sing = 1$ for the first type of nonsingular contributions have a stable and smooth behavior in all panels. Nevertheless, strictly speaking, the absorbing prescription used here is a naive procedure and is not an exact treatment of the subdominant singularities.

Hence, based on these observations we cannot conclude that $sing = 1$ is a priori better choice than $sing = 0$. In order to determine whether the choice of $sing = 0$ or $sing = 1$ is the proper prescription, we will perform a further examination in the following section, where we study the perturbative convergence between the corresponding cross sections at different orders of resummation.

In general for each of the upcoming analyses we will use similar examinations for the $sing = 1$ and $sing = 0$ choices. First we will verify the behavior of the first type of nonsingular contributions close to threshold and the corresponding effects on the total thrust distribution. Then we will study the perturbative convergence between the resulting cross section at NLL and N^{2}LL. This provides an individual guideline for each case to choose the most appropriate prescription. To summarize, these set of examinations lead us to the following results: I) for the bottom cross section both $sing = 1$ and $sing = 0$ are applicable, II) for the unstable top production $sing = 1$ lead to better perturbative convergence, III) for the stable top production $sing = 0$ is the only correct prescription which yields stable results.

Perturbative Convergence Examinations

In this section we discuss the perturbative behavior of the thrust distribution for bottom quark production. In particular we examine the impact of using different values for $sing$ and r_s on the convergence of the cross section between different orders of resummation. We recall that r_s is the slope of the soft function in the resummation region. In addition we discuss the impact of using renormalon-free schemes for the gap and mass parameters. To this end, we present the corresponding cross sections when, I) the gap parameter is absent and the result contains the soft renormalon ambiguities, II) we use the pole mass scheme for the heavy quark mass. We collect all the results in Figs. 3.15 and 3.16. Here, we display the hadronic cross section using the default theoretical parameters for $\{m, \alpha, \overline{\Omega}_1\}$ with resummation at NLL (green band) and N^{2}LL (red band) order. Figs. 3.15 and 3.16 display the peak and the tail regions of the distribution for the various cases, respectively. The error bands in the plots correspond to a theory parameter scan with 100 random points taken in the default range of values given in Tab. 3.4 .

The first row of panels in Figs. 3.15 and 3.16 illustrate the thrust distribution using the default theoretical parameters given in Tab. 3.4 , that correspond to $r_s = 2$ and $sing = 1$. The second row of panels is obtained by setting $sing = 0$ and leaving the rest of theoretical parameters unchanged. The third row of panels displays the results when the slope parameter is set to $r_s = 1$ and the rest of parameters are set to the default values. The fourth and fifth row of panels displays the thrust distribution, respectively, when we do not use the gap formalism and while we employ the pole mass scheme, keeping all the rest of theoretical parameters to the default values.

As we already discussed in Sec. 3.10 for most of the theoretical parameters in the massive profile functions we use the default values suggested by the massless profile functions in Ref. [158] . The first row of panels in Figs. 3.15 and 3.16 show that using the default values and the corresponding ranges of variations in Tab. 3.4 for the theoretical parameters in fact leads to a good convergence of the bottom cross section at NLL and N^2LL . Furthermore, the result exhibits good convergence in all regions of the distribution and at all energies. This is a clear evidence that we properly anticipated the Q dependence of the various terms in the profile functions.

Now let us turn back to the discussion on the choice of $sing$. Comparing the panels in the first ($sing = 1$) and second rows ($sing = 0$) of Figs. 3.15 and 3.16 we only notice a small difference between the resulting cross sections. In fact the relative size of the differences between the two choices is much smaller than the uncertainty from scale variation and both prescriptions illustrate a good perturbative convergence. Hence we conclude that the choice of $sing$ is in principle irrelevant for the bottom quark analysis. Nevertheless, based on the discussion in the previous section, we have taken the $sing = 1$ as the default value to ensure the suppression of the first type of nonsigular contributions relative to the singular contributions in the threshold region.

In the next study we examine the impact of using $r_s = 1$ instead of $r_s = 2$ on the convergence of the cross section. It is apparent from the set of plots in the peak region, shown in Fig. 3.15 , that for the slope 1 case the thrust distribution is somewhat reduced in comparison with the default case shown in the first row ($r_s = 2$). Moreover the distribution decreases in the tail region with a lower slope (so that the width of the distribution is slightly larger than the default case) and in the far tail with a steeper slope, in comparison to the corresponding panels in the first row. In addition, we observe for the slope 1 case that in the peak region the NLL band lies on the lower edge of the N^2LL band and does not entirely cover it, specially at low energies. In the tail region shown in Fig. 3.16 , the situation is more dramatic and the scan for NLL exhibits a bumpy shape close to the far tail. This behavior does not appear in the default case. In fact the bumpy shape here is induced by the singular contributions and it is originated from the rapid changes in the slope of the soft profile function that occurs at t_2 (see Fig. 3.17) while transiting from the canonical region (gray dashed line) to the multijet region (where all the scales are merging). Therefore, similar to Ref. [158] we conclude that, although $r_s = 1$ seems to be the natural choice for the slope of the soft profile function, using a larger value improves the convergence between the different orders of the cross section by smoothing out the profile functions in the tail and far-tail. In addition we observe in the panels of slope 1 case that already by increasing the accuracy of resummation form NLL to N^2LL, the bumpy shape vanishes. This observation confirms the statement of Ref. [158] that the slope choice has a smaller effect at higher orders than for the respective lower order predictions.

We emphasized in previous sections that it is essential to employ renormalon-free schemes such as the R-gap scheme for the soft function and short distance mass schemes to obtain stable results for the cross section. In the rest of this section we discuss the impact of subtracting these two renormalon ambiguities in the partonic corrections. The fourth rows in Figs. 3.15 and 3.16 display the cross section when employing the model function without the gap parameter. One can clearly observe in the fourth row of Fig. 3.15 that in the peak region the error bands at different orders have no meaningful overlap, indicating lack of convergence in the perturative results. Another interesting visible feature of the

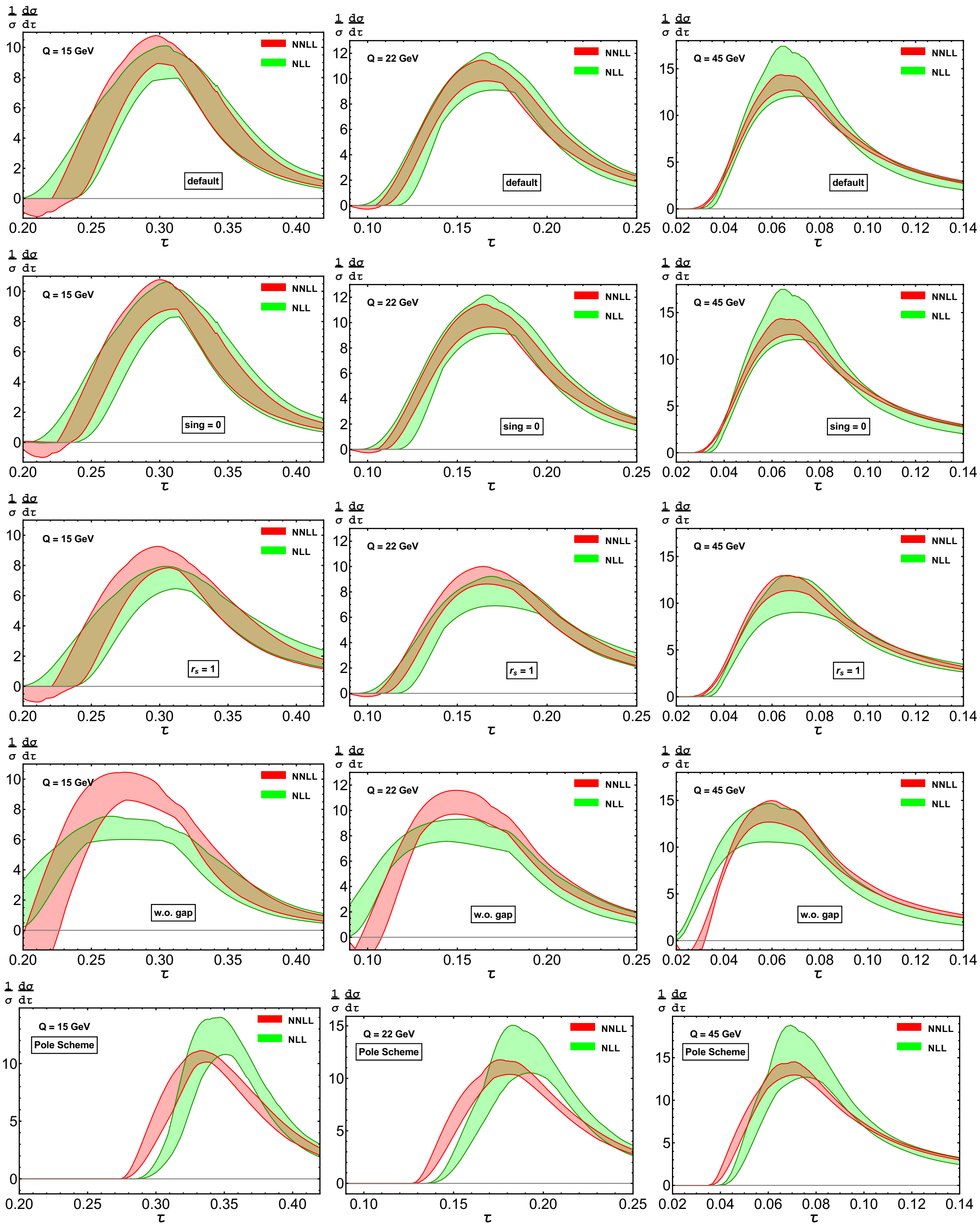

Figure 3.15: Theory scan for the bottom thrust distribution uncertainties in the peak region at various energies with resummation at N^{2}LL (red) and NLL (green) order. Here we display the hadronic cross sections when: we use the default theoretical parameters given in Tab. 3.4 (1st row), we set $sing = 0$ (2nd row), we set $r_s = 1$ (3rd row), we employ the model function without using the gap parameter to subtract the renormalon ambiguities (4th row), the pole mass scheme is used (5th row).

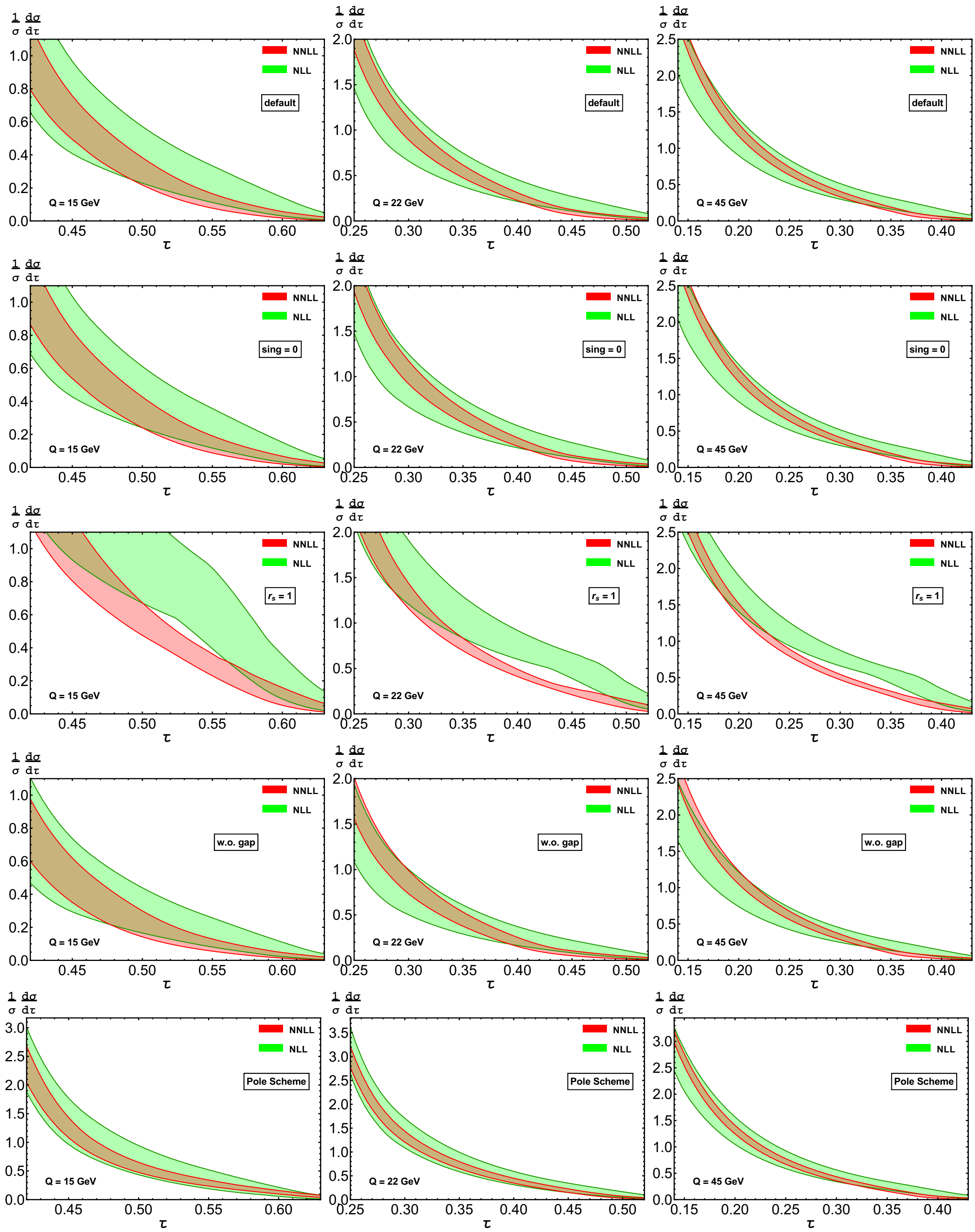

Figure 3.16: Theory scan for the bottom thrust distribution uncertainties in the tail region at various energies with resummation at N^{2}LL (red) and NLL (green) order. Here we display the hadronic cross sections when: we use the default theoretical parameters given in Tab. 3.4 (1st row), we set $sing = 0$ (2nd row), we set $r_s = 1$ (3rd row), we employ the model function without using the gap parameter to subtract the renormalon ambiguities (4th row), the pole mass scheme is used (5th row).

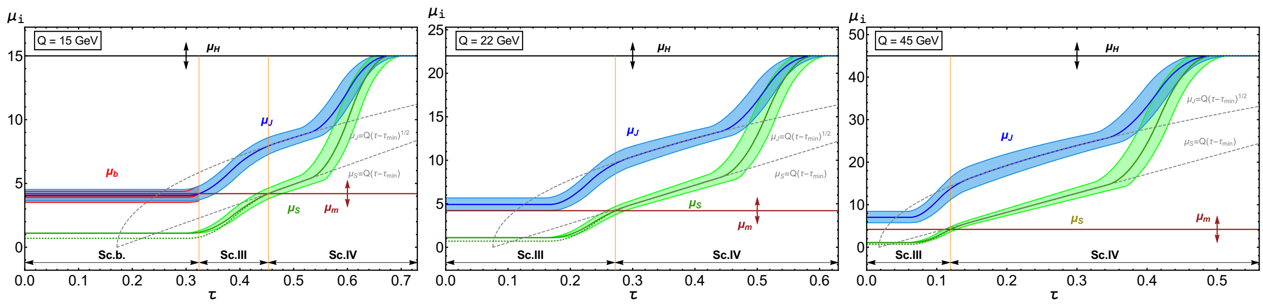

(a) Bottom Production

Figure 3.17: Massive profile functions when we set $r_s = 1$. We refer to Fig. 3.11 for more information about the convention used in the plot.

results is that the convergence of perturbation theory is getting worse at low c.m. energies. This confirms the expected behavior of the IR-sensitivity proportional to $\Lambda_{\rm QCD}/Q$. Moreover a set of new negative dips appears in the threshold region at N^{2}LL order which affects the total thrust distribution used for the normalization of the thrust distributions. Note that in the default result in the R-gap scheme (shown in the 1st row) such dips are less emphasized or completely removed. This particular feature of the soft function renormalon has been observed in Ref. [198] too. On the other hand, the result exhibits a good perturbative convergence in the OPE region which are consistent with the results for the default case. The reasoning for this behavior is that in the OPE region the nonperturbative effects are power suppressed and hence the IR-sensitivities has less impact.

The fifth row in Figs. 3.15 and 3.16 displays the bottom cross sections in the pole mass scheme with $m_b^{\rm pole} = 4.87\,{\rm GeV}$.[27] Here one can easily see that in the peak region the N^{2}LL bands are significantly shifted with respect to the NLL bands for all energies. This indicates a substantial instability that is due to the renormalon ambiguity in the pole mass scheme. In addition by comparing the result with the default cross sections, one can realize that the location of the peak has moved to higher thrust values in the pole mass scheme. This illustrates the high sensitivity of the peak position to the choice of the mass scheme. On the other hand in the tail region, the N^{2}LL band is entirely contained in the NLL band, exhibiting a good convergence. Hence one can simply conclude that the tail is not the appropriate region to extract the mass of the heavy quarks. In the next section we will discuss the sensitivity of the massive thrust distribution to the theoretical parameters m, α_s and $\overline{\Omega}_1$ in more details.

Sensitivity to the Theory Parameters

Here we discuss the sensitivity of the thrust distribution for bottom quark production to the theoretical parameters at different energies. In particular we concentrate on the impact on the peak region by separately varying the bottom quark mass, the strong coupling constant and the first moment of the soft model function. In Fig. 3.18 we display the resulting cross sections for bottom production at N^{2}LL using the R-gap and MSR mass schemes. The theoretical error bands are obtained by using 100 random scans over the theory parameters in the ranges given in Tab. 3.4 . In each panel the red band illustrates the default cross section using the default theoretical parameters and the blue and green error bands represent the cross section when we have changed a specific theoretical parameter from the default value, indicated on the top-right corner in each plot.

The first row of panels in Fig. 3.18 displays the impact of changing the bottom quark mass from $\overline{m}_b(\overline{m}_b) = 4.2\,{\rm GeV}$ by $\pm 0.5\,{\rm GeV}$ in the peak. Here one can see that at higher energies the error bands have a significant overlap in the peak region whereas at low energies the peak region with different colors are entirely distinguishable. Therefore we conclude that the bottom cross section at low energies

[27] The value of the bottom quark mass in the pole mass scheme is obtained from the four-loop relation between the pole and $\overline{\rm MS}$ scheme [63] and using the default theoretical value $\overline{m}_b(\overline{m}_b) = 4.2\,{\rm GeV}$.

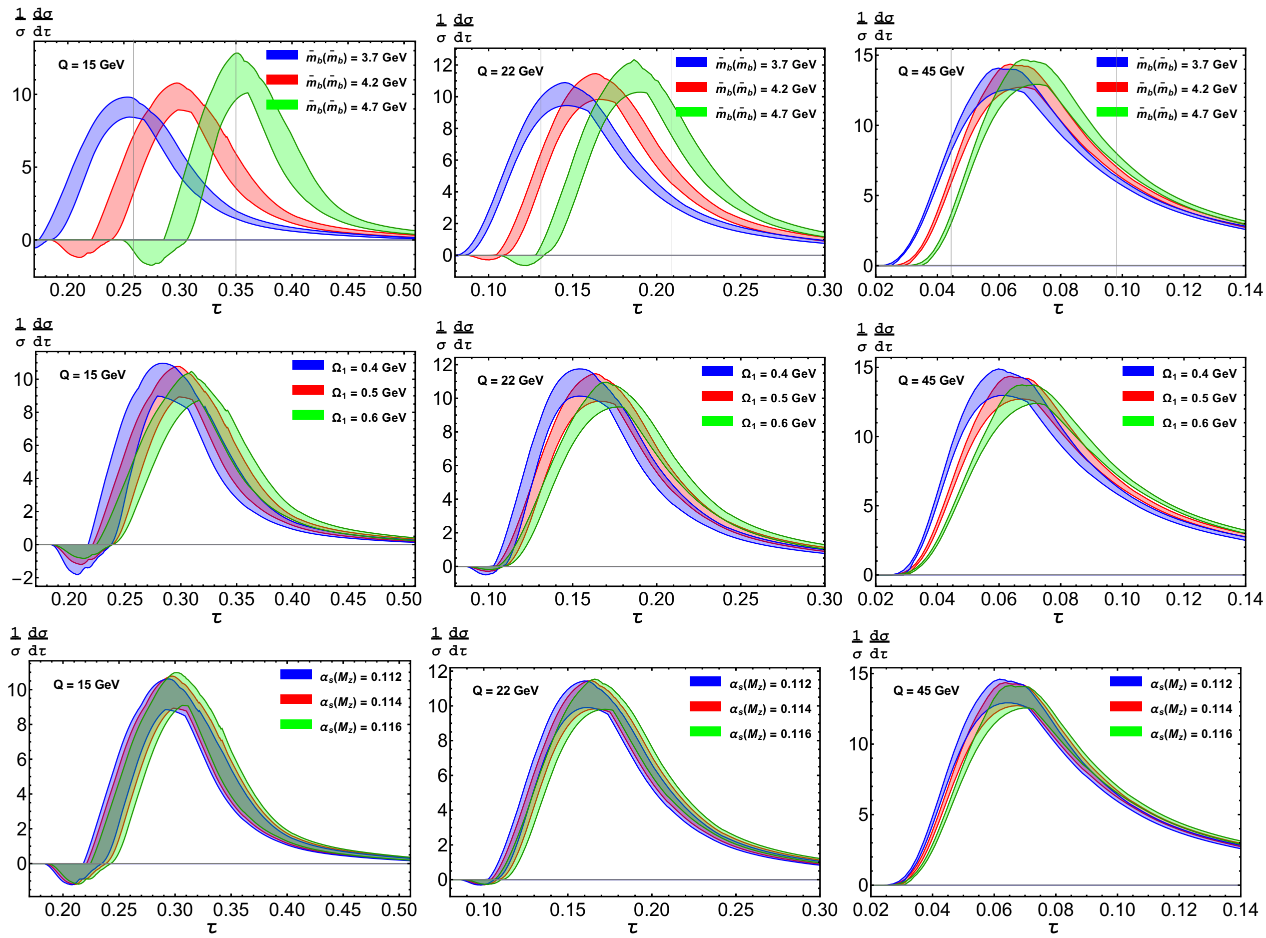

Figure 3.18: Sensitivity of the bottom thrust distribution at N^{2}LL order to the variation of the theoretical parameters at various energies. The theoretical uncertainty band is obtained by using 100 random scans over the theory parameters given in Tab. 3.4. We vary in the first row $\overline{m}_b(\overline{m}_b) = 4.2\,\mathrm{GeV}$ by $\pm 0.5\,\mathrm{GeV}$ while $\alpha_s(m_Z) = 0.114$ and $\overline{\Omega}_1(R_\Delta, \mu_\Delta) = 0.5$. In the second row we vary $\overline{\Omega}_1(R_\Delta, \mu_\Delta) = 0.5\,\mathrm{GeV}$ by $\pm 0.1\,\mathrm{GeV}$ when the mass and strong coupling constants are fixed, respectively to $\overline{m}_b(\overline{m}_b) = 4.2\,\mathrm{GeV}$ and $\alpha_s(m_Z) = 0.114$. In the third column we vary $\alpha_s(m_Z) = 0.114$ by ± 0.002 while we keep $\overline{m}_b(\overline{m}_b) = 4.2\,\mathrm{GeV}$ and $\overline{\Omega}_1(R_\Delta, \mu_\Delta) = 0.5\,\mathrm{GeV}$ unchanged. In all panels the red band is obtained from the central input parameters i.e. $\overline{m}_b(\overline{m}_b) = 4.2\,\mathrm{GeV}$, $\overline{\Omega}_1(R_\Delta, \mu_\Delta) = 0.5\,\mathrm{GeV}$ and $\alpha_s(m_Z) = 0.114$. The vertical gray lines in the first row of panel correspond to $X_{\mathrm{in/out}} = -0.5$ (left line) and $X_{\mathrm{in/out}} = 0.5$ (right line) which both indicate the thrust values where the relative size of the cross section is half of the peak height, see Sec. 3.11.1.

is more sensitive to the mass parameter (as it is of course expected) and the accuracy of the bottom mass extraction from the peak region is clearly better than 0.5 GeV. Note that the separation between the error bands is reduced in the tail region at all energies, showing the low sensitivity of the tail region to the bottom quark mass.

The second row of panels in Fig. 3.18 demonstrates the impact of varying the default value for the first moments of the soft function from $\overline{\Omega}_1(R_\Delta, \mu_\Delta) = 0.5\,\mathrm{GeV}$ by $\pm 0.1\,\mathrm{GeV}$. In this row, the various error bands show a considerable overlap and only at high energies the left side of the peak exhibits a visible separation between different colors. This leads us to the conclusion that the thrust distribution has less sensitivity to the nonperturbative parameter $\overline{\Omega}_1$ that might result to somewhat larger perturbative uncertainties when performing future fits.

The third row of panels in Fig. 3.18 illustrates the impact of varying the strong coupling constant from $\alpha_s(m_Z) = 0.114$ by ± 0.002 in the peak region. In this case all the respective error bands overlap entirely, except for a small range $0.03 < \tau < 0.06$ at $Q = 45\,\mathrm{GeV}$. We conclude that the sensitivity of the massive thrust to the coupling constant is substantially less than to the other theoretical parameters.

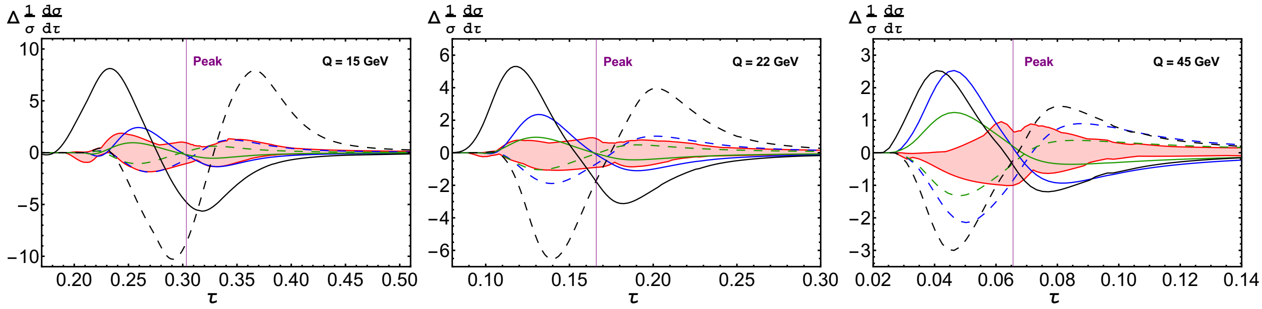

Figure 3.19: Comparison of the difference between the default bottom thrust distributions and the ones resulting by varying only one theory parameter. The red band is obtained after subtracting the default cross section from the theory scan for the cross section uncertainties. We vary $\alpha_s(m_Z) = 0.114$ by $-0.002(+0.002)$, displayed by the solid(dashed) green curves, $\overline{\Omega}_1(R_\Delta, \mu_\Delta) = 0.5\,\text{GeV}$ by $-0.1\,\text{GeV}(+0.1\,\text{GeV})$, displayed by the solid(dashed) blue curves, and $\overline{m}_b(\overline{m}_b) = 4.2\,\text{GeV}$ by $-0.5\,\text{GeV}(+0.5\,\text{GeV})$, displayed by the solid(dashed) black curves. The vertical purple line indicates the position of the peak for the default cross section.

So far we discussed the sensitivity of the thrust distribution to different theoretical parameters independently. In order to determine the capability of the method to extract various parameters from simultaneous fits to MC output (frequently called "data" in the following), we use Fig. 3.19 to visualize and compare the effect of various parameters on the cross section (different lines) in comparison with the theoretical uncertainty (red bands). The solid and dashed lines in Fig. 3.19 show the difference between the default bottom cross section and the ones that are yielded from varying one theory parameter, i.e. $\Delta_X(\mathrm{d}\sigma/\mathrm{d}\tau) = (\mathrm{d}\sigma/\mathrm{d}\tau)_\mathrm{X} - (\mathrm{d}\sigma/\mathrm{d}\tau)_\mathrm{def.}$ where $X \in \{m, \alpha_s, \overline{\Omega}_1\}$ refers to the parameter that is changed from the default value. The solid(dashed) green curves display the $\Delta_{\alpha_s}(\mathrm{d}\sigma/\mathrm{d}\tau)$ when we vary the default value $\alpha_s(m_Z) = 0.114$ by $-0.002(+0.002)$. The solid(dashed) blue curves illustrate the $\Delta_{\overline{\Omega}_1}(\mathrm{d}\sigma/\mathrm{d}\tau)$ when we vary the default value $\overline{\Omega}_1(R_\Delta, \mu_\Delta) = 0.5\,\text{GeV}$ by $-0.1\,\text{GeV}(+0.1\,\text{GeV})$. The solid(dashed) black curves show the $\Delta_m(\mathrm{d}\sigma/\mathrm{d}\tau)$ when we vary the default value $\overline{m}_b(\overline{m}_b) = 4.2\,\text{GeV}$ by $-0.5\,\text{GeV}(+0.5\,\text{GeV})$. The red band is obtained by subtracting the default cross section from the upper and lower edges of the error band obtained from the theory scan. The vertical purple line identifies the peak location in the default cross section.

In Fig. 3.19 the panel with $Q = 15\,\text{GeV}$ clearly shows that the relative changes in the cross section due to the bottom quark mass are dominant. It is clear that the major difference is arising from the shift in the peak region.[28] On the other hand, the changes due to $\overline{\Omega}_1$ and α_s variation are approximately covered everywhere by the theoretical uncertainties. In addition they reveal a similar behavior that indicates a degeneracy between these parameters, meaning that the effects of α_s on the cross section can be compensated by the changes in $\overline{\Omega}_1$ or vice verse. Hence this set of observations leads us to the conclusion that by using only the low energy data one can extract the bottom quark mass with high precision whereas the degeneracy of α_s and $\overline{\Omega}_1$ makes it difficult to determine them simultaneously with high precision. Furthermore due to the rather small size of relative changes one expects larger uncertainties for these parameters.

The panel with $Q = 22\,\text{GeV}$ in Fig. 3.19 illustrates a reduction in the relative differences between the $\Delta_m(\mathrm{d}\sigma/\mathrm{d}\tau)$ and the error band size. However, here the $\overline{\Omega}_1$ has a larger impact on the cross section. $\Delta_{\alpha_s}(\mathrm{d}\sigma/\mathrm{d}\tau)$ is still within the red error band. Therefore we conclude that by employing the data at intermediate energies in a fit we obtain a rather large uncertainty for the bottom mass in comparison with the low energy case. However a more precise measurement for $\overline{\Omega}_1$ is feasible.

Finally the last panel in Fig. 3.19 with $Q = 45\,\text{GeV}$ demonstrates an interesting situation, where the relative size of the changes due to m_b and $\overline{\Omega}_1$ are remarkably similar, indicating a high degeneracy between them. Here the impact of α_s has slightly increased such that the effects on the left side of the peak are distinct from the error band. However the $\Delta_{\alpha_s}(\mathrm{d}\sigma/\mathrm{d}\tau)$ curve still exhibits similar behavior

[28] In fact the peak position can also be used to extract the heavy quark mass [32,39]. However, by including the shape of the peak region we have increased the sensitivity of our method to the mass parameter.

to the $\Delta_{\overline{\Omega}_1}(\mathrm{d}\sigma/\mathrm{d}\tau)$ curve that infer the noted degeneracy between α_s and $\overline{\Omega}_1$. In this situation the simultaneous extraction of these theoretical parameters will result in large theoretical uncertainties for all parameters.

The obvious conclusion from these observations is that by combining the data from different energies one can simultaneously extract m_b and $\overline{\Omega}_1$ with high accuracy. The reason is that by performing the simultaneous fit using the available data for all ranges of energies, one obtains precise determinations for the mass variable from the low energy data, and consequently breaks the degeneracy between $\overline{\Omega}_1$ and m at high energies. This allows us to simultaneously determine $\overline{\Omega}_1$ with a better precision from the high energy data. Due to the apparent degeneracy between the effects of the strong coupling constant and the first moment of the model function on the cross section, we conclude that changes in $\overline{\Omega}_1$ can make up for the α_s effects such that one cannot extract α_s with good precision from the simultaneous fits. Hence it might be more convenient in future fits to fix the strong coupling constant as an external input and perform the fit for m and $\overline{\Omega}_1$. Note that the impact of m , α_s and $\overline{\Omega}_1$ in the tail region are comparable and the relative differences between $\Delta_{m,\alpha,\overline{\Omega}_1}(\mathrm{d}\sigma/\mathrm{d}\tau)$ and the error band sizes are substantially smaller than the peak region. Consequently we conclude that by including more data from the tail region we do not improve the precision of the results and we cannot resolve any degeneracies. Therefore at this accuracy it is more efficient to restrict the fitting procedures to the peak region.

Theoretical Uncertainties

Having demonstrated good control over the theoretical uncertainties of the bottom thrust distribution and explained the sensitivity of the results to different parameters of theory, we are now in the position to discuss the expected perturbative uncertainties in the MC mass determination using the thrust distribution.

To this end, here we use a simple χ^2 analysis, where we extract the heavy quark mass by fitting the theoretical thrust distribution (at NLL and N^{2}LL orders in the pole and MSR mass schemes) in the peak region to the most accurate theoretical predictions (i.e. at N^{2}LL order with the R-gap and MSR mass schemes) with the uncertainty bands obtained from the 100 random points in the theory parameter space. This analysis allows us to obtain an estimate of the theoretical uncertainty that can be achieved for the heavy quark mass determination. We stress that the following analysis and results should be considered only as a guideline for the more complicated actual fitting procedures and future analyses on the calibration of the MC top and bottom mass parameters.

For convenience let us first describe the notation that will be used in this section. We use a generic notation for the heavy quark mass i.e. m , to stress that the analysis can be applied analogously to both bottom and top quark productions. In the following analyses, we set the $\alpha_s(m_Z) = 0.114$ and $\overline{\Omega}_1(R_\Delta = 2, \mu_\Delta = 2) = 0.5\,\mathrm{GeV}$ as the fixed theoretical input parameters, so that we only concentrate on the heavy quark mass determination. We denote the resulting normalized thrust distribution (in the R-gap scheme) with

$$\frac{1}{\sigma}\frac{\mathrm{d}\sigma}{\mathrm{d}\tau}(\tau)\,[Q,m]\Big|^{X}_{n,j} . \tag{3.11.1}$$

Here, the subscript $n \in \{1,2\}$ indicates the order of logarithmic resummation in the singular contributions and the relevant nonsingular corrections in the partonic cross section, $\mathrm{N^nLL} + \mathrm{N^{n-1}LO}$. the subscript j denotes the scheme used for the heavy quark mass parameter in the theoretical description,

$$j = \begin{cases} 1 & \qquad\qquad \text{(Pole Mass Scheme)} \\ 2 & \qquad\qquad \text{(MSR Mass Scheme)} \end{cases} . \tag{3.11.2}$$

The superscript $X \in \{\mathrm{up.},\ \mathrm{low.},\ \mathrm{ave.},\ \mathrm{th.}\}$ in Eq. (3.11.1) is used for referring to a specific theoretical curve. The "up." and "low." labels, receptively, refer to the curves for the upper and lower edges of the error band of the distribution that are obtained from random variations of the parameters in the ranges given in Tab. 3.4 (illustrated in the first row of panels in Fig. 3.15). The "ave." indicates the resulting curve from taking the average of the upper and lower error band edges. As already said, in our fitting procedure we will use the most accurate theoretical description at different perturbative orders, i.e. $j = \{1, 2\}$, with $n = 2$, for the set of curves $X \in \{\text{up.}, \text{ low.}, \text{ ave.}\}$. Moreover we will fix the mass parameter in these distributions to a specific value $m = m_0$. The resulting distributions with theory errors will be employed instead of the data in the fitting procedure. The "$X = \text{th.}$" choice indicates the thrust distribution with variable n, j and m, where we use the default values for the theoretical parameters given in Tab. 3.4. The result for these choices will be used as the theory curve in our fitting procedure.

Our simple toy χ^2-analysis is based on the binning of the thrust distribution. We define the value of the thrust distribution in each bin as

$$R^i_{n,j}(Q,m)\big|^X \equiv \Big(\frac{1}{\Delta\tau(Q,m)}\Big) \int_{t^i_{\rm in}(Q,m)}^{t^i_{\rm out}(Q,m)} {\rm d}\tau' \, \frac{1}{\sigma}\frac{{\rm d}\sigma}{{\rm d}\tau}(\tau')[Q,m]\Big|^X_{n,j}\,, \tag{3.11.3}$$

where the superscript $i = 1, ..., n_{\rm bin}$ refers to the ith bin. The terms $t^i_{\rm in/out}(Q,m)$ are given by

$$\begin{aligned} t^i_{\rm in}(Q,m) &= \tau_{\rm in}(Q,m) + (i-1)\,\Delta\tau(Q,m)\,,\\ t^i_{\rm out}(Q,m) &= \tau_{\rm in}(Q,m) + i\,\Delta\tau(Q,m)\,, \end{aligned} \tag{3.11.4}$$

and

$$\Delta\tau(Q,m) = \frac{\tau_{\rm out}(Q,m) - \tau_{\rm in}(Q,m)}{n_{\rm bin}}\,, \tag{3.11.5}$$

is the size of bins. In order to adopt a common prescription for setting the $\tau_{\rm in/out}(Q,m)$ for different m and Q values, we use the additional variable $X_{\rm in/out}$ which represents the relative fraction of the size of the cross section at these thrust values w.r. to the peak height. We define the $X_{\rm in/out}$ variable using the following relation:

$$\frac{1}{\sigma}\frac{{\rm d}\sigma}{{\rm d}\tau}\Big(\tau_{\rm in/out}(Q,m)\Big)[Q,m] = \Big(1 - |X_{\rm in/out}|\Big)\,\frac{1}{\sigma}\frac{{\rm d}\sigma}{{\rm d}\tau}\Big(\tau_{\rm peak}(Q,m)\Big)[Q,m]. \tag{3.11.6}$$

where $X_{\rm in}$ and $X_{\rm out}$ are real numbers which can have positive or negative values. The negative (positive) value represents thrust values where the relative size of the cross section is $(1 - |X_{\rm in/out}|)$ of the peak height and are located on the left (right) side of the peak. For instance based on this definition, for each pair of Q and m the $X_{\rm in} = -0.5$ ($X_{\rm in} = +0.5$) corresponds to the $\tau_{\rm in}(Q,m) < \tau_{\rm peak}(Q,m)$ ($\tau_{\rm in}(Q,m) > \tau_{\rm peak}(Q,m)$) at which the height of the distribution is half of the peak height, see Fig. 3.11.1. Following this notation we simplify the task of addressing specific thrust values for all possible masses and energies for which the value of the distribution takes a certain fraction of the peak height. e.g. by referring to $X_{\rm in} = 0$ we simply indicate the peak position of the thrust distribution for any Q and m values.

After presenting the above notation, we are ready to describe our fitting procedure. Our χ^2 function reads

$$\chi^2_{n,j}(m) = \sum_Q \chi^2_{n,j}(Q,m)\,, \quad \text{with} \quad \chi^2_{n,j}(Q,m) = \frac{1}{n_{\rm bin}} \sum_{i=1}^{n_{\rm bin}} \left(\frac{R^i_{2,2}(Q,m_0)\big|^{\rm av.} - R^i_{n,j}(Q,m)\big|^{\rm th.}}{\Delta R^i_{n,2}(Q,m_0)\big|^{\rm av.}} \right)^2, \tag{3.11.7}$$

and

$$\begin{aligned} R^i_{2,2}(Q,m_0)\big|^{\rm av.} &= \frac{R^i_{2,2}(Q,m_0)\big|^{\rm up.} + R^i_{2,2}(Q,m_0)\big|^{\rm low.}}{2}\,,\\ \Delta R^i_{n,2}(Q,m_0)\big|^{\rm av.} &= \frac{R^i_{n,2}(Q,m_0)\big|^{\rm up.} - R^i_{n,2}(Q,m_0)\big|^{\rm low.}}{2}\,. \end{aligned} \tag{3.11.8}$$

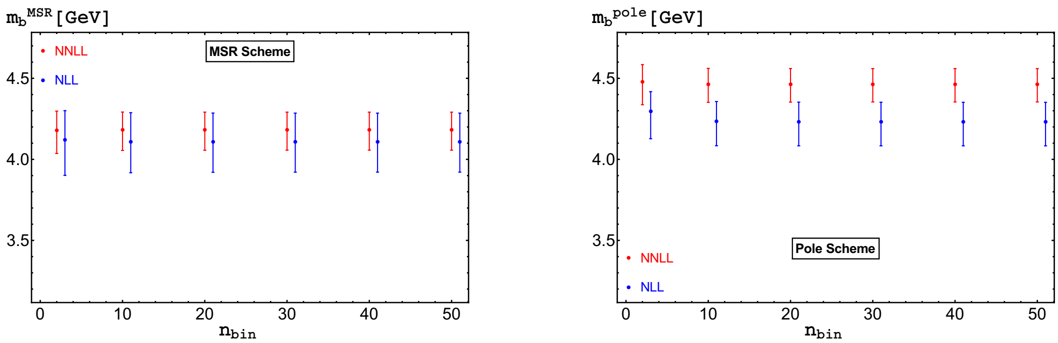

Figure 3.20: Bottom mass values and corresponding theoretical uncertainties at N^{2}LL (red) and NLL (blue) orders using the fitting procedure explained in the text. The left and right panels, respectively, illustrate the extracted mass in the MSR and pole mass schemes using different number of bins. For the input reference mass we use the $m_0 = m_b^{\rm MSR}(m_b^{\rm MSR}) = 4.2\,\text{GeV}$. Here, $m_b^{\rm MSR}(m_b^{\rm MSR})$ is abbreviated to $m_b^{\rm MSR}$. The respective numerical values for the MSR mass analysis results are given in Tab. 3.6 .

$n_{\rm bin}$	2	10	20	30	40	50
			$n=1$ (NLL)			
$m_b^{\rm MSR}$	4.1219	4.1110	4.1101	4.1099	4.1098	4.1098
$\Delta m_b^{\rm MSR}$	$-0.2205\vert 0.1785$	$-0.1932\vert 0.1768$	$-0.1895\vert 0.1756$	$-0.1888\vert 0.1753$	$-0.1885\vert 0.1753$	$-0.1884\vert 0.1752$
			$n=2$ (N^{2}LL)			
$m_b^{\rm MSR}$	4.1818	4.1825	4.1825	4.1826	4.1826	4.1826
$\Delta m_b^{\rm MSR}$	$-0.1453\vert 0.1158$	$-0.1274\vert 0.1094$	$-0.1261\vert 0.1087$	$-0.1258\vert 0.1086$	$-0.1257\vert 0.1085$	$-0.1256\vert 0.1085$

Table 3.6: Numerical values for bottom mass determinations at N^{2}LL and NLL orders using the fitting procedure explained in the text. For the input reference mass we use the $m_0 = m_b^{\rm MSR}(m_b^{\rm MSR}) = 4.2\,\text{GeV}$. Here, $m_b^{\rm MSR}(m_b^{\rm MSR})$ is abbreviated to $m_b^{\rm MSR}$. All numbers are given in units of GeV . The results in this table are visualized in Fig. 3.20 .

For the bottom mass analysis we set the reference mass value to $m_0 = \overline{m}_b(\overline{m}_b) = 4.2\,\text{GeV}$. Note that in Eq. (3.11.7) we take the most accurate theoretical cross section at N^{2}LL in the MSR mass scheme as the central values of the data in each bin, $R^i_{2,2}(Q,m_0)\big|^{\rm av.}$. For the perturbative QCD error $\Delta R^i_{n,2}(Q,m_0)\big|^{\rm av.}$, we take the MSR mass scheme however we set the resummation order n equal to the corresponding order in the theory curves $R^i_{n,j}(Q,m)\big|^{\rm th.}$.[29] Based on this fitting procedure, we can correctly estimate the theoretical uncertainties for the MSR mass extractions at NLL and N^{2}LL order. We employ this method for a pole mass analysis, to show the instability between the corresponding mass results at different orders.

We find out the best fit value, namely $m_{\rm min}$, minimizing the $\chi^2_{n,j}(m)$ function. In order to determine the theoretical uncertainty, we use $\chi^2_{\rm min}+1$ prescription, solving the following equation

$$\chi^2_{n,j}(m_{\rm min} \pm \Delta m) = \chi^2_{n,j}(m_{\rm min}) + 1\,, \tag{3.11.9}$$

for Δm . The results for $\pm\Delta m$ represent the up/down theoretical errors. We note that the theoretical uncertainties that are determined from this method should be interpreted with a bit of caution because they are based on 100 random points in the theory parameter space. By increasing the number of random points to 500 as used in similar analyses [155, 156, 158] , the theoretical error might come out slightly large.

It is clear from the notation that the best fit value for the mass $m_{\rm min}$ and its theoretical uncertainty $\pm\Delta m$ depends on the resummation order and the mass scheme used for the fit. However, to simplify the notation and avoid further labels for m , we will indicate the results for the extracted mass in the pole and MSR scheme with the conventional notation used so far and note the resummation order

[29] In other words, here we fit the theoretical cross section $R^i_{n,j}(Q,m)\big|^{\rm th.}$ to the error band average, produced from the random theory scan for the most accurate theoretical predictions $R^i_{2,2}(Q,m_0)\big|^{\rm av.}$ with the uncertainties $\Delta R^i_{n,2}(Q,m_0)\big|^{\rm av.}$.

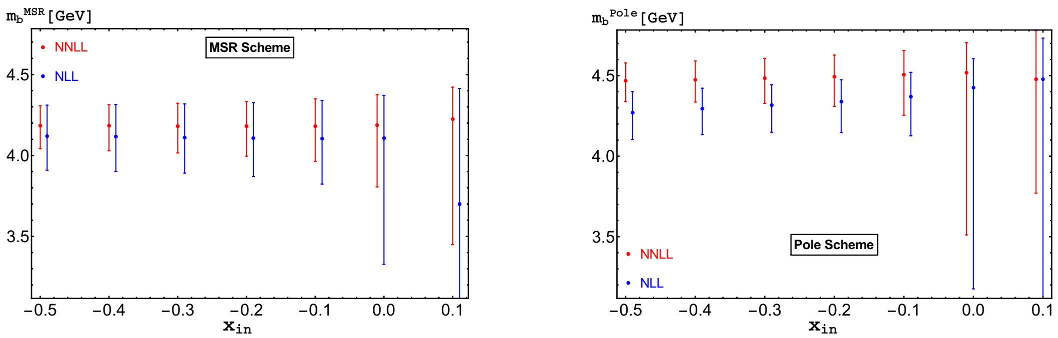

Figure 3.21: Bottom mass values and corresponding theoretical uncertainties at $\mathrm{N^2LL}$ (red) and NLL (blue) orders using the fitting procedure for the bottom thrust distribution explained in the text. The left and right panels display the fit results for different X_{in} values when we use the MSR and pole mass scheme for the theory, respectively. For the input reference mass we use the $m_0 = m_b^{\mathrm{MSR}}(m_b^{\mathrm{MSR}}) = 4.2\,\mathrm{GeV}$. Here, the term m_b^{MSR} refers to the $m_b^{\mathrm{MSR}}(m_b^{\mathrm{MSR}}) = \bar{m}_b(\bar{m}_b)$.

explicitly. In the MSR mass scheme case where $m = m^{\mathrm{MSR}}(R_m)$, one has to assign a reference scale for R_m. In the following analyses with the MSR mass scheme, the references scales are set as follows: $m = m_b^{\mathrm{MSR}}(m_b^{\mathrm{MSR}}) = \overline{m}_b(\overline{m}_b)$ for the bottom determination, and $m = m_t^{\mathrm{MSR}}(5\,\mathrm{GeV})$ for the top mass determination. In the pole mass analysis, we use $m = m_{b/t}^{\mathrm{pole}}$. Not that m indicates the mass parameter in the theory prediction used for the mass extraction, see Eq. (3.11.7). Furthermore one needs to set a reference value for the mass in the theory prediction used for obtaining the toy data in the fit, denoted with m_0. In our bottom and top analyses we use the $m_0 = 4.2\,\mathrm{GeV}$ and $m_0 = 168.8\,\mathrm{GeV}$, respectively.

Let us start the discussion on the mass analysis, by pointing out that the χ^2-function given in Eq. (3.11.7) is normalized with the number of bins. In fact, we found that by using the ordinary χ^2-function (that does not have the normalization factor), the size of resulting theoretical uncertainties reduces when increasing the number of bins. It turns out that this effect can be compensated by inserting the normalization factor $1/n_{\mathrm{bin}}$ in the χ^2-function definition, leading to stable results for the theoretical uncertainties in the mass determination. This stability is displayed in the left panel of Fig. 3.20 where we illustrated the fit values for the MSR bottom mass determination at both NLL (blue) and $\mathrm{N^2LL}$ (red) orders with respect to the number of bins. For the analysis shown in this plot, we used the thrust distribution in the peak region at $Q = \{15, 22, 45\}\,\mathrm{GeV}$. To set the intervals of fit region for all energies we fix $X_{\mathrm{in}} = -0.5$ and $X_{\mathrm{out}} = +0.5$ which is the interval between the two vertical gray lines shown in the first row of panel in Fig. 3.11.1. The respective numerical values are summarized in Tab. 3.6. Note that the theoretical uncertainties are asymmetric and the positive error values are more stable (and smaller) than the negative error values. Furthermore, the result at various resummation orders exhibit a good convergence and the difference between the best fit values for m_{min} at NLL and $\mathrm{N^2LL}$ is small.

For the sake of comparison, we also carry out a pole mass analysis, illustrated in the right panel of Fig. 3.20. Here, one can clearly see a significant discrepancy of $\mathcal{O}(250\,\mathrm{MeV})$ between the best fit values for m_{min} at NLL and $\mathrm{N^2LL}$ orders.[30] This feature was already anticipated in the convergence studies, visualized in the fourth row of panels in Fig. 3.15. This observation stresses once more that by using the MSR mass scheme we obtain more stable and reliable mass determinations at different orders of perturbation theory.

In the rest of this analysis we examine the sensitivity of the results to the fitting range window i.e. controlled by the X_{in} and X_{out} variables. Fig. 3.21 shows the results for the MSR (left panel) and pole (right panel) bottom mass determination at both NLL (blue) and $\mathrm{N^2LL}$ (red) orders for

[30] We remind the reader that in the pole mass analyses, we fit the theoretical cross section in the pole mass scheme to the data which is taken from the the MSR scheme predictions. Hence, the illustrated error bars in the pole mass analyses are related to the error bands in the MSR scheme predictions.

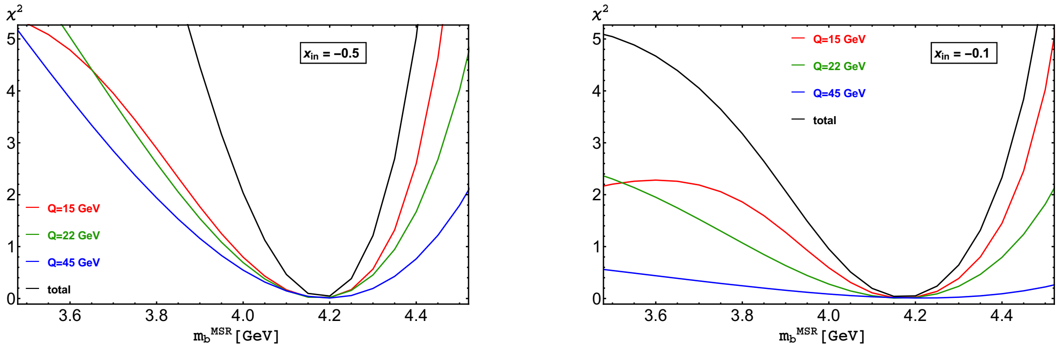

Figure 3.22: χ^2-functions for the simple fitting procedure, explained in the text, using the bottom thrust distribution at different energies. The left and right panels display the χ^2-functions for $X_{\rm in} = -0.5$ and $X_{\rm in} = -0.1$, respectively. For the input reference mass we use the $m_0 = m_b^{\rm MSR}(m_b^{\rm MSR}) = 4.2\,{\rm GeV}$. Here, $m_b^{\rm MSR}(m_b^{\rm MSR})$ is abbreviated to $m_b^{\rm MSR}$.

$Q = \{15, 22, 45\}\,{\rm GeV}$. In this plot we vary the range of fitting by taking different $X_{\rm in}$ values while we keep the $X_{\rm out} = 0.3$ unchanged. As a guideline to interpret this plot, we note that $X_{\rm in} > 0$ means that we do not include the peak of thrust distribution in the fitting procedure, $X_{\rm in} \simeq 0$ means that we fit only for the right half of the peak region and $X_{\rm in} < 0$ means that we have included more fractions of the peak region on the left side in the fit range. This setting is adopted for all energies which are used for the fit. In Fig. 3.22 we display the corresponding $\chi^2_{2,2}(Q, m)$-functions for two choices, $X_{\rm in} = -0.5$ (left panel) and $X_{\rm in} = -0.1$ (right panel). The red, blue, green curves illustrate the $\chi^2_{2,2}(15\,{\rm GeV}, m)$, $\chi^2_{2,2}(22\,{\rm GeV}, m)$ and $\chi^2_{2,2}(45\,{\rm GeV}, m)$. The black curve displays $\chi^2_{2,2}(m)$-function that is obtained from summing the χ^2 values for the three energies.

Based on the result observed in Fig. 3.21 and 3.22 we draw the following conclusions:

i) By including the peak region of the thrust distribution in the fitting procedure we obtain smaller theoretical uncertainties and more accurate determinations for mass values. This behavior is dictated by the steeper χ^2-functions as illustrated by the $X_{\rm in} = -0.5$ case in comparison with the $X_{\rm in} = -0.1$ case, shown in Fig. 3.22 . This result manifests the high mass sensitivity of the peak position that has been frequently referenced in previous sections as the appropriate observable to determine the mass of heavy quarks.

ii) In the left panel of Fig. 3.21 we observe that the results for $X_{\rm in} < -0.2$ are stable in the sense that the best fit value and relative theoretical uncertainties are not changing significantly by further reducing the $X_{\rm in}$ variable. This is a very important information for the future MC calibration, expressing that as for the fit range one needs to consider a sufficient size for a window over the peak region in order to obtain reliable results for mass determination.

iii) The result in Fig. 3.22 clearly demonstrates the higher sensitivity of our method for heavy quark mass determination at lower energies. Note that the illustrated χ^2-functions in this plot are asymmetric which leads to asymmetric theoretical errors for the fit values.

iv) By using the pole mass scheme, one obtains significant discrepancies between the best fit values $m_{\rm min}$ at NLL and N^{2}LL [see the right panel in Fig. 3.21]. This systematic difference is a clear evidence for the instabilities that arises from the renormalon ambiguities in this scheme. In contrast, the MSR mass analysis, shown in the left panel of Fig. 3.21 , exhibits a very good perturbative convergence between the mass values obtained at different resummation orders.

To conclude this section, based on the above discussion, we take the theoretical uncertainty given in the 4th column of Tab. 3.6 (where we use $n_{\rm bin} = 20$ and set the fit range to $X_{\rm in} = -0.5$ and

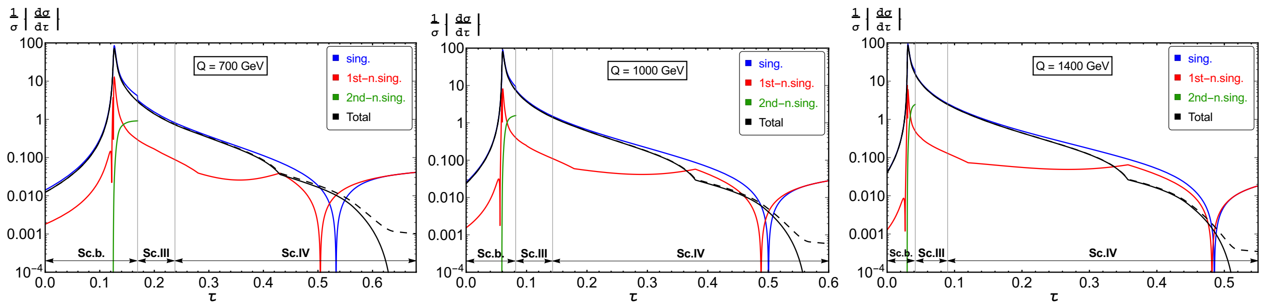

(a) Unstable Top Production

Figure 3.23: Singular and nonsingular contributions of the unstable top thrust distribution at various energies at N^{2}LL and including nonperturbative effects in the R-gap scheme. We use the default set of theoretical parameters for the top cross section given in Tab. 3.5 with $\alpha_s(m_Z) = 0.114$, $\overline{\Omega}_1(R_\Delta, \mu_\Delta) = 0.5\,\text{GeV}$ and $\overline{m}_t(\overline{m}_t) = 160\,\text{GeV}$. "1st-n.sing." and "2nd-n.sing." indicate the first and second type nonsingular components, respectively [see Sec. 3.5]. Here the subdominant singularities are not absorbed into the factorization theorem ($sing = 0$).

$X_{\text{out}} = 0.5$) as the final results of the theoretical error,

$$\Delta m_b^{\text{MSR}} \simeq \begin{array}{c} +0.18 \\ -0.19 \end{array} \text{GeV}\,, \quad \text{at NLL}\,,$$

$$\Delta m_b^{\text{MSR}} \simeq \begin{array}{c} +0.11 \\ -0.13 \end{array} \text{GeV}\,, \quad \text{at N}^2\text{LL}\,.$$

3.11.2 Unstable Top Analysis

Thrust Distribution: Singular v.s. Nonsingular Components

In this section we illustrate the relative size of singular and nonsingular contributions in different regions of the thrust distribution for the unstable top production. As explained in Sec. 3.8 to obtain the unstable top cross section one can employ an additional smearing of the stable thrust distribution with the Breit-Wigner function in the bHQET region to incorporate the finite width effects. To this end we applied the finite smearing to all singular contributions that are appearing in the bHQET regime in the peak region. Although this method provides a good description in the peak region, it fails to provide a continuous description between the bHQET regime and scenario III. Therefore to avoid this problem we construct a τ dependent function for the total width, denoted with $\Gamma_t(\tau)$, using a piecewise function in analogy with the profile function for the soft renormaliztion scale, such that it has a finite fixed value in the peak region and smoothly tending to zero in the far tail region, turning off the width effects. We refer to $\Gamma_t(\tau)$ as the total width profile function. Our profile function for the total width read

$$\Gamma_t(\tau) = \begin{cases} \Gamma_t^i & \tau < t_b \\ \zeta(\Gamma_t^i,\, 0,\, t_b,\, t_m,\, t_c,\, \tau) & t_b \le \tau \le t_c \\ 0 & t_c \le \tau \end{cases}. \tag{3.11.10}$$

where $\Gamma_t^i = 1.5\,\text{GeV}$ is the initial value for the top width employed in the peak region. Here we make use of the double quadratic function ζ given in Eq. (3.10.14) to smoothly connect the two flat functions Γ_t^i and 0 at the borders of the scenarios t_b and t_c.

In Fig. 3.23 we show the resulting cross sections for the unstable top production. Here we display different components of the thrust distribution at N^{2}LL using the default theoretical inputs and parameters given in Tab. 3.5. Note that in this case we do not absorb the subdominant singularities in the factorization theorems ($sing = 0$). We incorporate the finite width effects using the total width profile function in Eq. (3.11.10). We use the R-gap scheme for the nonperturbative model function

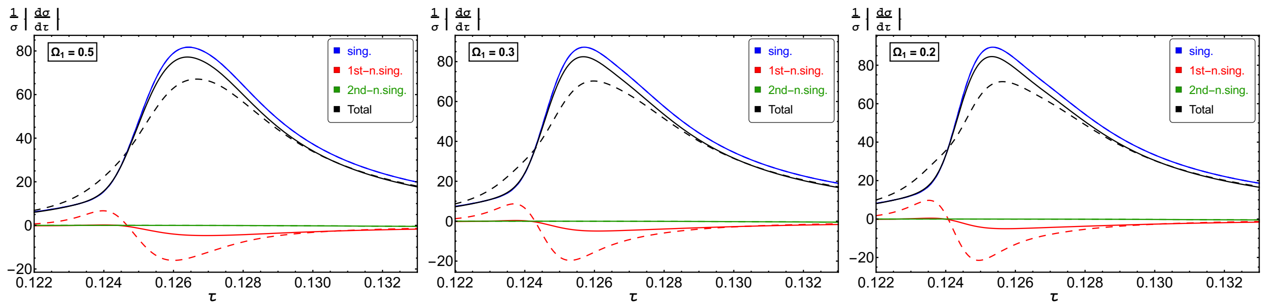

(a) Unstable Top Production

Figure 3.24: Singular and nonsingular contributions of the unstable top thrust distribution at N^{2}LL including nonperturbative effects in the R-gap scheme, when the subdominant singularities are absorbed ($sing = 1$), displayed with solid lines, or not absorbed ($sing = 0$), displayed with dashed lines. Here we set $e_h = 2$. For the rest of the theoretical parameters we use the default values given in Tab. 3.5 with $\alpha_s(m_Z) = 0.114$ and $\overline{m}_t(\overline{m}_t) = 160\,\mathrm{GeV}$. The left, center and right panels are obtained by setting $\overline{\Omega}_1(R_\Delta, \mu_\Delta) = 0.5\,\mathrm{GeV}$, $\overline{\Omega}_1(R_\Delta, \mu_\Delta) = 0.3\,\mathrm{GeV}$ and $\overline{\Omega}_1(R_\Delta, \mu_\Delta) = 0.2\,\mathrm{GeV}$, respectively. "1st-n.sing." and "2nd-n.sing." indicate the first and second type nonsingular components, respectively.

and the MSR mass scheme for the mass parameter. The red and green curves illustrate the first and second type of nonsingular components, respectively. The sum of the singular (solid blue) and nonsingular components gives the total thrust distribution (solid black). For the sake of comparison we also display the total thrust distribution using a constant value for the top width i.e. $\Gamma_t = 1.5\,\mathrm{GeV}$. The resulting cross sections are shown with the black dashed curves. The gray lines indicate the borders of kinematical scenarios.

The behavior of different components for the top cross section is similar to the bottom ones. In the peak region the singular contributions are dominant. In the tail region the relative size of the singular and the first type of nonsingular contributions are of the same order. In the far-tail region the singular and nonsinular contributions appear with the same size and opposite signs, canceling each other and consequently the total thrust distribution falls rapidly to zero. Furthermore, the difference between the solid and the dashed black lines in Fig. 3.23 clearly demonstrates the effects of finite width in the multijet region. It is easy to see that by using the profile function in Eq. (3.11.10) we achieved a perfect cancellation between singular and nonsingular pieces whereas by employing the constant finite width this cancellation is deteriorated. Note that the cross sections for these two cases are in good agreement in the region where $\tau < 0.5$. Therefore for the analyses carried out in Sec. 3.11.2 and Sec. 3.11.2 where we concentrate on the peak region, we employ the constant top width $\Gamma_t = 1.5\,\mathrm{GeV}$. This choice is only applied for convenience and will not affect the discussion and conclusion in the following sections.

In the rest of this section we study the effects of the subleading contributions for $sing = 0(1)$ on the unstable top cross section. In Fig. 3.24 we illustrate different components of the thrust distribution in the peak region at $Q = 700\,\mathrm{GeV}$ for $sing = 0$ (solid lines) and $sing = 1$ (dashed lines) using different values for the first moment of the soft model function. The left, center and right panels illustrate the cross section when the first moment of the soft model function at the reference scales $R_\Delta = \mu_\Delta = 2\,\mathrm{GeV}$ is set to $\overline{\Omega}_1(R_\Delta, \mu_\Delta) = 0.5\,\mathrm{GeV}$, $\overline{\Omega}_1(R_\Delta, \mu_\Delta) = 0.3\,\mathrm{GeV}$ and $\overline{\Omega}_1(R_\Delta, \mu_\Delta) = 0.2\,\mathrm{GeV}$, respectively. We set $e_h = 2$ since the impact of $sing = 0$ is more enhanced and leads to clear oscillating pattern in the threshold region. The rest of the theoretical parameters are set to the default values. Since the singular and the second type of nonsingular contributions are independent of $sing$ we only display one solid blue and one solid green curve in each panel.

From Fig. 3.24 one can see that the first type of nonsingular contributions with $sing = 0$ exhibits a smooth oscillating pattern close to the threshold. In fact, for unstable top production, the additional smearing with the finite top width effects is suppressing the subdominant singularities. On the other hand, the solid red curves in Fig. 3.24 illustrating the first type of nonsingular contributions with

$sing = 1$, show a stable behavior in all panels, obtained from the suppression of the subdominant singularities that are absorbed in the factorized cross section. Thus based on these observations we conclude that both $sing = 0$ and $sing = 1$ are in principle applicable. In order to determine whether one of these choices is more preferable, we provide a further examination of the convergence between the corresponding thrust distribution at different orders of resummation. In the next section it will be shown that the $sing = 0$ case displays a slightly better perturbative convergence.

Perturbative Convergence Examinations

In analogy with the bottom analysis here we present the perturbative behavior of the thrust distribution for unstable top quark production. The discussion in this section is organized as follows. First we examine the impact of using different values for $sing$, r_s, μ_0, R_0 and e_J on the convergence between the distributions at different orders of resummation. The cross sections for these cases are collected in Figs. 3.25 and 3.26, showing the peak and tail region of the distribution, respectively. In Fig. 3.27 we provide a closer comparison between the results of two different choices for e_J at NLL and $\mathrm{N^2LL}$. In Fig. 3.28, we illustrate the resulting distributions without implementing the gap parameter and the results using the pole mass scheme for the top quark mass.

We stress that, for the rest of the numerical results that will be presented in the unstable top quark analysis we use the flat profile function for the finite width $\Gamma_t = 1.5\,\mathrm{GeV}$. The reason is that in the following discussions we mainly concentrate on the peak region where the choice of top width profile function is not relevant and it is adequate to set it to a constant value, see Fig. 3.23. In particular for the special cases where the tail behavior matters (e.g. in the r_s examination) we have verified that using both profile functions lead to fully consistent results and the same conclusions.

The first row of panels in Figs. 3.25 and 3.26 shows the unstable top cross section using the default theoretical values as given in Tab. 3.5. The results exhibit good convergence between the NLL and $\mathrm{N^2LL}$ error bands in both peak and tail. The fact that this behavior persist at all energies coveys that the suggested parametrization of the profile functions has the appropriate energy dependence. In addition, note that we have employed the same profile functions for the bottom and the top quark cross sections. Thus, the perturbative convergence of the results indicates that we have properly accounted for the mass effects in various ingredients of the profile functions.

In the second row of panels in Figs. 3.25 and 3.26 we display the cross section for $sing = 1$. Here one can see that the overlap between the NLL (green band) and $\mathrm{N^2LL}$ error bands (red band) is worse than the default cross section with $sing = 0$ where the $\mathrm{N^2LL}$ error bands are almost entirely contained in the NLL error bands at all energies. It is clear that, as expected, the major discrepancies are appearing on the left side of the peak, close to the threshold of the cross section. On the other hand, the effects are negligible in the tail region. This behavior leads us to conclude that the $sing = 0$ choice has a better perturbative convergence and the results at various orders are clearly more consistent.

Next, we examine the impact of using $r_s = 1$ instead of $r_s = 2$ on the convergence of the unstable top cross section. The results in the peak and tail regions, shown in Fig. 3.25 and 3.26, indicate similar features of the bottom cross section, where the height of the cross section for the slope 1 case is reduced and the cross section falls down in the tail region more gradually. As a result, the NLL band does not cover the $\mathrm{N^2LL}$ band in the slope 1 case, neither in the peak, nor in the tail. This behavior is more significant at low energies. These observations acknowledge that the choice $r_s = 2$ leads to a better perturbative convergence for the unstable top cross section.

In the top profile function, presented in Tab. 3.5, we set the jet trumpet parameter to negative values where the default is $e_J = -1.5$ and varied by ± 1.5. Note that this implies the same variation for the bHQET scale since we set $e_b = e_J$. However, it would seem natural to set $e_J = 0$, which is also used for the default profile function of bottom and massless thrust in order to recover the exact canonical relations between the jet, soft and hard scales so that the logarithmic terms like $\ln(\mu_J^2/\mu_H\mu_S)$ and $\ln(\mu_b\mu_m/\mu_H\mu_S)$ in the factorization theorems are eliminated. Here, we examine the impact of these choices of e_J on the unstable top thrust distribution.

To this end, in the fourth row of panels in Figs. 3.25 and 3.26 we display the resulting cross section

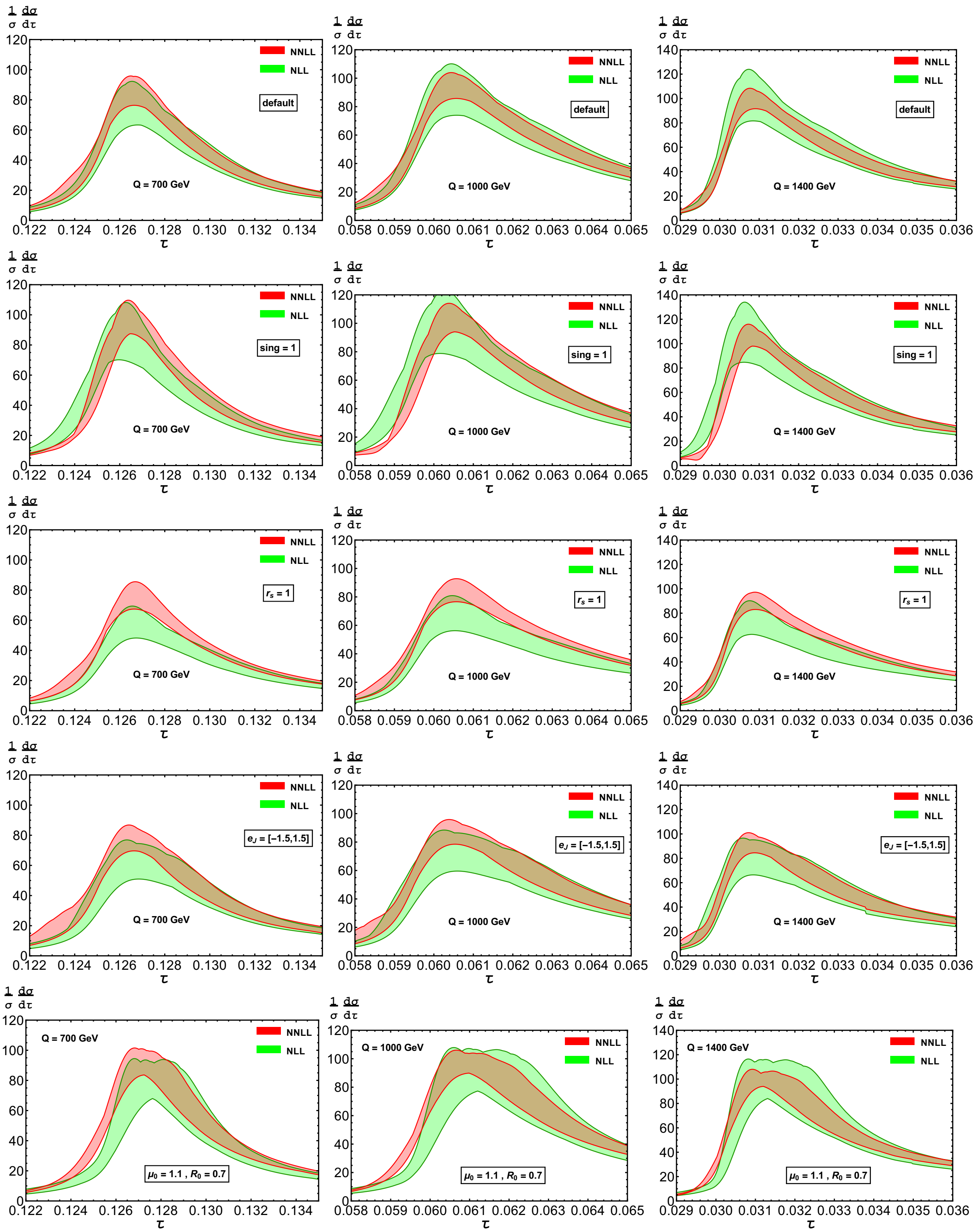

Figure 3.25: Theory scan for the thrust distribution uncertainties of the unstable top production in the peak region at various energies with resummation at N^{2}LL(red) and NLL(green). Here we display the hadronic cross sections when: we use the default theoretical parameters given in Tab. 3.5 (1st row), we set $sing = 1$ (2nd row), we set $r_s = 1$ (3rd row), the $e_{J/B} = 0$ is taken as default value and varied between -1.5 to 1.5 (4th row), we take $\mu_0 = 1.1\,\text{GeV}$ and $R_0 = 0.7\,\text{GeV}$ (5th row).

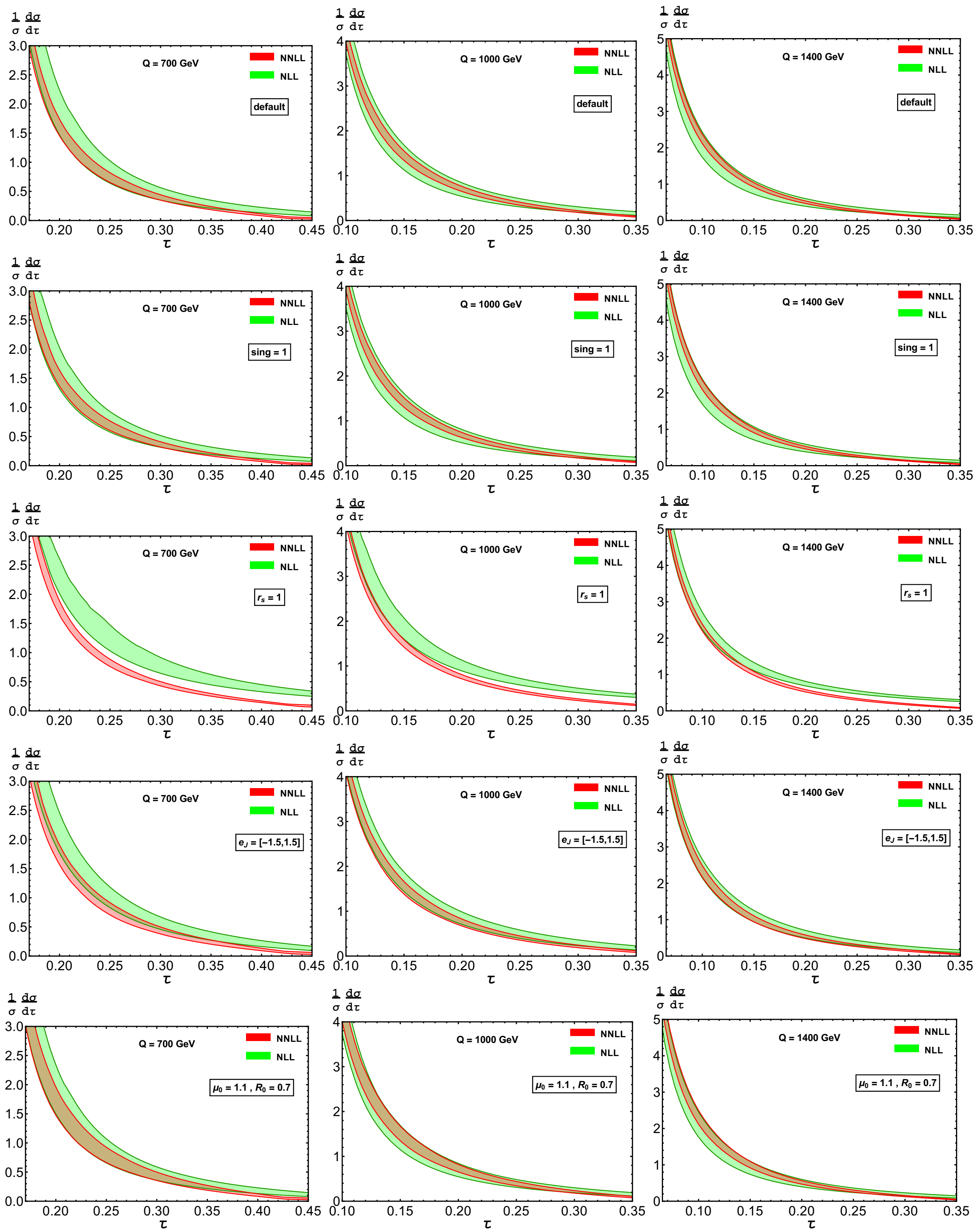

Figure 3.26: Theory scan for the thrust distribution uncertainties of the unstable top production in the tail region at various energies with resummation at N^{2}LL(red) and NLL(green). We display the hadronic cross sections when: we use the range of values in Tab. 3.5 (1st row), we set $sing = 1$ (2nd row), we set $r_s = 1$ (3rd row), the $e_{J/B} = 0$ is taken as default value and varied between -1.5 to 1.5 (4th row), we take $\mu_0 = 1.1\,\text{GeV}$ and $R_0 = 0.7\,\text{GeV}$ (5th row).

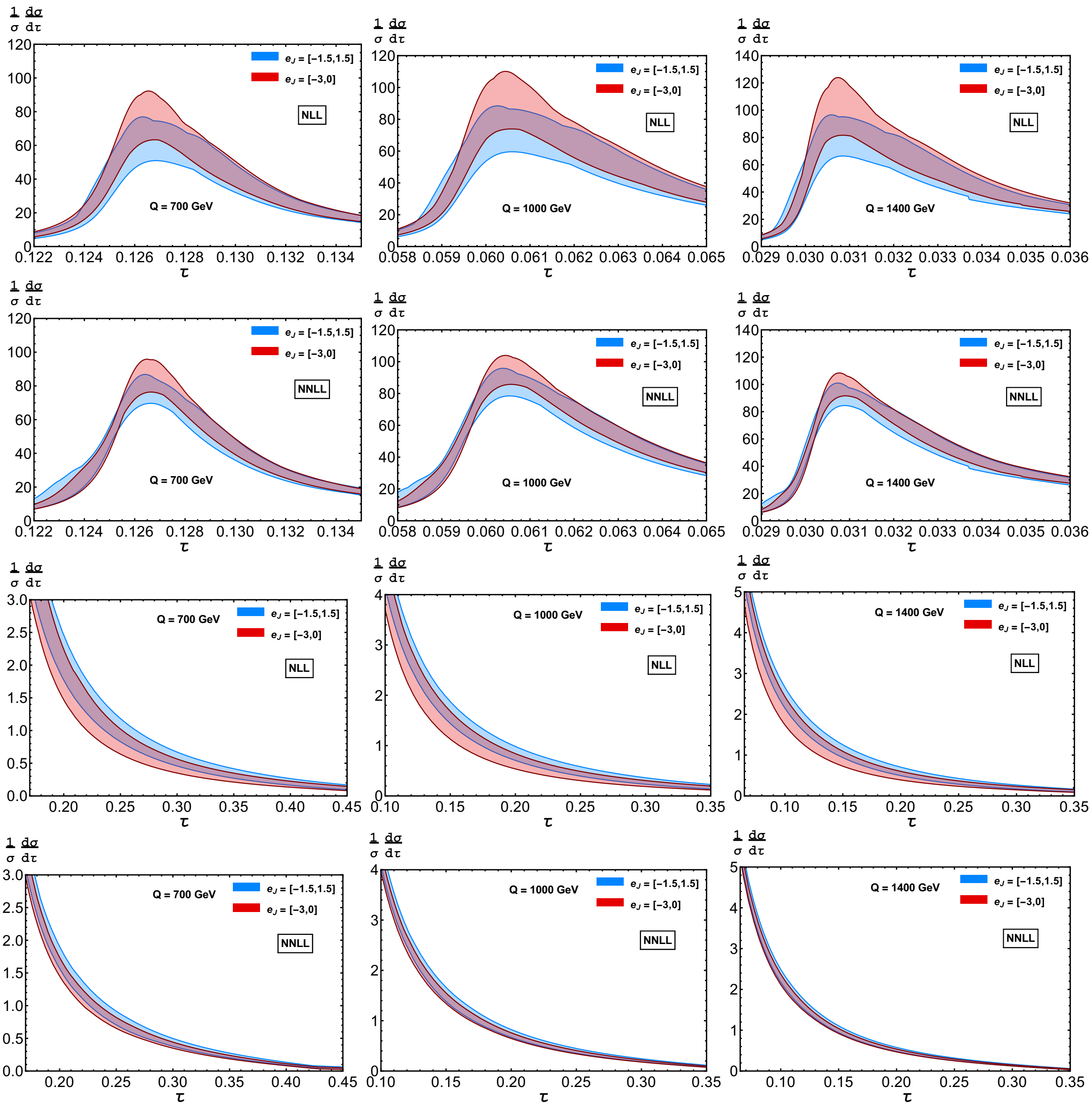

Figure 3.27: Theory scan for the thrust distribution uncertainties of the unstable top production in the peak (1st and 2nd rows) and tail (3rd and 4th rows) regions at various energies. The resummation order is explicitly indicated in each panel. The blue and red error bands are obtained by taking 100 random points using the $e_J = [-1.5, 1.5]$ and $e_J = [-3, 0]$ ranges of variation for the jet trumpet parameter. The rest of theoretical parameters are taken according to the default set in Tab. 3.5 .

by setting $e_J = 0$ as the default values, in the peak and tail region, respectively. The error bands are obtained by taking 100 random points using the modified range of variation for e_J in the interval $[-1.5, 1.5]$. The rest of theoretical parameters are taken according to default set in Tab. 3.5 . The results illustrate that the NLL error bands are slightly below the N^{2}LL error bands in the peak region, whereas the situation in the tail region is reversed and the red error bands cover the lower edge of the green band (at $Q = 700\,\text{GeV}$ they have marginal overlap). In contrast the results in the default panels where $e_J \in [-3, 0]$, exhibit a better perturbative convergence between the red and green bands. Thus from this set of plots we conclude that $e_J \in [-3, 0]$ is a more appropriate range of variation for the jet trumpet parameter.

To understand the origin of the visible improvement for $e_J \in [-3, 0]$ over the case $e_J \in [-1.5, 1.5]$,

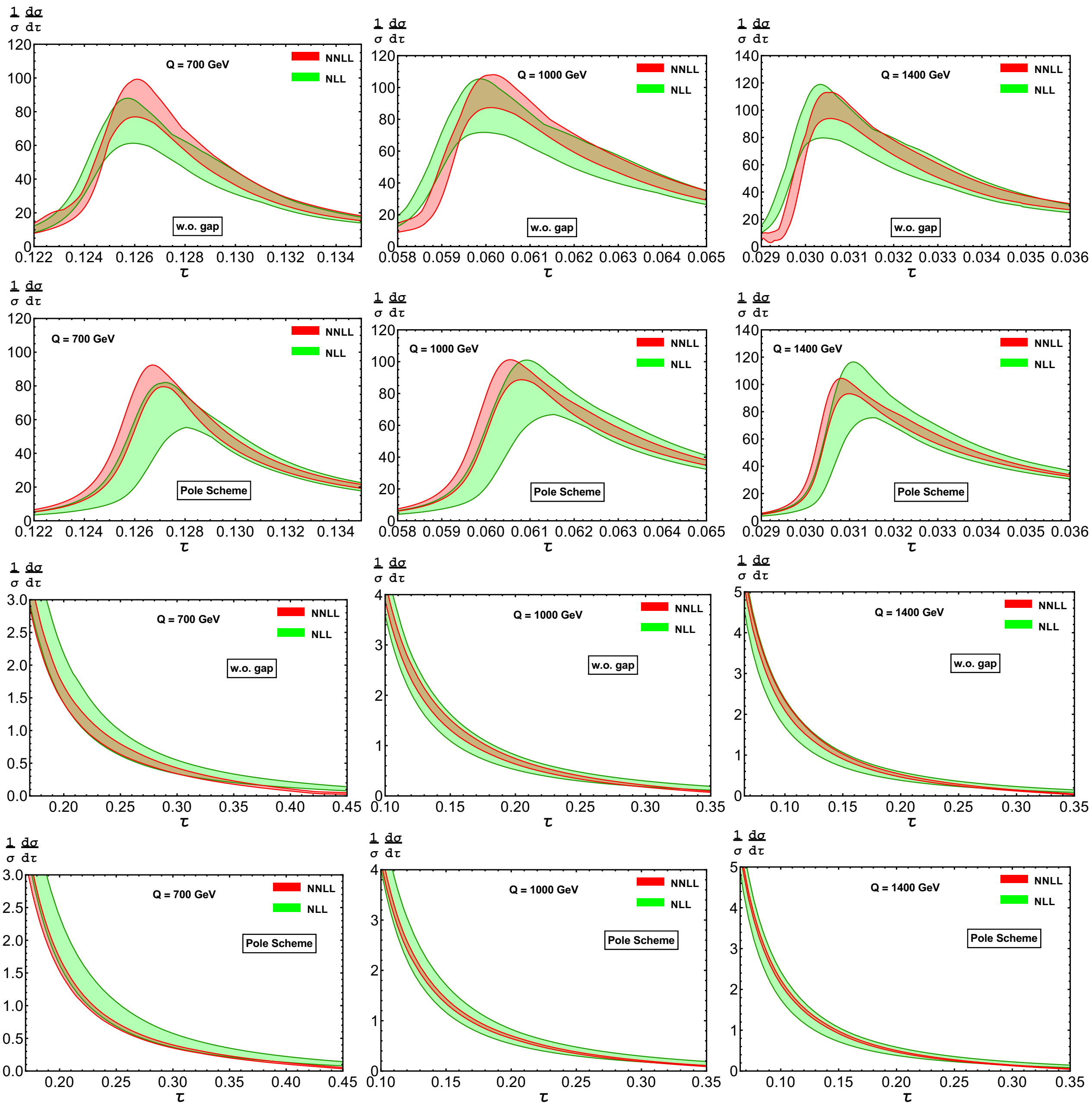

Figure 3.28: Theory scan for the thrust distribution uncertainties of the unstable top production in the peak (1st and 2nd row) and tail (3rd and 4th row) regions at various energies with resummation at $\mathrm{N^2LL}$(red) and NLL(green). Here we display the hadronic cross sections using the default theoretical parameters given in Tab. 3.5. In the 1st and 3rd row we employ the model function without using the gap parameter to subtract the renormalon ambiguities. For the 2nd and 4th row we use the pole mass scheme.

we compared the thrust distribution for these two choices at $\mathrm{N^2LL}$ (and NLL). The results are illustrated in Fig. 3.27 separately at NLL and $\mathrm{N^2LL}$ (3rd and 4th row). All the plots at different energies show good consistency between the consequent cross sections. Nevertheless it is clear from Fig. 3.27 that the impact of the e_J choice on the NLL error bands is more significant than on the $\mathrm{N^2LL}$ bands. In fact the slightly enhanced effects of the $e_J \in [-3, 0]$ choice on the NLL bands leads to notable improvements in the perturbative convergence of the results shown in the first rows w.r.t. to the 4th row of Figs. 3.25 and 3.26. Therefore we will use $e_J \in [-3, 0]$ for our final analysis. We stress that the choice of the e_J range is less relevant when including higher order perturbative corrections.

The last theoretical parameters that are examined here are μ_0 and R_0. We recall from Sec. 3.10 that these parameters are highly correlated and need to be set simultaneously. Note that in the top profile function given in Tab. 3.4 we have assigned different default values for the μ_0 and R_0 scales for the stable and unstable top production. The reason has been presented in Sec. 3.10 , where we discussed that the natural choices for the flat scales in the bHQET region for the stable heavy quark profile function (and massless profile functions) are $\mu_0 = 1.1\,\mathrm{GeV}$ and $R_0 = 0.7\,\mathrm{GeV}$. These values are based on the fact that in the nonperturbative regime, the dominant scale in the soft function is $\mathcal{O}(\Lambda_{\mathrm{QCD}}) \sim 1\,\mathrm{GeV}$. However, for the unstable massive quark production, the additional smearing with the Breit-Wigner function due to finite width effects, provides an additional IR-cutoff for the soft scale in the nonperturbative regime. Therefore we concluded that the μ_0 and R_0 should be set to larger values. We found that by setting $\mu_0 \sim 3\,\mathrm{GeV}$ and $R_0 \sim 2.25\,\mathrm{GeV}$ we obtain a good convergence between different resummation orders (shown in the default panels). To illustrate how these choices have improved the result, in the fifth row of panels in Figs. 3.25 and 3.26 , we show the cross section using $\mu_0 = 1.1\,\mathrm{GeV}$ and $R_0 = 0.7\,\mathrm{GeV}$ for unstable top production. Here, one can see that some parts of the N^{2}LL error bands are not within the NLL error bands. Note that the visible discrepancies between the two orders are appearing to the left of the peak region. This exactly corresponds to the flat part of the profile functions. Moreover the effects are more significant at lower c.m. energies which reflects the fact that the IR-cutoff scale is suppressed by an inverse power of the c.m. energy. This observation is in agreement with the form of the IR-cutoff scale $m\Gamma_t/Q$ given in Eq. (3.8.4).

Now let us discuss the impact of using renormalon-free schemes such as the R-gap scheme for the soft function and the short distance mass scheme on the unstable top thrust distribution. The first (peak) and third (tail) row of panels in Fig. 3.28 display the unstable top cross section when the soft model function does not contain the gap parameter. The second (peak) and fourth (tail) row of panels in Fig. 3.28 display the unstable top cross section in the pole mass scheme. Similar to the bottom cross section, in the corresponding panels for the peak region, we observe a significant shift between the N^{2}LL and NLL error bands for both cases. These behaviors are clear indications of the renormalon ambiguities in the soft function and pole mass scheme that turn out to have a significant effect on the peak of the thrust distribution. In the tail region, however, the N^{2}LL bands are entirely contained in the NLL band, exhibiting a good convergence. This observation leads us to conclude that in order to stabilize the perturbative behavior of the cross section in the peak region and extract a precise value for the mass of the top quark, it is necessary to use renormalon-free schemes for the soft function and the mass parameter.

Sensitivity to the Theory Parameters

In this section we illustrate the sensitivity to the theoretical parameters of the thrust distribution for the unstable top quark production at different energies. In analogy with the bottom case, here, we only focus on the impact of an independent variation of the top quark mass, the strong coupling constant and the first moment of the soft model function, in the peak region of the distribution. The Fig. 3.29 displays the resulting distribution at N^{2}LL using the R-gap and MSR mass scheme. The theoretical error bands are obtained as before by using the scan over 100 random points of theory parameters in the ranges given in Tab. 3.5 . In each panel the red band illustrates the default cross section using the default theoretical parameters and the blue and green error bands represent the cross section when we have changed a specific parameter of the theory, indicated on the top-right corner in each plot. The three rows in Fig. 3.29, respectively show the impact of changing the top quark mass from $\overline{m}_t(\overline{m}_t) = 160\,\mathrm{GeV}$ by $\pm 1\,\mathrm{GeV}$ (first row), the first moment of the shape function from $\overline{\Omega}_1(R_\Delta, \mu_\Delta) = 0.5\,\mathrm{GeV}$ by $-0.1\,\mathrm{GeV}(+0.1\,\mathrm{GeV})$ and the strong coupling constant from $\alpha_s(m_Z) = 0.114$ by ± 0.002 , in the peak region of the thrust distribution.

In the first row one can see that at high energies the error bands for different top mass values have an overlap in the right side of the peak region whereas at low energies the peak curve bands are entirely distinguishable. Note that by approaching the tail region the separation between different error bands reduces and they finally cover each other. Therefore, in analogy with the bottom case, here we conclude that the position of the peak at low energies is more sensitive to the heavy quark mass parameter, as expected. Moreover the plots at $Q = 700\,\mathrm{GeV}$ explicitly show that one can

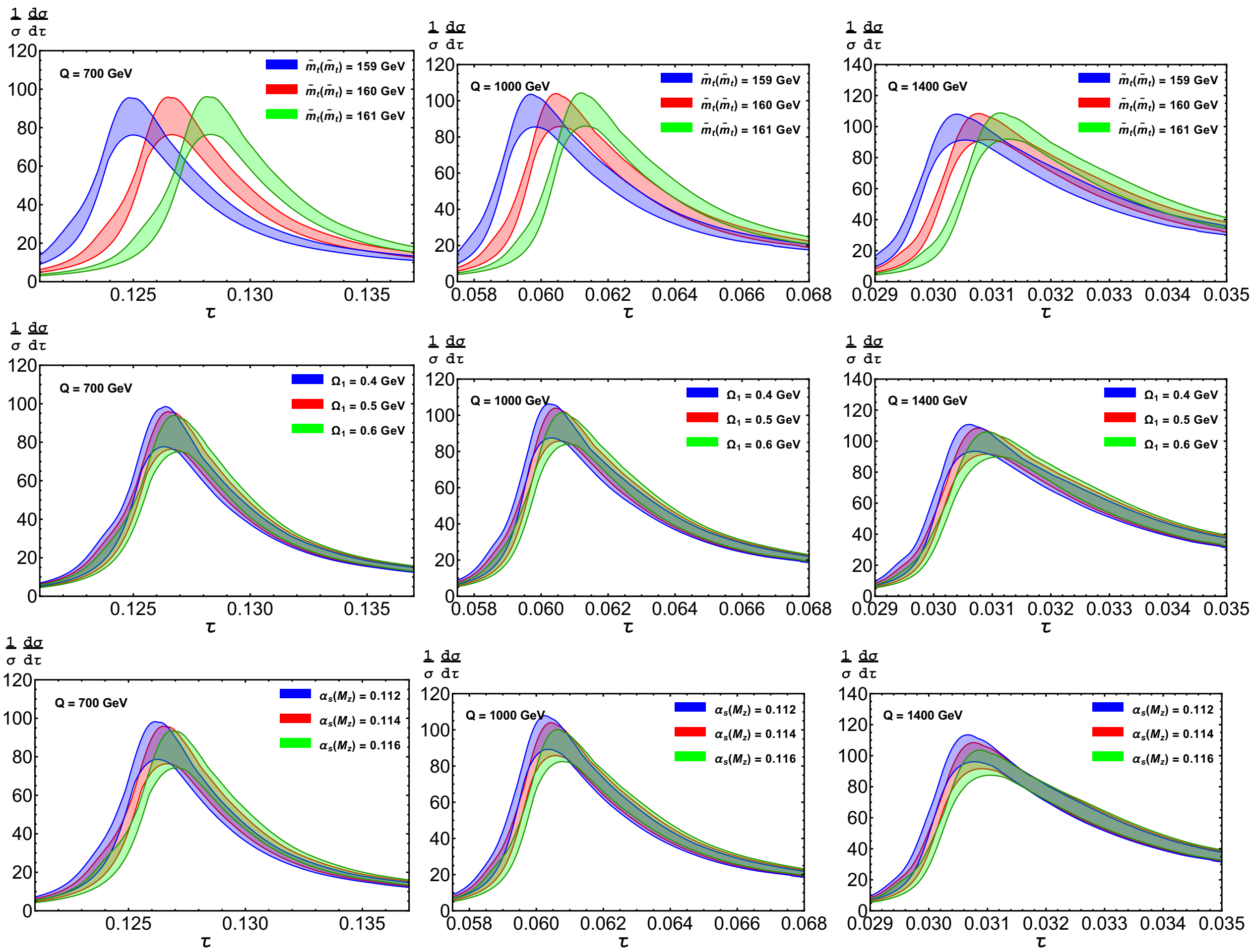

Figure 3.29: Sensitivity of the unstable top cross section at N^{2}LL to the variation of the theoretical parameters at various energies. The theoretical uncertainty band is obtained by using 100 random scans over the theory parameters given in Tab. 3.5 . We vary in the first row $\overline{m}_t(\overline{m}_t) = 160\,\text{GeV}$ by $\pm 1\,\text{GeV}$ while $\alpha_s(m_Z) = 0.114$ and $\overline{\Omega}_1(R_\Delta, \mu_\Delta) = 0.5$. In the second row we vary $\overline{\Omega}_1(R_\Delta, \mu_\Delta) = 0.5\,\text{GeV}$ by $\pm 0.1\,\text{GeV}$ when the mass and strong coupling constants are fixed, respectively to $\overline{m}_t(\overline{m}_t) = 160\,\text{GeV}$ and $\alpha_s(m_Z) = 0.114$. In the third column we vary the $\alpha_s(m_Z) = 0.114$ by ± 0.002 while we keep $\overline{m}_t(\overline{m}_t) = 160\,\text{GeV}$ and $\overline{\Omega}_1(R_\Delta, \mu_\Delta) = 0.5\,\text{GeV}$ unchanged. In all panels the red band yields from the central input parameters i.e. $\overline{m}_t(\overline{m}_t) = 160\,\text{GeV}$, $\overline{\Omega}_1(R_\Delta, \mu_\Delta) = 0.5\,\text{GeV}$ and $\alpha_s(m_Z) = 0.114$.

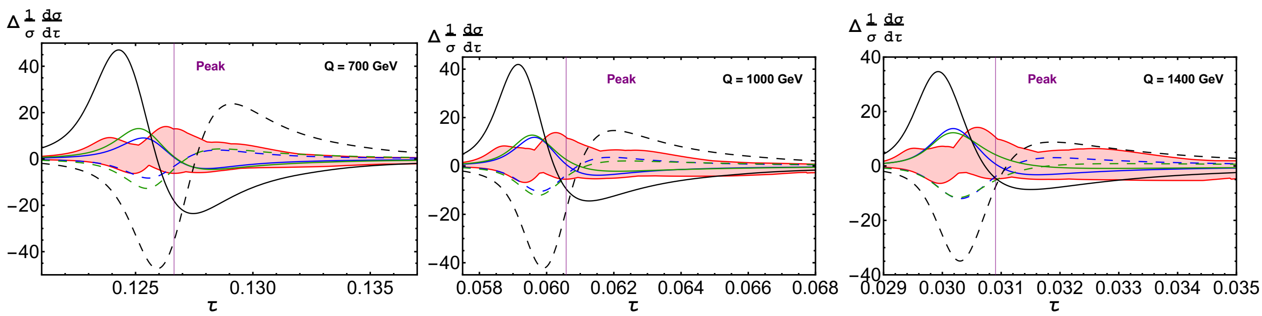

Figure 3.30: Comparison of the difference between the default unstable top cross section and the ones resulting by varying only one theory parameter. The red band is obtained after subtracting the default cross section from the theory scan for the cross section uncertainties. We vary $\alpha_s(m_Z) = 0.114$ by $-0.002(+0.002)$, displayed by the solid(dashed) green curves, $\overline{\Omega}_1(R_\Delta, \mu_\Delta) = 0.5\,\text{GeV}$ by $-0.1\,\text{GeV}(+0.1\,\text{GeV})$, displayed by the solid(dashed) blue curves, and $\overline{m}_t(\overline{m}_t) = 160\,\text{GeV}$ by $-1\,\text{GeV}(+1\,\text{GeV})$, displayed by the solid(dashed) black curves. The vertical purple line indicates the position of the peak for default cross section.

extract the top mass with accuracies better than 1 GeV using low energy data. On the other hand, the second row shows a very similar behavior to the third row, where all different error bands have a considerable overlap. This leads us to the conclusion that the thrust distribution has less sensitivity to the nonperturbative parameter $\overline{\Omega}_1$ and α_s that might result in large theoretical uncertainties while performing future fits.

In analogy with the bottom analysis, we also compare the effects of varying the three parameters to the theoretical uncertainties. This comparison is depicted in Fig. 3.30 . Here, the solid and dashed lines demonstrate different $\Delta_X(\mathrm{d}\sigma/\mathrm{d}\tau)$ with $X \in \{m, \alpha, \overline{\Omega}_1\}$. The solid(dashed) green curves display the $\Delta_{\alpha_s}(\mathrm{d}\sigma/\mathrm{d}\tau)$ when we vary the default value $\alpha_s(m_Z) = 0.114$ by $-0.002(+0.002)$. The solid(dashed) blue curve illustrates the $\Delta_{\overline{\Omega}_1}(\mathrm{d}\sigma/\mathrm{d}\tau)$ when we vary the default value $\overline{\Omega}_1(R_\Delta, \mu_\Delta) = 0.5\,\mathrm{GeV}$ by $-0.1\,\mathrm{GeV}(+0.1\,\mathrm{GeV})$. The solid(dashed) black curve shows the $\Delta_m(\mathrm{d}\sigma/\mathrm{d}\tau)$ when we vary the default value $\overline{m}_t(\overline{m}_t) = 160\,\mathrm{GeV}$ by $-1\,\mathrm{GeV}(+1\,\mathrm{GeV})$. The red bands are obtained by subtracting the default cross section from the upper and lower edges of the error bands in the theory scan. The vertical purple line identifies the peak location in the default cross section.

All the panels in Fig. 3.30 show that the relative changes in the cross section due to the top mass is dominant in the peak region of thrust. The origin is the strong mass dependence of the threshold and peak position of the thrust distribution. By increasing the energy the relative differences between the $\Delta_m(\mathrm{d}\sigma/\mathrm{d}\tau)$ and the error band size is slightly reduced. Hence we conclude that the presented method allows precise measurements of the top quark mass from future fits.

On the other hand, the changes due to the variation of $\overline{\Omega}_1$ or α_s are much closer in size to the theoretical uncertainties for all energies. Hence we anticipate to obtain larger uncertainties for $\overline{\Omega}_1$ and α_s from the simultaneous fits. Furthermore, $\Delta_{\alpha_s}(\mathrm{d}\sigma/\mathrm{d}\tau)$ and $\Delta_{\overline{\Omega}_1}(\mathrm{d}\sigma/\mathrm{d}\tau)$ illustrate a very similar behavior at all energies, which indicates a strong degeneracy between these parameters. This degeneracy might make it difficult to determine α_s and $\overline{\Omega}_1$ simultaneously with high precision. Note that in contrast to the bottom case by combining the data from different energies we do not achieve a better precision for $\overline{\Omega}_1$. Hence this analysis suggests that one might have to fix the strong coupling constant as an external parameter and perform the simultaneous fit for the rest of the theory parameters.

Note that in the tail region, the impact of changing m , α_s and $\overline{\Omega}_1$ on the cross section are comparable and the relative differences between $\Delta_{m,\alpha,\overline{\Omega}_1}(\mathrm{d}\sigma/\mathrm{d}\tau)$ and the error band size are substantially smaller than in the peak region. Hence by including more data from the tail region in the fit range we cannot resolve the degeneracies and achieve further improvements in the precision of the results. Therefore with the current resummation accuracy it is more convenient to use only the data in the peak region for extracting the top quark mass.

Theoretical Uncertainties

In this section we apply the simple fitting procedure, already explained in Sec. 3.11.1 , to the unstable top cross section in order to estimate the theoretical uncertainty that can be obtained for top quark mass determination. Similar to the bottom analysis use the hadronic predictions at NLL and N^{2}LL in the pole and MSR mass schemes. For the top mass analysis in the MSR mass scheme we take $m = m_t^{\mathrm{MSR}}(5\,\mathrm{GeV})$ as the reference mass and use $m_0 = 168.8\,\mathrm{GeV}$ as the input value for $m_t^{\mathrm{MSR}}(5\,\mathrm{GeV})$ in the fitting procedure. Furthermore, we set the $\alpha_s(m_Z) = 0.114$ and $\overline{\Omega}_1(R_\Delta = 2, \mu_\Delta = 2) = 0.5\,\mathrm{GeV}$ as the theoretical input parameters. We set all other theoretical parameters to the default values given in Tab. 3.5 .

First we discuss the stability of results w.r. to the number of bins in the fitting procedure. The left (right) panel of Fig. 3.31 illustrates the best fit values for the MSR (pole) top mass determination at both NLL (blue) and N^{2}LL (red) with respect to the number of bins. In this analysis, we have exploited the thrust distribution in the region between $X_{\mathrm{in}} = -0.5$ and $X_{\mathrm{out}} = +0.5$ at $Q = \{700, 1000, 1400\}\,\mathrm{GeV}$. The respective numerical values for the MSR mass analysis (i.e. the left panel of Fig. 3.31) are summarized in Tab. 3.7 .

Here, in analogy to the bottom mass analysis, we observe a very good convergence and stability between the fit values at NLL and N^{2}LL in the MSR mass scheme, see the left panel of Fig. 3.31 . On

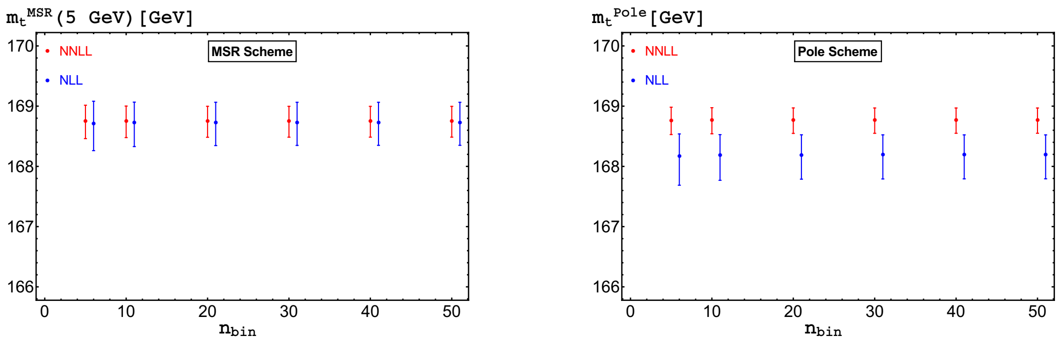

Figure 3.31: Top mass values and corresponding theoretical uncertainties at N^{2}LL (red) and NLL (blue) orders using the fitting procedure for the unstable top thrust distribution explained in the text. The left and right panels, respectively, illustrate the extracted mass in the MSR and pole mass schemes using different number of bins. For the input reference mass we use the $m_0 = m_t^{\rm MSR}(5\,{\rm GeV}) = 168.8\,{\rm GeV}$.

$n_{\rm bin}$	5	10	20	30	40	50
			$n = 1$ (NLL)			
$m_t^{\rm MSR}(5\,{\rm GeV})$ $\Delta m_t^{\rm MSR}(5\,{\rm GeV})$	168.719 $-0.458\vert 0.363$	168.729 $-0.400\vert 0.338$	168.733 $-0.388\vert 0.332$	168.734 $-0.385\vert 0.330$	168.734 $-0.384\vert 0.330$	168.734 $-0.384\vert 0.330$
			$n = 2$ (N^{2}LL)			
$m_t^{\rm MSR}(5\,{\rm GeV})$ $\Delta m_t^{\rm MSR}(5\,{\rm GeV})$	168.759 $-0.299\vert 0.256$	168.760 $-0.282\vert 0.242$	168.760 $-0.276\vert 0.238$	168.760 $-0.275\vert 0.237$	168.760 $-0.275\vert 0.236$	168.760 $-0.274\vert 0.236$

Table 3.7: Numerical values for top mass determinations at N^{2}LL and NLL using the fitting procedure explained in the text. For the input reference mass we use the $m_0 = 168.8\,{\rm GeV}$. The results in this table are visualized in Fig. 3.31 . All numbers are given in units of GeV .

the other hand, the analysis in the pole mass scheme, shown in right panel of Fig. 3.31 , exhibits a large difference between the best fit values for top mass at NLL and N^{2}LL . One can easily observe that the resulting discrepancies are at the level of 500 MeV which is clearly larger than the size of the theoretical uncertainties. Hence, as expected we conclude that using the pole mass scheme can in fact lead to a substantial systematic error in heavy quark mass determinations and should be avoided at our precision level. This observation acknowledges the same conclusion which was drawn form the perturbative convergence studies of unstable top cross section, shown in the fourth row of panels in Fig. 3.25 .

Note that the theoretical uncertainties quoted in Tab. 3.7 are asymmetric and again the positive error values are more stable (and smaller) than the negative ones. This behavior is more obvious at NLL and when we change the $X_{\rm in}$ variable [see Fig. 3.32 and relevant plots for χ^2-functions in Fig. 3.33] . The reasons for this behavior are simply: a) we use an asymmetric range w.r. to the peak position, b) the shapes of the distributions are asymmetric, so that it can rise with a sharp slope on the left side of the peak and fall off gradually on the right side, c) the sensitivity of the thrust distribution to the mass variation in the peak and tail regions of distribution are not uniform [see Figs. 3.29 and 3.30] .

Now let us examine the sensitivity of our results to the fit range which are parametrized by the fraction variables, $X_{\rm in}$ and $X_{\rm out}$. Fig. 3.32 shows the results for the MSR (left panel) and pole (right panel) top mass determination at both NLL (blue) and N^{2}LL (red) using the thrust distribution for $Q = \{700, 1000, 1400\}$ GeV . In analogy to the bottom case, here we vary the fit range by changing $X_{\rm in}$ values while we keep the $X_{\rm out} = 0.3$ fixed. In Fig. 3.33 we display the corresponding $\chi^2_{2,2}(Q, m)$-functions for two cases, $X_{\rm in} = -0.5$ (left panel) and $X_{\rm in} = -0.1$ (right panel). In this plot the red, blue and green curves illustrate the $\chi^2_{2,2}(700\,{\rm GeV}, m)$, $\chi^2_{2,2}(1000\,{\rm GeV}, m)$ and $\chi^2_{2,2}(1400\,{\rm GeV}, m)$, respectively. The black curve displays the $\chi^2_{2,2}(m)$-function that is obtained from summing the χ^2 values for the three energies.

According to the results in Figs. 3.32 and 3.33 we draw a set of conclusions which are analogous

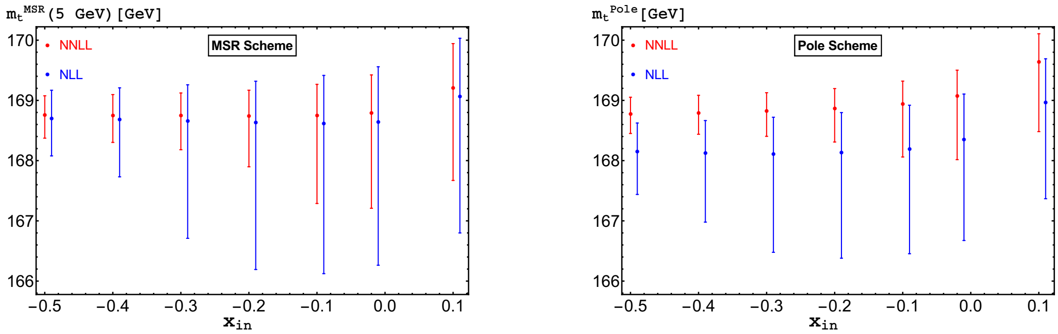

Figure 3.32: Top mass values and corresponding theoretical uncertainties at N^2LL (red) and NLL (blue) using the fitting procedure for the unstable top thrust distribution explained in the text. The left and right panels display the fit results for different $X_{\rm in}$ values when we use the MSR and pole mass schemes for the theory, respectively. Here, the reference mass in our numerical analysis is $m = m_t^{\rm MSR}(5\,{\rm GeV})$ [see Tab. 3.7]. For the input mass we use the $m_0 = 168.8\,{\rm GeV}$.

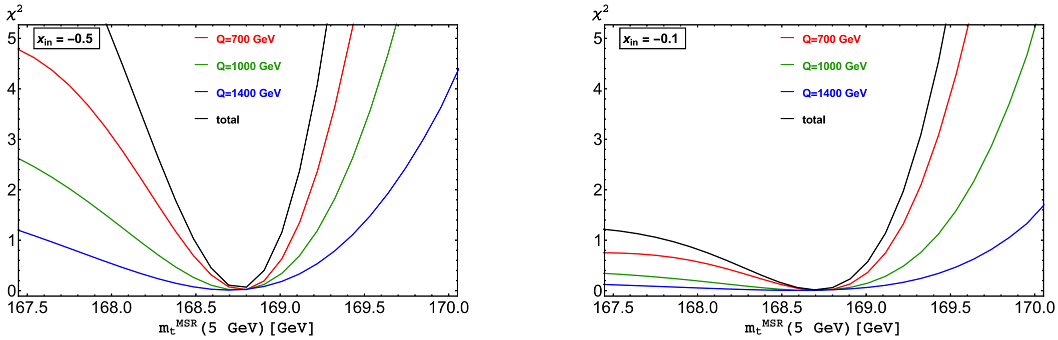

Figure 3.33: χ^2-functions for the simple fitting procedure, explained in the text, using the unstable top thrust distribution at different energies. The left and right panels display the χ^2-functions for $X_{\rm in} = -0.5$ and $X_{\rm in} = -0.1$, respectively. For the input reference mass we use the $m_0 = m_t^{\rm MSR}(5\,{\rm GeV}) = 168.8\,{\rm GeV}$.

to the bottom case in Sec. 3.11.1 :

i) Fig. 3.32 shows that in the top mass determination we obtain smaller theoretical uncertainties by including more information about the left side of the peak region of the distribution. This feature is clearly manifest in Fig. 3.33 where χ^2-functions for the $X_{\rm in} = -0.5$ case is much steeper than for $X_{\rm in} = -0.1$ case.

ii) In Fig. 3.32 , we observe that the results at NLL and N^2LL are stabilized, respectively, for $X_{\rm in} < -0.4$ and $X_{\rm in} < -0.3$. However, note that strictly speaking, only the lower theoretical uncertainty increases for larger $X_{\rm in}$ values. The reason for this behavior is that by excluding the left side of the peak region, we loose our sensitivity to the smaller top mass values.

iii) The result in Fig. 3.33 shows that we acquire higher mass sensitivity at lower energies. Note that the illustrated χ^2-functions in this plot are asymmetric which leads to different upper and lower theoretical errors for the fit values.

iv) Fig. 3.32, demonstrates that one obtains more stable results for mass determinations from the fits to the peak region in the MSR mass scheme than the pole mass scheme. This result is independent of the details of the fit range.

As the final outcome of our simple top mass analysis, we estimate the order of magnitude of the theoretical uncertainty that can be obtained from top mass determinations using the unstable top

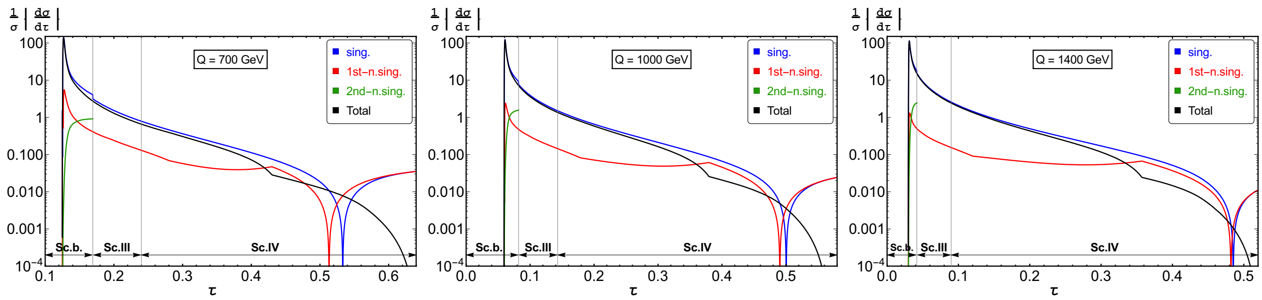

(a) Stable Top Production

Figure 3.34: Singular and nonsingular contributions of the stable top thrust distribution at various energies at N^{2}LL including nonperturbative effects in the R-gap scheme. We use the default set of theoretical parameter for the top production given in Tab. 3.5 with $\alpha_s(m_Z) = 0.114\,,\, \overline{\Omega}_1(R_\Delta, \mu_\Delta) = 0.5\,\mathrm{GeV}$ and $\overline{m}_t(\overline{m}_t) = 160\,\mathrm{GeV}$. "1st-n.sing." and "2nd-n.sing." indicate the first and second type nonsingular components, respectively [see Sec. 3.5]. Here the subdominant singularities are absorbed into the factorization theorem ($sing = 1$).

thrust distribution. Our final results at NLL and N^{2}LL read

$$\Delta m_t^{\mathrm{MSR}}(5\,\mathrm{GeV}) \simeq \begin{array}{c} +0.33 \\ -0.39 \end{array} \mathrm{GeV}\,, \quad \text{at NLL}\,,$$

$$\Delta m_t^{\mathrm{MSR}}(5\,\mathrm{GeV}) \simeq \begin{array}{c} +0.24 \\ -0.28 \end{array} \mathrm{GeV}\,, \quad \text{at N}^2\text{LL}\,.$$

These values are taken from the 4th column of Tab. 3.7 (where we used $n_{\mathrm{bin}} = 20$ and set the fit range to $X_{\mathrm{in}} = -0.5$ and $X_{\mathrm{out}} = 0.5$).

3.11.3 Stable Top Anlysis

Thrust Distribution: Singular v.s. Nonsingular Components

In the following we discuss the relative size of singular and nonsingular contributions in different regions of the thrust distribution for stable top production. In Fig. 3.34 we display the different components of the thrust distribution at N^{2}LL using the default theoretical inputs and parameters given in Tab. 3.5 where $sing = 1$, and we employ the R-gap scheme for the nonperturbative model function and the MSR mass scheme for the mass parameter.

The behavior of the different components for the stable top cross section is similar to the bottom and unstable top discussed above. In the peak region the singular contributions (blue line) are dominant to the first (red line) and second (green line) type of nonsingular contributions. Note that the second type of nonsigular is arising only in the bHQET region i.e. between the threshold of the distribution and the first gray line which is the border of the bHQET scenario t_b. The plots at $Q = 700\,\mathrm{GeV}$ clearly show that the contribution form the second type of nonsingular terms, appearing with negative sign, compensates the mismatch between the singular pieces in the bHQET and SCET III scenarios, so that the total thrust distribution (black line) is continuous at the border of the two scenarios. In the tail region the relative difference between the size of the singular and first type of nonsingular contributions reduces such that in the far-tail they appear with the same size and opposite signs. The consequent cancellation in the total thrust distribution is notable in the bottom-right corner of the corresponding plots.

Now let us have a look into the relative impact of the choices $sing = 0(1)$ on the stable top cross section. In Fig. 3.35 we illustrate different components of the thrust distribution in the peak region at $Q = 700\,\mathrm{GeV}$ for $sing = 0$ (solid lines) and $sing = 1$ (dashed lines) using different values for the first moment of the soft model function. The left, center and right panels illustrate the resulting cross section when the first moment of the soft model function at the reference scales $R_\Delta = \mu_\Delta = 2\,\mathrm{GeV}$

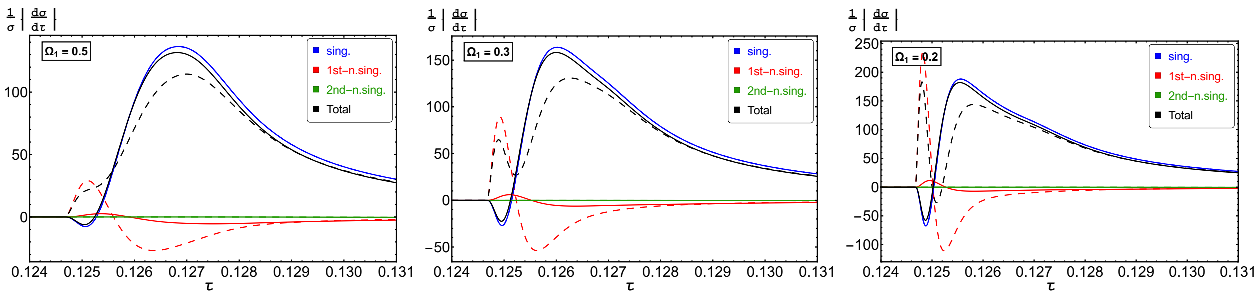

(a) Stable Top Production

Figure 3.35: Singular and nonsingular contributions of the stable top thrust distribution at N^{2}LL including nonperturbative effects in the R-gap scheme, when the subdominant singularities are absorbed ($sing = 1$), displayed with solid lines, or not absorbed ($sing = 0$), displayed with dashed lines. Here we set $e_h = 2$. For the rest of the theoretical parameters we use the default values given in Tab. 3.5 with $\alpha_s(m_Z) = 0.114$ and $\overline{m}_t(\overline{m}_t) = 160\,\text{GeV}$. The left, center and right panels are obtained by setting $\overline{\Omega}_1(R_\Delta, \mu_\Delta) = 0.5\,\text{GeV}$, $\overline{\Omega}_1(R_\Delta, \mu_\Delta) = 0.3\,\text{GeV}$ and $\overline{\Omega}_1(R_\Delta, \mu_\Delta) = 0.2\,\text{GeV}$, respectively. "1st-n.sing." and "2nd-n.sing." indicate the first and second type nonsingular components, respectively [see Sec. 3.5].

is set to $\overline{\Omega}_1(R_\Delta, \mu_\Delta) = 0.5\,\text{GeV}$, $0.3\,\text{GeV}$ and $0.2\,\text{GeV}$, respectively. Here we set $e_h = 2$ since the impact of $sing = 0$ is more enhanced and leads to clear instabilities in the threshold region. The rest of the theoretical parameters are set to the default values. The variable $sing$ is not relevant for the singular and the second type of nonsingular contribution, therefore the panels in Fig. 3.35 contains a single solid blue and one solid green curve.

Fig. 3.35 shows that the first type of nonsingular contributions with $sing = 0$ exhibits significant instabilities close to the threshold of the distribution. As its evident, the relative size of these effects for stable top production is significantly larger than for the unstable top and bottom case. These effects are considerably enhanced at $\overline{\Omega}_1 = 0.2$ where it leads to a new peak close to the threshold of the distribution. On the other hand, the solid red curves in Fig. 3.35 that are representing the first type of nonsingular contributions with $sing = 1$, exhibit a stable behavior in all panels. This clearly manifests the suppression of the subdominant singularities that are achieved by absorbing these terms in the factorized cross sections.

Based on these observations we conclude that for the stable top cross section it is crucial to set $sing = 1$. Nevertheless in the next section we examine the convergence of the thrust distribution with respect to different orders of resummation. This examination confirms that the choice of $sing = 1$ yields a better perturbative convergence in the peak region of the cross section.

Perturbative Convergence Examinations

This section is devoted to the analysis of the perturbative behavior of the thrust distribution for the stable top quark production. In the following discussion we first examine the impact of the different values for $sing$, r_s, μ_0 R_0 and e_J on the convergence of the cross section for different orders of resummation. The cross sections for these cases are collected in Figs. 3.36 and 3.37, showing the peak and tail region, respectively. We also present the stable top cross section, I) when we do not employ the gap formalism, II) when we use the pole mass scheme. The results are illustrated in Fig. 3.39. The analysis in this section is in close analogy with the analysis for the unstable top and bottom quark in Sec. 3.11.2 and Sec. 3.11.1, respectively.

The first row of panels in Figs. 3.36 and 3.37 shows the stable top distribution using the default theoretical values in the top profile function given in Tab. 3.5. The visible convergence w.r.t. to NLL and N^{2}LL in all regions is a further evidence that the constructed massive profile functions in Sec. 3.10 are correctly adapted for the massive thrust distribution at different energies.

In the second row of panels in Figs. 3.36 and 3.37 we display the cross section for $sing = 0$. Note that here, the overall overlap between the NLL and N^{2}LL error bands is similar to the default case

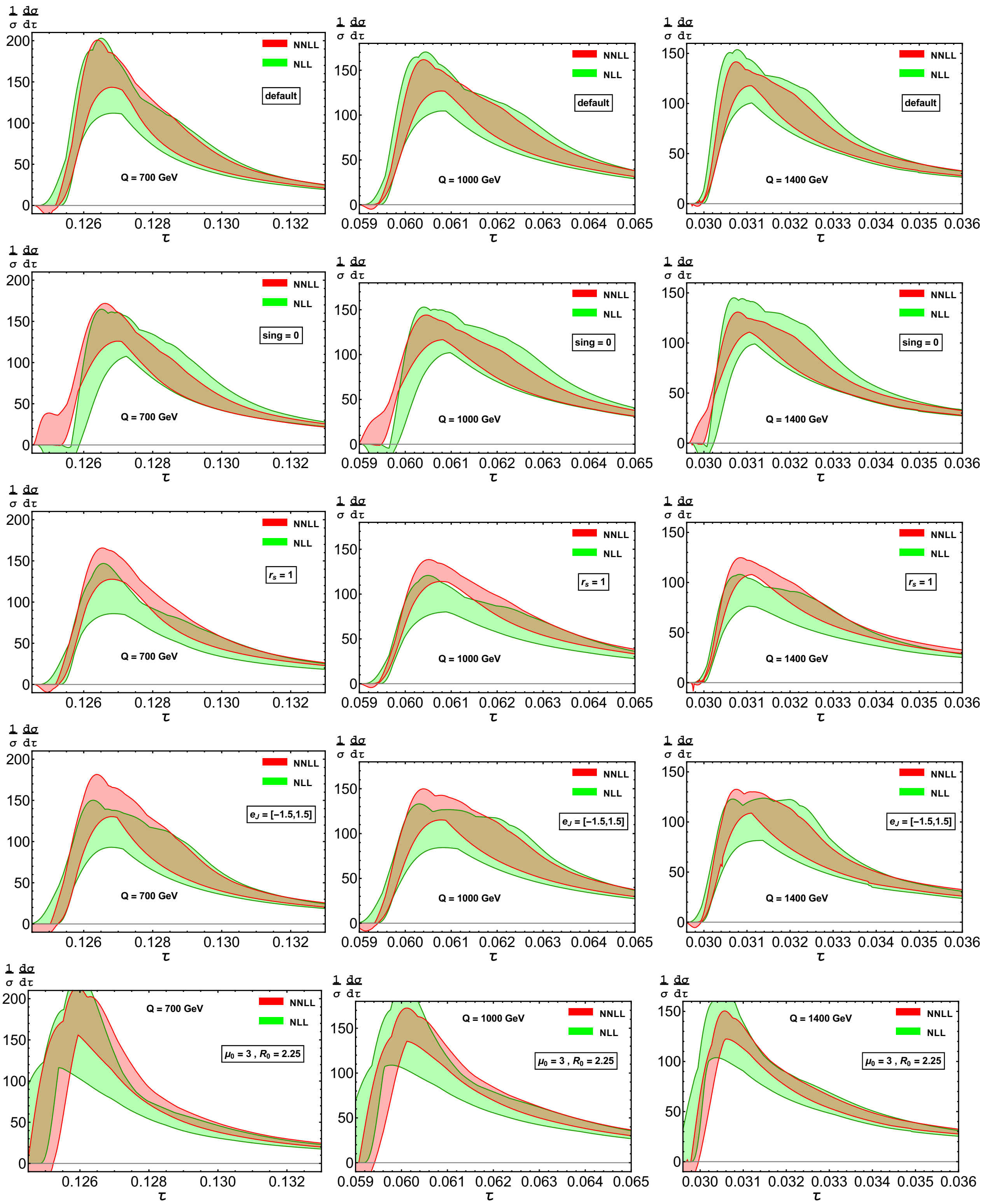

Figure 3.36: Theory scan for the thrust distribution uncertainties of the stable top production in the peak region at various energies at N^{2}LL(red) and NLL(green). Here we display the hadronic cross sections when: we use the default theoretical parameters given in Tab. 3.5 (1st row), we set $sing = 0$ (2nd row), we set $r_s = 1$ (3rd row), the $e_{J/B} = 0$ is taken as default value and varied between -1.5 to 1.5 (4th row), we take $\mu_0 = 3\,\mathrm{GeV}$ and $R_0 = 2.25\,\mathrm{GeV}$ (5th row). The tiny spikes in the last panel of the 4th and 5th rows are due to numerical instabilities and are not relevant for our discussion.

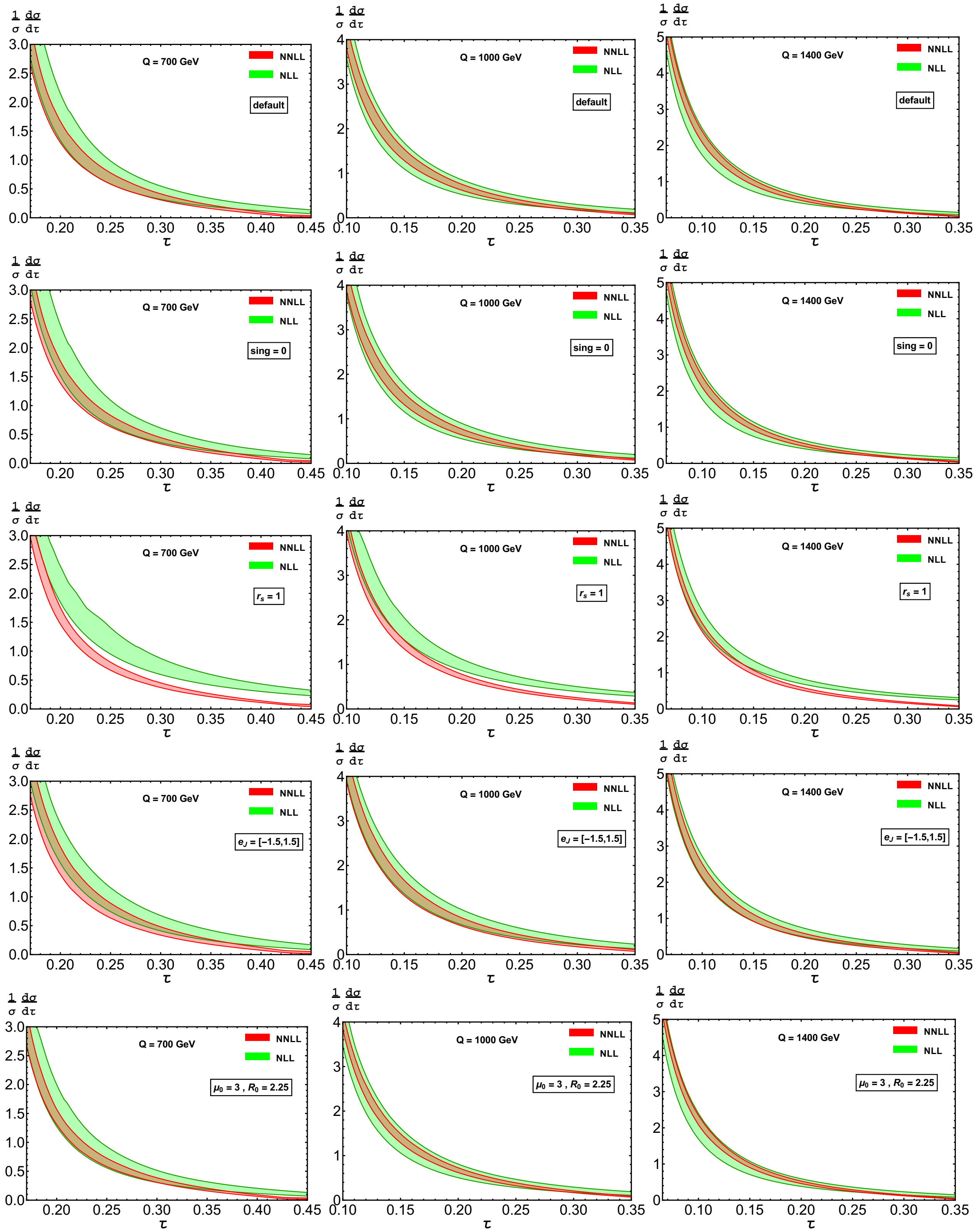

Figure 3.37: Theory scan for the thrust distribution uncertainties of the stable top production in the tail region at various energies at N^{2}LL(red) and NLL(green). We display the hadronic cross sections when: we use the range of values in Tab. 3.5 (1st row), we set $sing = 0$ (2nd row), we set $r_s = 1$ (3rd row), the $e_{J/B} = 0$ is taken as default value and varied between -1.5 to 1.5 (4th row), we take $\mu_0 = 3\,\mathrm{GeV}$ and $R_0 = 2.25\,\mathrm{GeV}$ (5th row).

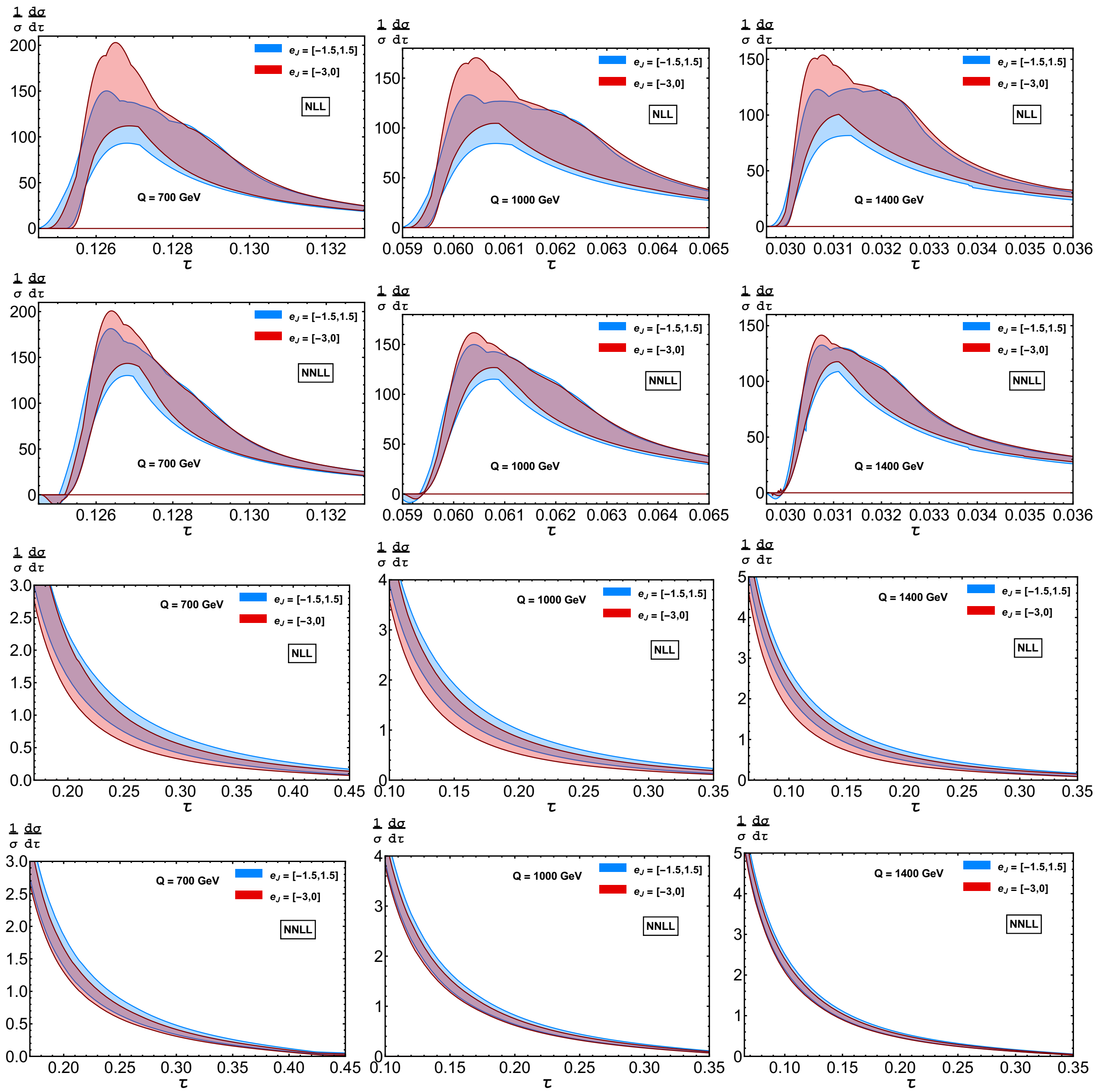

Figure 3.38: Theory scan for the thrust distribution uncertainties of the stable top production in the peak (1st and 2nd row) and tail (3rd and 4th row) regions at various energies. The resummation order is indicated in each panel. The blue and red error bands are obtained with a theory scan over 100 random points using the $e_J \in [-1.5, 1.5]$ and $e_J \in [-3, 0]$ ranges of variation for the jet trumpet parameter. The rest of the theoretical parameters are taken according to the default set in Tab. 3.5 . The tiny spikes in the last panel of the second row is due to numerical instabilities and is not relevant for our discussion.

with $sing = 1$. The only visible discrepancy between the green and red error bands in the $sing = 0$ case occurs in the threshold region. As already noted this behavior in the $sing = 0$ case is related to the subleading contributions (see Fig. 3.35 and the related discussion in the previous section). This observation explains the reason for setting $sing = 1$ as the default choice for the stable top cross section.

The impact of different choices for r_s on the convergence of the stable top cross section is very similar to the unstable top case. The results for different regions are shown in Fig. 3.36 and 3.37. The cross sections at NLL and N^{2}LL manifest the following features: I) in the peak region, the height of the cross sections for the slope 1 case is decreased and the error bands do not cover each other

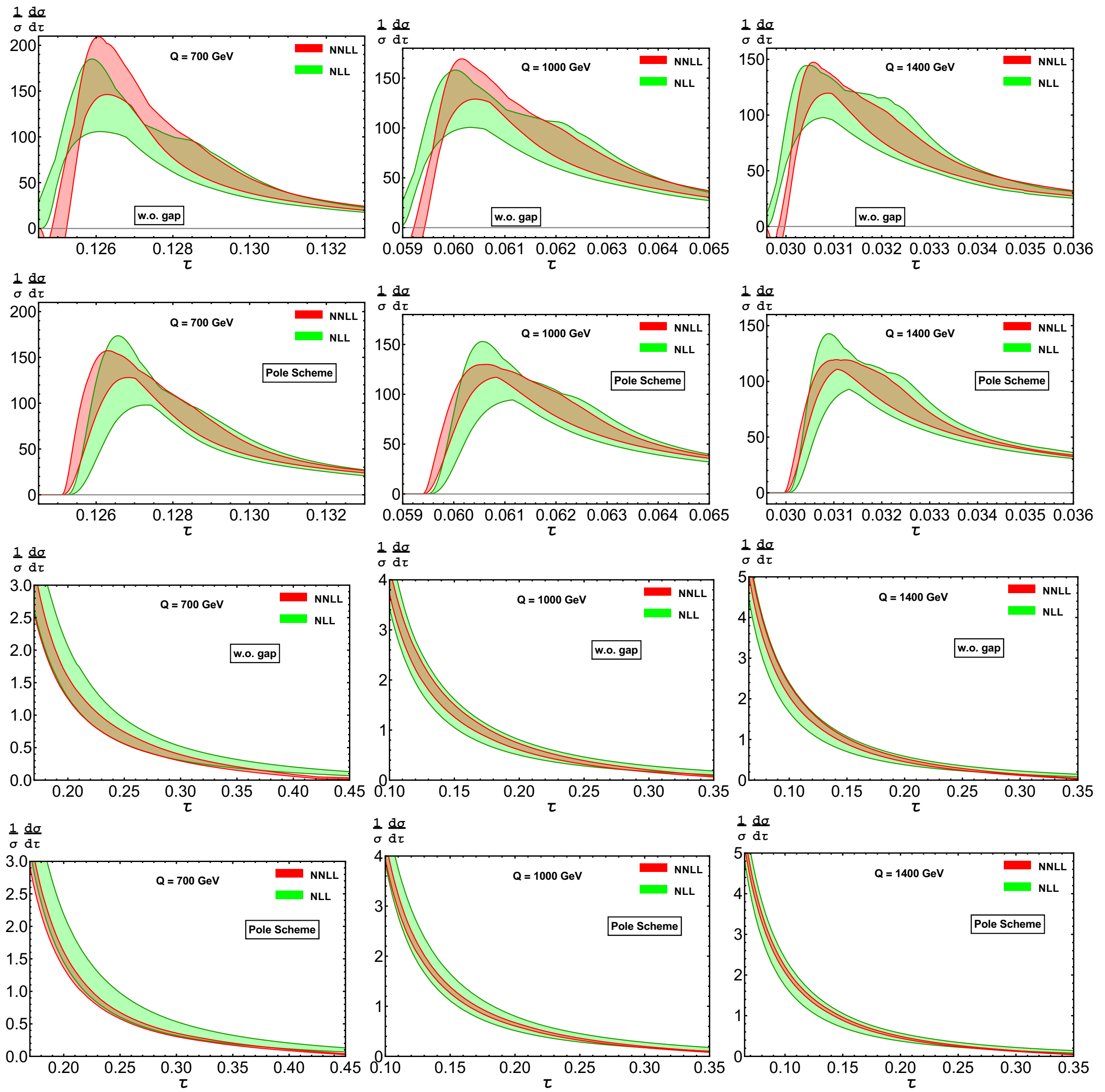

Figure 3.39: Theory scan for the thrust distribution uncertainties of the stable top production in the peak (1st and 2nd row) and tail (3rd and 4th row) regions at various energies at N^{2}LL(red) and NLL(green) order. Here we display the hadronic cross sections using the default theoretical parameters given in Tab. 3.5. In the 1st and 3rd row we employ the model function without using the gap parameter to subtract the renormalon ambiguities. For the 2nd and 4th row we use the pole mass scheme.

properly, II) in the tail region, the cross section falls down more gradually in comparison to the tail region for the slope 2 case, which leads to a visible inconsistency between the two error bands, III) the error bands exhibit no overlap in the far-tail, IV) the impact of the slope choice is more significant at low energies. According to the listed set of observations, once again we conclude that the choice of $r_s = 2$ leads to a better perturbative convergence.

Now let us study the impact of the jet trumpet parameter e_J on the cross sections. We already discussed that by taking $e_J \in [-3, 0]$ instead of $e_J \in [-1.5, 1.5]$ we obtain a better perturbative convergence for the unstable top cross section. In the 4th row of panels of Figs. 3.36 and 3.37 we examine the perturbative convergence of stable top cross section with $e_J \in [-1.5, 1.5]$. The results in the peak region show that the NLL error bands are slightly bellow the N^{2}LL error bands. However in the tail region, the N^{2}LL error bands are smaller and in particular they overlap with the lower edge of the NLL bands. By comparing these results with the default panels where $e_J \in [-3, 0]$ we conclude that the latter is a more appropriate range of variation for the jet trumpet parameter. The origin of the improvement in the perturbative convergence for the $e_J \in [-3, 0]$ is the bigger impact of the e_J choice on the NLL error bands relative to the N^{2}LL error bands. This behavior is illustrated in Fig. 3.38 .

As we already discussed in Sec. 3.11.2 , we adopt the default choices $\mu_0 = 1.1\,\mathrm{GeV}$ and $R_0 = 0.7\,\mathrm{GeV}$ for the soft and R-subtraction scales in the bHQET region (in the flat part) for stable top production. On the other hand, it has been shown in Sec. 3.11.2 that for the unstable top quark production, the finite width provides an IR-cutoff for the soft and R scale which shifts in particular μ_0 and R_0 . Therefore we concluded that larger values $\mu_0 = 3\,\mathrm{GeV}$ and $R_0 = 2.25\,\mathrm{GeV}$ should be used for unstable top quarks. In the fifth row of panels in Figs. 3.36 and 3.37 we show the stable top cross section for $\mu_0 = 3\,\mathrm{GeV}$ and $R_0 = 2.25\,\mathrm{GeV}$. Here, in the nonperturbative region i.e. on the left side of the peak , the NLL error band has a partial overlap with the N^{2}LL error band. It is clear that this choice has a larger impact at lower c.m. energies. We see that using a larger soft scale for the stable top quark leads to a worse perturbative convergence. This confirms our default choices for μ_0 and R_0 .

Before concluding this section let us also discuss the impact of renormalon-free schemes. The first and third row of panels in Fig. 3.39 display the stable top cross section when the soft model function does not contain the gap parameter. The second and fourth row of panels in Fig. 3.39 display the cross section in the pole mass scheme. The panels for both cases show a significant shift between the N^{2}LL and NLL error bands in the peak region and a good convergence in the tail. This illustrates how the renormalon ambiguities in the partonic correction are affecting the thrust distributions. Once again we stress that in general to achieve high precision in the heavy quark mass determination using event shapes, it is crucial to employ renormalon free schemes for the soft function and the heavy quark mass.

Sensitivity to the Theory Parameters

In analogy with previous analyses we now discuss the impact on the stable top distribution due to independent variations of m_t , α_s and $\overline{\Omega}_1$. Fig. 3.40 displays the cross sections for stable top production at N^{2}LL using the R-gap and MSR mass schemes. In Fig. 3.41 we compare the sensitivity of the distribution to m_t , α_s and $\overline{\Omega}_1$ to the theoretical uncertainty from the random scan. We also refer to the corresponding captions of Figs. 3.40 and 3.41 for the further description of the plots.

The first row of Fig. 3.40 manifests the high sensitivity of the peak region of the stable top cross section to the heavy quark mass parameter that can be used to determine the top quark mass with high precision. Clearly this sensitivity is enhanced at lower energies. In fact, the first panel of Fig. 3.40 at $Q = 700\,\mathrm{GeV}$ shows that the measurements of the top quark mass with accuracies better than $1\,\mathrm{GeV}$ are achievable. On the other hand, the second and third row of panels in Fig. 3.40 show a very similar dependence concerning the variation of $\overline{\Omega}_1$ and α_s , where all different error bands have a considerable overlap. Thus similar to the unstable top analysis, here, we conclude that using the thrust distribution with the current accuracy, one cannot determine $\overline{\Omega}_1$ and α_s with high precision.

The panels in Fig. 3.41 illustrate once again that the deviation due to the top quark mass $\Delta_{m_t}(\mathrm{d}\sigma/\mathrm{d}\tau)$ is dominant in the peak region and can be used to extract precise values for the top quark mass particularly at low energies. On the other hand, $\Delta_{\alpha_s}(\mathrm{d}\sigma/\mathrm{d}\tau)$ and $\Delta_{\overline{\Omega}_1}(\mathrm{d}\sigma/\mathrm{d}\tau)$ are much smaller and exhibit a strong degeneracy. Based on this behavior we conclude once again that the simultaneous extraction of the strong coupling constant and the first moment of model function seems difficult. Moreover the blue and green lines are smeared by the theoretical uncertainty band (red band). We expect that from a fit we would obtain uncertainties for $\overline{\Omega}_1$ that are much larger than $0.1\,\mathrm{GeV}$.

We note that the impact of m , α_s and $\overline{\Omega}_1$ on the tail region are all similar and the relative differences between the respective changes in the distribution and the error band size are significantly smaller

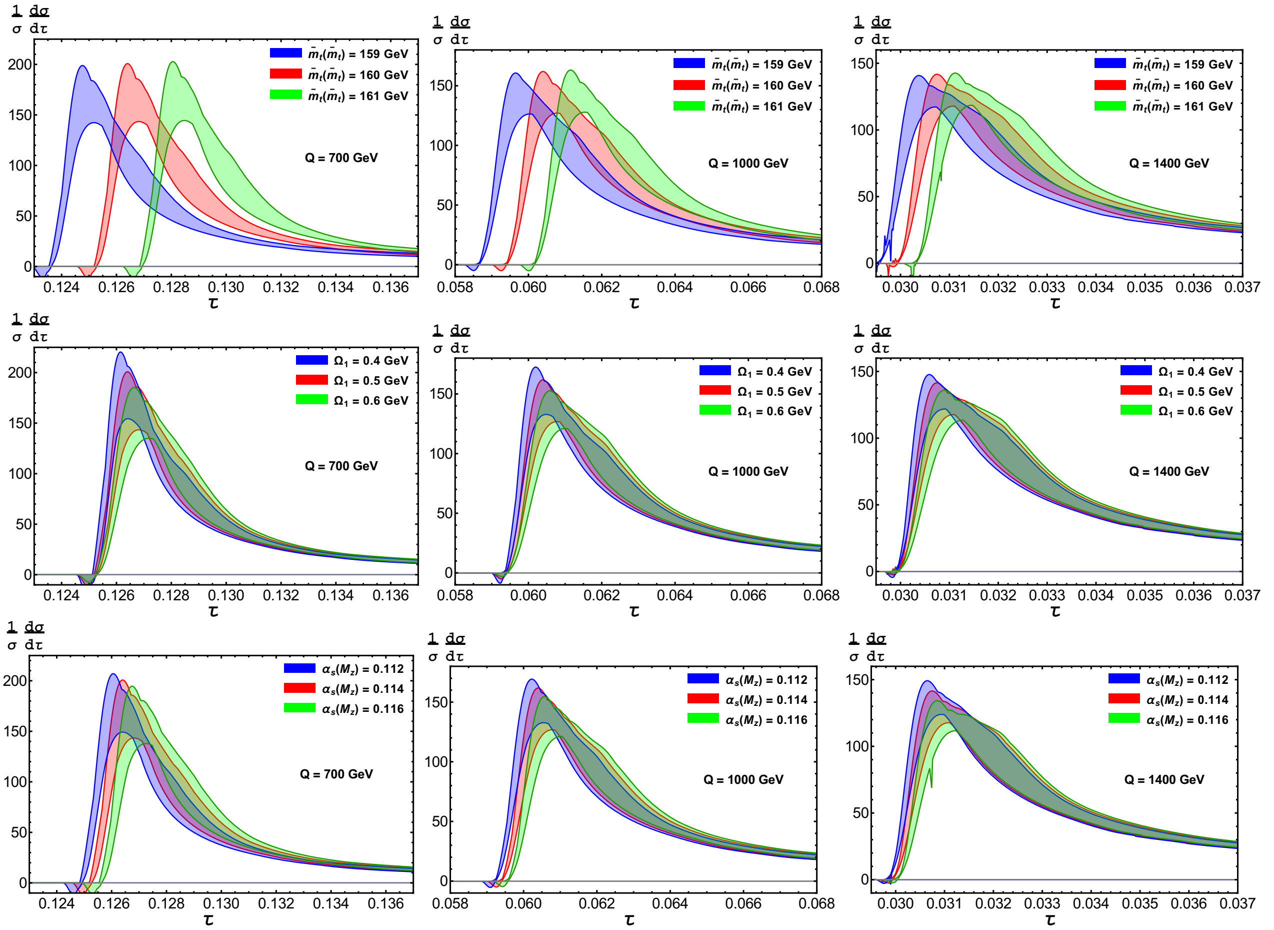

Figure 3.40: The sensitivity of the stable top distribution at N^{2}LL order to the variation of the theoretical parameters at various energies. The theoretical uncertainty band is obtained by using 100 random scans over the theory parameters given in Tab. 3.5 . We vary in the first row $\overline{m}_t(\overline{m}_t) = 160\,\mathrm{GeV}$ by $\pm 1\,\mathrm{GeV}$ while $\alpha_s(m_Z) = 0.114$ and $\overline{\Omega}_1(R_\Delta, \mu_\Delta) = 0.5$. In the second row we vary $\overline{\Omega}_1(R_\Delta, \mu_\Delta) = 0.5\,\mathrm{GeV}$ by $\pm 0.1\,\mathrm{GeV}$ when the mass and strong coupling constants are fixed, respectively to $\overline{m}_t(\overline{m}_t) = 160\,\mathrm{GeV}$ and $\alpha_s(m_Z) = 0.114$. In the third column we vary $\alpha_s(m_Z) = 0.114$ by ± 0.002 while we keep $\overline{m}_t(\overline{m}_t) = 160\,\mathrm{GeV}$ and $\overline{\Omega}_1(R_\Delta, \mu_\Delta) = 0.5\,\mathrm{GeV}$ unchanged. In all panels the red band yields from the central input parameters i.e. $\overline{m}_t(\overline{m}_t) = 160\,\mathrm{GeV}$, $\overline{\Omega}_1(R_\Delta, \mu_\Delta) = 0.5\,\mathrm{GeV}$ and $\alpha_s(m_Z) = 0.114$. The visible spikes in the panels of the last column are due to numerical instabilities and is not relevant for our discussion.

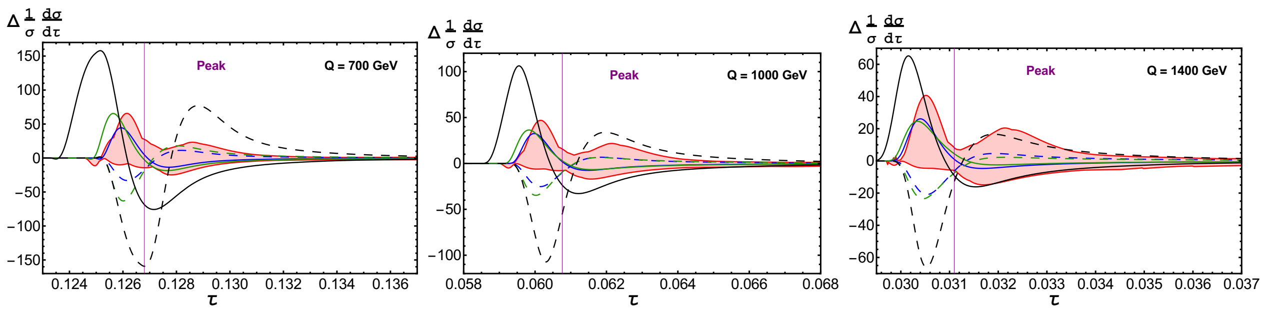

Figure 3.41: Comparison of the difference between the default stable top distribution and the ones resulting by varying only one theory parameter. The red band is obtained after subtracting the default cross section from the theory scan for the cross section uncertainties. We vary $\alpha_s(m_Z) = 0.114$ by $-0.002(+0.002)$, displayed by the solid(dashed) green curves, $\overline{\Omega}_1(R_\Delta, \mu_\Delta) = 0.5\,\mathrm{GeV}$ by $-0.1\,\mathrm{GeV}(+0.1\,\mathrm{GeV})$, displayed by the solid(dashed) blue curves, and $\overline{m}_t(\overline{m}_t) = 160\,\mathrm{GeV}$ by $-1\,\mathrm{GeV}(+1\,\mathrm{GeV})$, displayed by the solid(dashed) black curves. The vertical purple line indicates the position of the peak for the default cross section.

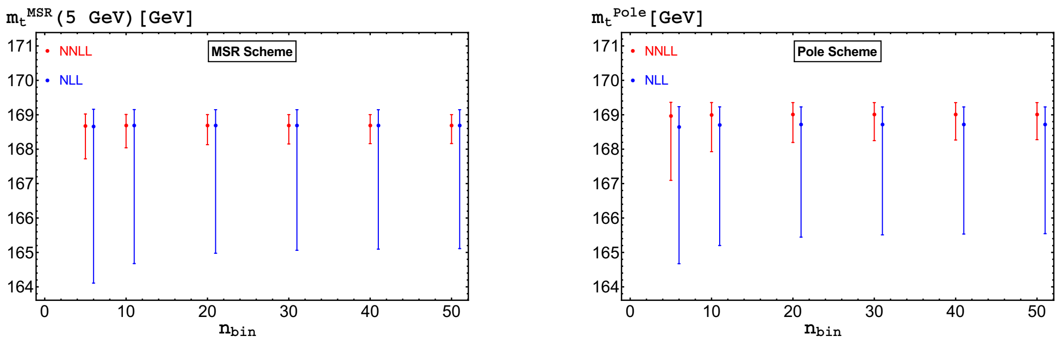

Figure 3.42: Top mass values and corresponding theoretical uncertainties at N^{2}LL (red) and NLL (blue) orders using the fitting procedure for the stable top thrust distribution explained in the text. The left and right panels, respectively, illustrate the extracted mass in the MSR and pole mass schemes using different number of bins. For the input reference mass we use the $m_0 = m_t^{\rm MSR}(5\,{\rm GeV}) = 168.8\,{\rm GeV}$.

than in the peak region. Therefore with the current resummation accuracy it seems more appropriate to only use the data in the peak region of the cross section to extract the top mass and $\overline{\Omega}_1$.

Theoretical Uncertainties

In the following we discuss the theoretical uncertainty that can be obtained from top top quark mass determination using the stable top thrust distribution at NLL and N^{2}LL in the pole and MSR mass schemes. Similar to previous analogous analysis in Sec. 3.11.3 , here we employ the simple fitting procedure, explained in Sec. 3.11.1 , and take $m = m_t^{\rm MSR}(5\,{\rm GeV})$ as the reference top mass and $m_0 = 168.8\,{\rm GeV}$ as the input value for $m_t^{\rm MSR}(5\,{\rm GeV})$. We set $\alpha_s(m_Z) = 0.114$ and $\overline{\Omega}_1(R_\Delta = 2, \mu_\Delta = 2) = 0.5\,{\rm GeV}$ as the theoretical input parameters. The rest of theoretical parameters are set according to the default values given in Tab. 3.5 for the unstable top cross section. To avoid repetition, we note that all the plots presented in this section are in one-to-one correspondence with the plots in Sec. 3.11.3 and the same conventions are employed. The only difference to the previous analyses is that here we use larger fit ranges, i.e. $X_{\rm in} = -0.3$ and $X_{\rm out} = 0.3$ in Fig. 3.42 , to improve the sensitivity of $\chi^2(m)$ to the quark mass variation and thus obtain meaningful results where the theoretical errors are comparable to the result from the stable top analysis.

$n_{\rm bin}$	5	10	20	30	40	50
			$n = 1$ (NLL)			
$m_t^{\rm MSR}(5\,{\rm GeV})$	168.670	168.689	168.697	168.698	168.699	168.699
$\Delta m_t^{\rm MSR}(5\,{\rm GeV})$	$-4.561\|0.490$	$-4.120\|0.461$	$-3.721\|0.450$	$-3.636\|0.448$	$-3.603\|0.448$	$-3.588\|0.447$
			$n = 2$ (N^{2}LL)			
$m_t^{\rm MSR}(5\,{\rm GeV})$	168.683	168.689	168.693	168.694	168.695	168.696
$\Delta m_t^{\rm MSR}(5\,{\rm GeV})$	$-0.964\|0.339$	$-0.648\|0.320$	$-0.563\|0.311$	$-0.542\|0.309$	$-0.535\|0.308$	$-0.532\|0.308$

Table 3.8: Numerical values for top mass determination at N^{2}LL and NLL using the fitting procedure explained in the text. For the input reference mass we use $m_0 = m_t^{\rm MSR}(5\,{\rm GeV}) = 168.8\,{\rm GeV}$. The results in this table are visualized in Fig. 3.42 . All numbers are given in units of GeV .

Fig. 3.42 clearly shows the stability of results w.r. to the number of bins in the fitting procedure. The respective numerical values for the MSR mass analysis are given in Tab. 3.8 . Note that here we have obtained larger theoretical errors at N^{2}LL and specially NLL in comparison with the corresponding results for the unstable top quark analysis, given in Tab. 3.7 . Nevertheless, we still obtain a good convergence and stability between the fit values at NLL and N^{2}LL in the MSR mass scheme, see the left panel of Fig. 3.42 . The reason for the smaller perturbative errors for the unstable top analysis is that in this distribution the total width of top quark serves as an IR-cutoff, which leads to larger values for the soft scale (which implies larger values for the jet scale as well). Therefore,

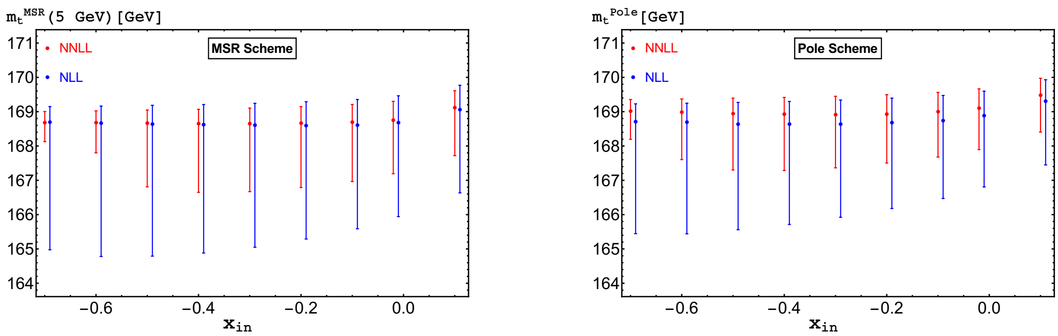

Figure 3.43: Top mass values and corresponding theoretical uncertainties at $\mathrm{N}^2\mathrm{LL}$ (red) and NLL (blue) using the fitting procedure for the stable top thrust distribution explained in the text. The left and right panels display the fit results for different $X_{\rm in}$ values when we use the MSR and pole mass scheme for the theory, respectively. Here, the reference mass in our numerical analysis is $m = m_t^{\rm MSR}(5\,\mathrm{GeV})$ [see Tab. 3.8]. For the input reference mass we use the $m_0 = 168.8\,\mathrm{GeV}$.

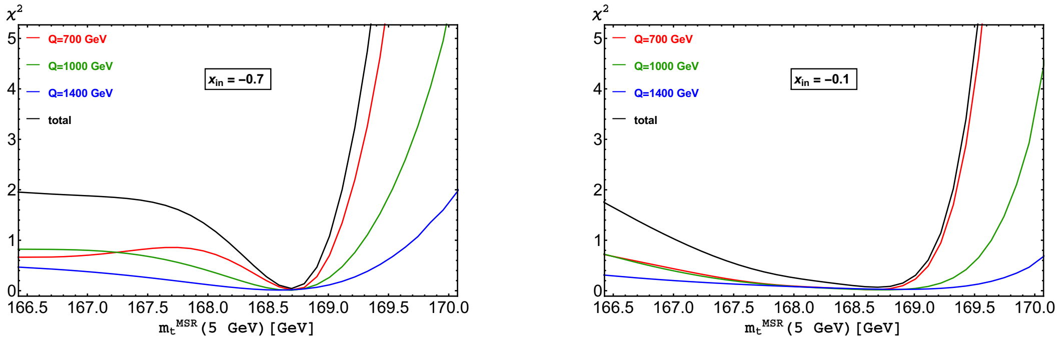

Figure 3.44: χ^2-functions for the simple fitting procedure, explained in the text, using the stable top thrust distribution at different energies. The left and right panels display the χ^2-functions for $X_{\rm in} = -0.7$ and $X_{\rm in} = -0.1$, respectively. For the input reference mass we use the $m_0 = m_t^{\rm MSR}(5\,\mathrm{GeV}) = 168.8\,\mathrm{GeV}$.

the perturbative series expansion of the partonic thrust distribution for unstable top quark exhibits a better convergence compared to the stable case.

On the other hand, the analysis in the pole mass scheme exhibit smaller differences of $\mathcal{O}(300)$ MeV between the best fit values for the top mass at NLL and $\mathrm{N}^2\mathrm{LL}$. The result in Fig. 3.42 shows that overall here we obtain much larger theoretical errors, particularly for smaller number of bins, in comparison with the unstable top quark analysis. We conclude that the impact of using renormalon free mass schemes for the stable top quark is much smaller than the unstable top quark. This has been already observed in Fig. 3.39 where the shift between the thrust distribution at NLL and $\mathrm{N}^2\mathrm{LL}$ is smaller for the stable top quark production than for the unstable top quark case, shown in Fig. 3.28 .

Finally let us discuss the sensitivity of our results to the fit range. The result are shown in Fig. 3.43 and 3.44 . In analogous to the bottom and stable top analyses we summarize the out comes as follows.

i) Fig. 3.43 shows that we obtain more precise mass determinations by including further the left side of the peak region of the top thrust distribution in the fitting procedure. The χ^2-functions have been illustrated in Fig. 3.44 for $X_{\rm in} = -0.7$ (left panel) and $X_{\rm in} = -0.1$ (right panel). Note that the χ^2-functions are shallower than the similar ones in the unstable case in Fig. 3.33 which leads to larger uncertainties.

ii) From Fig. 3.43 we conclude that the results are stabilized only for $X_{\rm in} < -0.6$. This means that one needs to account more information about the peak region for the stable top analysis to obtain a sufficient sensitivity in the χ^2 analysis in order to obtain a comparable precision for the mass as compared to the unstable analysis.

iii) Fig. 3.44 displays the higher sensitivity of the method to the quark mass parameter at lower energies. Again the asymmetric χ^2-functions in this plot explains the asymmetric theoretical error for the fit values.

Based on the analysis in this section, we estimate the order of magnitude of the theoretical uncertainty that can be obtained from top mass determinations using the stable top thrust distribution. We obtain

$$\Delta m_t^{\mathrm{MSR}}(5\,\mathrm{GeV}) \simeq \begin{array}{c} +0.45 \\ -3.72 \end{array} \mathrm{GeV}\,, \quad \text{at NLL}\,,$$

$$\Delta m_t^{\mathrm{MSR}}(5\,\mathrm{GeV}) \simeq \begin{array}{c} +0.31 \\ -0.56 \end{array} \mathrm{GeV}\,, \quad \text{at N}^2\text{LL}\,,$$

where the values are taken from the 4th column of Tab. 3.8 (for $n_{\mathrm{bin}} = 20$ and the fit range with $X_{\mathrm{in}} = -0.3$ and $X_{\mathrm{out}} = 0.3$).

Chapter 4

Conclusions

In this thesis I investigated two methods for high precision determination of the charm, bottom and top quark masses: (I) QCD sum rules, (II) jet physics.

In the first part of this work, we determined the $\overline{\rm MS}$ charm and bottom quark masses from quarkonium sum rules in the framework of the operator product expansion, using previous results for the $\mathcal{O}(\alpha_s^3)$ perturbative QCD computations, plus nonperturbative effects from the gluon condensate at $\mathcal{O}(\alpha_s)$. For the determination of the perturbative uncertainties we independently varied the renormalization scales of the strong coupling and the quark masses, in order to account for the variations due to different possible types of α_s expansions. In order to avoid a possible overestimate of the perturbative uncertainties, coming from the double scale variation in connection with a low scale of α_s , we have re-examined the charm mass determination from charmonium sum rules (vector correlator) supplementing the analysis with a convergence test. The convergence test is based on Cauchy's radical test, which is adapted to the situation in which only a few terms of the series are known, and quantifies the convergence rate of each series by the parameter V_c. We found that the distribution of the convergence parameter V_c coming from the complete set of series peaks around its mean value, and allows to quantify the overall convergence rate of the set of series for each moment. This justifies discarding (very few) series with values of V_c much larger than the average. For the final results in our analysis we discard 3% of the series having the highest V_c values.

In order to determine the charm mass from the vector current moments we fully exploited the available experimental data on the hadronic cross section. In this context we used a data clustering method [111–113] to combine the available data on the total e^+e^- hadronic cross section from many different experiments covering energies up to $\sqrt{s} = 10.538$ GeV. This allowed us to avoid any significant dependence of the experimental moments on ad-hoc assumptions on the "experimental" uncertainty being associated to the QCD theory input used for energies above 10.538 GeV. Our determination of the charm mass from the first moment (which is theoretically the cleanest) of the vector correlator reads:

$$\overline{m}_c(\overline{m}_c) = 1.288 \pm 0.020\,\mathrm{GeV}\,, \tag{4.0.1}$$

where all sources of uncertainty have been added in quadrature.

We applied the same method of theory uncertainty estimate to analyze the HPQCD lattice simulation results for the pseudoscalar correlator. Our convergence test indicates that the pseudoscalar moments have worse convergence than the vector moments. This translates into an uncertainty of 35 MeV due to the truncation of the perturbative series and the uncertainty from the error in α_s (roughly twice as big as for the vector determination). In contrast, using correlated scale variation (e.g. setting the scales in the mass and the strong coupling equal) the scale variation can be made smaller by a factor of 8. Our new determination from the first moment (again being the most reliable theoretical prediction) of the pseudoscalar correlator reads $\overline{m}_c(\overline{m}_c) = 1.267 \pm 0.041\,\mathrm{GeV}$, where again all individual errors have been added in quadrature. The combined total error is twice as big as for the vector correlator, and therefore we consider it as a validation of Eq. (4.0.1) in connection with the convergence test. The result is in sharp contrast with the analyses carried out by the HPQCD collaboration [6,14,15], where perturbative uncertainties of 4 MeV are claimed. We have checked that, as for the vector correlator, for the different possible types of α_s expansions the correlated variation - when the renormalization scales for the $\overline{\mathrm{MS}}$ mass and α_s are set equal - in general leads to a bad order-by-order convergence of the charm mass determination.

The second important result of this work is the determination of the bottom quark mass from the vector correlator. We have reanalyzed the experimental moments by combining experimental measurements of the first four narrow resonances, the threshold region covered by BABAR, and a theoretical model for the continuum. This theoretical model is an interpolation between a linear fit to the BaBar data points with highest energy and pQCD, to which we assign a 4% systematic uncertainty which decreases linearly to reach 0.3% at the Z-pole, and stays constant at 0.3% for higher energies. Our treatment is motivated by the error function yielded by the fit to BaBar data in the energy range between 11 and 11.2 GeV and the discrepancy between pQCD and experimental measurements at the Z-pole. This results into a large error for the first moment, and therefore we choose the second moment (which is theoretically as clean as the first one for the case of the bottom quark) for our final analysis, giving a total experimental uncertainty of 18 MeV. Our treatment of the experimental continuum uncertainty is in contrast to Ref. [9], where instead the very small perturbative QCD uncertainties (less than 1%) are used, claiming an experimental uncertainty of 6 MeV. In the light of the analysis carried out here, supported by the observations made in Ref. [124], we believe this is not justified. Our convergence test revealed that, as expected for the heavier bottom quark, the perturbative series converges faster than for the charm quark. Correspondingly, the perturbative and α_s uncertainties are $\sim 30\%$ smaller. Taking on the other hand correlated scale variation, as used in Refs. [9,114], the observed scale variation can shrink up to a factor of 20. We also find that the correlated variation $\mu_m = \mu_{\alpha_s}$ leads to incompatible results for the different types of α_s expansions. Our final result for the bottom mass from the second moment, with all errors added in quadrature, reads:

$$\overline{m}_b(\overline{m}_b) = 4.176 \pm 0.023\,\mathrm{GeV}\,, \tag{4.0.2}$$

were the total error is fairly dominated by the systematic one, which comes from the continuum region of the spectrum.

In order to further validate the results discussed above, we have also analyzed the ratios of consecutive moments for each one of the three correlators as alternative observables. In all cases the results from the moment ratios agree very well the regular moment analyses.

In the second part of this work, we provided a complete theoretical description of the entire thrust distribution for heavy quark production in $e^- e^+$ collisions that can be used to calibrate the top mass parameter in MCs in terms of a short distance mass. We discussed that the conceptual subtlety in this problem arises from the emergence of different hierarchies between the mass and the other kinematic scales. Hence for the full theoretical description one must take into account various kinematic scenarios where the role of the heavy quark mass is continuously changing from the threshold region to the asymptotic large energy limit. To this end we adopted a sequence of effective field theories within a variable flavor number scheme to describe the final state jets that are initiated by massive primary and secondary quarks. In the dijet limit, we used soft collinear effective theory (SCET) to describe the leading singular contributions in the jet cross section. The result has been formulated in terms of generic factorization theorems which allow to sum all the large logarithms between different kinematic scales. When the invariant mass of the jets are close to the heavy quark mass a new set of large logarithms arises. In order to sum up these term one has to integrate out the small heavy quark field components, and we matched the soft collinear effective theory to the boosted heavy quark effective theory. We discussed that this regime corresponds to the peak region of the thrust distribution. We provided the ingredients needed to achieve the full Next-to-Next-to-Leading logarithm summation. In particular we have accounted for secondary massive corrections which contains the leading set of rapidity logarithms of the form $\alpha_s^2 \ln(m^2/Q^2)$. We note that this framework is established based on previous works in Refs. [32,39,43].

In addition we considered the subleading contributions that are not accounted for by the factorization theorems. We extracted the full analytic expressions for these contribution from the $\mathcal{O}(\alpha_s)$ fixed order results of the thrust distribution. For certain pieces of the thrust distribution (the coefficients of Dirac delta function at threshold), we used the phase space slicing method which allowed us to compute the real and virtual contributions separately. The strategy of this calculation is generic and can be applied to any event shape.

These subleading contributions consist of nonsingular terms and subdominant singular terms that are suppressed by powers of (m/Q). For the stable top production, we demonstrated in Sec. 3.11 that these subdominant contributions, also enhanced by large logarithms, can be numerically large, leading to instabilities close to the threshold of the cross section. To suppress these effects we provided a prescription in Sec. 3.6 to absorb these subdominant singularities in the factorization formulas. It turned out from the convergence studies that this prescription is indeed suitable for the stable heavy quark production. For the unstable cases these effects are smeared by the total width of the unstable massive quark and absorbing these subleading contributions is not necessary.

We incorporated nonperturbative power corrections with a soft model function, whose moments are given by nonperturbative matrix elements. On the other hand the partonic soft function has IR-sensitivities which can spoil the perturbative convergence of the results. We used the gap formalism [198] where one accounts for an additional gap parameter $\Delta \sim \Lambda_{\rm QCD}$, as the minimum hadronic energy deposit due to soft radiations in the soft model function. By switching to the short distance scheme for Δ, we have removed the $\mathcal{O}(\Lambda_{\rm QCD})$ renormalon ambiguities in the partonic soft function, resulting in a considerably more stable perturbative behavior for the distribution.

In order to describe the decay of unstable heavy quarks in the peak region we used an effective treatment where the total width of the unstable massive quark enters the bHQET Lagrangian as an imaginary mass term at leading order given in Eq. (3.8.2). In turned out that the consequent width effects can be incorporated in the cross section via an additional factorization theorem where the stable jet function is convoluted with a Breit-Wigner function [see Eq. (3.8.3)]. We applied this smearing to the dominant singularities in the factorization scenarios and subdominant terms in the nonsingular contributions.

As a result, we obtained full control over the mass dependance in various kinematic regions of the thrust distribution. We formulated the theoretical framework of the pole mass scheme, however to remove the $\mathcal{O}(\Lambda_{\rm QCD})$-renormalon ambiguity in the pole mass scheme, we provided a prescription in Eq. (3.9.8) to switch from the pole mass scheme to the appropriate short distance mass schemes which are respecting the power counting of the corresponding EFTs for different kinematic scenarios and various matrix elements, see sec. 3.9. In particular for the bHQET region, we used the MSR mass scheme [245] which is a scale dependent short distance mass formally derived from the relation between the $\overline{\rm MS}$ and pole masses given in Eq. 3.9.7. We showed in Sec. 3.11 that using the short distance schemes one can indeed achieve a further improved perturbative convergence for the massive thrust distributions. This allowed us to determine the heavy quark mass with a precision better than $\Lambda_{\rm QCD}$.

We constructed τ-dependent profile functions for the various renormalization scales in the massive thrust distribution to sum up all the large logarithms and provide a smooth transition between different kinematic regions. The suggested massive profile functions are the natural extension of already available massless profile functions in the literature [155, 156, 158] and have consistent massless limits. Furthermore, in Sec. 3.11 we provided an extensive study of various choices for different parameters in the profile functions for bottom, stable top and unstable top cross section. We showed that using the default value and ranges of variation for the theoretical parameters given in Tab. 3.4 and Tab. 3.5 respectively for the bottom and top production, one achieves the best perturbative convergence for the resulting thrust distributions at various resummation orders.

In Sec. 3.11 we discussed the sensitivity of the thrust distribution for the stable(unstable) top and bottom production to the theoretical parameters at different energies. We concluded that: I) the peak region of the thrust distribution is very sensitive to the heavy quark mass, II) the impact of varying the leading nonperturbative correction on the thrust distribution is much smaller than the mass effects, so that one acquires a large theoretical uncertainty from the simultaneous fit to MC output, III) the α_s

variation exhibited similar effects to the leading nonperturbative correction on the thrust distribution, thus we concluded that it is more convenient to fix α_s as an external parameter when fitting.

Furthermore, we carried out a simple χ^2-fitting procedure to estimate the theoretical uncertainties that can be achieved in quark mass extractions from fitting the massive quark thrust distribution in the peak region. The χ^2-analysis was based on using the most accurate theoretical predictions (and the error bands from a random theory scan) as toy data. The main conclusions from the bottom, stable and unstable top analyses were: I) Using the MSR mass scheme instead of the pole mass, one obtains a much better perturbative convergence between the result of the analysis at different resummation orders. II) The perturbative errors are asymmetric. III) The top mass determination from the unstable top thrust distribution is more precise than the stable top case.

Finally we estimated the order of magnitude of the perturbative errors that can be obtained from the bottom and top mass determinations using the stable (unstable) thrust distribution. Our prediction for the theoretical error for the bottom quark mass reads

$$\Delta\, m_b^{\rm MSR}(m_b^{\rm MSR}) \simeq \begin{array}{c}+0.18\\-0.19\end{array} \;\text{GeV}\,, \quad \text{at NLL}\,,$$

$$\Delta\, m_b^{\rm MSR}(m_b^{\rm MSR}) \simeq \begin{array}{c}+0.11\\-0.13\end{array} \;\text{GeV}\,, \quad \text{at N}^2\text{LL}\,.$$

The results for the top quark mass using the unstable and stable top analyses are

$$\Delta\, m_t^{\rm MSR}(5\,\text{GeV}) \simeq \begin{array}{c}+0.33\\-0.39\end{array} \;\text{GeV}\,, \quad \text{at NLL}\,,$$

$$\Delta\, m_t^{\rm MSR}(5\,\text{GeV}) \simeq \begin{array}{c}+0.24\\-0.28\end{array} \;\text{GeV}\,, \quad \text{at N}^2\text{LL}\,.$$

and

$$\Delta\, m_t^{\rm MSR}(5\,\text{GeV}) \simeq \begin{array}{c}+0.45\\-3.72\end{array} \;\text{GeV}\,, \quad \text{at NLL}\,,$$

$$\Delta\, m_t^{\rm MSR}(5\,\text{GeV}) \simeq \begin{array}{c}+0.31\\-0.56\end{array} \;\text{GeV}\,, \quad \text{at N}^2\text{LL}\,,$$

respectively.

As an outlook its worth to note again that our theoretical predictions for the thrust distributions in the peak region can be used to extract a numerical relation between the mass parameters in MC generators and the well-defined short distance mass schemes, such as MSR mass, in QCD.

Appendix A

Results of the Fit Procedure

In this appendix we present in some more detail the numerical results of our fit procedure. In Tabs. A.1, A.2 and A.3, the results for the cluster energies and the cluster charmed R-values are shown for the standard, minimal and maximal selection of data sets, respectively, using our default setting for the correlations. We use the results for the standard data set selection for our final charm mass analysis. The numbers in the parentheses correspond to the statistical and systematical errors. The correlation matrices for the R-values is available, but cannot be displayed due to lack of space. They can be obtained by the authors on request. For the three data selections, the fit gives the following minimal χ^2 per degree of freedom,

$$\frac{\chi^2_{\rm standard}}{\rm dof} = 1.89\,, \qquad \frac{\chi^2_{\rm minimal}}{\rm dof} = 1.86\,, \qquad \frac{\chi^2_{\rm maximal}}{\rm dof} = 1.81\,, \tag{A.1}$$

and the following normalization constants for the non-charm background

$$\begin{aligned} n_{\rm ns}^{\rm standard} &= 1.039 \pm 0.003_{\rm stat} \pm 0.012_{\rm syst}\,,\; n_{\rm ns}^{\rm minimal} = 1.029 \pm 0.003_{\rm stat} \pm 0.015_{\rm syst}\,, \\ n_{\rm ns}^{\rm maximal} &= 1.023 \pm 0.003_{\rm stat} \pm 0.011_{\rm syst}\,. \end{aligned} \tag{A.2}$$

The fit results for the normalization constant $n_{\rm ns}$ is compatible with the corresponding normalization constant $n_- = 1.038$ used in Ref. [8] for the subtraction of the non-charm background for the BES 2001 dataset (our data set 2) but is not compatible with the result for the subtraction constant $n_- = 0.991$ concerning the BES 2006 data set (our dataset 5). Since the minimal χ^2/dof values are not close to unity, one has to conclude that the fit quality is not really very good. This is not at all visible from the agreement of the fit and the data for the total cross section (see Figs. 2.12) and thus might be related to the disparity between the fits of charm versus non-charm production rates [44].

In Eq. (A.3) we show for the correlation matrices of the first four experimental moments for the minimal and the maximal data set selection. The results for our standard selection are given in Eqs. (2.5.21) and (2.5.22). All numbers are related to moments $M_n^{\rm exp}$ normalized to units of $10^{-(n+1)}\,\text{GeV}^{-2n}$. We show the results accounting for the full set of correlated and uncorrelated uncertainties and the correlation matrices accounting only for uncorrelated systematical and statistical uncertainties (subscript uc).

$$\begin{aligned} C^{\rm exp}_{\rm min} &= \begin{pmatrix} 0.156 & 0.094 & 0.080 & 0.077 \\ 0.094 & 0.079 & 0.076 & 0.076 \\ 0.080 & 0.076 & 0.076 & 0.077 \\ 0.077 & 0.076 & 0.077 & 0.079 \end{pmatrix}, \; C^{\rm exp}_{\rm min,uc} = \begin{pmatrix} 0.046 & 0.037 & 0.034 & 0.034 \\ 0.037 & 0.034 & 0.034 & 0.035 \\ 0.034 & 0.034 & 0.035 & 0.036 \\ 0.034 & 0.035 & 0.036 & 0.037 \end{pmatrix}, \\ C^{\rm exp}_{\rm max} &= \begin{pmatrix} 0.107 & 0.079 & 0.075 & 0.075 \\ 0.079 & 0.074 & 0.074 & 0.075 \\ 0.075 & 0.074 & 0.075 & 0.077 \\ 0.075 & 0.075 & 0.077 & 0.079 \end{pmatrix}, \; C^{\rm exp}_{\rm max,uc} = \begin{pmatrix} 0.036 & 0.033 & 0.033 & 0.033 \\ 0.033 & 0.033 & 0.033 & 0.034 \\ 0.033 & 0.033 & 0.034 & 0.036 \\ 0.033 & 0.034 & 0.036 & 0.037 \end{pmatrix}. \end{aligned} \tag{A.3}$$

E	R	E	R	E	R	E	R
3.736	$-0.03(6\|2)$	3.749	$0.23(6\|2)$	3.751	$0.47(9\|3)$	3.753	$0.39(7\|3)$
3.755	$0.41(6\|3)$	3.757	$0.80(10\|3)$	3.759	$0.75(7\|3)$	3.761	$0.84(7\|3)$
3.763	$1.06(8\|3)$	3.765	$1.23(9\|4)$	3.767	$1.52(12\|4)$	3.769	$1.31(8\|3)$
3.771	$1.39(6\|4)$	3.773	$1.42(2\|4)$	3.775	$1.22(8\|3)$	3.777	$1.29(8\|4)$
3.78	$1.13(7\|3)$	3.781	$1.06(5\|3)$	3.783	$1.00(7\|3)$	3.785	$0.63(11\|3)$
3.787	$0.64(7\|3)$	3.79	$0.41(5\|2)$	3.808	$0.11(4\|2)$	3.846	$0.10(5\|2)$
3.883	$0.24(7\|2)$	3.928	$0.63(8\|2)$	3.967	$0.94(3\|2)$	4.002	$1.30(3\|3)$
4.033	$2.18(3\|4)$	4.069	$1.74(4\|3)$	4.117	$1.72(4\|3)$	4.156	$1.68(1\|4)$
4.191	$1.54(3\|3)$	4.23	$0.91(5\|2)$	4.261	$0.71(2\|2)$	4.307	$0.89(6\|2)$
4.346	$1.18(6\|2)$	4.382	$1.63(7\|3)$	4.416	$1.76(4\|3)$	4.452	$1.53(7\|3)$
4.492	$1.42(6\|3)$	4.529	$1.29(10\|3)$	4.715	$1.51(3\|3)$	5.326	$1.39(7\|7)$
6.006	$1.33(6\|7)$	6.596	$1.35(7\|7)$	7.202	$1.39(2\|4)$	7.852	$1.52(8\|5)$
8.417	$1.38(3\|5)$	9.04	$1.43(5\|6)$	9.54	$1.35(3\|5)$	10.327	$1.37(1\|5)$

Table A.1: Best fit values for the standard selection of data sets. The energy of the cluster is measured in GeV, and for R the first and second numbers in brackets are the statistical and systematical errors, respectively.

E	R	E	R	E	R	E	R
3.736	$-0.07(6\|2)$	3.749	$0.22(6\|2)$	3.751	$0.38(9\|3)$	3.753	$0.38(7\|3)$
3.755	$0.40(6\|3)$	3.757	$0.68(11\|3)$	3.759	$0.74(7\|3)$	3.761	$0.82(7\|4)$
3.763	$1.01(8\|4)$	3.765	$1.21(9\|4)$	3.767	$1.49(12\|4)$	3.769	$1.27(8\|4)$
3.772	$1.37(6\|4)$	3.773	$1.38(8\|4)$	3.775	$1.21(8\|4)$	3.777	$1.26(8\|4)$
3.78	$1.11(7\|3)$	3.781	$1.06(5\|4)$	3.783	$0.97(7\|4)$	3.785	$0.62(11\|3)$
3.787	$0.66(8\|3)$	3.79	$0.40(5\|3)$	3.808	$0.11(5\|2)$	3.845	$0.12(5\|2)$
3.879	$0.18(9\|2)$	3.935	$0.85(14\|3)$	3.969	$1.01(4\|3)$	4.002	$1.39(3\|4)$
4.032	$2.25(5\|5)$	4.066	$1.94(4\|5)$	4.118	$1.78(5\|5)$	4.157	$1.77(1\|5)$
4.191	$1.62(3\|5)$	4.232	$0.99(8\|3)$	4.261	$0.76(2\|3)$	4.309	$0.83(10\|3)$
4.35	$1.22(11\|3)$	4.385	$1.28(14\|4)$	4.415	$1.62(10\|4)$	4.45	$1.54(11\|4)$
4.492	$1.30(13\|4)$	4.529	$1.03(13\|3)$	4.716	$1.25(8\|3)$	5.378	$1.40(8\|8)$
6.008	$1.31(7\|8)$	6.622	$1.30(8\|8)$	7.206	$1.37(2\|6)$	7.856	$1.47(8\|7)$
8.417	$1.36(3\|6)$	9.037	$1.40(5\|7)$	9.544	$1.31(3\|6)$	10.252	$1.34(3\|6)$

Table A.2: Best fit values for the minimal selection of data sets. Conventions are as in Tab. A.1.

E	R	E	R	E	R	E	R
3.736	0.01(6|2)	3.749	0.29(5|2)	3.751	0.48(8|3)	3.753	0.40(7|2)
3.755	0.42(6|3)	3.757	0.80(10|3)	3.759	0.76(7|2)	3.761	0.85(6|3)
3.763	1.06(8|3)	3.765	1.24(8|3)	3.767	1.51(12|4)	3.769	1.31(7|3)
3.771	1.39(6|4)	3.773	1.41(2|4)	3.775	1.21(8|3)	3.777	1.28(8|4)
3.78	1.14(7|3)	3.781	1.06(5|3)	3.783	1.00(7|3)	3.785	0.61(9|3)
3.787	0.64(7|3)	3.79	0.41(5|2)	3.808	0.13(4|2)	3.846	0.10(4|2)
3.884	0.26(5|2)	3.927	0.66(7|2)	3.967	0.98(3|2)	4.002	1.30(2|2)
4.033	2.18(3|3)	4.07	1.74(3|3)	4.117	1.75(4|3)	4.156	1.70(1|4)
4.191	1.54(3|3)	4.23	0.91(5|2)	4.261	0.74(2|2)	4.307	0.87(6|2)
4.346	1.15(5|2)	4.382	1.55(6|3)	4.416	1.80(4|3)	4.452	1.52(6|3)
4.492	1.33(5|2)	4.53	1.19(8|2)	4.722	1.42(3|2)	5.36	1.39(6|4)
6.018	1.47(4|3)	6.608	1.66(4|3)	7.202	1.54(2|3)	7.851	1.63(8|5)
8.417	1.50(3|4)	9.04	1.55(5|5)	9.54	1.47(3|4)	10.327	1.48(1|4)

Table A.3: Best fit values for the maximal selection of data sets. Conventions are as in Tab. A.1.

Appendix B

Numerical Values for the Perturbative Coefficients

In this appendix we succinctly collect the numerical values in tables for all of the coefficients appearing in the perturbative series.

$n_f = 4$	$[C_V]^{0,0}_{0,i}$	$[C_V]^{1,0}_{0,i}$	$[C_V]^{0,1}_{0,i}$	$[C_V]^{0,2}_{0,i}$
$i = 0$	0	0	0	0
$i = 1$	1.44444	0	0	0
$i = 2$	2.83912	0	−3.00926	0
$i = 3$	−5.28158	6.01852	−16.4639	6.26929
$n_f = 5$	$[C_V]^{0,0}_{0,i}$	$[C_V]^{1,0}_{0,i}$	$[C_V]^{0,1}_{0,i}$	$[C_V]^{0,2}_{0,i}$
$i = 0$	0	0	0	0
$i = 1$	1.44444	0	0	0
$i = 2$	3.21052	0	− 2.76852	0
$i = 3$	− 6.28764	5.53704	− 15.7977	5.30633
$n_f = 4$	$[C_P]^{0,0}_{0,i}$	$[C_P]^{1,0}_{0,i}$	$[C_P]^{0,1}_{0,i}$	$[C_P]^{0,2}_{0,i}$
$i = 0$	1.33333	0	0	0
$i = 1$	3.11111	0	0	0
$i = 2$	0.115353	0	− 6.48148	0
$i = 3$	− 1.22241	12.963	− 10.4621	13.5031

Table B.1: Numerical values of the coefficients for Eq. (2.4.11) for $\widehat{\Pi}_V(0)$ in the $\overline{\mathrm{MS}}$ scheme and $n_f = 4, 5$, and $P(q^2 = 0)$ for $n_f = 4$.

	$n=1$	$n=2$	$n=3$	$n=4$
$[a_V(n_f=4)]_n^{0,0}$	-16.042	-26.7367	-38.8898	-52.3516
$[a_V(n_f=4)]_n^{1,0}$	-143.364	-272.186	-439.820	-646.690
$[a_V(n_f=5)]_n^{0,0}$	-4.011	-6.6842	-9.7224	-13.0879
$[a_V(n_f=5)]_n^{1,0}$	-36.9604	-69.9123	-112.669	-165.326
$[a_P(n_f=4)]_n^{0,0}$	8.02101	0	-9.72244	-20.9406
$[a_P(n_f=4)]_n^{1,0}$	39.1439	-36.3842	-152.67	-309.925

Table B.2: Numerical values for the coefficients of Eq. (2.4.13) for the vector correlator with $n_f = 4, 5$ (first four columns), and for the pseudoscalar correlator with $n_f = 4$ (last two columns). (Gluon condensate contribution).

	$[C_V]_{n,i}^{0,0}$	$[C_V]_{n,i}^{1,0}$	$[C_V]_{n,i}^{2,0}$	$[C_V]_{n,i}^{3,0}$	$[C_V]_{n,i}^{0,1}$	$[C_V]_{n,i}^{1,1}$	$[C_V]_{n,i}^{2,1}$	$[C_V]_{n,i}^{0,2}$	$[C_V]_{n,i}^{1,2}$
					$n=1$				
$i=0$	1.06667	0	0	0	0	0	0	0	0
$i=1$	2.55473	2.13333	0	0	0	0	0	0	0
$i=2$	2.49671	8.63539	4.35556	0	−5.32236	−4.44444	0	0	0
	3.15899	8.33909	4.17778	0	−4.89657	−4.08889	0	0	0
$i=3$	−5.64043	22.6663	32.696	8.95309	−18.5994	−42.8252	−18.1481	11.0882	9.25926
	−7.76244	18.2235	29.3221	8.12346	−18.2834	−37.1221	−16.0148	9.38509	7.83704
					$n=2$				
$i=0$	0.457143	0	0	0	0	0	0	0	0
$i=1$	1.10956	1.82857	0	0	0	0	0	0	0
$i=2$	2.77702	7.46046	5.5619	0	−2.31158	−3.80952	0	0	0
	3.23193	7.20649	5.40952	0	−2.12665	−3.50476	0	0	0
$i=3$	−3.49373	21.8523	38.6277	15.1407	−15.1307	−36.9519	−23.1746	4.81579	7.93651
	−2.64381	19.0805	35.2229	14.1249	−15.0705	−32.0439	−20.7365	4.07609	6.71746
					$n=3$				
$i=0$	0.270899	0	0	0	0	0	0	0	0
$i=1$	0.519396	1.6254	0	0	0	0	0	0	0
$i=2$	1.63882	5.8028	6.56931	0	−1.08207	−3.38624	0	0	0
	2.06768	5.57705	6.43386	0	−0.995509	−3.11534	0	0	0
$i=3$	−2.83951	16.0684	40.3042	22.2627	−8.4948	−29.3931	−27.3721	2.25432	7.05467
	−1.17449	14.8309	36.8953	21.0888	−9.18132	−25.3067	−24.6631	1.90806	5.97108
					$n=4$				
$i=0$	0.184704	0	0	0	0	0	0	0	0
$i=1$	0.203121	1.47763	0	0	0	0	0	0	0
$i=2$	0.795555	4.06717	7.44974	0	−0.42317	−3.0784	0	0	0
	1.22039	3.86194	7.3266	0	−0.389316,	−2.83213	0	0	0
$i=3$	−3.349	8.91524	38.2669	30.2128	−3.96649	−21.6873	−31.0406	0.881603	6.41334
	−1.386	9.10716	34.8581	28.8994	−5.16902	−18.3751	−28.0853	0.746189	5.42825

Table B.3: Numerical values of the coefficients for Eq. (2.4.2) for the vector current with $n_f = 4\,(5)$ for the upper (lower) number. (Standard fixed-order expansion).

	$[C_P]^{0,0}_{n,i}$	$[C_P]^{1,0}_{n,i}$	$[C_P]^{2,0}_{n,i}$	$[C_P]^{3,0}_{n,i}$	$[C_P]^{0,1}_{n,i}$	$[C_P]^{1,1}_{n,i}$	$[C_P]^{2,1}_{n,i}$	$[C_P]^{0,2}_{n,i}$	$[C_P]^{1,2}_{n,i}$
					$n=1$				
$i=0$	0.5333	0	0	0	0	0	0	0	0
$i=1$	2.0642	1.06667	0	0	0	0	0	0	0
$i=2$	7.23618	5.89136	2.17778	0	− 4.30041	− 2.22222	0	0	0
$i=3$	7.06593	29.1882	19.5609	4.47654	− 36.7734	− 27.9695	− 9.07407	8.95919	4.62963
					$n=2$				
$i=0$	0.30476	0	0	0	0	0	0	0	0
$i=1$	1.21171	1.21905	0	0	0	0	0	0	0
$i=2$	5.9992	6.86166	3.70794	0	− 2.5244	− 2.53968	0	0	0
$i=3$	14.5789	36.2468	31.4945	10.0938	− 28.8842	− 32.5014	−15.4497	5.25916	5.29101
					$n=3$				
$i=0$	0.20318	0	0	0	0	0	0	0	0
$i=1$	0.71276	1.21905	0	0	0	0	0	0	0
$i=2$	4.26701	6.29135	4.92698	0	− 1.48491	− 2.53968	0	0	0
$i=3$	13.3278	34.8305	38.066	16.697	− 20.066	− 30.1251	− 20.5291	3.09356	5.29101
					$n=4$				
$i=0$	0.147763	0	0	0	0	0	0	0	0
$i=1$	0.401317	1.18211	0	0	0	0	0	0	0
$i=2$	2.91493	5.1643	5.95979	0	− 0.836077	− 2.46272	0	0	0
$i=3$	9.9948	29.5129	40.2459	24.1703	−13.4331	−25.3105	−24.8325	1.74183	5.13067

Table B.4: Numerical values of the coefficients for Eq. (2.4.2) for the pseudoscalar correlator with $n_f = 4$. (Standard fixed-order expansion).

	$[\bar{C}_V]^{0,0}_{n,i}$	$[\bar{C}_V]^{1,0}_{n,i}$	$[\bar{C}_V]^{2,0}_{n,i}$	$[\bar{C}_V]^{3,0}_{n,i}$	$[\bar{C}_V]^{0,1}_{n,i}$	$[\bar{C}_V]^{1,1}_{n,i}$	$[\bar{C}_V]^{2,1}_{n,i}$	$[\bar{C}_V]^{0,2}_{n,i}$	$[\bar{C}_V]^{1,2}_{n,i}$
					$n=1$				
$i=0$	1.0328	0	0	0	0	0	0	0	0
$i=1$	1.2368	1.0328	0	0	0	0	0	0	0
$i=2$	0.46816	2.94379	1.59223	0	−2.57668	−2.15166	0	0	0
	0.788784	2.80034	1.50616	0	− 2.37054	− 1.97952	0	0	0
$i=3$	−3.2913	6.97983	10.9784	2.74217	−5.91875	−15.5793	−6.63428	5.36808	4.48262
	− 4.70257	4.68012	9.59148	2.42659	− 6.01262	− 13.2306	− 5.77361	4.54354	3.79409
					$n=2$				
$i=0$	0.822267	0	0	0	0	0	0	0	0
$i=1$	0.498944	0.822267	0	0	0	0	0	0	0
$i=2$	0.79463	1.85797	1.26766	0	−1.03947	−1.71306	0	0	0
	0.999196	1.74376	1.19914	0	− 0.956309	− 1.57601	0	0	0
$i=3$	−3.20128	3.15216	7.99164	2.1832	−4.91174	−10.3796	−5.28192	2.16555	3.56887
	−3.19148	1.49991	6.92794	1.93195	− 5.03603	− 8.67158	− 4.5967	1.83292	3.02069
					$n=3$				
$i=0$	0.804393	0	0	0	0	0	0	0	0
$i=1$	0.257044	0.804393	0	0	0	0	0	0	0
$i=2$	0.605688	1.58653	1.24011	0	−0.535508	−1.67582	0	0	0
	0.817928	1.4748	1.17307	0	− 0.492667	− 1.54175	0	0	0
$i=3$	−2.46047	1.56737	7.46171	2.13574	−3.34838	−9.19128	−5.1671	1.11564	3.49129
	−1.97558	0.0722677	6.44038	1.88995	− 3.75658	− 7.59737	− 4.49678	0.944279	2.95503
					$n=4$				
$i=0$	0.809673	0	0	0	0	0	0	0	0
$i=1$	0.111301	0.809673	0	0	0	0	0	0	0
$i=2$	0.382377	1.44951	1.24825	0	−0.231877	−1.68682	0	0	0
	0.615164	1.33706	1.18077	0	− 0.213327	− 1.55187	0	0	0
$i=3$	−2.21776	0.492406	7.2834	2.14976	−1.95033	−8.63733	−5.20102	0.483077	3.51421
	−1.36612	− 0.923734	6.26766	1.90236	− 2.62711	− 7.08209	− 4.5263	0.408876	2.97442

Table B.5: Numerical values of the coefficients for Eq. (2.4.3) for the vector current with $n_f = 4\,(5)$ for the upper (lower) number. (Linearized expansion).

	$[\bar{C}_P]^{0,0}_{n,i}$	$[\bar{C}_P]^{1,0}_{n,i}$	$[\bar{C}_P]^{2,0}_{n,i}$	$[\bar{C}_P]^{3,0}_{n,i}$	$[\bar{C}_P]^{0,1}_{n,i}$	$[\bar{C}_P]^{1,1}_{n,i}$	$[\bar{C}_P]^{2,1}_{n,i}$	$[\bar{C}_P]^{0,2}_{n,i}$	$[\bar{C}_P]^{1,2}_{n,i}$
$n=1$									
$i=0$	0.730297	0	0	0	0	0	0	0	0
$i=1$	1.41326	0.730297	0	0	0	0	0	0	0
$i=2$	3.58681	2.62028	1.12587	0	− 2.94429	− 1.52145	0	0	0
$i=3$	− 2.10344	11.3262	8.59338	1.93901	− 19.4793	− 13.2609	− 4.69114	6.13394	3.16969
$n=2$									
$i=0$	0.743002	0	0	0	0	0	0	0	0
$i=1$	0.738531	0.743002	0	0	0	0	0	0	0
$i=2$	2.55535	1.96655	1.14546	0	− 1.53861	− 1.54792	0	0	0
$i=3$	0.536147	6.35978	7.66478	1.97274	− 13.0167	− 10.5778	− 4.77276	3.20543	3.22484
$n=3$									
$i=0$	0.766734	0	0	0	0	0	0	0	0
$i=1$	0.448296	0.766734	0	0	0	0	0	0	0
$i=2$	2.02851	1.71554	1.18205	0	− 0.93395	− 1.59736	0	0	0
$i=3$	1.94168	4.12818	7.42578	2.03575	−9.89039	− 9.60801	− 4.9252	1.94573	3.32784
$n=4$									
$i=0$	0.787401	0	0	0	0	0	0	0	0
$i=1$	0.267317	0.787401	0	0	0	0	0	0	0
$i=2$	1.624	1.56872	1.21391	0	− 0.55691	− 1.64042	0	0	0
$i=3$	2.58251	2.65675	7.3283	2.09062	− 7.62431	− 9.06256	− 5.05796	1.16023	3.41754

Table B.6: Numerical values of the coefficients for Eq. (2.4.3) for the pseudoscalar current with $n_f = 4$. (Linearized expansion).

	$[\tilde{C}_V]^{0,0}_{n,i}$	$[\tilde{C}_V]^{1,0}_{n,i}$	$[\tilde{C}_V]^{2,0}_{n,i}$	$[\tilde{C}_V]^{3,0}_{n,i}$	$[\tilde{C}_V]^{0,1}_{n,i}$	$[\tilde{C}_V]^{1,1}_{n,i}$	$[\tilde{C}_V]^{2,1}_{n,i}$	$[\tilde{C}_V]^{0,2}_{n,i}$	$[\tilde{C}_V]^{1,2}_{n,i}$
$n=1$									
$i=0$	1	0	0	0	0	0	0	0	0
$i=1$	1.19753	1	0	0	0	0	0	0	0
$i=2$	2.84836	4.85031	1.54167	0	−2.49486	−2.08333	0	0	0
	3.1588	4.71142	1.45833	0	− 2.29527	−1.91667	0	0	0
$i=3$	1.92718	17.1697	14.7131	2.65509	−15.7102	−23.418	−6.42361	5.19762	4.34028
	1.32698	14.7867	13.2036	2.34954	− 15.0028	− 20.4771	− 5.59028	4.39926	3.67361
$n=2$									
$i=0$	1	0	0	0	0	0	0	0	0
$i=1$	0.60679	1	0	0	0	0	0	0	0
$i=2$	2.17997	4.25957	1.54167	0	−1.26415	−2.08333	0	0	0
	2.42875	4.12068	1.45833	0	− 1.16301	−1.91667	0	0	0
$i=3$	1.30653	14.3435	13.8024	2.65509	−11.03	−20.9565	−6.42361	2.63364	4.34028
	1.7702	11.9808	12.3421	2.34954	− 10.7766	− 18.2126	− 5.59028	2.22911	3.67361
$n=3$									
$i=0$	1	0	0	0	0	0	0	0	0
$i=1$	0.31955	1	0	0	0	0	0	0	0
$i=2$	1.39208	3.97233	1.54167	0	−0.66573	−2.08333	0	0	0
	1.65593	3.83344	1.45833	0	− 0.612471	− 1.91667	0	0	0
$i=3$	0.458292	12.5064	13.3595	2.65509	−6.82554	−19.7597	−6.42361	1.38694	4.34028
	1.53408	10.1987	11.9232	2.34954	− 7.11997	− 17.1115	− 5.59028	1.1739	3.67361
$n=4$									
$i=0$	1	0	0	0	0	0	0	0	0
$i=1$	0.137464	1	0	0	0	0	0	0	0
$i=2$	0.747189	3.79024	1.54167	0	−0.286383	−2.08333	0	0	0
	1.0347	3.65135	1.45833	0	− 0.263473	− 1.91667	0	0	0
$i=3$	−0.850143	11.1964	13.0788	2.65509	−3.55432	−19.001	−6.42361	0.596632	4.34028
	0.744809	8.93759	11.6576	2.34954	− 4.29854	− 16.4135	− 5.59028	0.504989	3.67361

Table B.7: Numerical values of the coefficients for Eq. (2.4.7) for the vector current$n_f = 4\,(5)$ for the upper (lower) number. (Iterative linearized expansion).

	$[\tilde{C}_P]^{0,0}_{n,i}$	$[\tilde{C}_P]^{1,0}_{n,i}$	$[\tilde{C}_P]^{2,0}_{n,i}$	$[\tilde{C}_P]^{3,0}_{n,i}$	$[\tilde{C}_P]^{0,1}_{n,i}$	$[\tilde{C}_P]^{1,1}_{n,i}$	$[\tilde{C}_P]^{2,1}_{n,i}$	$[\tilde{C}_P]^{0,2}_{n,i}$	$[\tilde{C}_P]^{1,2}_{n,i}$
					$n = 1$				
$i = 0$	1	0	0	0	0	0	0	0	0
$i = 1$	1.93519	1	0	0	0	0	0	0	0
$i = 2$	8.78182	5.58796	1.54167	0	− 4.03164	− 2.08333	0	0	0
$i = 3$	9.22126	25.7977	15.8503	2.65509	− 42.7996	− 26.4915	− 6.42361	8.39924	4.34028
					$n = 2$				
$i = 0$	1	0	0	0	0	0	0	0	0
$i = 1$	0.99398	1	0	0	0	0	0	0	0
$i = 2$	5.42718	4.64676	1.54167	0	−2.07079	−2.08333	0	0	0
$i = 3$	11.733	19.005	14.3993	2.65509	−25.8023	−22.5698	−6.42361	4.31416	4.34028
					$n = 3$				
$i = 0$	1	0	0	0	0	0	0	0	0
$i = 1$	0.584683	1	0	0	0	0	0	0	0
$i = 2$	3.81501	4.23746	1.54167	0	− 1.21809	− 2.08333	0	0	0
$i = 3$	11.0126	15.8978	13.7683	2.65509	− 17.7717	− 20.8644	− 6.42361	2.53768	4.34028
					$n = 4$				
$i = 0$	1	0	0	0	0	0	0	0	0
$i = 1$	0.339493	1	0	0	0	0	0	0	0
$i = 2$	2.74147	3.99227	1.54167	0	− 0.707277	− 2.08333	0	0	0
$i = 3$	9.51996	13.9286	13.3903	2.65509	− 12.512	− 19.8428	− 6.42361	1.47349	4.34028

Table B.8: Numerical values of the coefficients for Eq. (2.4.7) for the pseudoscalar current with $n_f = 4$. (Iterative linearized expansion).

	$[R_V]^{0,0}_{n,i}$	$[R_V]^{1,0}_{n,i}$	$[R_V]^{2,0}_{n,i}$	$[R_V]^{3,0}_{n,i}$	$[R_V]^{0,1}_{n,i}$	$[R_V]^{1,1}_{n,i}$	$[R_V]^{2,1}_{n,i}$	$[R_V]^{0,2}_{n,i}$	$[R_V]^{1,2}_{n,i}$
					$n = 1$				
$i = 0$	0.428571	0	0	0	0	0	0	0	0
$i = 1$	0.0137566	0.857143	0	0	0	0	0	0	0
$i = 2$	1.56736	1.44418	1.75	0	− 0.0286596	− 1.78571	0	0	0
	1.72775	1.32513	1.67857	0	− 0.0263668	− 1.64286	0	0	0
$i = 3$	− 4.79526	2.66831	9.00161	3.59722	− 6.57481	− 8.76742	− 7.29167	0.0597075	3.72024
	− 3.53855	1.29072	7.81479	3.26389	− 6.65629	− 7.1511	− 6.43452	0.0505364	3.14881
					$n = 2$				
$i = 0$	0.592593	0	0	0	0	0	0	0	0
$i = 1$	− 0.302139	1.18519	0	0	0	0	0	0	0
$i = 2$	0.718416	1.35457	2.41975	0	0.629455	− 2.46914	0	0	0
	1.06685	1.18996	2.32099	0	0.579099	− 2.2716	0	0	0
$i = 3$	− 1.59081	− 1.60786	11.1353	4.97394	− 2.02404	− 9.44651	− 10.0823	− 1.31137	5.14403
	0.404636	− 3.06309	9.54776	4.51303	− 3.35942	− 7.42572	− 8.89712	− 1.10994	4.35391
					$n = 3$				
$i = 0$	0.681818	0	0	0	0	0	0	0	0
$i = 1$	− 0.557447	1.36364	0	0	0	0	0	0	0
$i = 2$	− 0.119176	1.13889	2.78409	0	1.16135	− 2.84091	0	0	0
	0.369655	0.949499	2.67045	0	1.06844	− 2.61364	0	0	0
$i = 3$	− 1.61506	− 5.30928	11.9551	5.72285	2.28504	− 9.12039	− 11.6004	− 2.41948	5.91856
	1.3858	− 6.67953	10.1636	5.19255	− 0.0698462	−6.9352	− 10.2367	− 2.04785	5.00947

Table B.9: Numerical values for the coefficients of the standard fixed-order expansion of the ratios of vector moments. We display results for the vector current with $n_f = 4, (5)$ for the upper (lower) number.

	$[R_P]^{0,0}_{n,i}$	$[R_P]^{1,0}_{n,i}$	$[R_P]^{2,0}_{n,i}$	$[R_P]^{3,0}_{n,i}$	$[R_P]^{0,1}_{n,i}$	$[R_P]^{1,1}_{n,i}$	$[R_P]^{2,1}_{n,i}$	$[R_P]^{0,2}_{n,i}$	$[R_P]^{1,2}_{n,i}$
					$n = 1$				
$i = 0$	0.571429	0	0	0	0	0	0	0	0
$i = 1$	0.0603175	1.14286	0	0	0	0	0	0	0
$i = 2$	3.262	2.00952	2.33333	0	− 0.125661	− 2.38095	0	0	0
$i = 3$	6.32118	6.21577	12.1735	4.7963	− 13.7852	− 12.0397	− 9.72222	0.261795	4.96032
					$n = 2$				
$i = 0$	0.666667	0	0	0	0	0	0	0	0
$i = 1$	− 0.311887	1.33333	0	0	0	0	0	0	0
$i = 2$	2.1179	1.57993	2.72222	0	0.649765	− 2.77778	0	0	0
$i = 3$	9.55945	1.01989	12.6416	5.59568	− 7.82395	− 10.8608	− 11.3426	− 1.35368	5.78704
					$n = 3$				
$i = 0$	0.727273	0	0	0	0	0	0	0	0
$i = 1$	− 0.57611	1.45455	0	0	0	0	0	0	0
$i = 2$	1.09403	1.25182	2.9697	0	1.20023	− 3.0303	0	0	0
$i = 3$	9.74702	− 3.08269	12.8277	6.10438	− 2.71009	− 9.88258	− 12.3737	− 2.50048	6.31313

Table B.10: Numerical values for the coefficients of the linearized expansion of the ratios of pseudoscalar moments with $n_f = 4$.

	$[\bar{R}_V]^{0,0}_{n,i}$	$[\bar{R}_V]^{1,0}_{n,i}$	$[\bar{R}_V]^{2,0}_{n,i}$	$[\bar{R}_V]^{3,0}_{n,i}$	$[\bar{R}_V]^{0,1}_{n,i}$	$[\bar{R}_V]^{1,1}_{n,i}$	$[\bar{R}_V]^{2,1}_{n,i}$	$[\bar{R}_V]^{0,2}_{n,i}$	$[\bar{R}_V]^{1,2}_{n,i}$
					$n = 1$				
$i = 0$	0.654654	0	0	0	0	0	0	0	0
$i = 1$	0.0105068	0.654654	0	0	0	0	0	0	0
$i = 2$	1.19701	1.0925	1.00926	0	− 0.0218891	− 1.36386	0	0	0
	1.31951	1.00158	0.954703	0	− 0.020138	− 1.25475	0	0	0
$i = 3$	− 3.68165	0.823415	5.76639	1.73817	− 5.02124	− 6.65245	− 4.20524	0.0456024	2.84138
	− 2.72379	− 0.349776	4.95174	1.53813	− 5.0835	− 5.42147	− 3.6597	0.0385979	2.40494
					$n = 2$				
$i = 0$	0.7698	0	0	0	0	0	0	0	0
$i = 1$	− 0.196245	0.7698	0	0	0	0	0	0	0
$i = 2$	0.441611	1.07606	1.18678	0	0.408843	− 1.60375	0	0	0
	0.667925	0.969147	1.12263	0	0.376136	− 1.47545	0	0	0
$i = 3$	− 0.92068	− 1.21163	6.45905	2.04389	− 1.21043	− 6.95338	− 4.9449	− 0.851757	3.34115
	0.433093	− 2.4104	5.5185	1.80867	− 2.08612	− 5.57542	− 4.3034	− 0.720927	2.82795
					$n = 3$				
$i = 0$	0.825723	0	0	0	0	0	0	0	0
$i = 1$	− 0.337551	0.825723	0	0	0	0	0	0	0
$i = 2$	− 0.141159	1.02719	1.27299	0	0.703232	− 1.72026	0	0	0
	0.154843	0.912501	1.20418	0	0.646973	− 1.58264	0	0	0
$i = 3$	− 1.03567	−2.65386	6.7324	2.19237	1.67114	− 6.92913	− 5.30412	− 1.46507	3.58387
	0.902443	−3.82647	5.73411	1.94007	0.222185	− 5.49342	− 4.61602	− 1.24003	3.03338

Table B.11: Numerical values for the coefficients of the linearized expansion of the ratios of vector moments. We display results for the vector current with $n_f = 4, (5)$ for the upper (lower) number.

	$[\bar{R}_P]^{0,0}_{n,i}$	$[\bar{R}_P]^{1,0}_{n,i}$	$[\bar{R}_P]^{2,0}_{n,i}$	$[\bar{R}_P]^{3,0}_{n,i}$	$[\bar{R}_P]^{0,1}_{n,i}$	$[\bar{R}_P]^{1,1}_{n,i}$	$[\bar{R}_P]^{2,1}_{n,i}$	$[\bar{R}_P]^{0,2}_{n,i}$	$[\bar{R}_P]^{1,2}_{n,i}$
$n=1$									
$i=0$	0.7559290	0	0	0	0	0	0	0	0
$i=1$	0.0398962	0.755929	0	0	0	0	0	0	0
$i=2$	2.15656	1.28928	1.16539	0	− 0.0831172	− 1.57485	0	0	0
$i=3$	4.06725	1.88674	6.70126	2.00706	− 9.11366	− 7.79727	− 4.85579	0.173161	3.28094
$n=2$									
$i=0$	0.816497	0	0	0	0	0	0	0	0
$i=1$	− 0.190991	0.816497	0	0	0	0	0	0	0
$i=2$	1.27461	1.1585	1.25877	0	0.397898	− 1.70103	0	0	0
$i=3$	6.15209	− 0.379067	6.87731	2.16787	− 4.6981	− 7.44666	− 5.24486	− 0.828954	3.54382
$n=3$									
$i=0$	0.852803	0	0	0	0	0	0	0	0
$i=1$	− 0.337775	0.852803	0	0	0	0	0	0	0
$i=2$	0.574538	1.07172	1.31474	0	0.703697	− 1.77667	0	0	0
$i=3$	5.94225	− 1.95744	6.96991	2.26427	− 1.31021	− 7.20157	− 5.47807	− 1.46604	3.7014

Table B.12: Numerical values for the coefficients of the linearized expansion of the ratios of pseudoscalar moments with $n_f = 4$.

	$[\tilde{R}_V]^{0,0}_{n,i}$	$[\tilde{R}_V]^{1,0}_{n,i}$	$[\tilde{R}_V]^{2,0}_{n,i}$	$[\tilde{R}_V]^{3,0}_{n,i}$	$[\tilde{R}_V]^{0,1}_{n,i}$	$[\tilde{R}_V]^{1,1}_{n,i}$	$[\tilde{R}_V]^{2,1}_{n,i}$	$[\tilde{R}_V]^{0,2}_{n,i}$	$[\tilde{R}_V]^{1,2}_{n,i}$
$n=1$									
$i=0$	1	0	0	0	0	0	0	0	0
$i=1$	0.0160494	1	0	0	0	0	0	0	0
$i=2$	1.86056 2.04768	3.66883 3.52994	1.54167 1.45833	0 0	− 0.0334362 − 0.0307613	− 2.08333 − 1.91667	0 0	0 0	0 0
$i=3$	− 1.85046 − 0.0174324	11.8662 9.52394	12.8916 11.4806	2.65509 2.34954	−7.80382 − 7.88822	−18.4951 − 15.9481	−6.42361 − 5.59028	0.0696588 0.0589592	4.34028 3.67361
$n=2$									
$i=0$	1	0	0	0	0	0	0	0	0
$i=1$	− 0.254929	1	0	0	0	0	0	0	0
$i=2$	0.0638103 0.357801	3.39785 3.25896	1.54167 1.45833	0 0	0.531103 0.488615	− 2.08333 − 1.91667	0 0	0 0	0 0
$i=3$	− 2.11686 0.322201	9.07965 6.88187	12.4739 11.0854	2.65509 2.34954	0.552022 − 0.755491	− 17.366 − 14.9093	− 6.42361 − 5.59028	− 1.10646 − 0.936512	4.34028 3.67361
$n=3$									
$i=0$	1	0	0	0	0	0	0	0	0
$i=1$	− 0.408795	1	0	0	0	0	0	0	0
$i=2$	− 0.988542 − 0.630066	3.24398 3.10509	1.54167 1.45833	0 0	0.851656 0.783523	− 2.08333 − 1.91667	0 0	0 0	0 0
$i=3$	− 5.11183 − 1.87845	7.46526 5.35334	12.2367 10.861	2.65509 2.34954	5.43048 3.40317	− 16.7249 − 14.3195	− 6.42361 − 5.59028	− 1.77428 − 1.50175	4.34028 3.67361

Table B.13: Numerical values for the coefficients of the iterative linearized expansion of the ratios of vector moments. We display results for the vector current with $n_f = 4, (5)$ for the upper (lower) number.

	$[\tilde{R}_P]^{0,0}_{n,i}$	$[\tilde{R}_P]^{1,0}_{n,i}$	$[\tilde{R}_P]^{2,0}_{n,i}$	$[\tilde{R}_P]^{3,0}_{n,i}$	$[\tilde{R}_P]^{0,1}_{n,i}$	$[\tilde{R}_P]^{1,1}_{n,i}$	$[\tilde{R}_P]^{2,1}_{n,i}$	$[\tilde{R}_P]^{0,2}_{n,i}$	$[\tilde{R}_P]^{1,2}_{n,i}$
					$n=1$				
$i=0$	1	0	0	0	0	0	0	0	0
$i=1$	0.0527778	1	0	0	0	0	0	0	0
$i=2$	2.95841	3.70556	1.54167	0	− 0.109954	− 2.08333	0	0	0
$i=3$	11.4629	13.0982	12.9483	2.65509	− 12.4961	− 18.6481	− 6.42361	0.22907	4.34028
					$n=2$				
$i=0$	1	0	0	0	0	0	0	0	0
$i=1$	− 0.233915	1	0	0	0	0	0	0	0
$i=2$	1.09324	3.41886	1.54167	0	0.487324	− 2.08333	0	0	0
$i=3$	8.77473	10.1858	12.5063	2.65509	− 3.80468	− 17.4536	− 6.42361	− 1.01526	4.34028
					$n=3$				
$i=0$	1	0	0	0	0	0	0	0	0
$i=1$	− 0.3960760	1	0	0	0	0	0	0	0
$i=2$	− 0.118446	3.2567	1.54167	0	0.825158	− 2.08333	0	0	0
$i=3$	4.92499	8.38182	12.2563	2.65509	1.76427	− 16.7779	− 6.42361	− 1.71908	4.34028

Table B.14: Numerical values for the coefficients of the iterative linearized expansion of the ratios of pseudoscalar moments with $n_f = 4$.

Appendix C

Evolution Factors and Anomalous Dimensions

The RG equations for various elements of the factorization theorems read [39]

$$\begin{aligned}
\mu\frac{\mathrm{d}}{\mathrm{d}\mu}U_{H_Q}^{(n_f)}(Q,\mu_H,\mu) &= \gamma_{H_Q}^{(n_f)}(Q,\mu)U_{H_Q}^{(n_f)}(Q,\mu_H,\mu)\,,\\
\mu\frac{\mathrm{d}}{\mathrm{d}\mu}U_{H_m}^{(n_f)}(Q,\frac{Q}{m},\mu) &= \gamma_{H_m}^{(n_f)}(Q/m,\mu)U_{H_m}^{(n_f)}(Q,\frac{Q}{m},\mu)\,,\\
\mu\frac{\mathrm{d}}{\mathrm{d}\mu}U_{F}^{(n_f)}(s,\mu,\mu_F) &= \int \mathrm{d}\,s\,\gamma_{F}^{(n_f)}(s-s',\mu)U_{F}^{(n_f)}(s',\mu,\mu_F)\,,
\end{aligned}\tag{C.1}$$

with $F=\{J,S,B\}$ where the J,S and B subscripts indicate whether the evolution factor corresponds to the jet, soft or bHEQT jet function, respectively. We indicated the number of active flavors with n_f. The functions U_{H_Q}, U_{H_m}, U_J, U_S and U_B are respectively the RG evolution factors for the hard function, bQHET current matching coefficient, SCET jet function, soft function and bHQET jet function and the terms γ_{H_Q}, γ_{H_m}, γ_J, γ_S and γ_B are the corresponding anomalous dimensions, respectively. The generic form of the anomalous dimension for different sectors is given by

$$\begin{aligned}
\gamma_{H_Q}^{(n_f)}(Q,\mu) &= \Gamma_{H_Q}^{(n_f)}[\alpha_s]\ln\left(\frac{\mu^2}{Q^2}\right)+\gamma_{H_Q}^{(n_f)}[\alpha_s]\,,\\
\gamma_{H_m}^{(n_f)}(Q/m,\mu) &= \Gamma_{H_m}^{(n_f)}[\alpha_s]\ln\left(\frac{m^2}{Q^2}\right)+\gamma_{H_m}^{(n_f)}[\alpha_s]\,,\\
\gamma_{F}^{(n_f)}(s-s',\mu) &= -\frac{2\Gamma_F^{(n_f)}[\alpha_s]}{j_F\mu^{j_F}}\ln\left[\frac{\mu^{j_F}\theta(s-s')}{s-s'}\right]_+ +\gamma_F^{(n_f)}[\alpha_s]\delta(s-s')\,,
\end{aligned}\tag{C.2}$$

where $j_S=1$, $j_J=2\,,j_B=1\,.$ The terms $\Gamma_{H_Q}[\alpha_s]\,,\ \Gamma_{H_m}[\alpha_s]$ and $\Gamma_F[\alpha_s]$ are given by a constant of proportionality times the QCD cusp anomalous dimension and the $\gamma[\alpha_s]$ are known as the non-cusp anomalous dimensions

$$\Gamma_X(\alpha_s)=\sum_{n=0}^{\infty}\Gamma_n^X\left(\frac{\alpha_s}{4\pi}\right)^{n+1},\qquad \gamma_X(\alpha_s)=\sum_{n=0}^{\infty}\gamma_n^X\left(\frac{\alpha_s}{4\pi}\right)^{n+1},$$

where we dropped the superscript (n_f) for convenience. In the rest of this presentation we use this notation so that the (n_f) dependence is implicit. It is conventional to present the anomalous dimensions for the hard $(\Gamma_i^{H_Q},\gamma_i^{H_Q})$, thrust jet function (Γ_i^J,γ_i^J) and thrust soft function (Γ_i^S,γ_i^S) in terms of the anomalous dimensions for the hard current matching $(\Gamma_i^{\tilde{C}},\gamma_i^{\tilde{C}})$, hemisphere jet function $(\Gamma_i^{J_n},\gamma_i^{J_{n,\bar{n}}})$ and hemisphere soft function $(\Gamma_i^{S_n},\gamma_i^{S_{n,\bar{n}}})$, respectively. The set of relations among these variables read

$$\begin{aligned}
\Gamma_i^{H_Q} &= 2\Gamma_i^{C}\,, \quad \gamma_i^{H_Q} = \gamma_i^{\tilde{C}} + \left(\gamma_i^{\tilde{C}}\right)^* = 2\gamma_i^{C}\,, \\
\Gamma_i^{J} &= 2\Gamma_i^{J_n}\,, \quad \gamma_i^{J} = \gamma_i^{J_n} + \gamma_i^{J_{\bar{n}}} = 2\gamma_i^{J_n}\,, \\
\Gamma_i^{S} &= 2\Gamma_i^{S_n}\,, \quad \gamma_i^{S} = \gamma_i^{S_n} + \gamma_i^{S_{\bar{n}}} = 2\gamma_i^{S_n}\,,
\end{aligned} \tag{C.3}$$

where $\gamma_i^C \equiv \mathrm{Re}\left[\gamma_i^{\tilde{C}}\right]$ and we have used the fact that $\gamma_i^{S_n} = \gamma_i^{S_{\bar{n}}}$ and $\gamma_i^{J_n} = \gamma_i^{J_{\bar{n}}}$. The cusp and non-cusp anomalous dimensions for the hard current matching are given by [224]

$$\begin{aligned}
\Gamma_n^C &= -\,\Gamma_n^{\text{cusp}}\,, \qquad \gamma_0^C = -6C_F, \\
\gamma_1^C &= C_F^2\Big(-3+4\pi^2-48\zeta_3\Big) + C_AC_F\Big(-\frac{961}{27}-\frac{11}{3}\pi^2+52\zeta_3\Big) + C_FT_{n_f}\Big(\frac{260}{27}+\frac{4}{3}\pi^2\Big), \\
\gamma_2^C &= C_F^3\Big(-29-6\pi^2-\frac{16}{5}\pi^4-136\zeta_3+\frac{32}{3}\pi^2\zeta_3+480\zeta_5\Big) \\
&\quad + C_F^2C_A\Big(-\frac{151}{2}+\frac{410}{9}\pi^2+\frac{494}{135}\pi^4-\frac{1688}{3}\zeta_3-\frac{16}{3}\pi^2\zeta_3-240\zeta_5\Big) \\
&\quad + C_FC_A^2\Big(-\frac{139345}{1458}-\frac{7163}{243}\pi^2-\frac{83}{45}\pi^4+\frac{7052}{9}\zeta_3-\frac{88}{9}\pi^2\zeta_3-272\zeta_5\Big) \\
&\quad + C_F^2T_{n_f}\Big(\frac{5906}{27}-\frac{52}{9}\pi^2-\frac{56}{27}\pi^4+\frac{1024}{9}\zeta_3\Big) \\
&\quad + C_AC_FT_{n_f}\Big(-\frac{34636}{729}+\frac{5188}{243}\pi^2+\frac{44}{45}\pi^4-\frac{3856}{27}\zeta_3\Big) + C_FT_{n_f}^2\Big(\frac{19336}{729}-\frac{80}{27}\pi^2-\frac{64}{27}\zeta_3\Big),
\end{aligned} \tag{C.4}$$

where Γ_n^{cusp} are the cusp anomalous dimension series coefficients [229],

$$\begin{aligned}
\Gamma_0^{\text{cusp}} &= 4C_F \qquad \Gamma_1^{\text{cusp}} = C_FC_A\Big(\frac{268}{9}-\frac{4}{3}\pi^2\Big) - \frac{80}{9}C_FT_{n_f}\Big), \\
\Gamma_2^{\text{cusp}} &= C_FC_A^2\Big(\frac{490}{3}-\frac{536}{27}\pi^2+\frac{44}{45}\pi^4+\frac{88}{3}\zeta_3\Big) + C_FC_AT_{n_f}\Big(-\frac{1672}{27}+\frac{160}{27}\pi^2-\frac{224}{3}\zeta_3\Big) \\
&\quad + C_F^2T_{n_f}\Big(-\frac{220}{3}+64\zeta_3\Big) - \frac{64}{27}C_FT_{n_f}^2\,, \\
\Gamma_3^{\text{cusp}} &= (1\pm 2)\frac{(\Gamma_2^{\text{cusp}})^2}{\Gamma_1^{\text{cusp}}}\,,
\end{aligned} \tag{C.5}$$

with $C_F = 4/3$, $C_A = 3$ and $T_{n_f} = n_f/2$. The unknown four-loop cusp anomalous dimension is determined by the Padè approximation, assigning 200% uncertainty. The cusp and non-cusp anomalous dimensions for the jet functions are given by [229, 246]

$$\begin{aligned}
\Gamma_n^{J_n} &= 2\,\Gamma_n^{\text{cusp}}\,, \qquad \gamma_0^{J_n} = 6C_F, \\
\gamma_1^{J_n} &= C_FT_{n_f}\Big(-\frac{484}{27}-\frac{8}{9}\pi^2\Big) + C_AC_F\Big(\frac{1769}{27}+\frac{22}{9}\pi^2-80\zeta_3\Big) + C_F^2\Big(3-4\pi^2+48\zeta_3\Big), \\
\gamma_2^{J_n} &= C_F^3\Big(29+6\pi^2+\frac{16}{5}\pi^4+136\zeta_3-\frac{32}{3}\pi^2\zeta_3-480\zeta_5\Big) \\
&\quad + C_F^2C_A\Big(\frac{151}{2}-\frac{510}{9}\pi^2-\frac{494}{135}\pi^4+\frac{1688}{3}\zeta_3+\frac{16}{3}\pi^2\zeta_3+240\zeta_5\Big) \\
&\quad + C_FC_A^2(\frac{412907}{1458}+\frac{838}{243}\pi^2+\frac{19}{5}\pi^4-\frac{1100}{9}\zeta_3+\frac{176}{9}\pi^2\zeta_3+464\zeta_5\Big) \\
&\quad + C_F^2T_{n_f}\Big(-\frac{9328}{27}+\frac{64}{9}\pi^2+\frac{328}{135}\pi^4-\frac{416}{9}\zeta_3\Big) + C_FT_{n_f}^2\Big(-\frac{27656}{729}+\frac{160}{81}\pi^2+\frac{512}{27}\zeta_3\Big) \\
&\quad + C_AC_FT_{n_f}\Big(\frac{10952}{729}-\frac{2360}{243}\pi^2-\frac{92}{45}\pi^4+\frac{5312}{27}\zeta_3\Big)\,.
\end{aligned} \tag{C.6}$$

The anomalous dimensions for the soft function can be derived from the consistency relations [39] for the factorization theorem,

$$\Gamma_i^{S_n} = -\,\Gamma_i^{\rm cusp}, \quad \gamma_i^{S_n} = -\,\gamma_i^{C} - \gamma_i^{J_n}. \tag{C.7}$$

Similarly we present the anomalous dimension of the bHQET matching coefficient ($\Gamma_i^{H_m}, \gamma_i^{H_m}$) and the bHQET thrust jet function ($\Gamma_i^{B}, \gamma_i^{B}$) in terms of the anomalous dimesnion for the bHQET current matching coefficient ($\Gamma_i^{\tilde{C}_m}, \gamma_i^{\tilde{C}_m}$) and the bHQET hemisphere jet function ($\Gamma_i^{B_n}, \gamma_i^{B_{n,\bar{n}}}$), given by

$$\begin{aligned}\Gamma_i^{H_m} &= 2\Gamma_i^{C_m}\,, \quad \gamma_i^{H_m} = \gamma_i^{\tilde{C}_m} + \left(\gamma_i^{\tilde{C}_m}\right)^* = 2\gamma_i^{C_m}\,,\\ \Gamma_i^{B} &= 2\Gamma_i^{B_n}\,, \quad \gamma_i^{B} = \gamma_i^{B_n} + \gamma_i^{B_{\bar{n}}} = 2\gamma_i^{B_n}\,,\end{aligned} \tag{C.8}$$

where $\gamma_i^{C_m} \equiv \mathrm{Re}\left[\gamma_i^{\tilde{C}_m}\right]$ and we use the fact that $\gamma_i^{B_n} = \gamma_i^{B_{\bar{n}}}$. The anomalous dimension for the bHQET hemisphere jet function is known up to two loops [39, 178],

$$\begin{aligned}\Gamma_i^{B_n} &= \Gamma_n^{\rm cusp},\\ \gamma_0^{B_n} &= 4C_F,\\ \gamma_1^{B_n} &= C_A C_F\left(\frac{1396}{27} - \frac{23}{9}\pi^2 - 20\zeta_3\right) + C_F T_{n_f}\left(\frac{4}{9}\pi^2 - \frac{464}{27}\right).\end{aligned} \tag{C.9}$$

The anomalous dimensions of the bHQET current matching coefficient, H_m, are known up to two loops [39, 178, 181]. One can also use the consistency relation for the bHQET factorization theorem to derive the H_m anomalous dimensions

$$\Gamma_i^{C_m} = -\,\Gamma_i^{\rm cusp}, \quad \gamma_i^{C_m} = -\,\gamma_i^{B_n} - \gamma_i^{S_n}\,. \tag{C.10}$$

The general solutions for the evolution factors in the SCET and bHQET factorization read [39]

$$\begin{aligned}U_{H_Q}(Q,\mu_0,\mu) &= e^{K_{H_Q}}\left(\frac{\mu_0^2}{Q^2}\right)^{\omega_{H_Q}},\\ U_{H_m}\Big(\frac{Q}{m},\mu_0,\mu\Big) &= e^{K_{H_m}}\left(\frac{m^2}{Q^2}\right)^{\omega_{H_m}},\\ U_F(t-t',\mu,\mu_0) &= \frac{e^{K_F}(e^{\gamma_E})^{\omega_F}}{\mu_0^{j_F}\,\Gamma(-\omega_F)}\Big[\frac{(\mu_0^{j_F})^{1+\omega_F}\theta(t-t')}{(t-t')^{1+\omega_F}}\Big]_+,\end{aligned} \tag{C.11}$$

where $\omega_F = \omega(\Gamma_F,\mu,\mu_0)$, $K_F = K_F(\Gamma_F,\gamma_F,\mu,\mu_0)$ are given by [155]

$$\begin{aligned}&\omega(\Gamma,\mu,\mu_0) = 2\int_{\alpha_s(\mu_0)}^{\alpha_s(\mu)}\frac{\mathrm{d}\,\alpha}{\beta(\alpha)}\,\Gamma(\alpha)\\ &= -\frac{\Gamma_0}{j_F\beta_0}\bigg\{\ln r + \frac{\alpha_s(\mu_0)}{4\pi}\Big(\frac{\Gamma_1}{\Gamma_0} - \frac{\beta_1}{\beta_0}\Big)(r-1) + \frac{1}{2}\frac{\alpha_s^2(\mu_0)}{(4\pi)^2}\Big(\frac{\beta_1^2}{\beta_0^2} - \frac{\beta_2}{\beta_0} + \frac{\Gamma_2}{\Gamma_0} - \frac{\Gamma_1\beta_1}{\Gamma_0\beta_0}\Big)(r^2-1)\\ &+ \frac{1}{3}\frac{\alpha_s^3(\mu_0)}{(4\pi)^3}\Big[\frac{\Gamma_3}{\Gamma_0} - \frac{\beta_3}{\beta_0} + \frac{\Gamma_1}{\Gamma_0}\Big(\frac{\beta_1^2}{\beta_0^2} - \frac{\beta_2}{\beta_0}\Big) - \frac{\beta_1}{\beta_0}\Big(\frac{\beta_1^2}{\beta_0^2} - 2\frac{\beta_2}{\beta_0} + \frac{\Gamma_2}{\Gamma_0}\Big)\Big](r^3-1)\bigg\},\end{aligned} \tag{C.12}$$

and

$$
\begin{aligned}
&K(\Gamma,\gamma,\mu,\mu_0)-\omega\Big(\frac{\gamma}{2},\mu,\mu_0\Big)=2\int_{\alpha_s(\mu_0)}^{\alpha_s(\mu)}\frac{\mathrm{d}\,\alpha}{\beta(\alpha)}\,\Gamma(\alpha)\int_{\alpha_s(\mu_0)}^{\alpha}\frac{\mathrm{d}\alpha'}{\beta(\alpha')}\\
&=\frac{\Gamma_0}{2\beta_0^2}\bigg\{\frac{4\pi}{\alpha_s(\mu_0)}\Big(\ln r+\frac{1}{r}-1\Big)+\Big(\frac{\Gamma_1}{\Gamma_0}-\frac{\beta_1}{\beta_0}\Big)(r-1-\ln r)-\frac{\beta_1}{2\beta_0}\ln^2 r\\
&+\frac{\alpha_s(\mu_0)}{4\pi}\bigg[\Big(\frac{\Gamma_1\beta_1}{\Gamma_0\beta_0}-\frac{\beta_1^2}{\beta_0^2}\Big)(r-1-r\ln r)-B_2\ln r+\Big(\frac{\Gamma_2}{\Gamma_0}-\frac{\Gamma_1\beta_1}{\Gamma_0\beta_0}+B_2\Big)\frac{(r^2-1)}{2}\\
&+\Big(\frac{\Gamma_2}{\Gamma_0}-\frac{\Gamma_1\beta_1}{\Gamma_0\beta_0}\Big)(1-r)\bigg]+\frac{\alpha_s^2(\mu_0)}{(4\pi)^2}\bigg[\Big[\Big(\frac{\Gamma_1}{\Gamma_0}-\frac{\beta_1}{\beta_0}\Big)B_2+\frac{B_3}{2}\Big]\frac{(r^2-1)}{2}\\
&+\Big(\frac{\Gamma_3}{\Gamma_0}-\frac{\Gamma_2\beta_1}{\Gamma_0\beta_0}+\frac{B_2\Gamma_1}{\Gamma_0}+B_3\Big)\Big(\frac{r^3-1}{3}-\frac{r^2-1}{2}\Big)\\
&-\frac{\beta_1}{2\beta_0}\Big(\frac{\Gamma_2}{\Gamma_0}-\frac{\Gamma_1\beta_1}{\Gamma_0\beta_0}+B_2\Big)\Big(r^2\ln r-\frac{r^2-1}{2}\Big)-\frac{B_3}{2}\ln r-B_2\Big(\frac{\Gamma_1}{\Gamma_0}-\frac{\beta_1}{\beta_0}\Big)(r-1)\bigg]\bigg\},
\end{aligned}
\tag{C.13}
$$

where $r=\alpha_s(\mu)/\alpha_s(\mu_0)$ depends on the 4-loop running couplings, and the coefficients are $B_2=\beta_1^2/\beta_0^2-\beta_2/\beta_0$ and $B_3=-\beta_1^3/\beta_0^3+2\beta_1\beta_2/\beta_0^2-\beta_3/\beta_0$. These results are expressed in terms of series expansion coefficients of the QCD β function $\beta[\alpha_s]$, given by

$$
\beta(\alpha_s)=-2\,\alpha_s\sum_{n=0}^{\infty}\beta_n\Big(\frac{\alpha_s}{4\pi}\Big)^{n+1},
\tag{C.14}
$$

where the β_n are given by

$$
\begin{aligned}
&\beta_0=11-\frac{2}{3}n_f\,,\qquad \beta_1=102-\frac{38}{3}n_f\,,\qquad \beta_2=\frac{2857}{2}-\frac{5033}{18}n_f+\frac{325}{54}n_f^2,\\
&\beta_3=\frac{149753}{6}+3564\zeta_3+\bigg(-\frac{1078361}{162}-\frac{6508}{27}\zeta_3\bigg)n_f+\bigg(\frac{50065}{162}+\frac{6472}{81}\zeta_3\bigg)n_f^2+\frac{1093}{729}n_f^3\,.
\end{aligned}
\tag{C.15}
$$

We remark that for the anomalous dimensions of the bHQET current matching coefficient the cusp angle is fixed at m^2/Q^2, therefore the K_F factor for U_{H_m} reads

$$
K_{H_m}(\Gamma_{H_m},\gamma_{H_m},\mu,\mu_0)=\omega\Big(\frac{\gamma_{H_m}}{2},\mu,\mu_0\Big)\,.
\tag{C.16}
$$

Appendix D

Threshold Region for Event Shapes

In this section we provide a generic method to specify the boundaries of the phase space of the threshold region for different event shape variables in the x_1–x_2 plane. Let us represent a 2-jet event shape variable with $e(x_1, x_2)$. The Taylor series expansion of $e(x_1, x_2)$ at $x_1 = x_2 = 1$ (i.e. the point of minimal gluon energy) at leading order reads

$$e(x_1, x_2) = e(1,1) + \frac{\partial e(x_1, 1)}{\partial x_1}\bigg|_{x_1=1}(x_1 - 1) + \frac{\partial e(1, x_2)}{\partial x_2}\bigg|_{x_2=1}(x_2 - 1) + \mathcal{O}\Big[(x_i - 1)^2\Big]\,, \qquad \text{(D.1)}$$

where the we have neglected higher order terms in the power series. We note that the threshold of a 2-jet event shape is defined as $e_{\min} \equiv e(1,1)$. Using the Taylor series in Eq. (D.1) one obtains the following equation for the threshold boundaries

$$\delta = e(x_1, x_2) - e_{\min} = \frac{\partial e(x_1, 1)}{\partial x_1}\bigg|_{x_1=1}(x_1 - 1) + \frac{\partial e(1, x_2)}{\partial x_2}\bigg|_{x_2=1}(x_2 - 1)\,, \qquad \text{(D.2)}$$

where $\delta \ll 1$. The resulting equation represents a simple straight line that is determined with the first derivative of the event shape variable with respect to x_1 and x_2 at the threshold region close to $x_1 = x_2 = 1$. Now by calculating the intersection of this line with the diagonal line in phase space $x_1 = x_2$, one can find the term $x_3^{\max}$ that enters the equation for the boundary of the soft gluon region given by $x_3 = 2 - (x_2 + x_1) = x_3^{\max}$. We obtain

$$x_3^{\max} = \delta\left(\frac{\partial e(x_1, 1)}{\partial x_1}\bigg|_{x_1=1} + \frac{\partial e(1, x_2)}{\partial x_2}\bigg|_{x_2=1}\right)^{-1}. \qquad \text{(D.3)}$$

Appendix E

Analytic Convolution of Distributions with Breit-Wigner

The procedure to obtain an analytic convolution of the soft function, jet function and corresponding evolution kernel distributions is to use the Fourier transformation. In Fourier space (referred to as configuration space as well) convolutions are transformed into simple products of various terms. The resulting expressions at the end can be transformed back into momentum space for the numerical analysis. After employing such transformations for the various convolutions in the factorization scenarios and transforming back to momentum space, before performing the convolution with the model function, the analytic expressions present the following generic structure,

$$\frac{\mathrm{d}}{\mathrm{d}\tilde{\omega}^n}\Big[\frac{1}{\ell}\Big(\frac{\mu\, e^{\gamma_E}}{\ell}\Big)^{\tilde{\omega}}\frac{1}{\Gamma(-\tilde{\omega})}\Big]\,, \tag{E.1}$$

where the parameters $\{\tilde{\omega}, \ell, \mu\}$ are determined from the exact factorization formulas in Eqs. (3.5.4 , 3.5.2 , 3.5.9) . We apply the convolution of the Breit-Wigner function with these structures,

$$\frac{\mathrm{d}}{\mathrm{d}\tilde{\omega}^n}\left[\frac{\big(\mu\, e^{\gamma_E}\big)^{\tilde{\omega}}}{\Gamma(-\tilde{\omega})}\int_{-\infty}^{\ell}\mathrm{d}\ell'\,(\ell-\ell')^{-\tilde{\omega}-1}\frac{\Gamma_q}{\pi\,(\ell'^2+\Gamma_q^2)}\right], \tag{E.2}$$

where $\Gamma_q = \frac{m\Gamma}{Q^2}$. This integration can be performed analytically. The final outcome reads

$$\frac{\mathrm{d}}{\mathrm{d}\tilde{\omega}^n}\left\{\frac{\big(\mu\, e^{\gamma_E}\big)^{\tilde{\omega}}}{\Gamma(-\tilde{\omega})}\Big(1+\frac{\ell^2}{\Gamma_q^2}\Big)^{\frac{-\tilde{\omega}-1}{2}}\Gamma(\tilde{\omega}+1)\sin\left[\frac{1+\tilde{\omega}}{2}\Big(\pi+2\arctan\big(\frac{\ell}{\Gamma_q}\big)\Big)\right]\right\}. \tag{E.3}$$

The analytic results can be expanded for the small width limit, $\Gamma_q \to 0$, to obtain the stable top cross section. We used this limit to cross check the direct integrations of plus distributions that are performed for the stable top analysis.

Appendix F

Series Coefficients of $\overline{\mathrm{MS}}$ Residual Mass Term

The $a_{nk}(n_h, n_l)$ coefficients of perturbative expansion of residual mass term in $\overline{\mathrm{MS}}$ mass scheme up to 4 loops read [62, 63],

$$
\begin{aligned}
a_{10} &= \frac{16}{3}\,, \qquad a_{11} = 8\,,\\
a_{20} &= \frac{3049}{18} + \frac{32}{9}\pi^2 + \frac{16}{9}\pi^2\ln 2 - \frac{8}{3}\zeta_3 + \Big(-\frac{71}{9} - \frac{8}{9}\pi^2\Big)n_l + \Big(-\frac{143}{9} + \frac{16}{9}\pi^2\Big)n_h\,,\\
a_{21} &= \frac{692}{3} - \frac{104}{9}(n_l + n_h)\,, \qquad a_{22} = 120 - \frac{16}{3}(n_l + n_h)\,,\\
a_{30} &= \frac{1145453}{162} + \frac{50758}{81}\pi^2 + \frac{7520}{27}\pi^2\ln 2 - \frac{682}{81}\pi^4 - \frac{448}{27}\pi^2\ln^2 2 - \frac{608}{27}\ln^4 2 - 72\zeta_3 - \frac{5324}{27}\pi^2\zeta_3\\
&\quad + \frac{13640}{27}\zeta_5 - \frac{4864}{9}\mathrm{Li}_4\Big(\frac{1}{2}\Big)\\
&\quad + n_l\bigg(\frac{488}{243}\pi^4 - \frac{162454}{243} - \frac{7720}{81}\pi^2 - \frac{704}{81}\pi^2\ln 2 + \frac{128}{81}\pi^2\ln^2 2 + \frac{64}{81}\ln^4 2 - \frac{5656}{27}\zeta_3 + \frac{512}{27}\mathrm{Li}_4\Big(\frac{1}{2}\Big)\bigg)\\
&\quad + n_h\bigg(-\frac{310846}{243} + \frac{109016}{243}\pi^2 - \frac{40960}{81}\pi^2\ln 2 + \frac{656}{243}\pi^4 - \frac{64}{81}\pi^2\ln^2 2 + \frac{64}{81}\ln^4 2 - \frac{6008}{27}\zeta_3 - 16\pi^2\zeta_3\\
&\quad + 80\zeta_5 + \frac{512}{27}\mathrm{Li}_4\Big(\frac{1}{2}\Big)\bigg) + n_l\,n_h\bigg(\frac{23668}{729} - \frac{208}{81}\pi^2 - \frac{128}{27}\zeta_3\bigg) + n_l^2\bigg(\frac{4708}{729} + \frac{208}{81}\pi^2 + \frac{224}{27}\zeta_3\bigg)\\
&\quad + n_h^2\bigg(\frac{18962}{729} - \frac{256}{405}\pi^2 - \frac{352}{27}\zeta_3\bigg)\,,\\
a_{31} &= \frac{91708}{9} + \frac{1664}{9}\pi^2 + \frac{832}{9}\pi^2\ln 2 - \frac{416}{3}\zeta_3 + n_l\bigg(-\frac{9512}{9} - \frac{1504}{27}\pi^2 - \frac{128}{27}\pi^2\ln 2 - \frac{896}{9}\zeta_3\bigg)\\
&\quad + n_h\bigg(-\frac{13256}{9} + \frac{2240}{27}\pi^2 - \frac{128}{27}\pi^2\ln 2 - \frac{896}{9}\zeta_3\bigg) + n_l\,n_h\bigg(\frac{4576}{81} - \frac{64}{27}\pi^2\bigg)\\
&\quad + n_h^2\bigg(\frac{3152}{81} - \frac{128}{27}\pi^2\bigg) + n_l^2\bigg(\frac{1424}{81} + \frac{64}{27}\pi^2\bigg)\,,\\
a_{32} &= 6392 - \frac{6160}{9}(n_l + n_h) + \frac{832}{27}n_h n_l + \frac{416}{27}(n_l^2 + n_h^2)\,,\\
a_{33} &= 2080 - \frac{1792}{9}(n_l + n_h) + \frac{256}{27}n_h n_l + \frac{128}{27}(n_l^2 + n_h^2)\,. \qquad \text{(F.1)}
\end{aligned}
$$

Appendix G

Jet Mass Scheme

The jet mass is a particular short distance scheme for boosted heavy quarks in jets and it is defined via the jet function in position space. We define the jet mass scheme using its relation to the pole mass,

$$m_{\rm pole} = m_J^{(n_l)}(R_m,\mu) + \delta m_J^{(n_l)}(R_m,\mu)\,, \tag{G.1}$$

where n_l denotes the number of massless active flavors. The residual mass term in the jet scheme $\delta m_J^{(n_l)}(R_m,\mu)$ is extracted directly from the bHQET jet function,

$$\delta m_J^{(n_l)}(R_m,\mu) = e^{\gamma_E}\frac{R_m}{2}\frac{\mathrm{d}}{\mathrm{d}\ln(iy)}\ln\tilde{B}(y,\mu)\big|_{iye^{\gamma_E}=1/R_m}\,, \tag{G.2}$$

such that it precisely cancels the renormalon ambiguity of the pole mass scheme to all orders in perturbation theory [178]. Here $\tilde{B}(y,\mu)$ is the bHQET jet function in position-space i.e. $\tilde{B}(x,\mu) = \int \mathrm{d}\hat{s}\, B(\hat{s},\Gamma,m,\mu)e^{-i\hat{s}x}$. The subscript J indicates that the mass parameter is in the jet mass scheme. Note that the definition of the residual mass term $\delta m_J^{(n_l)}(R_m,\mu)$ is in close analogy with the gap subtraction $\delta^{(n_l)}(R,\mu)$ in the R-gap scheme defined via position-space soft function, see Eq. (3.7.2). The resulting expression for the residual mass term has a perturbative series expansion of the following form

$$\delta m_J^{(n_l)}(R_m,\mu) = R_m\sum_{n=1}^{\infty}\sum_{k=0}^{n} a_{nk}^J\left[\frac{\alpha_s(\mu)}{4\pi}\right]^n \ln^k\left(\frac{\mu}{R_m}\right), \tag{G.3}$$

where the coefficients a_{nk}^J have been calculated up to two-loops in Ref. [178],

$$\begin{aligned}
a_{10}^J &= e^{\gamma_E}\frac{8}{3}\,, \quad a_{11}^J = e^{\gamma_E}\frac{16}{3}\,, \quad a_{20}^J = e^{\gamma_E}\Big(\frac{4376}{27} - \frac{8}{3}\pi^2 - 40\zeta_3 - \frac{752}{81}n_l\Big)\,,\\
a_{21}^J &= e^{\gamma_E}\Big(\frac{1600}{9} - \frac{16}{3}\pi^2 - \frac{256}{27}n_l\Big)\,, \quad a_{22}^J = e^{\gamma_E}\Big(\frac{176}{3} - \frac{32}{9}n_l\Big)\,.
\end{aligned} \tag{G.4}$$

The RGE flow in the two-dimensional $R_m - \mu$ plane is given by [245]

$$R_m\frac{\mathrm{d}}{\mathrm{d}R_m}m_J^{(n_l)}(R_m,R_m) = -R_m\frac{\mathrm{d}}{\mathrm{d}R_m}\delta m_J^{(n_l)}(R_m,R_m) = -R_m\sum_{n=0}^{\infty}\gamma_n^{R_m}\left(\frac{\alpha_s(R_m)}{4\pi}\right)^{n+1}, \tag{G.5}$$

$$\mu\frac{\mathrm{d}}{\mathrm{d}\mu}m_J^{(n_l)}(R_m,\mu) = -R_m\,e^{\gamma_E}\sum_{n=0}^{\infty}\Gamma_n^{\rm cusp}\left(\frac{\alpha_s(\mu)}{4\pi}\right)^{n+1}, \tag{G.6}$$

where the μ-anomalous dimension of the jet mass is completely determined by the cusp-anomalous dimension [178] , i.e. known up to three-loop order. Note that in Eq. (G.5) the R_m-evolution is carried out on the diagonal i.e. $R_m = \mu$, so that we do not encounter any large logarithms in the

R_m-anomalous dimensions. On the other hand the running of the mass on the diagonal ensures that the renormalon contributions are exactly canceled at all scales and we do not generate any further renormalon enhancement while the evolution of mass. The LO, NLO and NNLO terms of the R_m-anomalous dimension can be extracted from the following relations [178]

$$\gamma_0^{R_m} = a_{10}^J\,, \qquad \gamma_1^{R_m} = a_{20}^J - 2\,\beta_0\, a_{10}^J\,, \qquad \gamma_2^{R_m} = a_{30}^J - 4\,\beta_0\, a_{20}^J - 2\,\beta_1\, a_{10}^J\,, \tag{G.7}$$

where β_i are the coefficients of the QCD β-function given in Eq. (C.15).

In order to derive the matching relation between the jet mass and other short-distance mass schemes one can use the relation between the jet and pole mass schemes given in Eq. (G.1) and consider the fact that the pole mass scheme is a unique scheme defined via the partonic pole of green function, i.e. scale invariant and flavor independent. For instance to connect the $m_J(R_m,\mu)$ to the $\overline{m}(\mu)$, we first evolve the jet mass on the diagonal of $R_m - \mu$ plane to the scale $R_m = \mu = \overline{m}(\overline{m})$. At this scale we carry out the matching by eliminating the pole mass from Eqs. (G.1) and (3.9.4) . Following this procedure, we obtain the matching relation between the jet and $\overline{\text{MS}}$ masses at two-loop order,

$$\begin{aligned} m_J^{(n_l)}\big(R_m=\overline{m},\mu=\overline{m}\big) = \overline{m}\bigg\{1 + \bigg(\frac{\alpha_s^{(n_l+1)}(\overline{m})}{\pi}\bigg)\bigg[\frac{4}{3} - \frac{2}{3}e^{\gamma_E}\bigg] + \bigg(\frac{\alpha_s^{(n_l+1)}(\overline{m})}{\pi}\bigg)^2\bigg[\frac{307}{32} + \frac{\pi^2}{3} \\ + \frac{\pi^2}{9}\ln 2 - \frac{1}{6}\zeta_3 - \Big(\frac{\pi^2}{18} + \frac{71}{144}\Big)n_l + e^{\gamma_E}\Big(- \frac{547}{54} + \frac{47}{81}n_l + \frac{\pi^2}{6} + \frac{5}{2}\zeta_3\Big)\bigg]\bigg\}, \end{aligned} \tag{G.8}$$

where $\overline{m} = \overline{m}^{(n_l+1)}\big(\overline{m}^{(n_l+1)}\big)$.

Bibliography

[1] **LHC Higgs Cross Section Working Group** Collaboration, S. Heinemeyer *et al.*, "Handbook of LHC Higgs Cross Sections: 3. Higgs Properties," `arXiv:1307.1347 [hep-ph]`.

[2] A. A. Petrov, S. Pokorski, J. D. Wells, and Z. Zhang, "Role of low-energy observables in precision Higgs boson analyses," *Phys.Rev.* **D91** no. 7, (2015) 073001, `arXiv:1501.02803 [hep-ph]`.

[3] M. Antonelli *et al.*, "Flavor Physics in the Quark Sector," *Phys. Rept.* **494** (2010) 197–414, `arXiv:0907.5386 [hep-ph]`.

[4] M. A. Shifman, A. I. Vainshtein, and V. I. Zakharov, "QCD and Resonance Physics. Sum Rules," *Nucl. Phys.* **B147** (1979) 385–447.

[5] M. A. Shifman, A. I. Vainshtein, and V. I. Zakharov, "QCD and Resonance Physics: Applications," *Nucl. Phys.* **B147** (1979) 448–518.

[6] **HPQCD** Collaboration, I. Allison *et al.*, "High-Precision Charm-Quark Mass from Current-Current Correlators in Lattice and Continuum QCD," *Phys. Rev.* **D78** (2008) 054513, `arXiv:0805.2999 [hep-lat]`.

[7] R. Boughezal, M. Czakon, and T. Schutzmeier, "Charm and bottom quark masses from perturbative QCD," *Phys. Rev.* **D74** (2006) 074006, `arXiv:hep-ph/0605023`.

[8] J. H. Kuhn, M. Steinhauser, and C. Sturm, "Heavy quark masses from sum rules in four-loop approximation," *Nucl. Phys.* **B778** (2007) 192–215, `arXiv:hep-ph/0702103`.

[9] K. G. Chetyrkin *et al.*, "Charm and Bottom Quark Masses: an Update," *Phys. Rev.* **D80** (2009) 074010, `arXiv:0907.2110 [hep-ph]`.

[10] S. Bodenstein, J. Bordes, C. A. Dominguez, J. Penarrocha, and K. Schilcher, "Charm-quark mass from weighted finite energy QCD sum rules," *Phys. Rev.* **D82** (2010) 114013, `arXiv:1009.4325 [hep-ph]`.

[11] S. Narison, "Gluon condensates and c, b quark masses from quarkonia ratios of moments," *Phys. Lett.* **B693** (2010) 559–566, `arXiv:1004.5333 [hep-ph]`.

[12] S. Narison, "Gluon Condensates and $m_{c,b}$ from QCD-Moments and their ratios to Order α_s^3 and $\langle G^4 \rangle$," *Phys.Lett.* **B706** (2012) 412–422, `arXiv:1105.2922 [hep-ph]`.

[13] S. Bodenstein, J. Bordes, C. Dominguez, J. Penarrocha, and K. Schilcher, "QCD sum rule determination of the charm-quark mass," *Phys.Rev.* **D83** (2011) 074014, `arXiv:1102.3835 [hep-ph]`.

[14] C. McNeile, C. T. H. Davies, E. Follana, K. Hornbostel, and G. P. Lepage, "High-Precision c and b Masses, and QCD Coupling from Current-Current Correlators in Lattice and Continuum QCD," *Phys. Rev.* **D82** (2010) 034512, `arXiv:1004.4285 [hep-lat]`.

[15] B. Chakraborty, C. Davies, B. Galloway, P. Knecht, J. Koponen, *et al.*, "High-precision quark masses and QCD coupling from $n_f = 4$ lattice QCD," *Phys.Rev.* **D91** no. 5, (2015) 054508, `arXiv:1408.4169 [hep-lat]`.

[16] K. G. Chetyrkin, J. H. Kuhn, and C. Sturm, "Four-loop moments of the heavy quark vacuum polarization function in perturbative QCD," *Eur. Phys. J.* **C48** (2006) 107–110, `arXiv:hep-ph/0604234`.

[17] C. Sturm, "Moments of Heavy Quark Current Correlators at Four-Loop Order in Perturbative QCD," *JHEP* **0809** (2008) 075, `arXiv:0805.3358 [hep-ph]`.

[18] A. Maier, P. Maierhofer, and P. Marqaurd, "The second physical moment of the heavy quark vector correlator at $O(\alpha_s^3)$," *Phys. Lett.* **B669** (2008) 88–91, `arXiv:0806.3405 [hep-ph]`.

[19] A. Maier, P. Maierhofer, P. Marquard, and A. V. Smirnov, "Low energy moments of heavy quark current correlators at four loops," *Nucl. Phys.* **B824** (2010) 1–18, `arXiv:0907.2117 [hep-ph]`.

[20] A. H. Hoang, V. Mateu, and S. Mohammad Zebarjad, "Heavy Quark Vacuum Polarization Function at $O(\alpha_s^2)$ and $O(\alpha_s^3)$," *Nucl. Phys.* **B813** (2009) 349–369, `arXiv:0807.4173 [hep-ph]`.

[21] Y. Kiyo, A. Maier, P. Maierhofer, and P. Marquard, "Reconstruction of heavy quark current correlators at $O(\alpha_s^3)$," *Nucl. Phys.* **B823** (2009) 269–287, `arXiv:0907.2120 [hep-ph]`.

[22] D. Greynat and S. Peris, "Resummation of Threshold, Low- and High-Energy Expansions for Heavy-Quark Correlators," *Phys. Rev.* **D82** (2010) 034030, `arXiv:1006.0643 [hep-ph]`.

[23] D. Greynat, P. Masjuan, and S. Peris, "Analytic Reconstruction of heavy-quark two-point functions at $\mathcal{O}(\alpha_s^3)$," *Phys.Rev.* **D85** (2012) 054008, `arXiv:1104.3425 [hep-ph]`.

[24] J. H. Kuhn and M. Steinhauser, "Determination of α_s and heavy quark masses from recent measurements of $R(s)$," *Nucl. Phys.* **B619** (2001) 588–602, `arXiv:hep-ph/0109084`.

[25] **Tevatron Electroweak Working Group, CDF, D0** Collaboration, "A Combination of CDF and D0 Results on the Mass of the Top Quark," `arXiv:0803.1683 [hep-ex]`.

[26] **CDF, D0** Collaboration, T. Aaltonen *et al.*, "Combination of the top-quark mass measurements from the Tevatron collider," *Phys. Rev.* **D86** (2012) 092003, `arXiv:1207.1069 [hep-ex]`.

[27] **ATLAS** Collaboration, "Combination of ATLAS and CMS results on the mass of the top quark using up to 4.9 fb1 of data,".

[28] S. Adomeit, "Top-quark mass measurements: Alternative techniques (LHC + Tevatron)," in *7th International Workshop on Top Quark Physics (TOP2014) Cannes, France, September 28-October 3, 2014*. 2014. `arXiv:1411.7917 [hep-ex]`. `http://inspirehep.net/record/1331406/files/arXiv:1411.7917.pdf`.

[29] A. Juste, S. Mantry, A. Mitov, A. Penin, P. Skands, E. Varnes, M. Vos, and S. Wimpenny, "Determination of the top quark mass circa 2013: methods, subtleties, perspectives," *Eur. Phys. J.* **C74** (2014) 3119, `arXiv:1310.0799 [hep-ph]`.

[30] S. Moch *et al.*, "High precision fundamental constants at the TeV scale," `arXiv:1405.4781 [hep-ph]`.

[31] **ATLAS, CDF, CMS, D0** Collaboration, "First combination of Tevatron and LHC measurements of the top-quark mass," `arXiv:1403.4427 [hep-ex]`.

[32] S. Fleming, A. H. Hoang, S. Mantry, and I. W. Stewart, "Jets from massive unstable particles: Top-mass determination," *Phys. Rev.* **D77** (2008) 074010, `arXiv:hep-ph/0703207 [hep-ph]`.

[33] A. H. Hoang and I. W. Stewart, "Top Mass Measurements from Jets and the Tevatron Top-Quark Mass," *Nucl. Phys. Proc. Suppl.* **185** (2008) 220–226, `arXiv:0808.0222 [hep-ph]`.

[34] A. H. Hoang, "The Top Mass: Interpretation and Theoretical Uncertainties," in *7th International Workshop on Top Quark Physics (TOP2014) Cannes, France, September 28-October 3, 2014*. 2014. `arXiv:1412.3649 [hep-ph]`. `http://inspirehep.net/record/1333866/files/arXiv:1412.3649.pdf`.

[35] B. Colquhoun, R. Dowdall, C. Davies, K. Hornbostel, and G. Lepage, "Υ and Υ' Leptonic Widths, a_μ^b and m_b from full lattice QCD," *Phys.Rev.* **D91** no. 7, (2015) 074514, `arXiv:1408.5768 [hep-lat]`.

[36] C. W. Bauer, S. Fleming, D. Pirjol, and I. W. Stewart, "An Effective field theory for collinear and soft gluons: Heavy to light decays," *Phys. Rev.* **D63** (2001) 114020, `arXiv:hep-ph/0011336 [hep-ph]`.

[37] C. W. Bauer and I. W. Stewart, "Invariant operators in collinear effective theory," *Phys. Lett.* **B516** (2001) 134–142, `arXiv:hep-ph/0107001 [hep-ph]`.

[38] C. W. Bauer, D. Pirjol, and I. W. Stewart, "Soft collinear factorization in effective field theory," *Phys. Rev.* **D65** (2002) 054022, `arXiv:hep-ph/0109045 [hep-ph]`.

[39] S. Fleming, A. H. Hoang, S. Mantry, and I. W. Stewart, "Top Jets in the Peak Region: Factorization Analysis with NLL Resummation," *Phys. Rev.* **D77** (2008) 114003, `arXiv:0711.2079 [hep-ph]`.

[40] M. A. G. Aivazis, J. C. Collins, F. I. Olness, and W.-K. Tung, "Leptoproduction of heavy quarks. 2. A Unified QCD formulation of charged and neutral current processes from fixed target to collider energies," *Phys. Rev.* **D50** (1994) 3102–3118, `arXiv:hep-ph/9312319 [hep-ph]`.

[41] M. A. G. Aivazis, F. I. Olness, and W.-K. Tung, "Leptoproduction of heavy quarks. 1. General formalism and kinematics of charged current and neutral current production processes," *Phys. Rev.* **D50** (1994) 3085–3101, `arXiv:hep-ph/9312318 [hep-ph]`.

[42] S. Gritschacher, A. H. Hoang, I. Jemos, and P. Pietrulewicz, "Secondary Heavy Quark Production in Jets through Mass Modes," *Phys. Rev.* **D88** (2013) 034021, `arXiv:1302.4743 [hep-ph]`.

[43] P. Pietrulewicz, S. Gritschacher, A. H. Hoang, I. Jemos, and V. Mateu, "Variable Flavor Number Scheme for Final State Jets in Thrust," *Phys. Rev.* **D90** no. 11, (2014) 114001, `arXiv:1405.4860 [hep-ph]`.

[44] B. Dehnadi, A. H. Hoang, V. Mateu, and S. M. Zebarjad, "Charm Mass Determination from QCD Charmonium Sum Rules at Order α_s^3," *JHEP* **1309** (2013) 103, `arXiv:1102.2264 [hep-ph]`.

[45] B. Dehnadi, A. H. Hoang, and V. Mateu, "Bottom and Charm Mass Determinations with a Convergence Test," *JHEP* **08** (2015) 155, `arXiv:1504.07638 [hep-ph]`.

[46] V. Mateu, A. H. Hoang, B. Dehnadi, and S. M. Zebarjad, "Charm mass determination from QCD sum rules: A revision of the classical method," *Few Body Syst.* **50** (2011) 207–209.

[47] B. Dehnadi, A. H. Hoang, V. Mateu, and S. M. Zebarjad, "Charm mass determination from QCD sum rules at O(alpha**3(s))," *AIP Conf. Proc.* **1441** (2012) 628–630.

[48] B. Dehnadi, A. H. Hoang, and V. Mateu, "Charm and Bottom Masses from Sum Rules with a Convergence Test," `arXiv:1411.5597 [hep-ph]`.

[49] B. Dehnadi, A. H. Hoang, and V. Mateu, "New Charm and Bottom Quark Mass Determinations from QCD Sum Rules," in *Proceedings, 18th High-Energy Physics International Conference in Quantum Chromodynamics (QCD 15)*, vol. 270-272, pp. 113–117. 2016.

[50] A. Hoang, "Fully massive thrust distribution." `http://www.ph.tum.de/scet2014`, 2014. [Online; accessed 23-May-2014].

[51] B. Dehnadi, "Primary massive quark production in thrust distribution: theory vs MC." `https://indico.fnal.gov/conferenceDisplay.py?ovw=True&confId=9397`, 2016. [Online; accessed 27-March-2015].

[52] M. Preisser, "Effective field theory approach to massive event-shape distributions." `http://www.lupm.univ-montp2.fr/users/qcd/qcd15/Welcome.html`, 2015. [Online; accessed 02-July-2015].

[53] A. Hoang, "Interpretation of top quark mass measurements." `https://indico.cern.ch/event/301787/`, 2015. [Online; accessed 13-January-2014].

[54] A. Hoang, "The top mass and Monte Carlos." `http://indico.cern.ch/event/340357/`, 2015. [Online; accessed 13-January-2015].

[55] A. Hoang, "Top mass: interpretation and theoretical uncertainties." `https://indico.in2p3.fr/event/10114/`, 2015. [Online; accessed 03-October-2014].

[56] A. Hoang, "Subtleties in precise top quark mass determinations at the LHC and ILC." `http://www.icepp.s.u-tokyo.ac.jp/lcws13/`, 2013. [Online; accessed 15-November-2013].

[57] M. Preisser, "Top quark mass calibration for Pythia with thrust." `http://SCET2016.desy.de/`, 2016. [Online; accessed 21-March-2016].

[58] A. Hoang, "Precise measurement of the top mass at proton and electron colliders." `https://indico.in2p3.fr/event/12279/`, 2016. [Online; accessed 19-March-2016].

[59] I. Wolfram Research, *Mathematica Edition: Version 10.0*. Wolfram Research, Inc., Champaign, Illinois, 2014.

[60] *GFortran, Gnu compiler collection (gcc), Version 5.0.0*. Copyright (C) 2014 Free Software Foundation, Inc., 2014.

[61] M. Beneke, "Renormalons," *Phys. Rept.* **317** (1999) 1–142, `arXiv:hep-ph/9807443 [hep-ph]`.

[62] K. Melnikov and T. v. Ritbergen, "The Three loop relation between the MS-bar and the pole quark masses," *Phys. Lett.* **B482** (2000) 99–108, `arXiv:hep-ph/9912391 [hep-ph]`.

[63] K. G. Chetyrkin, J. H. Kuhn, and M. Steinhauser, "RunDec: A Mathematica package for running and decoupling of the strong coupling and quark masses," *Comput. Phys. Commun.* **133** (2000) 43–65, `arXiv:hep-ph/0004189 [hep-ph]`.

[64] **E142** Collaboration, P. L. Anthony *et al.*, "Determination of the neutron spin structure function.," *Phys. Rev. Lett.* **71** (1993) 959–962.

[65] **E143** Collaboration, K. Abe *et al.*, “Precision measurement of the proton spin structure function g1(p),” *Phys. Rev. Lett.* **74** (1995) 346–350.

[66] H. D. Politzer, “Reliable Perturbative Results for Strong Interactions?,” *Phys. Rev. Lett.* **30** (1973) 1346–1349.

[67] D. J. Gross and F. Wilczek, “Ultraviolet Behavior of Nonabelian Gauge Theories,” *Phys. Rev. Lett.* **30** (1973) 1343–1346.

[68] D. J. Gross and F. Wilczek, “Asymptotically Free Gauge Theories. 1,” *Phys. Rev.* **D8** (1973) 3633–3652.

[69] D. J. Gross and F. Wilczek, “Asymptotically Free Gauge Theories. 2.,” *Phys. Rev.* **D9** (1974) 980–993.

[70] H. Fritzsch, M. Gell-Mann, and H. Leutwyler, “Advantages of the Color Octet Gluon Picture,” *Phys. Lett.* **B47** (1973) 365–368.

[71] R. K. Ellis, W. J. Stirling, and B. R. Webber, “QCD and collider physics,” *Camb. Monogr. Part. Phys. Nucl. Phys. Cosmol.* **8** (1996) 1–435.

[72] M. E. Peskin and D. V. Schroeder, *An Introduction to quantum field theory.* 1995.

[73] S. Mandelstam, “Vortices and Quark Confinement in Nonabelian Gauge Theories,” *Phys. Rept.* **23** (1976) 245–249.

[74] G. ’t Hooft, “Topology of the Gauge Condition and New Confinement Phases in Nonabelian Gauge Theories,” *Nucl. Phys.* **B190** (1981) 455.

[75] T. Suzuki, “A Ginzburg-Landau Type Theory of Quark Confinement,” *Prog. Theor. Phys.* **80** (1988) 929.

[76] S. Maedan and T. Suzuki, “An Infrared Effective Theory of Quark Confinement Based on Monopole Condensation,” *Prog. Theor. Phys.* **81** (1989) 229–240.

[77] T. Suzuki, “Abelian Confinement Mechanism in QCD,” *Prog. Theor. Phys.* **81** (1989) 752.

[78] T. Suzuki and I. Yotsuyanagi, “A possible evidence for Abelian dominance in quark confinement,” *Phys. Rev.* **D42** (1990) 4257–4260.

[79] M. Czakon, “The Four-loop QCD beta-function and anomalous dimensions,” *Nucl. Phys.* **B710** (2005) 485–498, `arXiv:hep-ph/0411261 [hep-ph]`.

[80] T. van Ritbergen, J. A. M. Vermaseren, and S. A. Larin, “The four-loop beta function in quantum chromodynamics,” *Phys. Lett.* **B400** (1997) 379–384, `arXiv:hep-ph/9701390 [hep-ph]`.

[81] W. Zimmermann, “Normal products and the short distance expansion in the perturbation theory of renormalizable interactions,” *Annals Phys.* **77** (1973) 570–601. [Lect. Notes Phys.558,278(2000)].

[82] K. G. Wilson, “Nonlagrangian models of current algebra,” *Phys. Rev.* **179** (1969) 1499–1512.

[83] **Particle Data Group** Collaboration, K. Olive *et al.*, “Review of Particle Physics,” *Chin. Phys.* **C38** (2014) 090001.

[84] **Particle Data Group** Collaboration, W. M. Yao *et al.*, “Review of particle physics,” *J. Phys.* **G33** (2006) 1–1232.

[85] A. O. G. Kallen and A. Sabry, "Fourth order vacuum polarization," *Kong. Dan. Vid. Sel. Mat. Fys. Med.* **29N17** (1955) 1–20.

[86] K. Chetyrkin, J. H. Kuhn, and M. Steinhauser, "Heavy quark vacuum polarization to three loops," *Phys.Lett.* **B371** (1996) 93–98, `arXiv:hep-ph/9511430 [hep-ph]`.

[87] K. Chetyrkin, J. H. Kuhn, and M. Steinhauser, "Three loop polarization function and $\mathcal{O}(\alpha_s^2)$ corrections to the production of heavy quarks," *Nucl.Phys.* **B482** (1996) 213–240, `arXiv:hep-ph/9606230 [hep-ph]`.

[88] R. Boughezal, M. Czakon, and T. Schutzmeier, "Four-loop tadpoles: Applications in QCD," *Nucl. Phys. Proc. Suppl.* **160** (2006) 160–164, `arXiv:hep-ph/0607141`.

[89] M. Czakon and T. Schutzmeier, "Double fermionic contributions to the heavy-quark vacuum polarization," *JHEP* **0807** (2008) 001, `arXiv:0712.2762 [hep-ph]`.

[90] A. Maier, P. Maierhofer, and P. Marquard, "Higher Moments of Heavy Quark Correlators in the Low Energy Limit at $O(\alpha_s^2)$," *Nucl. Phys.* **B797** (2008) 218–242, `arXiv:0711.2636 [hep-ph]`.

[91] D. J. Broadhurst *et al.*, "Two loop gluon condensate contributions to heavy quark current correlators: Exact results and approximations," *Phys. Lett.* **B329** (1994) 103–110, `arXiv:hep-ph/9403274`.

[92] **BES** Collaboration, J. Z. Bai *et al.*, "Measurement of the Total Cross Section for Hadronic Production by e^+e^- Annihilation at Energies between 2.6-5 Gev," *Phys. Rev. Lett.* **84** (2000) 594–597, `arXiv:hep-ex/9908046`.

[93] **BES** Collaboration, J. Z. Bai *et al.*, "Measurements of the Cross Section for $e^+e^- \to$ hadrons at Center-of-Mass Energies from 2 to 5 GeV," *Phys. Rev. Lett.* **88** (2002) 101802, `arXiv:hep-ex/0102003`.

[94] **BES** Collaboration, M. Ablikim *et al.*, "Measurement of Cross Sections for $D^0\bar{D}^0$ and D^+D^- Production in e^+e^- Annihilation at $\sqrt{s} = 3.773$ GeV," *Phys. Lett.* **B603** (2004) 130–137, `arXiv:hep-ex/0411013`.

[95] **BES** Collaboration, M. Ablikim *et al.*, "Measurements of the cross sections for $e^+e^- \to$ hadrons at 3.650-GeV, 3.6648-GeV, 3.773-GeV and the branching fraction for $\psi(3770) \to$ non $D\ \bar{D}$," *Phys. Lett.* **B641** (2006) 145–155, `arXiv:hep-ex/0605105`.

[96] M. Ablikim *et al.*, "Measurements of the continuum R_{uds} and R values in e^+e^- annihilation in the energy region between 3.650-GeV and 3.872-GeV," *Phys. Rev. Lett.* **97** (2006) 262001, `arXiv:hep-ex/0612054`.

[97] **BES Bollaboration** Collaboration, M. Ablikim *et al.*, "R value measurements for e^+e^- annihilation at 2.60, 3.07 and 3.65 GeV," *Phys. Lett.* **B677** (2009) 239–245, `arXiv:0903.0900 [hep-ex]`.

[98] A. Osterheld *et al.*, "Measurements of total hadronic and inclusive D^* cross-sections in e^+e^- annihilations between 3.87-GeV and 4.5- GeV,". SLAC-PUB-4160.

[99] C. Edwards *et al.*, "Hadron production in e^+e^- annihilation from $s^{1/2} = 5$- GeV to 7.4-GeV,". SLAC-PUB-5160.

[100] **CLEO** Collaboration, R. Ammar *et al.*, "Measurement of the total cross section for $e^+e^- \to$ hadrons at $s^{1/2} = 10.52\,\mathrm{GeV}$," *Phys. Rev.* **D57** (1998) 1350–1358, `arXiv:hep-ex/9707018`.

[101] **CLEO** Collaboration, D. Besson *et al.*, "Observation of New Structure in the e^+e^- Annihilation Cross-Section Above B $\bar{\mathrm{B}}$ Threshold," *Phys. Rev. Lett.* **54** (1985) 381.

[102] **CLEO** Collaboration, D. Besson *et al.*, "Measurement of the Total Hadronic Cross Section in e^+e^- Annihilations below 10.56 GeV," *Phys. Rev.* **D76** (2007) 072008, `arXiv:0706.2813 [hep-ex]`.

[103] **CLEO** Collaboration, D. Cronin-Hennessy *et al.*, "Measurement of Charm Production Cross Sections in e^+e^- Annihilation at Energies between 3.97 and 4.26 GeV," *Phys. Rev.* **D80** (2009) 072001, `arXiv:0801.3418 [hep-ex]`.

[104] A. E. Blinov *et al.*, "The Measurement of R in e^+e^- annihilation at center-of- mass energies between 7.2-GeV and 10.34-GeV," *Z. Phys.* **C70** (1996) 31–38.

[105] L. Criegee and G. Knies, "Review of e^+e^- experiments with PLUTO from 3-GeV to 31-GeV," *Phys. Rept.* **83** (1982) 151.

[106] J. Siegrist *et al.*, "Observation of a Resonance at 4.4-GeV and Additional Structure Near 4.1-GeV in e^+e^- Annihilation," *Phys. Rev. Lett.* **36** (1976) 700.

[107] P. A. Rapidis *et al.*, "Observation of a Resonance in e^+e^- Annihilation Just Above Charm Threshold," *Phys. Rev. Lett.* **39** (1977) 526.

[108] G. S. Abrams *et al.*, "Measurement of the parameters of the $\psi''(3770)$ resonance," *Phys. Rev.* **D21** (1980) 2716.

[109] J. Siegrist *et al.*, "Hadron Production by e^+e^- Annihilation at Center-Of-Mass Energies Between 2.6-GeV and 7.8-GeV. Part 1. Total Cross-Section, Multiplicities and Inclusive Momentum Distributions," *Phys. Rev.* **D26** (1982) 969.

[110] J. Penarrocha and K. Schilcher, "QCD Duality and the Mass of the Charm Quark," *Phys. Lett.* **B515** (2001) 291–296, `arXiv:hep-ph/0105222`.

[111] G. D'Agostini, "On the use of the covariance matrix to fit correlated data," *Nucl. Instrum. Meth.* **A346** (1994) 306–311.

[112] T. Takeuchi, "The Status of the determination of $\alpha(m_Z)$ and $\alpha_s(m_Z)$," *Prog. Theor. Phys. Suppl.* **123** (1996) 247–264, `arXiv:hep-ph/9603415`.

[113] K. Hagiwara, A. D. Martin, D. Nomura, and T. Teubner, "Predictions for g-2 of the muon and $\alpha_{QED}(M_Z^2)$," *Phys. Rev.* **D69** (2004) 093003, `arXiv:hep-ph/0312250`.

[114] S. Bodenstein, J. Bordes, C. A. Dominguez, J. Penarrocha, and K. Schilcher, "Bottom-quark mass from finite energy QCD sum rules," *Phys. Rev.* **D85** (2012) 034003, `arXiv:hep-ph/1111.5742v2`.

[115] F. Le Diberder and A. Pich, "The perturbative QCD prediction to R_τ revisited," *Phys. Lett.* **B286** (1992) 147–152.

[116] A. A. Pivovarov, "Renormalization group analysis of the tau-lepton decay within QCD," *Z. Phys.* **C53** (1992) 461–464, `arXiv:hep-ph/0302003`.

[117] E. Braaten, S. Narison, and A. Pich, "QCD analysis of the tau hadronic width," *Nucl. Phys.* **B373** (1992) 581–612.

[118] S. Narison and A. Pich, "QCD Formulation of the tau Decay and Determination of Λ_{MS}," *Phys. Lett.* **B211** (1988) 183.

[119] E. Braaten, "The Perturbative QCD Corrections to the Ratio R for tau Decay," *Phys. Rev.* **D39** (1989) 1458.

[120] E. Braaten, "QCD Predictions for the Decay of the tau Lepton," *Phys. Rev. Lett.* **60** (1988) 1606–1609.

[121] A. H. Hoang and M. Jamin, "$\overline{\mathrm{MS}}$ Charm Mass from Charmonium Sum Rules with Contour Improvement," *Phys. Lett.* **B594** (2004) 127–134, `arXiv:hep-ph/0403083`.

[122] V. A. Novikov *et al.*, "Charmonium and Gluons: Basic Experimental Facts and Theoretical Introduction," *Phys. Rept.* **41** (1978) 1–133.

[123] P. A. Baikov, V. A. Ilyin, and V. A. Smirnov, "Gluon condensate fit from the two loop correction to the coefficient function," *Phys. Atom. Nucl.* **56** (1993) 1527–1530.

[124] K. Chetyrkin *et al.*, "Precise Charm- and Bottom-Quark Masses: Theoretical and Experimental Uncertainties," `arXiv:1010.6157 [hep-ph]`.

[125] S. Narison and R. Tarrach, "Higher dimension renormalization group invariant vacuum condensates in Quantum Chromodynamics," *Phys. Lett.* **B125** (1983) 217.

[126] B. L. Ioffe, "QCD at low energies," *Prog. Part. Nucl. Phys.* **56** (2006) 232–277, `arXiv:hep-ph/0502148`.

[127] O. V. Tarasov, A. A. Vladimirov, and A. Y. Zharkov, "The Gell-Mann-Low Function of QCD in the Three Loop Approximation," *Phys. Lett.* **B93** (1980) 429–432.

[128] S. A. Larin and J. A. M. Vermaseren, "The Three loop QCD Beta function and anomalous dimensions," *Phys. Lett.* **B303** (1993) 334–336, `arXiv:hep-ph/9302208`.

[129] K. G. Chetyrkin, "Quark mass anomalous dimension to $O(\alpha_s^4)$," *Phys. Lett.* **B404** (1997) 161–165, `arXiv:hep-ph/9703278`.

[130] J. A. M. Vermaseren, S. A. Larin, and T. van Ritbergen, "The 4-loop quark mass anomalous dimension and the invariant quark mass," *Phys. Lett.* **B405** (1997) 327–333, `arXiv:hep-ph/9703284`.

[131] *D. Nomura and T. Teubner, private communication.*

[132] K. Chetyrkin, A. Kataev, and F. Tkachov, "Higher Order Corrections to $\sigma_t(e^+e^- \to \mathrm{Hadrons})$ in Quantum Chromodynamics," *Phys.Lett.* **B85** (1979) 277.

[133] M. Dine and J. Sapirstein, "Higher Order QCD Corrections in e^+e^- Annihilation," *Phys.Rev.Lett.* **43** (1979) 668.

[134] W. Celmaster and R. J. Gonsalves, "An Analytic Calculation of Higher Order Quantum Chromodynamic Corrections in e^+e^- Annihilation," *Phys.Rev.Lett.* **44** (1980) 560.

[135] S. Gorishnii, A. Kataev, and S. Larin, "Next-To-Leading $O(\alpha_s^3)$ QCD Correction to $\sigma_t(e^+e^- \to \mathrm{Hadrons})$: Analytical Calculation and Estimation of the Parameter Lambda (MS)," *Phys.Lett.* **B212** (1988) 238–244.

[136] S. Gorishnii, A. Kataev, and S. Larin, "Correction $O(\alpha_s^3)$ to $\sigma_{\mathrm{tot}}(e^+e^- \to \mathrm{hadrons})$ in quantum chromodynamics," *JETP Lett.* **53** (1991) 127–131.

[137] W. Bernreuther and W. Wetzel, "Order α_s^2 Massive Quark Contribution to the Vacuum Polarization of Massless Quarks," *Z.Phys.* **C11** (1981) 113.

[138] S. Gorishnii, A. Kataev, and S. Larin, "Three Loop Corrections of Order $O(M^2)$ to the Correlator of Electromagnetic Quark Currents," *Nuovo Cim.* **A92** (1986) 119–131.

[139] K. Chetyrkin and A. Kwiatkowski, "Mass corrections to the tau decay rate," *Z.Phys.* **C59** (1993) 525–532, `arXiv:hep-ph/9805232 [hep-ph]`.

[140] K. Chetyrkin and J. H. Kuhn, "Quartic mass corrections to R_{had}," *Nucl.Phys.* **B432** (1994) 337–350, `arXiv:hep-ph/9406299 [hep-ph]`.

[141] K. Chetyrkin, R. Harlander, and J. H. Kuhn, "Quartic mass corrections to R_{had} at order α_s^3," *Nucl.Phys.* **B586** (2000) 56–72, `arXiv:hep-ph/0005139 [hep-ph]`.

[142] A. H. Hoang and T. Teubner, "Analytic calculation of two loop corrections to heavy quark pair production vertices induced by light quarks," *Nucl. Phys.* **B519** (1998) 285–328, `arXiv:hep-ph/9707496`.

[143] A. H. Hoang, M. Jezabek, J. H. Kuhn, and T. Teubner, "Radiation of heavy quarks," *Phys. Lett.* **B338** (1994) 330–335, `arXiv:hep-ph/9407338`.

[144] **Particle Data Group** Collaboration, K. Nakamura *et al.*, "Review of particle physics," *J. Phys.* **G37** (2010) 075021.

[145] **Particle Data Group** Collaboration, J. Beringer *et al.*, "Review of Particle Physics (RPP)," *Phys.Rev.* **D86** (2012) 010001.

[146] **BABAR Collaboration** Collaboration, B. Aubert *et al.*, "Measurement of the $e^+e^- \to b\bar{b}$ cross section between $\sqrt{s} = 10.54\,\mathrm{GeV}$ and $11.20\,\mathrm{GeV}$," *Phys.Rev.Lett.* **102** (2009) 012001, `arXiv:0809.4120 [hep-ex]`.

[147] **CLEO** Collaboration, J. Rosner *et al.*, "Di-electron widths of the Υ(1S,2S,3S) resonances," *Phys.Rev.Lett.* **96** (2006) 092003, `arXiv:hep-ex/0512056 [hep-ex]`.

[148] **CLEO** Collaboration, G. Huang *et al.*, "Measurement of $B(\Upsilon(5S) \to B_s^* \bar{B}_s^*)$ Using ϕ Mesons," *Phys.Rev.* **D75** (2007) 012002, `arXiv:hep-ex/0610035 [hep-ex]`.

[149] D. Lovelock, J. Horstkotte, C. Klopfenstein, J. Lee-Franzini, L. Romero, *et al.*, "Masses, Widths, and Leptonic Widths of the Higher Upsilon Resonances," *Phys.Rev.Lett.* **54** (1985) 377–380.

[150] S. Jadach and B. Ward, "Yfs2: The Second Order Monte Carlo for Fermion Pair Production at LEP / SLC With the Initial State Radiation of Two Hard and Multiple Soft Photons," *Comput.Phys.Commun.* **56** (1990) 351–384.

[151] K. Chetyrkin, J. H. Kuhn, and T. Teubner, "Extracting α_s from electron - positron annihilation around 10 GeV," *Phys.Rev.* **D56** (1997) 3011–3018, `arXiv:hep-ph/9609411 [hep-ph]`.

[152] **Tevatron Electroweak Working Group, CDF, DELPHI, SLD Electroweak and Heavy Flavour Groups, ALEPH, LEP Electroweak Working Group, SLD, OPAL, D0, L3** Collaboration, L. E. W. Group, "Precision Electroweak Measurements and Constraints on the Standard Model," `arXiv:1012.2367 [hep-ex]`.

[153] G. Corcella and A. Hoang, "Uncertainties in the $\overline{\mathrm{MS}}$ bottom quark mass from relativistic sum rules," *Phys.Lett.* **B554** (2003) 133–140, `arXiv:hep-ph/0212297 [hep-ph]`.

[154] M. Beneke, A. Maier, J. Piclum, and T. Rauh, "The bottom-quark mass from non-relativistic sum rules at NNNLO," *Nucl.Phys.* **B891** (2015) 42–72, `arXiv:1411.3132 [hep-ph]`.

[155] R. Abbate, M. Fickinger, A. H. Hoang, V. Mateu, and I. W. Stewart, "Thrust at N^{3}LL with Power Corrections and a Precision Global Fit for $\alpha_s(m_Z)$," *Phys. Rev.* **D83** (2011) 074021, `arXiv:1006.3080 [hep-ph]`.

[156] R. Abbate, M. Fickinger, A. H. Hoang, V. Mateu, and I. W. Stewart, "Precision Thrust Cumulant Moments at N^{3}LL," *Phys. Rev.* **D86** (2012) 094002, `arXiv:1204.5746 [hep-ph]`.

[157] T. Gehrmann, G. Luisoni, and P. F. Monni, "Power corrections in the dispersive model for a determination of the strong coupling constant from the thrust distribution," *Eur. Phys. J.* **C73** (2013) 2265, `arXiv:1210.6945 [hep-ph]`.

[158] A. H. Hoang, D. W. Kolodrubetz, V. Mateu, and I. W. Stewart, "Precise determination of α_s from the C-parameter distribution," *Phys. Rev.* **D91** no. 9, (2015) 094018, `arXiv:1501.04111 [hep-ph]`.

[159] S. Alekhin, J. Blumlein, and S. Moch, "Parton Distribution Functions and Benchmark Cross Sections at NNLO," *Phys. Rev.* **D86** (2012) 054009, `arXiv:1202.2281 [hep-ph]`.

[160] S. Bethke, A. H. Hoang, S. Kluth, J. Schieck, I. W. Stewart, *et al.*, "Workshop on Precision Measurements of α_s," `arXiv:1110.0016 [hep-ph]`.

[161] S. Bethke, "World Summary of α_s (2012)," *Nucl.Phys.Proc.Suppl.* **234** (2013) 229–234, `arXiv:1210.0325 [hep-ex]`.

[162] A. Pich, "Review of α_s determinations," *PoS* **ConfinementX** (2012) 022, `arXiv:1303.2262 [hep-ph]`.

[163] A. Hoang, P. Ruiz-Femenia, and M. Stahlhofen, "Renormalization Group Improved Bottom Mass from Upsilon Sum Rules at NNLL Order," *JHEP* **1210** (2012) 188, `arXiv:1209.0450 [hep-ph]`.

[164] A. Signer, "The Charm quark mass from non-relativistic sum rules," *Phys.Lett.* **B672** (2009) 333–338, `arXiv:0810.1152 [hep-ph]`.

[165] A. A. Penin and N. Zerf, "Bottom Quark Mass from Υ Sum Rules to $\mathcal{O}(\alpha_s^3)$," *JHEP* **1404** (2014) 120, `arXiv:1401.7035 [hep-ph]`.

[166] J. Erler and M.-x. Luo, "Precision determination of heavy quark masses and the strong coupling constant," *Phys.Lett.* **B558** (2003) 125–131, `arXiv:hep-ph/0207114 [hep-ph]`.

[167] J. Bordes, J. Penarrocha, and K. Schilcher, "Bottom quark mass and QCD duality," *Phys.Lett.* **B562** (2003) 81–86, `arXiv:hep-ph/0212083 [hep-ph]`.

[168] C. F. Berger, T. Kucs, and G. F. Sterman, "Event shape / energy flow correlations," *Phys. Rev.* **D68** (2003) 014012, `arXiv:hep-ph/0303051 [hep-ph]`.

[169] E. Farhi, "A QCD Test for Jets," *Phys. Rev. Lett.* **39** (1977) 1587–1588.

[170] S. Catani, G. Turnock, and B. R. Webber, "Jet broadening measures in e^+e^- annihilation," *Phys. Lett.* **B295** (1992) 269–276.

[171] T. Chandramohan and L. Clavelli, "Consequences of Second Order QCD for Jet Structure in e^+e^- Annihilation," *Nucl. Phys.* **B184** (1981) 365.

[172] R. K. Ellis, D. A. Ross, and A. E. Terrano, "The Perturbative Calculation of Jet Structure in $e^+ e^-$ Annihilation," *Nucl. Phys.* **B178** (1981) 421.

[173] M. Dasgupta and G. P. Salam, "Event shapes in $e^+ e^-$ annihilation and deep inelastic scattering," *J. Phys.* **G30** (2004) R143, `arXiv:hep-ph/0312283 [hep-ph]`.

[174] T. Becher and M. D. Schwartz, "A precise determination of α_s from LEP thrust data using effective field theory," *JHEP* **07** (2008) 034, `arXiv:0803.0342 [hep-ph]`.

[175] R. Kelley, M. D. Schwartz, R. M. Schabinger, and H. X. Zhu, "The two-loop hemisphere soft function," *Phys. Rev.* **D84** (2011) 045022, `arXiv:1105.3676 [hep-ph]`.

[176] A. Hornig, C. Lee, I. W. Stewart, J. R. Walsh, and S. Zuberi, "Non-global Structure of the $O(\alpha_s^2)$ Dijet Soft Function," *JHEP* **08** (2011) 054, `arXiv:1105.4628 [hep-ph]`.

[177] P. F. Monni, T. Gehrmann, and G. Luisoni, "Two-Loop Soft Corrections and Resummation of the Thrust Distribution in the Dijet Region," *JHEP* **08** (2011) 010, `arXiv:1105.4560 [hep-ph]`.

[178] A. Jain, I. Scimemi, and I. W. Stewart, "Two-loop Jet-Function and Jet-Mass for Top Quarks," *Phys. Rev.* **D77** (2008) 094008, `arXiv:0801.0743 [hep-ph]`.

[179] T. Matsuura and W. L. van Neerven, "Second Order Logarithmic Corrections to the Drell-Yan Cross-section," *Z. Phys.* **C38** (1988) 623.

[180] T. Matsuura, S. C. van der Marck, and W. L. van Neerven, "The Calculation of the Second Order Soft and Virtual Contributions to the Drell-Yan Cross-Section," *Nucl. Phys.* **B319** (1989) 570.

[181] A. H. Hoang, A. Pathak, P. Pietrulewicz, and I. W. Stewart, "Hard Matching for Boosted Tops at Two Loops," *JHEP* **12** (2015) 059, `arXiv:1508.04137 [hep-ph]`.

[182] S. Weinzierl, "NNLO corrections to 3-jet observables in electron-positron annihilation," *Phys. Rev. Lett.* **101** (2008) 162001, `arXiv:0807.3241 [hep-ph]`.

[183] S. Weinzierl, "Event shapes and jet rates in electron-positron annihilation at NNLO," *JHEP* **06** (2009) 041, `arXiv:0904.1077 [hep-ph]`.

[184] A. Gehrmann-De Ridder, T. Gehrmann, E. W. N. Glover, and G. Heinrich, "Second-order QCD corrections to the thrust distribution," *Phys. Rev. Lett.* **99** (2007) 132002, `arXiv:0707.1285 [hep-ph]`.

[185] A. Gehrmann-De Ridder, T. Gehrmann, E. W. N. Glover, and G. Heinrich, "NNLO corrections to event shapes in $e^+ e^-$ annihilation," *JHEP* **12** (2007) 094, `arXiv:0711.4711 [hep-ph]`.

[186] Y. L. Dokshitzer, D. Diakonov, and S. I. Troian, "Hard Processes in Quantum Chromodynamics," *Phys. Rept.* **58** (1980) 269–395.

[187] S. Catani, L. Trentadue, G. Turnock, and B. R. Webber, "Resummation of large logarithms in $e^+ e^-$ event shape distributions," *Nucl. Phys.* **B407** (1993) 3–42.

[188] J. C. Collins and D. E. Soper, "Back-To-Back Jets in QCD," *Nucl. Phys.* **B193** (1981) 381. [Erratum: Nucl. Phys.B213,545(1983)].

[189] J. C. Collins, D. E. Soper, and G. F. Sterman, "Transverse Momentum Distribution in Drell-Yan Pair and W and Z Boson Production," *Nucl. Phys.* **B250** (1985) 199.

[190] J. C. Collins and D. E. Soper, "Back-To-Back Jets: Fourier Transform from B to K-Transverse," *Nucl. Phys.* **B197** (1982) 446.

[191] G. Parisi and R. Petronzio, "Small Transverse Momentum Distributions in Hard Processes," *Nucl. Phys.* **B154** (1979) 427.

[192] J. Kodaira and L. Trentadue, "Summing Soft Emission in QCD," *Phys. Lett.* **B112** (1982) 66.

[193] C. W. Bauer, S. P. Fleming, C. Lee, and G. F. Sterman, "Factorization of $e^+ e^-$ Event Shape Distributions with Hadronic Final States in Soft Collinear Effective Theory," *Phys. Rev.* **D78** (2008) 034027, `arXiv:0801.4569 [hep-ph]`.

[194] J.-Y. Chiu, A. Jain, D. Neill, and I. Z. Rothstein, "A Formalism for the Systematic Treatment of Rapidity Logarithms in Quantum Field Theory," *JHEP* **05** (2012) 084, `arXiv:1202.0814 [hep-ph]`.

[195] J.-y. Chiu, A. Jain, D. Neill, and I. Z. Rothstein, "The Rapidity Renormalization Group," *Phys. Rev. Lett.* **108** (2012) 151601, `arXiv:1104.0881 [hep-ph]`.

[196] Y.-T. Chien and M. D. Schwartz, "Resummation of heavy jet mass and comparison to LEP data," *JHEP* **08** (2010) 058, `arXiv:1005.1644 [hep-ph]`.

[197] T. Becher and G. Bell, "NNLL Resummation for Jet Broadening," *JHEP* **11** (2012) 126, `arXiv:1210.0580 [hep-ph]`.

[198] A. H. Hoang and I. W. Stewart, "Designing gapped soft functions for jet production," *Phys. Lett.* **B660** (2008) 483–493, `arXiv:0709.3519 [hep-ph]`.

[199] G. P. Salam and D. Wicke, "Hadron masses and power corrections to event shapes," *JHEP* **05** (2001) 061, `arXiv:hep-ph/0102343 [hep-ph]`.

[200] C. Lee and G. F. Sterman, "Momentum Flow Correlations from Event Shapes: Factorized Soft Gluons and Soft-Collinear Effective Theory," *Phys. Rev.* **D75** (2007) 014022, `arXiv:hep-ph/0611061 [hep-ph]`.

[201] V. Mateu, I. W. Stewart, and J. Thaler, "Power Corrections to Event Shapes with Mass-Dependent Operators," *Phys. Rev.* **D87** no. 1, (2013) 014025, `arXiv:1209.3781 [hep-ph]`.

[202] I. W. Stewart, F. J. Tackmann, and W. J. Waalewijn, "N-Jettiness: An Inclusive Event Shape to Veto Jets," *Phys. Rev. Lett.* **105** (2010) 092002, `arXiv:1004.2489 [hep-ph]`.

[203] G. T. Bodwin, E. Braaten, and G. P. Lepage, "Rigorous QCD analysis of inclusive annihilation and production of heavy quarkonium," *Phys. Rev.* **D51** (1995) 1125–1171, `arXiv:hep-ph/9407339 [hep-ph]`. [Erratum: Phys. Rev.D55,5853(1997)].

[204] W. E. Caswell and G. P. Lepage, "Effective Lagrangians for Bound State Problems in QED, QCD, and Other Field Theories," *Phys. Lett.* **B167** (1986) 437.

[205] N. Brambilla, A. Pineda, J. Soto, and A. Vairo, "Effective field theories for heavy quarkonium," *Rev. Mod. Phys.* **77** (2005) 1423, `arXiv:hep-ph/0410047 [hep-ph]`.

[206] S. Weinberg, "Dynamical approach to current algebra," *Phys. Rev. Lett.* **18** (1967) 188–191.

[207] S. Weinberg, "Nonlinear realizations of chiral symmetry," *Phys. Rev.* **166** (1968) 1568–1577.

[208] S. R. Coleman, J. Wess, and B. Zumino, "Structure of phenomenological Lagrangians. 1.," *Phys. Rev.* **177** (1969) 2239–2247.

[209] C. G. Callan, Jr., S. R. Coleman, J. Wess, and B. Zumino, "Structure of phenomenological Lagrangians. 2.," *Phys. Rev.* **177** (1969) 2247–2250.

[210] R. F. Dashen, “Chiral SU(3) x SU(3) as a symmetry of the strong interactions,” *Phys. Rev.* **183** (1969) 1245–1260.

[211] L.-F. Li and H. Pagels, “Perturbation theory about a Goldstone symmetry,” *Phys. Rev. Lett.* **26** (1971) 1204–1206.

[212] H. Pagels, “Departures from Chiral Symmetry: A Review,” *Phys. Rept.* **16** (1975) 219.

[213] H. Leutwyler, “On the foundations of chiral perturbation theory,” *Annals Phys.* **235** (1994) 165–203, `arXiv:hep-ph/9311274 [hep-ph]`.

[214] H. Georgi, “An Effective Field Theory for Heavy Quarks at Low-energies,” *Phys. Lett.* **B240** (1990) 447–450.

[215] E. Eichten and B. R. Hill, “An Effective Field Theory for the Calculation of Matrix Elements Involving Heavy Quarks,” *Phys. Lett.* **B234** (1990) 511.

[216] B. Grinstein, “The Static Quark Effective Theory,” *Nucl. Phys.* **B339** (1990) 253–268.

[217] T. Mannel, W. Roberts, and Z. Ryzak, “A Derivation of the heavy quark effective Lagrangian from QCD,” *Nucl. Phys.* **B368** (1992) 204–220.

[218] A. V. Manohar and M. B. Wise, “Heavy quark physics,” *Camb. Monogr. Part. Phys. Nucl. Phys. Cosmol.* **10** (2000) 1–191.

[219] T. Becher, A. Broggio, and A. Ferroglia, “Introduction to Soft-Collinear Effective Theory,” `arXiv:1410.1892 [hep-ph]`.

[220] M. D. Schwartz, “Resummation and NLO matching of event shapes with effective field theory,” *Phys. Rev.* **D77** (2008) 014026, `arXiv:0709.2709 [hep-ph]`.

[221] J. C. Collins, F. Wilczek, and A. Zee, “Low-Energy Manifestations of Heavy Particles: Application to the Neutral Current,” *Phys. Rev.* **D18** (1978) 242.

[222] P. A. Baikov, K. G. Chetyrkin, A. V. Smirnov, V. A. Smirnov, and M. Steinhauser, “Quark and gluon form factors to three loops,” *Phys. Rev. Lett.* **102** (2009) 212002, `arXiv:0902.3519 [hep-ph]`.

[223] T. Gehrmann, T. Huber, and D. Maitre, “Two-loop quark and gluon form-factors in dimensional regularisation,” *Phys. Lett.* **B622** (2005) 295–302, `arXiv:hep-ph/0507061 [hep-ph]`.

[224] S. Moch, J. A. M. Vermaseren, and A. Vogt, “The Quark form-factor at higher orders,” *JHEP* **08** (2005) 049, `arXiv:hep-ph/0507039 [hep-ph]`.

[225] R. N. Lee, A. V. Smirnov, and V. A. Smirnov, “Analytic Results for Massless Three-Loop Form Factors,” *JHEP* **04** (2010) 020, `arXiv:1001.2887 [hep-ph]`.

[226] E. Lunghi, D. Pirjol, and D. Wyler, “Factorization in leptonic radiative $B \to \gamma\, e\, \nu$ decays,” *Nucl. Phys.* **B649** (2003) 349–364, `arXiv:hep-ph/0210091 [hep-ph]`.

[227] C. W. Bauer and A. V. Manohar, “Shape function effects in $B \to X_s\, \gamma$ and $B \to X_u\, l\, \bar{\nu}$ decays,” *Phys. Rev.* **D70** (2004) 034024, `arXiv:hep-ph/0312109 [hep-ph]`.

[228] T. Becher and M. Neubert, “Toward a NNLO calculation of the $\bar{B} \to X_s\, \gamma$ decay rate with a cut on photon energy. II. Two-loop result for the jet function,” *Phys. Lett.* **B637** (2006) 251–259, `arXiv:hep-ph/0603140 [hep-ph]`.

[229] S. Moch, J. A. M. Vermaseren, and A. Vogt, "The Three loop splitting functions in QCD: The Nonsinglet case," *Nucl. Phys.* **B688** (2004) 101–134, `arXiv:hep-ph/0403192 [hep-ph]`.

[230] Z. Ligeti, I. W. Stewart, and F. J. Tackmann, "Treating the b quark distribution function with reliable uncertainties," *Phys. Rev.* **D78** (2008) 114014, `arXiv:0807.1926 [hep-ph]`.

[231] A. H. Hoang, A. Jain, I. Scimemi, and I. W. Stewart, "R-evolution: Improving perturbative QCD," *Phys. Rev.* **D82** (2010) 011501, `arXiv:0908.3189 [hep-ph]`.

[232] A. H. Hoang and S. Kluth, "Hemisphere Soft Function at $\mathcal{O}(\alpha_s^2)$ for Dijet Production in $e^+ e^-$ Annihilation," `arXiv:0806.3852 [hep-ph]`.

[233] S. Gritschacher, A. Hoang, I. Jemos, and P. Pietrulewicz, "Two loop soft function for secondary massive quarks," *Phys. Rev.* **D89** no. 1, (2014) 014035, `arXiv:1309.6251 [hep-ph]`.

[234] A. K. Leibovich, Z. Ligeti, and M. B. Wise, "Comment on quark masses in SCET," *Phys. Lett.* **B564** (2003) 231–234, `arXiv:hep-ph/0303099 [hep-ph]`.

[235] K. G. Chetyrkin, J. H. Kuhn, and A. Kwiatkowski, "QCD corrections to the e^+e^- cross-section and the Z boson decay rate: Concepts and results," *Phys. Rept.* **277** (1996) 189–281.

[236] H. P. Nilles, "Isolating Gloun Jets," *Phys. Rev. Lett.* **45** (1980) 319.

[237] B. L. Ioffe, "Associated Production of Gluonic Jets and Heavy Mesons in $e^+ e^-$ Annihilation," *Phys. Lett.* **B78** (1978) 277.

[238] H. Yamamoto, "An Efficient Algorithm for Calculating Thrust in High Multiplicity Reactions," *J. Comput. Phys.* **52** (1983) 597–601.

[239] B. W. Harris and J. F. Owens, "The Two cutoff phase space slicing method," *Phys. Rev.* **D65** (2002) 094032, `arXiv:hep-ph/0102128 [hep-ph]`.

[240] G. Grammer, Jr. and D. R. Yennie, "Improved treatment for the infrared divergence problem in quantum electrodynamics," *Phys. Rev.* **D8** (1973) 4332–4344.

[241] A. Bassetto, M. Ciafaloni, and G. Marchesini, "Jet Structure and Infrared Sensitive Quantities in Perturbative QCD," *Phys. Rept.* **100** (1983) 201–272.

[242] F. Fiorani, G. Marchesini, and L. Reina, "Soft Gluon Factorization and Multi - Gluon Amplitude," *Nucl. Phys.* **B309** (1988) 439.

[243] S. Catani and M. Grazzini, "The soft gluon current at one loop order," *Nucl. Phys.* **B591** (2000) 435–454, `arXiv:hep-ph/0007142 [hep-ph]`.

[244] M. Beneke, A. P. Chapovsky, M. Diehl, and T. Feldmann, "Soft collinear effective theory and heavy to light currents beyond leading power," *Nucl. Phys.* **B643** (2002) 431–476, `arXiv:hep-ph/0206152 [hep-ph]`.

[245] A. H. Hoang, A. Jain, I. Scimemi, and I. W. Stewart, "Infrared Renormalization Group Flow for Heavy Quark Masses," *Phys. Rev. Lett.* **101** (2008) 151602, `arXiv:0803.4214 [hep-ph]`.

[246] T. Becher, M. Neubert, and B. D. Pecjak, "Factorization and Momentum-Space Resummation in Deep-Inelastic Scattering," *JHEP* **01** (2007) 076, `arXiv:hep-ph/0607228 [hep-ph]`.